

REPORT DOCUMENTATION PAGE			Form Approved OMB No. 0704-0188	
Public reporting burden for this collection of information is estimated to average 1 hour per response, including the time for reviewing instructions, searching existing data sources, gathering and maintaining the data needed, and completing and reviewing the collection of information. Send comments regarding this burden estimate or any other aspect of this collection of information, including suggestions for reducing this burden, to Washington Headquarters Services, Directorate for Information Operations and Reports, 1215 Jefferson Davis Highway, Suite 1204, Arlington, VA 22202-4302, and to the Office of Management and Budget, Paperwork Reduction Project (0704-0188), Washington, DC 20503.				
1. AGENCY USE ONLY (Leave blank)		2. REPORT DATE 14.Jan.03	3. REPORT TYPE AND DATES COVERED DISSERTATION	
4. TITLE AND SUBTITLE LOCALIZED FLOW CONTROL WITH ENERGY DEPOSITION			5. FUNDING NUMBERS	
6. AUTHOR(S) MAJ ADELGREN RUSSELL G				
7. PERFORMING ORGANIZATION NAME(S) AND ADDRESS(ES) RUTGERS UNIVERSITY NEW BRUNSWICK			8. PERFORMING ORGANIZATION REPORT NUMBER CI02-798	
9. SPONSORING/MONITORING AGENCY NAME(S) AND ADDRESS(ES) THE DEPARTMENT OF THE AIR FORCE AFIT/CIA, BLDG 125 2950 P STREET WPAFB OH 45433			10. SPONSORING/MONITORING AGENCY REPORT NUMBER	
11. SUPPLEMENTARY NOTES				
12a. DISTRIBUTION AVAILABILITY STATEMENT Unlimited distribution In Accordance With AFI 35-205/AFIT Sup 1			12b. DISTRIBUTION CODE	
13. ABSTRACT (Maximum 200 words)				
<div style="display: flex; justify-content: space-between; align-items: center;"> <div style="text-align: center;"> DISTRIBUTION STATEMENT A Approved for Public Release Distribution Unlimited </div> <div style="font-size: 2em; font-weight: bold;">20030225 104</div> </div>				
14. SUBJECT TERMS			15. NUMBER OF PAGES 358	
			16. PRICE CODE	
17. SECURITY CLASSIFICATION OF REPORT	18. SECURITY CLASSIFICATION OF THIS PAGE	19. SECURITY CLASSIFICATION OF ABSTRACT	20. LIMITATION OF ABSTRACT	

This material is declared a work of the U.S. Government and is not subject to copyright protection in the United States. Approved for public release; distribution unlimited. Any opinions expressed in this material are those of the author and do not represent the opinions of the U.S. Government.

LOCALIZED FLOW CONTROL WITH ENERGY DEPOSITION

by

RUSSELL G. ADELGREN

A dissertation submitted to the
Graduate School-New Brunswick
Rutgers, The State University of New Jersey
in partial fulfillment of the requirements

for the degree of

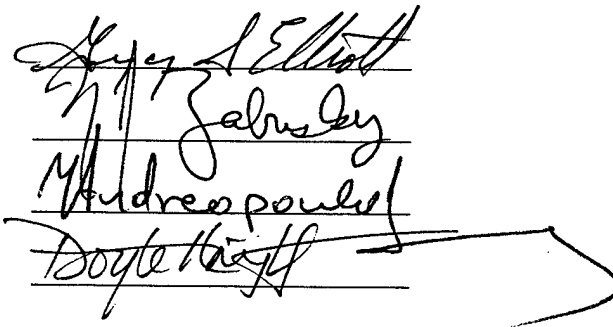
Doctor of Philosophy

Graduate Program in Mechanical and Aerospace Engineering

written under the direction of

Professor Gregory S. Elliott

and approved by



New Brunswick, New Jersey

October, 2002

ABSTRACT OF THE DISSERTATION

LOCALIZED FLOW CONTROL WITH ENERGY DEPOSITION

By Russell G. Adelgren

Dissertation Director:
Professor Gregory S. Elliott

A series of experiments with energy deposition via laser-induced optical breakdown of air, i.e., a laser spark, have been performed. These experiments have demonstrated the possibility of using a laser spark for supersonic flow control. A focused Nd:YAG laser (pulse time of 10 nanoseconds, pulse frequency of 10 Hz, and capable of energy levels up to 600 milli-Joules per pulse) was used to create the energy deposition laser spark. This laser energy deposition was then tested in quiescent air, upstream of a Mach 3.45 sphere with and without shock impingement, into shock structures within the dual solution domain, and into a compressible shear layer.

In the first of these experiments, Rayleigh scattering flow visualization was taken for energy deposition into quiescent air. A time sequence of images showed the post breakdown fluid motion created by the laser spark for different laser energy levels. Blast wave radius and wave speed measurements were made and correlated to five different laser energy deposition levels. Pressure probe measurements of the propagating blast wave were made for two different laser energy deposition levels. The blast wave measurements correlate well with the numerical simulations. However, the intrusive pressure probe measurements differed by 40% from the model and this is attributed to shock reflections off of the probe surface.

Laser energy was deposited upstream of a sphere in Mach 3.45 flow. The energy was deposited one sphere diameter and 0.6 diameters upstream of the front of the sphere. The frontal surface pressure on the sphere was recorded as the laser spark perturbed region interacted with the flow about the sphere. Tests for three different energy levels and two different incident laser beam diameters were completed. Schlieren

images were also taken of the flow and correlated in time to the surface pressure measurements. In addition, surface heat transfer and temperature measurements were made of the interaction process. The surface temperature and heat transfer measurements were made with instrumentation designed and constructed in-house. Radiation heating, blast wave heating, and thermal heating effects were measured as the laser energy deposition upstream of the Mach 3.45 sphere interacted with the steady state flow structure. Two deposition locations of 0.6 and 1.0 diameters upstream and single and double pulses were investigated with the heat transfer instrumentation. Moreover, laser energy was deposited upstream of the sphere subjected to an Edney Type IV shock/shock interaction. The surface pressure on the sphere was measured and correlated in time to shadowgraph images taken of the flow interaction process. Two locations of energy deposition were investigated with the surface pressure measurements. Surface heat transfer and temperature measurements were also made on the sphere with the Edney Type IV shock/shock interaction. Two deposition locations with single and double discharges were investigated with the heat transfer instrumentation for the sphere with shock impingement. A significant effect on the flow for laser spark energy deposition has been demonstrated for these experimental cases described. It has been demonstrated that the peak surface pressure associated with the Edney IV interaction can be momentarily reduced by 30% by the interaction with the thermal spot created by the laser spark.

The effects of laser energy deposition on another shock interaction phenomena were studied. Laser energy deposition was used to modify the shock structure formed by symmetric wedges at Mach 3.45 within the dual solution domain. Various energy deposition locations were studied, and two different wedge spans were tested. Schlieren images were taken, phase locked to the time of energy deposition, and used to visualize the time sequence of flow events. Experimental and numerical results were compared for one test case. It was demonstrated experimentally that the Mach reflection could be reduced by 80% momentarily. The numerical simulations show a transition from the stable Mach reflection to a stable regular reflection.

Two energy deposition methods (electric arcing and laser energy deposition) were used to force and control compressible mixing layers of axisymmetric jets. The energy deposition forcing methods have been experimentally investigated with the schlieren technique, particle image velocimetry, Mie scattering, and static pressure probe diagnostic techniques. Two jets perfectly expanded with nozzle exit Mach

numbers of 0.85 and 1.38 were tested and examined with schlieren imaging for electric arc frequencies ranging from 1-18 kHz. Similar structures were observed for comparable Strouhal numbers between the subsonic and supersonic jets. The Mach 1.38 jet shear layer was forced with a single pulse laser energy deposition. The large-scale structure forced with the laser perturbation was characterized with schlieren imaging, measurements of the velocity and vorticity fields, and the pressure history. The core and braid regions were identified and correlated with the pressure data. The single pulse laser perturbation was demonstrated as an effective way to induce large-scale structures in a compressible shear layer. It was demonstrated that the laser spark (capable of 40 mJ/pulse) was more effective at inducing a large-scale structure than the electric arc (capable of 1 mJ/pulse) in the compressible shear layer.

Acknowledgement

First and foremost, I would like to thank my wife. Actually, I should also thank the good Lord for blessing me with someone so loving and caring as my wife. Thanks for putting up with all of the long nights, missed weekends, and my numerous quirks. I also thank my kids for all of their great support, for their great artwork they continually supply for my office at home and at work, and for the breaks from work they give to me at the park and at home. You all have grown so much these past three years, and I thank the Lord for allowing me to witness it.

I also thank the Lord for blessing me with such great parents and parents-in-laws. Thank you each for your love, support, and caring.

I would like to thank Professors Knight and Elliott for including me in such exciting ideas while I have been here at Rutgers. Professor Knight, the Air Force lost a good officer when you decided to leave and become a scholar. Your leadership and organizational skills are phenomenal and rival those of senior officers I know. Professor Elliott, thanks for all of the things you have taught me in the lab about experimentation, exploration, and instrumentation. Your tremendous enthusiasm is a vital source of inspiration to me and to those around you. It has been a true pleasure working for you these past three years. Doctor Hong Yan, thanks for the numerical modeling of some of the experimental work for the wedges, and more importantly for your cheerful and most delightful personality.

Thanks to Martin, Visilije, Vijay, Kate, and Katherine for their friendship over the last three years. I also thank Val, Bill, and Eric in the Physics machine shop and all of the good stories we had the chance to swap. I would also like to thank Professor Benaroya and Mrs. Mazzucco for their tremendous support. I wish you each the best in your future endeavors.

Thanks to Senior Airman Patel for being so unselfish and for so courageously serving this country this past Fall. God Bless you and the others like you in this country, and good luck with your future studies. You are going to be a great officer.

John Petrowski, whatever the department is paying you, it is not enough. I dearly thank you for helping me and devoting so much of your time with the heat transfer electronics. Also, thanks for all you have taught me in the machine shop.

I thank Doctors Carter, Buetner, Ivanov, and Zheltovodov for all the great times we had working on experiments together, for all of the enthusiasm, and great support. I look forward to more experiments with you each in the future. I also thank Doctors Schmisser and Walker from the Air Force Office of Scientific Research for their support of this research.

I also thank Professors Zabusky and Andreopoulos for being on my committee and reviewing this document.

Lastly, I would like to thank Colonel Litwhiler, and Lieutenant Colonel Cooley at the Air Force Academy for giving me the chance to pursue this opportunity.

We are all travelers in the wilderness of this world, and the best that we find in our travels is an honest friend.

Robert Louis Stevenson

Dedication

To my wife, children, my sisters, my Mom and Dad, and my in-laws. Thank you each for all of your love and support.

Also, to Jonn J. Edmunds, Kristofer T. Stonesifer, Johnny M. Spann, Jefferson D. Davis, Daniel H. Petithory, Brian C. Prosser, Nathan R. Chapman, Matthew W. Bancroft, Daniel G. McCollum, Stephen L. Bryson, Scott N. Germosen, Nathan P. Hays, Bryan P. Bertrand, Jeannette L. Winters, Walter F. Cohee III, Dwight J. Morgan, Stanley L. Harriman, Neil C. Roberts, Marc A. Anderson, Matthew A. Commons, Bradley S. Crose, Philip J. Svitak, John A. Chapman, Jason D. Cunningham, Matthew J. Bourgeois, Brian T. Craig, Justin J. Galewski, Jamie O. Maugans, Daniel A. Romero, Gene A. Vance Jr, Sean M. Corlew, Anissa A. Shero, Peter P. Tycz II, all of their parents, spouses, children, and other loved ones for giving such an enormous sacrifice. You are not, and will not be forgotten. God bless you all, and peace be with you. It is my sincerest hope that some of my work someday will lead to less of such sacrifice.

Table of Contents

ABSTRACT OF THE DISSERTATION.....	ii
Acknowledgement.....	v
Dedication	vii
Table of Contents	viii
Lists of tables.....	xi
List of illustrations.....	xii
Chapter 1 Introduction.....	1
1.1 Motivation.....	1
1.2 Research Objectives	7
Chapter 2 Background and Literature Survey	9
2.1 Governing Equations.....	9
2.2 Flow Control with Energy Addition.....	12
2.3 Energy Deposition Techniques	13
2.3.1 Laser Induced Optical Breakdown	13
2.3.2 Spherically Symmetric Laser Perturbation Model.....	17
2.3.3 Electric Arc.....	18
2.4 Shock Interaction Phenomena	20
2.4.1 Edney Type IV Shock Interaction	20
2.4.2 Mach Reflection and Regular Reflection Dual Solution Domain.....	22
2.5 Compressible Jet Shear Layer	26
Chapter 3 Experimental Facilities	30
3.1 Wind Tunnel.....	30
3.2 Flow Visualization	32
3.2.1 Schlieren and Shadowgraph	32
3.2.2 Filtered Rayleigh Scattering	37
3.2.3 Mie Scattering	43
3.3 Laser Perturbation	44

3.4 Electric Arc	45
3.5 Surface Pressure	46
3.6 Surface Heat Transfer.....	51
3.6.1 Thin Film Gauge Theory	52
3.6.2 Heat Transfer Model Description	55
3.6.2.1 Model Construction	55
3.6.2.2 Low-noise Signal Conditioner Design.....	59
3.6.3 Heat Transfer Gauge Calibration.....	62
3.6.3.1 Static.....	62
3.6.3.2 Blunt Body Heat Transfer and Dynamic Tests	66
3.7 Intersecting Shocks	78
3.8 Axisymmetric Jets.....	81
3.9 Particle Image Velocimetry.....	83
3.10 Pressure Probe.....	83
Chapter 4 Laser Energy Deposition in Quiescent Air	87
4.1 Overview of Laser Energy Deposition in Quiescent Air Experiments.....	87
4.2 Flow Visualization	87
4.3 Energy and Deposition Volume	106
4.4 Blast Wave	106
4.4.1 Wave Propagation Speed.....	106
4.4.2 Pressure	116
4.5 Summary	127
Chapter 5 Laser Energy Deposition Upstream of Mach 3.45 Sphere.....	128
5.1 Overview of Sphere Tests	128
5.2 Sphere Without Shock Impingement	129
5.2.1 Steady State	129
5.2.2 Flow Visualization.....	134
5.2.3 Surface Pressure	147

5.2.4 Surface Heat Transfer	167
5.3 Sphere With Shock Impingement.....	185
5.3.1 Steady State	185
5.3.2 Flow Visualization.....	187
5.3.3 Surface Pressure	200
5.3.4 Surface Heat Transfer.....	213
5.4 Summary	232
Chapter 6 Crossing Shocks.....	234
6.1 Overview of Crossing Shock Tests	234
6.2 Flow Visualization	236
6.3 Comparison with Computational Model	266
6.4 Summary	279
Chapter 7 Electric Arc and Laser Energy Excitation of Compressible Axisymmetric Jet Shear Layer	281
7.1 Overview of Shear Layer Tests	281
7.2 Electric Arc Forcing.....	282
7.3 Laser Discharge Forcing	289
7.4 Summary	308
Chapter 8 Conclusion	309
8.1 Key Discoveries	309
8.2 Areas for Further Research	310
References	313
Vita.....	322

Lists of tables

Table 3.1 Operating Parameters for the Rutgers Mach 3.45 Supersonic Wind Tunnel	31
Table 3.2 Index of refraction for air at 20 C and one atmosphere [43]	33
Table 3.3 Electric arc characteristics	46
Table 3.4 Thermal properties.....	55
Table 3.5 Gauge locations for eight gauge model	58
Table 3.6 Wedge model parameters	78
Table 3.7 Test nozzles' stagnation conditions	81
Table 3.8 Test nozzles' exit conditions	82
Table 3.9 Test nozzles' Reynolds number and calculated convective Mach and velocities	82
Table 3.10 Electric arc characteristics	82
Table 3.11 Nd:YAG excitation laser characteristics	82
Table 4.1 Perturbation laser characteristics	109
Table 4.2. Atmospheric test conditions	109
Table 5.1 Tunnel operating parameters for sphere without shock impingement surface pressure tests	131
Table 5.2 Tunnel operating parameters for surface heat transfer measurement experiments.....	167
Table 5.3 Tunnel operating parameters for shock impingement surface pressure tests.....	200
Table 5.4 Tunnel operating parameters for heat transfer measurements on sphere with shock impingement	213
Table 6.1 Laser deposition position and energy levels for wedges with span $b = 2.2w$	235
Table 6.2 Laser deposition position and energy levels for wedges with span $b = 4w$	235
Table 6.3 Tunnel operational parameters for wedge tests	240
Table 6.4 Wedge flow parameters for Mach 3.45	240
Table 6.5 Tunnel operation parameters for the wedge tests	270
Table 7.1 Summary of axisymmetric jet shear layer perturbation experiments.....	282
Table 7.2 Comparison of convective velocity for forced large-scale structure	293

List of illustrations

Figure 1.1 X-15A-2 flight test vehicle launch from B-52 aircraft, note the external fuel tanks were jettisoned at Mach 2 (photo courtesy of NASA)	1
Figure 1.2 Hypersonic research engine dummy model mounted on X-15A-2 ventral fin (photo courtesy of NASA).....	2
Figure 1.3 X-15A-2 ventral fin shock impingement damage after Mach 6.7 test flight (photos courtesy of NASA).....	4
Figure 1.4 X-15 wind tunnel test (photo courtesy of NASA).....	5
Figure 1.5 Hyper-X (X-43) vehicle (image courtesy of NASA)	5
Figure 1.6 Potential flow control areas on high speed aerospace vehicle.....	6
Figure 2.1 Laser induced optical breakdown process.....	14
Figure 2.2 Pictures of laser sparks in quiescent air for (left) $13 \text{ mJ}/1 \pm 0.5 \text{ mm}^3$, (middle) $127 \text{ mJ}/1.3 \pm 0.7 \text{ mm}^3$, and (right) $258 \text{ mJ}/3 \pm 1 \text{ mm}^3$. Laser incidence is from bottom to top.....	16
Figure 2.3 Edney's shock/shock interaction classification [33]	22
Figure 2.4 Edney Type IV shock/shock interaction [33].....	22
Figure 2.5 Simplified inviscid two fin model	24
Figure 2.6 Pressure deflection diagram with the von Neumann and detachment angles for Mach 3.45	25
Figure 2.7 Crossing shock dual solution domain.....	25
Figure 2.8 Nomenclature associated with the symmetric wedges and regular reflection	26
Figure 2.9 Nomenclature associated with the symmetric wedges and Mach reflection	26
Figure 2.10 Forcing of large-scale structure in compressible axisymmetric shear layer.....	29
Figure 3.1 Mach 3.45 wind tunnel schematic.....	31
Figure 3.2 Mach 3.45 wind tunnel photo.....	31
Figure 3.3 Z-path schlieren apparatus	35
Figure 3.4 Pulse width comparison between Xenon flash lamp and laser-Argon flash.....	36
Figure 3.5 Elements of laser-Argon spark source.....	36
Figure 3.6 Comparison of schlieren flash sources for images taken of laser energy deposition in quiescent air next to 25.4 mm diameter hemisphere model.....	37

Figure 3.7 Rayleigh scattering distributions for various y values.....	40
Figure 3.8 Overlapping scattering and absorption bands.....	40
Figure 3.9 Filtered Rayleigh scattering experimental apparatus.....	41
Figure 3.10 Laser sheet and excitation laser orientation for quiescent air energy deposition tests	41
Figure 3.11 Filtered Rayleigh scattering test apparatus; camera, iodine filter, and lens arrangement.....	42
Figure 3.12 Filtered Rayleigh scattering apparatus; camera and iodine filter	43
Figure 3.13 Rutgers University Gasdynamics Lab Nd:YAG lasers	45
Figure 3.14 Sphere surface pressure model.....	47
Figure 3.15 Pressure model mounted in wind tunnel	47
Figure 3.16 Schematic of sphere model, wedge, and approximate energy deposition locations.....	48
Figure 3.17 Mach cone diagram for three dimensional effects of wedge in tunnel test section (dimensions in inches)	48
Figure 3.18 Endevco pressure transducer calibration for 24 Jun 2000 for laser energy deposition upstream of Mach 3.45 sphere with shock impingement tests.....	49
Figure 3.19 Endevco pressure transducer calibration for 27 Jun 2000 for laser energy deposition upstream of Mach 3.45 sphere with shock impingement tests.....	49
Figure 3.20 Endevco pressure transducer calibration for the 27 Nov 2000 tests, 258 mJ/pulse laser energy deposition 1.0 diameter upstream of Mach 3.45 sphere without shock impingement.....	50
Figure 3.21 Endevco pressure transducer calibration for the 28 Nov 2000 tests, 127 mJ/pulse laser energy deposition 1.0 diameter upstream of Mach 3.45 sphere without shock impingement.....	50
Figure 3.22 Endevco pressure transducer calibration for the 29 Nov 2000 tests, 13 mJ/pulse laser energy deposition 1.0 diameter upstream of Mach 3.45 sphere without shock impingement.....	51
Figure 3.23 One dimensional, semi-infinite heat conduction model	55
Figure 3.24 Eight gauge heat transfer hemisphere model mounted in wind tunnel test section with shock impingement ramp.....	59
Figure 3.25 Eight gauge model showing platinum films and silver leads on MACOR hemisphere	59
Figure 3.26 Signal conditioner schematic for one channel.....	61
Figure 3.27 Front view of four channel signal conditioner	61

Figure 3.28 Four channel signal conditioner components.....	62
Figure 3.29 Static calibration of stagnation point heat transfer gauge.....	63
Figure 3.30 Calibration data for gauges 1-4 of eight gauge heat transfer model.....	64
Figure 3.31 Internal sphere temperature during gauge 1-4 calibration.....	64
Figure 3.32 Calibration data for gauges 5-8 of eight gauge heat transfer model.....	65
Figure 3.33 Internal sphere temperature during gauges 5-8 calibration	65
Figure 3.34 Sphere stagnation point gauge, test run 1	70
Figure 3.35 Sphere stagnation point gauge, test run 2 with corresponding shadowgraph times	70
Figure 3.36 Comparison of test run 1 and 2	71
Figure 3.37 Tunnel parameters for test run 1	71
Figure 3.38 Tunnel parameters for test run 2	72
Figure 3.39 Drop in wind tunnel air storage tank temperature for polytropic expansion process; 10 s wind tunnel operation time and stagnation pressure of 150 psi.....	72
Figure 3.40 Stagnation point heat flux from test run 1 computed from raw temperature data	73
Figure 3.41 Stagnation point heat flux from test run 1 computed from smoothed temperature data and comparison to theoretical heat flux	73
Figure 3.42 Stagnation point heat flux from test run 2 computed from smoothed temperature data and comparison to theoretical heat flux	74
Figure 3.43 Shadowgraphs for test run 2.....	75
Figure 3.44 Embedded thermocouple temperature and comparison to thin film platinum gauge surface temperature.....	76
Figure 3.45 Time response for gauges 1-3, a) – c), respectively, for radiation and blast wave heating from laser energy deposition into quiescent air 1.0 diameter upstream of sphere.....	77
Figure 3.46 Symmetric wedge models (dimensions given in inches).....	79
Figure 3.47 Test section blockage comparison between symmetric wedge models and the sphere and wedge model for the Edney Type IV shock impingement tests (dimensions given in inches).....	79
Figure 3.48 55.8 mm span symmetric wedge models mounted in wind tunnel test section	80
Figure 3.49 101.4 mm span, 22 degree symmetric wedge models	80

Figure 3.50 Test apparatus for axisymmetric jet 3 component PIV measurements.....	81
Figure 3.51 Pressure probe with Endevco 8514-20 piezoresistive pressure transducer	84
Figure 3.52 Pressure probe with Kistler 211B5 piezoelectric pressure transducer.....	85
Figure 3.53 Calibration of Kistler piezoelectric pressure transducer used for quiescent blast wave measurements	85
Figure 3.54 Calibration of Endevco piezoresistive pressure transducer used for the jet shear layer pressure measurements	86
Figure 4.1 Blast wave formation and vortex ring development for laser induced optical breakdown in quiescent air.....	90
Figure 4.2 Filtered Rayleigh Scattering images of laser induced breakdown in quiescent air at various times, time $t = 0$ corresponds to laser spark pulse	91
Figure 4.3 Vortex ring diameter growth as a function of time (measured from Filtered Rayleigh Scattering images)	92
Figure 4.4 Vortex ring motion along optical axis (measured from Filtered Rayleigh Scattering images, negative direction is motion away from the focusing lens)	93
Figure 4.5 Filtered Rayleigh scattering images and blast wave measurement points for 112 mJ/pulse, 5 – 14 μ s	94
Figure 4.6 Filtered Rayleigh scattering images and blast wave measurement points for 112 mJ/pulse, 16 – 40 μ s	95
Figure 4.7 Filtered Rayleigh scattering images and blast wave measurement points for 98 mJ/pulse, 5 – 14 μ s	96
Figure 4.8 Filtered Rayleigh scattering images and blast wave measurement points for 98 mJ/pulse, 16 – 40 μ s	97
Figure 4.9 Filtered Rayleigh scattering images and blast wave measurement points for 76 mJ/pulse, 5 – 14 μ s	98
Figure 4.10 Filtered Rayleigh scattering images and blast wave measurement points for 76 mJ/pulse, 16 – 40 μ s	99

Figure 4.11 Filtered Rayleigh scattering images and blast wave measurement points for 50 mJ/pulse, 5 – 14 μ s	100
Figure 4.12 Filtered Rayleigh scattering images and blast wave measurement points for 50 mJ/pulse, 16 – 40 μ s	101
Figure 4.13 Filtered Rayleigh scattering images and blast wave measurement points for 20 mJ/pulse, 5 – 14 μ s	102
Figure 4.14 Filtered Rayleigh scattering images and blast wave measurement points for 20 mJ/pulse, 16 – 35 μ s	103
Figure 4.15 Filtered Rayleigh scattering images and blast wave measurement points for 116 mJ/pulse, 5 – 14 μ s	104
Figure 4.16 Filtered Rayleigh scattering images and blast wave measurement points for 116 mJ/pulse, 16 – 40 μ s	105
Figure 4.17 Shock wave radius as a function of time for varying incident laser absorption energies	110
Figure 4.18 Shock wave speed as a function of time for varying incident laser absorption energies	111
Figure 4.19 Shock wave Mach number as a function of time for varying laser absorption energies	112
Figure 4.20 Comparison of experimental fit for time exponent for energy deposition levels	113
Figure 4.21 Shock wave propagation for 112 mJ/pulse	113
Figure 4.22 Shock wave propagation for 98 mJ/pulse	114
Figure 4.23 Shock wave propagation for 50 mJ/pulse	114
Figure 4.24 Shock wave propagation for 20 mJ/pulse	115
Figure 4.25 Shock wave propagation for 116 mJ/pulse	115
Figure 4.26 Measured and simulated pressure traces at $r = 6.9$ mm and corresponding schlieren image at t = 10.8 μ s for energy deposition of 58 mJ/pulse	118
Figure 4.27 Measured and simulated pressure traces at $r = 9.6$ mm and corresponding schlieren image at t = 18.4 μ s for energy deposition of 58 mJ/pulse	118
Figure 4.28 Measured and simulated pressure traces at $r = 12.0$ mm and corresponding schlieren image at t = 24.4 μ s for energy deposition of 58 mJ/pulse	119

Figure 4.29 Measured and simulated pressure traces at $r = 17.4$ mm and corresponding schlieren image at $t = 38.4$ μ s for energy deposition of 58 mJ/pulse.....	119
Figure 4.30 Measured and simulated pressure traces at $r = 22.2$ mm and corresponding schlieren image at $t = 52.4$ μ s for energy deposition of 58 mJ/pulse.....	120
Figure 4.31 Measured and simulated pressure traces at $r = 27.3$ mm and corresponding schlieren image at $t = 66.4$ μ s for energy deposition of 58 mJ/pulse.....	120
Figure 4.32 Measured and simulated pressure traces at $r = 32.4$ mm and corresponding schlieren image at $t = 81.2$ μ s for energy deposition of 58 mJ/pulse.....	121
Figure 4.33 Measured and simulated pressure traces at $r = 36.6$ mm and corresponding schlieren image at $t = 94.4$ μ s for energy deposition of 58 mJ/pulse.....	121
Figure 4.34 Measured and simulated pressure traces at $r = 41.7$ mm and corresponding schlieren image at $t = 107.2$ μ s for energy deposition of 58 mJ/pulse.....	122
Figure 4.35 Measured and simulated pressure traces at $r = 6.9$ mm and corresponding schlieren image at $t = 10.4$ μ s for energy deposition of 115 mJ/pulse.....	122
Figure 4.36 Measured and simulated pressure traces at $r = 9.6$ mm and corresponding schlieren image at $t = 16.4$ μ s for energy deposition of 115 mJ/pulse.....	123
Figure 4.37 Measured and simulated pressure traces at $r = 12.0$ mm and corresponding schlieren image at $t = 22.4$ μ s for energy deposition of 115 mJ/pulse.....	123
Figure 4.38 Measured and simulated pressure traces at $r = 17.1$ mm and corresponding schlieren image at $t = 36.4$ μ s for energy deposition of 115 mJ/pulse.....	124
Figure 4.39 Measured and simulated pressure traces at $r = 22.2$ mm and corresponding schlieren image at $t = 49.2$ μ s for energy deposition of 115 mJ/pulse.....	124
Figure 4.40 Measured and simulated pressure traces at $r = 27.3$ mm and corresponding schlieren image at $t = 63.2$ μ s for energy deposition of 115 mJ/pulse.....	125
Figure 4.41 Measured and simulated pressure traces at $r = 32.4$ mm and corresponding schlieren image at $t = 77.6$ μ s for energy deposition of 115 mJ/pulse.....	125

Figure 4.42 Measured and simulated pressure traces at $r = 36.6$ mm and corresponding schlieren image at $t = 91.2$ μ s for energy deposition of 115 mJ/pulse.....	126
Figure 4.43 Comparison of peak pressures associated with the blast wave for energy deposition of 58 mJ/pulse.....	126
Figure 4.44 Comparison of peak pressures associated with the blast wave for energy deposition of 112 mJ/pulse.....	127
Figure 5.1 Laser energy deposition locations for Mach 3.45 experiments	128
Figure 5.2 Laser energy deposition locations for Mach 3.45 sphere with Edney Type IV shock/shock interaction.....	129
Figure 5.3 Computational density contours and experimental schlieren comparison for Mach 3.45 sphere	131
Figure 5.4 Grid convergence for sphere computations.....	132
Figure 5.5 Experimental, numerical, and Lobb model [85] comparison for shock standoff distance for Mach 3.45 sphere	132
Figure 5.6 Comparison of Euler computations and experimental pressure distribution.....	133
Figure 5.7 Flow features for the laser energy deposition upstream of a Mach 3.45 sphere, a) initial deposition, b) blast wave effects, c) bow shock lensing due to shock thermal interface interaction, and d) thermal heating to sphere surface from thermal spot impingement and bow shock collapse back to steady state	138
Figure 5.8 Instantaneous argon/laser generated schlieren images of Mach 3.45 sphere with laser energy deposition one diameter upstream, 0, 10, 20, and 30 μ s after laser energy deposition, 283 mJ/pulse, 150 mm focal length lens	139
Figure 5.9 Instantaneous argon/laser generated schlieren images of Mach 3.45 sphere with laser energy deposition one diameter upstream, 40, 50, 60, and 70 μ s after laser energy deposition, 283 mJ/pulse, 150 mm focal length lens	140
Figure 5.10 Instantaneous argon/laser generated schlieren images of Mach 3.45 sphere with laser energy deposition one diameter upstream, 80, 90, 100, and 120 μ s after laser energy deposition, 283 mJ/pulse, 150 mm focal length lens	141

Figure 5.11 Instantaneous argon/laser generated schlieren images of Mach 3.45 sphere with laser energy deposition one diameter upstream, 130, 140, 150, and 160 μ s after laser energy deposition, 283 mJ/pulse, 150 mm focal length lens	142
Figure 5.12 Instantaneous argon/laser generated schlieren images of Mach 3.45 sphere with laser energy deposition 0.6 diameters upstream, 0, 10, 20, and 30 μ s after laser energy deposition, 283 mJ/pulse, 150 mm focal length lens	143
Figure 5.13 Instantaneous argon/laser generated schlieren images of Mach 3.45 sphere with laser energy deposition 0.6 diameters upstream, 40, 50, 60, and 70 μ s after laser energy deposition, 283 mJ/pulse, 150 mm focal length lens	144
Figure 5.14 Instantaneous argon/laser generated schlieren images of Mach 3.45 sphere with laser energy deposition 0.6 diameters upstream, 80, 90, 100, and 110 μ s after laser energy deposition, 283 mJ/pulse, 150 mm focal length lens	145
Figure 5.15 Instantaneous argon/laser generated schlieren images of Mach 3.45 sphere with laser energy deposition 0.6 diameters upstream, 120, 130, and 140 μ s after laser energy deposition, 283 mJ/pulse, 150 mm focal length lens	146
Figure 5.16 Surface pressure traces for various pressure port locations on the vertical symmetry plane around front of sphere with laser energy deposition (incident laser beam energy at 13 mJ/pulse) one diameter upstream and focused on model centerline.....	151
Figure 5.17 Surface pressure traces for various pressure port locations on the vertical symmetry plane around front of sphere with laser energy deposition (incident laser beam energy at 127 mJ/pulse) one diameter upstream and focused on model centerline.....	152
Figure 5.18 Surface pressure traces for various pressure port locations on the vertical symmetry plane around front of sphere with laser energy deposition (incident laser beam energy at 258 mJ/pulse) one diameter upstream and focused on model centerline.....	152
Figure 5.19 Comparison of stagnation point pressure traces for sphere for three energy deposition levels 1.0 diameter upstream of the sphere.....	153
Figure 5.20 Space – time diagram for the shock interaction with the leading edge of the thermal interface boundary.....	154

Figure 5.21 Shock wave and interface interaction.....	154
Figure 5.22 Phase averaged xenon Strobotac flash generated schlieren images of Mach 3.45 sphere with laser energy deposition 1.0 diameter upstream, 0, 10, 20, and 30 μ s after laser energy deposition, 13 mJ/pulse, 150 mm focal length lens, and correlated with polar steady state and instantaneous pressure plots	155
Figure 5.23 Phase averaged xenon Strobotac flash generated schlieren images of Mach 3.45 sphere with laser energy deposition 1.0 diameter upstream, 40, 50, 60, and 70 μ s after laser energy deposition, 13 mJ/pulse, 150 mm focal length lens, and correlated with polar steady state and instantaneous pressure plots	156
Figure 5.24 Phase averaged xenon Strobotac flash generated schlieren images of Mach 3.45 sphere with laser energy deposition 1.0 diameter upstream, 80, 90, 100, and 110 μ s after laser energy deposition, 13 mJ/pulse, 150 mm focal length lens, and correlated with polar steady state and instantaneous pressure plots.....	157
Figure 5.25 Phase averaged xenon Strobotac flash generated schlieren images of Mach 3.45 sphere with laser energy deposition 1.0 diameter upstream, 120, and 130 μ s after laser energy deposition, 13 mJ/pulse, 150 mm focal length lens, and correlated with polar steady state and instantaneous pressure plots	158
Figure 5.26 Phase averaged xenon Strobotac flash generated schlieren images of Mach 3.45 sphere with laser energy deposition 1.0 diameter upstream, 0, 10, 20, and 30 μ s after laser energy deposition, 127 mJ/pulse, 150 mm focal length lens, and correlated with polar steady state and instantaneous pressure plots	159
Figure 5.27 Phase averaged xenon Strobotac flash generated schlieren images of Mach 3.45 sphere with laser energy deposition 1.0 diameter upstream, 40, 50, 60, and 70 μ s after laser energy deposition, 127 mJ/pulse, 150 mm focal length lens, and correlated with polar steady state and instantaneous pressure plots	160
Figure 5.28 Phase averaged xenon Strobotac flash generated schlieren images of Mach 3.45 sphere with laser energy deposition 1.0 diameter upstream, 80, 90, 100, and 110 μ s after laser energy deposition,	

127 mJ/pulse, 150 mm focal length lens, and correlated with polar steady state and instantaneous pressure plots.....	161
Figure 5.29 Phase averaged xenon Strobotac flash generated schlieren images of Mach 3.45 sphere with laser energy deposition 1.0 diameter upstream, 120, and 130 μ s after laser energy deposition, 127 mJ/pulse, 150 mm focal length lens, and correlated with polar steady state and instantaneous pressure plots.....	162
Figure 5.30 Phase averaged xenon Strobotac flash generated schlieren images of Mach 3.45 sphere with laser energy deposition 1.0 diameter upstream, 0, 10, 20, and 30 μ s after laser energy deposition, 258 mJ/pulse, 150 mm focal length lens, and correlated with polar steady state and instantaneous pressure plots.....	163
Figure 5.31 Phase averaged xenon Strobotac flash generated schlieren images of Mach 3.45 sphere with laser energy deposition 1.0 diameter upstream, 40, 50, 60, and 70 μ s after laser energy deposition, 258 mJ/pulse, 150 mm focal length lens, and correlated with polar steady state and instantaneous pressure plots.....	164
Figure 5.32 Phase averaged xenon Strobotac flash generated schlieren images of Mach 3.45 sphere with laser energy deposition 1.0 diameter upstream, 80, 90, 100, and 110 μ s after laser energy deposition, 258 mJ/pulse, 150 mm focal length lens, and correlated with polar steady state and instantaneous pressure plots.....	165
Figure 5.33 Phase averaged xenon Strobotac flash generated schlieren images of Mach 3.45 sphere with laser energy deposition 1.0 diameter upstream, 120, and 130 μ s after laser energy deposition, 258 mJ/pulse, 150 mm focal length lens, and correlated with polar steady state and instantaneous pressure plots.....	166
Figure 5.34 Wall temperature for the hemisphere without laser spark.....	172
Figure 5.35 Wall heat flux without laser spark.....	173
Figure 5.36 Measured wall heat flux on Mach 3.45 sphere and with laser energy deposition 1.0 diameter upstream and on the centerline axis, one laser pulse (10 Hz) at 283 mJ/pulse, 150 mm focal length lens.....	174

Figure 5.37 Measured wall heat flux and temperature for gauge 1 on Mach 3.45 sphere and with laser energy deposition 1.0 diameter upstream and on the centerline axis, one laser pulse (10 Hz) at 283 mJ/pulse, 150 mm focal length lens	174
Figure 5.38 Measured wall heat flux and temperature for gauge 2 on Mach 3.45 sphere and with laser energy deposition 1.0 diameter upstream and on the centerline axis, one laser pulse (10 Hz) at 283 mJ/pulse, 150 mm focal length lens	175
Figure 5.39 Measured wall heat flux and temperature for gauge 3 on Mach 3.45 sphere and with laser energy deposition 1.0 diameter upstream and on the centerline axis, one laser pulse (10 Hz) at 283 mJ/pulse, 150 mm focal length lens	175
Figure 5.40 Measured wall heat flux and temperature for gauge 4 on Mach 3.45 sphere and with laser energy deposition 1.0 diameter upstream and on the centerline axis, one laser pulse (10 Hz) at 283 mJ/pulse, 150 mm focal length lens	176
Figure 5.41 Measured wall heat flux and temperature for gauge 5 on Mach 3.45 sphere and with laser energy deposition 1.0 diameter upstream and on the centerline axis, one laser pulse (10 Hz) at 283 mJ/pulse, 150 mm focal length lens	176
Figure 5.42 Measured wall heat flux and temperature for gauge 6 on Mach 3.45 sphere and with laser energy deposition 1.0 diameter upstream and on the centerline axis, one laser pulse (10 Hz) at 283 mJ/pulse, 150 mm focal length lens	177
Figure 5.43 Measured wall heat flux and temperature for gauge 7 on Mach 3.45 sphere and with laser energy deposition 1.0 diameter upstream and on the centerline axis, one laser pulse (10 Hz) at 283 mJ/pulse, 150 mm focal length lens	177
Figure 5.44 Measured wall heat flux and temperature for gauge 8 on Mach 3.45 sphere and with laser energy deposition 1.0 diameter upstream and on the centerline axis, one laser pulse (10 Hz) at 283 mJ/pulse, 150 mm focal length lens	178
Figure 5.45 Measured wall heat flux on Mach 3.45 sphere and with laser energy deposition 1.0 diameter upstream and on the centerline axis, double laser pulse with 5 μ s separation (10 Hz) at 263 mJ/(double pulse), 150 mm focal length lens.....	178

Figure 5.46 Measured wall heat flux on Mach 3.45 sphere and with laser energy deposition 0.6 diameters upstream and on the centerline axis, single laser pulse (10 Hz) at 283 mJ/pulse, 150 mm focal length lens	179
Figure 5.47 Measured wall heat flux and temperature for gauge 1 on Mach 3.45 sphere and with laser energy deposition 0.6 diameters upstream and on the centerline axis, one laser pulse (10 Hz) at 283 mJ/pulse, 150 mm focal length lens	179
Figure 5.48 Measured wall heat flux and temperature for gauge 2 on Mach 3.45 sphere and with laser energy deposition 0.6 diameters upstream and on the centerline axis, one laser pulse (10 Hz) at 283 mJ/pulse, 150 mm focal length lens	180
Figure 5.49 Measured wall heat flux and temperature for gauge 3 on Mach 3.45 sphere and with laser energy deposition 0.6 diameters upstream and on the centerline axis, one laser pulse (10 Hz) at 283 mJ/pulse, 150 mm focal length lens	180
Figure 5.50 Measured wall heat flux and temperature for gauge 4 on Mach 3.45 sphere and with laser energy deposition 0.6 diameters upstream and on the centerline axis, one laser pulse (10 Hz) at 283 mJ/pulse, 150 mm focal length lens	181
Figure 5.51 Measured wall heat flux and temperature for gauge 5 on Mach 3.45 sphere and with laser energy deposition 0.6 diameters upstream and on the centerline axis, one laser pulse (10 Hz) at 283 mJ/pulse, 150 mm focal length lens	181
Figure 5.52 Measured wall heat flux and temperature for gauge 6 on Mach 3.45 sphere and with laser energy deposition 0.6 diameters upstream and on the centerline axis, one laser pulse (10 Hz) at 283 mJ/pulse, 150 mm focal length lens	182
Figure 5.53 Measured wall heat flux and temperature for gauge 7 on Mach 3.45 sphere and with laser energy deposition 0.6 diameters upstream and on the centerline axis, one laser pulse (10 Hz) at 283 mJ/pulse, 150 mm focal length lens	182
Figure 5.54 Measured wall heat flux and temperature for gauge 8 on Mach 3.45 sphere and with laser energy deposition 0.6 diameters upstream and on the centerline axis, one laser pulse (10 Hz) at 283 mJ/pulse, 150 mm focal length lens	183

Figure 5.55 Measured wall heat flux on Mach 3.45 sphere and with laser energy deposition 0.6 diameters upstream and on the centerline axis, double laser pulse separated by 5 μ s (10 Hz) at 263 mJ/(double pulse), 150 mm focal length lens.....	183
Figure 5.56 Time integrated heat flux for each of the gauges from small time scale data, 1c1 = single laser pulse 1.0 diameter upstream, 1c2 = single laser pulse 0.6 diameters upstream, 2c1 = double laser pulse 1.0 diameter upstream, and 2c2 = double laser pulse 0.6 diameters upstream	184
Figure 5.57 Measured surface pressure for Mach 3.45 sphere with Edney Type IV shock impingement.	187
Figure 5.58 Flow features associated with laser energy deposition upstream of Mach 3.45 sphere with shock impingement, a) initial deposition, b) shearing of thermal spot, oblique shock distortion, and blast wave distortion, c) perturbation to Edney IV shock/shock interaction, and d) complex bow shock lensing, thermal spot interaction with sphere, and three-dimensional shock interactions	190
Figure 5.59 Instantaneous argon/laser generated schlieren images of Mach 3.45 sphere with Edney Type IV shock impingement and with laser energy deposition 1.0 diameter upstream and 0.45 diameters above the centerline axis, 0, 10, 20, and 30 μ s after laser energy deposition, 283 mJ/pulse, 150 mm focal length lens.....	191
Figure 5.60 Instantaneous argon/laser generated schlieren images of Mach 3.45 sphere with Edney Type IV shock impingement and with laser energy deposition 1.0 diameter upstream and 0.45 diameters above the centerline axis, 40, 50, 60, and 70 μ s after laser energy deposition, 283 mJ/pulse, 150 mm focal length lens.....	192
Figure 5.61 Instantaneous argon/laser generated schlieren images of Mach 3.45 sphere with Edney Type IV shock impingement and with laser energy deposition 1.0 diameter upstream and 0.45 diameters above the centerline axis, 80, 90, 100, and 110 μ s after laser energy deposition, 283 mJ/pulse, 150 mm focal length lens.....	193
Figure 5.62 Instantaneous argon/laser generated schlieren images of Mach 3.45 sphere with Edney Type IV shock impingement and with laser energy deposition 1.0 diameter upstream and 0.45 diameters above the centerline axis, 120, 130, 140, and 150 μ s after laser energy deposition, 283 mJ/pulse, 150 mm focal length lens	194

Figure 5.63 Instantaneous argon/laser generated schlieren images of Mach 3.45 sphere with Edney Type IV shock impingement and with laser energy deposition 1.0 diameter upstream and 0.45 diameters above the centerline axis, 160 μ s after laser energy deposition, 283 mJ/pulse, 150 mm focal length lens	195
Figure 5.64 Filtered Rayleigh scattering image in vertical symmetry plane to verify one impinging shock	195
Figure 5.65 Instantaneous argon/laser generated schlieren images of Mach 3.45 sphere with Edney Type IV shock impingement and with laser energy deposition 0.6 diameter upstream and 0.2 diameters above the centerline axis, 0, 10, 20, and 30 μ s after laser energy deposition, 283 mJ/pulse, 150 mm focal length lens.....	196
Figure 5.66 Instantaneous argon/laser generated schlieren images of Mach 3.45 sphere with Edney Type IV shock impingement and with laser energy deposition 0.6 diameter upstream and 0.2 diameters above the centerline axis, 40, 50, 60, and 70 μ s after laser energy deposition, 283 mJ/pulse, 150 mm focal length lens.....	197
Figure 5.67 Instantaneous argon/laser generated schlieren images of Mach 3.45 sphere with Edney Type IV shock impingement and with laser energy deposition 0.6 diameter upstream and 0.2 diameters above the centerline axis, 80, 90, 100, and 110 μ s after laser energy deposition, 283 mJ/pulse, 150 mm focal length lens.....	198
Figure 5.68 Instantaneous argon/laser generated schlieren images of Mach 3.45 sphere with Edney Type IV shock impingement and with laser energy deposition 0.6 diameter upstream and 0.2 diameters above the centerline axis, 120, and 130 μ s after laser energy deposition, 283 mJ/pulse, 150 mm focal length lens	199
Figure 5.69 Pressure port locations with port diameter indicated and relative jet impingement region for surface pressure measurements for the energy deposition 0.7 diameters upstream and 0.15 diameters above model centerline.....	202
Figure 5.70 Pressure port locations with port diameter indicated and relative jet impingement region for surface pressure measurements for the energy deposition 0.7 diameters upstream and 0.28 diameters above model centerline.....	203

Figure 5.71 Surface pressure traces on the vertical symmetry plane around front of sphere in an Edney IV interaction with energy deposition 0.7 diameters upstream and 0.15 diameters above model centerline	204
Figure 5.72 Surface pressure traces on the vertical symmetry plane around front of sphere in an Edney IV interaction with energy deposition 0.7 diameters upstream and 0.28 diameters above model centerline	205
Figure 5.73 Phase averaged xenon Strobotac flash generated schlieren images of Mach 3.45 sphere with an Edney IV interaction with energy deposition 0.7 diameters upstream and 0.15 diameters above model centerline, 10, 20, 30, and 40 μ s after laser energy deposition, 258 mJ/pulse, 150 mm focal length lens, and correlated with polar steady state and instantaneous pressure	206
Figure 5.74 Phase averaged xenon Strobotac flash generated schlieren images of Mach 3.45 sphere with an Edney IV interaction with energy deposition 0.7 diameters upstream and 0.15 diameters above model centerline, 50, 60, 70, and 80 μ s after laser energy deposition, 258 mJ/pulse, 150 mm focal length lens, and correlated with polar steady state and instantaneous pressure	207
Figure 5.75 Phase averaged xenon Strobotac flash generated schlieren images of Mach 3.45 sphere with an Edney IV interaction with energy deposition 0.7 diameters upstream and 0.15 diameters above model centerline, 90, 100, 110, and 120 μ s after laser energy deposition, 258 mJ/pulse, 150 mm focal length lens, and correlated with polar steady state and instantaneous pressure	208
Figure 5.76 Phase averaged xenon Strobotac flash generated schlieren images of Mach 3.45 sphere with an Edney IV interaction with energy deposition 0.7 diameters upstream and 0.15 diameters above model centerline, 130, and 140 μ s after laser energy deposition, 258 mJ/pulse, 150 mm focal length lens, and correlated with polar steady state and instantaneous pressure	209
Figure 5.77 Phase averaged xenon Strobotac flash generated schlieren images of Mach 3.45 sphere with an Edney IV interaction with energy deposition 0.7 diameters upstream and 0.28 diameters above model centerline, 10, 20, 30, and 40 μ s after laser energy deposition, 258 mJ/pulse, 150 mm focal length lens, and correlated with polar steady state and instantaneous pressure	210
Figure 5.78 Phase averaged xenon Strobotac flash generated schlieren images of Mach 3.45 sphere with an Edney IV interaction with energy deposition 0.7 diameters upstream and 0.28 diameters above model	

centerline, 50, 60, 70, and 80 μ s after laser energy deposition, 258 mJ/pulse, 150 mm focal length lens, and correlated with polar steady state and instantaneous pressure	211
Figure 5.79 Phase averaged xenon Strobotac flash generated schlieren images of Mach 3.45 sphere with an Edney IV interaction with energy deposition 0.7 diameters upstream and 0.28 diameters above model centerline, 90, 100, 120, and 140 μ s after laser energy deposition, 258 mJ/pulse, 150 mm focal length lens, and correlated with polar steady state and instantaneous pressure.....	212
Figure 5.80 Thin film platinum gauge locations with gauge width indicated and relative jet impingement region for surface temperature and heat flux measurements	217
Figure 5.81 Hemisphere wall temperature with impinging shock and no laser spark	218
Figure 5.82 Wall heat flux, no laser spark.....	219
Figure 5.83 Comparison of stagnation point surface temperature for sphere with and without Edney Type IV shock/shock interaction.....	220
Figure 5.84 Comparison of stagnation point heat transfer for sphere with and without Edney Type IV shock/shock interaction	221
Figure 5.85 Measured wall heat flux on Mach 3.45 sphere with Edney Type IV shock impingement and with laser energy deposition 1.0 diameter upstream and 0.45 diameters above the centerline axis, one laser pulse (10 Hz) at 283 mJ/pulse, 150 mm focal length lens	222
Figure 5.86 Measured wall heat flux and wall temperature for gauge 1 on Mach 3.45 sphere with Edney Type IV shock impingement and with laser energy deposition 1.0 diameter upstream and 0.45 diameters above the centerline axis, one laser pulse (10 Hz) at 283 mJ/pulse, 150 mm focal length lens	222
Figure 5.87 Measured wall heat flux and wall temperature for gauge 2 on Mach 3.45 sphere with Edney Type IV shock impingement and with laser energy deposition 1.0 diameter upstream and 0.45 diameters above the centerline axis, one laser pulse (10 Hz) at 283 mJ/pulse, 150 mm focal length lens	223
Figure 5.88 Measured wall heat flux and wall temperature for gauge 3 on Mach 3.45 sphere with Edney Type IV shock impingement and with laser energy deposition 1.0 diameter upstream and 0.45	

diameters above the centerline axis, one laser pulse (10 Hz) at 283 mJ/pulse, 150 mm focal length lens	223
Figure 5.89 Measured wall heat flux and wall temperature for gauge 4 on Mach 3.45 sphere with Edney Type IV shock impingement and with laser energy deposition 1.0 diameter upstream and 0.45 diameters above the centerline axis, one laser pulse (10 Hz) at 283 mJ/pulse, 150 mm focal length lens	224
Figure 5.90 Measured wall heat flux and wall temperature for gauge 5 on Mach 3.45 sphere with Edney Type IV shock impingement and with laser energy deposition 1.0 diameter upstream and 0.45 diameters above the centerline axis, one laser pulse (10 Hz) at 283 mJ/pulse, 150 mm focal length lens	224
Figure 5.91 Measured wall heat flux and wall temperature for gauge 6 on Mach 3.45 sphere with Edney Type IV shock impingement and with laser energy deposition 1.0 diameter upstream and 0.45 diameters above the centerline axis, one laser pulse (10 Hz) at 283 mJ/pulse, 150 mm focal length lens	225
Figure 5.92 Measured wall heat flux and wall temperature for gauge 7 on Mach 3.45 sphere with Edney Type IV shock impingement and with laser energy deposition 1.0 diameter upstream and 0.45 diameters above the centerline axis, one laser pulse (10 Hz) at 283 mJ/pulse, 150 mm focal length lens	225
Figure 5.93 Measured wall heat flux and wall temperature for gauge 8 on Mach 3.45 sphere with Edney Type IV shock impingement and with laser energy deposition 1.0 diameter upstream and 0.45 diameters above the centerline axis, one laser pulse (10 Hz) at 283 mJ/pulse, 150 mm focal length lens	226
Figure 5.94 Measured wall heat flux on Mach 3.45 sphere with Edney Type IV shock impingement and with laser energy deposition 1.0 diameter upstream and 0.45 diameters above the centerline axis, double laser pulse separated by 5 μ s (10 Hz) at 263 mJ/pulse, 150 mm focal length lens	226
Figure 5.95 Measured wall heat flux on Mach 3.45 sphere with Edney Type IV shock impingement and with laser energy deposition 0.6 diameters upstream and 0.2 diameters above the centerline axis, one laser pulse (10 Hz) at 283 mJ/pulse, 150 mm focal length lens	227

Figure 5.96 Measured wall heat flux and wall temperature for gauge 1 on Mach 3.45 sphere with Edney Type IV shock impingement and with laser energy deposition 0.6 diameters upstream and 0.2 diameters above the centerline axis, one laser pulse (10 Hz) at 283 mJ/pulse, 150 mm focal length lens	227
Figure 5.97 Measured wall heat flux and wall temperature for gauge 2 on Mach 3.45 sphere with Edney Type IV shock impingement and with laser energy deposition 0.6 diameters upstream and 0.2 diameters above the centerline axis, one laser pulse (10 Hz) at 283 mJ/pulse, 150 mm focal length lens	228
Figure 5.98 Measured wall heat flux and wall temperature for gauge 3 on Mach 3.45 sphere with Edney Type IV shock impingement and with laser energy deposition 0.6 diameters upstream and 0.2 diameters above the centerline axis, one laser pulse (10 Hz) at 283 mJ/pulse, 150 mm focal length lens	228
Figure 5.99 Measured wall heat flux and wall temperature for gauge 4 on Mach 3.45 sphere with Edney Type IV shock impingement and with laser energy deposition 0.6 diameters upstream and 0.2 diameters above the centerline axis, one laser pulse (10 Hz) at 283 mJ/pulse, 150 mm focal length lens	229
Figure 5.100 Measured wall heat flux and wall temperature for gauge 5 on Mach 3.45 sphere with Edney Type IV shock impingement and with laser energy deposition 0.6 diameters upstream and 0.2 diameters above the centerline axis, one laser pulse (10 Hz) at 283 mJ/pulse, 150 mm focal length lens	229
Figure 5.101 Measured wall heat flux and wall temperature for gauge 6 on Mach 3.45 sphere with Edney Type IV shock impingement and with laser energy deposition 0.6 diameters upstream and 0.2 diameters above the centerline axis, one laser pulse (10 Hz) at 283 mJ/pulse, 150 mm focal length lens	230
Figure 5.102 Measured wall heat flux and wall temperature for gauge 7 on Mach 3.45 sphere with Edney Type IV shock impingement and with laser energy deposition 0.6 diameters upstream and 0.2 diameters above the centerline axis, one laser pulse (10 Hz) at 283 mJ/pulse, 150 mm focal length lens	230

Figure 5.103 Measured wall heat flux and wall temperature for gauge 8 on Mach 3.45 sphere with Edney Type IV shock impingement and with laser energy deposition 0.6 diameters upstream and 0.2 diameters above the centerline axis, one laser pulse (10 Hz) at 283 mJ/pulse, 150 mm focal length lens	231
Figure 5.104 Measured wall heat flux on Mach 3.45 sphere with Edney Type IV shock impingement and with laser energy deposition 0.6 diameters upstream and 0.2 diameters above the centerline axis, double laser pulse separated by 5 μ s (10 Hz) at 263 mJ/pulse, 150 mm focal length lens	231
Figure 5.105 Time integrated heat flux for each of the gauges from small time scale data, 1w1 = single laser pulse 1.0 diameter upstream and 0.45 diameters above centerline, 1w2 = single laser pulse 0.6 diameters upstream and 0.2 diameters above centerline, 2w1 = double laser pulse 1.0 diameter upstream and 0.45 diameters above centerline, and 2w2 = double laser pulse 0.6 diameters upstream and 0.2 diameters above centerline.....	232
Figure 6.1 Energy deposition locations for wedges with span $b = 2.2w$ (image is drawn to scale)	234
Figure 6.2 Energy deposition locations for wedges with span $b = 4.0w$ (image is drawn to scale)	235
Figure 6.3 Instantaneous laser/argon schlieren time sequence of laser energy deposition at 215 mJ/pulse with deposition location $-0.02w$ from leading edge of wedges and $0.25w$ above leading edge for 0, 10, 20, 30, 40, and 50 μ s delays, $2g = 1.14w$, and $b = 2.2w$	241
Figure 6.4 Instantaneous laser/argon schlieren time sequence of laser energy deposition at 215 mJ/pulse with deposition location $-0.02w$ from leading edge of wedges and $0.25w$ above leading edge for 60, 70, 80, 90, 100, and 110 μ s delays, $2g = 1.14w$, and $b = 2.2w$	242
Figure 6.5 Instantaneous laser/argon schlieren time sequence of laser energy deposition at 215 mJ/pulse with deposition location $-0.02w$ from leading edge of wedges and $0.25w$ above leading edge for 120, 130, 140, 160, 180, and 200 μ s delays, $2g = 1.14w$, and $b = 2.2w$	243
Figure 6.6 Instantaneous laser/argon schlieren time sequence of laser energy deposition at 215 mJ/pulse with deposition location $-0.02w$ from leading edge of wedges and $0.25w$ above leading edge for 220 and 300 μ s delays, $2g = 1.14w$, and $b = 2.2w$	244

Figure 6.7 Instantaneous laser/argon schlieren time sequence of laser energy deposition at 105 mJ/pulse with deposition location $-0.02w$ from leading edge of wedges and $0.25w$ above leading edge for 0, 10, 20, 30, 40, and 50 μs delays, $2g = 1.14w$, and $b = 2.2w$	245
Figure 6.8 Instantaneous laser/argon schlieren time sequence of laser energy deposition at 105 mJ/pulse with deposition location $-0.02w$ from leading edge of wedges and $0.25w$ above leading edge for 60, 70, 80, 90, 100, and 110 μs delays, $2g = 1.14w$, and $b = 2.2w$	246
Figure 6.9 Instantaneous laser/argon schlieren time sequence of laser energy deposition at 105 mJ/pulse with deposition location $-0.02w$ from leading edge of wedges and $0.25w$ above leading edge for 120, 130, 140, and 340 μs delays, $2g = 1.14w$, and $b = 2.2w$	247
Figure 6.10 Instantaneous laser/argon schlieren time sequence of laser energy deposition at 215 mJ/pulse with deposition location $-0.05w$ from leading edge of wedges and $0.58w$ above leading edge for 0, 10, 20, 30, 40, and 50 μs delays, $2g = 1.14w$, and $b = 2.2w$	248
Figure 6.11 Instantaneous laser/argon schlieren time sequence of laser energy deposition at 215 mJ/pulse with deposition location $-0.05w$ from leading edge of wedges and $0.58w$ above leading edge for 60, 70, 80, 90, 100, and 110 μs delays, $2g = 1.14w$, and $b = 2.2w$	249
Figure 6.12 Instantaneous laser/argon schlieren time sequence of laser energy deposition at 215 mJ/pulse with deposition location $-0.05w$ from leading edge of wedges and $0.58w$ above leading edge for 120, 140, 160, 180, and 300, μs delays, $2g = 1.14w$, and $b = 2.2w$	250
Figure 6.13 Instantaneous laser/argon schlieren time sequence of laser energy deposition at 215 mJ/pulse with deposition location $-0.02w$ from leading edge of wedges and $0.95w$ above leading edge for 0, 10, 20, 30, 40, and 50 μs delays, $2g = 1.14w$, and $b = 2.2w$	251
Figure 6.14 Instantaneous laser/argon schlieren time sequence of laser energy deposition at 215 mJ/pulse with deposition location $-0.02w$ from leading edge of wedges and $0.95w$ above leading edge for 60, 70, 80, 90, 100, and 110 μs delays, $2g = 1.14w$, and $b = 2.2w$	252
Figure 6.15 Instantaneous laser/argon schlieren time sequence of laser energy deposition at 215 mJ/pulse with deposition location $-0.02w$ from leading edge of wedges and $0.95w$ above leading edge for 120, 130, 160, 180, 200, and 300 μs delays, $2g = 1.14w$, and $b = 2.2w$	253

Figure 6.16 Instantaneous laser/argon schlieren time sequence of laser energy deposition at 215 mJ/pulse with deposition location $-1.31w$ from leading edge of wedges and $0.98w$ above leading edge for 0, 2, 4, 6, 8, and 10 μs delays, $2g = 1.14w$, and $b = 2.2w$	254
Figure 6.17 Instantaneous laser/argon schlieren time sequence of laser energy deposition at 215 mJ/pulse with deposition location $-1.31w$ from leading edge of wedges and $0.98w$ above leading edge for 12, 14, 16, 18, 20, and 22 μs delays, $2g = 1.14w$, and $b = 2.2w$	255
Figure 6.18 Instantaneous laser/argon schlieren time sequence of laser energy deposition at 215 mJ/pulse with deposition location $-1.31w$ from leading edge of wedges and $0.98w$ above leading edge for 24, 26, 30, 40, 50, and 60 μs delays, $2g = 1.14w$, and $b = 2.2w$	256
Figure 6.19 Instantaneous laser/argon schlieren time sequence of laser energy deposition at 215 mJ/pulse with deposition location $-1.31w$ from leading edge of wedges and $0.98w$ above leading edge for 70 μs delay, $2g = 1.14w$, and $b = 2.2w$	257
Figure 6.20 Instantaneous laser/argon schlieren time sequence of laser energy deposition at 215 mJ/pulse with deposition location $0.59w$ from leading edge of wedges and $0.05w$ above leading edge for 0, 20, 40, 60, 80, and 100 μs delays, $2g = 1.14w$, and $b = 2.2w$	258
Figure 6.21 Instantaneous laser/argon schlieren time sequence of laser energy deposition at 215 mJ/pulse with deposition location $0.59w$ from leading edge of wedges and $0.05w$ above leading edge for 120, 140, 160, 180, 200, and 300 μs delays, $2g = 1.14w$, and $b = 2.2w$	259
Figure 6.22 Mach stem heights after laser energy deposition at various locations for symmetric 22° wedges, $2g = 1.14w$ and $b = 2.2w$, the measurement uncertainty of the Mach stem height is $\pm 10\%$ (the position numbers and associated energy levels are noted in the legend and correspond to the numbers given in Figure 6.1)	260
Figure 6.23 Instantaneous laser/argon schlieren time sequence of laser energy deposition at 215 mJ/pulse with deposition location $0.12w$ upstream of leading edge and $0.47w$ above leading edge for 0, 10, 20, 30, 40, and 50 μs delays, $2g = 1.19w$, and $b = 4w$	261
Figure 6.24 Instantaneous laser/argon schlieren time sequence of laser energy deposition at 215 mJ/pulse with deposition location $0.12w$ upstream of leading edge and $0.47w$ above leading edge for 60, 70, 80, 90, 100, and 110 μs delays, $2g = 1.19w$, and $b = 4w$	262

Figure 6.25	Instantaneous laser/argon schlieren time sequence of laser energy deposition at 215 mJ/pulse with deposition location $0.12w$ upstream of leading edge and $0.47w$ above leading edge for 120, 130, 140, 160, 180, and 200 μs delays, $2g = 1.19w$, and $b = 4w$	263
Figure 6.26	Instantaneous laser/argon schlieren time sequence of laser energy deposition at 215 mJ/pulse with deposition location $0.12w$ upstream of leading edge and $0.47w$ above leading edge for 220 μs delay, $2g = 1.19w$, and $b = 4w$	264
Figure 6.27	Instantaneous laser/argon schlieren time sequence of laser energy deposition at 215 mJ/pulse with deposition location $0.23w$ upstream of leading edge and $0.25w$ above leading edge for 120, 130, 140, 160, 180, and 200 μs delays, $2g = 1.19w$, and $b = 4w$	265
Figure 6.28	Experimental and numerical schlieren comparison for laser energy deposition upstream of 22 degree symmetric wedges at Mach 3.45 for time delays of 0 and 10 μs	271
Figure 6.29	Experimental and numerical schlieren comparison for laser energy deposition upstream of 22 degree symmetric wedges at Mach 3.45 for time delays of 20 and 30 μs	272
Figure 6.30	Experimental and numerical schlieren comparison for laser energy deposition upstream of 22 degree symmetric wedges at Mach 3.45 for time delays of 40 and 50 μs	273
Figure 6.31	Experimental and numerical schlieren comparison for laser energy deposition upstream of 22 degree symmetric wedges at Mach 3.45 for time delays of 60 and 70 μs	274
Figure 6.32	Experimental and numerical schlieren comparison for laser energy deposition upstream of 22 degree symmetric wedges at Mach 3.45 for time delays of 80 and 90 μs	275
Figure 6.33	Experimental and numerical schlieren comparison for laser energy deposition upstream of 22 degree symmetric wedges at Mach 3.45 for time delays of 100 and 110 μs	276
Figure 6.34	Experimental and numerical schlieren comparison for laser energy deposition upstream of 22 degree symmetric wedges at Mach 3.45 for time delays of 120 and 130 μs	277
Figure 6.35	Experimental and numerical schlieren comparison for laser energy deposition upstream of 22 degree symmetric wedges at Mach 3.45 for time delays of 140 and 150 μs	278

Figure 6.36 Mach stem height measurements from experimental and numerical simulation schlieren images as a function of time after the laser energy deposition (the uncertainty in the measurements is $\pm 10\%$)	279
Figure 7.1 Schlieren images of electric arc shear layer perturbation in Mach 0.85 jet (top numbers are pulse frequency in kHz and bottom are Strouhal numbers)	286
Figure 7.2 Schlieren images of electric arc shear layer perturbation in Mach 1.38 jet (top numbers are pulse frequency in kHz and bottom are Strouhal numbers)	287
Figure 7.3 Contour plots of three Cartesian velocity components with u - v vector field overlays (the vector fields are plotted with the convective velocity subtracted from the v component) and z -component of vorticity for the Mach 1.38 jet with no perturbation.....	288
Figure 7.4 Contour plots of three Cartesian velocity components with u - v vector field overlays (the vector fields are plotted with the convective velocity subtracted from the v component) and z -component of vorticity for the Mach 1.38 jet with 10kHz 1mJ electric arc perturbation.....	288
Figure 7.5 Schlieren images for increasing time delays (given in μs below each image) after 40 mJ laser excitation pulse in shear layer of Mach 1.38 jet	294
Figure 7.6 Contour plots of three Cartesian velocity components with u - v vector field overlays (the vector fields are plotted with the convective velocity subtracted from the v component) and z -component of vorticity for Mach 1.38 jet 220 μs after a 40 mJ laser spark perturbation	295
Figure 7.7 Comparison of the velocity and z -component of vorticity for laser perturbations of 5, 10, 20, and 40 mJ/pulse at 220 μs (note the convective rate has been subtracted from the v component in the vector field plots).....	296
Figure 7.8 Deformation of jet core due to 40 mJ laser excitation pulse (320 m/s velocity magnitude isosurface)	297
Figure 7.9 Vorticity magnitude in jet 220 μs after 40 mJ laser excitation pulse	298
Figure 7.10 The x -component of vorticity at 220 μs after 40 mJ laser excitation pulse	299
Figure 7.11 The y -component of vorticity at 220 μs after 40 mJ laser excitation pulse	300
Figure 7.12 The z -component of vorticity at 220 μs after 40 mJ laser excitation pulse	301

Figure 7.13 Temporal evolution of the x -component of velocity, u , y -component of velocity, v , and z -component of vorticity, Ω_z , correlated with Mie scattering images and pressure probe data at 100 - 120 μs	302
Figure 7.14 Temporal evolution of the x -component of velocity, u , y -component of velocity, v , and z -component of vorticity, Ω_z , correlated with Mie scattering images and pressure probe data at 140 - 160 μs	303
Figure 7.15 Temporal evolution of the x -component of velocity, u , y -component of velocity, v , and z -component of vorticity, Ω_z , correlated with Mie scattering images and pressure probe data at 180 - 200 μs	304
Figure 7.16 Temporal evolution of the x -component of velocity, u , y -component of velocity, v , and z -component of vorticity, Ω_z , correlated with Mie scattering images and pressure probe data at 220 - 240 μs	305
Figure 7.17 Temporal evolution of the x -component of velocity, u , y -component of velocity, v , and z -component of vorticity, Ω_z , correlated with Mie scattering images and pressure probe data at 260 μs	306
Figure 7.18 Vertical pressure probe (upstream, middle, and downstream) traces and correlation with large-scale structures	307

If there had been any question that the airplane was going to come back in that shape, we never would have flown it.

Jack Kolf
X-15 Project Engineer
Statement on the Oct. 3, 1967 X-15A-2 test flight
[69]

Chapter 1

Introduction

1.1 Motivation

On October 3, 1967, NASA test pilot "Pete" Knight flew the X-15A-2 (see Figure 1.1) to an altitude of 102,700 feet and to Mach 6.7. This flight would set a speed record for a winged-vehicle that would stand until the first orbital return of the Space Shuttle in 1981. [69]

However, this hypersonic test flight of the X-15A-2 was not without incident. Nearly catastrophic damage occurred to the aircraft due to severe aerothermodynamic loading caused by shock impingement. [16, 69, 146, 147] During this test flight, an oblique shock generated from the leading edge of a dummy

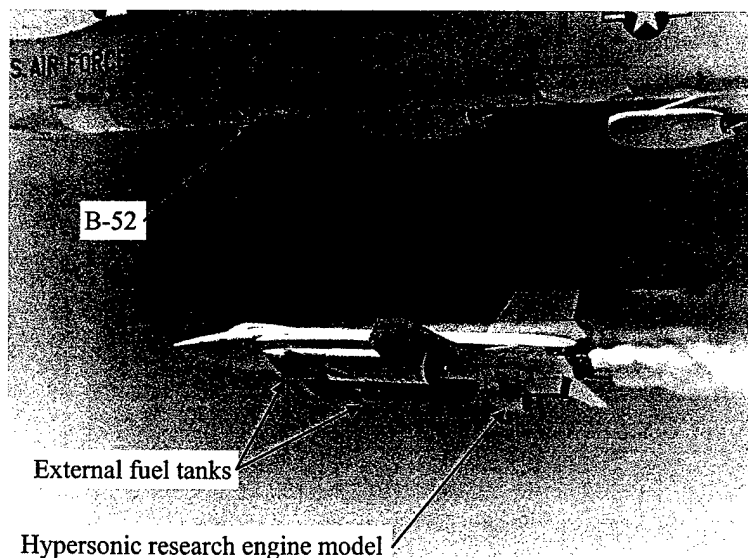


Figure 1.1 X-15A-2 flight test vehicle launch from B-52 aircraft, note the external fuel tanks were jettisoned at Mach 2 (photo courtesy of NASA)

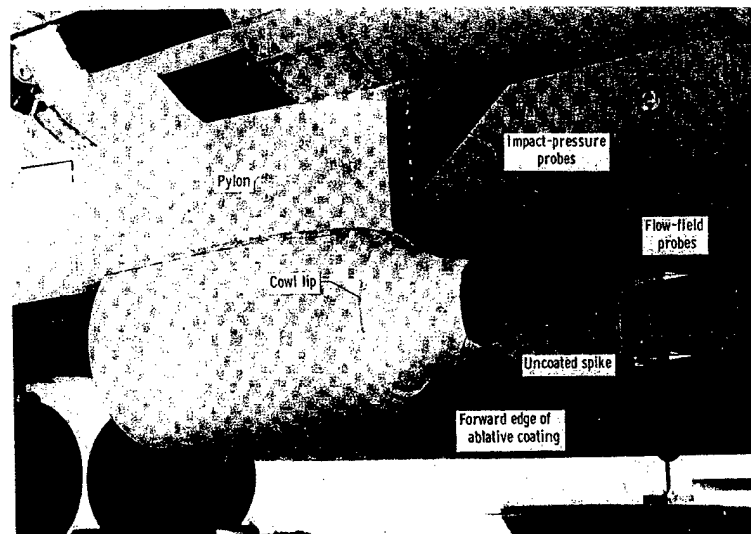


Figure 1.2 Hypersonic research engine dummy model mounted on X-15A-2 ventral fin (photo courtesy of NASA)

hypersonic research engine model (see Figure 1.2) and the main wing leading edge impinged on the model support pylon. The pylon supporting the model was the ventral fin on the bottom of the X-15A-2 (see Figure 1.1). The subsequent Edney Type IV [33] shock/shock interaction (see Section 2.4.1) led to severe burn damage of the pylon skin. This damage occurred approximately 160 seconds into the test flight and completely burned through the Inconel skin (Inconel has a melting temperature of 2800 degrees Fahrenheit). Figure 1.3 shows the severity of the burn damage caused by the shock impingement, and Figure 1.4 shows the flow with shock structures around the vehicle simulated in a subsequent wind tunnel test. [16]

Furthermore, the heat generated by the shock impingement was conducted through the skin and airframe structure, and this heat prematurely set off three of four explosive separation bolts holding the engine model to the ventral fin. The fourth bolt failed prior to landing causing the model to separate from the fin and crash to the ground. The premature firing of the bolts and the separation of the engine model shows how close the X-15A-2 came to in-flight catastrophic failure due to the severe aerothermal loading caused by the shock impingement. Jack Kolf dramatically underscored this proximity with disaster (see quote on page 1).

The resulting burn damage caused by the aerothermal loads encountered on this Mach 6.7 test flight of the X-15A-2 vividly emphasizes the necessity for proper flow control at high speeds. By proper design (body shaping, thermal protection materials, etc.) hypersonic aerospace vehicles would account for severe

aerothermal loading at design conditions. However, there is a need for a *robust* flow control mechanism to handle off design conditions such as gust response or an unplanned maneuver condition. For instance, a vehicle in hypersonic flight might encounter atmospheric gust, respond, and have a flow situation where an off nominal design shock impingement occurred on the aircraft. If there were a system to perturb the flow momentarily to reduce the severity of the aerothermal loading, the survivability of the aircraft would be significantly enhanced. The last pilot to fly the X-15, William Dana, wrote, [28]

The first lesson from the X-15 is to make the airplane robust. ... Examples exist of where the X-15 survived a major stress in spite of operating with a major malfunction.

The *robustness* of the X-15 made it a great test program. The design margins allowed the X-15 not only to overcome severe, unforeseen conditions, but to also be used for a myriad of flight test experiments, not all of which were originally considered by the X-15 designers. [69] Likewise, the *robustness* of future high speed aerospace vehicles will be a critical factor in their survivability, both technically and politically.

More recently, aerothermal loading was identified as a technical issue during the design phases of the National AeroSpace Plane (NASP). [143] Analysis showed the heat transfer rate to the engine inlet cowl to be on the order of $1.2 \times 10^9 \text{ W/m}^2$ when at hypersonic flight conditions and due to a shock/shock interaction at the inlet cowl lip (see Figure 1.6).

As a point of reference, the entire output of a moderate-size nuclear power plant would be required to provide this heating rate to a 1-m² piece of material.

Wie *et al* [143]

This simple analogy gives a feeling for the severity and the extremeness of the aerothermal loading associated with shock impingements. Furthermore, the NATO Research Technology Organization recently studied the shock impingement problem as one of the critical flow phenomena for hypersonic flight. [76, 58, 49]

Energy deposition could be an in-flight mechanism used to mitigate such an extreme pressure and heat load associated with the Edney IV phenomena. For instance, severe aerothermal loads encountered due to unforeseen conditions, such as a pitch up of the vehicle due to gust, could be controlled through energy

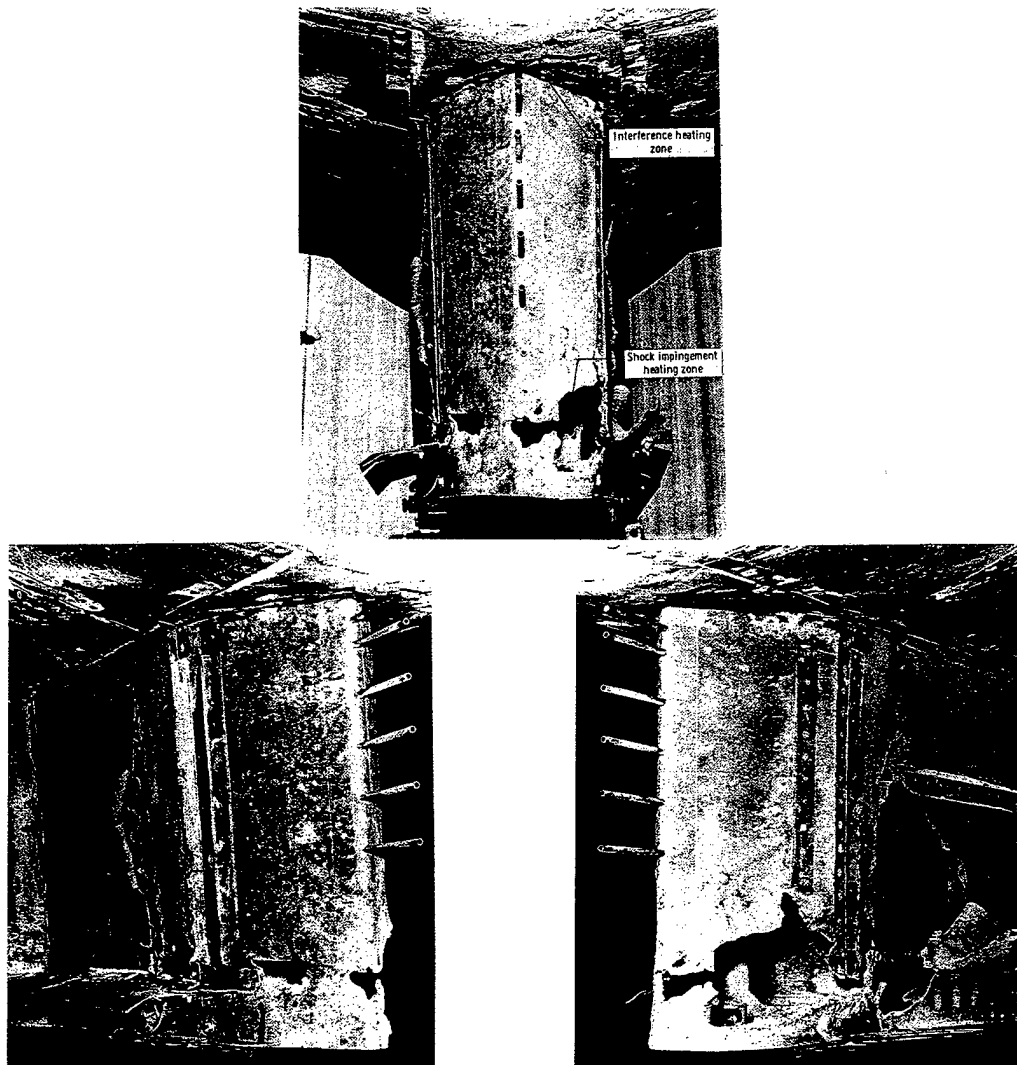


Figure 1.3 X-15A-2 ventral fin shock impingement damage after Mach 6.7 test flight (photos courtesy of NASA)

deposition into the flow. This would be an example of a dynamic, robust, and localized flow control system.

In addition to the extreme aerothermal loads due to shock impingements encountered in high speed flight conditions, other critical engine inlet conditions are encountered on vehicles (see Figure 1.5) operating in the hypersonic flight regime. Two other such critical flow issues are the compression of the air in the engine inlet, and the mixing of the fuel and air for combustion (see Figure 1.6). Because of the critical operation of high speed engines at extreme flight conditions, proper flow control must be carefully taken into account.

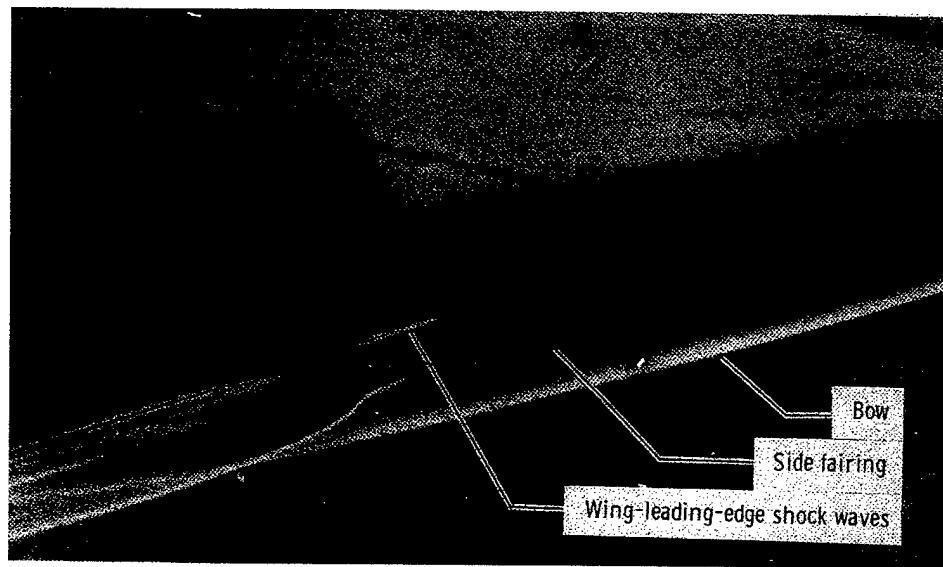


Figure 1.4 X-15 wind tunnel test (photo courtesy of NASA)

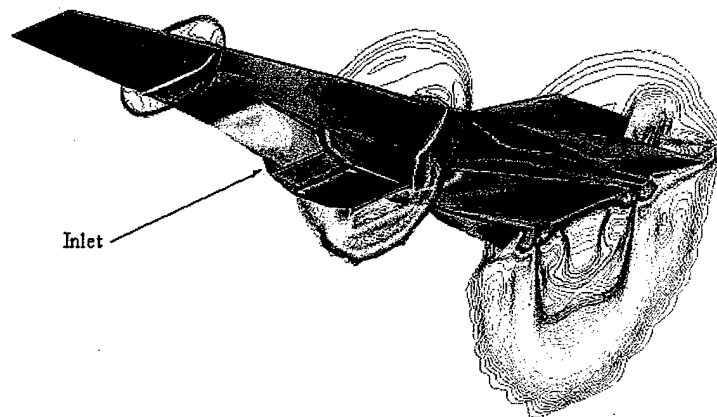


Figure 1.5 Hyper-X (X-43) vehicle (image courtesy of NASA)

Dynamic flow control by energy deposition has recently gained widespread interest. Knight *et al* [77] recently surveyed research efforts where aerodynamic flow control was obtained by energy deposition. They reviewed recent research efforts focused on the possibility of using energy deposition for drag reduction, modification of shock structures, and MHD control.

Researchers [18, 78, 99, 109, 118, 140] have studied the possibility of using energy deposition as a means of global flow control, i.e., drag reduction of a supersonic body by means of energy deposition. On the other hand, energy deposition could also be used to modify localized flow problems. For instance, critical flow areas on a high speed aerospace vehicle such as the X-43 are shown in Figure 1.6. Energy deposition could be used in a localized manner to control the flow about these critical areas.

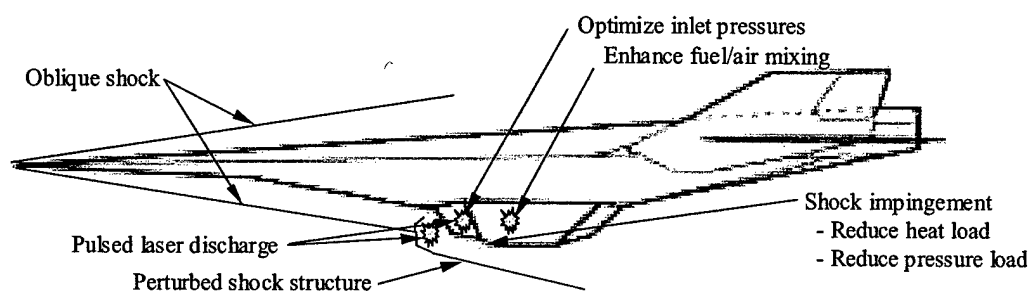


Figure 1.6 Potential flow control areas on high speed aerospace vehicle

High speed aircraft might use shocks to decelerate the flow in the inlet of the vehicle such as the Hyper-X (see Figure 1.5 and Figure 1.6). The ability to control the shock structures is critical to the performance of the engine. For example, at Mach 5 the total pressure downstream of a regular reflection with an incident shock angle of 35° is 4.5 times greater than downstream of a normal shock. The stagnation pressure and the pressure recovery as the flow decelerates through the inlet are critical to the operation of high speed engines. Energy deposition could be used to control the shock structures within the inlet for optimal inlet conditions.

Moreover, fuel/oxidizer mixing through high speed engine chambers is critical for efficient combustion. Enhanced mixing and efficient combustion are necessary for the successful operation of high speed engines. Energy deposition could be used to enhance this fuel/oxidizer mixing process and, therefore, enhance the combustion.

The application of energy deposition for local flow control would require low power in terms of the energy deposition into the flow. These lower power requirements translate to small, low weight energy generation systems, i.e., small lasers with optics or small electric arc units both with their appropriate control systems. Therefore, these smaller systems have real near-term potential applications for localized flow control. In addition, the use of a laser facilitates the ability to modify the flow remotely from a

vehicle. For instance, it would eliminate the need to have electrodes protruding into the flow to induce an electrically generated discharge.

1.2 Research Objectives

Research was undertaken to investigate the potential of using energy deposition for local flow control in the areas highlighted in the previous section. An experimental and computational effort was put forth for this investigation. However, this dissertation focuses mainly on the experimental results. As part of this research effort four flow types were investigated.

First, the laser energy deposition into quiescent air was characterized. The blast wave propagation speed was measured with schlieren and Filtered Rayleigh scattering. Pressure probe measurements were made. Flow geometry parameters of energy deposition volume were measured and energy absorption levels were measured. These measurements were made in an effort to verify and validate the on-going computational modeling development of the laser energy deposition physics.

Second, pressure and heat transfer measurements were made for laser energy deposition upstream of a hemisphere at Mach 3.45 with and without an impinging shock. These tests were completed to assess the effectiveness of using energy deposition to ameliorate the adverse aerothermal loads associated with the Edney Type IV shock/shock interaction upstream of a blunt body. Schlieren flow visualization was used to observe the flow with the laser perturbation and correlate with the surface pressure and heat transfer measurements.

Third, the effectiveness of using energy deposition to control shock structures with bimodal stability was assessed. Laser perturbation was used to control transition from Mach reflection to regular reflection within the dual solution domain for crossing shocks. Schlieren flow visualization was used to visualize the unsteady flow interaction process and compared to Euler computations.

Lastly, large-scale structures were forced in a compressible axisymmetric jet mixing layer with laser perturbation and electric arcing. Particle Image Velocimetry (PIV) data was used to assess the effect on the shear layer and to compare the effectiveness of the laser and electric perturbation methods. Emphasis was placed on determining the effectiveness of enhanced mixing.

The outlay of the chapters in this document follows the four areas above with the exception of chapters 2 and 3. Chapter 2 gives the necessary background information and the results of a literature survey covering the four research efforts. Chapter 3 describes the experimental facilities used to make the measurements. Then Chapters 4 – 7 give the results for the above outlined research areas. Chapter 4 gives the results for laser perturbation in quiescent air. Chapter 5 gives the results for the laser deposition upstream of the hemisphere at Mach 3.45 with and without the shock impingement. Chapter 6 gives the results for the perturbations to the crossing shock structures, and Chapter 7 gives the results of forcing the shear layer with the laser and electric arc. Finally, chapter 8 summarizes the key findings and gives some recommendations on future research and potential applications.

The X-15 was the only aircraft I ever flew where I was glad when the engine quit.

Milton Thompson

Test Pilot

Statement about the accelerations felt during X-15 test flights [28]

Chapter 2

Background and Literature Survey

2.1 Governing Equations

The equations governing a compressible, continuous fluid are briefly outlined in this section. Complete derivations of these equations are not given here but can be found in the literature. [80, 134]

The continuity equation in Cartesian coordinate tensor notation is given by

$$\frac{\partial \rho}{\partial t} + \frac{\partial \rho u_i}{\partial x_i} = 0 \quad (2.1)$$

where $i=1,2,3$, ρ is the density, u_i is the i^{th} velocity component, t is time, and x_i is the Cartesian coordinate. Repeated indices indicate the conventional summation operation unless otherwise noted.

The momentum equation is given by

$$\rho \frac{\partial u_i}{\partial t} + \rho u_j \frac{\partial u_i}{\partial x_j} = -\frac{\partial p}{\partial x_i} + \frac{\partial}{\partial x_j} \left(\mu \left(\frac{\partial u_i}{\partial x_j} + \frac{\partial u_j}{\partial x_i} - \frac{2}{3} \frac{\partial u_k}{\partial x_k} \right) \right) \quad (2.2)$$

where the Stokes' hypothesis is assumed, p is the pressure, and μ is the viscosity coefficient. The viscosity can be defined by the well known Sutherland formula relating viscosity and temperature, T , by

$$\frac{\mu}{\mu_0} = \frac{T_0 + 110.3}{T + 110.3} \left(\frac{T}{T_0} \right)^{3/2} \quad (2.3)$$

where $\mu_0 = 1.789 \times 10^{-5} \frac{\text{kg}}{\text{m} \cdot \text{s}}$ for standard air at $T_0 = 288 \text{ K}$.

The energy equation is given by

$$\rho \frac{\partial}{\partial t} \left(e + \frac{1}{2} V^2 \right) + \rho u_j \frac{\partial}{\partial x_j} \left(e + \frac{1}{2} V^2 \right) = \rho \dot{q} + \frac{\partial}{\partial x_j} \left(k \frac{\partial}{\partial x_j} \right) - \frac{\partial}{\partial x_j} \tau_{ij} u_i \quad (2.4)$$

where e is the internal energy, V is the magnitude of velocity, \dot{q} is the volumetric heating, k is the thermal conductivity, and τ_{ij} is the stress tensor defined by

$$\tau_{ij} = -p \delta_{ij} + \mu \left(\frac{\partial u_i}{\partial x_j} + \frac{\partial u_j}{\partial x_i} - \frac{2}{3} \frac{\partial u_k}{\partial x_k} \right) \quad (2.5)$$

where, as in Equation (2.2), Stokes' hypothesis relating viscosity and bulk viscosity is assumed.

The equation of state for an ideal gas is given by

$$p = \rho R T \quad (2.6)$$

where the gas constant, $R = 286.9 \frac{\text{J}}{\text{kg} \cdot \text{K}}$ for air. The gas constant, R , is related to the specific heats by the relation

$$R = c_p - c_v \quad (2.7)$$

where c_p is the specific heat at constant pressure and c_v is the specific heat at constant volume. Typical

values for air are $c_p = 1005 \frac{\text{J}}{\text{kg} \cdot \text{K}}$ and $c_v = 717.6 \frac{\text{J}}{\text{kg} \cdot \text{K}}$. [72] The ratio of specific heats is defined as

$$\gamma = \frac{c_p}{c_v} \quad (2.8)$$

For a calorically perfect gas, the specific heats are related to the internal energy, e , and the enthalpy, h , by

$$\begin{aligned} e &= c_v T \\ h &= c_p T \end{aligned} \quad (2.9)$$

Following the above equations, the isentropic relations for a gas are given by

$$\frac{T_0}{T} = 1 + \frac{\gamma-1}{2} M^2 \quad (2.10)$$

$$\frac{p_0}{p} = \left(1 + \frac{\gamma-1}{2} M^2 \right)^{\gamma/(\gamma-1)} \quad (2.11)$$

$$\frac{\rho_0}{\rho} = \left(1 + \frac{\gamma-1}{2} M^2 \right)^{1/(\gamma-1)} \quad (2.12)$$

where M is the Mach number, and the subscript 0 indicates the stagnation condition. The Mach number is given by

$$M = \frac{V}{a} \quad (2.13)$$

where a is the speed of sound of the gas and is defined by

$$a^2 = \gamma RT \quad (2.14)$$

The Rankine-Hugoniot relations for a normal shock wave are now summarized. The subscripts 1 and 2 are, respectively, the upstream and downstream conditions. The relations for the pressure, temperature, density, and Mach number upstream and downstream of a normal shock are

$$\frac{p_2}{p_1} = 1 + \frac{2\gamma}{\gamma+1} (M_1^2 - 1) \quad (2.15)$$

$$\frac{T_2}{T_1} = \left(1 + \frac{2\gamma}{\gamma+1} (M_1^2 - 1) \right) \left(\frac{2 + (\gamma-1)M_1^2}{(\gamma+1)M_1^2} \right) \quad (2.16)$$

$$\frac{\rho_2}{\rho_1} = \frac{(\gamma+1)M_1^2}{2 + (\gamma-1)M_1^2} \quad (2.17)$$

$$M_2^2 = \frac{1 + \frac{\gamma-1}{2} M_1^2}{\gamma M_1^2 - \frac{(\gamma-1)}{2}} \quad (2.18)$$

The relations for the Pitot conditions, or the stagnation conditions downstream of the shock, are given by

$$T_{02} = T_{01} \quad (2.19)$$

$$\frac{P_{02}}{P_{01}} = \left(\frac{\gamma + 1}{2\gamma M_1^2 - (\gamma - 1)} \right)^{\gamma/(\gamma-1)} \left(\frac{(\gamma + 1)M_1^2}{(\gamma - 1)M_1^2 + 2} \right)^{\gamma/(\gamma-1)} \quad (2.20)$$

where the subscripts 01 and 02 are the upstream and downstream stagnation conditions, respectively.

These equations are referenced throughout the document and are listed above for convenience.

2.2 Flow Control with Energy Addition

Knight *et al* [77] recently describe the fundamentals of energy deposition into a high speed flow. Neglecting the viscous terms in Equations (2.1), (2.2), and (2.4), the governing equations for energy deposition into a three-dimensional inviscid perfect gas flow become

$$\frac{\partial \rho}{\partial t} + \nabla \cdot \rho \bar{v} = 0 \quad (2.21)$$

$$\frac{\partial \bar{v}}{\partial t} + \bar{v} \cdot \nabla \bar{v} = -\frac{1}{\rho} \nabla p \quad (2.22)$$

$$\frac{\partial T}{\partial t} + \bar{v} \cdot \nabla T = -(\gamma - 1)T \nabla \cdot \bar{v} + \frac{\dot{Q}}{\rho c_v} \quad (2.23)$$

where $\dot{Q} = \rho \dot{q}$ and \dot{Q} is the energy added per unit volume per time, and \dot{q} is the energy added per unit mass per time (same as in Equation (2.4)). The total energy added per unit time is defined as

$$\dot{Q}_t = \iiint \dot{Q} dV. \quad (2.24)$$

Knight *et al* [77] further define the dimensionless energy deposition ratio, ε , as

$$\varepsilon = \frac{M_\infty^2 Q_0 L}{\rho_\infty U_\infty^3} \quad (2.25)$$

where Q_0 is the characteristic value for Q , and L is the characteristic length of the energy deposition region. Thus, Q_0 is defined as

$$Q_0 = \frac{\dot{Q}_t}{L^3}. \quad (2.26)$$

The energy deposition ratio, ε , is a ratio of the energy added per unit time to the static enthalpy flux through the region of energy addition. An alternative formulation for ε is given by

$$\varepsilon = \frac{M_\infty^2 q_0 L}{U_\infty^3} \quad (2.27)$$

where q_0 is defined as

$$q_0 = \frac{Q_t}{\rho_\infty L^3}. \quad (2.28)$$

Lastly, a parameter for unsteady periodic energy deposition is defined as

$$\tau = \frac{U_\infty t_0}{L} \quad (2.29)$$

where t_0 is the period of the energy deposition. The parameter τ is a ratio of the period of the energy pulse to the time of the flow to traverse the region of energy deposition. For more details on various simulations for energy deposition upstream of bodies see Knight *et al* [77]. They review recent research efforts focused on the possibility of using energy deposition for drag reduction, modification of shock structures, and MHD control.

Moreover, research has been done on the use of energy deposition to control the sonic boom problem. [93] Others have considered it for transonic problems, and still others for boundary layer separation problems, [124] boundary layer control, [23] and shear layer perturbation. [1]

2.3 Energy Deposition Techniques

Two types of energy deposition were investigated as a means of local flow control. First, a Nd:YAG laser was focused down to create a laser induced optical breakdown in air. Secondly, electric arcing was used to force structures in an axisymmetric jet in addition to the laser energy deposition forcing.

2.3.1 Laser Induced Optical Breakdown

The deposition of energy into a gas medium with a focused laser beam has been studied since the discovery of a laser-induced spark in 1963. [26, 86, 94] Subsequent research since the discovery has led to an extensive list of publications, and this research has been detailed and summarized quite nicely by Raizer [114, 116], Morgan [97], Root [119], and Smith. [132] The overall process, described in greater detail by both Root and Raizer, starts when a laser beam with sufficient power is focused down, and a sufficient

radiation flux density is achieved, leading to a discharge (somewhat similar to the electric arc discharge). The pressure and temperature of the gas in the region of this discharge will be increased significantly as the energy of the laser is absorbed to cause this so called laser induced optical breakdown. The energy deposition into a gas by a focused laser beam can be described by five progressive steps (see Figure 2.1): 1) initial release of seed electrons by multi-photon ionization, 2) rapid ionization of the gas in the focal region by the cascade release of electrons, 3) absorption and reflection of laser energy by the gaseous plasma, rapid expansion of the plasma and detonation wave formation and propagation up the focal axis, and 4) the propagation of the detonation wave into the surrounding gas and relaxation of focal region plasma, and 5) a residual vortex ring formation [2, 32] due to the asymmetric formation of the plasma.

In step 1) of the breakdown process, the initial release of electrons occur due to a molecule in the focal region taking multi-photon hits, from the laser light, until an electron overcomes its binding potential energy (≈ 14.5 eV for Nitrogen) and is released. Most gases require energy above 10 eV for ionization. Meyerand and Haught describe an experimental technique to determine the radiation threshold of various gases. [90, 91] Multi-photon hits on an atom or molecule in the gas medium are needed because the energy required to release an electron is greater than the energy absorbed by a collision with a single photon hit.

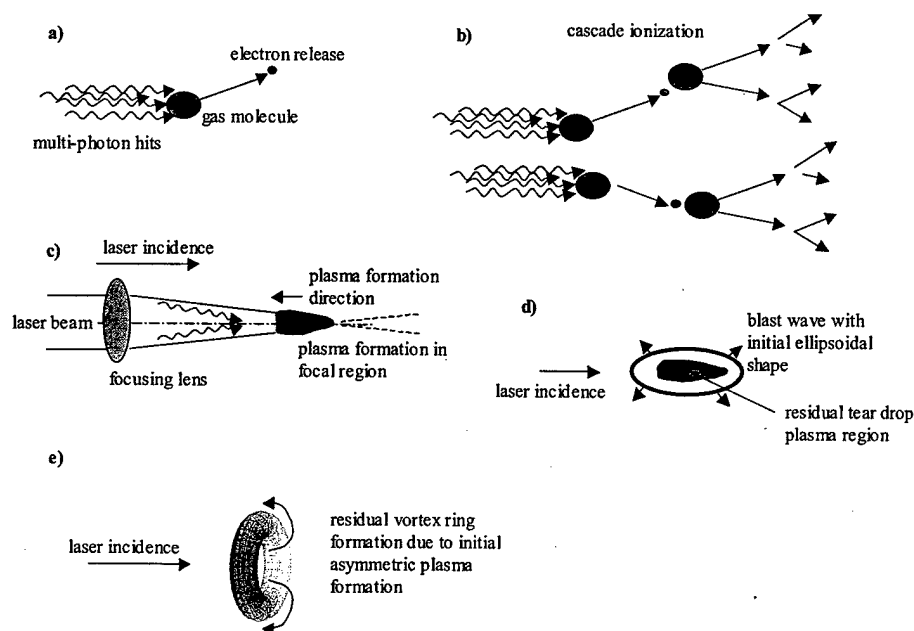


Figure 2.1 Laser induced optical breakdown process

The photon energy, E , is given by

$$E = h\nu \quad (2.30)$$

where h is Planck's constant ($h = 6.626 \times 10^{-34} \text{ J}\cdot\text{s}$ [5]), and ν is the frequency of the radiation. For the Nd:YAG laser with a wavelength of 532 nm, $E = 2.34 \text{ eV}$.

The probability of an electron release by multi-photon hits will not occur unless a threshold of radiation flux density is met. This leads to the necessity of focusing the laser beam diameter down through a lens increasing the radiation flux density to induce the probability of multi-photon hits on an atom or molecule. By focusing the laser beam down, the intensity of light increases over a smaller cross-sectional area, i.e., the increase in radiation flux density. Baravian *et al* [8] determined the probabilities of multi-photon ionization of Nitrogen given a radiation flux density of $2.44 \times 10^{12} \text{ W/m}^2$. Keldysh [73] also estimates the probabilities of multi-photon ionization, and Niemz [100] estimates the threshold dependence on laser pulse duration.

Next in step 2), a cascade release of electrons occurs. Once seed electrons are generated by multi-photon hits, these electrons will collide with other atoms and molecules causing a further release of electrons. The electrons in the field of radiation gain energy due to the inverse bremsstrahlung [44] collisions with photons before and after electrons collide with molecules. [97] This process is the reverse of the bremsstrahlung process [44] whereby electrons emit photons as they slow down. A cascade effect, as multi-photon hits continue in the focal region, and as free electrons collide with other atoms, leads to the cascade release of electrons. The ionization of the gas rapidly takes place at this point and the plasma forms.

The process continues in step 3), as the plasma now absorbs a significant portion of the photon energy of the remaining laser pulse. The plasma becomes more opaque to the light energy of the laser due to the inverse-bremsstrahlung effect in contrast to the transparent nature of the non-plasma gas. Thus, the plasma region will absorb the laser radiation as compared to the non-plasma region. The plasma also propagates up the axis in the direction of incident laser light. This propagation up the laser beam axis leads to an elongated region for the plasma formation. A tear drop shape for the plasma region results. Figure 2.2 contains three CCD images of the flash from a laser spark for three different incident laser energy levels and two different incident beam diameters. All three clearly indicate the elongation of the spark along the

direction of laser incidence. Another phenomena that occurs is that a detonation type wave forms in the rapidly expanding gas, and this wave will also absorb energy as it forms and travels along the axis towards the lens. [119]



Figure 2.2 Pictures of laser sparks in quiescent air for (left) $13 \text{ mJ}/1 \pm 0.5 \text{ mm}^3$, (middle) $127 \text{ mJ}/1.3 \pm 0.7 \text{ mm}^3$, and (right) $258 \text{ mJ}/3 \pm 1 \text{ mm}^3$. Laser incidence is from bottom to top.

In step 4), the laser pulse ends, electron releases cease, and plasma formation subsides. However, a blast wave formed by the formation of the plasma and rapid expansion of gas in the focal region propagates into the surrounding gas. Moreover, the focal region of the laser has been substantially heated leaving behind a region with higher specific internal energy as compared to before the pulse. The pressure has correspondingly increased, and conversely the density due to the expansion and rarefaction process has decreased. At this point we say some of the laser energy has been deposited into the gas. Not all of the laser energy is absorbed. Some of the energy is reflected, transmitted, scattered, and emitted by the plasma. [71]

Finally, in step 5) there is a residual vortex ring formed by the asymmetric formation of the plasma. Adelgren *et al* [2] and Dors *et al* [32] have observed this vortex ring formation by asymmetric plasma formation. Similarly, Svetsov *et al* [137] have experimentally and numerically analyzed the post fluid motion of a laser discharge. Their findings also show a vortex formation due to an initial asymmetry. Jiang, *et al* [70] and Stiener, *et al* [135] have also numerically analyzed laser-induced blast waves. These latter two models mentioned assume a symmetric sphere shape for the initial region. Yan *et al* [150] (see Section 2.3.2) also have developed a spherical laser deposition model. This model is a simplified perfect gas model that neglects the initial plasma formation process. This model is being developed for use in simulations of the laser energy deposition by flow control research effort.

Recently, Kandala and Candler, have modeled the plasma formation process, steps 1-4 above for a Nd:YAG focused laser discharge. [71] Their model solves the conservation (mass, momentum, and energy) equations for twelve species along with a chemical kinetics model. The eleven species in their model are: N_2 , O_2 , NO , N , O , N_2^+ , O_2^+ , NO^+ , O^+ , N^+ , and the electrons.

In addition to discharging the laser in quiescent air, the beam can be focused onto a solid surface. Root [119] describes the laser induced breakdown process when a laser beam is focused on a target surface. When the beam is focused on a target surface, the plasma formation can initiate at a lower radiation flux density, i.e., lower incident beam energy. The laser irradiation incident on surface will generate seed electrons from the target surface for the transient gaseous plasma generation phase as opposed to seed electrons generated by multi-photon ionization of the gaseous molecules. These seed electrons initiate the breakdown and the plasma formation. Moreover, it should also be noted that dust particles in the air, or tracer particles, i.e., PIV aluminum-oxide particles placed in the flow for tracking, can also lower the radiation flux density threshold needed for breakdown. These dust or trace particles will provide seed electrons more readily than gaseous multi-photon ionization. [132]

2.3.2 Spherically Symmetric Laser Perturbation Model

Yan *et al* [150] modeled a laser discharge and assumed an instantaneous perturbation, spherical symmetry, and perfect gas. With these assumptions the laser energy deposition region can be modeled as an instantaneous initial condition defined as

$$\Delta T = \Delta T_0 e^{-r^2/r_0^2} \quad (2.31)$$

where ΔT is the one-dimensional Gaussian temperature distribution, with ΔT_0 being the peak temperature value, and r is the spherical radius coordinate. The peak temperature is determined by the total energy deposited into a spherical volume element given by

$$E = \int_0^{2\pi} \int_0^\pi \int_0^\infty \rho_\infty c_v \Delta T \, r^2 dr \sin \theta \, d\theta \, d\phi, \quad (2.32)$$

and with the peak temperature determined by

$$\Delta T_0 = \frac{E}{\pi^{3/2} r_0^3 \rho_\infty c_v}. \quad (2.33)$$

The width of the distributed temperature profile is determined by r_0 and given as $\frac{R_0}{2}$, where the deposition volume is given by $V = \frac{4}{3}\pi R_0^3$. The deposition volume is estimated from experimental measurement of the energy deposition region. From Equation (2.31) the value for the temperature will reach 2% of the peak value for $r_0 = R_0$. The initial conditions for the density, velocity, temperature, and pressure become

$$\rho = \rho_\infty \quad (2.34)$$

$$u = u_\infty \quad (2.35)$$

$$v = 0 \quad (2.36)$$

$$w = 0 \quad (2.37)$$

$$T = T_\infty + \Delta T \quad (2.38)$$

$$p = \rho RT. \quad (2.39)$$

An initial constant density profile is assumed for the energy deposition region. This assumption is valid due to conservation of mass – there can be no instantaneous mass flux from the region of deposition during the essentially instantaneous laser pulse. The heat addition term, Q , in Equation (2.23) is thereby modeled as a disturbance to the pressure, temperature and density fields, and these in turn are used as an initial condition to the Euler simulation where Q is neglected.

2.3.3 Electric Arc

The more familiar electric arc can also be used as an energy deposition mechanism. In contrast to the laser deposition, the electric arc must have electrodes to generate the plasma region, i.e., arc.

Historically, the electric discharge in a gaseous medium has been characterized by the pressure of the gas, the potential of the electric field between the electrodes, and the amount of current flowing between

these electrodes. The types of gas discharge have been divided into three categories based on the amount of current flow. Currents ranging up to 10^{-6} amperes are dark or Townsend discharges. Glow discharges range from 10^{-6} to 10^{-1} amperes, and arc discharges occur for currents approximately over 10^{-1} amperes. [64, 65, 115]

When an arc discharge occurs between the anode and cathode, plasma formation with increased ion and electron densities takes place in the arc channel within the gas. Various mechanisms, such as thermionic emission from the cathode, ion collisions with the cathode, and radiation induced emissions at the electrodes and in the gaseous gap between the electrodes, can generate electrons for the current flow between the electrodes. Once electrons are present in the gap, they are accelerated by the applied electric field across the gap. As the electrons gain energy they will begin to collide with atoms and molecules of the gas leading to further ionization and more electrons. If there are a sufficient number of collisions, there will be an electron avalanche and rapid ionization of the gas. An electric arc is generated if this avalanche takes place. Electrons and ions gain energy from the electric field across the anode and cathode. Electrons lose energy to collisions with molecules. Pressure and temperature are increased through the acceleration of ions by the electric field. Within the arc channel, the ion temperature can increase up to the order of 10,000 K and the electron temperature can be on the order of 50,000 K. The transient or steady-state nature of the discharge along with the equilibrium or non-equilibrium properties between the electrodes all depend on the gas composition and pressure, the material (and temperatures) of the anode and cathode, the circuitry driving the electric field between the electrodes, external and internal radiation sources, and the presence of any magnetic fields.

Industrially, electric arcs have been used as circuit control devices, light sources, and heat sources. Two prominent arc heat sources are the arc welder and the arc furnace. A typical arc welder uses the high temperatures generated by an electric arc in atmospheric air to melt and join various metals. Industrial arc furnaces use the heat of electric arcs to melt metals for industrial processing. A third heat source application involves the plasma torch used for cutting and material processing.

By controlling these same physical principles mentioned above, the electric arc can be used as an energy deposition source into compressible gas flows. This energy source can then in turn be used as an active flow control mechanism. Recently, Buck and Li [15] experimentally and numerically studied the

effect of an electric spark disturbance in a Mach-3 flow. Likewise, the electric glow discharge has been used for flow control. Glow discharge was used as an active shear layer control by Martens *et al* [87], and Roth *et al* [120, 121] have demonstrated the use of glow discharge for boundary layer control. Likewise, Corke *et al* [23] have used a glow discharge for boundary layer separation control on wing surfaces.

As part of this experimental study, the electric arc energy deposition provides a means of perturbation to an axisymmetric jet shear layer. By controlling the frequency of the electrical arc perturbation, a method of active flow control is demonstrated. As will be shown, the electric arc perturbation can enhance the mixing within the shear layer of a supersonic jet and a comparison is made to laser energy deposition technique.

2.4 Shock Interaction Phenomena

After investigating the effects of laser energy deposition in quiescent air, the effects of energy deposition on three other types of flow phenomena were examined. The first two, involved intersecting shock phenomena. The third flow consisted of electric arc and laser deposition in the compressible shear layer of axisymmetric jets.

2.4.1 Edney Type IV Shock Interaction

We decided to determine the effects of depositing energy upstream of the Edney IV interaction as an example of a detrimental localized flow phenomena where energy deposition might be used as a mitigation flow control technique.

Even though damage due to shock/shock interactions, i.e., the X-15A-2 1967 Mach 6.7 test flight (see 1.1) [146, 147], was observed prior to Edney's 1968 report [33], he was the first to categorize and fully characterize the shock/shock interactions. He studied the effect of an oblique shock interacting with a blunt body shock and developed six categories of interactions (see Figure 2.3). The fourth, known as the Edney Type IV interaction, is the most severe case leading to highly localized regions of surface pressure and heat transfer rates on the body downstream of the interaction. When the oblique shock propagating from an upstream compression turn intersects the bow shock of the blunt body within the sonic region, i.e., the subsonic region behind the bow shock, an Edney Type IV interaction occurs (see Figure 2.4). A supersonic

jet embedded in the subsonic region behind the blunt body bow shock develops and impinges on the blunt body. This impinging, embedded supersonic jet causes high, localized heat transfer regions and high, localized surface pressures on the blunt body. These surface thermal and pressure stresses can be 10 to 20 times greater than stagnation conditions, thus leading to catastrophic failure of the blunt body material, e.g., the X-15A-2 flight test mentioned above. More recently, Yamamoto *et al* [149] have simulated the severity of shock impingement when space-lift booster vehicles are separated during a launch environment. Pandey [103] has simulated the structural response to the severe aerothermal loads associated with shock/shock interactions upstream of an engine cowl.

The Type IV interaction has been studied both numerically and experimentally, [58, 49, 54, 55, 148, 59] and the Type IV shock/shock interaction has been identified as a critical hypersonic flight vehicle design issue. [76] However, no completely successful mitigation scheme has been developed to date. Holden *et al* [56, 57, 101] studied the Type III and IV interactions experimentally and achieved a 10 percent decrease in the peak heating loads with a transpiration cooling technique. Also, Modlin and Colwell [95] develop a heat exchange design to deal with the extreme heat loads generated by the Type IV interaction on a hypersonic aerospace plane engine cowl. In this design, Modlin and Colwell propose using a liquid metal in a heat exchanger inside the body (an inlet cowl in this case) in addition with transpiration cooling techniques. Other researchers have further examined and characterized the shock impingement interactions. Frame and Lewis [40] developed an analytical model for the Type IV interaction in a calorically perfect gas without the requirement of empirical or experimental data. This analytical method is limited to two-dimensional analysis. Lind *et al* [83, 84] and Zhong [154] studied the unsteady behavior of the Type IV interaction with various numerical schemes. Hsu and Parpia [66] added complexity and studied, with numerical simulation, the effect of dual impinging oblique shocks with a bow shock interaction. Hannemann and Schnieder [48] numerically studied the Type III and IV interaction and developed a new classification of Type IVa. Researchers have also extended the experimental analysis since Edney's classic and well organized experimental results. Carl *et al* [17], Purpura *et al* [112], and Pot *et al* [111] measured the characteristics of the interaction experimentally. Lind [82] and Berry *et al* [12] studied the effect of body geometry on the interaction.

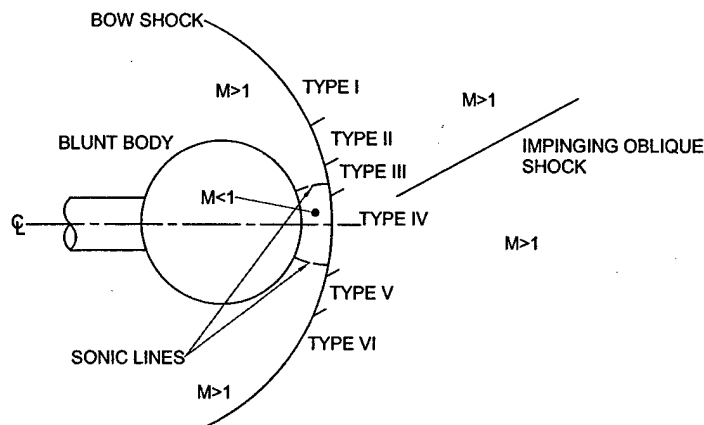


Figure 2.3 Edney's shock/shock interaction classification [33]

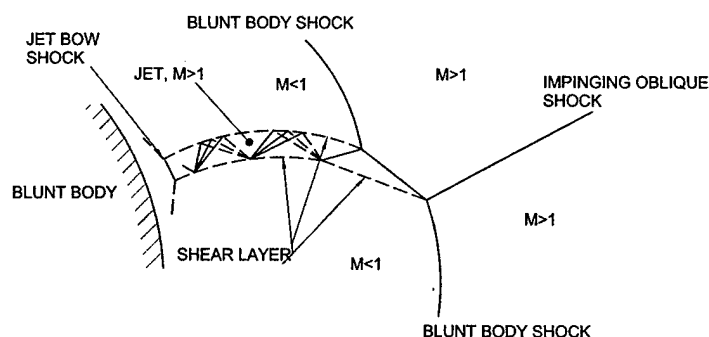


Figure 2.4 Edney Type IV shock/shock interaction [33]

2.4.2 Mach Reflection and Regular Reflection Dual Solution Domain

Another shock/shock interaction phenomena concerns the intersection of two shocks, one a right running wave and the other a left running wave, and the reflected shock structure within what is known as the dual solution domain. J. von Neumann [144] proved the existence of a dual solution domain, defined by the von Neumann angle, α_N , and the detachment angle, α_d . Within these two shock angles, either a regular reflection or a Mach reflection can occur (see Figure 2.5, and Figure 2.7).

The crossing shock interaction is a canonical example of a sidewall compression inlet (see Figure 2.5). An aircraft engine inlet would not be designed to operate in the dual solution domain due where a Mach

reflection could occur. However, due to gust response or vehicle maneuver, the dual solution domain could be encountered for a short time, and any freestream disturbance could lead to a Mach reflection. The ability to control the shock structures is critical to the performance of the engine. For example, as stated in Section 1.1, at Mach 5 the total pressure downstream of a regular reflection with an incident shock angle of 35° is 4.5 times greater than downstream of a normal shock. The losses in total pressure due to a Mach reflection going into the combustion chamber would be severe and could lead to an engine unstart.

Figure 2.6 illustrates the criteria for the regular reflection and the Mach reflection. The boundary for the von Neumann angle occurs where the pressure rise across the primary and reflected shock is equal to the pressure rise across a freestream normal shock. This point is the intersection of the primary shock pressure deflection plot and the reflected shock pressure deflection plot where the flow deflection angle is zero after passing through the reflected shock. Likewise, the boundary for the detachment angle occurs when the pressure rise across the primary shock is too strong for an attached shock when the flow is turned back to a zero flow deflection. The von Neumann and the detachment flow angles, θ_N and θ_D , respectively, are identified in Figure 2.6. Within the boundary set by these two angles, either a Mach reflection or a regular reflection is possible. At Mach numbers below 2.2 the boundary for the von Neumann and the detachment angles coincide. However, at high Mach numbers the dual solution domain is quite large. For example, at Mach 5 and above the dual solution domain spans 10 degrees. Henderson [50] and Hornung and Robinson [63] proved the existence of the dual solution through experimentation.

Hornung *et al* [62] proposed the existence of hysteresis within the dual solution domain, and this phenomena has been confirmed by Ivanov [68], Schmisser and Gaitonde [125], Chpoun *et al* [19], and Vuillon *et al*. [145] Below the von Neumann angle, only regular reflection occurs. If the boundary is slowly approached from below the von Neumann angle, a regular reflection will remain and transition to a Mach reflection at the detachment boundary of the dual solution domain. Above the detachment boundary, only a Mach reflection is possible. If the boundary is slowly approached from above, a Mach reflection will remain until transition to a regular reflection at the von Neumann boundary. Li and Ben-Dor [79] have proposed an analytical model for Mach reflections and regular reflections within the dual solution domain. They also show the existence of a minimum entropy production boundary that coincides with the detachment boundary. Chpoun *et al* [19] also prove the regular reflection solution stability within the dual

solution domain. However, Khotyanovsky *et al* [74] and Molder *et al* [96] have shown the transition of the steady state regular reflection to the Mach reflection within the dual solution domain by freestream disturbances. In addition, Markelov *et al* [88] have studied the effect of boundary effects on the shock structure within the dual solution domain. Moreover, Ivanov *et al* [67] have studied the boundary effects associated with three dimensional wedge span and these effects have been confirmed by Schmisser and Gaitonde [125]. These effects are associated with the variance of Mach stem height along the wedge span due to the Mach wave interaction from the wedge leading edge outer corners. The Mach stem height decreases due to the Mach wave interaction from these corners.

As part of this research effort, laser perturbations were deposited upstream of symmetric shock structures in the dual solution domain. The objective is to better understand the physics of the flow and determine if shock structures can be controlled, whereby, optimal shock structures for optimal engine performance could be positively controlled in high speed inlets.

Figure 2.8 shows the nomenclature associated with the regular reflection shock structure, and Figure 2.9 shows the nomenclature associated with the Mach reflection.

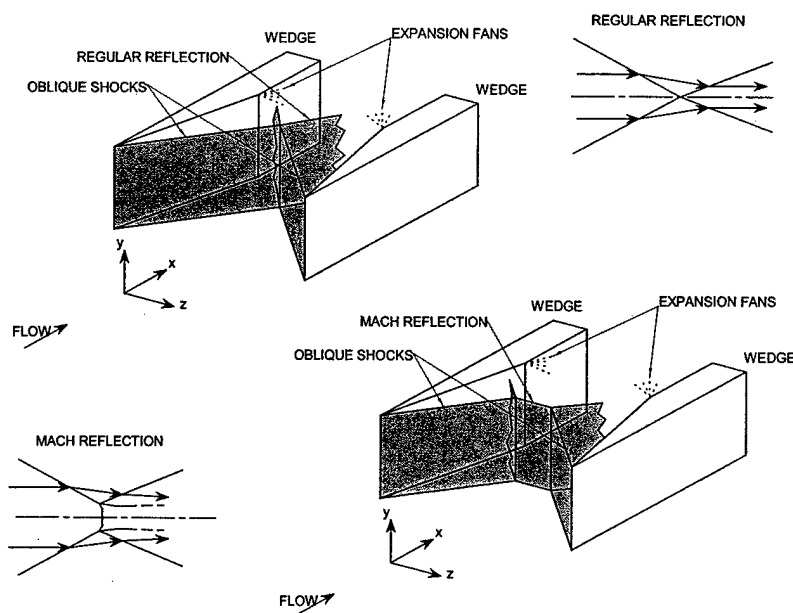


Figure 2.5 Simplified inviscid two fin model

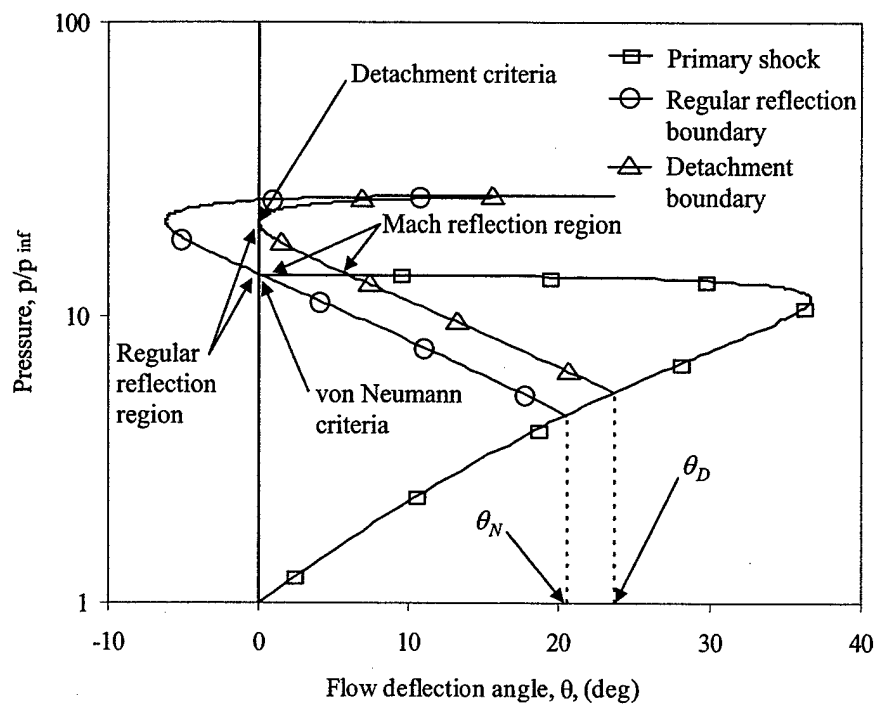


Figure 2.6 Pressure deflection diagram with the von Neumann and detachment angles for Mach 3.45

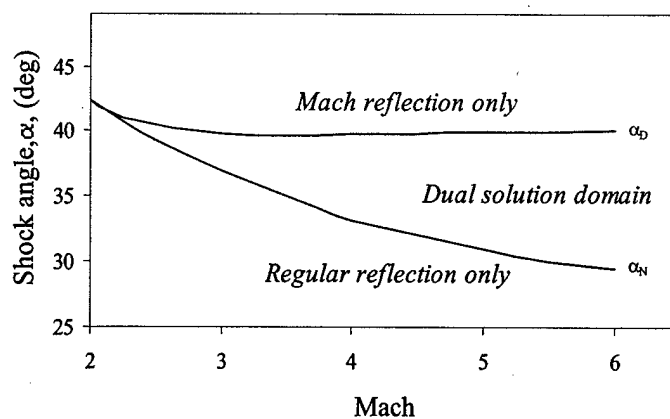


Figure 2.7 Crossing shock dual solution domain

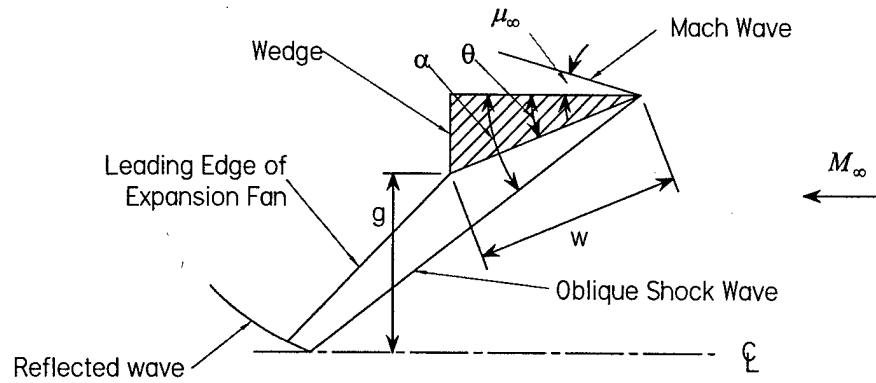


Figure 2.8 Nomenclature associated with the symmetric wedges and regular reflection

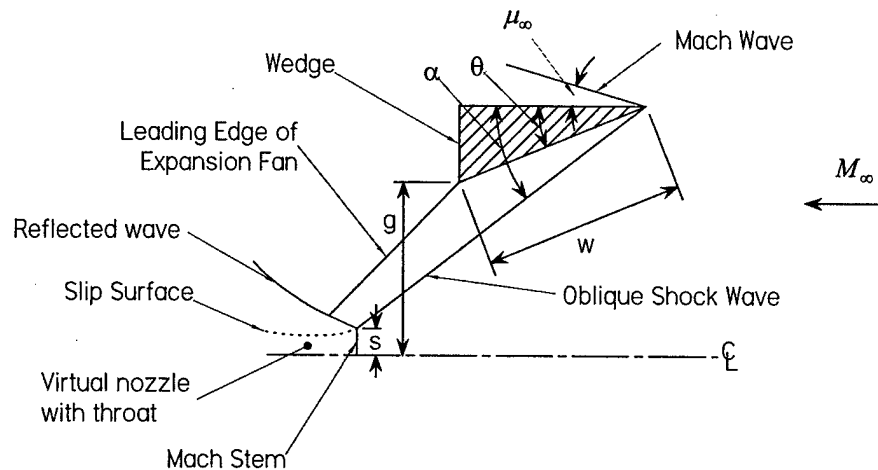


Figure 2.9 Nomenclature associated with the symmetric wedges and Mach reflection

2.5 Compressible Jet Shear Layer

For many years it has been known that supersonic (compressible) mixing layers have a much slower growth rate than their subsonic (incompressible) counter parts. Bogdanoff [13] and Papamoschou [104] provided detailed derivations of a convective velocity and Mach number – based on the differences between the velocities from each of the two streams and the defined convective velocity – and the two speeds of sound. The convective Mach number is given by

$$M_c = \frac{U_1 - U_c}{a_1} \quad (2.40)$$

for mixing layers with the same specific heat ratio, where U_c is given by

$$U_c = \frac{a_1 U_2 + a_2 U_1}{a_1 + a_2} \quad (2.41)$$

Hileman and Samimy [52] correlated acoustic measurements with the turbulent structures of a Mach 1.3 jet. Their measurements postulated the empirical convective equations developed by Murakami and Papamoschou [98] were better suited for determining the convective velocity of the structures. The empirical equations give the convection rates as

$$U_c = -M_{c1} a_1 + U_1, \quad (2.42)$$

$$M_{c1} = M_c + \frac{-dM_c}{\sqrt{1 + (a_1/a_2)^2}}, \text{ and} \quad (2.43)$$

$$dM_c = 1.25 \ln(M_c) + 1.11. \quad (2.44)$$

Papamoschou [105] and Hall *et al* [47] have also modified the convective Mach number relation to take into account recompression shocks which may be present within the shear layer at high compressibility levels.

Flow visualization experiments by Clemens and Mungal in 1992 [21] showed that at $M_c \leq 0.5$, the shear layer contained the two-dimensional structures that are characteristic of the incompressible shear layer. In 1993 Elliott *et al* [38] found that the pairing processes typical of an incompressible shear layer was still occurring at $M_c = 0.51$, but was not seen at $M_c = 0.86$. Other investigators have shown the convective Mach number also correlates trends in the turbulence profiles and shear layer characteristics. [37, 42]

Several recent investigations have shifted attention to the problem of controlling and enhancing the growth rate of supersonic mixing layers, and subsequently, supersonic jets. The ability to force and control the mixing layer not only allows one to study spatially stable large-scale structures, but it is also desirable in numerous applications of interest today. Increased mixing of fuel and oxidizer streams for combustion enhancement is an active area of research. For example, Slessor *et al* [131] experimentally studied the effect of shear layer inflow perturbations on the mixing and growth rates. Day *et al* [29] have analyzed

compressible shear layer flow instabilities where heat was released. Urban *et al* [141] have investigated the velocity fields of a planar compressible mixing layer with induced mixing also with a motivation of enhanced combustion. Another area of research is motivated by noise abatement of turbulent shear layers. [52, 138, 106, 30, 102]

In 1995 Gutmark *et al* [46] wrote a complete review of current control and enhancement techniques. They classified the excitation techniques into three categories: passive excitation, active excitation, and techniques of increasing the streamwise vorticity.

Because of the shortcomings of current control methodologies, there is a desire to develop more flexible and controllable forcing techniques. Shortcomings of current control methodologies are manifested by the fact that most are designed for specific flow conditions and geometries, i.e. fixed Mach number and nozzle configuration. On the other hand, flow control with energy deposition could adapt to changes in flow conditions, such as the Mach number, by adapting the frequency and energy level of the depositions.

As part of this research effort, energy deposition is investigated as a method of enhancing and controlling large-scale structures in the shear layer of axisymmetric jets (see Figure 2.10). Two excitation methods were investigated: a multiple pulse 1 mJ electric arc and a focused pulse from a Nd:YAG laser. Both methods ionize the flow near the nozzle surface (see Figure 2.10), and provide single (laser excitation) or multiple (electric arc) bursts of excitation to the exit of the jet where the shear layer is formed. This energy deposition forces the formation of large-scale structures, and these structures can be studied using modern diagnostic techniques.

Previously, Elliott, Crawford, and Mosedale demonstrated the use of a laser to force a large-scale structure in axisymmetric jets with single [35, 36] and double pulse [24] discharges. The goal of the work presented here is to further characterize the flow field created by an electric arc as well as the laser perturbation to the compressible shear layer in an axisymmetric jet evaluating the turbulence structure and effectiveness of the excitation.

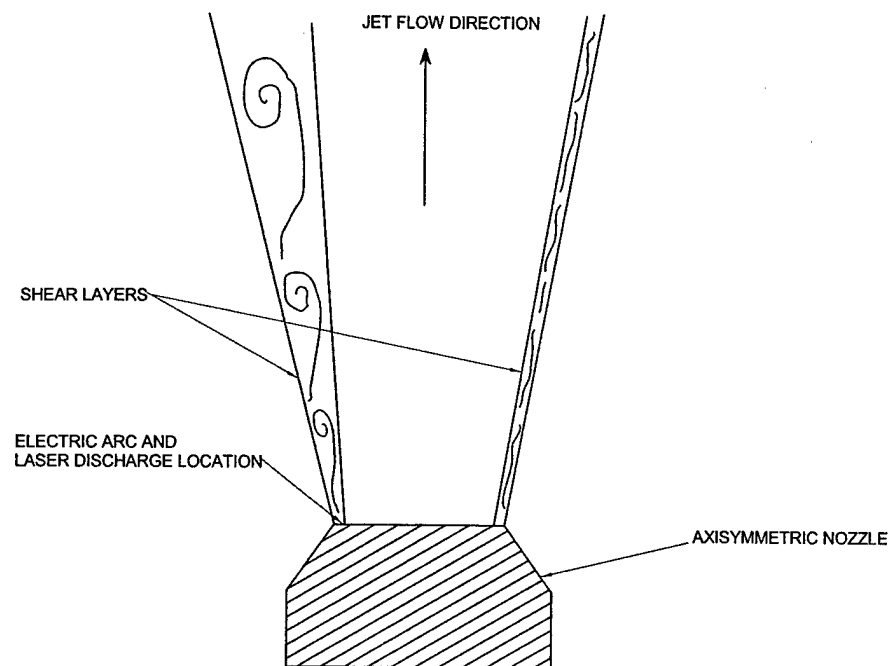


Figure 2.10 Forcing of large-scale structure in compressible axisymmetric shear layer

Chapter 3

Experimental Facilities

3.1 Wind Tunnel

The energy deposition tests upstream of a 25.4 mm diameter sphere with and without the Edney Type IV interaction (see Chapter 5) and the symmetric crossing shock structures in the dual solution domain (see Chapter 6) were conducted in the Rutgers University Mach 3.45 supersonic wind tunnel. Figure 3.1 is a schematic, Figure 3.2 is a picture of this supersonic wind tunnel facility, and Table 3.1 lists the typical operating parameters for this facility. [136] This tunnel is a basic blowdown tunnel with an exhaust into atmospheric pressure. [110] The nozzle of the tunnel is an asymmetric one-sided nozzle that expands the flow to Mach 3.45 in the test section. The test section cross area is 15 cm by 15 cm, has two side windows, and also has windows that can be placed in the top and bottom of the test section. Typically, these windows support optical measurement techniques and access for the laser perturbation experiments (see Chapter 5 and 6).

A main component of the wind tunnel is a compressed air storage system. Compressed air is supplied to the tunnel from high pressure (16.6 MPa) air storage tanks with a total volume of 8 m³ offering run times on the order of minutes to continuous operation for the other smaller facilities within the Gasdynamics lab. Three four-stage air compressors supply the compressed air to these storage tanks after the moisture is removed by a regenerative air dryer.

The tunnel stagnation chamber pressure and temperature data and the atmospheric pressure for the tests are digitally recorded by a computer system. The computer system consists of a Gateway Pentium II computer with a National Instruments PCI-6031 series board. The tunnel data acquisition system is operated with Labview software.

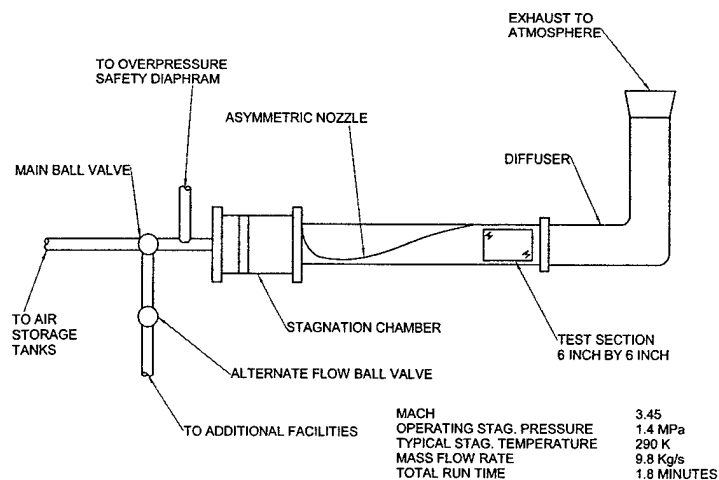


Figure 3.1 Mach 3.45 wind tunnel schematic

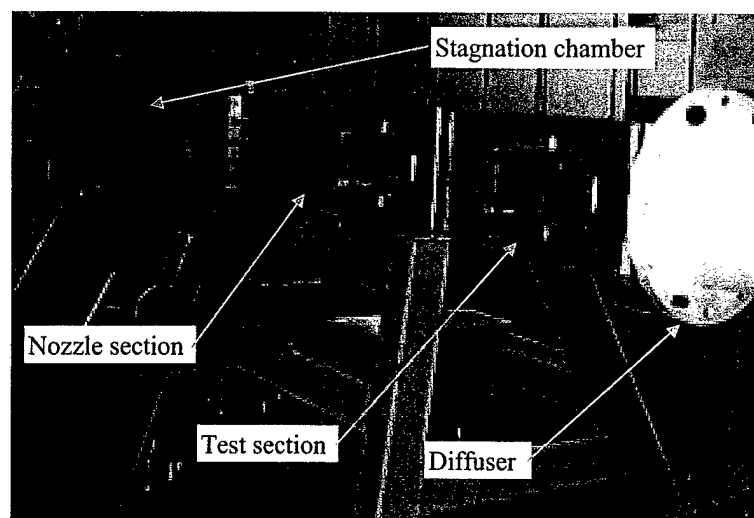


Figure 3.2 Mach 3.45 wind tunnel photo

Table 3.1 Operating Parameters for the Rutgers Mach 3.45 Supersonic Wind Tunnel

Mach Number	3.45
Operating Stagnation Pressure	1.4 MPa
Typical Stagnation Temperature	290 K
Mass Flow Rate	9.8 Kg/s
Typical Run Time	≈ 20 s
Total Run Time	1.8 minutes
Test Area Cross Section	15 cm x 15 cm
Test Area Length	30 cm
Test Section Reynolds Number	$4.44 - 8.88 \times 10^7/m$

3.2 Flow Visualization

Four techniques were used for flow visualization. The shadowgraph and schlieren techniques are discussed in Section 3.2.1, filtered Rayleigh scattering in 3.2.2, and Mie scattering in 3.2.3.

3.2.1 Schlieren and Shadowgraph

The schlieren and shadowgraph techniques are optical methods that determine density fields by changes in the index of refraction within a transparent medium. [43] The changes to the index of refraction within the transparent medium, the compressible gas in our case, is measured by determining the effects on a light beam passed through the test region. The shadowgraph technique measures the second derivative of the index of refraction normal to and integrated along the light beam. The schlieren technique measures the first derivative of the index of refraction normal to the light beam and perpendicular to the knife-edge and is also integrated along the light beam. Both methods are well suited for compressible flows with shock structures due to the high density gradients associated with shock waves.

The density is related to the index of refraction for a transparent medium through the Lorenz-Lorentz relation and the Gladstone-Dale constant. [43] The relation is given by

$$\frac{\rho}{\rho_0} = \frac{n-1}{n_0-1} \quad (3.1)$$

where ρ is the density, ρ_0 is the reference density, n is the index of refraction, and n_0 is the reference index of refraction. Table 3.2 lists values for the index of refraction for air at standard temperature and pressure for two wavelengths of light.

The schlieren system measures the first derivative of the density with respect to the direction perpendicular to the knife-edge and normal to the light beam, and the relation is given by

$$\frac{\partial \rho}{\partial y} = \frac{\rho_0}{n_0-1} \frac{\partial n}{\partial y} \quad (3.2)$$

where y is normal to the light beam and perpendicular to the knife edge. The relation for the shadowgraph is given by

$$\frac{\partial^2 \rho}{\partial y^2} = \frac{\rho_0}{n_0 - 1} \frac{\partial^2 n}{\partial y^2} \quad (3.3)$$

where y in this case is normal to the light path. Equation (3.2) can be related to the intensity changes of light in the image to obtain

$$\frac{\Delta I}{I_K} = \pm \frac{f_2}{a_K n_a} \frac{n_0 - 1}{\rho_0} \int \frac{\partial \rho}{\partial y} dz \quad (3.4)$$

where z is the coordinate along the light path, ΔI is the change in light intensity, I_K is the reduction in image intensity due to the knife edge without any flow disturbances, f_2 is the distance from the mirror to the knife edge, i.e., the focal length of the mirror, a_K is the amount of focal light area not removed by the knife edge, and n_a is the index of refraction for the ambient air. For a shadowgraph system the changes in light intensity become

$$\frac{\Delta I}{I_T} = - \frac{z_{sc}}{n_a} \frac{n_0 - 1}{\rho_0} \int \frac{\partial^2 \rho}{\partial y^2} dz \quad (3.5)$$

where z_{sc} is the distance from the test section to the camera, and I_T is initial intensity at the screen with out disturbances in the flow.

Table 3.2 Index of refraction for air at 20 C and one atmosphere [43]

Light wavelength, λ , (nm)	$n_{air} - 1$
546.1	2.733×10^{-4}
632.8	2.719×10^{-4}

Both the schlieren and the shadowgraph technique are integrals along the light path. Therefore, in this study the schlieren and shadowgraph techniques were used exclusively for qualitative flow visualization and no attempt was made to determine quantitative density, pressure, or temperature measurements. Please see Goldstein [43] for more details on schlieren, shadowgraph, and also interferometer techniques.

The shadowgraph and schlieren images for the Mach 3.45 tunnel tests were taken in the standard Z-path arrangement [43] with 150 mm diameter concave mirrors with a focal length of 2 meters (see Figure 3.3). The images were recorded on a PixelVision back illuminated CCD camera with a resolution of 512 by 512 pixels. Background and flat-field images were taken to correct for uneven illumination and improve the image quality.

A Stanford Research Systems pulse generator is used to control the timing delay between the pulses of the laser used for the energy deposition and the schlieren flash source. This control of the time delay allows for images to be captured for precise delays after the laser spark discharge.

For the images in the initial phase of this research effort, a General Radio Company Stobotac type 1538-A xenon arc flash-lamp provided a light pulse with a temporal pulse width of $2.76 \mu\text{s}$ (see Figure 3.4). This temporal pulse width was measured as the half-peak value recorded with a photodiode. The flow speed in the wind tunnel test section is typically 640 m/s so the typical flow transit during the flash is 1.77 mm .

A new flash source was developed and used for the latter tests discussed in Chapters 4, 5 and 6. A 532 nm wavelength Nd:YAG laser beam was focused down and discharged on a two-percent thoriated tungsten rod in an Argon flow for the schlieren light source. As described previously, a plasma is created above the rod after seed electrons have been generated from the rod. Moreover, Argon has a lower ionization threshold compared to Nitrogen. For example, Minck [94, 114] gives results showing the threshold laser power required to ionize Argon at one atmosphere of pressure is 70 kW , and for Nitrogen at one atmosphere the laser power required is 500 kW . These results are for a Q-switched ruby laser, and, therefore, will differ slightly for the Nd:YAG laser used for this apparatus. In any case, the breakdown and plasma formation will be initiated more readily in the Argon.

This new technique for generating a spark for the schlieren images was found to be superior to the Strobotac flash lamp described above. Figure 3.4 compares the pulse width measured with a photodiode for the Strobotac flash lamp and the laser/argon flash source. The half-peak pulse width for the Nd:YAG discharge in argon is $0.12 \mu\text{s}$ and the flow transit for this time in the test section of the wind tunnel is 0.08 mm . Figure 3.5 is a schematic showing the components of the Nd:YAG laser/argon flash source. Figure 3.6 compares the two flash sources for the schlieren system for a laser discharge in quiescent air next to a 25.4 mm sphere. The obvious improvement in image quality can be seen in the image on the right, taken with the laser/argon light source. The increase in quality is attributable to two aspects: 1) the decreased pulse width of the flash source, and 2) the ability to filter the light emitted from the laser energy deposition spark. The effect of decreasing the pulse width can be seen in the blast wave emanating from the laser discharge. It is much more distinct for the image on the right when compared to the blast wave on the left. Moreover, the flash from the laser spark formation can be filtered from the laser/argon source since the light emitted from the discharge in argon has a

much narrower bandwidth than the Strobotac arc flash. The effect of this filtering can be seen by the near elimination of dark "blotch" seen in the image on the left through the center of the energy deposition discharge location. This darkened region, or "blotch" is due to the shutter of the camera being open during the laser discharge and for the strobe for the schlieren. The light emitted (due to the bremsstrahlung effect during the plasma formation and relaxation) saturates the pixels of the CCD camera in this region. This light cannot be filtered since it has a broader band of frequencies compared to the light emitted by the laser discharge in argon used for the schlieren source. A third benefit also comes from the ability to control the jitter of the light source when it is time synced with the laser discharge. Since the laser/argon spark source is driven by the laser, its time can be controlled within 10 ns to the laser used for the laser energy deposition discharge. The Strobotac light source can only be controlled within 2 μ s when time synced with the discharge laser. Therefore, phase locked images produced by the laser/argon source have three orders of magnitude less variation when compared to phase locked images produced with the Strobotac light source.

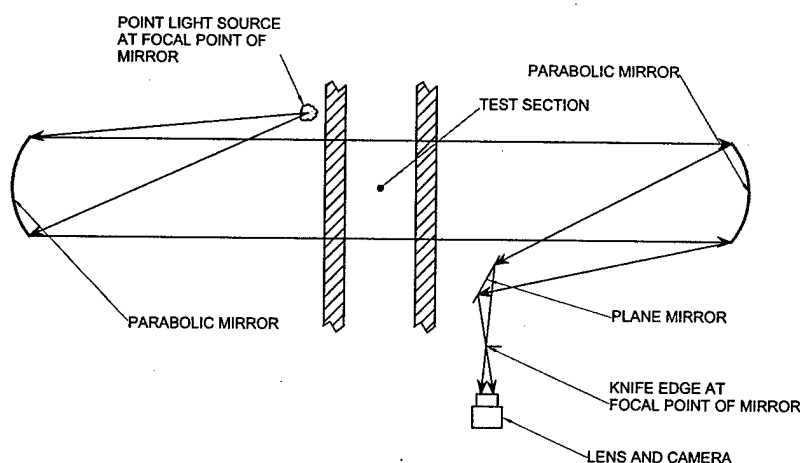


Figure 3.3 Z-path schlieren apparatus

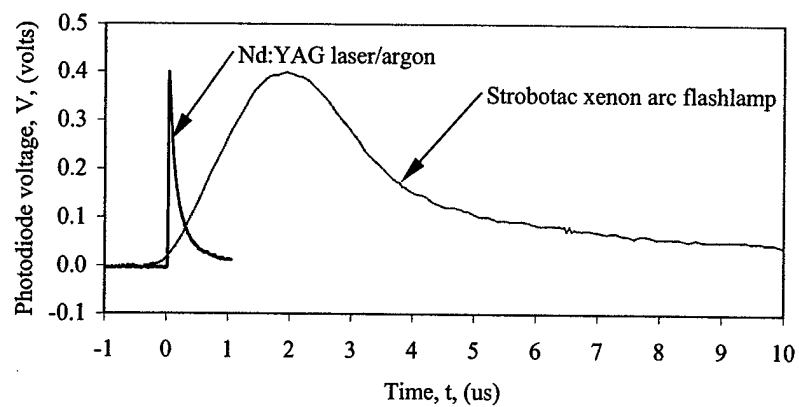


Figure 3.4 Pulse width comparison between Xenon flash lamp and laser-Argon flash

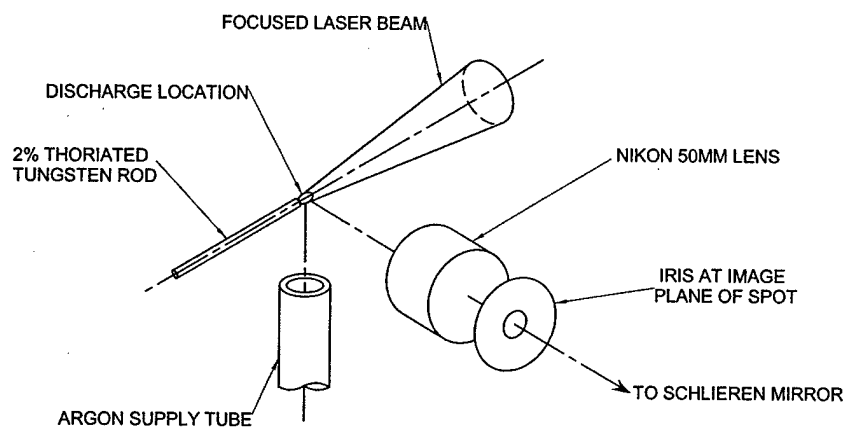


Figure 3.5 Elements of laser-Argon spark source

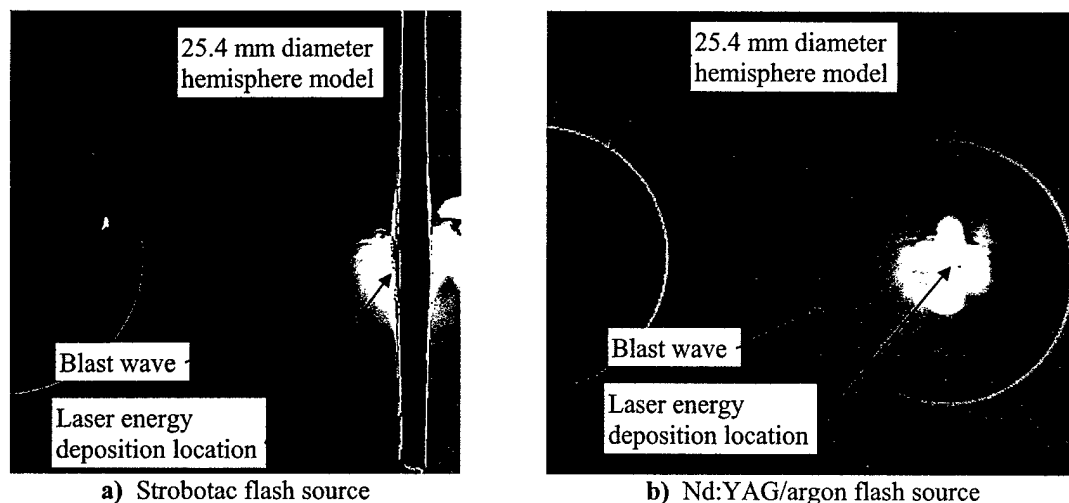


Figure 3.6 Comparison of schlieren flash sources for images taken of laser energy deposition in quiescent air next to 25.4 mm diameter hemisphere model

3.2.2 Filtered Rayleigh Scattering

Rayleigh scattering was used to image the flow for the laser spark deposition tests in quiescent air. Elliott and Beutner [34] and Miles and Lempert [92] give a thorough explanation of this technique. A brief description of the technique is given here.

Rayleigh scattering is the scattering produced when light encounters a particle, and this particle diameter is less than $1/10$ the wavelength of the incident light. The scattering is centered at the particle and is distributed in all directions. For wavelengths of light in the visible range, the Rayleigh scattering produced occurs from air molecules. The intensity of the Rayleigh scattering is proportional to the number of scatter producing particles per unit volume, and is, therefore, related to the density of the gas. The Rayleigh scattering profile is a function of the velocity, pressure, and temperature. The random motion of air molecules causes a broadening of the Rayleigh scattering spectral distribution. There are two parameters which characterize the spectral profile, and they are the x and y parameters. The x parameter is the non-dimensional frequency and the y parameter is the ratio of the collisional frequency to the acoustic spatial frequency. They are given by

$$x = \frac{\lambda |\nu - \nu_0|}{4\mu \sin(\theta/2)} \sqrt{\frac{M}{2kT}} \quad (3.6)$$

$$y = \frac{\lambda p}{4\mu \sin(\theta/2)} \sqrt{\frac{M}{2kT}} \quad (3.7)$$

where λ is the wavelength of the incident light, p is the pressure, μ is the viscosity, θ is the angle between the incident and the scattered wave vectors, M is the molecular mass, k is the Boltzmann constant, T is the temperature, ν is the frequency, and ν_0 is the incoming light frequency. Figure 3.7 shows the distribution for various y values. The frequency of the scattered light can also be Doppler shifted when a bulk velocity component is also present in the gas. The Doppler shifted frequency, ν_D , is given by

$$\nu_D = \frac{1}{\lambda} (\vec{k}_s - \vec{k}_0) \cdot \vec{V} \quad (3.8)$$

where \vec{k}_s and \vec{k}_0 are the observed and incident light wave vectors, and \vec{V} is the flow velocity.

Filtered Rayleigh scattering is the technique of placing a molecular filter with absorption wells located within the frequency range of the imaging laser (see Figure 3.8) in front of the light detecting device, such as the camera. This molecular filter (see Figure 3.11 and Figure 3.12) is placed in front of the receiving optics to modify the frequency spectrum of the scattering signal from the imaged flow region. The imaging laser can be tuned to the absorption wells of the molecule (iodine for these tests) in the filter, and unwanted scattering from walls, windows, etc. is absorbed while the Doppler shifted Rayleigh scattering from molecules in the flow field is shifted and thermally broadened outside the absorption well (see Figure 3.8). If the Doppler shift is small (due to the optical arrangement), planar images are obtained where the intensity is representative of the qualitative density and temperature variations. [14]

Currently, this filtered Rayleigh scattering technique, in addition to giving qualitative images for the density, is being investigated to give average flow properties, such as pressure, velocity, and temperature, at each point in the illuminated plane and also instantaneous flow properties. [14]

For these experiments with the Rayleigh scattering technique, a molecular iodine filter was used with an injection seeded, frequency-doubled Nd:YAG laser with a 532 nm wavelength, capable of 600 mJ per pulse, and a 10 ns pulse width (see Figure 3.9 and Figure 3.10). Since the linewidth of the of the laser is

narrow, it is tuned to match the transition absorption wells of the iodine filter. The laser beam is sent through a cylindrical lens and a spherical lens to produce a planar laser sheet in the flow region of interest. A Princeton Instruments integrated charge couple device camera is used to record the filtered Rayleigh scattering images of the flow region (see also Figure 3.11 and Figure 3.12).

A Stanford Research Systems pulse generator is used to control the timing delay between the pulses of the laser used for the energy deposition and the laser used for the Rayleigh scattering. This control of the time delay allows for images to be captured for precise delays after the laser spark discharge. The images are stored on a Pentium class computer system with Winview control software for the Princeton Instruments camera.

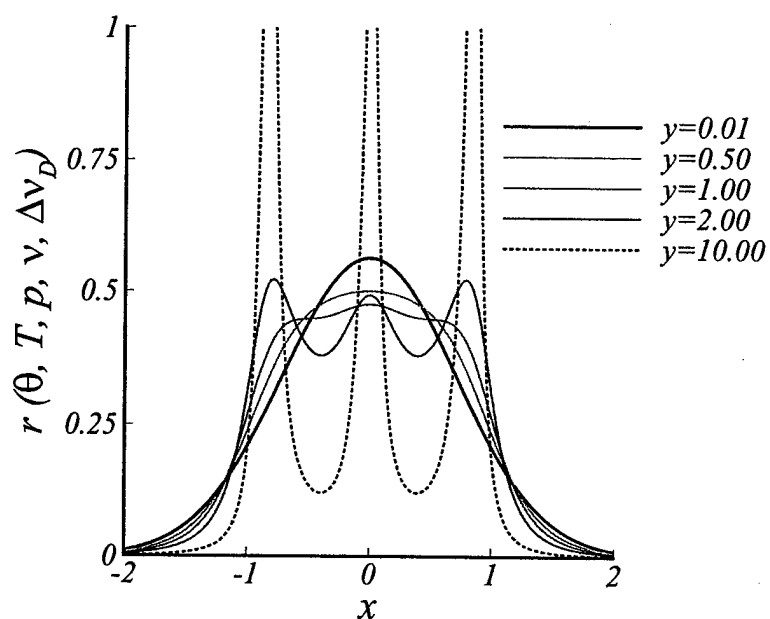


Figure 3.7 Rayleigh scattering distributions for various y values

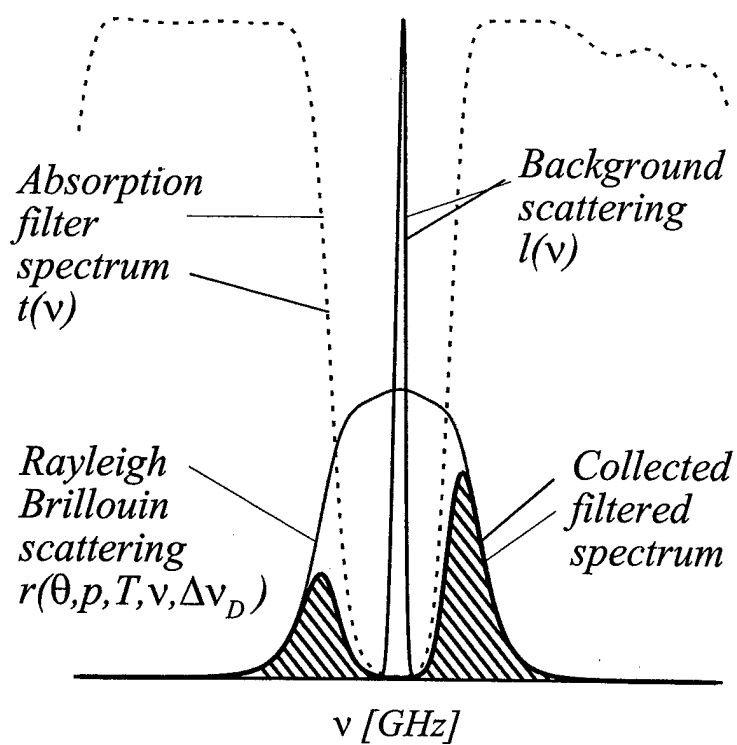


Figure 3.8 Overlapping scattering and absorption bands

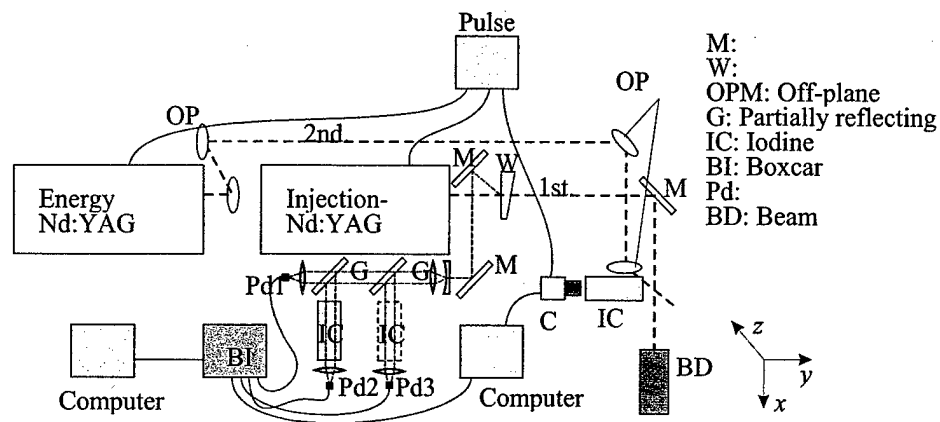


Figure 3.9 Filtered Rayleigh scattering experimental apparatus

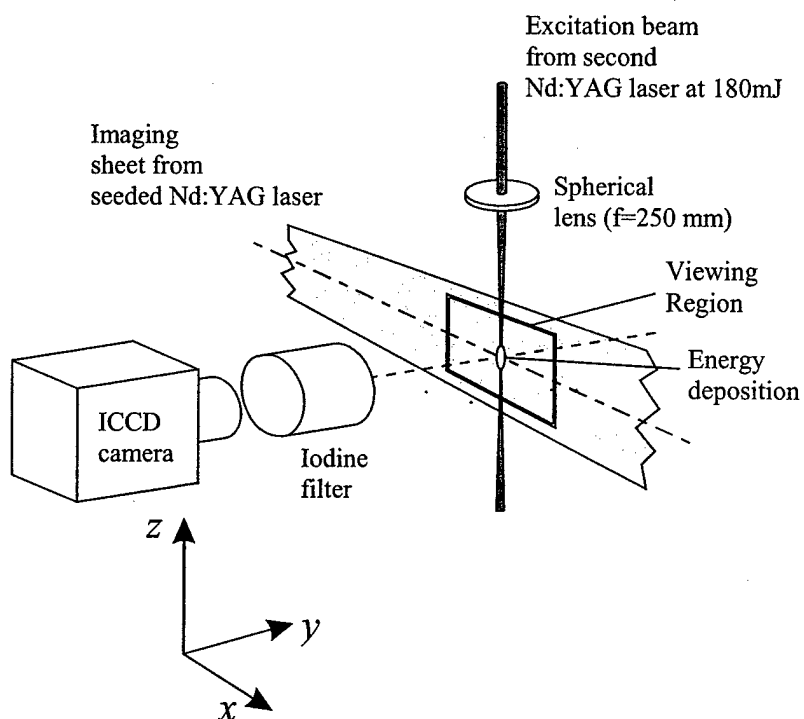


Figure 3.10 Laser sheet and excitation laser orientation for quiescent air energy deposition tests

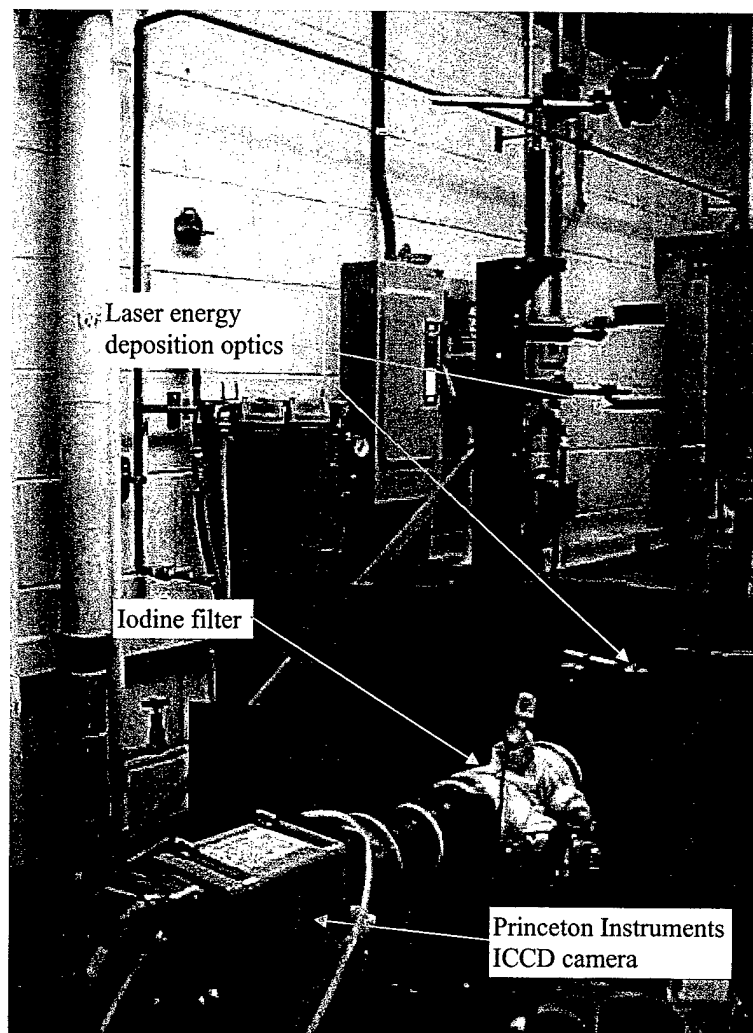


Figure 3.11 Filtered Rayleigh scattering test apparatus; camera, iodine filter, and lens arrangement

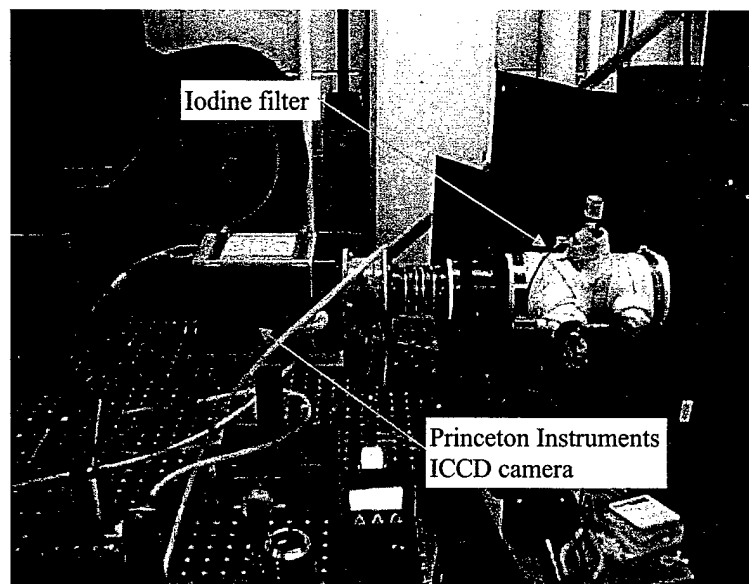


Figure 3.12 Filtered Rayleigh scattering apparatus; camera and iodine filter

3.2.3 Mie Scattering

A planar Mie scattering technique was used to image the laser perturbed shear layer structure of a compressible axisymmetric jet (see Chapter 7). In contrast to the Rayleigh scattering (see Section 3.2.2), Mie scattering is produced when light encounters a particle, and this particle diameter is greater than $1/10$ the wavelength of the incident light. Therefore, Mie scattering typically occurs off of seeded particles, dust, or condensation droplets within the flow. A single pulsed Nd:YAG laser (wavelength of 532 nm) was formed into a sheet at the same location as the double pulsed laser sheet used for the PIV measurements (discussed below in Section 3.9). A Princeton Instruments intensified CCD camera was placed normal to the laser sheet to record the images of the Mie scattering - the laser light scattered from the condensation - produced in the jet shear layer. [21] The jet was exhausted into the moist ambient air, whereby condensation formed in the shear layer due to entrainment of the moist air into the cooler jet flow (see for instance the jet exit temperatures in Table 3.8). For the planar Mie scattering images, the jet was operated without the dry co-flow around the jet nozzle as used for the PIV measurements (see Section 3.9).

3.3 Laser Perturbation

For the laser excitation experiments, a beam from a pulsed Neodymium: Yttrium Aluminum Garnet (Nd:YAG), 532 nm, laser was focused down to create a laser induced optical breakdown in air (see Section 2.3.1). Figure 3.13 shows the Gasdynamic Nd:YAG lasers used for the energy deposition and laser diagnostics. For the laser energy deposition tests into the shear layer of a compressible axisymmetric jet (see Chapter 7), the laser was focused onto the tungsten electrode used for the electric arc experiments so the energy deposition would be located similarly to the electric arc excitation. The Nd:YAG laser could provide only a single pulse, but at much higher energies than capable from the arc. The excitation beam was focused with a 250 mm focal length lens resulting in a focal diameter of approximately less than 0.1 mm. The Nd:YAG laser was frequency doubled to a wavelength of 532 nm with a temporal pulse width of about 10 ns and a repetition rate of 10 Hz. At this pulse frequency each perturbation can be analyzed independently; the pulses are considered as isolated events because the separation distance between pulses in the shear layer is quite large (≈ 25 meters). The amount of energy delivered by the excitation pulse was measured using an Ophir Optonics 30A-P-SH meter. Timing with the flow diagnostics was controlled with a Quantum Composer pulse generator.

Figure 3.10 and Figure 3.11 shows the experimental components used to conduct the energy deposition tests in quiescent air.

The Nd:YAG laser was also used to create the laser energy deposition upstream of the sphere and for the wedges in the wind tunnel (see Chapter 5 and Chapter 6).

For all of the laser energy deposition tests, the laser was pulsed at 10 Hz. The timing of the laser was controlled with a Stanford Research Systems pulse generator used to control the timing delay between the pulses of the laser used for the energy deposition and imaging instrumentation.

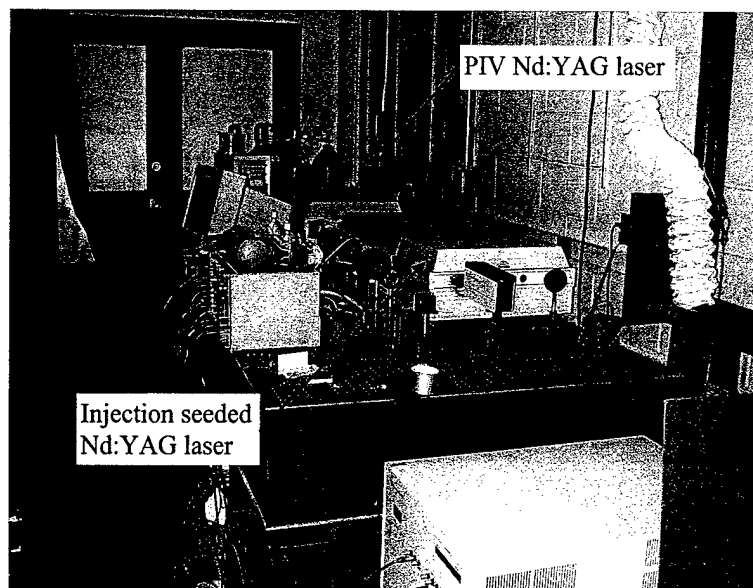


Figure 3.13 Rutgers University Gasdynamics Lab Nd:YAG lasers

3.4 Electric Arc

The arc for the jet experiments was produced using a Velonex Model 360 High Voltage Pulse Generator (HVPG) equipped with a V1728 plugin output unit providing a maximum pulse output of 3 amps at 10 kV. Instead of pulsing continuously at a given frequency, short bursts of pulses were produced to minimize the power needed, but still have a long enough train of pulses so that the flow field could reach "steady state". The HVPG was triggered using an 8013B pulse generator to give a 1 ms burst of 7 μ sec-wide pulses at frequencies from 1 to 18 kHz. The arc was created across a 1 mm gap between the lip of the nozzle exit and a 1 mm diameter, 2% thoriated-tungsten welding rod. A 3.3 kohm resistor is placed in series with the arc to limit the current and match the impedance of the HVPG. The breakdown of the arc occurred at approximately 4 kV on the leading edge of the pulse; the arc voltage reduces to 50 V once the arc is formed. The voltage drop of the arc is determined by the physics of the plasma created, and the current is primarily a function of the power-supply voltage and series resistor. Energy deposition into the arc was approximately 1 mJ/pulse. Table 3.3 summarizes the electric arc characteristics.

Table 3.3 Electric arc characteristics

Pulse Width (μ s)	Energy (mJ)	Current (Amp)	Voltage (volt)	Pulse Frequency (kHz)
7	1	3	50	1-18

3.5 Surface Pressure

An Edney Type IV interaction is generated in the test section by the intersection of an oblique shock generated by a 15 degree wedge mounted on the test section ceiling and the bow shock of the 25.4 mm sphere mounted in the test section. The sphere model contains a pressure transducer used to measure the surface pressure (see Figure 3.14). The sphere model is mounted on a u-joint, and the u-joint in turn is mounted to a sting and splitter plate at the back of the test section (see Figure 3.15 and Figure 3.16).

A single Endevco 8530C-100 pressure transducer is mounted inside the 25.4 mm sphere model behind a 1.32 mm diameter port and at a depth of 1.78 mm from the front of the model's spherical surface (see Figure 3.14). The uncertainty of the recorded pressure measurements is estimated to be ± 0.7 psi, and the pressure data is recorded in 1 μ s increments. The model is vertically rotated by means of the u-joint to position the location of the pressure port. The uncertainty of the angle port position is ± 3 degrees.

The model was mounted such that the Mach cone coming off of the wedge corners did not impact on the sphere model (see Figure 3.17). This positioning of the model was done to minimize any three dimensional effects of the Mach cone's impact on the model.

The electronic leads connected to the transducer are secured to the sting, sting mount, and are taken out along a channel in the sting mount through the top, rear of the test section. The signal from the transducer is conditioned by the Endevco Model 109 Piezoresistive Conditioner. The signal is low pass filtered and read into an HP oscilloscope. The pressure data is digitally recorded from the oscilloscope and stored in ASCII text format. The pressure data was averaged for multiple pressure traces.

Figure 3.18 and Figure 3.19 give the calibration results for the Endevco pressure transducer mounted in the sphere model prior to the shock impingement tests. Likewise, Figure 3.20 - Figure 3.22 give the calibration results for the pressure transducer mounted in the model prior to the laser energy deposition

tests upstream of the sphere without the shock impingement. The calibrations all show the linearity of the Endevco gauges used for the surface pressure tests.

The gauges typically lasted anywhere from one to thirty wind tunnel runs. Particle (dust, paint chips, etc. from the tanks, piping, and stagnation chamber) hits on the gauge during a wind tunnel run destroyed the gauges during the testing. The gauge diaphragm is very delicate and is susceptible to destruction caused by high speed particle impacts. Four gauges were utilized in the test program, and the wind tunnel nozzle area and test section were continually cleaned to eliminate as much particulate matter as possible.

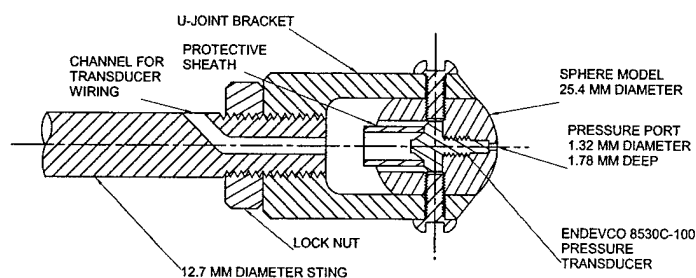


Figure 3.14 Sphere surface pressure model

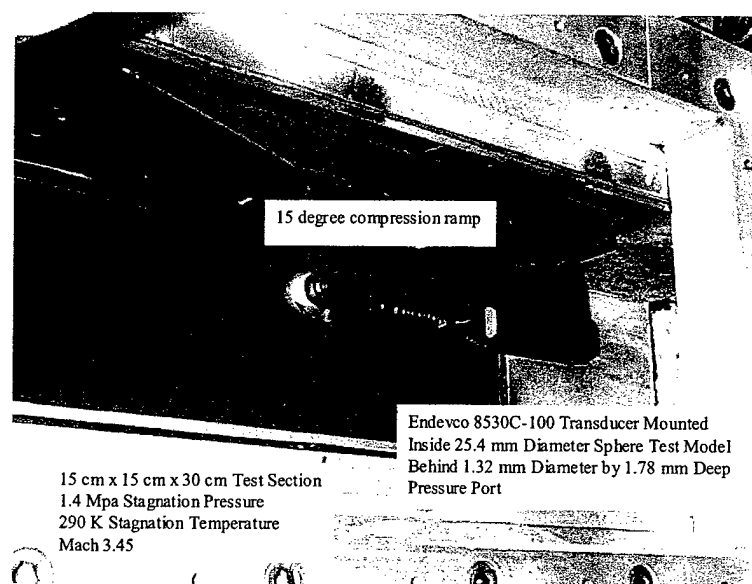


Figure 3.15 Pressure model mounted in wind tunnel

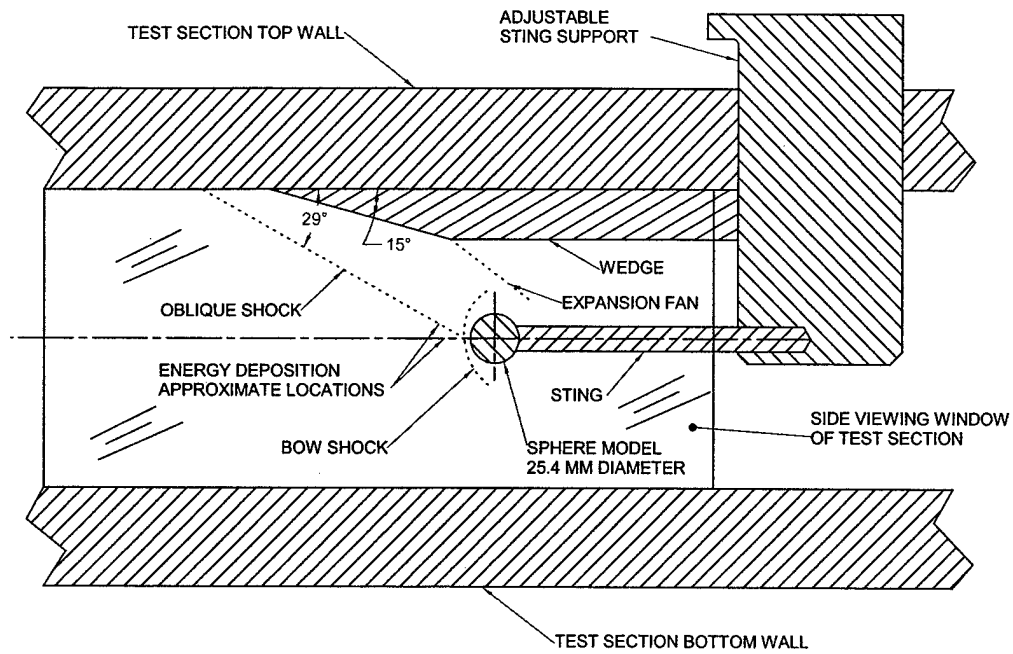


Figure 3.16 Schematic of sphere model, wedge, and approximate energy deposition locations

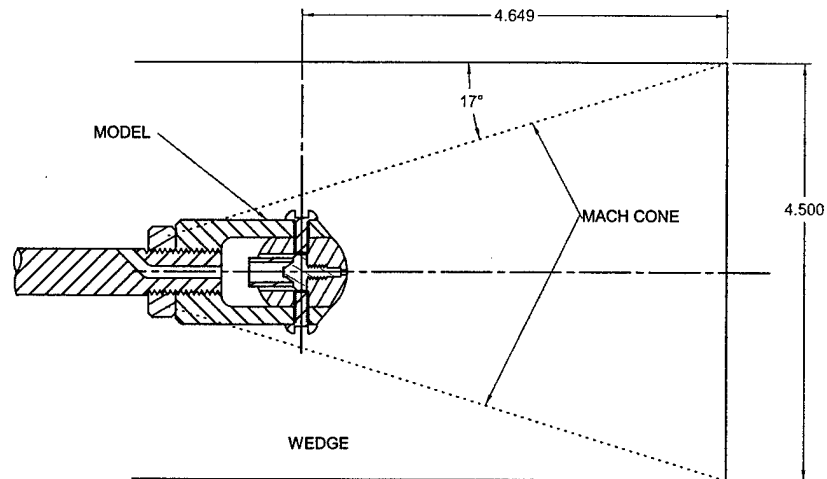


Figure 3.17 Mach cone diagram for three dimensional effects of wedge in tunnel test section (dimensions in inches)

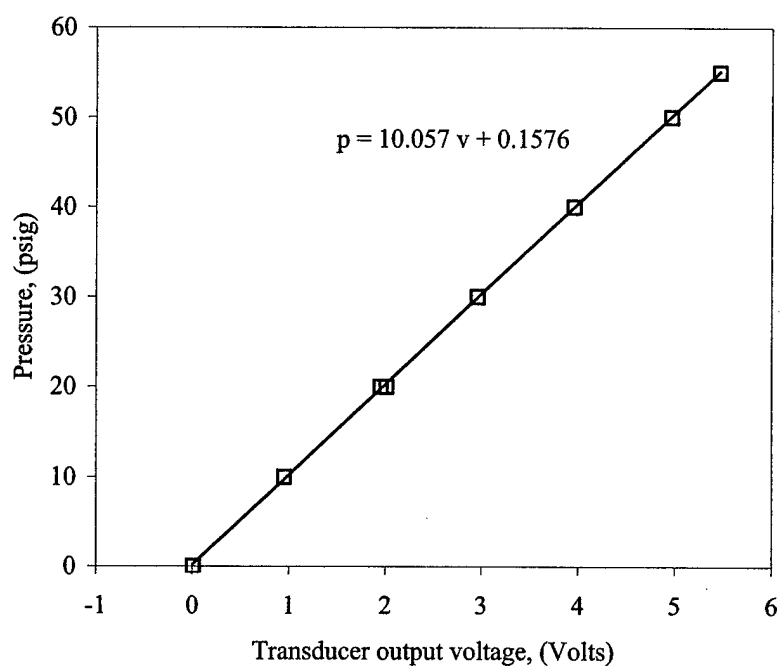


Figure 3.18 Endeveco pressure transducer calibration for 24 Jun 2000 for laser energy deposition upstream of Mach 3.45 sphere with shock impingement tests

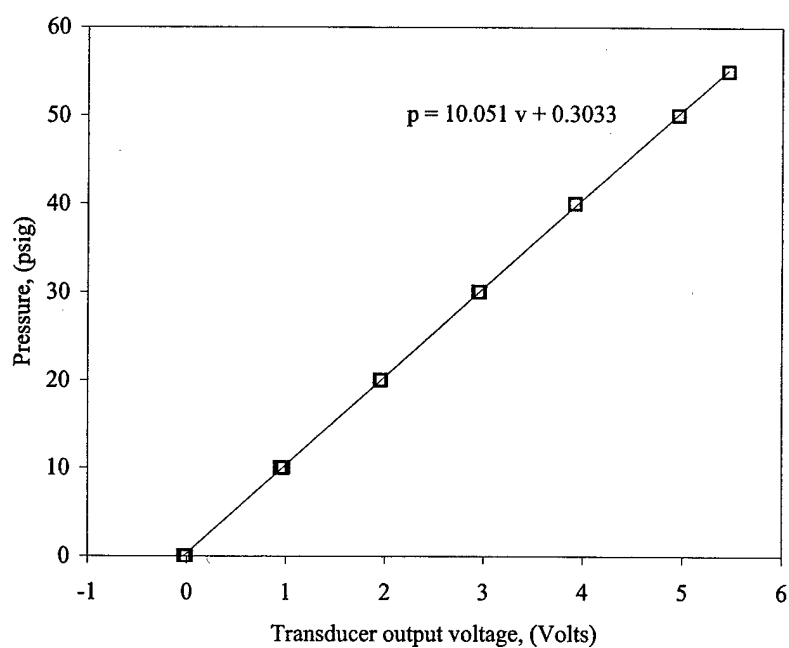


Figure 3.19 Endeveco pressure transducer calibration for 27 Jun 2000 for laser energy deposition upstream of Mach 3.45 sphere with shock impingement tests

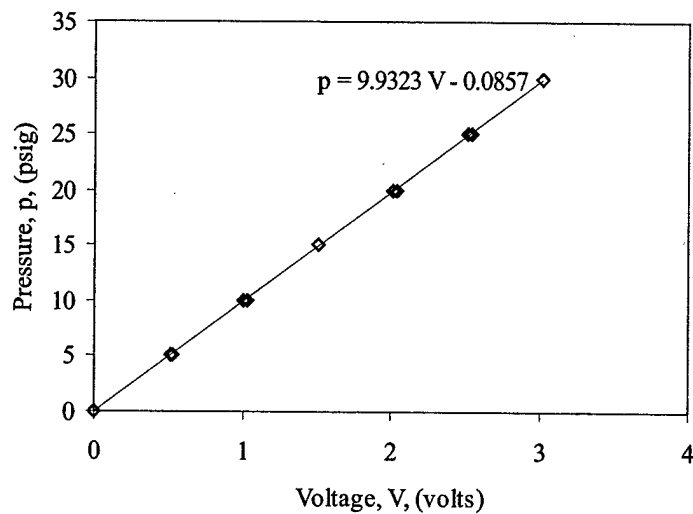


Figure 3.20 Endeeco pressure transducer calibration for the 27 Nov 2000 tests, 258 mJ/pulse laser energy deposition 1.0 diameter upstream of Mach 3.45 sphere without shock impingement

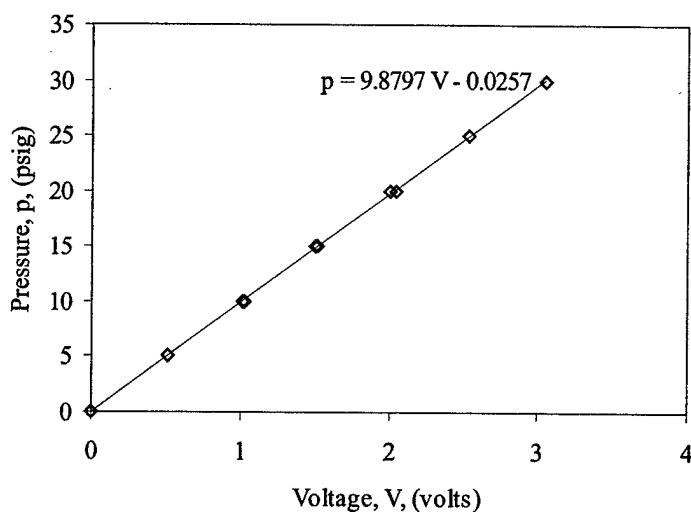


Figure 3.21 Endeeco pressure transducer calibration for the 28 Nov 2000 tests, 127 mJ/pulse laser energy deposition 1.0 diameter upstream of Mach 3.45 sphere without shock impingement

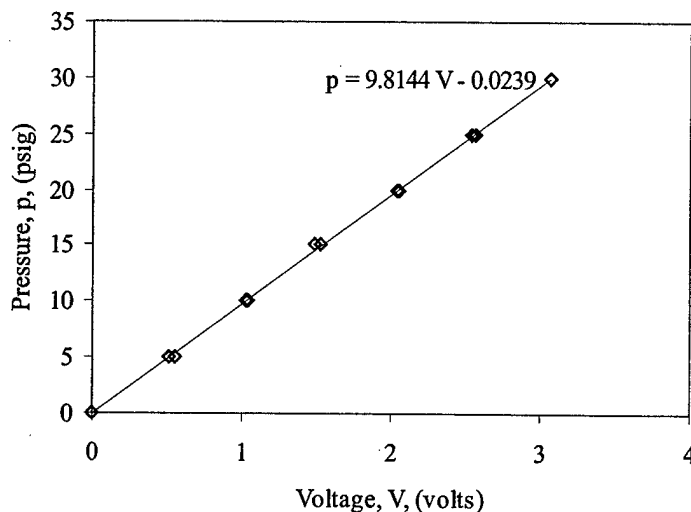


Figure 3.22 Endeveco pressure transducer calibration for the 29 Nov 2000 tests, 13 mJ/pulse laser energy deposition 1.0 diameter upstream of Mach 3.45 sphere without shock impingement

3.6 Surface Heat Transfer

The determination of heat transfer to a body immersed in a compressible fluid is a complex problem. The equations governing the heat transfer involve the fluid dynamic equations and the body heat conduction equations. These equations must be solved in a coupled fashion to determine the heat transfer and temperature profile within the boundary layer and within the body.

However, heat transfer measurements can be made by the use of thin film resistance gauges, thick film calorimeters, surface thermocouples, and embedded differential gauges. The time response for thin film gauges are typically on the order of 10^{-7} seconds, [127] and for thick film calorimeters the time response can be comparable. However, for thick film gauges small heat fluxes cannot be determined. The heat flux can be two orders of magnitude more sensitive for the thin film gauges when compared to the thick film gauges. [127] Another common temperature transducer is the thermocouple. Thermocouples operate on the Seebeck effect due to dissimilar metal junctions. [128] The limitation for using thermocouples is that the Seebeck voltage produced by temperature changes is on the order of microvolts or tens of microvolts. These microvolt signals, especially during measurements of transient temperature fluctuations, are very susceptible to noise. On the other hand, thin film gauges supplied with current in either a potentiometer or

a bridge circuit will produce signals in the tens of millivolts range. These millivolt signals can be further amplified. Thus, the signals from the resistance based thermometers are much less susceptible to external noise when compared to the lower level Seebeck signals of the thermocouples. Thus, the response time, simplicity of construction, and the simplicity of operation, led to the selection of thin film gauges for the heat transfer measurements, and besides, the use of thin film gauges is a proven technique in transient and short duration facilities with operating times of 10 milliseconds and less. [53]

3.6.1 Thin Film Gauge Theory

The basic concept of using metallic films to measure heat flux lies in the physical principle that conducting metals have an electrical resistance that is a function of temperature. The resistance of metallic conductors increases as temperature increases and, conversely, decreases as temperature decreases. This physical phenomena of metallic conductors occurs due to the vibrational excitation dependence on temperature of the atoms in the metallic crystalline structure. [133] As the temperature increases the atoms vibrate more rigorously. As the temperature decreases the atoms vibrate less. Theoretically, if the temperature is decreased to absolute zero, vibration of the atoms cease. The valence electrons in metals are shared with all atoms within the crystal structure (thus, metals are good conductors because of these "free" electrons). If an electrical potential is applied, the electrons have a net drift and a current is established. The principle of electrical resistance comes about due to the collisions of electrons with the atoms in the metallic crystalline structure. These collisions impede the motion, or the net drift, of the electrons. As the atoms vibrate more rigorously, more collisions are mathematically probable, and therein lies the temperature – resistance relationship for metallic conductors. [133] If metals are cooled to temperatures approaching absolute zero, superconductivity is approached (i.e., zero resistivity due to the lower probabilities of electron – atom collisions).

As a side note, semi-conductors behave oppositely. As temperature increases, electrical conductivity *increases*. [133] This phenomena is due to electrons in the valence bonds of the semi-conductor crystalline structure being released as atomic vibrations are increased due to temperature. As opposed to metals, the semi-conductor does not have the free, shared electrons mentioned above. The electrons kicked free from the valence bonds by the increase in atomic vibrations leads to the increase in conductivity for the semi-

conductor material. This is why thermistors (common semi-conductor temperature transducers) have a negative temperature – resistance slope as opposed to the positive slope for metals such as platinum.

The heat transfer measured from thin film gauges assumes heat conduction into a one-dimensional, semi-infinite material (see Figure 3.23). Schultz and Jones [126] give the details of this theory. A brief summary of the methodology is presented here.

The temperature profile in the materials shown in Figure 3.23 is governed by the Fourier heat conduction equation for each region

$$\frac{\partial^2 T_1}{\partial x^2} = \frac{1}{\alpha_1} \frac{\partial T_1}{\partial t} \quad (3.9)$$

$$\frac{\partial^2 T_2}{\partial x^2} = \frac{1}{\alpha_2} \frac{\partial T_2}{\partial t} \quad (3.10)$$

where T is the temperature, α is the thermal diffusivity, x is the one-dimensional spatial coordinate into the material, and t is the time. The boundary conditions are

$$-k \frac{\partial T_1}{\partial x} = \dot{q} \quad \text{at } x = 0 \quad (3.11)$$

$$k_1 \frac{\partial T_1}{\partial x} = k_2 \frac{\partial T_2}{\partial x} \quad \text{at } x = \varepsilon \quad (3.12)$$

$$T_1 = T_2 \quad \text{at } x = \varepsilon \quad (3.13)$$

$$T_2 \rightarrow 0 \quad \text{as } x \rightarrow \infty \quad (3.14)$$

where k is the thermal conductivity, \dot{q} is the heat flux, and ε is the gauge thickness. The initial conditions are

$$T_1 = T_2 = 0 \quad \text{at } t = 0. \quad (3.15)$$

The temperature, T , is a temperature difference referenced to another temperature such as the ambient temperature, or the temperature at the infinite boundary, $x \rightarrow \infty$. Taking the Laplace transform, applying the boundary and initial conditions, and then taking the inverse Laplace transform, the surface temperature and surface heat transfer rate at $x = 0$ become

$$T_s(t) = \frac{1}{\sqrt{\pi} \sqrt{\rho_2 c_2 k_2}} \int_0^t \frac{\dot{q}_s(\tau)}{(t-\tau)} d\tau \quad (3.16)$$

$$\dot{q}_s(t) = \sqrt{\frac{\rho_2 c_2 k_2}{\pi}} \int_0^t \frac{\frac{dT_s(\tau)}{d\tau}}{(t-\tau)^{3/2}} d\tau. \quad (3.17)$$

where the subscript s refers to the condition at the surface. The integral can be integrated by parts to eliminate the derivative term in Equation (3.17). Because of the derivative term, any noise imposed on the signal for T_s will be greatly amplified by the heat flux calculation. Finally, the heat transfer equation is given by

$$\dot{q}_s(t) = \sqrt{\frac{\rho_2 c_2 k_2}{\pi}} \left[\frac{T_s(t)}{\sqrt{t}} + \frac{1}{2} \int_0^t \frac{T_s(t) - T_s(\tau)}{(t-\tau)^{3/2}} d\tau \right] \quad (3.18)$$

where it has been assumed $\varepsilon \rightarrow 0$ for the thin film. This equation can be numerically integrated to obtain the heat flux as a function of time based on discrete measurements for the surface temperature. The equation in numerical form, based on the Cook-Felderman technique, [22] then becomes

$$\dot{q}_s(t_j) = 2 \sqrt{\frac{\rho_2 c_2 k_2}{\pi}} \sum_{i=1}^j \frac{T_s(t_i) - T_s(t_{i-1})}{\sqrt{t_j - t_i} + \sqrt{t_j - t_{i-1}}}. \quad (3.19)$$

Simeonides [129] gives a detailed derivation of Equation (3.19), and a detailed derivation of the above equations for the one dimensional analysis.

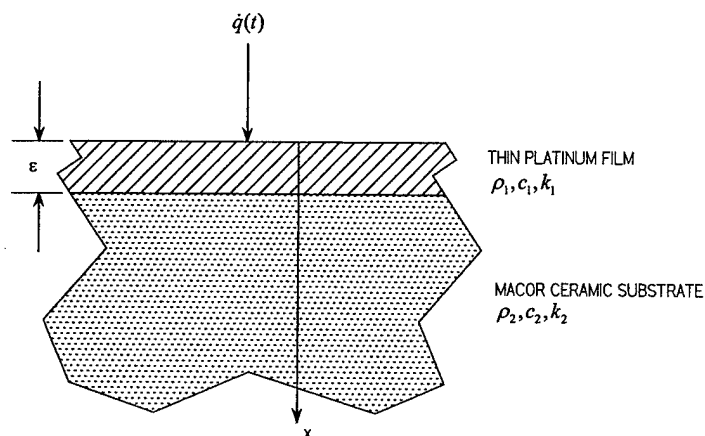


Figure 3.23 One dimensional, semi-infinite heat conduction model

Table 3.4 Thermal properties

Attribute	Units	MACOR	Platinum	Steel
Density, ρ	g/cm^3	2.52	21.45	7.80
Thermal conductivity, k	$\text{W/m}^\circ\text{C}$	1.46	69.1	43
Specific heat, c	$\text{kJ/kg}^\circ\text{C}$	0.79	0.134	0.473
Thermal diffusivity, α	m^2/s	7.33×10^{-7}	2.4×10^{-5}	1.17×10^{-5}

3.6.2 Heat Transfer Model Description

The thin-film heat transfer gauges were constructed by painting and kiln firing thin platinum strips to a MACOR ceramic substrate. Electrical leads connected the gauges to a signal conditioner whereby the resistance changes were transformed to voltages, amplified, and sent to a computer for data logging and analysis.

3.6.2.1 Model Construction

The model material selection process was based on functionality. The most common materials used for the substrate are MACOR, a machinable ceramic, and Pyrex, a high temperature glass. There are two reasons for using a ceramic or a glass material. The first reason is the ceramic is an electrical insulator and will not interfere, or short, the electrically conducting temperature resistance gauge. The second reason for

using the ceramic is the need for a thermally non-conducting material. The one-dimensional and semi-infinite assumptions for the heat flux measurements (see Section 3.6.1) are also a limiting factor for the substrate material. The thermal insulating property of the ceramic or glass maintains the validity of the one-dimensional and semi-infinite assumptions of the theory. MACOR was chosen because of the relative ease for which it can be formed into different shapes by machining. MACOR can be machined similar to low-grade steel. In contrast, Pyrex, or other types of glass, must be either ground and polished, or heated and blown to desired shapes. MACOR also has better strength and crack resistant properties when compared to glass. These characteristics lead to better mounting options for the models in the wind tunnel. For instance, the MACOR models can be drilled and tapped with threads for mounting to the test section sting in the wind tunnel. The knowledge obtained with MACOR will allow for more flexibility in future heat transfer model construction for the Gasdynamics lab.

Platinum was selected for the thin film temperature resistance material. Platinum has the best resistance temperature characteristics compared to other conductor materials such as silver, gold, nickel, steel, copper, etc. [126, 129] Furthermore, platinum is the standard for short duration, shock tunnel facilities. It is also the standard by which other temperature probes are calibrated. [117]. Table 3.4 lists the thermal properties for MACOR, platinum, and, for comparison, steel.

One-inch diameter MACOR rods were machined with a hemisphere nose. A $3/8 - 24 - \text{UNF}$ hole was drilled and tapped in the back of the ceramic rod, and this threaded hole was mated to the wind tunnel sting. A 0.1 inch port was drilled into the center of the rod at the back of the hemisphere to mount a K-type thermocouple to monitor the internal substrate temperature during the tunnel tests. This internal temperature was measured to validate the semi-infinite temperature boundary condition. The surface of the hemisphere was polished. The surface was inspected with a microscope and no visible scratches were observed prior to the application of the platinum gauges and silver contact leads.

The metallo-organic (Englehard Liquid Bright Platinum 05X) platinum paint for the gauges was applied with one stroke of a 10/0 Sable brush. The widths of the platinum gauges were approximately 0.6 mm and the length approximately 2 mm. The thickness of the gauges was estimated to be approximately $1 \mu\text{m}$, similar to gauges used in other research facilities. [81, 75]

After the metallo-organic platinum was painted, they were allowed to dry under a heat lamp for 10 minutes. Next, the substrate and gages were fired in a kiln. The Fast-glaze program was used with a setting of Cone-21. A pre-heat time of 30 minutes and hold time of 30 minutes was found to work best for firing the platinum gauges and silver leads. The firing time was about 5 hours and 20 minutes (depending on the starting ambient temperature), and the maximum temperature at the hold time was 1112 F. The top vent hole in the side of the kiln was left open to allow the metallo-organic solvent vapors to vent off during the firing. After the firing program had completed, the gauges were left in the oven for another 5 to 6 hours to allow the gauges to cool slowly without quenching. If the gauges are quenched, the metallic gauges, leads, and MACOR can crack. The slow cooling process also allows the gauges and substrates to relieve internal stresses.

Silver contact leads were painted on the MACOR to provide contact to the platinum gauges. Metallo-organic silver A2282 paint was used. The silver leads were fired with the same temperature-time profile as for the platinum.

Wire-wrap 30 gage leads were connected to the silver contacts with CircuitWorks CW2400 silver loaded epoxy. Prior to epoxying the leads to the silver contacts, the wire was tacked in place with CircuitWorks CW 4300 Quick-Bond Gel and Adhesive. Shielded 24-gauge, 7 strand, Belden cable, in turn, was soldered to the 30 gage leads. There are two reasons for using the multi-strand cabling. First, the multi-strand cable provides more conductor surface area. For metallic conductors, the high frequency signal is carried at the surface. Therefore, for the optimal transmission of high frequency signals, conductors with maximum surface area should be used. Thus, multi-strand cabling should be used for high frequency signal transmission. Second, the multi-strand cabling can have smaller radius bends when compared to the single strand cabling. This "tighter bending" gives more flexibility for running the transmission cables from the test section to the signal conditioner. The shielded cable was then brought to the custom-built signal conditioner (see Section 3.6.2.2). The cable shielding was grounded to the signal conditioner through the 9-pin standard serial connector. The silver leads were over coated with CircuitWorks Overcoat CW3300C to provide some abrasion resistance protection for the silver contacts. No overcoat was applied to the platinum and the silver contacts across the hemisphere surface to minimize any unnecessary distortion to the spherical surface. Non-conductive epoxy was applied over the contact

area to protect the cabling from flow environment of the wind tunnel. Moreover, the shielded cabling was epoxied to the sting and splitter plate to protect the cabling in the test section. The cables along the sting were also wrapped with copper tape to provide additional electrical shielding.

Loops in the cabling were kept to a minimum, and twisted cabling was used to minimize the noise pick up from external sources. [27] A minimum of length of cabling was also used from the gauge to the signal conditioner to minimize the noise from external sources and the loss of signal due to low voltage transmission losses.

Figure 3.24 shows the eight gauge model mounted in the test section with the compression ramp used to generate the impinging shock. Figure 3.25 is a close up view of the model mounted in the test section. A k-type thermocouple was also epoxied into the center of the sphere to monitor the temperature of the inside of the sphere during the wind tunnel testing. This temperature was needed to verify the semi-infinite theory for the gauges (see Section 3.6.1).

The eight gauge model was mounted in the tunnel such that the gauges were in the vertical symmetry plane for the hemisphere. Table 3.1 lists the angle locations for the gauges.

Table 3.5 Gauge locations for eight gauge model

Gauge number	Angle (degrees from horizontal)
1	0.0 ± 1.7
2	5.7 ± 1.7
3	11.1 ± 1.7
4	16.9 ± 1.7
5	23.2 ± 1.7
6	29.6 ± 1.7
7	36.1 ± 1.7
8	42.2 ± 1.7

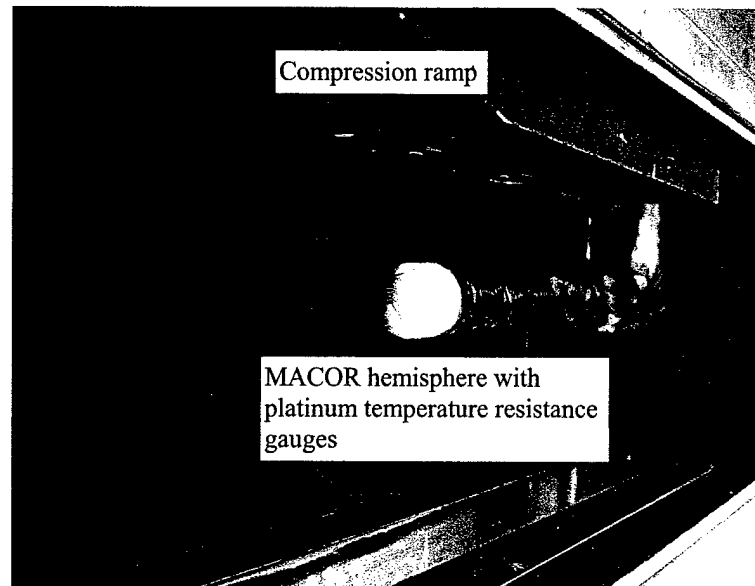


Figure 3.24 Eight gauge heat transfer hemisphere model mounted in wind tunnel test section with shock impingement ramp

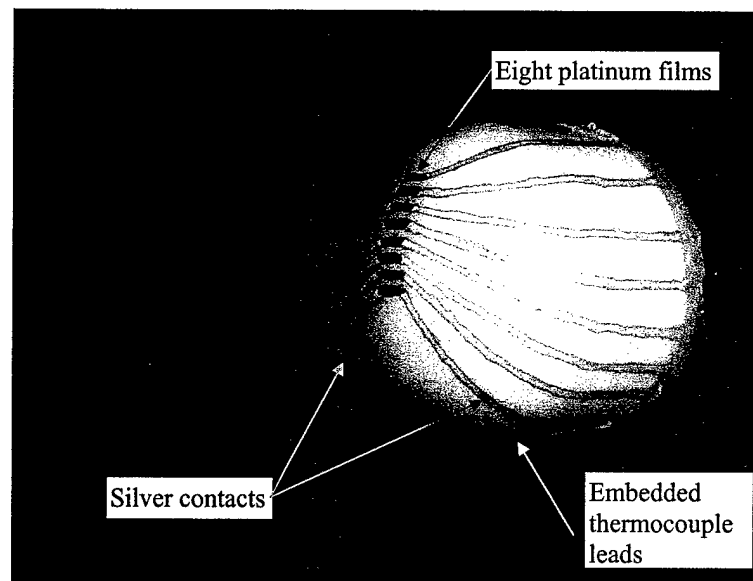


Figure 3.25 Eight gauge model showing platinum films and silver leads on MACOR hemisphere

3.6.2.2 Low-noise Signal Conditioner Design

Figure 3.26 is a schematic for one channel of the four channel signal conditioner for the platinum thin film resistance temperature gauges. A wheatstone bridge converts the resistance of the platinum gauge to a

voltage signal. The bridge is powered with constant voltage from a low-noise linear Power One 179-2071-ND power supply. The voltage to the bridge is controlled with a 317 JRC voltage regulator. The regulator voltage output to the bridge can be controlled with an adjustable trim potentiometer, and, moreover, the regulator supplies additional noise suppression for the applied bridge voltage. In addition, capacitive filters supply even more noise suppression. These components are also shown in Figure 3.28.

The bridge can be balanced by a trim potentiometer for each channel (see Figure 3.27). The bridge will be balanced when

$$R_{gage}R_{100} = R_{trim}R_{100} \quad (3.20)$$

where R_{gage} is the gauge resistance (100 to 350 ohms), R_{100} are the bridge resistors (100 ohms), and R_{trim} is the potentiometer resistance (0 to 500 ohms). The output signal from the balanced bridge will be

$$\Delta V_o = \frac{R_{gage}R_{trim}}{(R_{gage} + R_{trim})^2} \left(\frac{\Delta R_{gage}}{R_{gage}} \right) V_i \quad (3.21)$$

where ΔV_o is the output signal, ΔR_{gage} is the change in the gauge resistance, and V_i is the applied bridge voltage.

A low-noise precision Maxim Max 427 op amp amplifies the signal output from the bridge circuit (see Figure 3.26 and Figure 3.28). The gain of the amp is 10 (set by the ratio of the feedback resistors) and the amp is wired for differential signal input mode. Differential mode suppresses additional external signal noise pickup. [27]

The power and signal input from the gauge is passed to the signal conditioner through a standard 9-pin serial connector (see Figure 3.27). The shielding from the gauge leads were grounded to the signal conditioner through the external 9-pin cover. This shielding provides additional external noise suppression. [27] The power for the signal conditioner is supplied with standard 120 volt AC. A special thanks to Mr John Petrowski for his help in the design, and for constructing this signal conditioner with the utmost in workmanship.

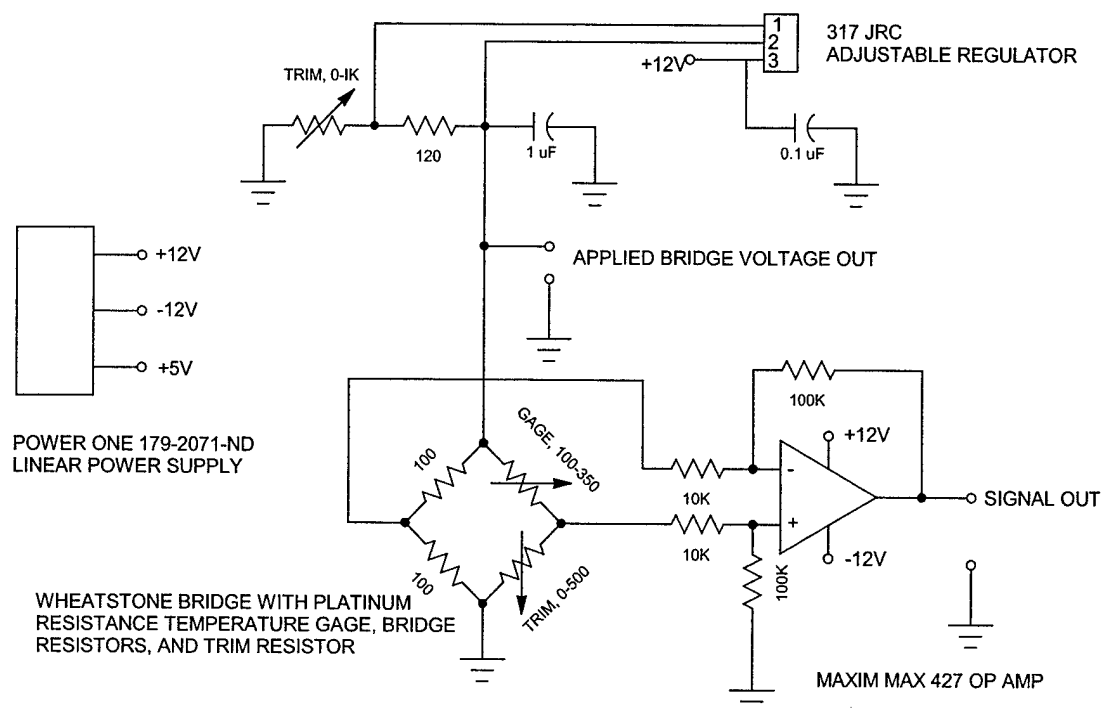


Figure 3.26 Signal conditioner schematic for one channel

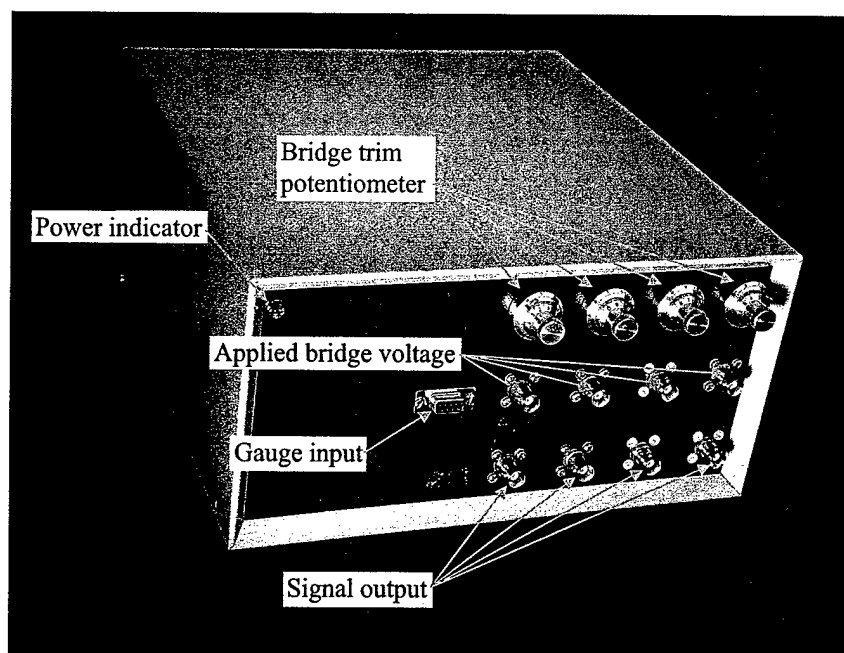


Figure 3.27 Front view of four channel signal conditioner

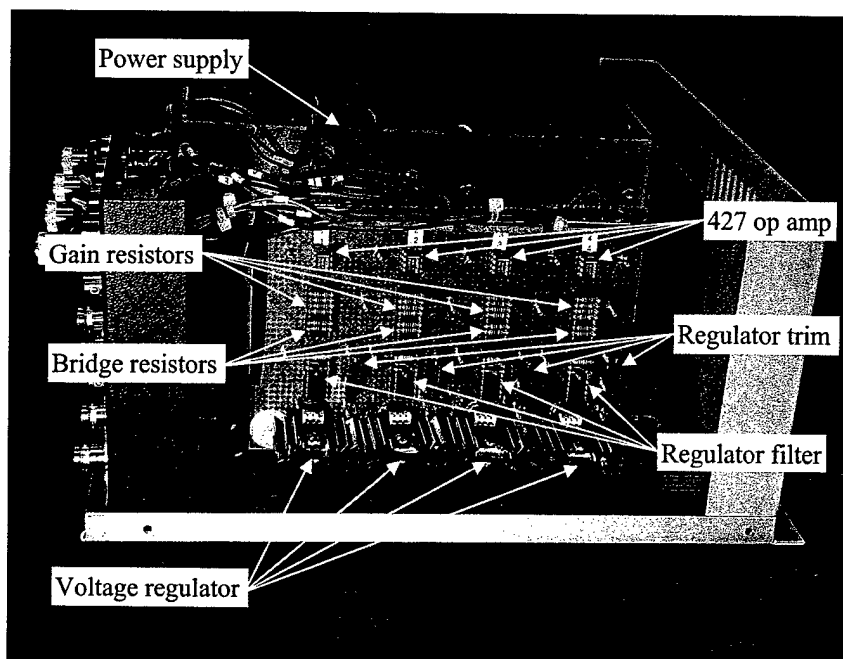


Figure 3.28 Four channel signal conditioner components

3.6.3 Heat Transfer Gauge Calibration

The heat transfer gauges were calibrated in a static temperature bath. A single stagnation point gauge on a hemisphere was then dynamically tested in the wind tunnel.

3.6.3.1 Static

The thin film platinum gauges were calibrated in a glycerin bath. Glycerin is used because it is electrically non-conducting. It also has a high boiling temperature and can be used to calibrate over a broad range of temperatures. A k-type thermocouple was used to monitor the temperature of the bath, and the gauges were connected to the signal conditioner set at the operational applied bridge voltage, i.e., 2 volts. The static bath data was recorded with National Instruments Labview software and a BNC 2120 board connected to a PCMI card inserted in a laptop computer. Figure 3.29 is the results for the calibration of the single stagnation point gauge on the MACOR hemisphere. The range of calibration temperatures for this gauge was 22 to 45 C. The calibration shows the gauge to be linear over the temperature range of interest.

Figure 3.30 is the glycerin bath calibration for gauges 1 through 4 of the eight gauge hemisphere model. Figure 3.31 is the internal temperature of the embedded k-type thermocouple inside the sphere during the calibration. Likewise, Figure 3.32 and Figure 3.33 are the calibration results for gauges 5 through 8. The lower temperature were calibrated using an ice bath. These lower temperatures were calibrated after the first wind tunnel results for the stagnation point gauge were obtained (see Section 3.6.3.2).

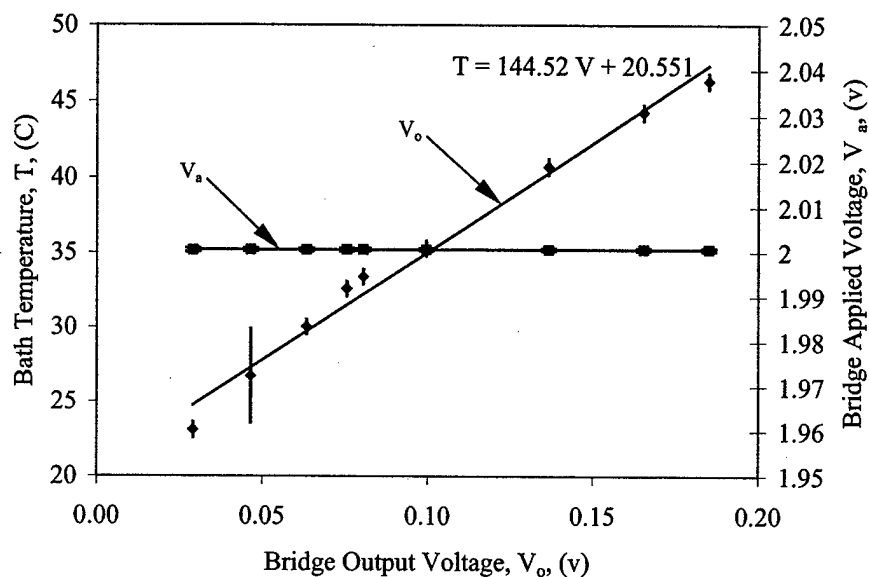


Figure 3.29 Static calibration of stagnation point heat transfer gauge

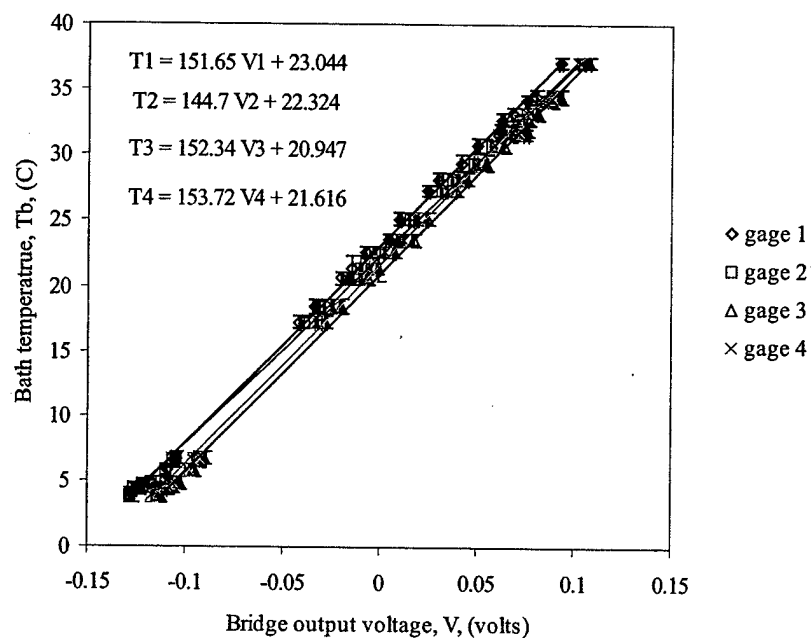


Figure 3.30 Calibration data for gauges 1-4 of eight gauge heat transfer model

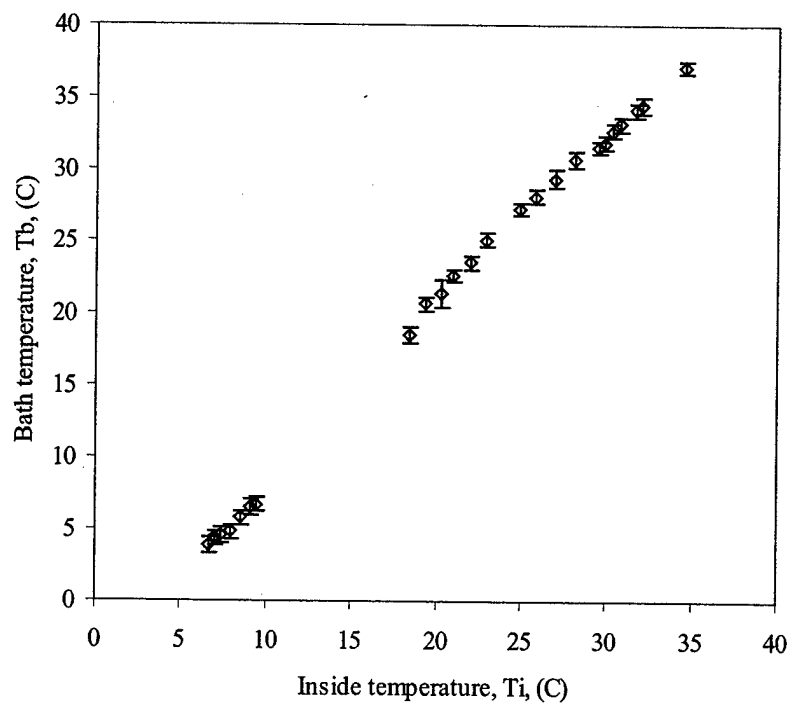


Figure 3.31 Internal sphere temperature during gauge 1-4 calibration

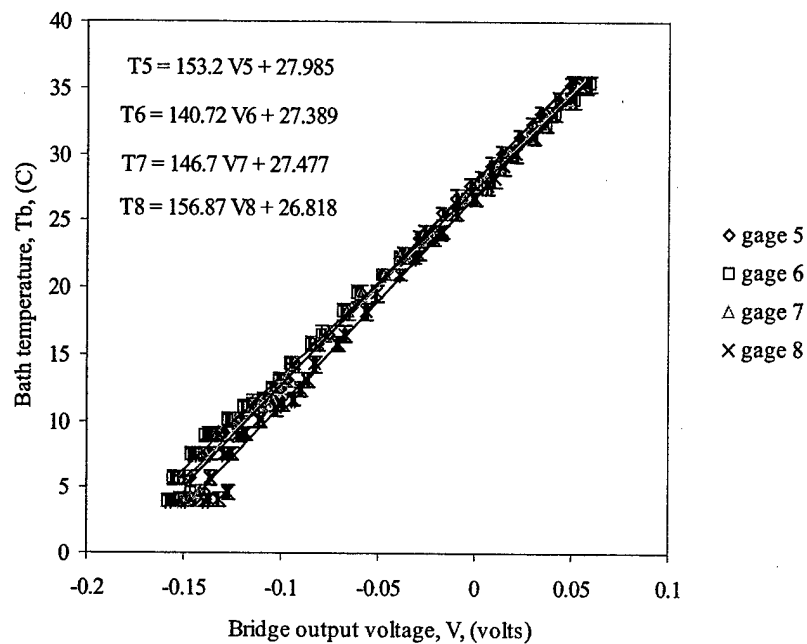


Figure 3.32 Calibration data for gauges 5-8 of eight gauge heat transfer model

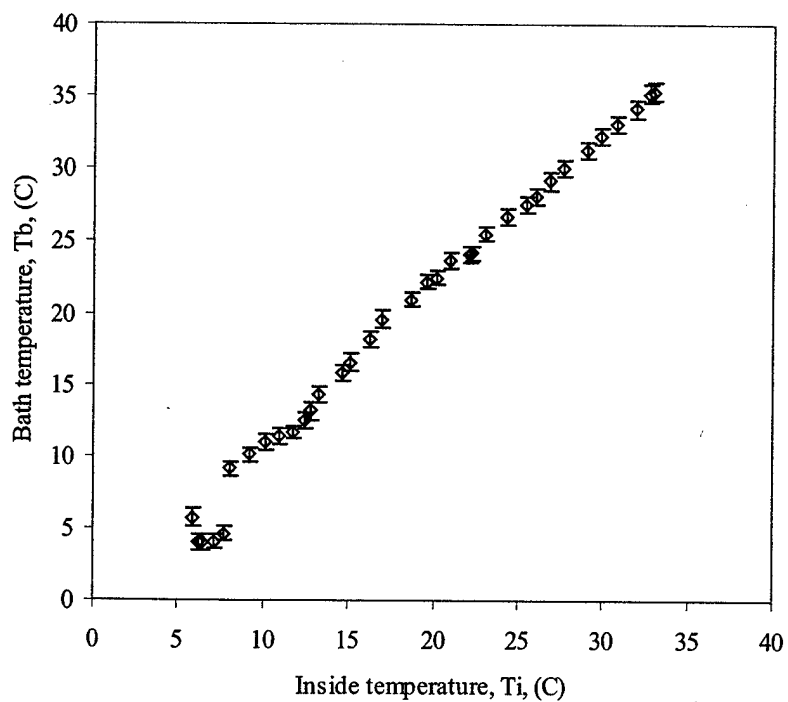


Figure 3.33 Internal sphere temperature during gauges 5-8 calibration

3.6.3.2 Blunt Body Heat Transfer and Dynamic Tests

The platinum temperature resistance and surface heat flux gauges were tested in the wind tunnel on a sphere. These results were compared to theoretical results for stagnation point blunt body heat transfer. The single stagnation point hemisphere gauge was tested in the wind tunnel and compared to the van Driest stagnation point heat flux equation. [142] van Driest estimates the stagnation point heat flux for a sphere as

$$q_0 = 0.763 \text{Pr}^{-0.6} \sqrt{\rho_e \mu_e} \sqrt{\frac{du_e}{dx}} (h_{aw} - h_w) \quad (3.22)$$

where q_0 is the wall heat flux at the stagnation point, Pr is the Prandtl number (Pr = 0.72 for air), ρ_e is the density at the edge of the boundary layer, μ_e is the viscosity at the edge of the boundary layer, $\frac{du_e}{dx}$ is the velocity gradient at the edge of the boundary layer where x is the coordinate in the azimuthal direction, h_{aw} is the enthalpy at the adiabatic wall, and h_w is the enthalpy at the wall. For an ideal gas, Equation (3.22) becomes

$$q_0 = 0.763 \text{Pr}^{-0.6} \sqrt{\rho_{02} \mu_{02}} \sqrt{\frac{du_e}{dx}} c_p (T_0 - T_w) \quad (3.23)$$

where the edge conditions are defined by the pitot conditions since the evaluation is on the stagnation streamline. The viscosity is determined with Equations (2.3) and (2.10). The pitot density is defined by Equations (2.6), (2.19), and (2.20). The enthalpy for an ideal gas is defined by Equation (2.9). Finally, Anderson [6], from Newtonian theory, derives a relationship for the velocity gradient for the stagnation streamline for a sphere as

$$\frac{du_e}{dx} = \frac{1}{R} \sqrt{\frac{2(p_{02} - p_\infty)}{\rho_{02}}} \quad (3.24)$$

where R is the radius of the sphere, p_{02} is the pitot pressure given by Equation (2.19), p_∞ is the freestream pressure given by Equation (2.11), and ρ_{02} is the pitot density as defined in Equation (3.23). More details on the derivation of Equations (3.22) and (3.24) can be found in Anderson [6] and Schlichting [123].

Equation (3.22) works for an ideal gas non-reacting flow, in other words, a cold flow. If the flow is a high enthalpy flow, and the gas is reacting, a more correct expression for the stagnation point heat transfer is given by the analysis of Fay and Riddell. [39]

Figure 3.34 shows the temperature for the single point stagnation gauge for test run 1. The tunnel startup is shown by the heating of the gauge from 6 – 8 seconds. This heating occurs due to the starting of the test section and the propagation of the shock through the test section and past the model. Once the tunnel starts, the gauge records a steady cooling of the stagnation point. This cooling is due to the fact that the stagnation temperature is cooler than the ambient. When the tunnel shuts down, there is a significant decrease in temperature.

Figure 3.35 is the temperature for test run 2, and Figure 3.36 compares test run 1 and 2. In Figure 3.35 the strobe flash is marked on the plot for shadowgraph images taken during run 2. Some of these shadowgraph images are shown in Figure 3.43. Most significant is the image for the shut down of the tunnel, shadowgraph number 16. This image shows a shock impinging upon the model due to the tunnel shutdown. This shock impingement gives significant decrease in temperature during the tunnel shutdown. Figure 3.37 and Figure 3.38 show the tunnel stagnation pressure and the stagnation temperature during the run. Both of these figures show the stagnation temperature drop during the wind tunnel run. Most of the stagnation temperature drop is due to the drop in the temperature of the air in the compressed air storage tanks. The tank air temperature drops due to the expansion of the air in the tanks as the air is removed during the operation of the wind tunnel. A simple analysis shows that the final temperature, T_f , of the air in the tanks is given by

$$T_f = \left(\frac{p_i}{\frac{p_i}{T_i} - \Delta m \frac{R}{V}} \right)^{1-n} T_i^n \quad (3.25)$$

where p_i is the initial tank pressure, T_i is the initial tank temperature, Δm is the mass of air removed from the tanks, R is the ideal gas constant for air, V is the tank volume, and n is the exponent describing a polytropic expansion. For a polytropic gas, the relation between the temperature and pressure is

$$\frac{T_i}{T_f} = \left(\frac{p_i}{p_f} \right)^{\frac{n}{n-1}} \quad (3.26)$$

where p_f is the final pressure. For an isothermal process, n is equal to one. For an adiabatic process n is equal to 1.4.

The amount of air mass used during a wind tunnel run can be determined by the continuity equation and assuming an isentropic expansion through the wind tunnel nozzle. Thus, the mass used, Δm , is given by

$$\Delta m = \Delta t p_0 M A \sqrt{\frac{\gamma}{RT_0}} \left(1 + \frac{\gamma+1}{2} M^2 \right)^{-\frac{\gamma+1}{2(\gamma+1)}} \quad (3.27)$$

where Δt is the time of the wind tunnel run, γ is the ratio of specific heats, R is the gas constant for air, p_0 is the stagnation pressure, T_0 is the stagnation temperature, M is the Mach number in the test section, and A is the test section cross sectional area. Assuming no other losses through the piping system, the tank temperature will drop according to Equations (3.25) and (3.27) during the operation of the wind tunnel, and this temperature will then become the stagnation temperature in the wind tunnel. Figure 3.39 shows the temperature drop associated with the tank expansion process for isothermal to adiabatic processes for a typical 10 second run time, for various initial tank pressures, and a typical initial tank temperature of 293 K. Pope and Goin [110] also give results for stagnation temperature drops that can occur due to throttling through the pressure control valve. For most of the data, the starting tank pressure was above 1000 psi, so the drop in tank temperature was typically less than 15 K.

Figure 3.40 is the heat transfer for test run 1 without any filtering applied to the temperature data. Figure 3.41, and Figure 3.42 show the computed heat transfer, temperature, and the van Driest (see Equation (3.23)) heat transfer for the test runs. In Equation (3.23), an estimated value at the end of the operation of the wind tunnel run is used for the stagnation temperature value. For these latter two plots the temperature has been filtered prior to the computation of the heat transfer (see Equation (3.19)). The temperature was filtered with a sliding least squares second order polynomial smoothing routine. By comparing Figure 3.40, Figure 3.41, and Figure 3.42 the necessity of filtering the temperature can be seen. Any noise in the temperature will be greatly amplified by the derivative term in Equation (3.17) for the heat

flux. For both test runs the measured heat flux asymptotically approaches the van Driest heat flux. At the end of the run, the difference between the measured and van Driest heat flux is within 10%.

For the eight gauge model surface heat flux tests, a k-type thermocouple was mounted on the inside of the hemisphere. This k-type thermocouple was placed here to determine the extent to which the semi-infinite gauge theory would be valid for the 25.4 mm diameter sphere tests in the wind tunnel. Figure 3.44 shows the results for one of the wind tunnel runs. The theory for the measurement of the heat transfer, based on this measurement result, would be valid for wind tunnel runs of 12 seconds, or less, from the start of supersonic flow within the test section. Therefore, tunnel run times were targeted at 10 seconds for the heat transfer tests. The thermocouple measurements were logged for each test discussed in Chapter 5.

Figure 3.45 shows the response of gauges 1-3 on the eight-gauge hemisphere model with a laser discharge 0.6 sphere diameters from the front of the hemisphere in quiescent air. The rise time for each gauge is 0.7 μ s. The response time is estimated to be 2 μ s based on the heating due to the laser spark. The temperature trace for each of the three gauges is unfiltered data, and $T - T_a$ is the measured temperature relative to the ambient temperature, T_a . The data signal has been converted to a temperature based on the bath calibration results of Section 3.6.3.1. The rise in temperature associated with the blast wave corresponds to the time a blast wave would hit the sphere based on the results to be given in Chapter 4 and the distance from the sphere. The low level of noise present on the temperature data is readily apparent. The noise level is estimated to be ± 0.1 K. The heating signal from the spark flash was verified by blocking the gauge with a cover and firing the laser. This verified that the gauge was not picking up a electromagnetic noise from the laser power supply during the laser pulsing. It also verified the heating produced from the blast wave emanating from the laser discharge location.

The thin film gauges were considered operational at this point. Tests continued to measure the surface temperature and heat flux for the energy deposition upstream of the sphere with and without shock impingement (see Chapters 5 and 6).

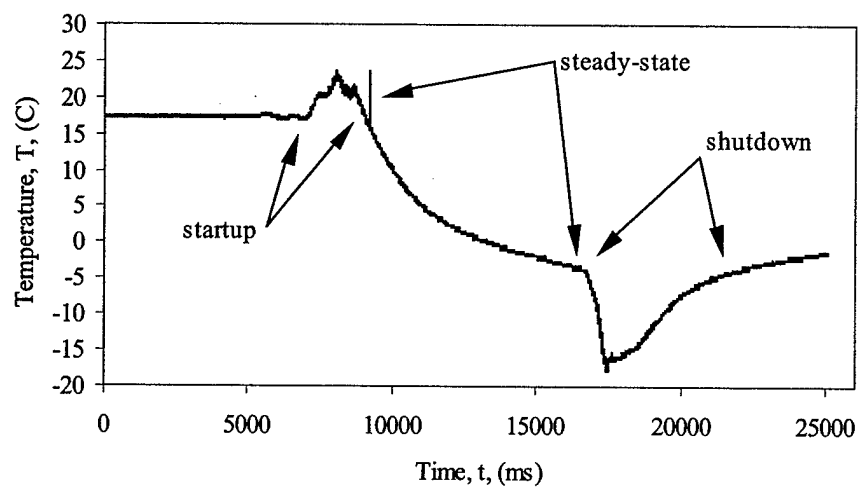


Figure 3.34 Sphere stagnation point gauge, test run 1

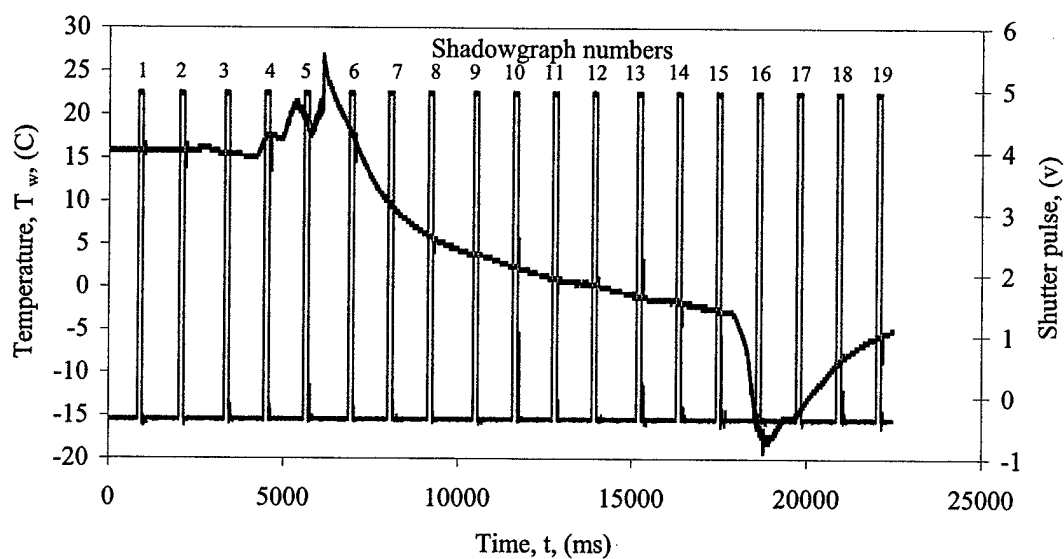


Figure 3.35 Sphere stagnation point gauge, test run 2 with corresponding shadowgraph times

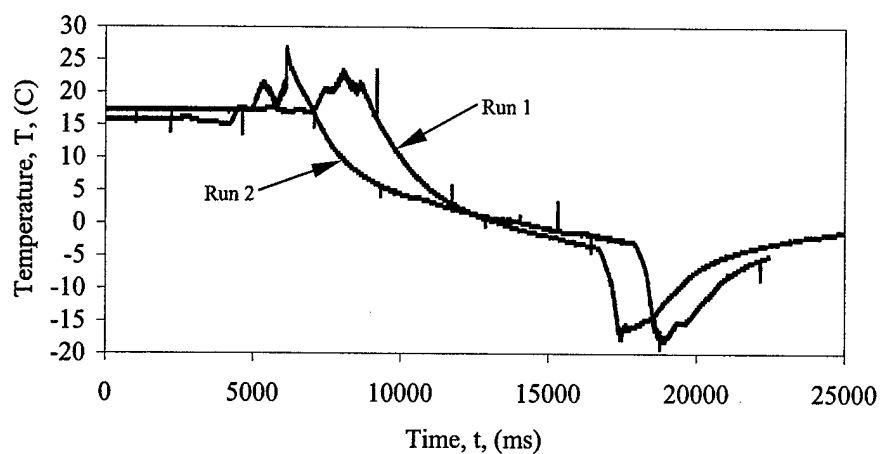


Figure 3.36 Comparison of test run 1 and 2

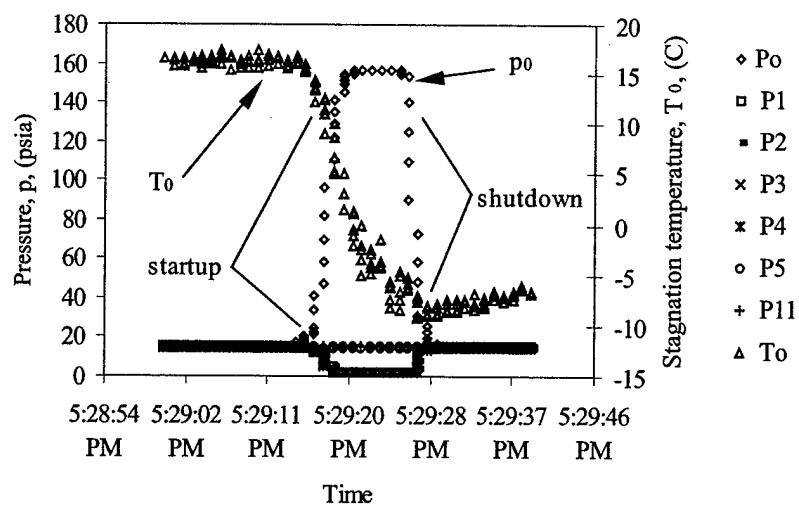


Figure 3.37 Tunnel parameters for test run 1

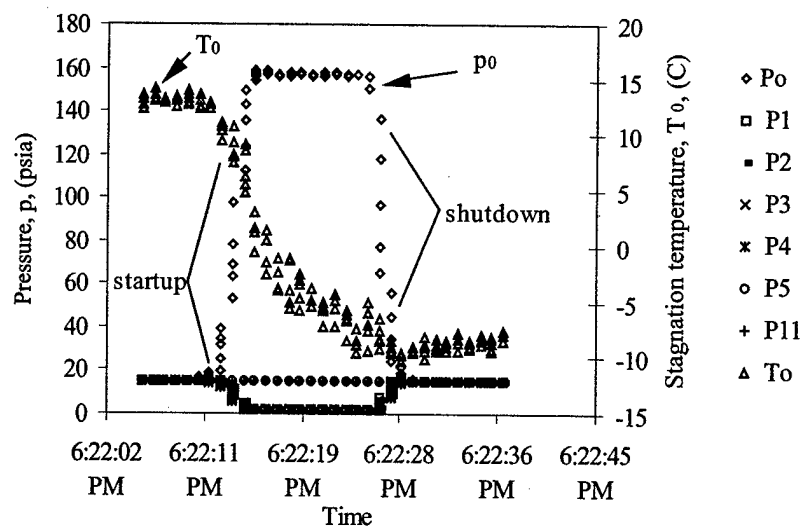


Figure 3.38 Tunnel parameters for test run 2

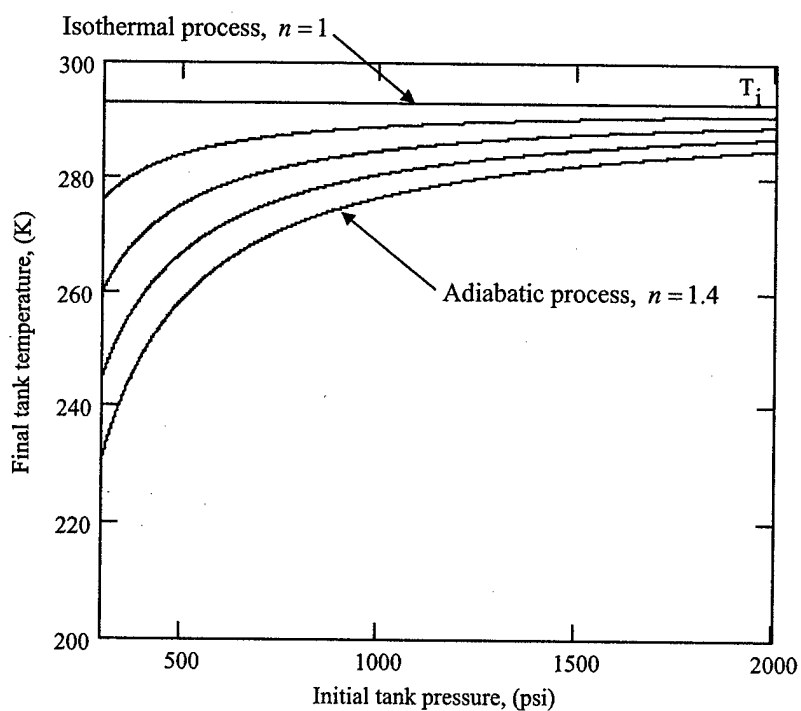


Figure 3.39 Drop in wind tunnel air storage tank temperature for polytropic expansion process; 10 s wind tunnel operation time and stagnation pressure of 150 psi

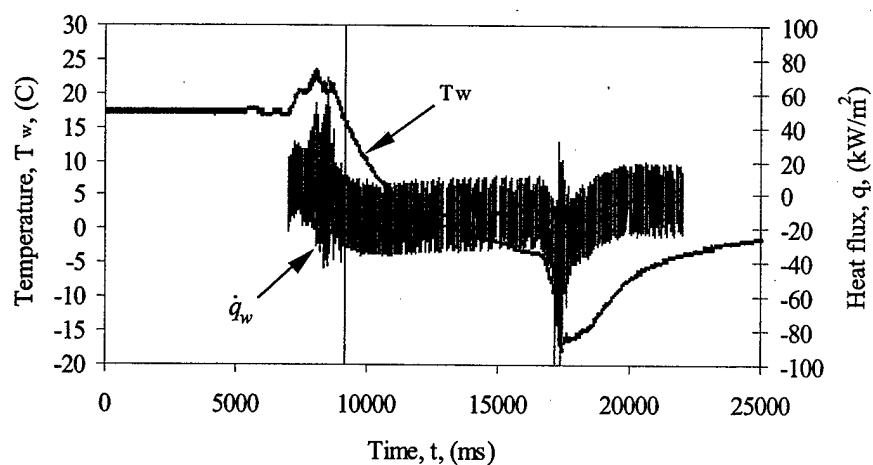


Figure 3.40 Stagnation point heat flux from test run 1 computed from raw temperature data

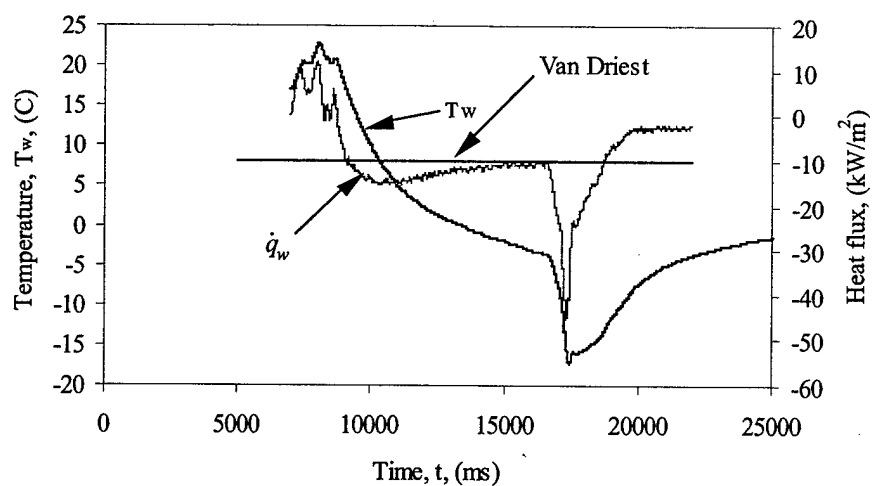


Figure 3.41 Stagnation point heat flux from test run 1 computed from smoothed temperature data and comparison to theoretical heat flux

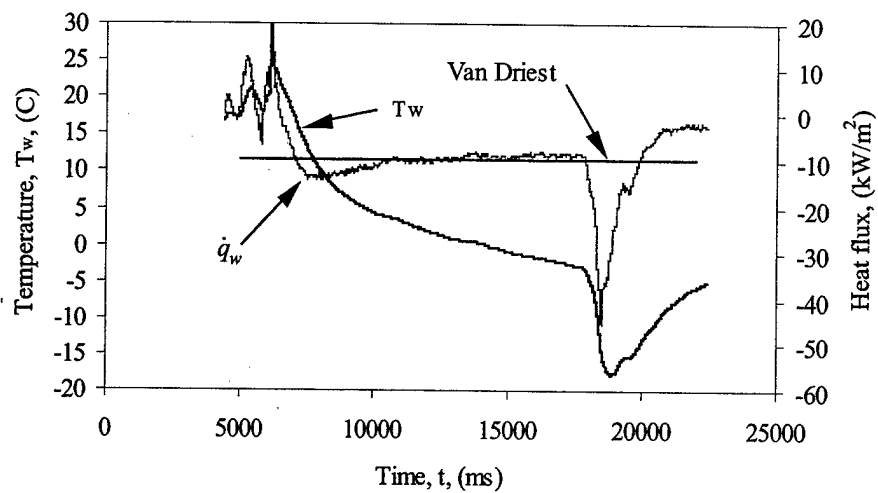
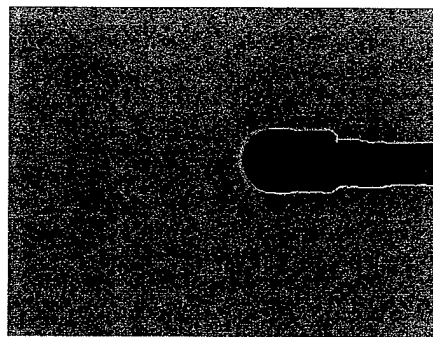
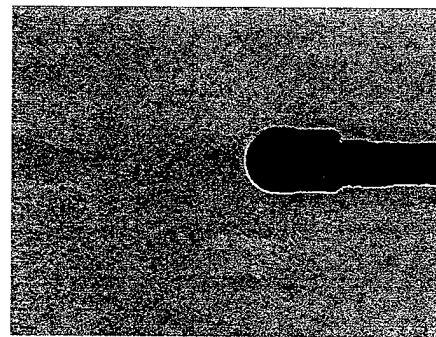


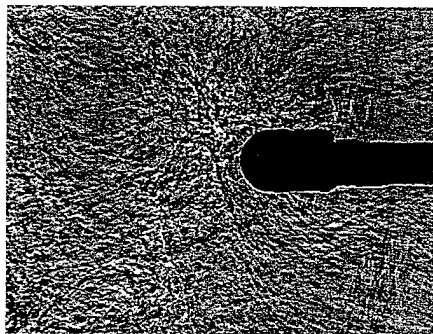
Figure 3.42 Stagnation point heat flux from test run 2 computed from smoothed temperature data and comparison to theoretical heat flux



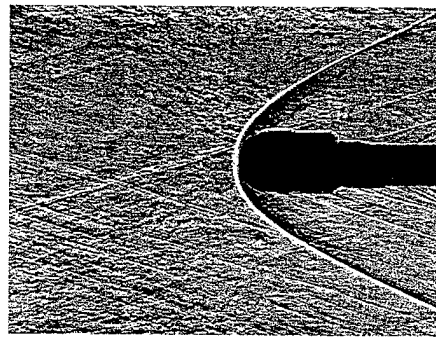
Shadowgraph 2 (2007 ms)



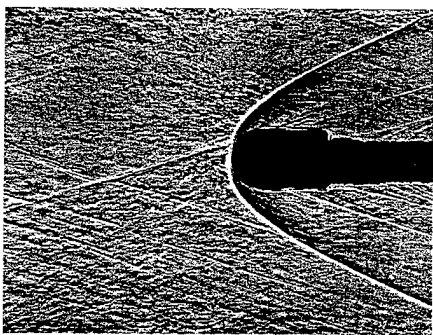
Shadowgraph 4 (4438 ms)



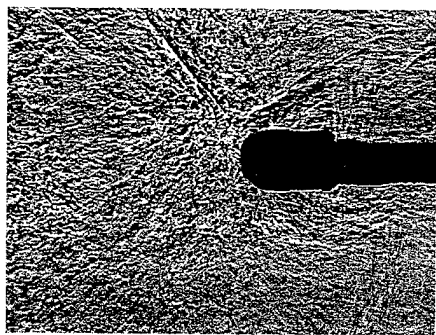
Shadowgraph 5 (5578 ms)



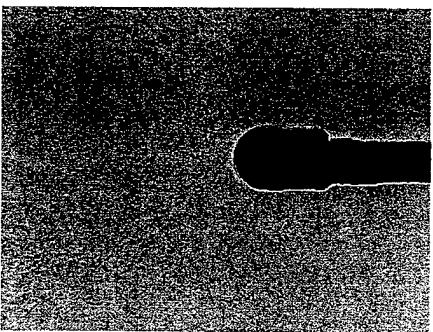
Shadowgraph 6 (6867 ms)



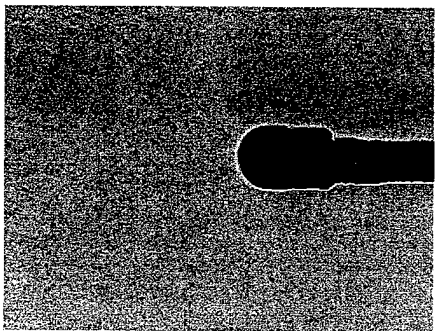
Shadowgraph 15 (17422 ms)



Shadowgraph 16 (18562 ms)



Shadowgraph 17 (19702 ms)



Shadowgraph 18 (20842 ms)

Figure 3.43 Shadowgraphs for test run 2

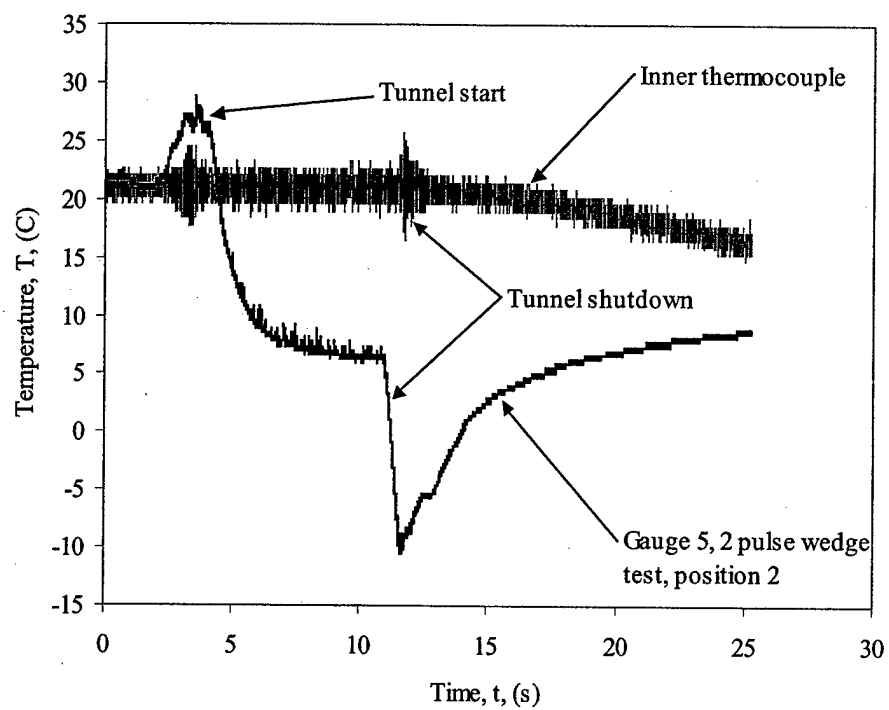


Figure 3.44 Embedded thermocouple temperature and comparison to thin film platinum gauge surface temperature

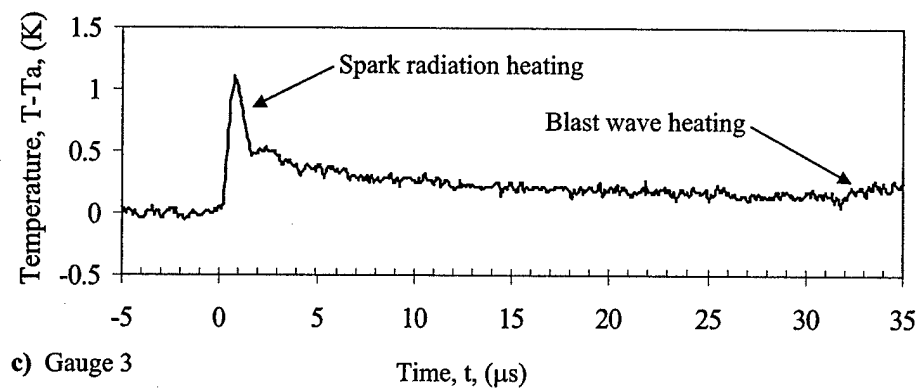
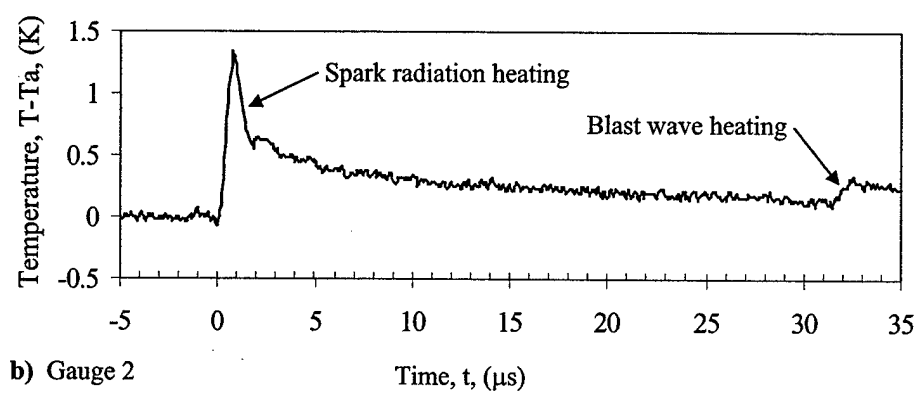
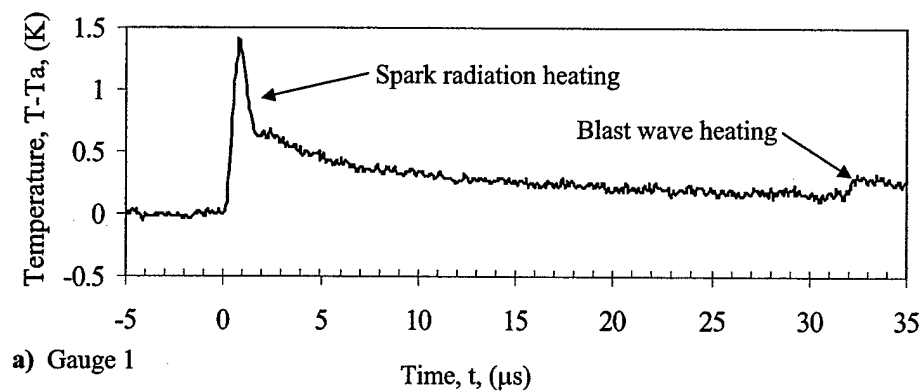


Figure 3.45 Time response for gauges 1-3, a) – c), respectively, for radiation and blast wave heating from laser energy deposition into quiescent air 1.0 diameter upstream of sphere

3.7 Intersecting Shocks

Figure 3.46 is a schematic and Figure 3.48 - Figure 3.49 are photos of the wedge models mounted in the wind tunnel. Table 3.6 lists the wedge parameters used for the laser energy deposition tests upstream of the crossing shocks within the dual solution domain.

The two different span wedges were used to determine the effect of the span on the three-dimensional effects of the energy deposition. There was difficulty in starting the wind tunnel with the original wedges of $4w$ span, where w is the wedge length (see Figure 2.8). Figure 3.47 compares the tunnel test section blockage between the symmetric wedge models and the sphere and wedge model used for the Edney shock impingement tests. The model used for the shock impingement tests had successfully started in the wind tunnel. However, the initial $4w$ span models did not. The sting for these wedges had an upper bracket for mounting wedges of different wedge angles. The original $4w$ span wedges with this upper mounting bracket would not start in the wind tunnel. The span of the wedges was reduced to $2.2w$ to allow the tunnel to start. The wedges were sized with the wedge length, $w = 25.4$ mm, to give comparable blockage in the test section as for previous test programs. New wedges were made with a span of $4w$ without the upper mounting bracket. In addition, the sting was modified to reduce the amount of blockage in the test section. The modified wedge and sting configurations reduced the amount of blockage in the tunnel test section. Moreover, by not having the mounting bracket, the oblique shock from this bracket was not present. This oblique shock, generated by the mounting bracket, tended to trip the boundary layer in the test section for the original $4w$ span wedges leading to the tunnel not starting.

Finally, having the two different span wedges allowed for a study of laser energy deposition and a correlation with the three-dimensional effects associated with the intersecting shocks in the dual solution domain. Ivanov *et al* [67] and Schmisser and Gaitonde [125] have demonstrated the three-dimensional dependence of the Mach stem for crossing shocks within the dual solution domain.

Table 3.6 Wedge model parameters

wedge length, w	25.4 mm
wedge span, b	55.8 and 101.4 mm
wedge separation, $2g$	30.2 mm

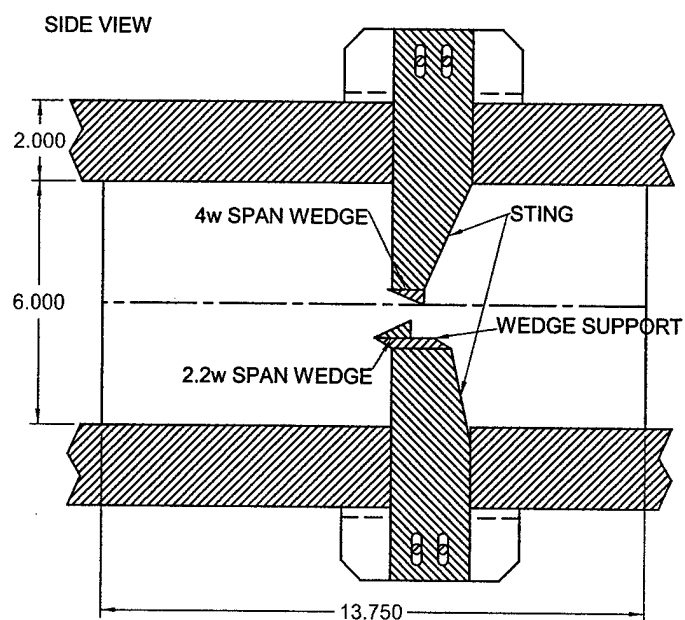


Figure 3.46 Symmetric wedge models (dimensions given in inches)

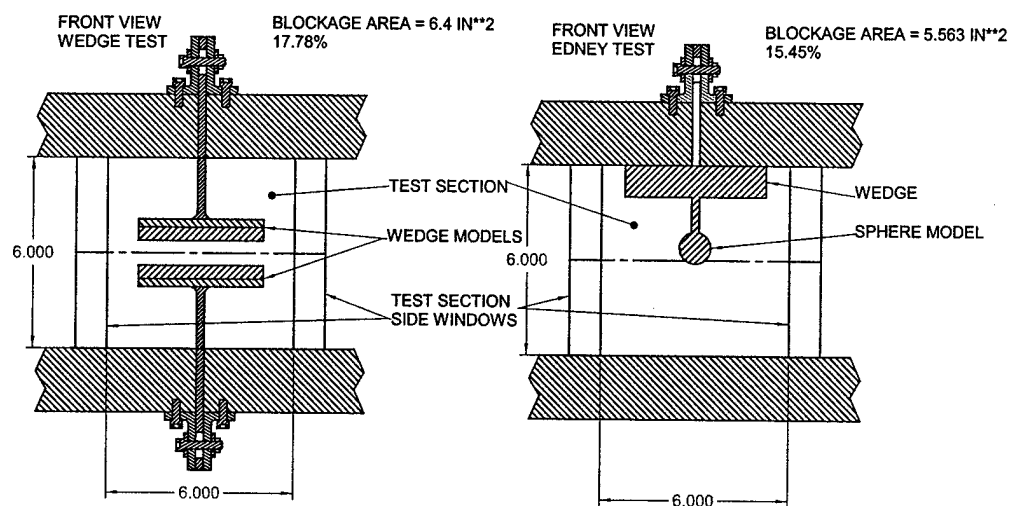


Figure 3.47 Test section blockage comparison between symmetric wedge models and the sphere and wedge model for the Edney Type IV shock impingement tests (dimensions given in inches)

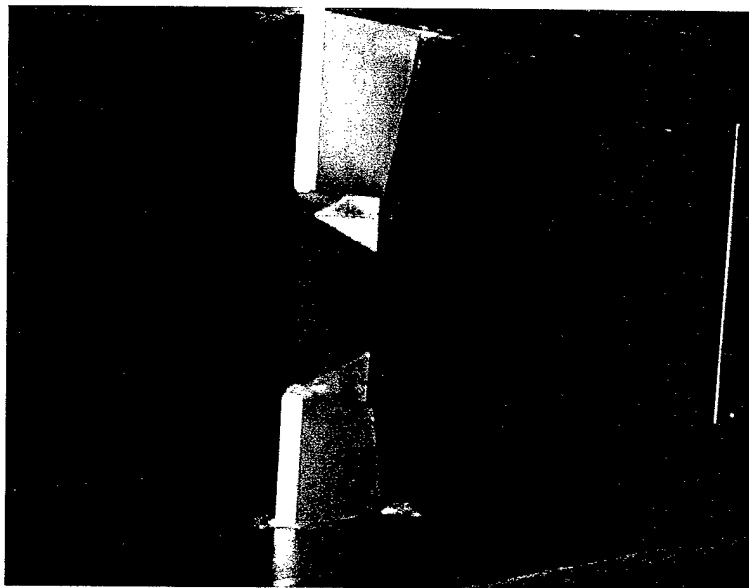


Figure 3.48 55.8 mm span symmetric wedge models mounted in wind tunnel test section

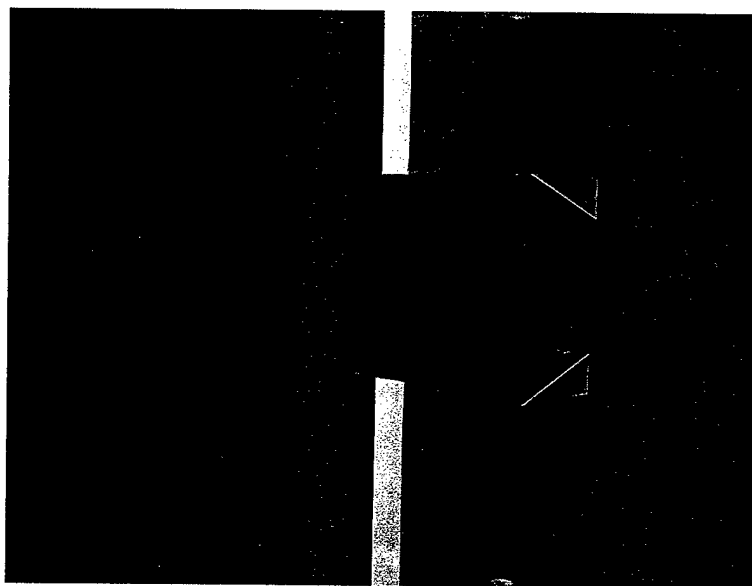


Figure 3.49 101.4 mm span, 22 degree symmetric wedge models

3.8 Axisymmetric Jets

Two axisymmetric nozzles with exit diameters of 12.5 mm were investigated. The Mach 0.85 and 1.38 nozzles were designed for perfect expansion at atmospheric conditions. Therefore, they were converging and converging-diverging nozzles, respectively. A small co-flow was provided for seeding purposes as the perfectly expanded jet exhausted into the atmosphere. Cross jet (x), streamwise (y), and transverse (z) directions are indicated in Figure 3.50. Since the jet was not heated, the stagnation temperature remained at room temperature. The stagnation conditions are summarized in Table 3.7, and the exit conditions are summarized in Table 3.8. Table 3.9 summarizes the Reynolds numbers and convective Mach and velocities for the nozzles.

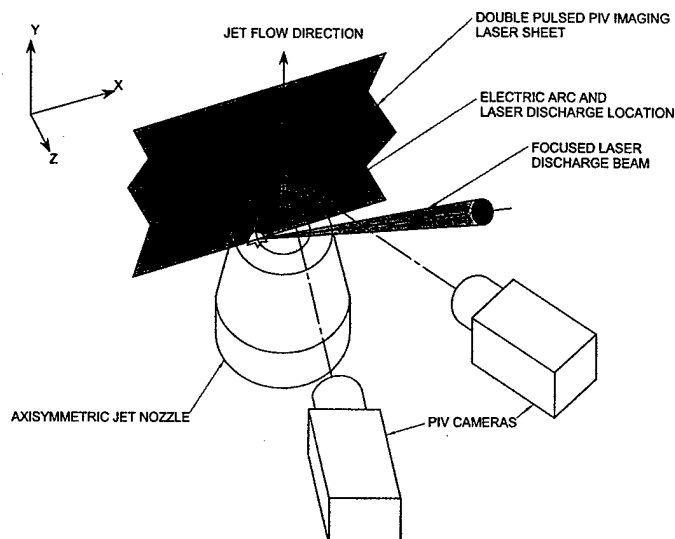


Figure 3.50 Test apparatus for axisymmetric jet 3 component PIV measurements

Table 3.7 Test nozzles' stagnation conditions

Nozzle Exit Mach	Stagnation Pressure (MPa)	Stagnation Temperature (K)	Stagnation Density (kg/m^3)
0.85	0.16	300	1.89
1.38	0.31	300	3.54

Table 3.8 Test nozzles' exit conditions

Nozzle Exit Mach	Velocity (m/s)	Temperature (K)	Pressure (MPa)	Density (kg/m ³)
0.85	276	262	0.10	1.35
1.38	408	219	0.10	1.61

Table 3.9 Test nozzles' Reynolds number and calculated convective Mach and velocities

Nozzle Exit Mach	Re_D	M_c^*	M_c^\dagger	U_c^* (m/s)	U_c^\dagger (m/s)
0.85	2.3×10^5	-	-	-	-
1.38	5.3×10^5	0.63	0.23	220	342

* Calculated from Eqs. (2.40) and (2.41)

† Calculated from Eqs. (2.42), (2.43), and (2.44)

Table 3.10 Electric arc characteristics

Pulse Width (μ s)	Energy (mJ)	Current (Amp)	Voltage (volt)	Pulse Frequency (kHz)
7	1	3	50	1-18

Table 3.11 Nd:YAG excitation laser characteristics

Pulse Width (ns)	Energy (mJ)	Wavelength (nm)	Pulse Frequency (Hz)
10	5 - 40	532	10

The under-expanded jet was created with a 12.7 mm diameter converging nozzle operated at a stagnation pressure of 500 kPa in ambient air. A Mach disk formed in the jet with the nozzle operated at this condition. The stagnation temperature was increased to 400 degrees K to avoid condensation from the moisture in the air. The purpose of heating the air was to avoid scattering signals from ice particles (Mie scattering) instead of the air molecules (Rayleigh scattering). In the case of energy deposition in quiescent

air, the jet nozzle was removed from the experimental set up to eliminate any blast wave reflections from the nozzle surfaces.

3.9 Particle Image Velocimetry

A LaVision 3-component PIV system was used to measure the complete velocity field at each measurement plane. This system uses two views (i.e. cameras) to construct all three velocity components (see Figure 3.50). The two cameras are corrected for oblique optical distortion and use image processing software to align the fields of view. This stereo camera setup allows for the out-of-plane velocity component to be calculated. Each of the interline transfer cameras allow two frames to be taken with 2 μ s separation between frames. From the two frames, the velocity field was calculated using standard cross correlation techniques with 32 by 32 pixels and 50 percent overlap. [113] The spatial resolution of the cameras is 1280 by 1024 pixels, and the images were digitized to 12-bit resolution. The two illumination pulses were from a pair of Q-switched Nd:YAG lasers, each providing about 20 mJ per pulse. Cylindrical and spherical optics were used to form a 1-mm thick laser sheet, which was passed transversely through the jet so that the compressible shear layer could be visualized. Both the supersonic jet and co-flow were seeded with 0.5- μ m Aluminum oxide particles. Based on this size, the particles sufficiently followed the flow structures.

The accuracy of the PIV measurements is estimated to be $\pm 2\%$ (or ± 4 m/s) based on the designed nozzle exit conditions, and PIV measurements taken at the nozzle exit.

3.10 Pressure Probe

Pressure probe measurements were made for the laser discharge in quiescent air (see Chapter 4) and outside of the shear layer for the axisymmetric jet tests (see Chapter 7).

Pressure measurements were recorded outside of the jet shear layer with an Endevco 8514-20 pressure transducer mounted in a probe (see Figure 3.51). Power was supplied to the transducer with an Endevco Model 106 power supply, and an Endevco Model 109 signal conditioner amplified the transducer signal. The signal was filtered with a Krohn-Hite 3103A filter with cut-off high and low frequencies of 70 kHz and 10 Hz respectively. The output from the signal conditioner was displayed on a HP 500 MHz oscilloscope, and the data was digitally recorded through a National Instruments GPIB-PCMI card connected to a laptop

PC. The pressure transducer was statically calibrated over the range of expected pressures (see Figure 3.54).

The pressure across the blast wave generated with the laser induced breakdown was recorded with a Kistler 211B5 pressure transducer mounted to a probe (see Figure 3.52). The signal from the pressure transducer was amplified with a Kistler signal conditioner and then recorded with a HP 500 MHz oscilloscope. The data was digitally recorded with a National Instruments GPIB-PCMI card connected to a laptop PC.

Figure 3.53 gives the results for the calibration of the Kistler pressure probe, and Figure 3.54 gives the results for the calibration of the Endevco pressure probe. The Endevco probe was statically calibrated over a range of pressures. The data was fit with a linear least squares, and this fit determined the calibration coefficient for converting the voltage output signal to the pressure data. The Kistler transducer was dynamically calibrated in the Rutgers University Undergraduate Lab Shock Tunnel over the range of expected pressures for the experiment (see Figure 3.53). Both of the pressure probes are linear over the pressure ranges measured in the experiments. The uncertainty for the Endevco probe is ± 0.05 psi and ± 0.1 psi for the Kistler probe.

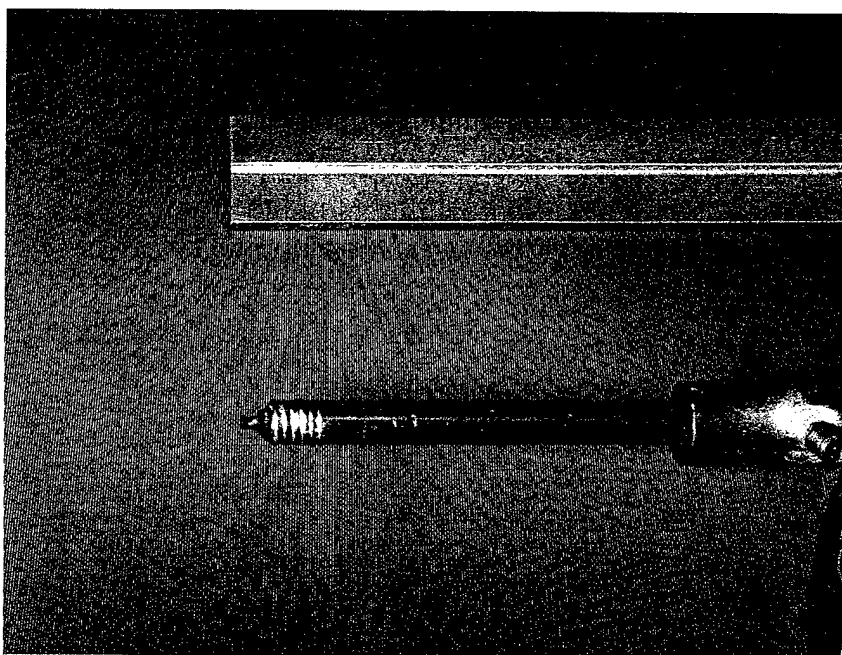


Figure 3.51 Pressure probe with Endevco 8514-20 piezoresistive pressure transducer

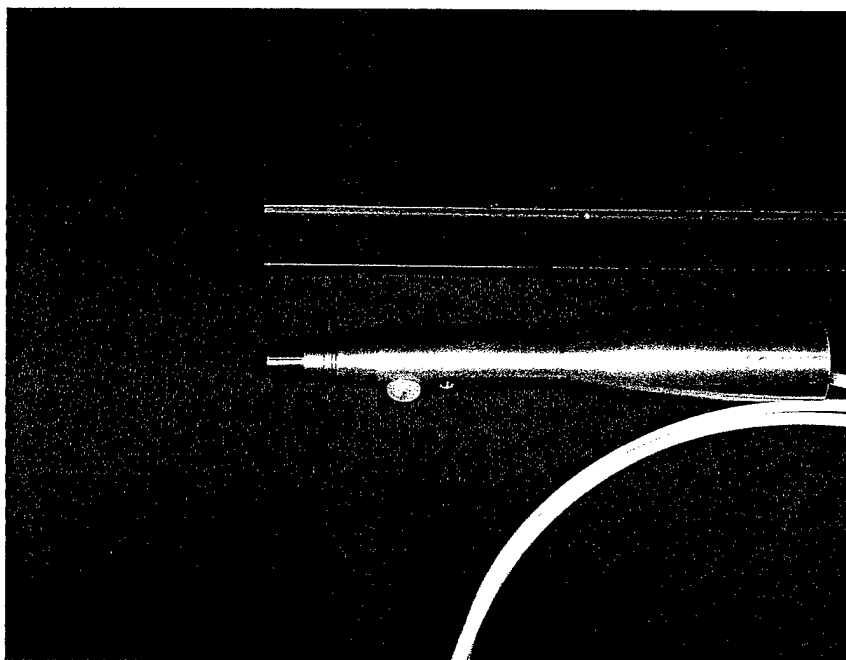


Figure 3.52 Pressure probe with Kistler 211B5 piezoelectric pressure transducer

Kistler Pressure Transducer Calibration - Rutgers Shock Tube - 21 Feb 2002
Model 211B5, SN C193161

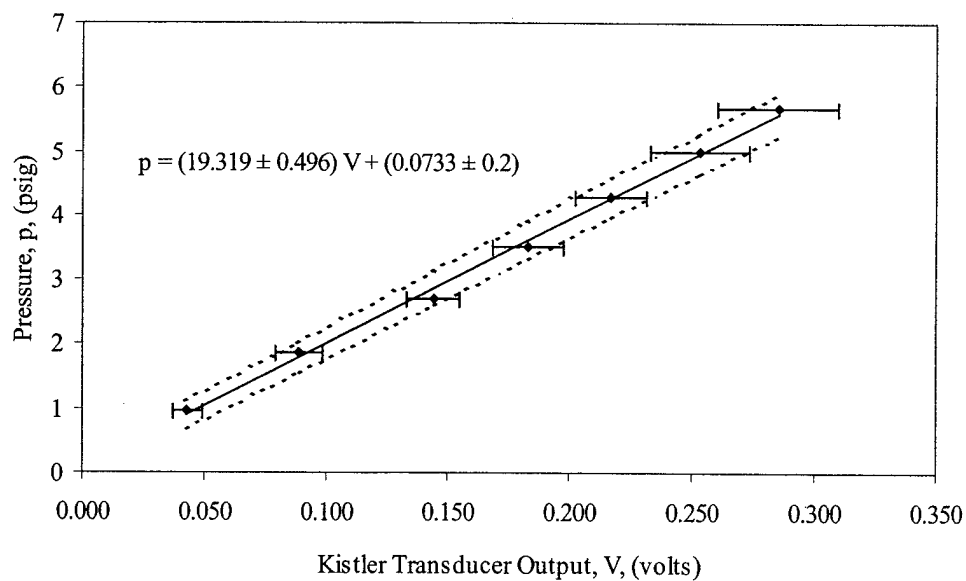


Figure 3.53 Calibration of Kistler piezoelectric pressure transducer used for quiescent blast wave measurements

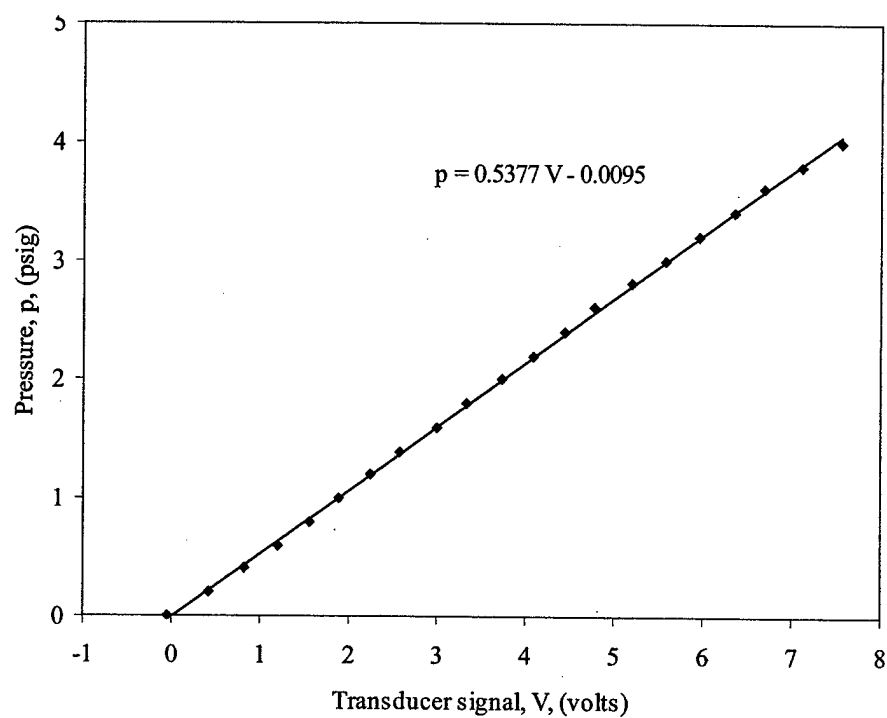


Figure 3.54 Calibration of Endevco piezoresistive pressure transducer used for the jet shear layer pressure measurements

Chapter 4

Laser Energy Deposition in Quiescent Air

4.1 Overview of Laser Energy Deposition in Quiescent Air Experiments

The objective of these quiescent air tests was to determine some of the flow characteristics associated with depositing laser energy into air, and then use these characteristics to verify and validate the numerical models being developed. These flow characteristics, i.e., blast wave propagation and blast wave pressure, are needed for the verification and validation of the gasdynamic model development of Yan *et al* [151], and the plasmadynamic model development of Kandala and Candler. [71] Moreover, the energy deposition into quiescent air provides the initial step in a building block approach for a basic understanding of the flow physics of the deposition process, and as it is applied to more complex flows (see Chapter 5 - Chapter 7).

4.2 Flow Visualization

Filtered Rayleigh scattering (see Section 3.2.2) was used to visualize the process of laser induced breakdown in quiescent air and to give a qualitative assessment of the flow associated with the laser energy deposition. First, images are provided to show flow visualization of the entire process. Second, images are taken of the early times of the process at various energy deposition levels to characterize the blast wave for model verification.

The laser induced breakdown process has been described in Section 2.3.1. The asymmetric formation of the laser deposition region will lead to an initial ellipsoidal blast wave and then a subsequent vortex ring formation at later times (see Figure 4.1). In the early stages of the formation process, the plasma forms and a laser supported detonation wave [119] will propagate up the laser incidence axis towards the focal lens (see Figure 4.1 a) and b)). The laser supported detonation wave will induce fluid motion within the plasma region up the axis towards the lens (see Figure 4.1 b) and c)). This fluid motion will create shearing stresses with the adjacent cooler ambient fluid. The cooler ambient fluid will also begin to move into the back of the plasma region, and the heated fluid will be ejected forward, towards the lens (see Figure 4.1 d)). A blast wave begins to move out from the heated region and is initially ellipsoidal in shape due to the

asymmetric plasma region. However, the blast wave becomes spherical by 5 to 10 μs (see Figure 4.1 c) and d)). Baker [7] also observes the spherical blast wave from asymmetric energy sources for larger explosions. A primary vortex ring structure resides at later times due to the asymmetric plasma formation process and the initial asymmetric blast wave and expansion processes. These initial asymmetric temperature and pressure distributions have been modeled by Dors *et al* [32] and have been shown to induce the formation of the observed vortex ring. More recently, Kandala and Candler [71] have modeled the plasma formation process and have shown a similar asymmetric temperature distribution along the optical axis as used by Dors *et al* [32].

Figure 4.2 shows filtered Rayleigh scattering images for the laser induced breakdown in air for various times after the laser pulse. At 2 μs the asymmetric blast wave is observed, and by 10 μs the wave becomes spherically symmetric in shape. At 30 μs the formation of a vortex ring is apparent. The vortex ring and ejected heated fluid can be seen at the later times. Figure 4.3 shows the growth of the vortex ring, and Figure 4.4 shows the motion of the vortex ring. These measurements were taken from filtered Rayleigh scattering images in two series of experiments. The vortex ring moves away from the focusing lens along the optical axis. This motion of the vortex ring, away from the focusing lens and along the optical axis, also verifies the sign of the vorticity as indicated in Figure 4.1 e), and as simulated by Dors *et al.* [32] The uncertainty in the measurements given in Figure 4.3 and Figure 4.4 is ± 0.2 mm.

The radiation from the bremsstrahlung process subsides by approximately 10 μs and is dependent on the incident radiation energy. Likewise, the strength of the blast wave, magnitude of asymmetry, size of the deposition region, and the strength of the vortex ring depend on the incident energy. These characteristics also depend on the optics of the incident laser, i.e., focal length, beam diameter, and beam divergence.

In addition, filtered Rayleigh scattering images were taken for six different laser energy levels and with two different focal length lenses. The incident energy level was measured, and blast wave measurements were made from these Rayleigh scattering images to quantify the energy levels associated with the blast wave. The objective of these flow visualization quiescent experiments is to provide gross flow features, i.e., the blast wave characteristics, for verification and validation of the energy deposition models.

Figure 4.5 and Figure 4.6 show the filtered Rayleigh scattering time sequence of images for the laser induced breakdown from 5 to 40 μs for a laser incidence of 112 mJ/pulse. Likewise, Figure 4.7 and Figure 4.8 show the time sequence of images for 98 mJ/pulse, Figure 4.9 and Figure 4.10 show the time sequence of images for 76 mJ/pulse, Figure 4.11 and Figure 4.12 show the time sequence of images for 50 mJ/pulse, and Figure 4.13 and Figure 4.14 show the time sequence of images for 20 mJ/pulse. Finally, Figure 4.15 and Figure 4.16 show the time sequence of images for the laser induced breakdown from 5 to 40 μs for 116 mJ/pulse. Each image is an average of 50 images where the laser sheet for the Rayleigh scattering image is phase locked to the energy deposition laser. The energy deposition source laser is incident from the top, and the laser sheet for the Rayleigh scattering visualization cuts through the center plane of the laser spark. The blast wave propagates out from the spark location. The blast wave measurements taken from these images are given in Section 4.4.1.

The deposition region is characterized by the bright tear drop shaped region where the plasma releases radiation by the bremsstrahlung process. Even though the laser energy deposition pulse only lasts 10 ns, the emission of visible radiation can be seen from 5 to 14 μs for the 112 mJ/pulse case (see Figure 4.5). By comparison, this bremsstrahlung effect has subsided by 5 μs for the 20 mJ/pulse case (see Figure 4.13). For the other energy levels the bremsstrahlung emission subsides between the times for these to boundary energy levels. The blast wave can be seen propagating out from the laser deposition region for each of the energy levels. The asymmetric deposition region is formed by the plasma formation process and is observed for each case. However, the asymmetry decreases with the decreasing energy levels. Although the energy deposition region is asymmetric, the blast wave becomes spherical by 6 to 7 μs . Baker [7] has noted that the blast wave becomes spherical with increasing radial distance for any finite shaped energy source region. A vortex formation is observed for times after 25 μs . This vortex is due to the asymmetric plasma formation (see Figure 4.1) and is observed by Adelgren *et al* at later delay times out to 900 μs . [2] This vortex formation has also been observed by Dors *et al*. [32]

The energy deposition levels and optical characteristics are summarized in Table 4.1 and the ambient conditions are given in Table 4.2 for these test cases.

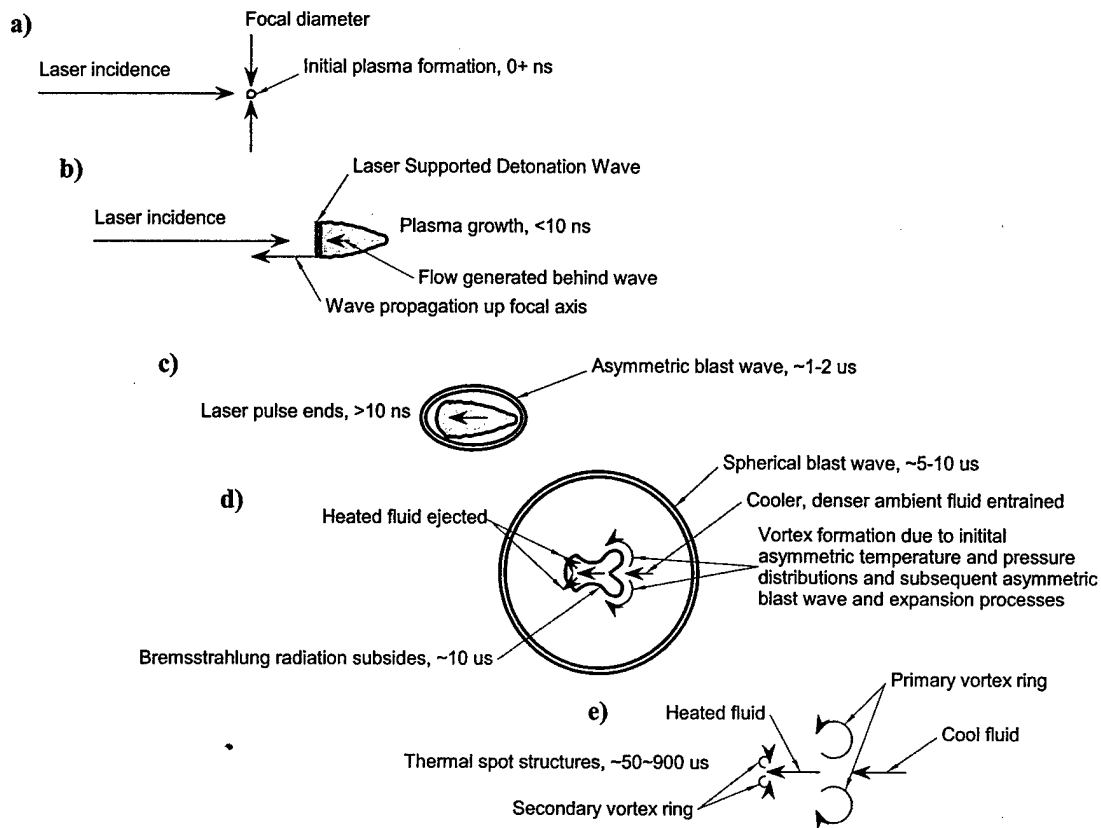


Figure 4.1 Blast wave formation and vortex ring development for laser induced optical breakdown in quiescent air

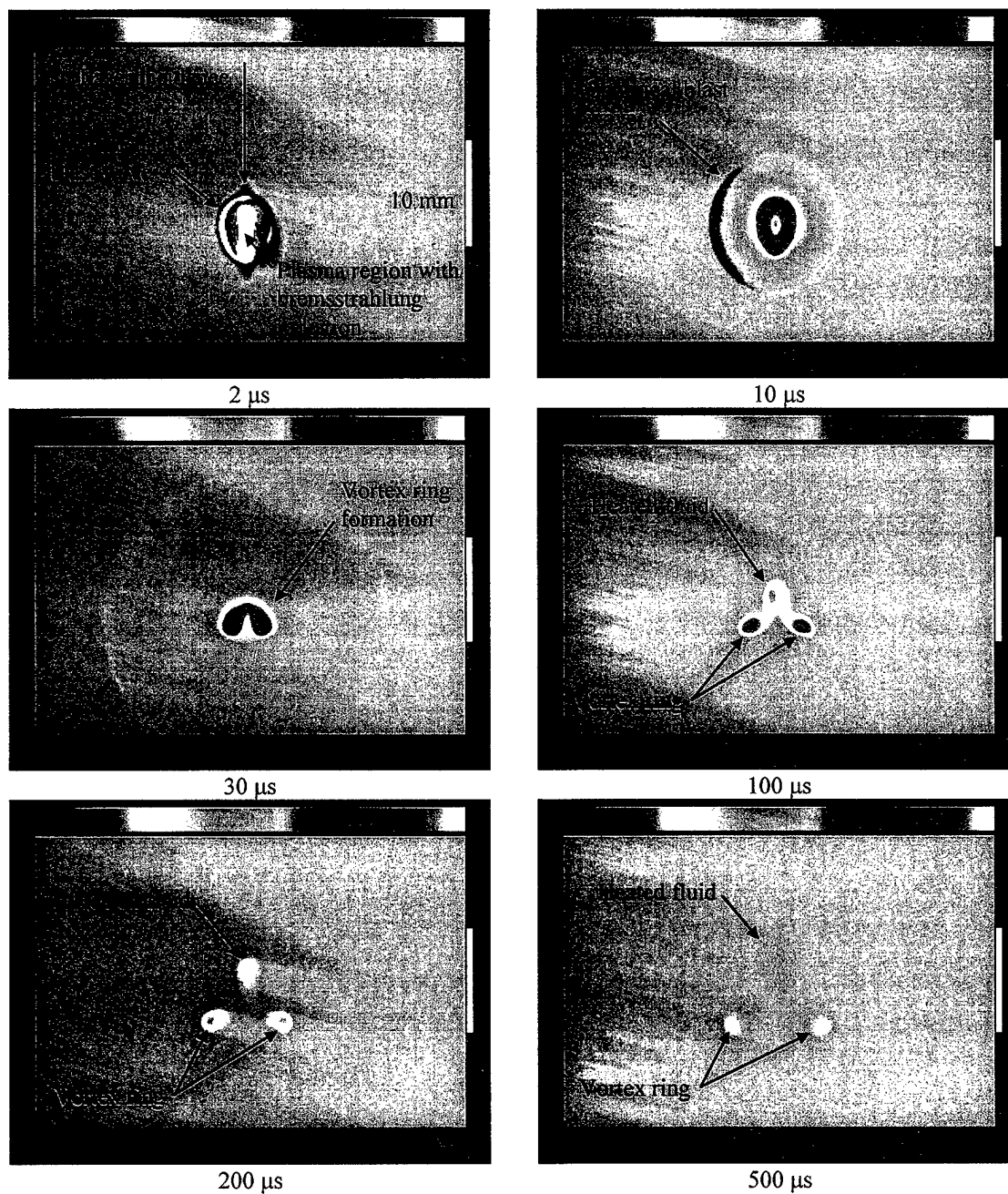


Figure 4.2 Filtered Rayleigh Scattering images of laser induced breakdown in quiescent air at various times, time $t = 0$ corresponds to laser spark pulse

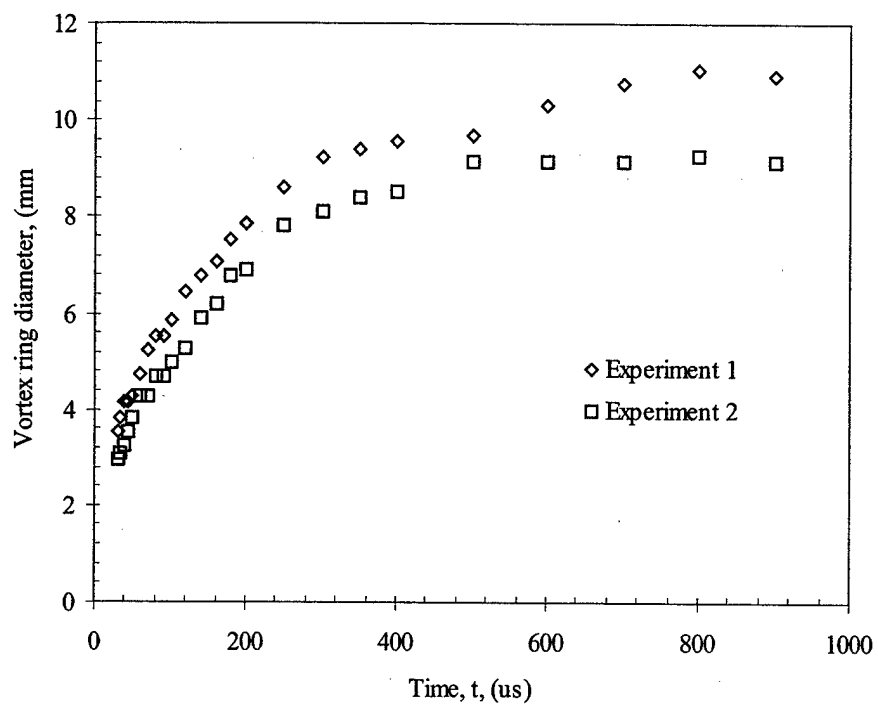


Figure 4.3 Vortex ring diameter growth as a function of time (measured from Filtered Rayleigh Scattering images)

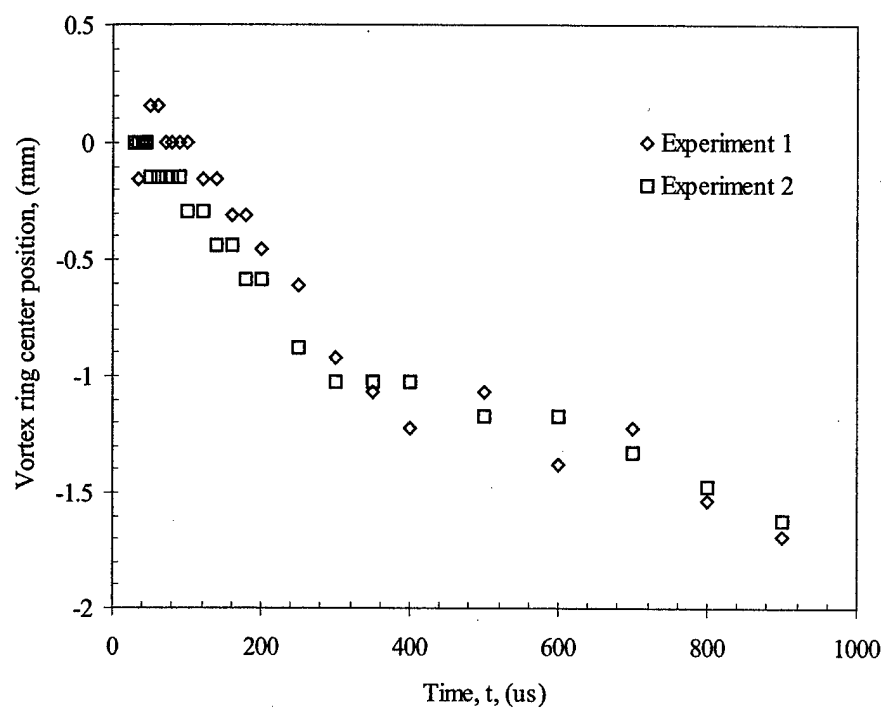


Figure 4.4 Vortex ring motion along optical axis (measured from Filtered Rayleigh Scattering images, negative direction is motion away from the focusing lens)

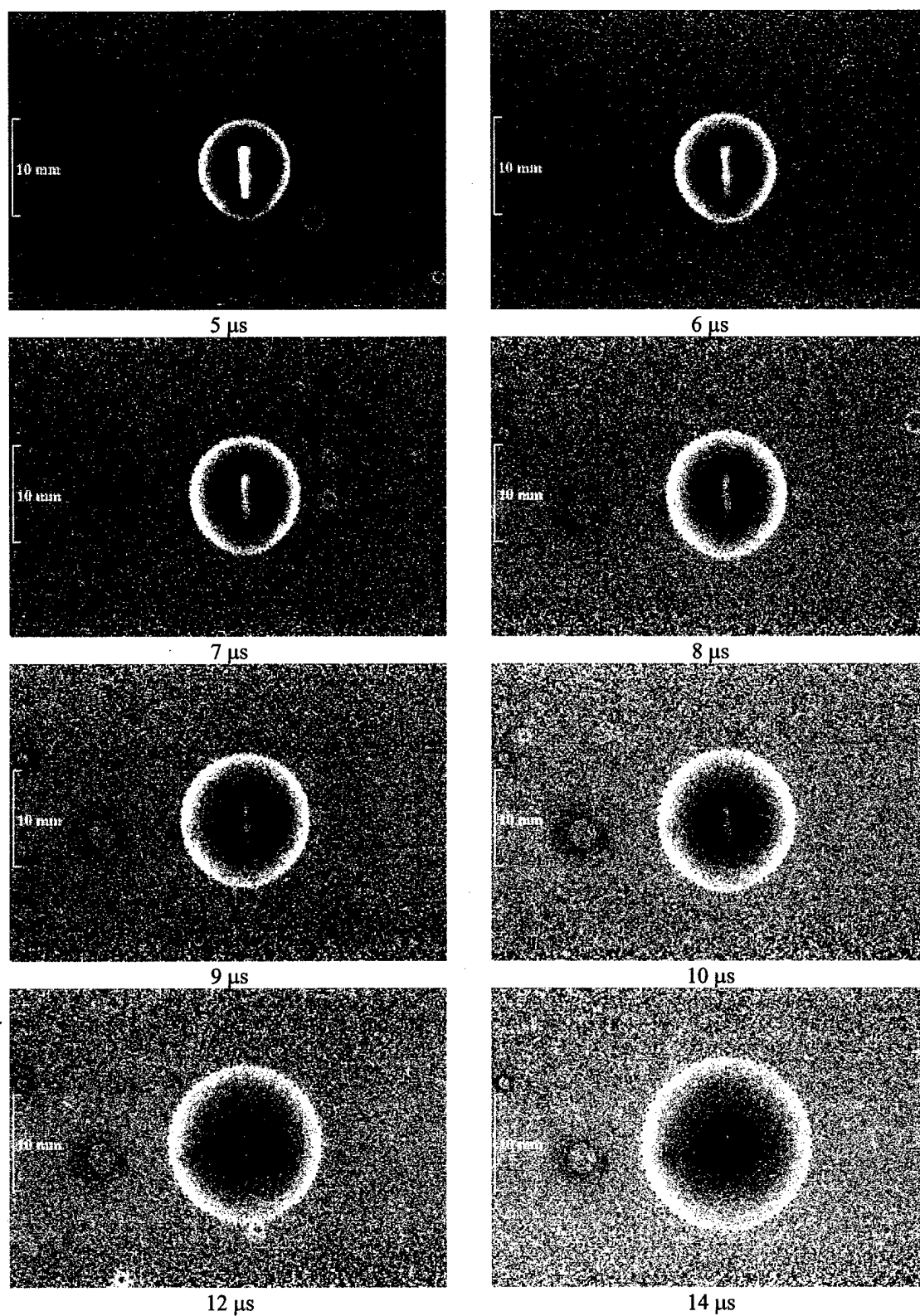


Figure 4.5 Filtered Rayleigh scattering images and blast wave measurement points for 112 mJ/pulse, 5 – 14 μs

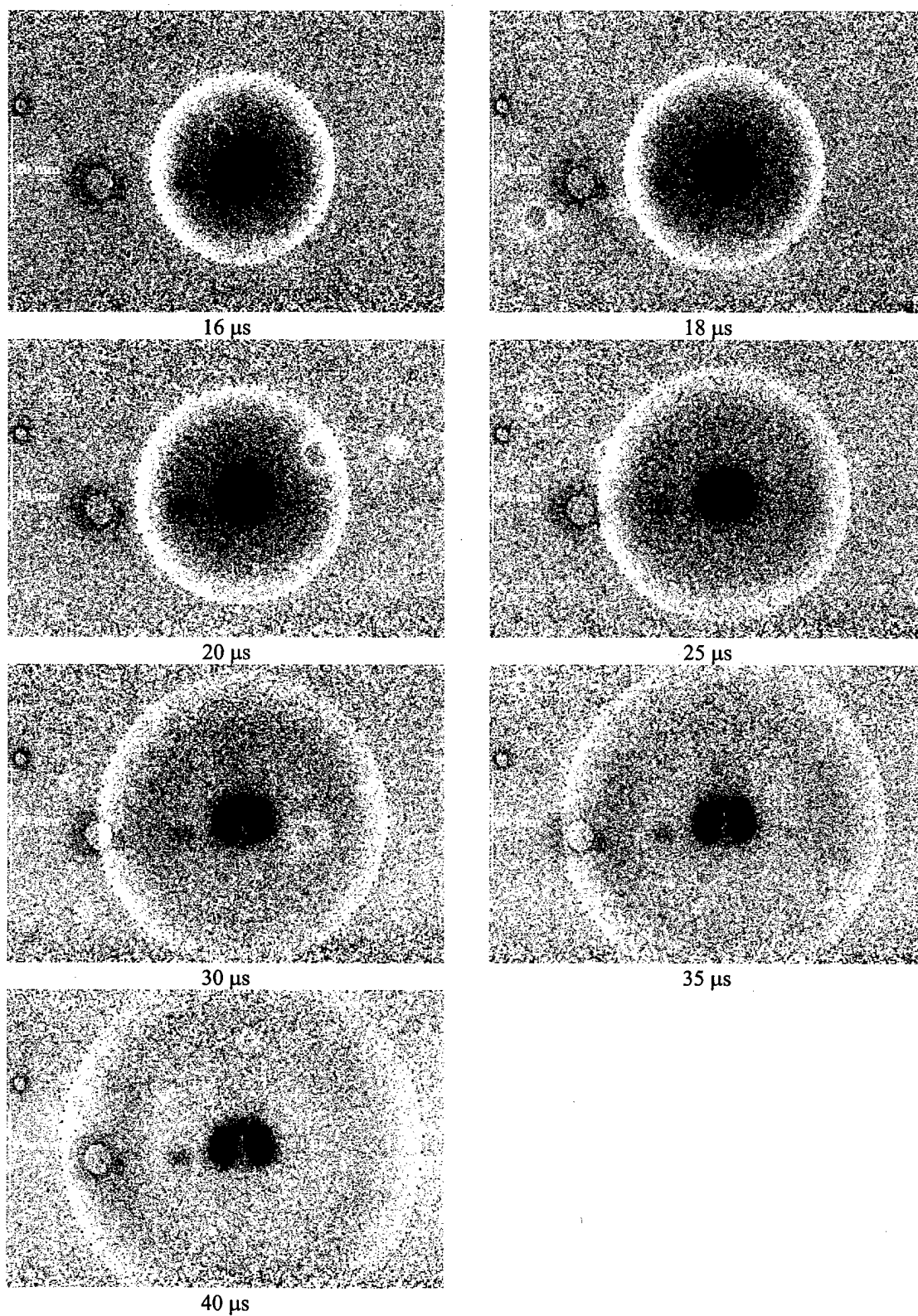


Figure 4.6 Filtered Rayleigh scattering images and blast wave measurement points for 112 mJ/pulse, 16–40 μs

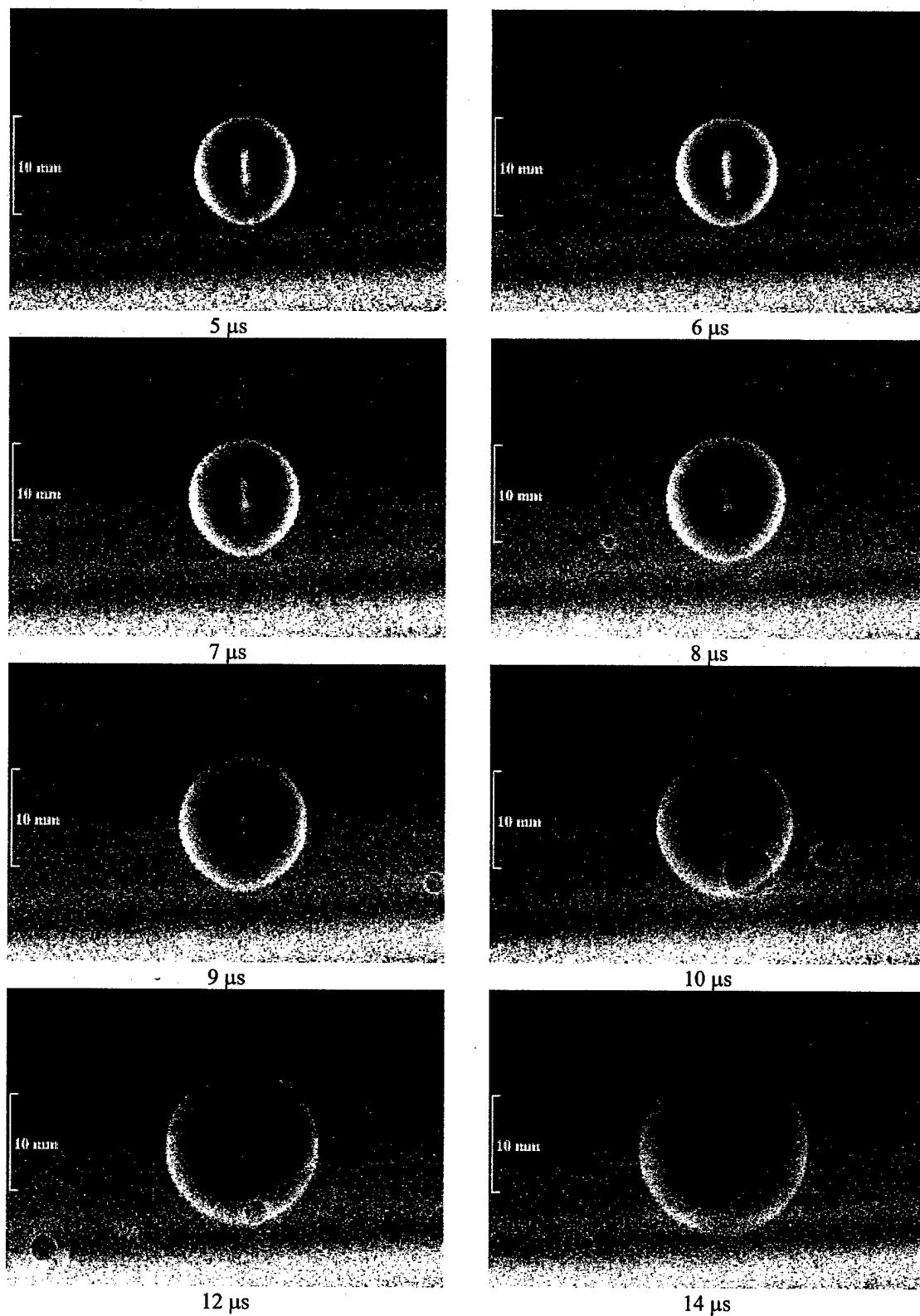


Figure 4.7 Filtered Rayleigh scattering images and blast wave measurement points for 98 mJ/pulse, 5 – 14 μs

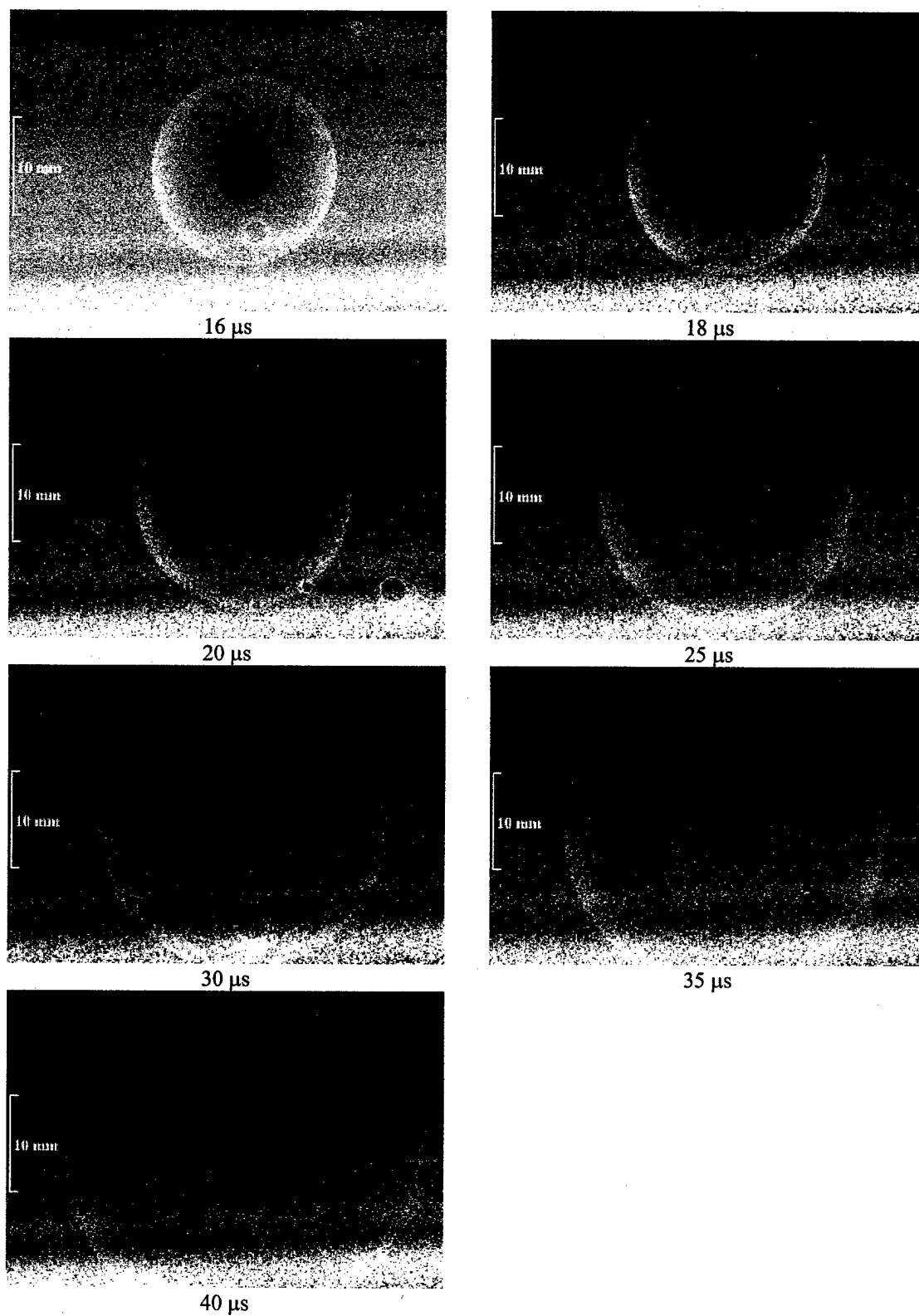


Figure 4.8 Filtered Rayleigh scattering images and blast wave measurement points for 98 mJ/pulse, 16 – 40 μ s

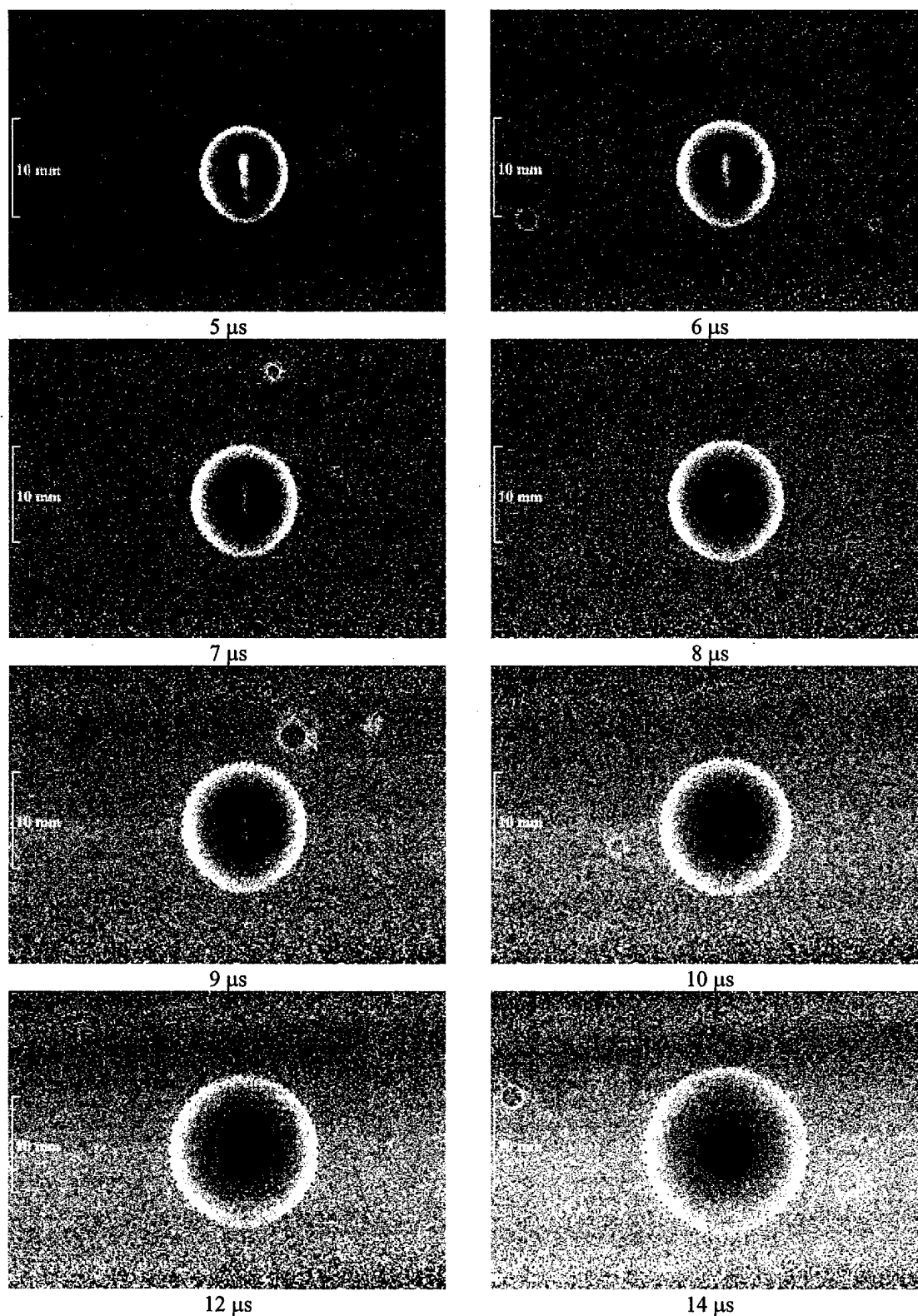


Figure 4.9 Filtered Rayleigh scattering images and blast wave measurement points for 76 mJ/pulse, 5 – 14 μ s

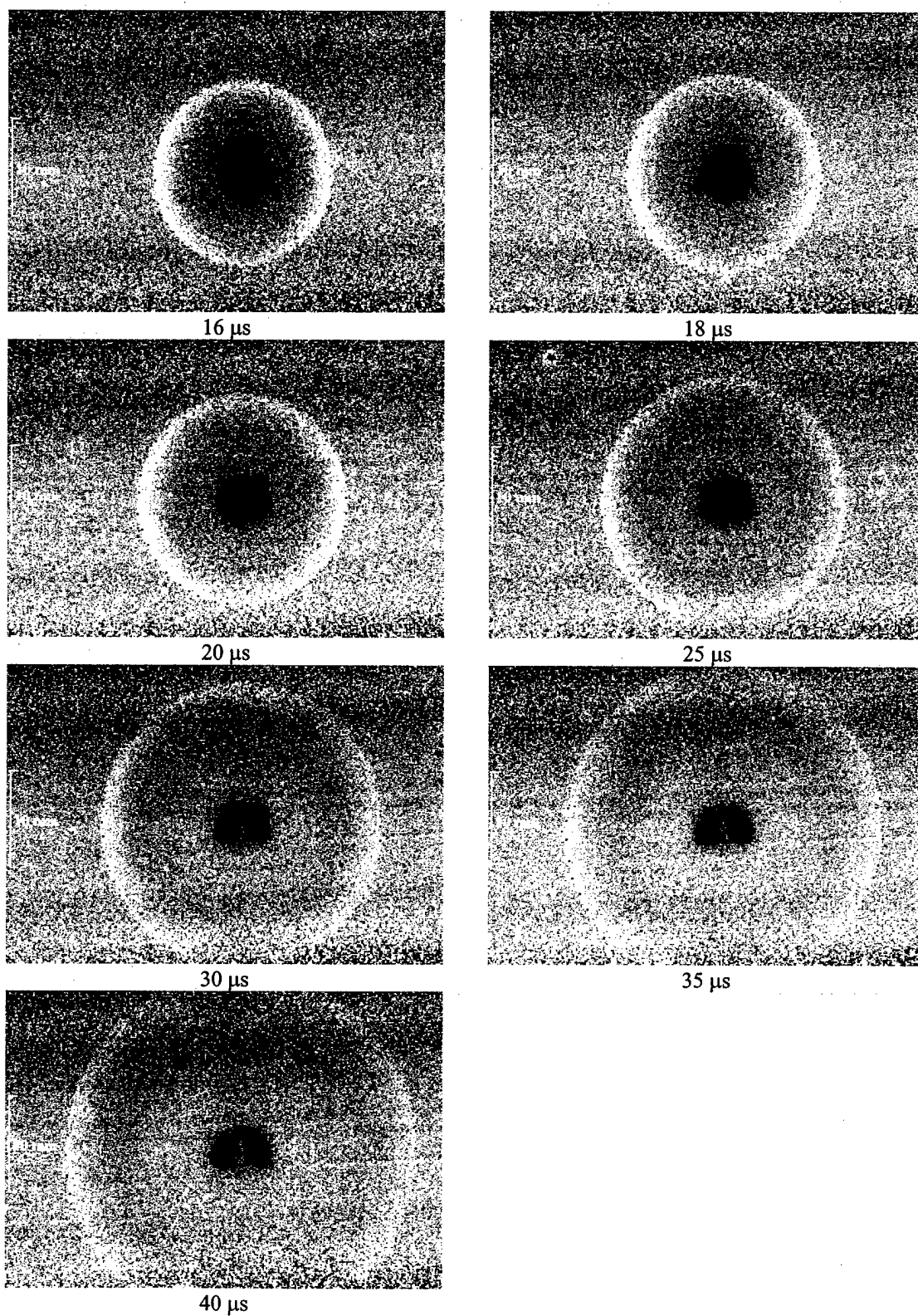


Figure 4.10 Filtered Rayleigh scattering images and blast wave measurement points for 76 mJ/pulse, 16 – 40 μ s

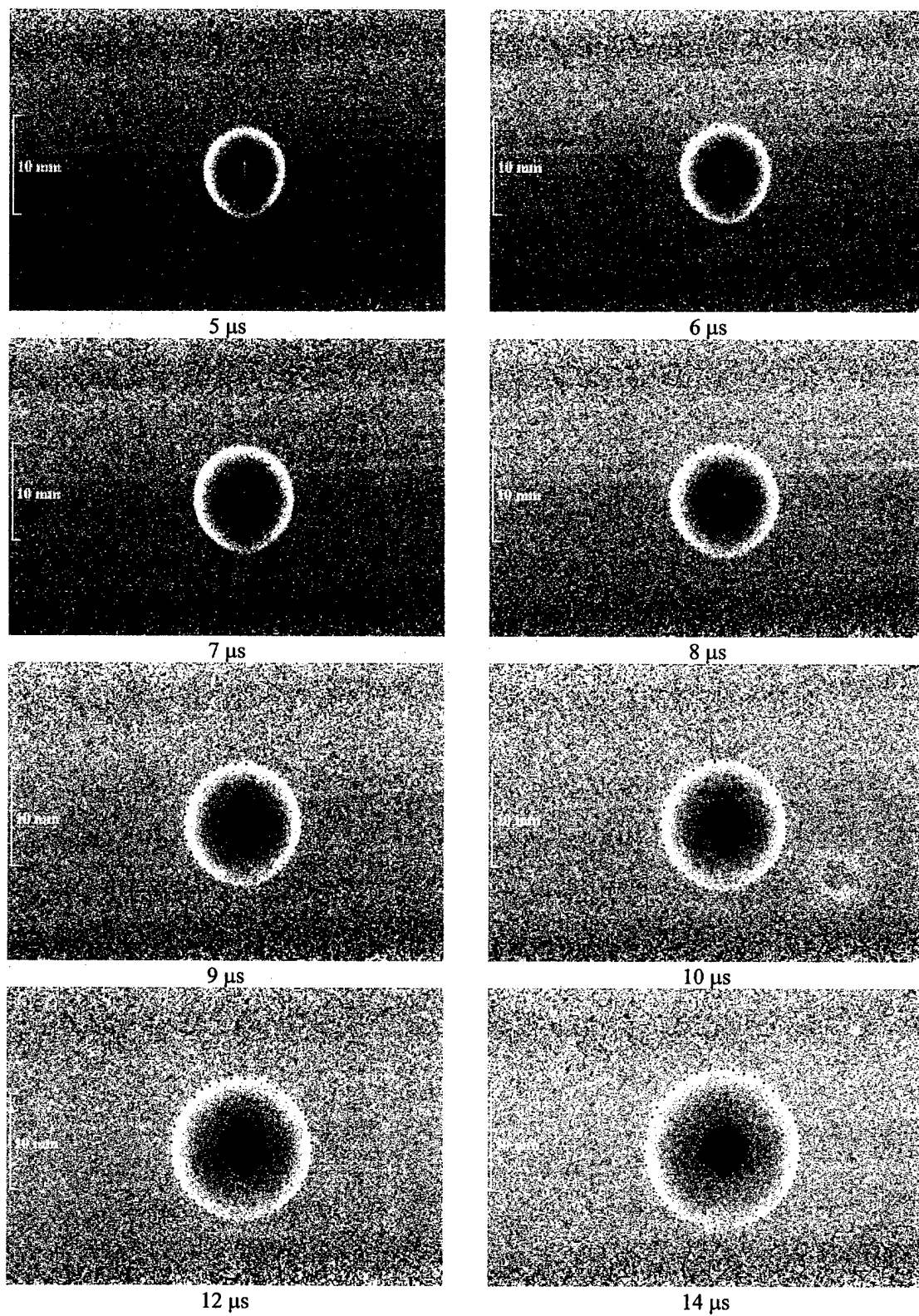


Figure 4.11 Filtered Rayleigh scattering images and blast wave measurement points for 50 mJ/pulse, 5 – 14 μ s

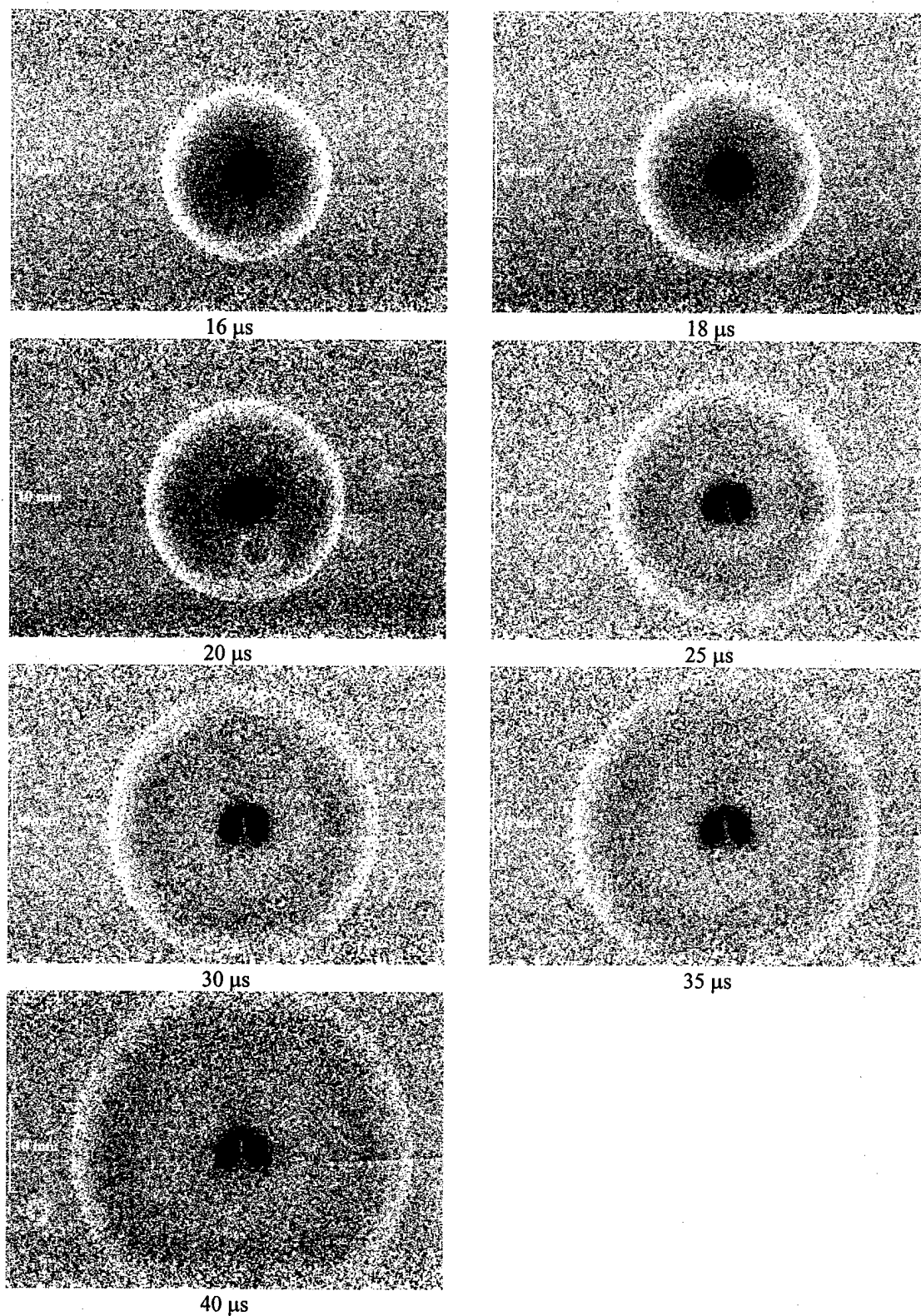


Figure 4.12 Filtered Rayleigh scattering images and blast wave measurement points for 50 mJ/pulse, 16 – 40 μ s

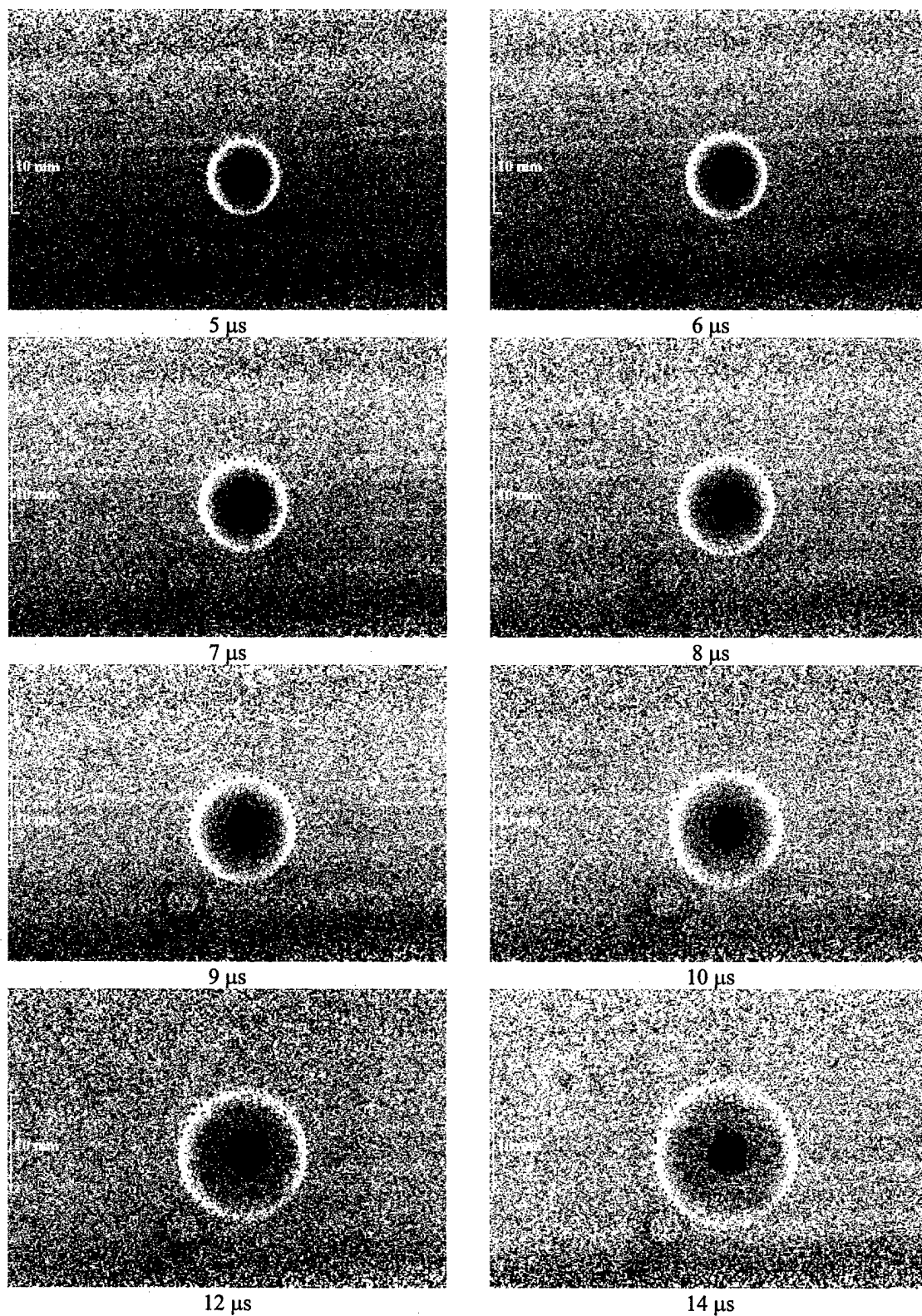


Figure 4.13 Filtered Rayleigh scattering images and blast wave measurement points for 20 mJ/pulse, 5 – 14 μ s

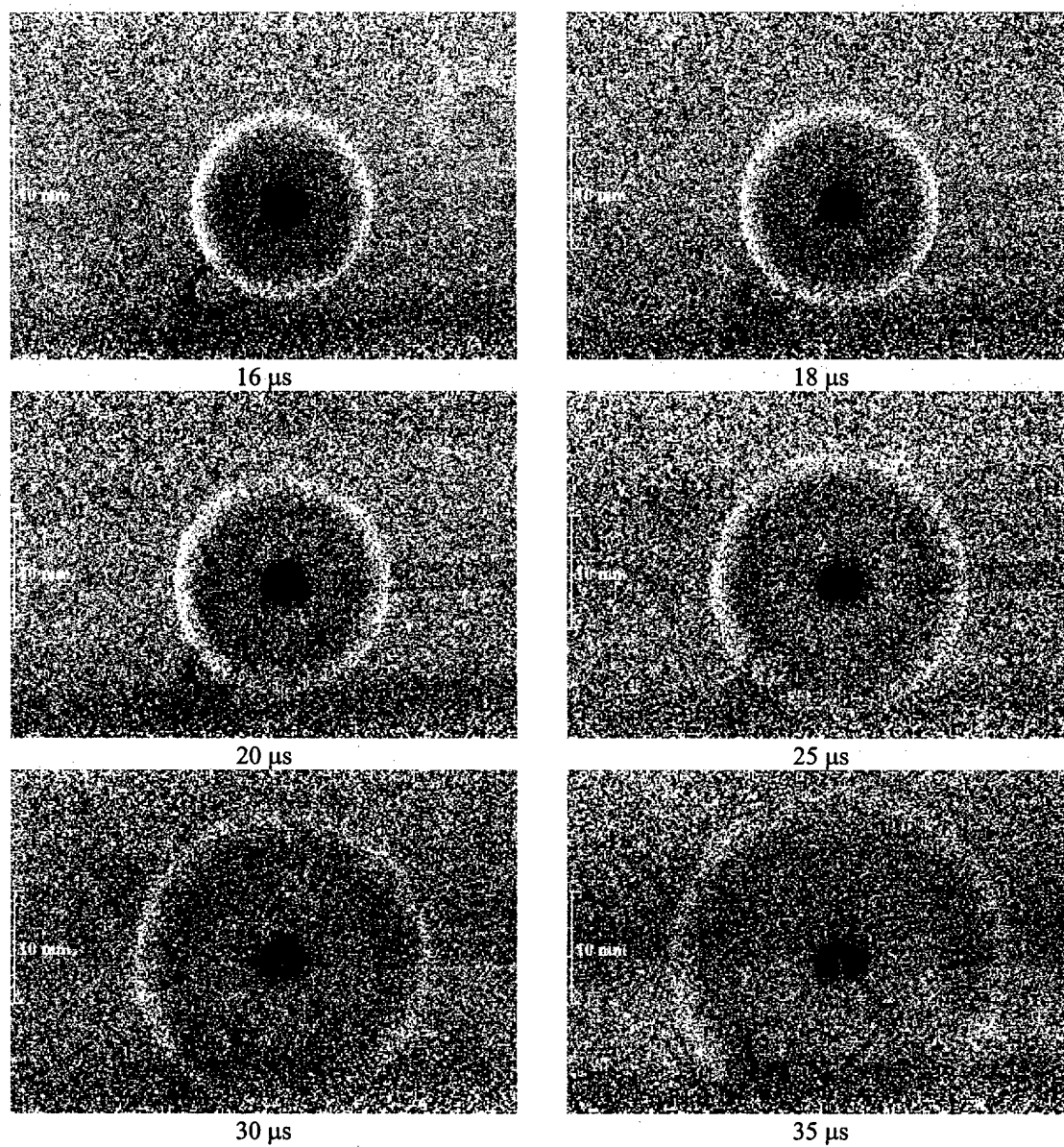


Figure 4.14 Filtered Rayleigh scattering images and blast wave measurement points for 20 mJ/pulse, 16–35 μ s

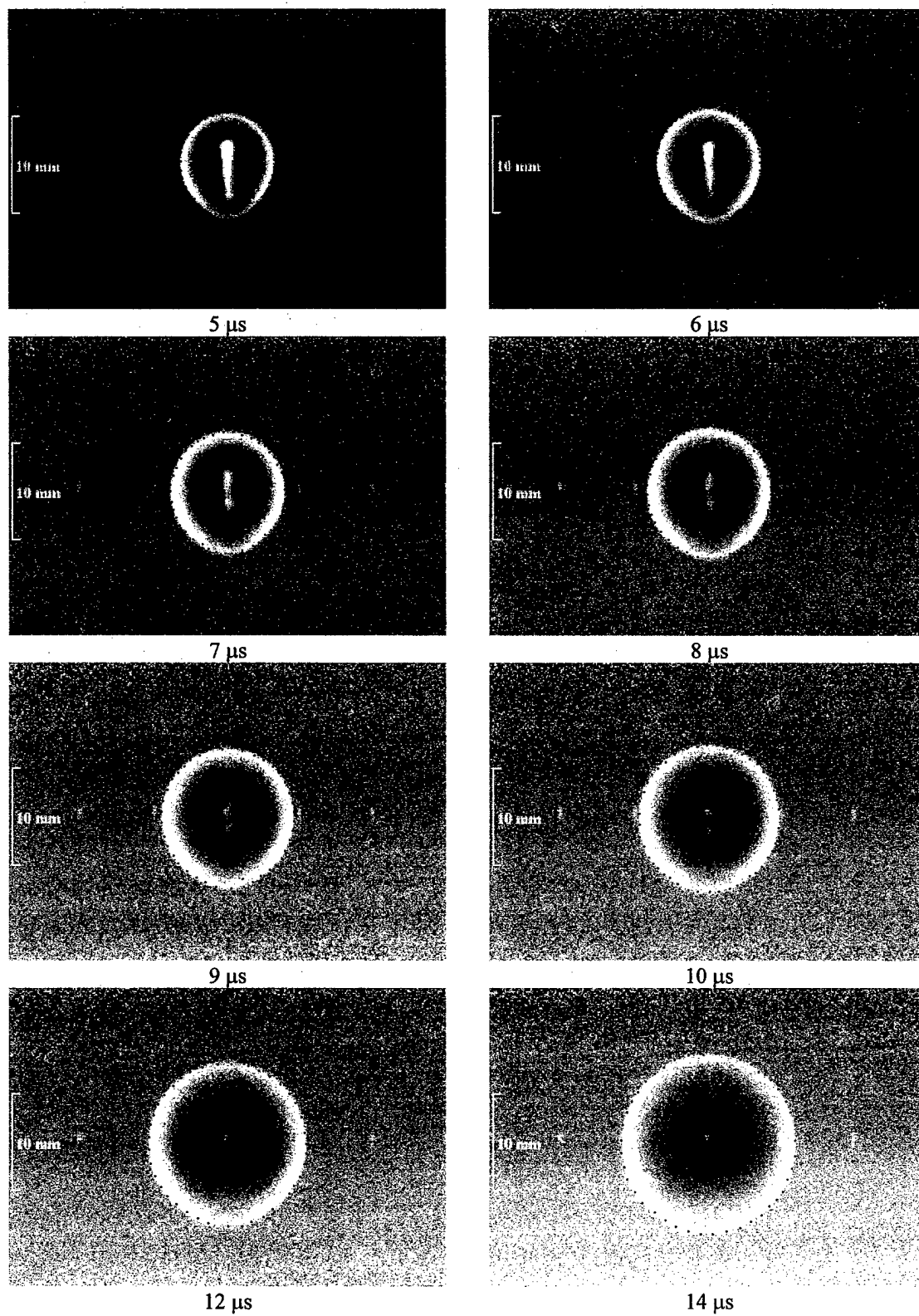


Figure 4.15 Filtered Rayleigh scattering images and blast wave measurement points for 116 mJ/pulse, 5 – 14 μ s

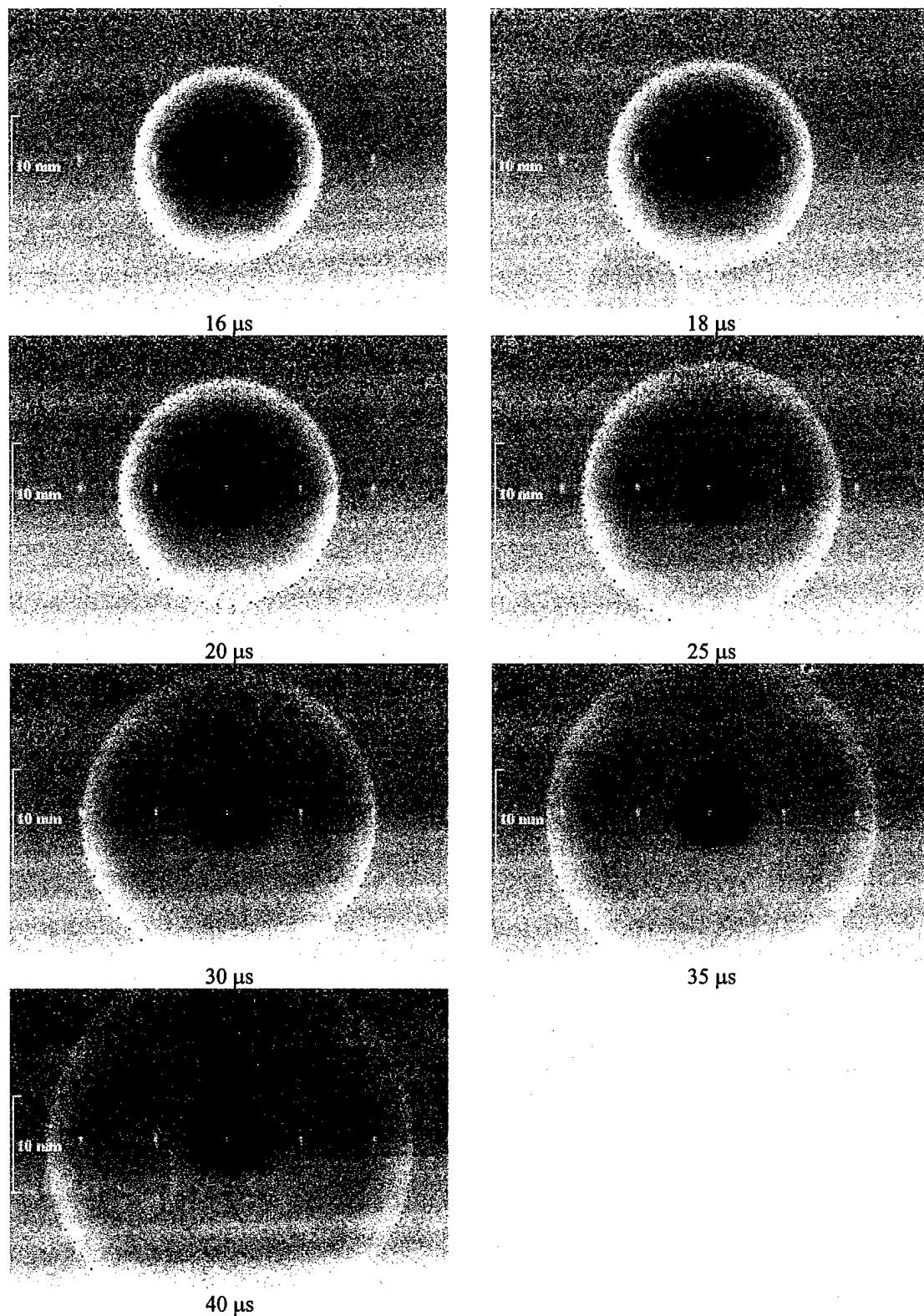


Figure 4.16 Filtered Rayleigh scattering images and blast wave measurement points for 116 mJ/pulse, 16 – 40 μ s

4.3 Energy and Deposition Volume

The energy for the deposition was estimated by taking laser beam power readings before and after the laser breakdown region. This is, of course, an upper bound for the energy deposited into the flow. There will be losses associated with radiation and scattering off-axis not recorded by the power meter after the breakdown region. Some of the energy is reflected, transmitted, scattered, and emitted by the plasma. Kandala and Candler [71] have modeled the plasma formation process and have quantitatively estimated some of the losses associated with the Nd:YAG laser plasma formation. The energy deposition levels for the various tests are reported throughout the document. The estimated accuracy of the energy deposition levels is ± 5 mJ/pulse. In addition, the blast wave propagation speed was measured as a parameter of the energy deposition level (see Section 4.4.1).

The diameter of the focal point region is governed by

$$d = f\theta \quad (4.1)$$

where d is the focal diameter, f is the focal length, and θ is the beam divergence. The estimated deposition volumes for the various tests are given throughout this document based on various optical arrangements.

4.4 Blast Wave

4.4.1 Wave Propagation Speed

Table 4.1 lists the characteristics of the energy deposition laser used for the quiescent air blast measurements. Table 4.2 lists the atmospheric conditions for laser energy deposition into quiescent air tests.

Figure 4.17 summarizes the shock wave radius versus time data for the test cases described in Section 4.2 above. The measurements for the blast wave radius were taken from the FRS images taken at each time increment and for each energy level. At each individual time increment, a sample of 30 to 40 points were manually read from the FRS images. Each point's pixel location was then least squares fit to determine the blast wave radius, given by

$$(x_{i,t} - x_{0,t})^2 + (y_{i,t} - y_{0,t})^2 = r_t^2 \quad (4.2)$$

where the point $(x_{0,t}, y_{0,t})$ is the center, r_t is the radius, and the point $(x_{i,t}, y_{i,t})$ is the i th data point. The subscript t refers to the time of the image. This reference time is the time delay between the laser pulse for the energy deposition and the time the image is recorded.

In turn, the blast wave radius versus time data was least squares curve fit to determine the values for a power function defined by

$$r = at^b + c \quad (4.3)$$

where r is the radius of the blast wave, t is the time, and a , b , and c are the fitting parameters. The wave propagation speed was then simply determined by taking the derivative of Equation (4.3). Figure 4.18 shows the shock speed as a function of time, and Figure 4.19 gives the shock Mach number as a function of time.

Figure 4.20 compares the experimentally determined time exponent, b in Equation (4.3), with the well known Taylor-Sedov [139] point source explosion equation for blast wave radius given by

$$r = C \left(\frac{E_0}{\rho_0} \right)^{1/5} t^{2/5} \quad (4.4)$$

where r is the blast wave radius, C is a constant depending the gas, E_0 is the energy of the explosion, ρ_0 is the initial density, and t is the time. As can be seen in Figure 4.20 the time exponent for the laser energy deposition experiments (~ 0.9) is significantly different than the Taylor-Sedov time exponent of 0.4. The difference comes from the similarity solution assumption used to derive Equation (4.4) of the ambient pressure being much less than the pressure after the blast wave. This requirement of a strong wave is not met by the laser energy deposition where for the times observed in the experiments the wave speed quickly approaches the acoustic speed as seen in Figure 4.19. Initially, Sedov [153] analyzed the wave propagation characteristics for the case where the back pressure cannot be neglected. More recently McGuire [89] verified the Sedov theory for pressure measurements made to determine the wave characteristics with significant back pressure for the blast wave generated with laser energy deposition.

The blast wave radius versus time data for each energy deposition level is presented in Figure 4.21 through Figure 4.25. The number of points read to fit the radius according to Equation (4.2) was

determined by the number needed to approach a normal distribution of residuals for the fit. This normal distribution of residuals was then used to give an estimate on the uncertainty in the measured radius. The residuals are shown for each energy test case in the figures by an error bar at each experimental data point. The error bars plotted on the radius versus time plot are the $\pm\sigma$ (one standard deviation) distribution for the residuals. The numerical simulation outlined in Section 2.3.2 is also shown for each energy case on the plots for comparison with the experimental data.

In summary, experimental measurements were made of the blast wave propagation for varying laser energy deposition levels. These measurements were then used to verify and calibrate the model development effort of Yan *et al* [151]. This model can now be used to verify and validate the energy deposition into more complex three-dimensional flow fields. In addition, the energy deposition levels can be estimated with this model when the energy levels are not easily measured by experiment. For instance, if the blast wave propagation speed can be measured from wind tunnel schlieren images, then an estimate can be made of the amount of energy deposited into the flow with this calibrated one-dimensional model.

Table 4.1 Perturbation laser characteristics

Differential Beam Energy (mJ)	Incident Beam Wavelength (nm)	Lens Focal Length (mm)
112	532	120
98	532	120
76	532	120
50	532	120
20	532	120
116	532	90

Table 4.2. Atmospheric test conditions

Differential Beam Energy (mJ)	Ambient Pressure (Pa)	Ambient Temperature (K)
112	1.013×10^5	291
98	1.013×10^5	291
76	1.013×10^5	291
50	1.013×10^5	291
20	1.013×10^5	291
116	1.013×10^5	294

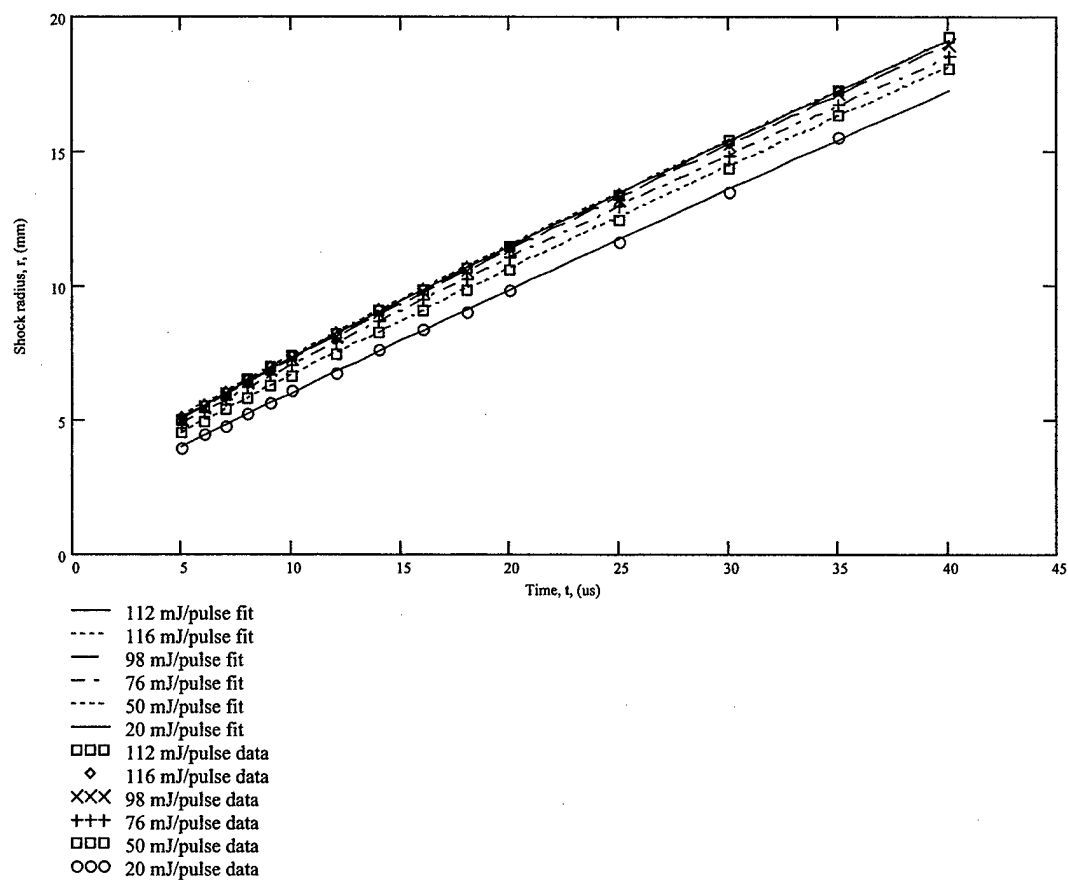


Figure 4.17 Shock wave radius as a function of time for varying incident laser absorption energies

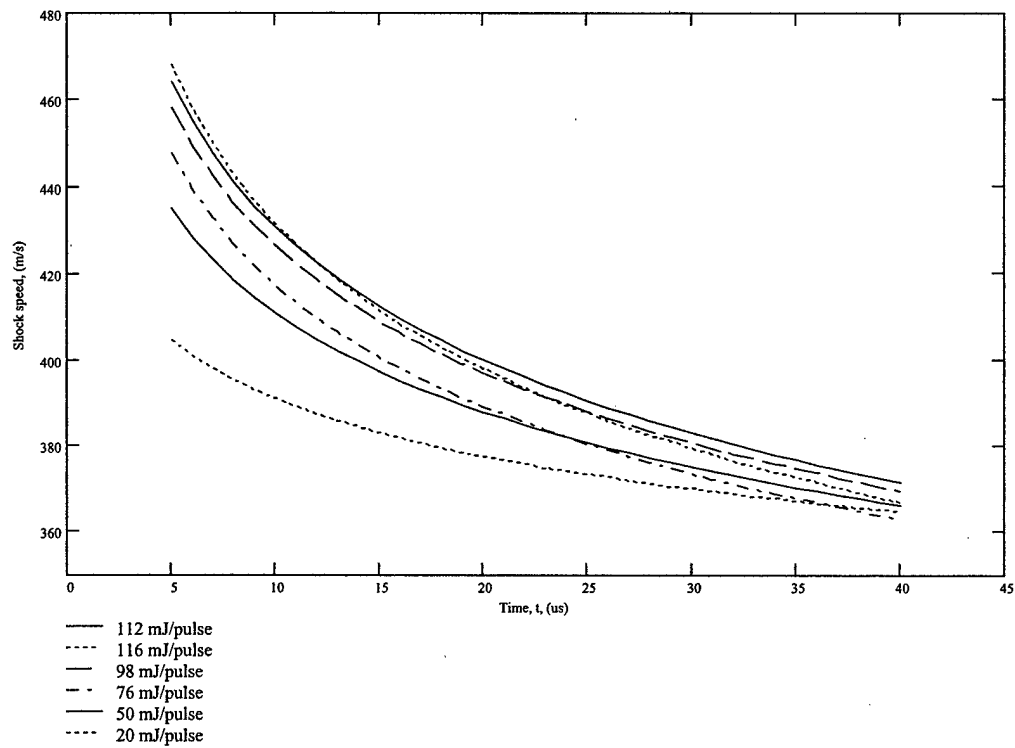


Figure 4.18 Shock wave speed as a function of time for varying incident laser absorption energies

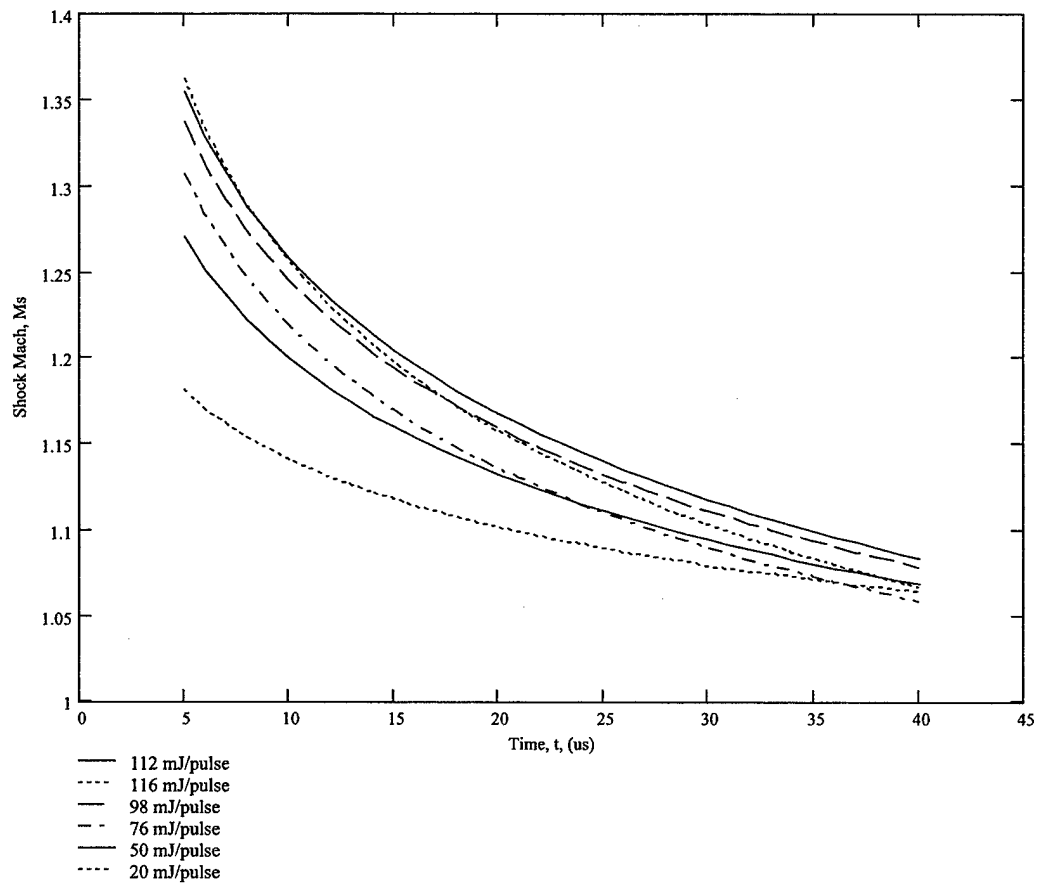


Figure 4.19 Shock wave Mach number as a function of time for varying laser absorption energies

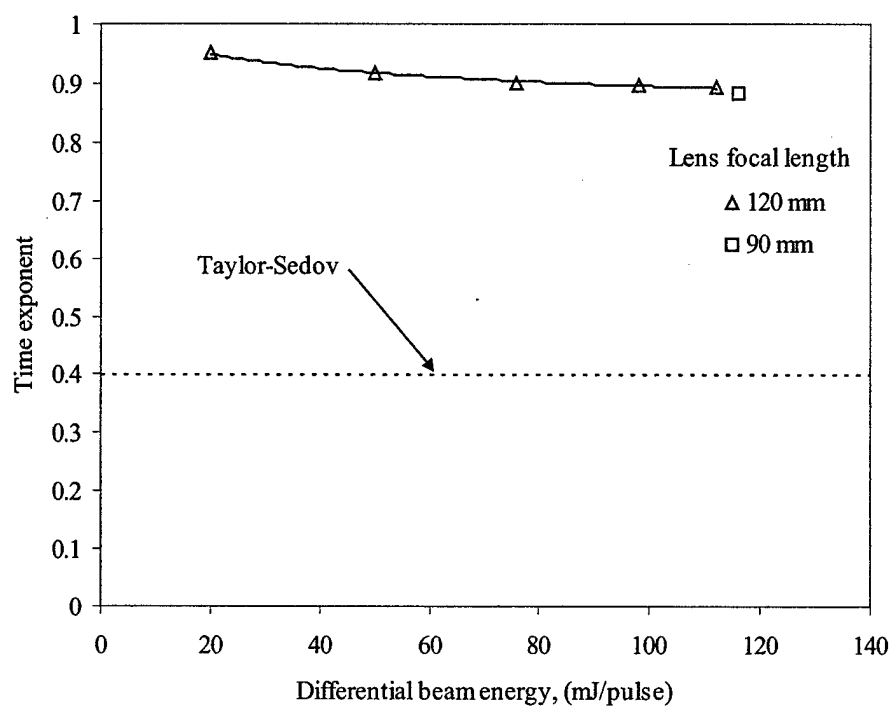


Figure 4.20 Comparison of experimental fit for time exponent for energy deposition levels

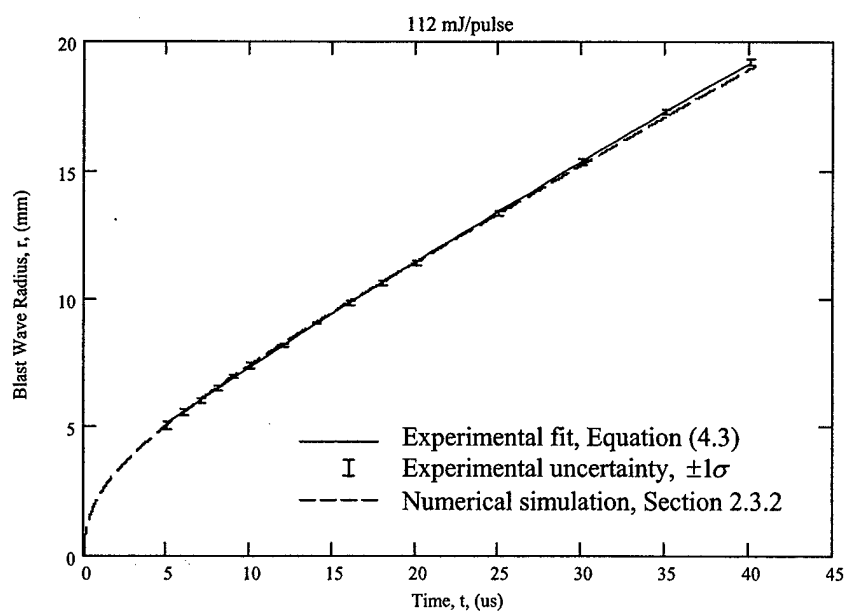


Figure 4.21 Shock wave propagation for 112 mJ/pulse

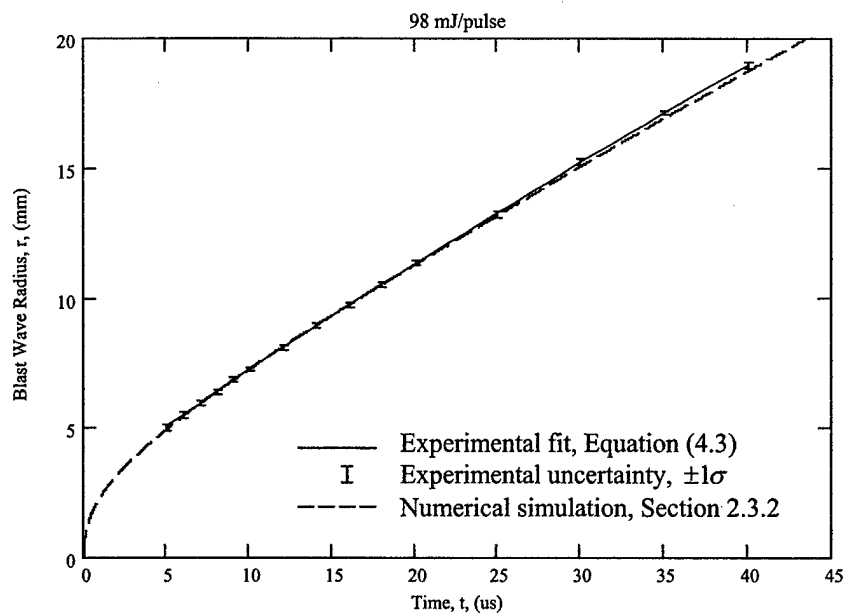


Figure 4.22 Shock wave propagation for 98 mJ/pulse

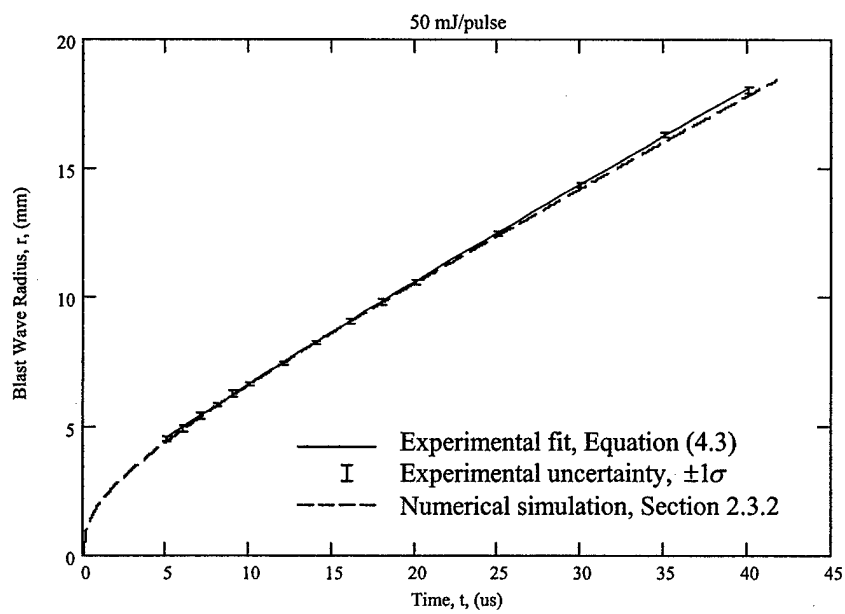


Figure 4.23 Shock wave propagation for 50 mJ/pulse

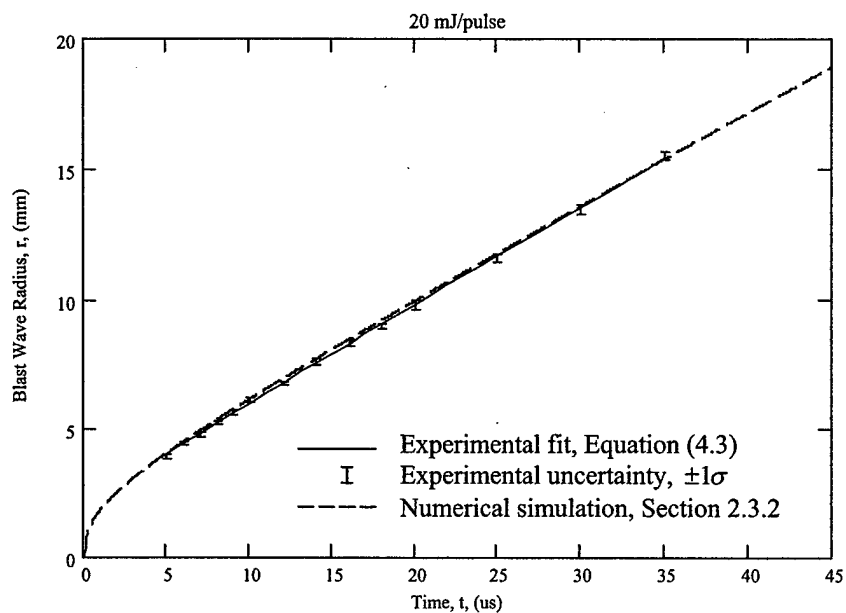


Figure 4.24 Shock wave propagation for 20 mJ/pulse

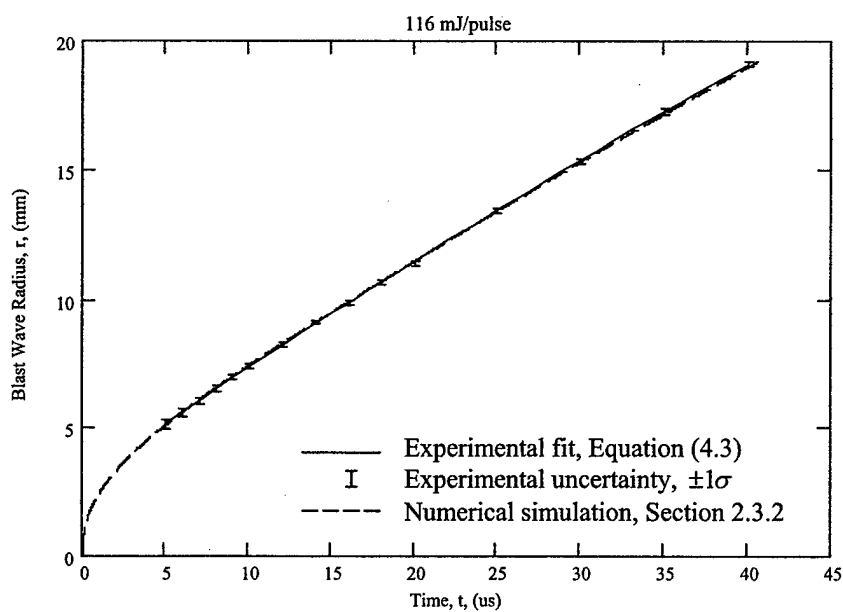


Figure 4.25 Shock wave propagation for 116 mJ/pulse

4.4.2 Pressure

Pressure measurements were made to compare against the results of the numerical simulation of Yan *et al* [151]. The objective of collecting this data is, again, to verify and validate the model development effort.

Two different energy levels of 58 and 112 mJ/pulse were tested. Figure 4.26 through Figure 4.34 give the pressure probe results for the 58 mJ/pulse laser energy deposition tests into quiescent air. In each figure the numerically simulated pressure is also presented for comparison. A corresponding schlieren image (taken with the laser/argon spark system Section 3.2.1) is also shown. The pressures have been scaled with the ambient air pressure. In each case the experimentally pressure is higher than the numerically simulated pressure. This higher pressure recorded by the Kistler probe is due to the shock reflection off of the surface of the probe. The reflection of the shock wave from the surface leads to a higher pressure measurement than is expected from the compression of the blast wave alone. However, the measured pressure shows the proper characteristics of the passage of a moving shock wave. The sharp increase in pressure due to the initial compression is observed along with the following expansion wave. The measured expansion is also greater in magnitude than the simulated expansion. In a like manner, this increase in measured expansion is due to the reflection of the expansion wave from the surface of the pressure probe. Figure 4.35 through Figure 4.42 gives the results for the pressures for the 112 mJ/pulse test case. Again, the magnitudes of the compressions and expansions due to the passage of the blast wave are greater for the experimental data. This, likewise, is attributable to the reflections of the waves from the surface of the intrusive probe.

For each of the energy levels, the decaying shock strength is observed by the decaying pressure levels. This decay is observed in both the numerical simulation and the experimental probe measurements. Figure 4.43 shows a comparison of the peak pressure levels associated with the blast wave for the probe measurements, the simulation, and as calculated from the normal shock relations for the 58 mJ/pulse case. Likewise, Figure 4.44 gives the comparison for the 112 mJ/pulse case. In each case the, the experimental peak pressure is larger than the simulation and as determined from the normal shock relations.

For each of the energy levels tested, the difference in the peak pressure measured from the probe to the simulated pressure was 40 percent. The errors associated with the intrusive probe measurements definitely

justify the effort to measure the thermodynamic properties for the quiescent laser energy deposition non-intrusively. Boguszko *et al* [14] is developing the Filtered Rayleigh Scattering technique to make these non-intrusive measurements for pressure. Their measurements agree with the model within 1%. Moreover, Boguszko's measurements will non-intrusively measure the density and temperature as well. These measurements will be a key factor in the verification of the model development effort of Yan *et al* [151] and Kandala and Candler [71].

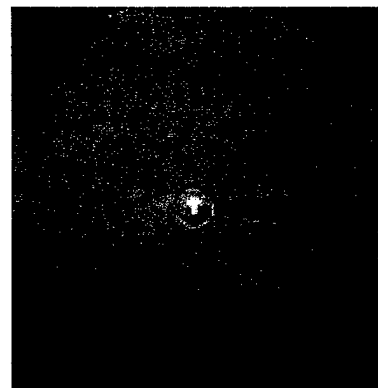
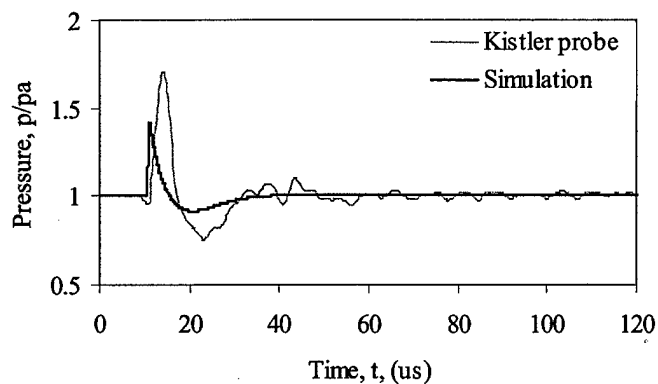


Figure 4.26 Measured and simulated pressure traces at $r = 6.9$ mm and corresponding schlieren image at $t = 10.8 \mu\text{s}$ for energy deposition of 58 mJ/pulse

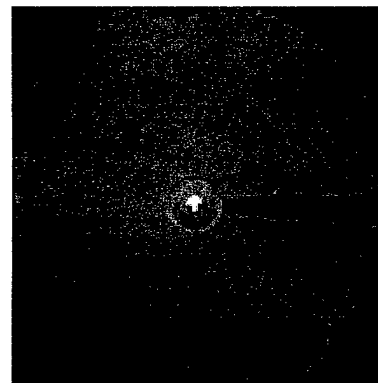
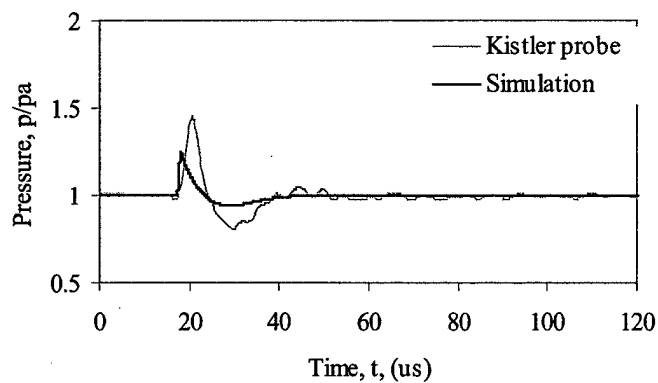


Figure 4.27 Measured and simulated pressure traces at $r = 9.6$ mm and corresponding schlieren image at $t = 18.4 \mu\text{s}$ for energy deposition of 58 mJ/pulse

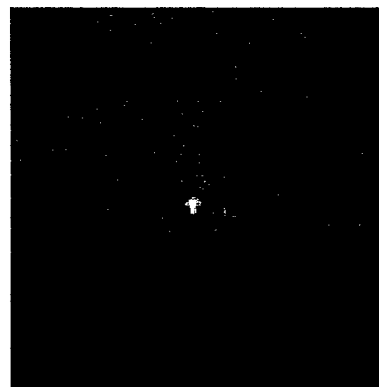
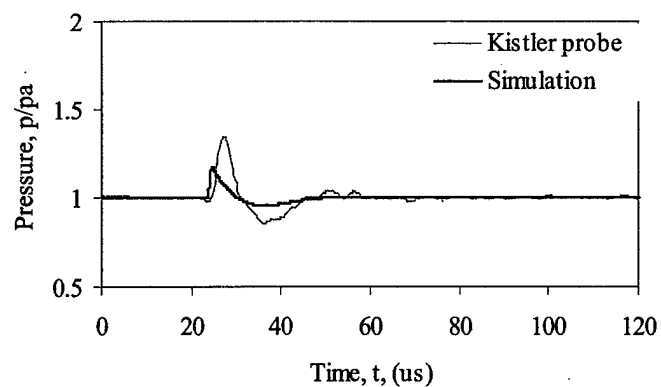


Figure 4.28 Measured and simulated pressure traces at $r = 12.0$ mm and corresponding schlieren image at $t = 24.4 \mu\text{s}$ for energy deposition of 58 mJ/pulse

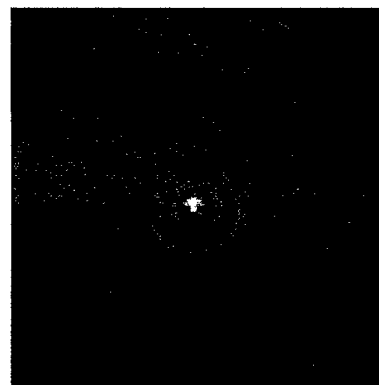
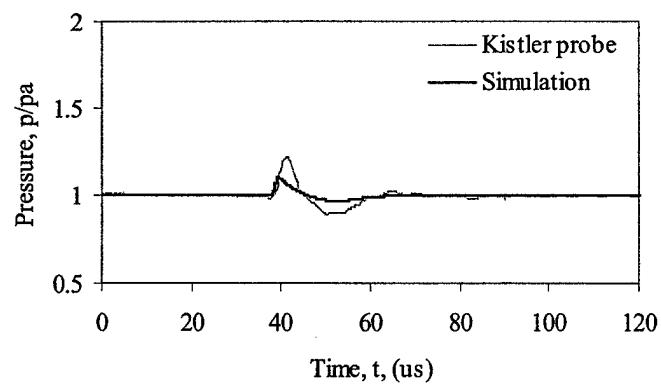


Figure 4.29 Measured and simulated pressure traces at $r = 17.4$ mm and corresponding schlieren image at $t = 38.4 \mu\text{s}$ for energy deposition of 58 mJ/pulse

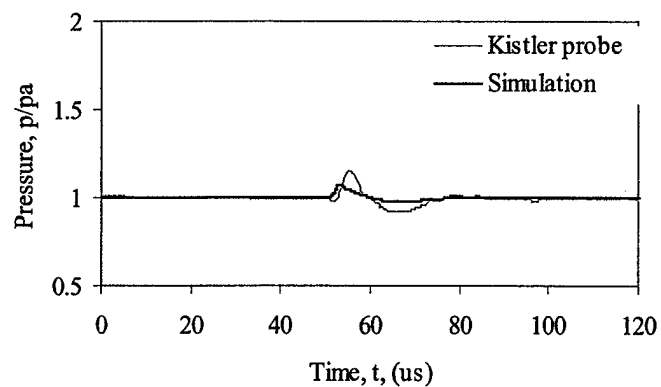


Figure 4.30 Measured and simulated pressure traces at $r = 22.2$ mm and corresponding schlieren image at $t = 52.4$ μ s for energy deposition of 58 mJ/pulse

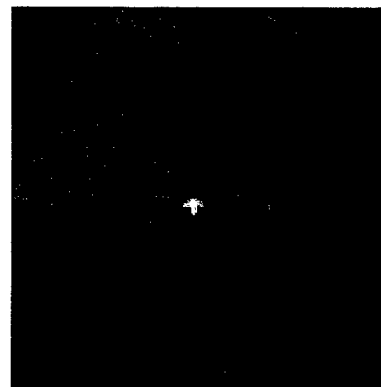
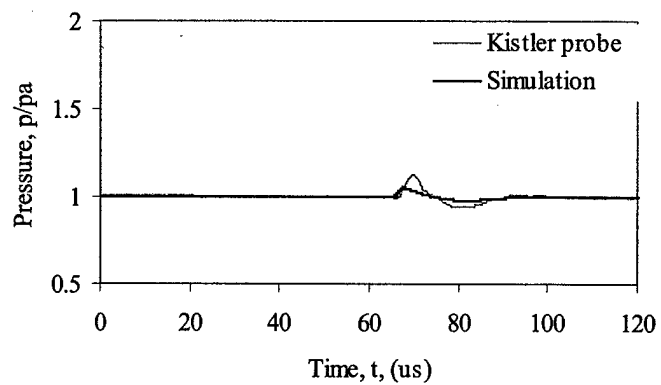


Figure 4.31 Measured and simulated pressure traces at $r = 27.3$ mm and corresponding schlieren image at $t = 66.4$ μ s for energy deposition of 58 mJ/pulse

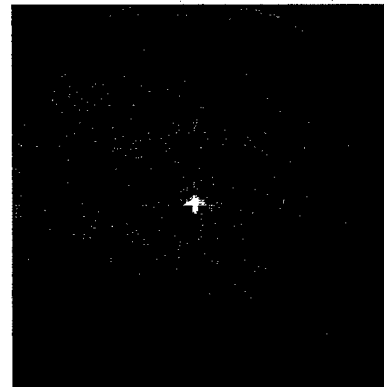
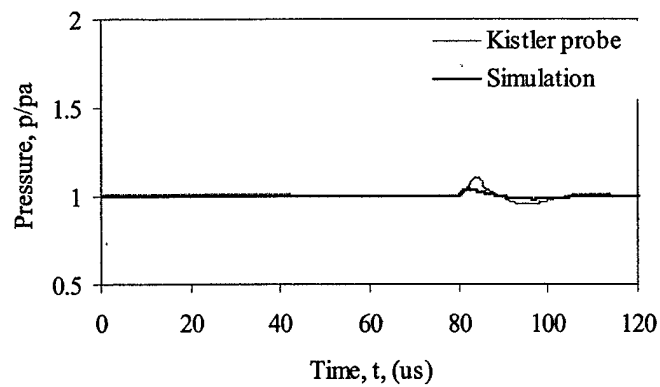


Figure 4.32 Measured and simulated pressure traces at $r = 32.4$ mm and corresponding schlieren image at $t = 81.2$ μ s for energy deposition of 58 mJ/pulse

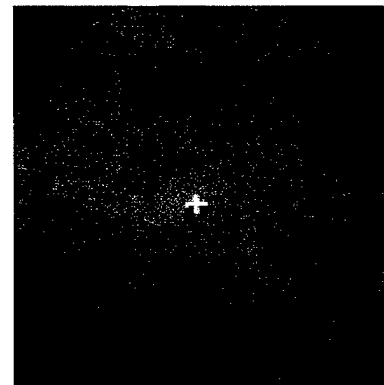
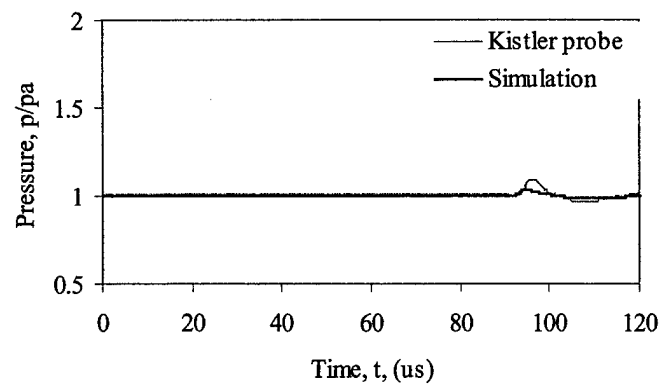


Figure 4.33 Measured and simulated pressure traces at $r = 36.6$ mm and corresponding schlieren image at $t = 94.4$ μ s for energy deposition of 58 mJ/pulse

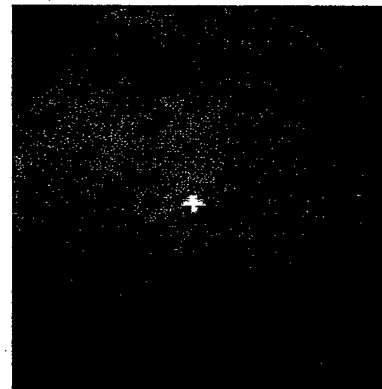
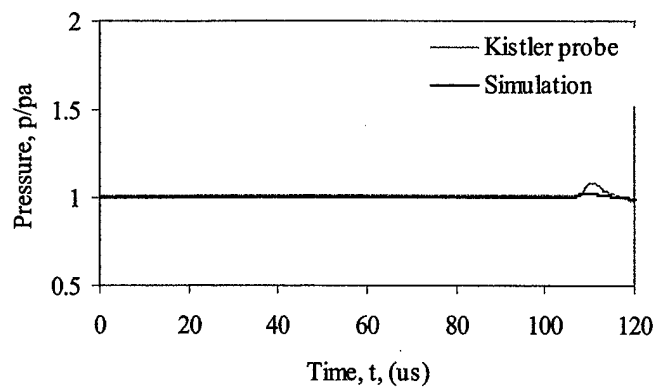


Figure 4.34 Measured and simulated pressure traces at $r = 41.7 \text{ mm}$ and corresponding schlieren image at $t = 107.2 \mu\text{s}$ for energy deposition of 58 mJ/pulse

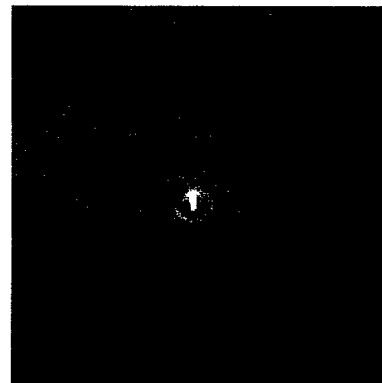
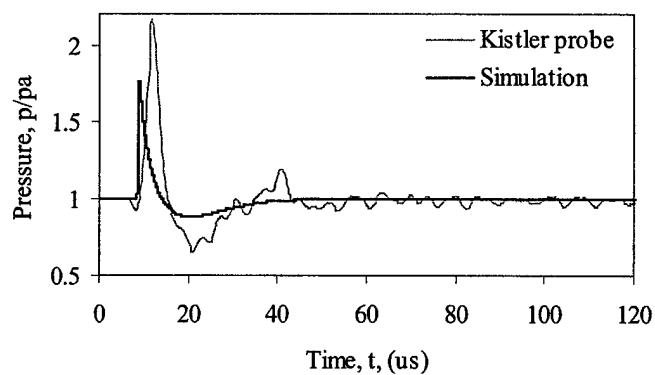


Figure 4.35 Measured and simulated pressure traces at $r = 6.9 \text{ mm}$ and corresponding schlieren image at $t = 10.4 \mu\text{s}$ for energy deposition of 115 mJ/pulse

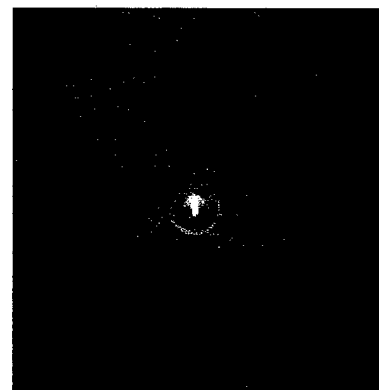
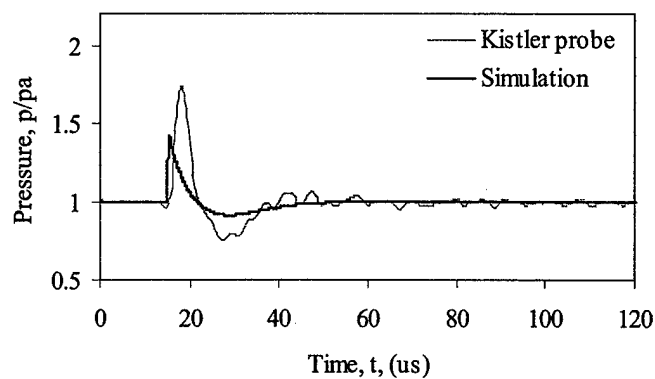


Figure 4.36 Measured and simulated pressure traces at $r = 9.6$ mm and corresponding schlieren image at $t = 16.4$ μ s for energy deposition of 115 mJ/pulse

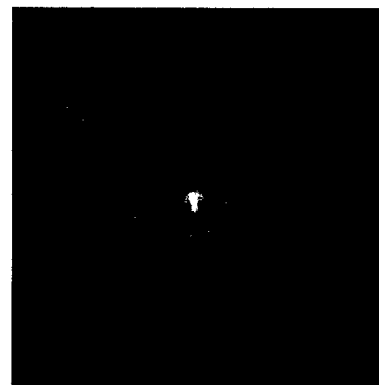
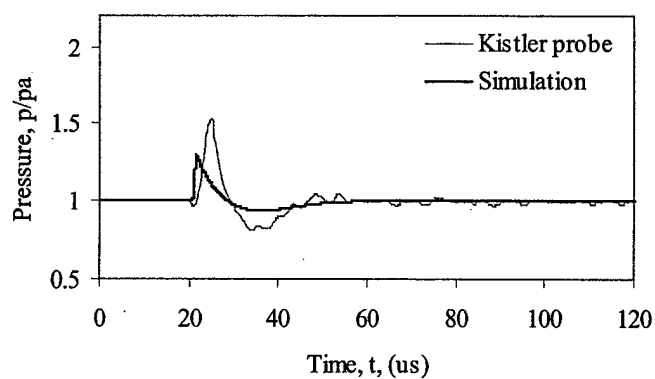


Figure 4.37 Measured and simulated pressure traces at $r = 12.0$ mm and corresponding schlieren image at $t = 22.4$ μ s for energy deposition of 115 mJ/pulse

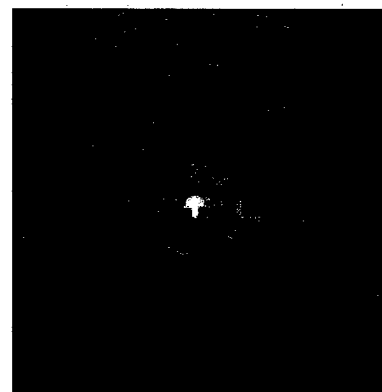
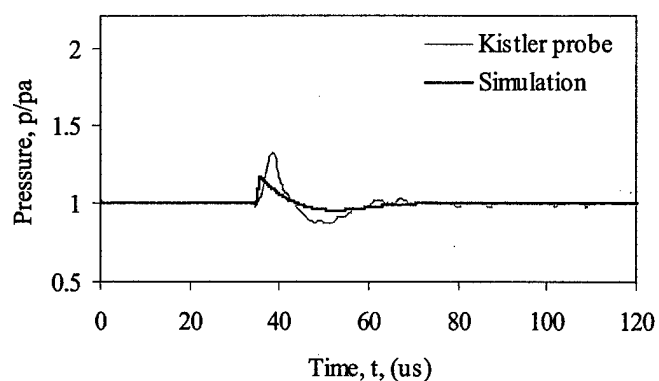


Figure 4.38 Measured and simulated pressure traces at $r = 17.1$ mm and corresponding schlieren image at $t = 36.4$ μ s for energy deposition of 115 mJ/pulse

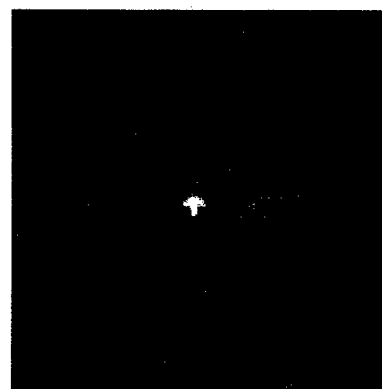
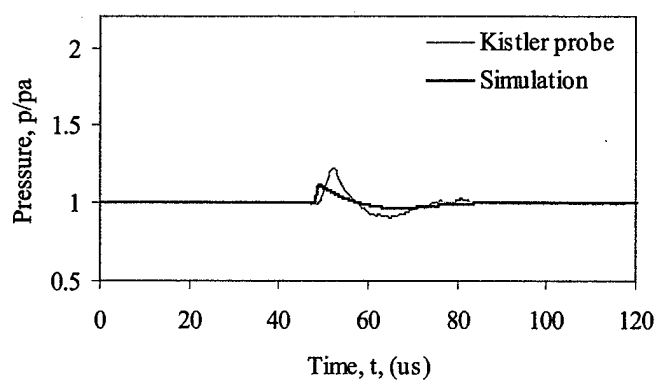


Figure 4.39 Measured and simulated pressure traces at $r = 22.2$ mm and corresponding schlieren image at $t = 49.2$ μ s for energy deposition of 115 mJ/pulse

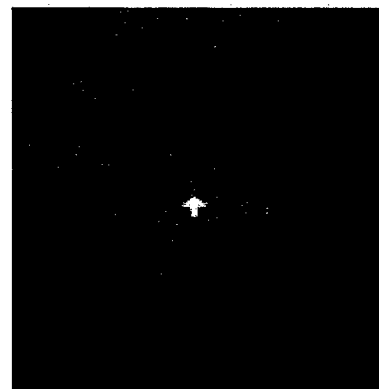
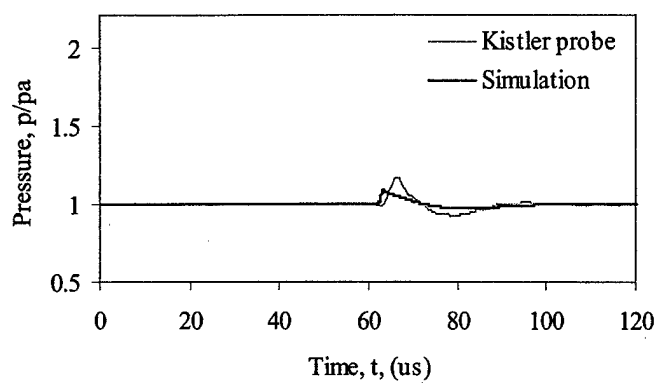


Figure 4.40 Measured and simulated pressure traces at $r = 27.3$ mm and corresponding schlieren image at $t = 63.2$ μ s for energy deposition of 115 mJ/pulse

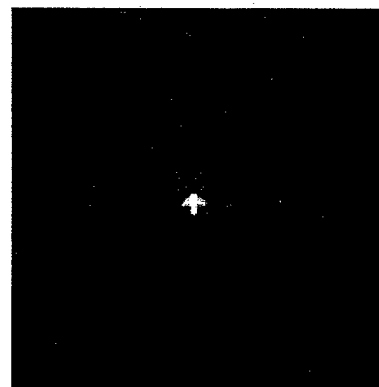
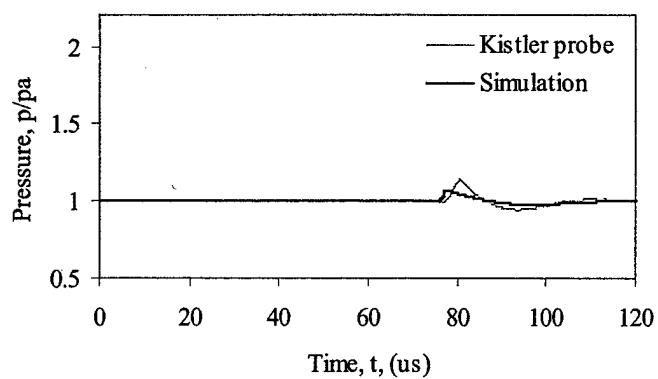


Figure 4.41 Measured and simulated pressure traces at $r = 32.4$ mm and corresponding schlieren image at $t = 77.6$ μ s for energy deposition of 115 mJ/pulse

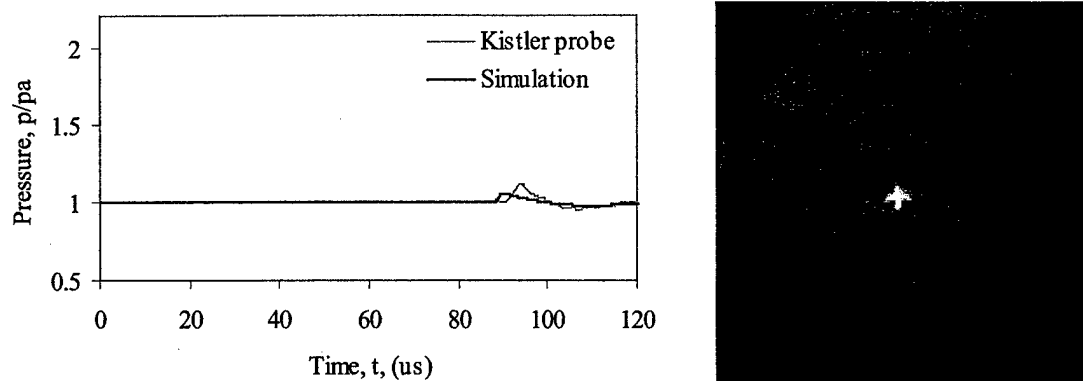


Figure 4.42 Measured and simulated pressure traces at $r = 36.6$ mm and corresponding schlieren image at $t = 91.2$ μ s for energy deposition of 115 mJ/pulse

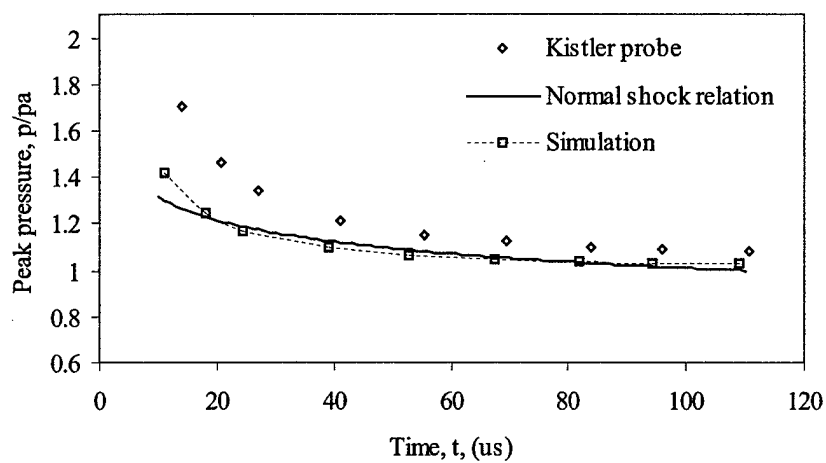


Figure 4.43 Comparison of peak pressures associated with the blast wave for energy deposition of 58 mJ/pulse

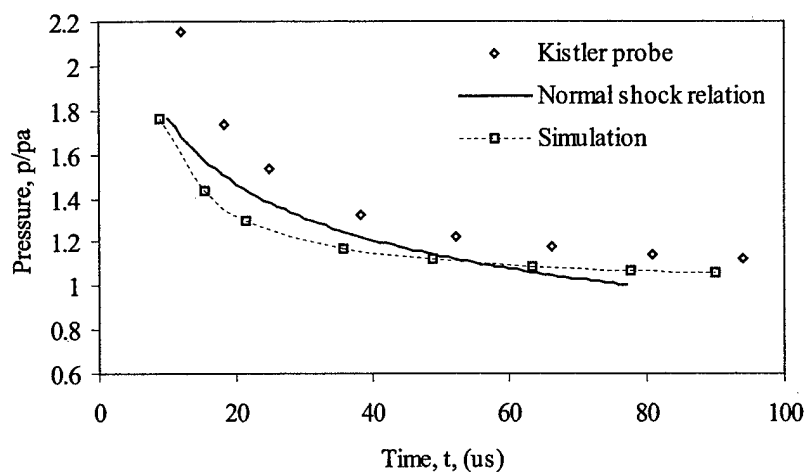


Figure 4.44 Comparison of peak pressures associated with the blast wave for energy deposition of 112 mJ/pulse

4.5 Summary

Qualitative and quantitative experiments have been completed for laser energy deposition into air. The blast wave propagation speed and pressure have been measured for various laser energy deposition levels. The wave speed measurements show good agreement with the numerical simulation results. The pressure probe measurements, however, have errors of 40% and can be attributed to the intrusive probe. This justifies the work by Boguszko *et al* [14] in making non-intrusive velocity, density, pressure, and temperature measurements for further simulation verification and validation. The blast wave measurements will provide a means of calibrating the levels of laser energy deposition for future experiments when the blast wave speed can be measured.

Chapter 5

Laser Energy Deposition Upstream of Mach 3.45 Sphere

5.1 Overview of Sphere Tests

Experiments were completed for a sphere at Mach 3.45 with laser energy deposition upstream of the sphere. Surface pressure, temperature, and heat transfer measurements were made for the cases of the sphere with and without shock impingement. The overarching goal of these tests was to determine if the laser energy deposition could be used to mitigate the adverse aerothermal loads associated with the Edney Type IV shock/shock interaction. Schlieren images were made to record the interaction of the laser perturbation with the sphere and to correlate with the pressure and heat transfer data. Figure 5.1 shows the laser energy deposition locations for the tests with the sphere alone. These tests were completed as a baseline case for comparison to the shock impingement test cases. Figure 5.2 shows the laser energy deposition locations for the sphere with the Edney Type IV shock/shock interaction.

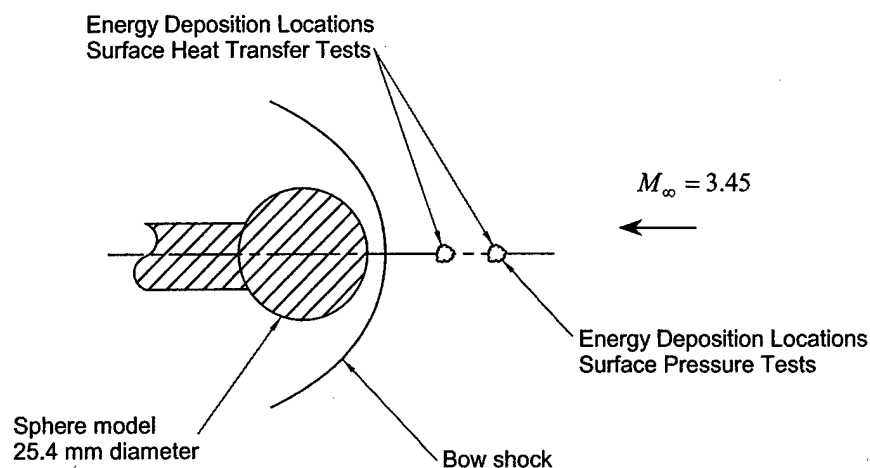


Figure 5.1 Laser energy deposition locations for Mach 3.45 experiments

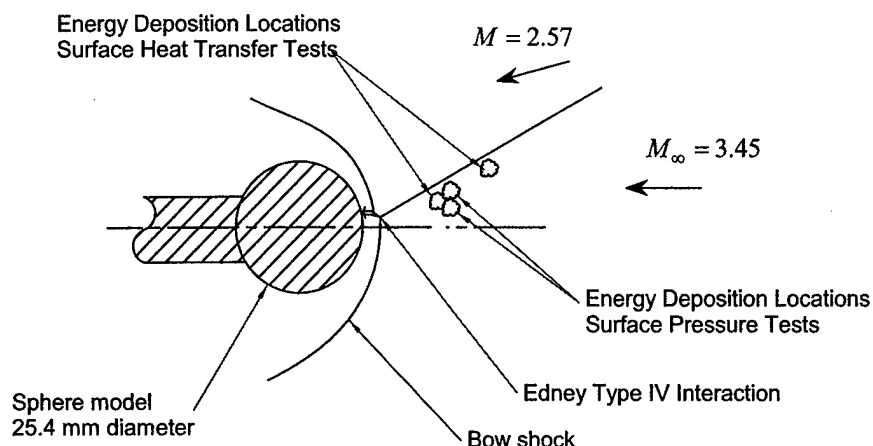


Figure 5.2 Laser energy deposition locations for Mach 3.45 sphere with Edney Type IV shock/shock interaction

5.2 Sphere Without Shock Impingement

Surface pressure and heat transfer measurements were made on a 25.4 mm diameter sphere in the Mach 3.45 wind tunnel with laser energy deposition upstream of the sphere. The pressure and heat transfer measurements recorded the unsteady interaction of the laser-induced perturbation. Schlieren images were recorded to visualize the effect of the laser energy deposition. The data collected for the sphere without the shock impingement provided a baseline to compare against for the shock impingement test cases.

5.2.1 Steady State

Figure 5.3 compares the computed density field with an experimental schlieren image at Mach 3.45. The flow is from left to right in these images. The three-dimensional Euler simulation was run with freestream conditions matched with the conditions in the wind tunnel. The General Aerodynamic Simulation Program (GASP) version 3.2 [3] was used for the Euler simulation for the steady-state flow about the sphere. The grids for the simulations were generated in FORTRAN. Various grid sizes were used, and the results of a grid convergence study are shown in Figure 5.4. The grid domain consisted of the hemisphere region in front of the sphere. Freestream boundary conditions were applied at the upstream

boundary of the grid. Inviscid boundary conditions were applied at the sphere surface, i.e., the flow velocity is tangent to the sphere surface. First order extrapolation from the interior applied to the primitive flow variables was applied at the boundary for the flow exiting the downstream boundary. The flux algorithm was the 2nd order accurate Van Leer flux-vector splitting scheme. The time integration was performed with the two-factor approximate factorization method with a maximum CFL of 5. [3] The simulation conditions were matched to the tunnel test conditions (see Table 5.1).

For the steady state conditions, the computational and experimental shock stand-off distances are both within 3% of the Lobb model [85] given by

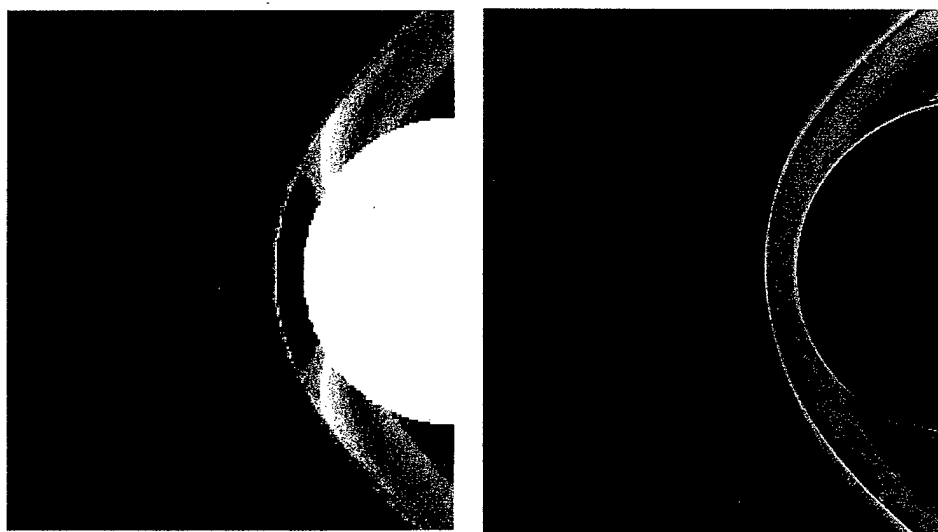
$$\Delta = 0.41 D \frac{(\gamma - 1)M_{\infty}^2 + 2}{(\gamma + 1)M_{\infty}^2} \quad (5.1)$$

where, Δ is the stand-off distance, D is the sphere diameter, γ is the ratio of specific heats, and M_{∞} is the freestream Mach number. Figure 5.5 shows the experimental measurements, the Euler simulation, and the Lobb model for the shock standoff distance for the sphere. In this figure, the density along the centerline is plotted from the Euler simulation and compared to the measurements for the shock standoff distance taken from the schlieren images and the computed distance given by Equation (5.1).

Figure 5.6 compares the Euler computational results with the measured surface pressure distribution for the sphere at Mach 3.45 at steady state with no perturbation. The computational results fall within the experimental uncertainty of the data. The three sets of data points (indicated by diamonds, squares, and triangles) were test data collected on three subsequent days of testing. The repeatability of the measured surface pressure is representative of the data collected on the separate days of testing. The surface pressure is non-dimensionalized with the freestream pitot pressure, p_{02} , (see Equation (2.20)). The horizontal error bars in the figure show the uncertainty in the angular position of the pressure port. The uncertainty for the pressure is $\pm 1\%$. Figure 5.4 gives the grid convergence for the Euler computations for the sphere model for four increasing grid sizes.

Table 5.1 Tunnel operating parameters for sphere without shock impingement surface pressure tests

Mach number	3.45
Reynolds number based on sphere diameter, $Re_D = \frac{\rho V D}{\mu}$	1.711×10^6
Freestream viscosity, μ	$5.316 \times 10^{-6} \frac{\text{kg}}{\text{m s}}$
Stagnation pressure, p_0	$9.308 \times 10^5 \text{ Pa}$
Stagnation temperature, T_0	263 K
Stagnation density, ρ_0	$12.336 \frac{\text{kg}}{\text{m}^3}$
Freestream temperature, T	77.8 K
Freestream pressure, p	$1.310 \times 10^4 \text{ Pa}$
Freestream density, ρ	$0.587 \frac{\text{kg}}{\text{m}^3}$
Freestream velocity, V	609.9 m/s
Freestream speed of sound, a	176.8 m/s
Pitot pressure, p_{02}	$2.070 \times 10^5 \text{ Pa}$
Pitot density, ρ_{02}	$2.743 \frac{\text{kg}}{\text{m}^3}$

**Figure 5.3** Computational density contours and experimental schlieren comparison for Mach 3.45 sphere

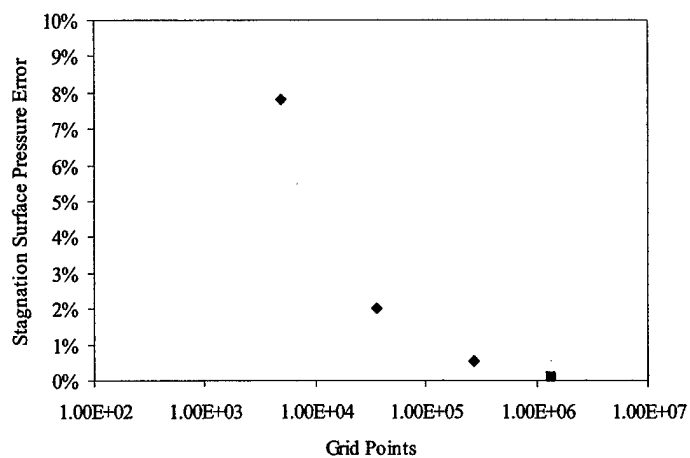


Figure 5.4 Grid convergence for sphere computations

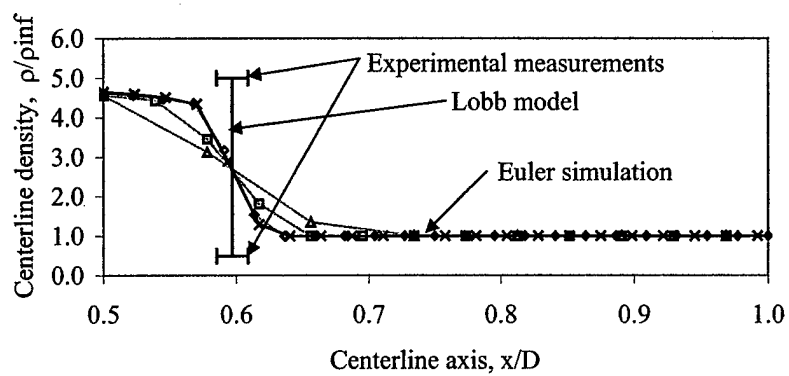


Figure 5.5 Experimental, numerical, and Lobb model [85] comparison for shock standoff distance for Mach 3.45 sphere

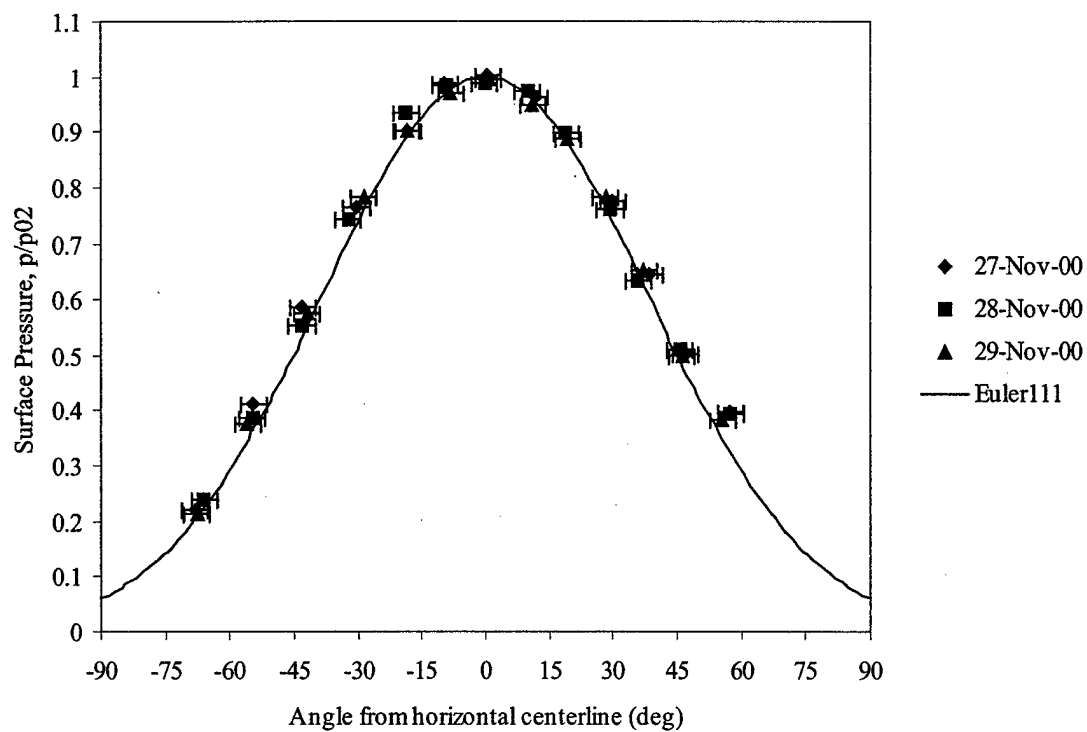


Figure 5.6 Comparison of Euler computations and experimental pressure distribution

5.2.2 Flow Visualization

The laser energy deposition technique was applied as a perturbation upstream of the 25.4 mm sphere model in the Mach 3.45 wind tunnel. Two deposition locations (1.0 and 0.6 diameters) on the centerline axis were tested upstream of the sphere (see Figure 5.1). In this section, schlieren images are presented to qualitatively describe the unsteady flow phenomena as the laser perturbation interacts with the model. Surface pressure and heat transfer measurements are made in the subsequent sections and quantitatively describe the interaction processes.

As a starting point and to give an overview of the process, Figure 5.7 is a schematic illustrating some of the unsteady flow features created by depositing the laser energy upstream of the sphere. In all cases, for both the sphere with and without shock impingement, the energy deposition location was upstream of the bow shock, and, therefore, in the supersonic region of the flow. The pulse width of the laser is 10 ns. Thus, the energy deposited into the flow can be considered an instantaneous event (see Figure 5.7 a)). After the laser energy has been deposited, the spot will begin to convect downstream, and a blast wave will propagate outward from the spot (see Chapter 4). The blast wave will reach the bow shock where a weak two-shock interaction will take place (see Figure 5.7 b)). The blast wave is relatively weak compared to the bow shock (blast wave Mach numbers for the quiescent air tests quickly approached sonic conditions (see Chapter 4)). However, a transmitted wave will propagate to the sphere surface. The effects of the blast wave reflecting off of the sphere were detected by the heat transfer measurements and will be presented in Section 5.2.4. The pressure measurements did not detect this reflection due to the frequency response limitation of the pressure gauges. The thermal spot then reaches the bow shock where an interface and shock interaction takes place (see Figure 5.7 c)). From this interaction the bow shock lenses forward, and an expansion wave is transmitted to the sphere surface where the pressure and temperature are reduced. These pressure and temperatures were detected by the surface pressure and temperature measurements and will be presented in the next Sections. Finally, at the latter times, the thermal spot impacts the sphere, convects around the sphere, and the bow shock collapses back to its steady state position (see Figure 5.7 d)).

Figure 5.8 - Figure 5.11 are a time sequence of instantaneous schlieren images for laser energy deposition 1.0 diameter upstream of a 25.4 mm diameter sphere in the Mach 3.45 wind tunnel. The laser/argon schlieren system described in Section 3.2.1 was used for this sequence of images. The laser for the energy deposition is repetitively fired at 10 Hz, and the flow in the test section effectively travels 64 m between laser pulses. Therefore, the schlieren images represent isolated events, however, the main features of the flow are linked in time sequence from image-to-image. The schlieren flash and the laser energy deposition are phase locked. The flow is from right-to-left in each image, and the time between the laser pulse and the schlieren spark is given beneath each image. The laser deposition location is indicated in the 0 time delay image in Figure 5.8. This spot is in each image and is due to the flash, bremsstrahlung effect (see Section 2.3.1), from the formation of the plasma region. This bright spot is visible in each image due to the fact that the shutter for the camera is open for all events, i.e., the laser deposition and the schlieren flash.

The laser incidence direction for the laser energy deposition is shown in the 0 μ s in Figure 5.8. The spark is formed by focusing the 1.0 cm diameter Nd:YAG laser beam down through a 150 mm focal length lens (see Section 3.3). The optics for focusing the beam down were located below the wind tunnel test section and the beam was brought the bottom test section observation window (see Section 3.1). The energy of the beam was measured at 283 mJ/pulse, and the energy deposition size is estimated at $3 \pm 1 \text{ mm}^3$ (see Section 4.3 for details on energy measurements and for deposition volume estimates).

The blast wave is clearly visible in the schlieren image for a time delay of 10 μ s between the laser pulse and the schlieren flash. At a time delay of 10 μ s, the thermal spot and blast wave and the sphere/bow shock are isolated features in the flow. The knife-edge for the schlieren images is oriented vertically (see Section 3.2.1). The density gradients are clearly visible across the hemisphere model bow shock and the blast wave emanating from the laser energy deposition. The density gradients are in the horizontal direction for this orientation of the schlieren knife-edge.

Between 20 and 30 μ s after the laser energy deposition, the blast wave for the deposition hits the bow shock of the sphere, is transmitted, and then reflected off of the sphere surface. The reflected shock from the surface of the sphere can be seen in the 30 μ s image. At 40 μ s the thermally heated region created by the laser energy deposition begins to interact with the bow shock of the hemisphere. Between 40 and 50 μ s

the bow shock is distorted and blooms forward due to the decrease in local Mach number in the thermally heated region. In the Russian literature, Georgievski and Levin [41], call this effect the lensing of the bow shock. In the 40 and 50 μs images, streamwise striations are observed. These striations represent streamwise vorticity as the three-dimensional thermal region interacts with the three-dimensional bow shock of the hemisphere. The vorticity evolution equation for compressible flow can be developed by taking the curl of the momentum equation, Equation (2.2). The resulting equation in Cartesian component form for the vorticity transport is then [134]

$$\frac{\partial}{\partial t} \left(\frac{\Omega_k}{\rho} \right) + u_j \frac{\partial}{\partial x_j} \left(\frac{\Omega_k}{\rho} \right) = \frac{\Omega_j}{\rho} \frac{\partial u_k}{\partial x_j} + \frac{1}{\rho^3} (\nabla \rho \times \nabla p) + \frac{1}{\rho} \varepsilon_{ijk} \frac{\partial^2}{\partial x_i \partial x_j} \left(\mu \left(\frac{\partial u_i}{\partial x_j} + \frac{\partial u_j}{\partial x_i} \right) \right) \quad (5.2)$$

where Ω_k is the k th component of vorticity, ρ is the density, u_j is the j th component of velocity, t is time, x_j is the Cartesian component, and μ is the viscosity (see Equation (2.3)). The terms on the left hand side describe the evolution of the vorticity in time and space. The first term on the right gives rise to vorticity due to the stretching and tilting of the vorticity due to velocity gradients in the flow. The second term is the baroclinic term. The baroclinic term can generate vorticity due to the misalignment of the density and pressure gradients within the flow. The third term on the right gives the change of vorticity due to viscosity and diffusion processes. For more details on the compressible vorticity transport equation see Smits and Dussauge. [134]

First, there is vorticity in the laser energy deposition region. The laser induced breakdown of air generates a vortex ring due to the asymmetric formation of the plasma (see Sections 2.3.1 and 4.1). This vortex ring in the images of Figure 5.8 through Figure 5.15 is aligned with its center axis along the laser incidence axis. This vortex ring will stretch and tilt according to the first term on the left hand side of Equation (5.2).

The second source of vorticity in the flow comes from the curved bow shock interaction with the thermal spot interface. As the spot migrates into the bow shock, vorticity will be generated by the baroclinic term, the second term of Equation (5.2). Samtaney [122] has studied various density bubble interface interactions with shock structures in two and three dimensions. These interactions of shock waves

with density stratifications, and the associated vorticity generation, are known as the Richtmeyer-Meshkov instability environment.

From 60 to 70 μs (see Figure 5.9) the thermal spot generated streamwise vorticity begins to breakdown to the smaller scales of turbulent flow. The distorted bow shock begins to collapse backward, and the upstream portion of the laser energy deposition blast wave moves into the bow shock. From 80 to 120 μs the bow shock collapses back more, and the thermally heated flow convects around the sphere. Finally at 160 μs the sphere is back at its steady state condition.

Figure 5.12 through Figure 5.15 shows the interaction process for the laser energy deposition 0.6 diameters upstream of the sphere and at Mach 3.45. Compared to the energy deposition 1.0 diameters upstream, the interaction process begins, as expected, earlier for the closer deposition location. The blast wave impacts the bow shock and the sphere from 10-20 μs . The lensing of the bow shock occurs from 20-30 μs . Streamwise vorticity is also observed in the schlieren image at 30 μs and the breakdown of the vorticity to the smaller scales of turbulence from 40-70 μs . The upstream portion of the blast wave interacts from 30 to 40 μs . By 120 μs the thermal spot convects around the sphere, and the bow shock resumes its steady state shape.

In both of these energy deposition locations, the fluid dynamic processes occur on the order of tens of microseconds, and the wave interactions on the order of microseconds. With this time scale, the data acquisition frequency for the surface pressure and temperature measurements were needed in the 100 kHz range. The surface pressure and temperature measurements are presented in the next Sections.

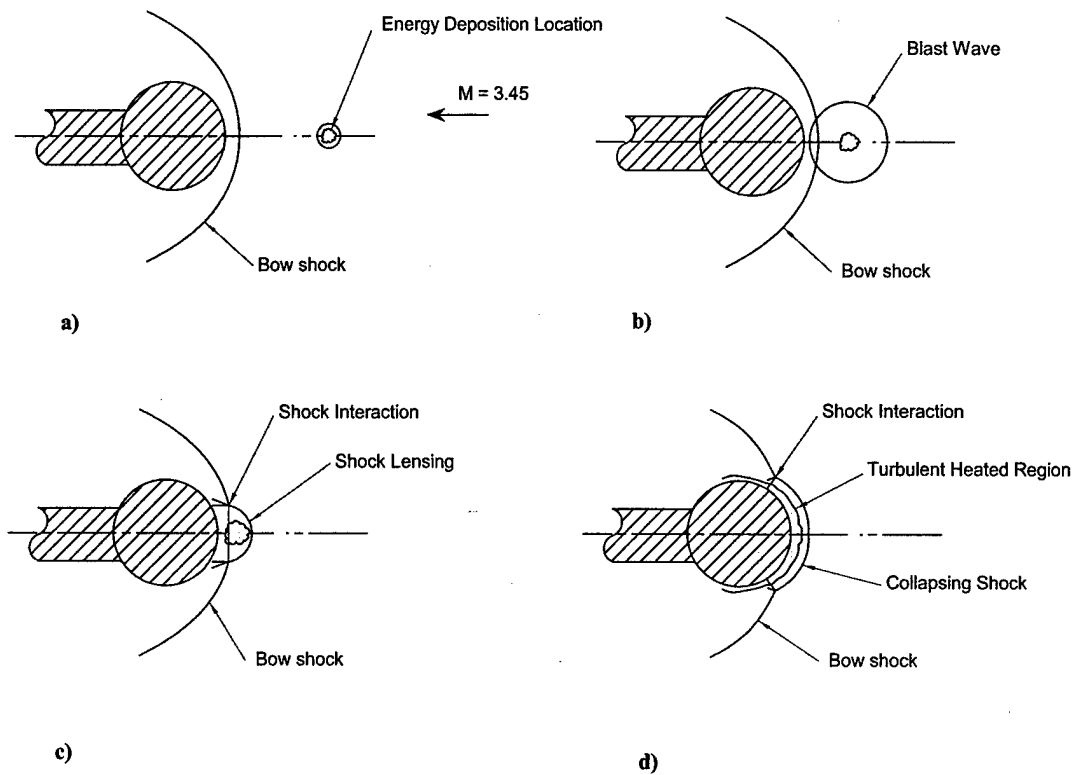


Figure 5.7 Flow features for the laser energy deposition upstream of a Mach 3.45 sphere, **a)** initial deposition, **b)** blast wave effects, **c)** bow shock lensing due to shock thermal interface interaction, and **d)** thermal heating to sphere surface from thermal spot impingement and bow shock collapse back to steady state

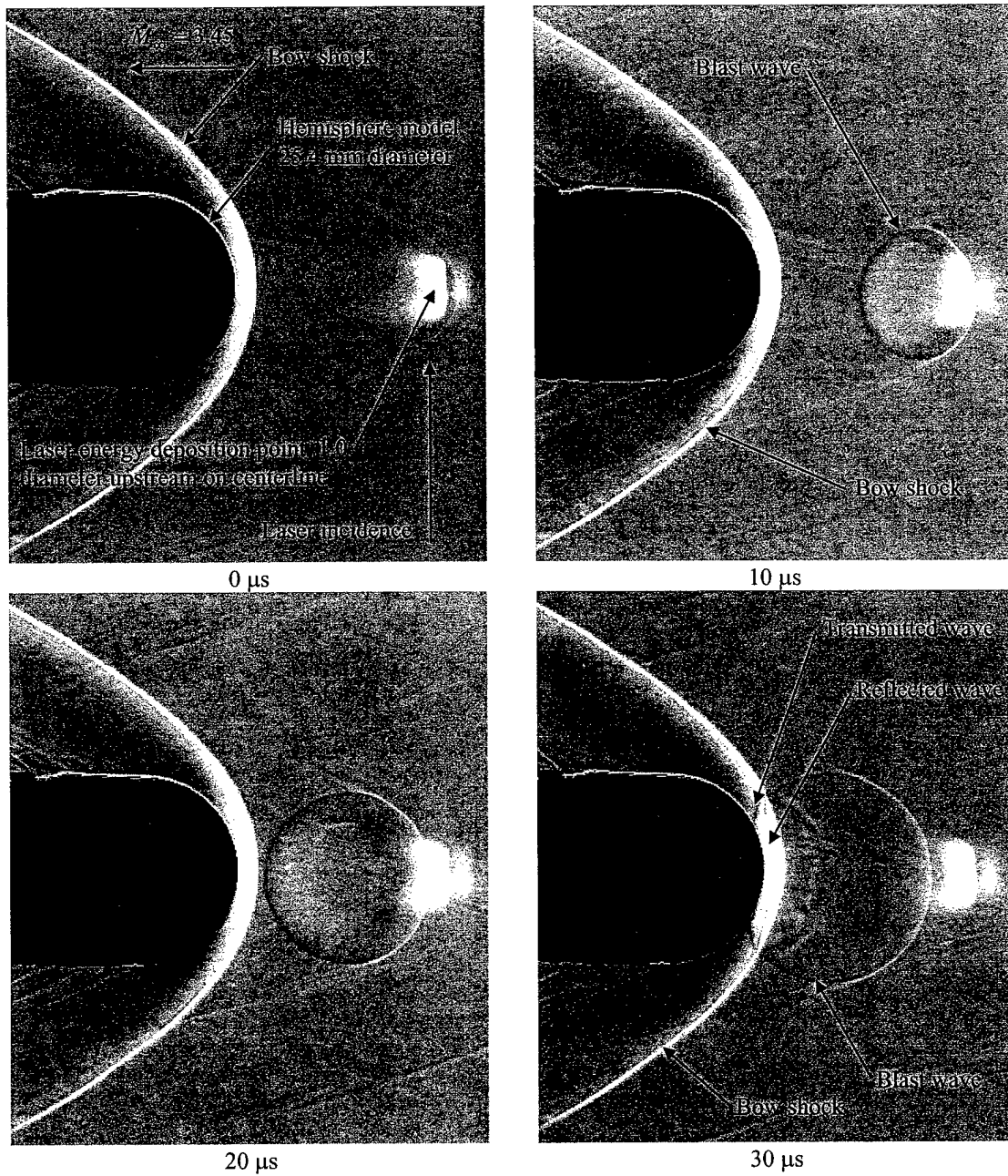


Figure 5.8 Instantaneous argon/laser generated schlieren images of Mach 3.45 sphere with laser energy deposition one diameter upstream, 0, 10, 20, and 30 μ s after laser energy deposition, 283 mJ/pulse, 150 mm focal length lens

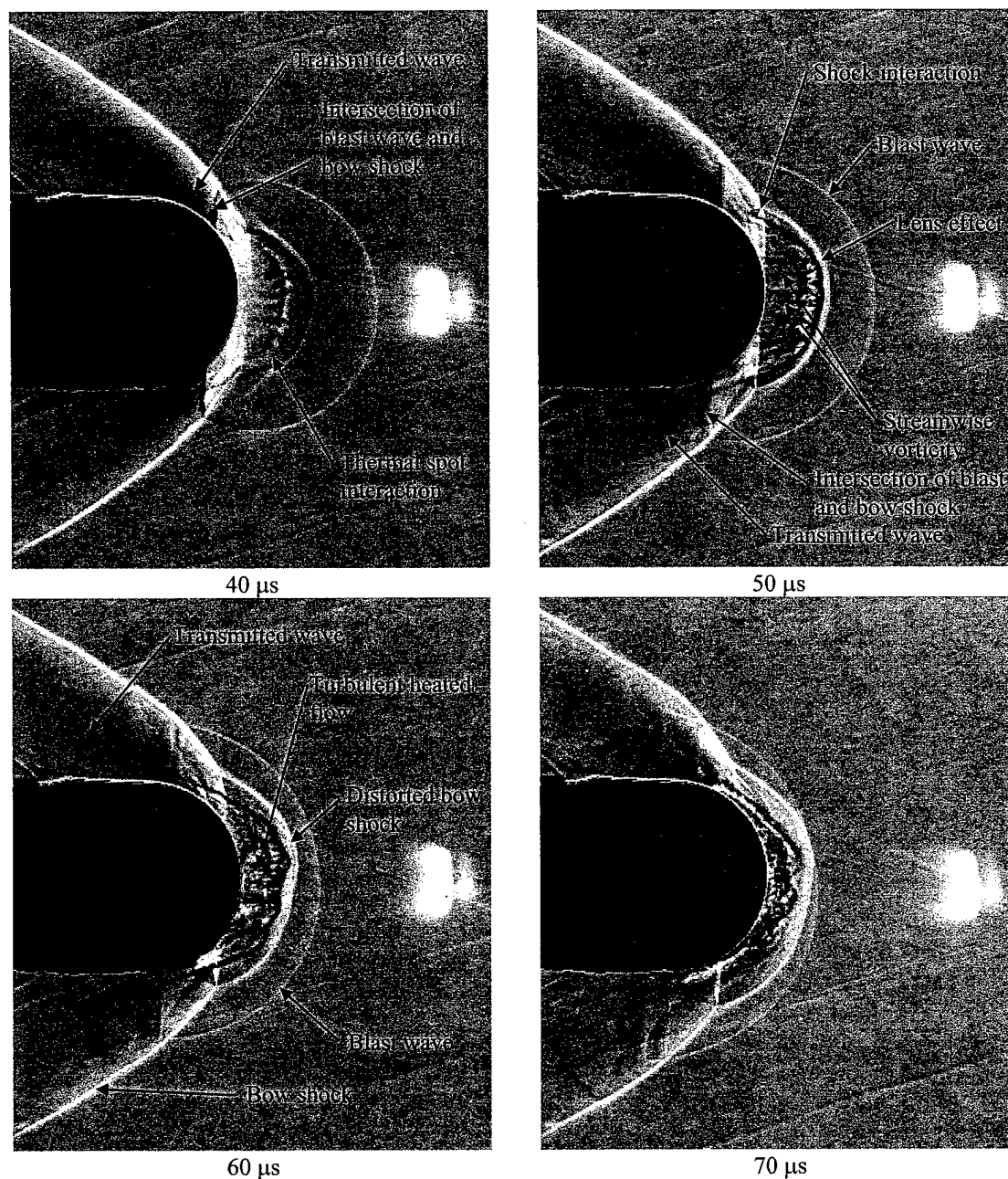


Figure 5.9 Instantaneous argon/laser generated schlieren images of Mach 3.45 sphere with laser energy deposition one diameter upstream, 40, 50, 60, and 70 μ s after laser energy deposition, 283 mJ/pulse, 150 mm focal length lens

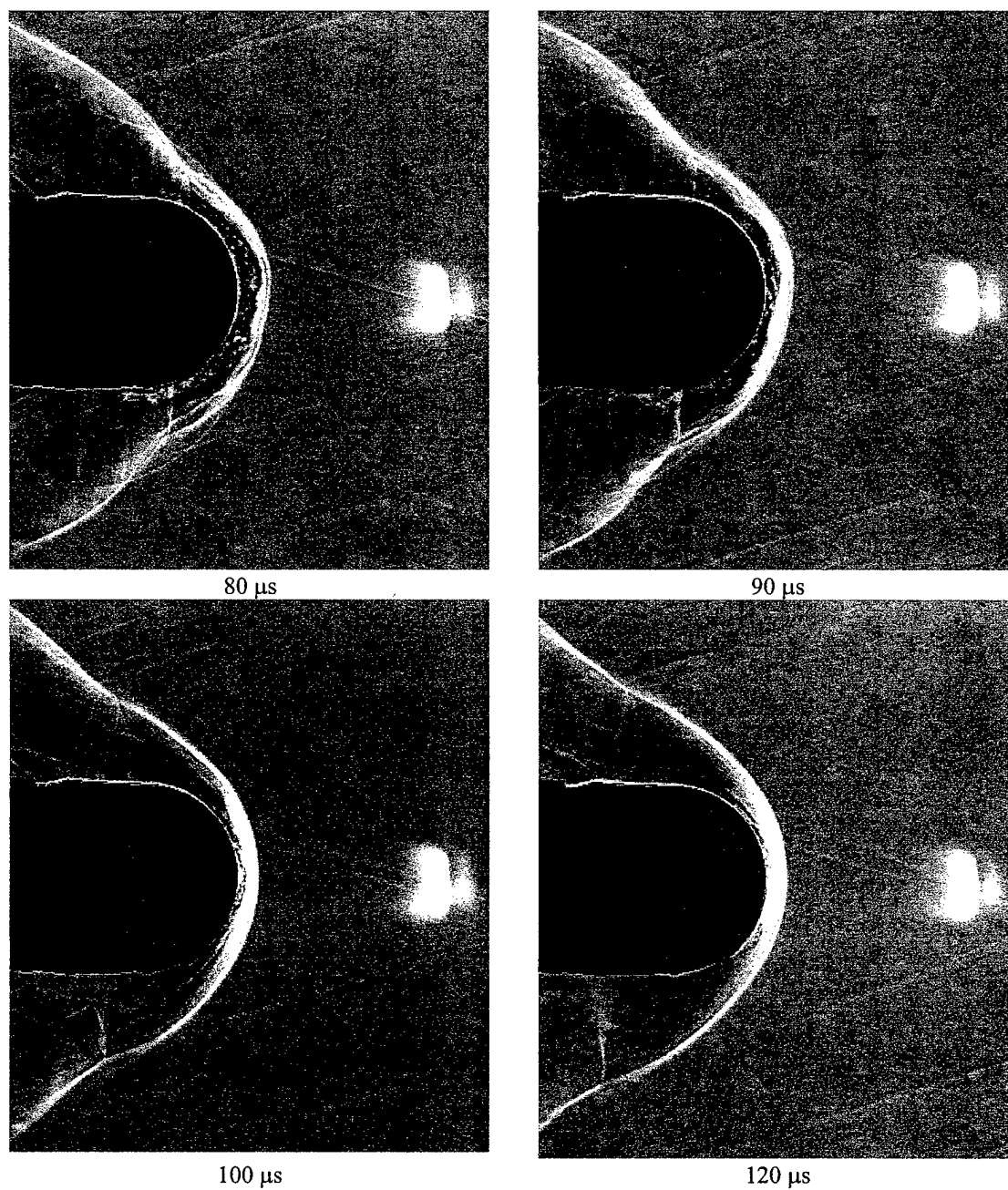


Figure 5.10 Instantaneous argon/laser generated schlieren images of Mach 3.45 sphere with laser energy deposition one diameter upstream, 80, 90, 100, and 120 μ s after laser energy deposition, 283 mJ/pulse, 150 mm focal length lens

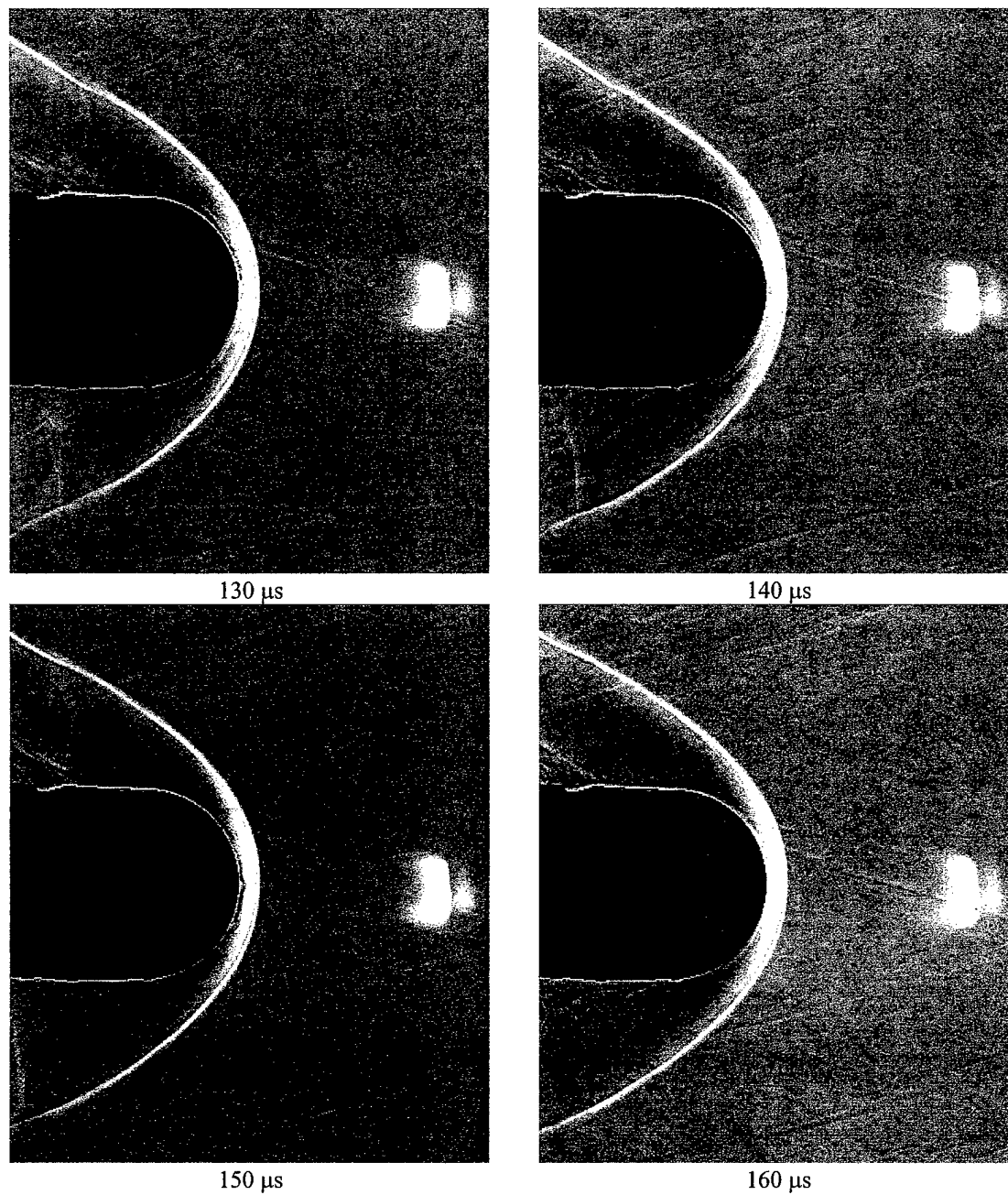


Figure 5.11 Instantaneous argon/laser generated schlieren images of Mach 3.45 sphere with laser energy deposition one diameter upstream, 130, 140, 150, and 160 μs after laser energy deposition, 283 mJ/pulse, 150 mm focal length lens

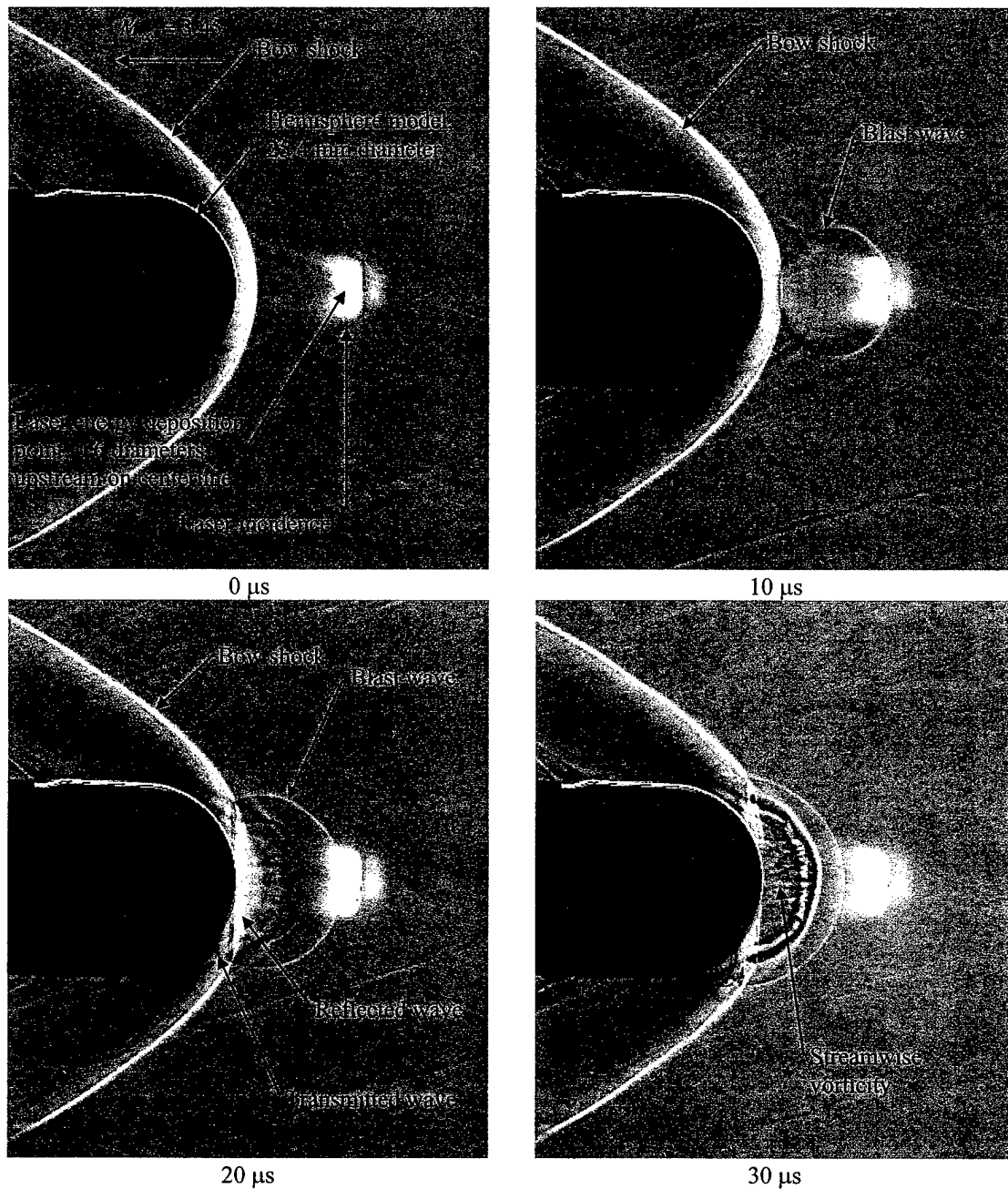


Figure 5.12 Instantaneous argon/laser generated schlieren images of Mach 3.45 sphere with laser energy deposition 0.6 diameters upstream, 0, 10, 20, and 30 μ s after laser energy deposition, 283 mJ/pulse, 150 mm focal length lens

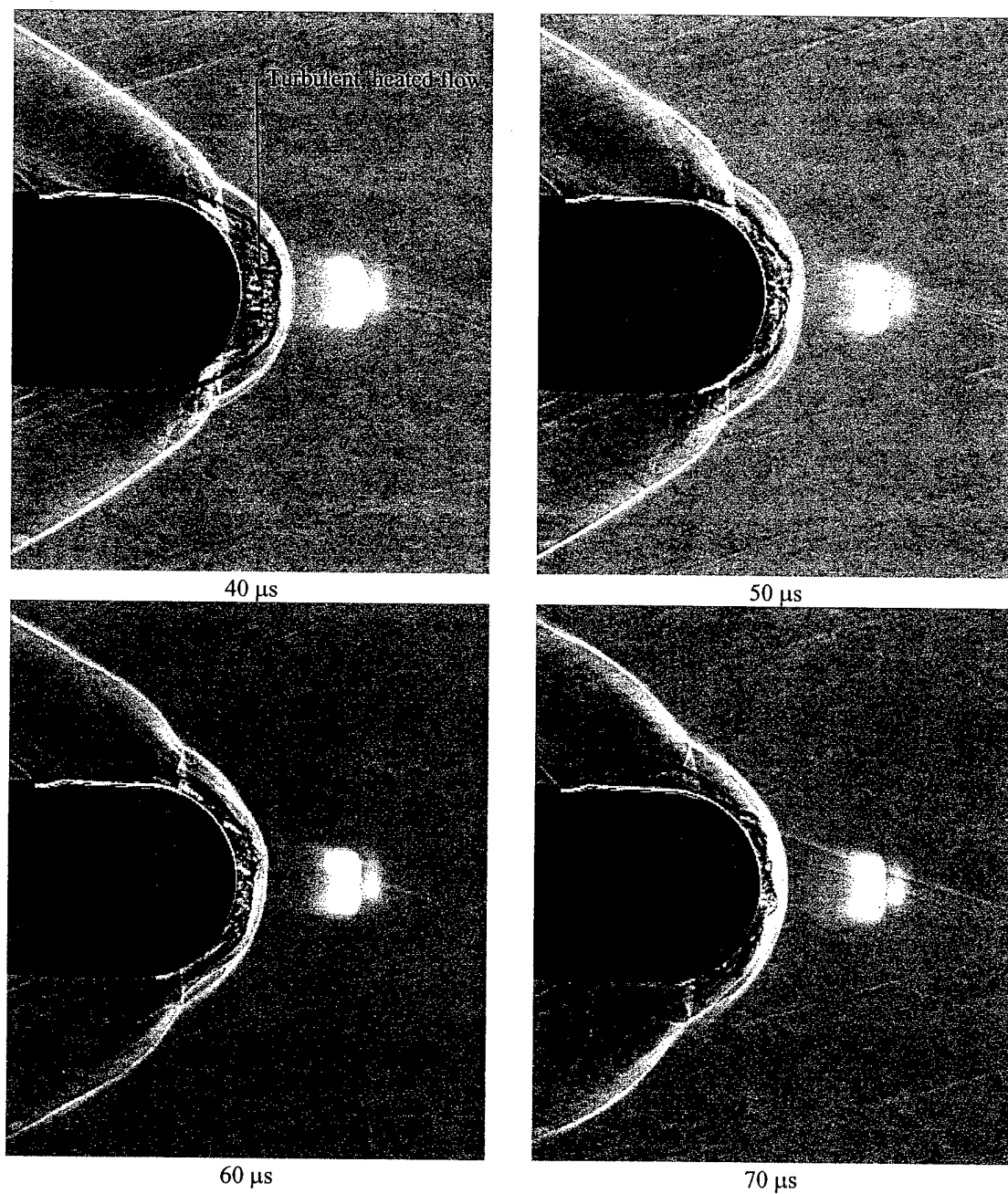


Figure 5.13 Instantaneous argon/laser generated schlieren images of Mach 3.45 sphere with laser energy deposition 0.6 diameters upstream, 40, 50, 60, and 70 μs after laser energy deposition, 283 mJ/pulse, 150 mm focal length lens

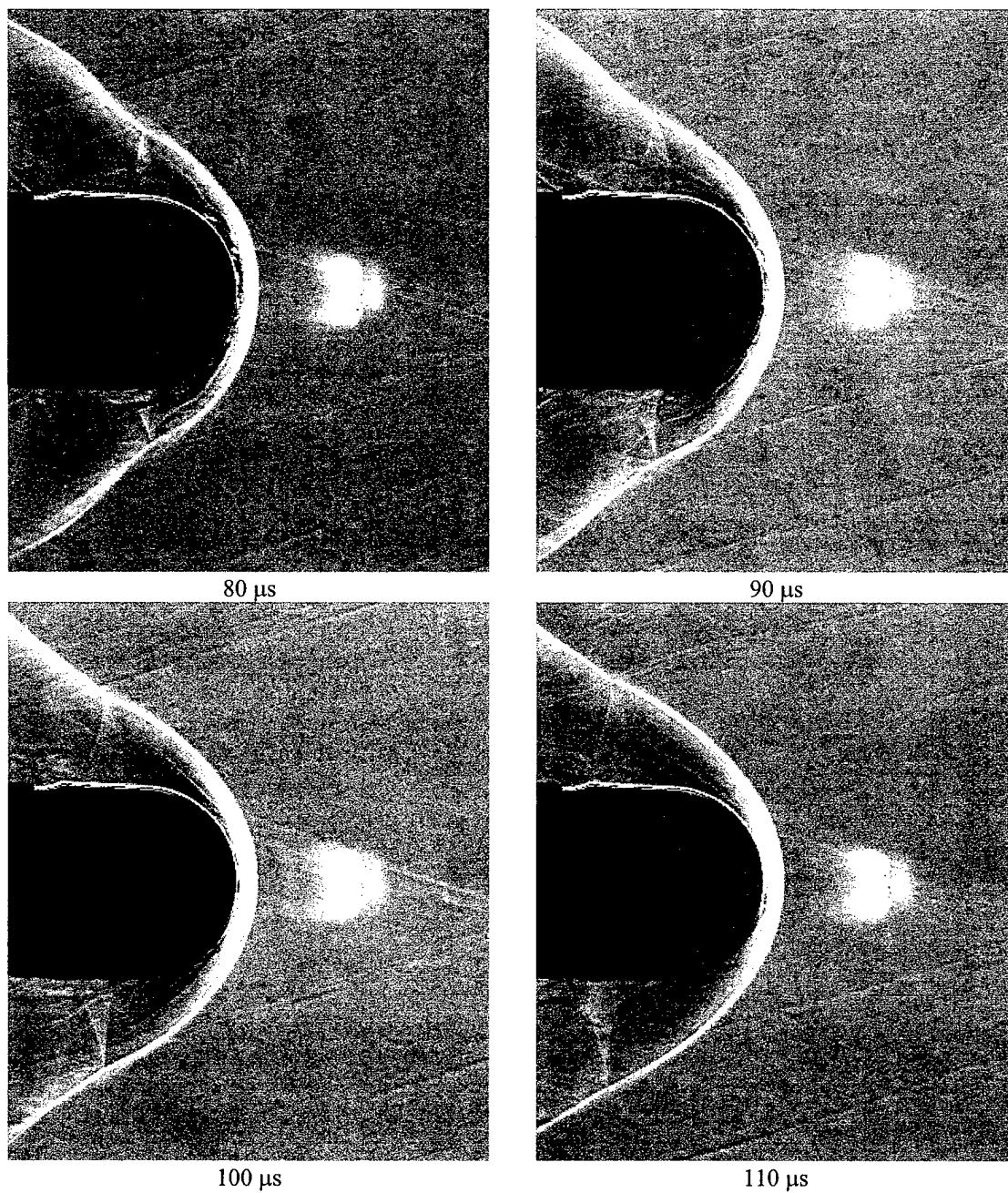


Figure 5.14 Instantaneous argon/laser generated schlieren images of Mach 3.45 sphere with laser energy deposition 0.6 diameters upstream, 80, 90, 100, and 110 μ s after laser energy deposition, 283 mJ/pulse, 150 mm focal length lens

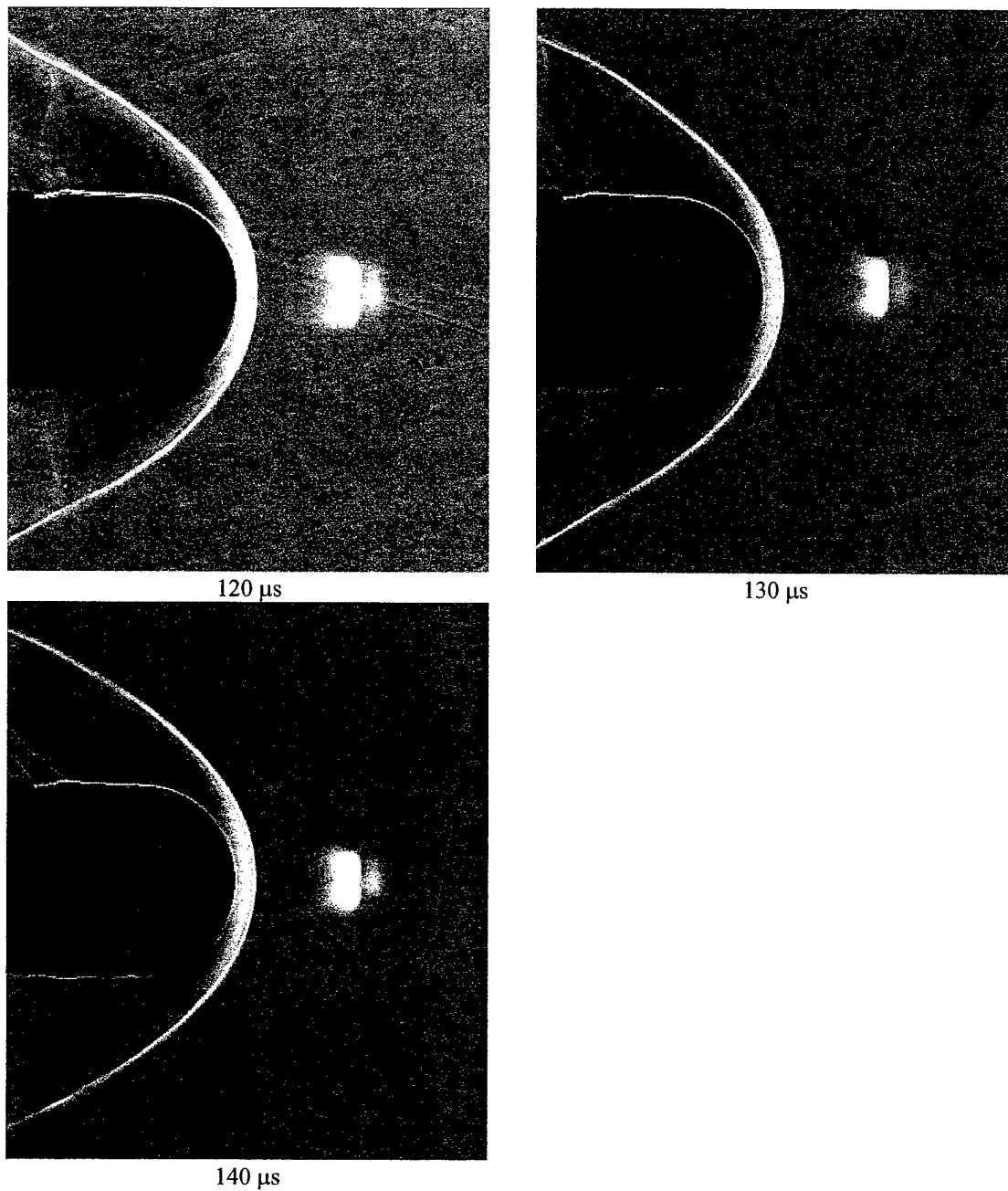


Figure 5.15 Instantaneous argon/laser generated schlieren images of Mach 3.45 sphere with laser energy deposition 0.6 diameters upstream, 120, 130, and 140 μs after laser energy deposition, 283 mJ/pulse, 150 mm focal length lens

5.2.3 Surface Pressure

The surface pressure was measured across the vertical symmetry plane of the sphere for laser energy deposition 1.0 diameter upstream of the front of the sphere for three energy levels: 13, 127, and 258 mJ/pulse. Figure 5.16, Figure 5.17, and Figure 5.18 show the surface pressure from ± 60 degrees as a function of time, and pressure port location for the three energy levels. The pressure has been non-dimensionalized with the freestream pitot pressure, p_{02} , (see Equation (2.20)). The interaction of the thermal spot, generated by the laser discharge, with the bow shock (in the time interval of 40-90 microseconds) causes a blooming of the bow shock (Georgievski and Levin [41] call this the lensing effect). This behavior is consistent with the simulations of Georgievski and Levin and Aleksandrov *et al.* [4]. It can be noted that the energy deposition effects the flow over a period on the order of 50 microseconds. This flow transient effect is much greater than the energy deposition whereby the excitation laser has a pulse width of 10 nanoseconds.

Figure 5.19 compares the stagnation point pressure traces for the three energy deposition levels. The reduction in stagnation pressure is independent of the energy deposition magnitude.

The lensing effect and the expansion observed by the surface pressure measurements can be described by the one-dimensional analysis of a shock wave interaction with an interface. In this analysis the shock wave represents the blunt body bow shock and the interface represents the leading edge of the thermal region created by the energy deposition. Figure 5.20 is a space-time diagram for the interaction process. The interaction begins with the interface approaching the shock for $t < 0$. After the interface hits the shock, $t > 0$, there will be an expansion fan that hits the surface of the body, and the shock moving upstream for the case when the gas is heated upstream of the interface, $T_2 > T_1$. The coordinates are fixed to the initial shock such that the transformation is given by

$$\hat{u} = u - u_\infty \quad (5.3)$$

where \hat{u} is the gas velocity relative to the initial shock ($t < 0$), u is the gas velocity relative to the wave velocity of the shock, and u_∞ is the freestream velocity. The wave velocity of the shock is determined by the shock strength, i.e. the pressure jump across the shock, and is determined by Equation (2.15). The

velocities and pressures across the interface are respectively equal such that, $u_1 = u_2$, $p_1 = p_2$, $u_3 = u_4$, and $p_3 = p_4$.

The properties on either side of the expansion fan can be related by a characteristic through the fan such that

$$u_4 + \frac{2}{\gamma-1} a_4 = u_0 + \frac{2}{\gamma-1} a_0 \quad (5.4)$$

and the speed of sound can be related to the pressure in regions 4 and 0 by

$$\frac{a_4}{a_0} = \left(\frac{p_4}{p_0} \right)^{\frac{\gamma-1}{2\gamma}}. \quad (5.5)$$

By using the normal shock relations, Equations (5.4) and (5.5), and the interface conditions, the relation for the shock after $t > 0$ is given by the implicit equation for the pressure ratio, p_3/p_1 ,

$$\frac{a_2}{a_1} \frac{1}{\gamma} \left(\frac{p_3}{p_1} - 1 \right) \left[\frac{\frac{2\gamma}{\gamma+1}}{\frac{p_3}{p_1} + \frac{\gamma-1}{\gamma+1}} \right]^{\frac{1}{2}} + \frac{2}{\gamma-1} \frac{a_0}{a_1} \left(\left(\frac{p_3/p_1}{p_0/p_1} \right)^{\frac{\gamma-1}{2\gamma}} - 1 \right) - \frac{1}{\gamma} \left(\frac{p_0}{p_1} - 1 \right) \left[\frac{\frac{2\gamma}{\gamma+1}}{\frac{p_0}{p_1} + \frac{\gamma-1}{\gamma+1}} \right]^{\frac{1}{2}} = 0 \quad (5.6)$$

where $\frac{p_0}{p_1}$ is determined by the shock for $t < 0$, $\frac{a_2}{a_1}$ is determined by the temperature across the interface,

and $\frac{a_0}{a_1}$ is given by

$$\frac{a_0}{a_1} = \left[\left(\frac{\gamma-1}{\gamma+1} \right)^2 + \frac{\gamma-1}{\gamma+1} \frac{p_0}{p_1} \right]^{\frac{1}{2}}. \quad (5.7)$$

Now, Equation (5.6) is completely determined by the initial shock strength and the temperature ratio across the interface. For a freestream Mach number of 3.45, and an initial range of temperature ratios of

$1 \leq \frac{T_2}{T_1} \leq 1000$ across the interface, the values for the velocities of the edges of the expansion fan, the

interface, and the shock for $t > 0$ are relative to the initial shock are

$$\frac{\hat{u}_f}{a_1} = \frac{u_0 - a_0}{a_1} - M_\infty = -2.619$$

$$-2.619 \leq \frac{\hat{u}_f}{a_1} = \frac{u_4 - a_4}{a_1} - M_\infty \leq 0.510$$

$$-0.817 \leq \frac{\hat{u}_3}{a_1} = \frac{u_3}{a_1} - M_\infty \leq 1.790$$

$$0 \leq \frac{\hat{c}_{s,t>0}}{a_1} = \frac{c_{s,t>0}}{a_1} - M_\infty \leq 31.473$$

where \hat{u}_f is the left edge velocity of the expansion fan, \hat{u}_f is the right edge of the expansion fan, \hat{u}_3 is the velocity of the interface for $t > 0$, $\hat{c}_{s,t>0}$ is the wave speed of the shock after the interaction, and $a_1 = a_\infty$ is the freestream speed of sound in region 1 (see Figure 5.20).

From the above one-dimensional analysis, we observe that the expansion fan does move downstream and strike the surface of the body ($\hat{u}_f < 0$ relative to the original bow shock), and the shock lenses forward ($\hat{c}_{s,t>0} > 0$ relative to the original bow shock), or upstream. Figure 5.21 shows the one-dimensional interaction process for $t < 0$ and for $t > 0$. However, for the experiments performed, the process is entirely three-dimensional and includes viscous effects. The physics of the expansion process and the shock lensing, even in the three-dimensional case, can be explained by the one-dimensional, inviscid, analysis outlined above.

Figure 5.22, through Figure 5.25 correlate the surface pressure measurements with the schlieren images for the sphere with energy deposition of 13 mJ/pulse. The schlieren images are ensemble averaged images taken with the xenon flash system described in Section 3.2.1. The schlieren flash and the laser energy deposition are phase locked. The time delay between the laser energy deposition and the schlieren flash is given below each image.

Figure 5.26 through Figure 5.29 correlate the surface pressure measurements with the schlieren images for the sphere with energy deposition of 127 mJ/pulse. Figure 5.30 through Figure 5.33 correlate the surface pressure measurements with the schlieren images for the sphere with energy deposition of 258 mJ/pulse.

Due to the smaller energy deposition volume of the low energy level, a shock interaction process is also observed in the images for 40 to 100 μs for the 13 mJ/pulse case (see Figure 5.23 and Figure 5.24). The compressions due to this shock interaction process are also observed and noted in Figure 5.16.

In summary, laser energy deposition upstream of the sphere reduces the stagnation point pressure by 40% due to the shock lensing process. The flow interaction time lasts for 40-50 μs in contrast to the energy deposition time for the laser pulse of 10 ns. The basic physics of the shock lensing process can be described by a one-dimensional gasdynamic analysis.

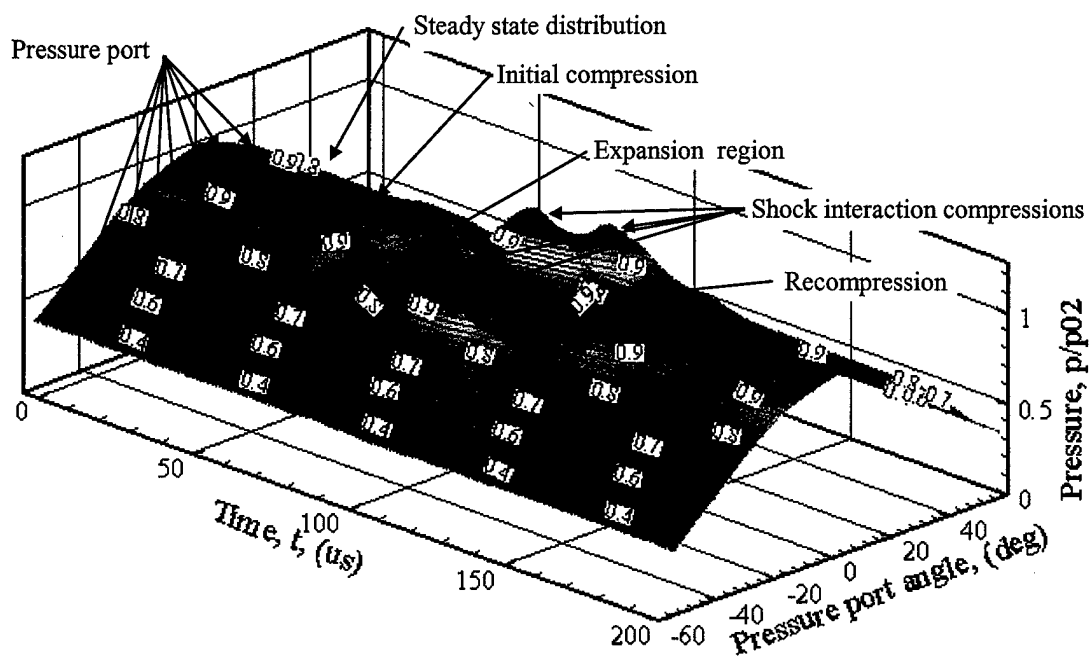


Figure 5.16 Surface pressure traces for various pressure port locations on the vertical symmetry plane around front of sphere with laser energy deposition (incident laser beam energy at 13 mJ/pulse) one diameter upstream and focused on model centerline

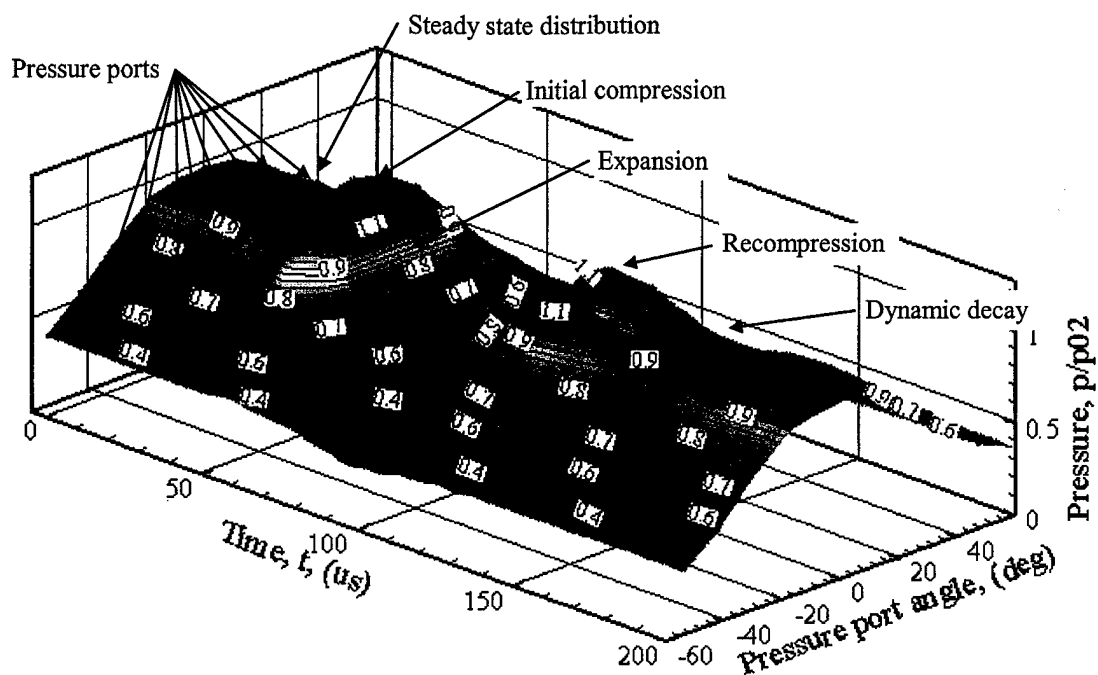


Figure 5.17 Surface pressure traces for various pressure port locations on the vertical symmetry plane around front of sphere with laser energy deposition (incident laser beam energy at 127 mJ/pulse) one diameter upstream and focused on model centerline

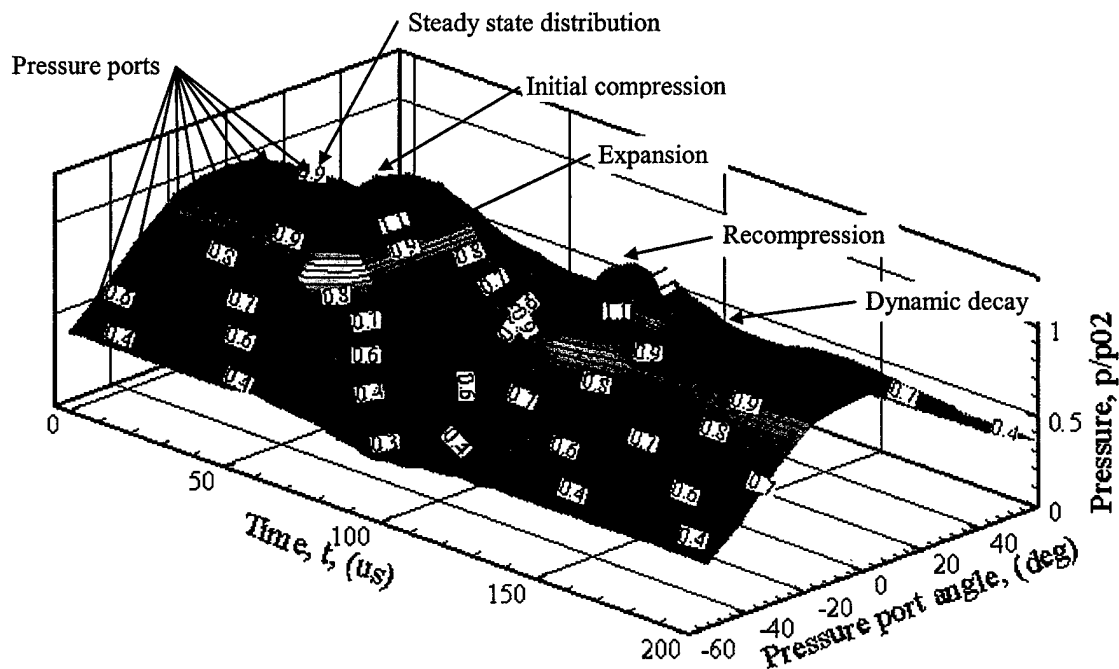


Figure 5.18 Surface pressure traces for various pressure port locations on the vertical symmetry plane around front of sphere with laser energy deposition (incident laser beam energy at 258 mJ/pulse) one diameter upstream and focused on model centerline

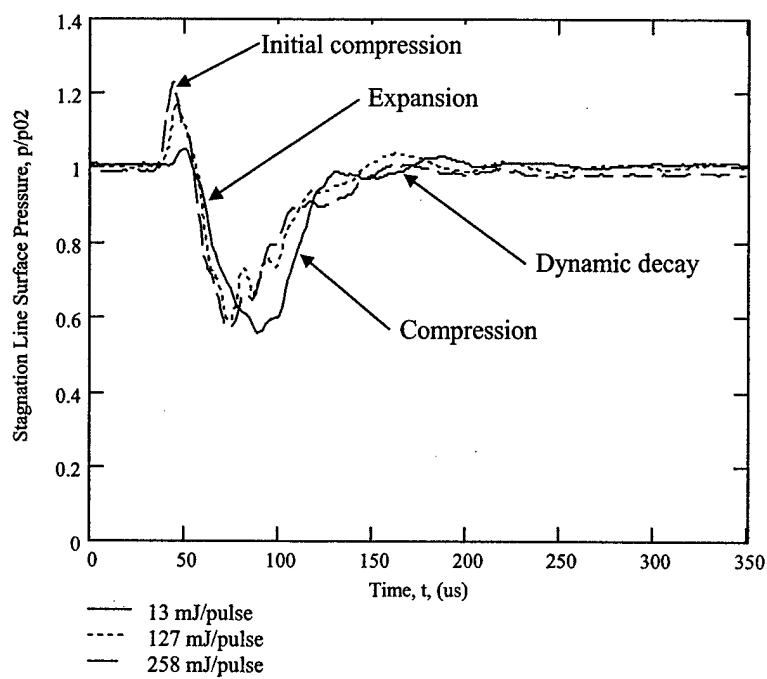


Figure 5.19 Comparison of stagnation point pressure traces for sphere for three energy deposition levels 1.0 diameter upstream of the sphere

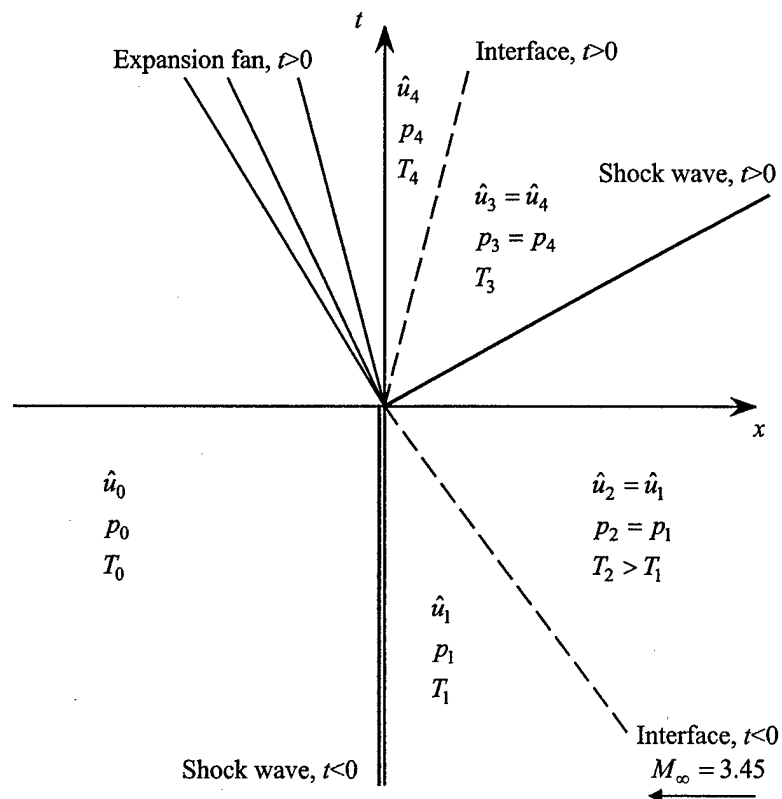


Figure 5.20 Space – time diagram for the shock interaction with the leading edge of the thermal interface boundary

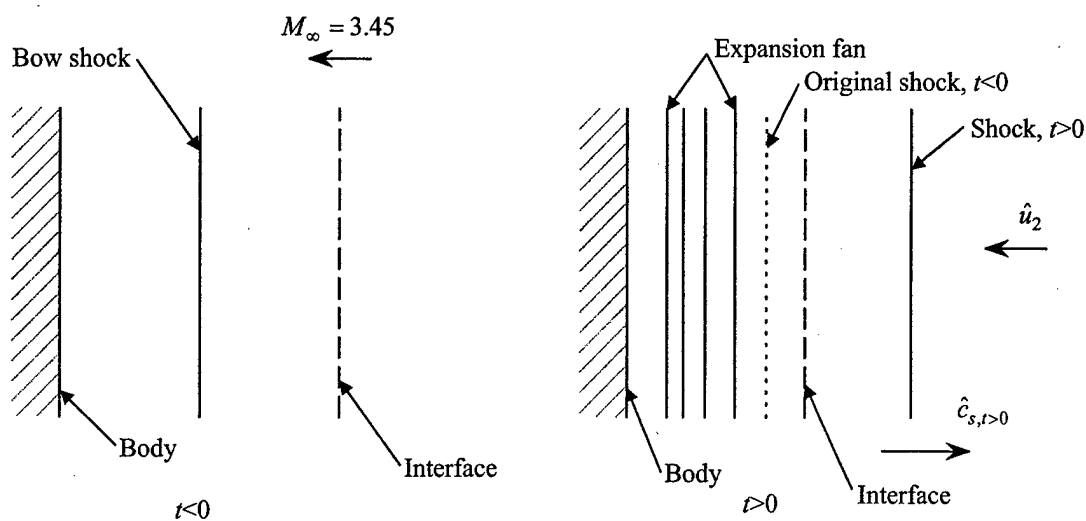


Figure 5.21 Shock wave and interface interaction

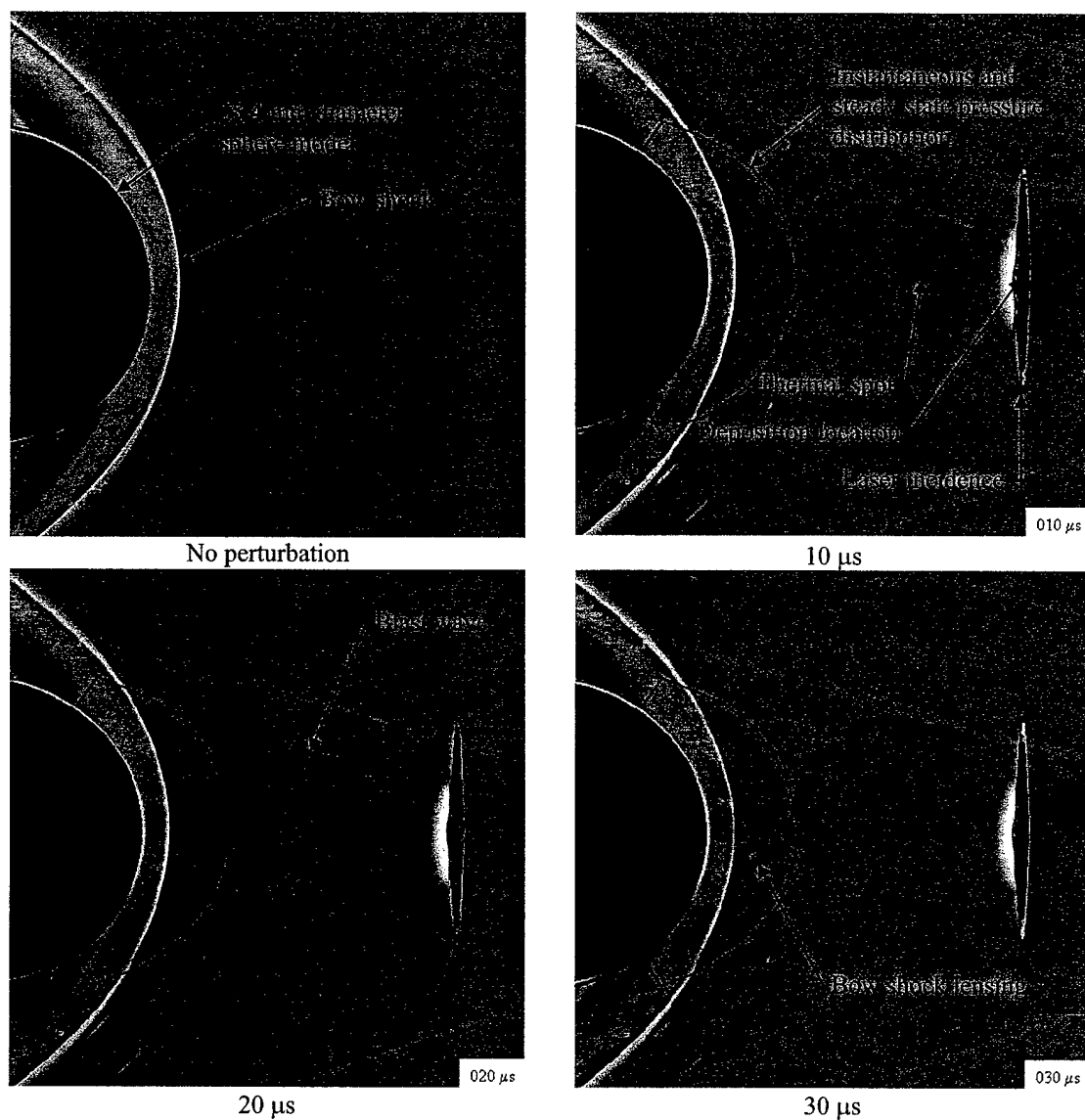


Figure 5.22 Phase averaged xenon Strobotac flash generated schlieren images of Mach 3.45 sphere with laser energy deposition 1.0 diameter upstream, 0, 10, 20, and 30 μ s after laser energy deposition, 13 mJ/pulse, 150 mm focal length lens, and correlated with polar steady state and instantaneous pressure plots

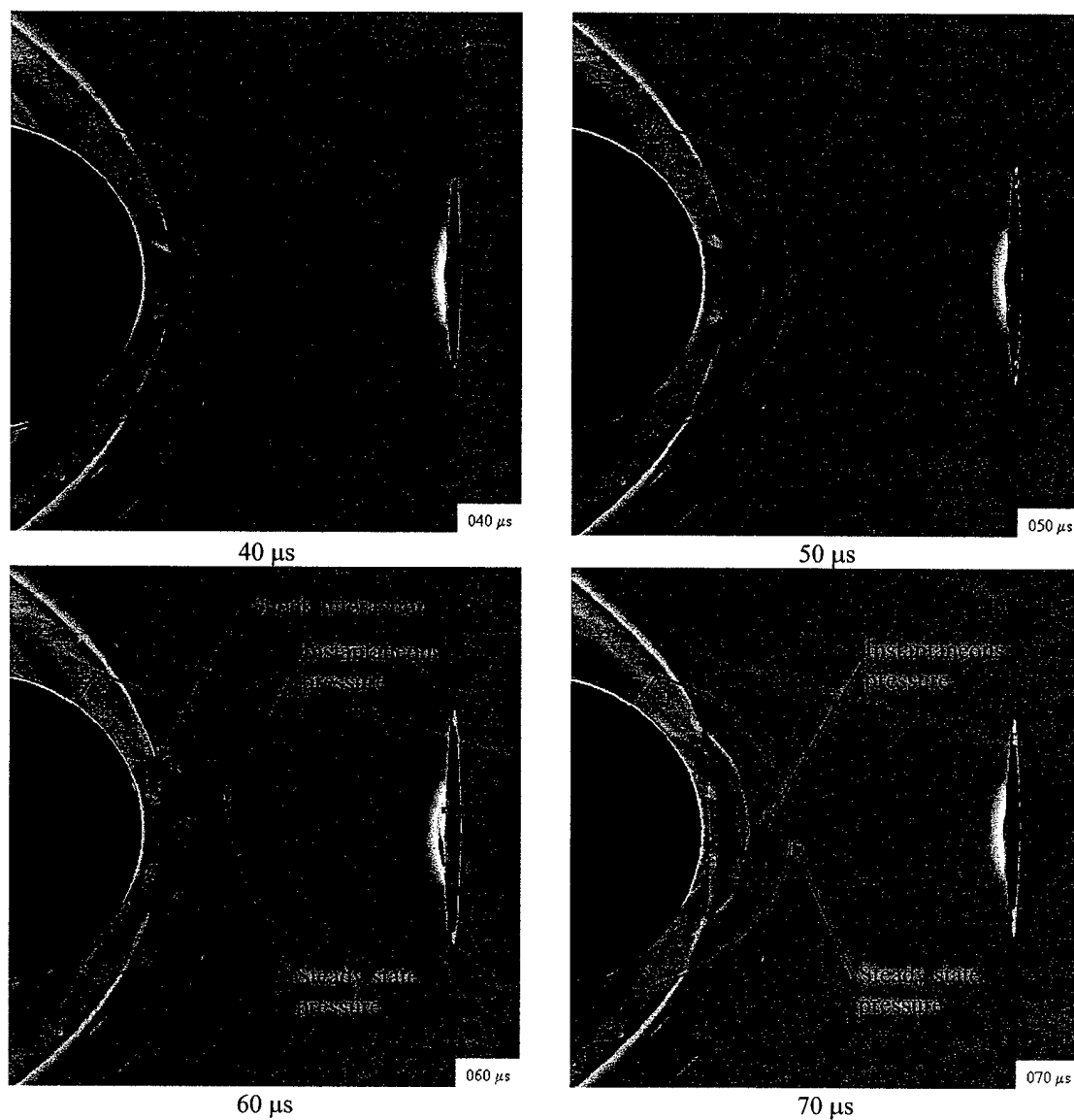


Figure 5.23 Phase averaged xenon Strobotac flash generated schlieren images of Mach 3.45 sphere with laser energy deposition 1.0 diameter upstream, 40, 50, 60, and 70 μ s after laser energy deposition, 13 mJ/pulse, 150 mm focal length lens, and correlated with polar steady state and instantaneous pressure plots

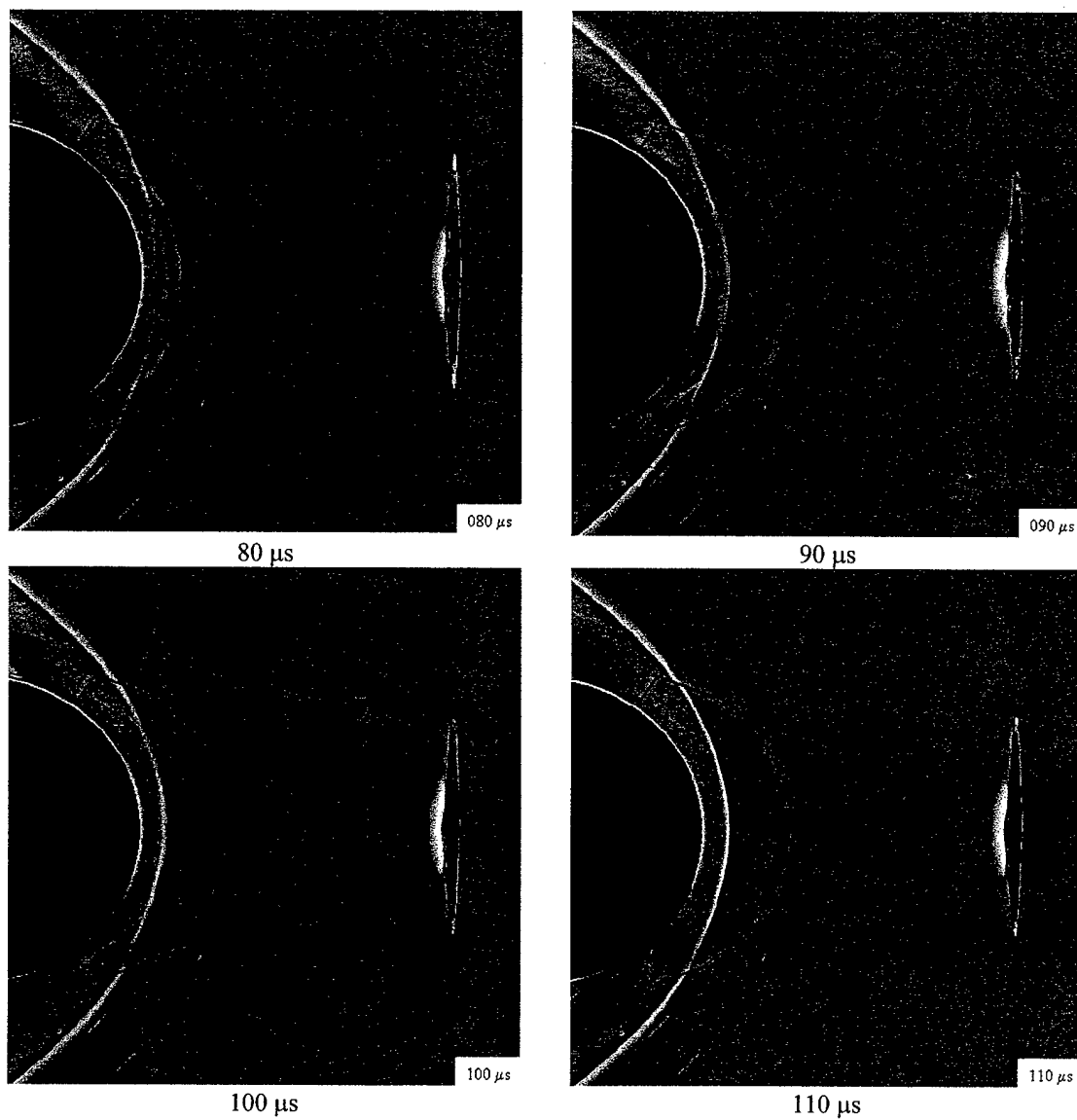


Figure 5.24 Phase averaged xenon Strobotac flash generated schlieren images of Mach 3.45 sphere with laser energy deposition 1.0 diameter upstream, 80, 90, 100, and 110 μs after laser energy deposition, 13 mJ/pulse, 150 mm focal length lens, and correlated with polar steady state and instantaneous pressure plots

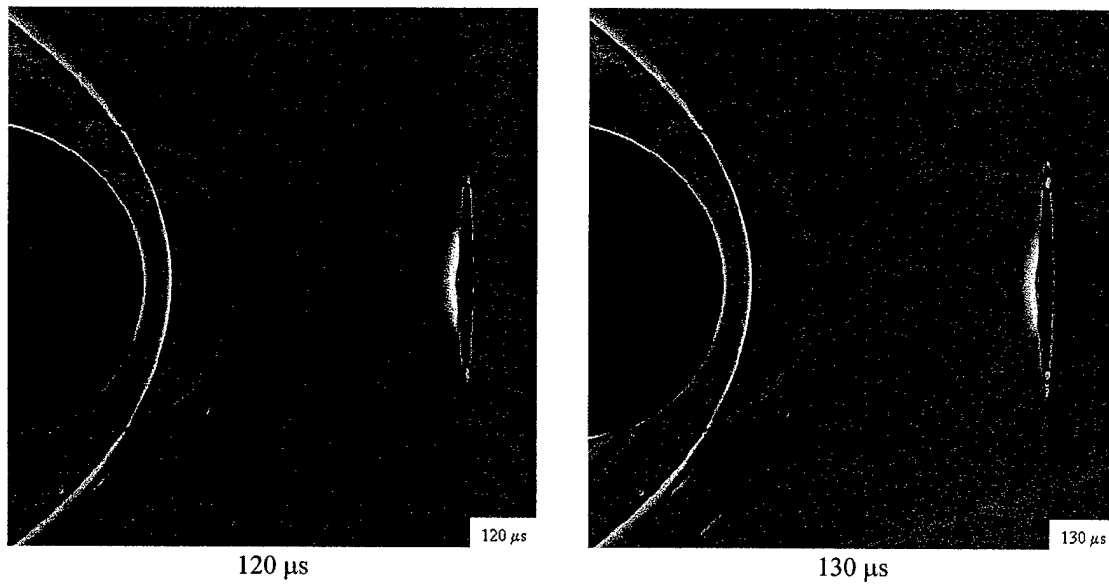


Figure 5.25 Phase averaged xenon Strobotac flash generated schlieren images of Mach 3.45 sphere with laser energy deposition 1.0 diameter upstream, 120, and 130 μ s after laser energy deposition, 13 mJ/pulse, 150 mm focal length lens, and correlated with polar steady state and instantaneous pressure plots

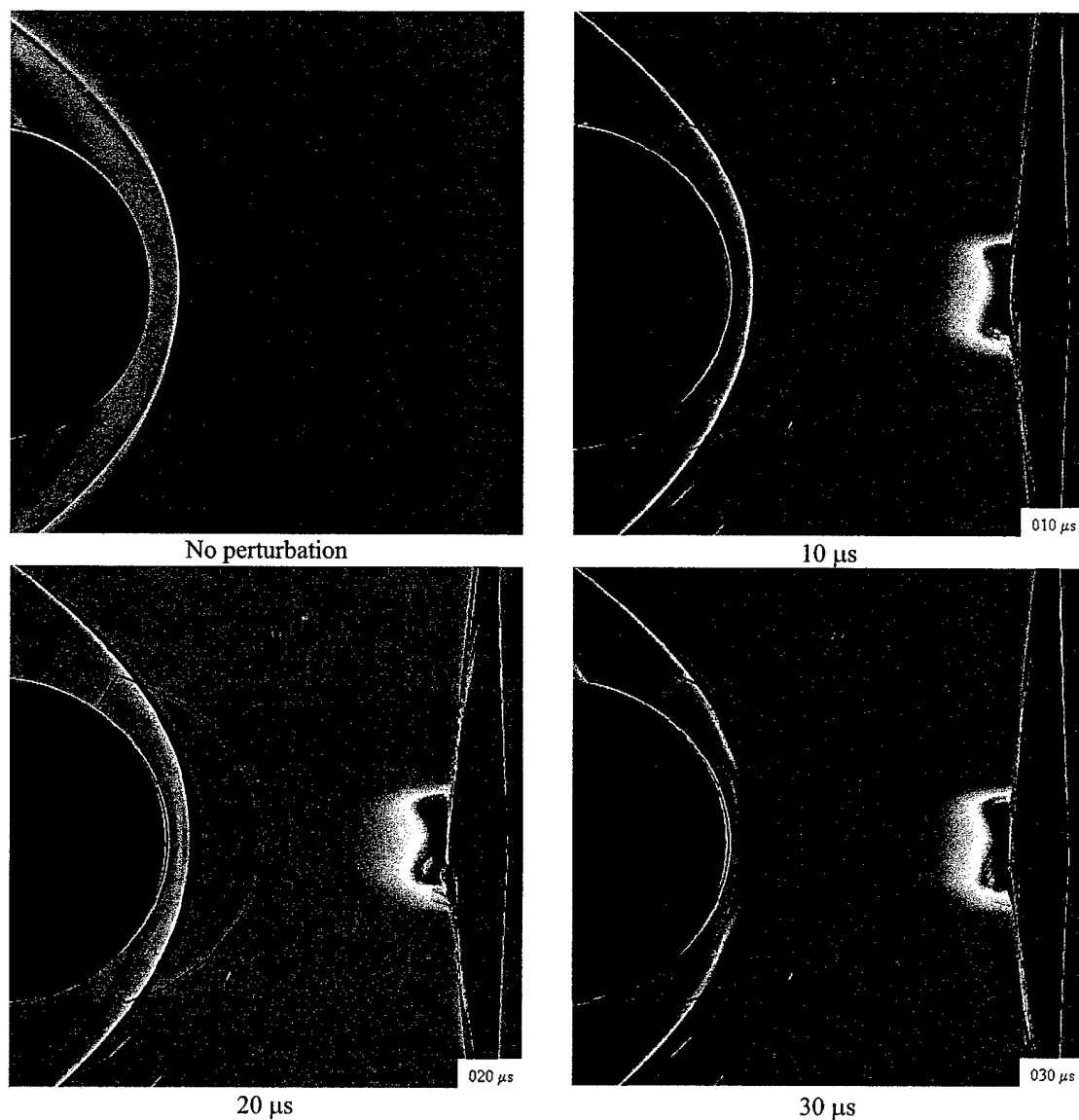


Figure 5.26 Phase averaged xenon Strobotac flash generated schlieren images of Mach 3.45 sphere with laser energy deposition 1.0 diameter upstream, 0, 10, 20, and 30 μs after laser energy deposition, 127 mJ/pulse, 150 mm focal length lens, and correlated with polar steady state and instantaneous pressure plots

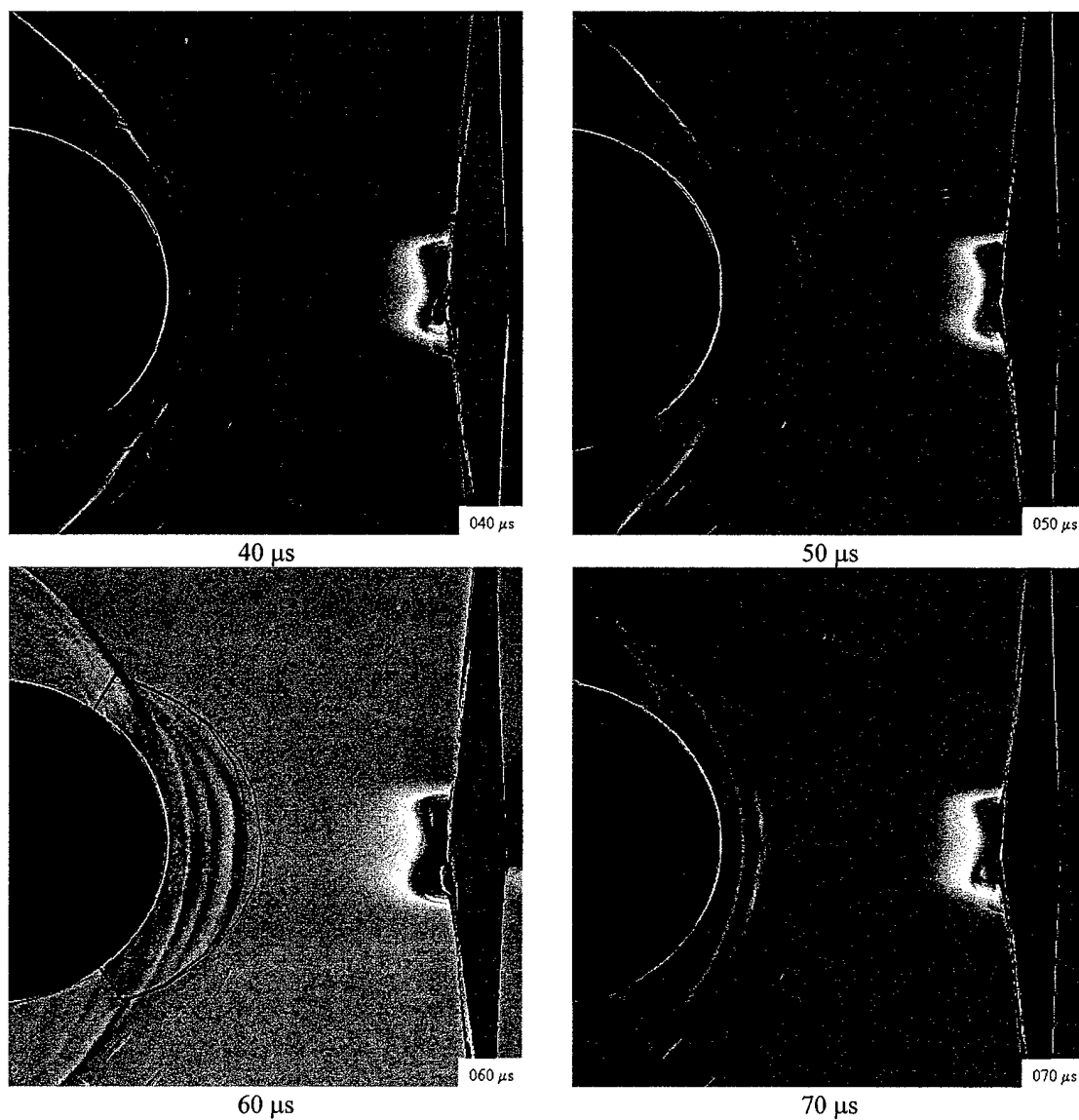


Figure 5.27 Phase averaged xenon Strobotac flash generated schlieren images of Mach 3.45 sphere with laser energy deposition 1.0 diameter upstream, 40, 50, 60, and 70 μs after laser energy deposition, 127 mJ/pulse, 150 mm focal length lens, and correlated with polar steady state and instantaneous pressure plots

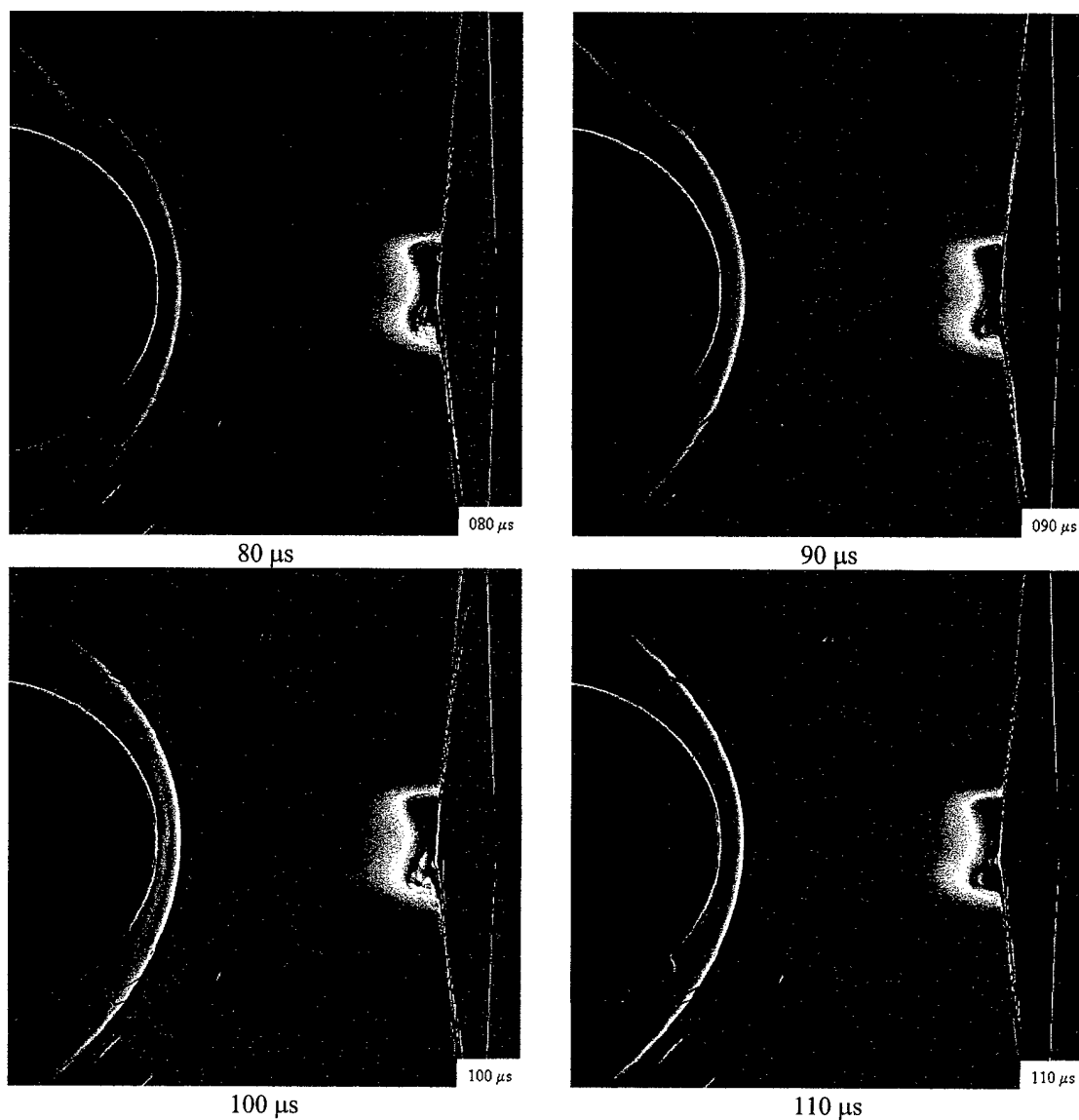


Figure 5.28 Phase averaged xenon Strobotac flash generated schlieren images of Mach 3.45 sphere with laser energy deposition 1.0 diameter upstream, 80, 90, 100, and 110 μs after laser energy deposition, 127 mJ/pulse, 150 mm focal length lens, and correlated with polar steady state and instantaneous pressure plots

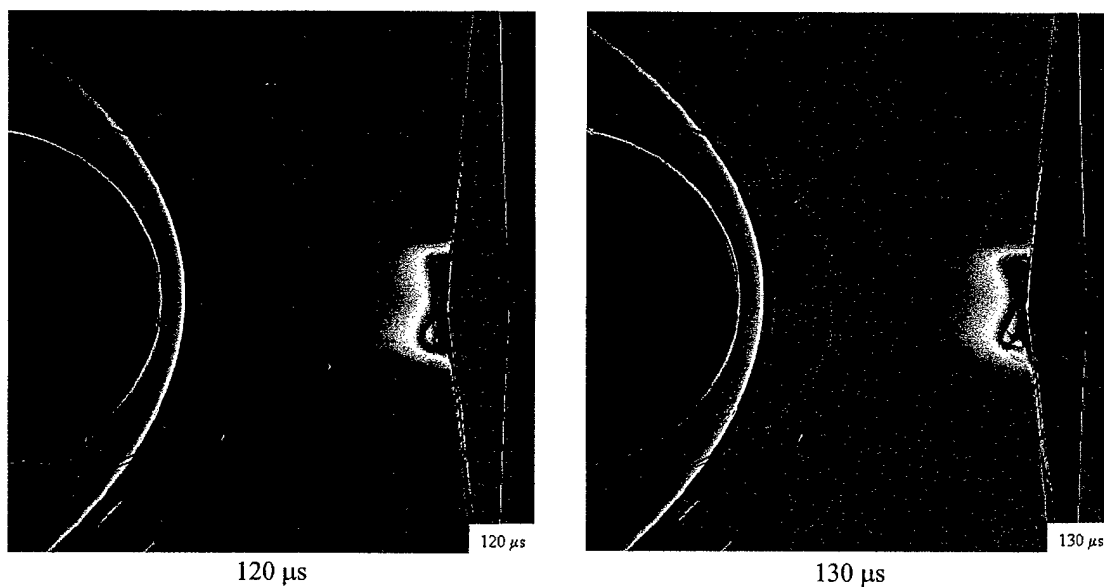


Figure 5.29 Phase averaged xenon Strobotac flash generated schlieren images of Mach 3.45 sphere with laser energy deposition 1.0 diameter upstream, 120, and 130 μ s after laser energy deposition, 127 mJ/pulse, 150 mm focal length lens, and correlated with polar steady state and instantaneous pressure plots

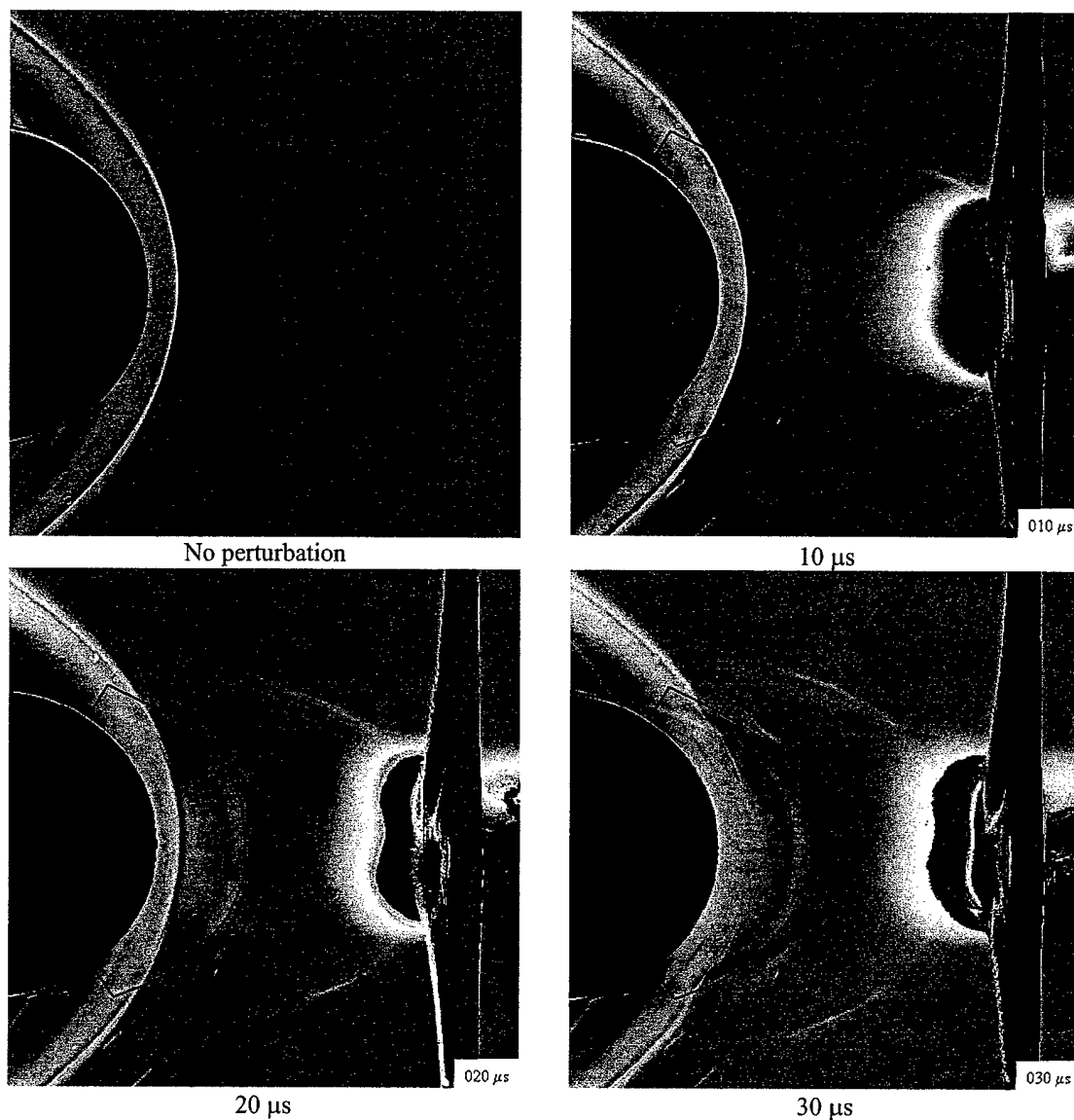


Figure 5.30 Phase averaged xenon Strobotac flash generated schlieren images of Mach 3.45 sphere with laser energy deposition 1.0 diameter upstream, 0, 10, 20, and 30 μs after laser energy deposition, 258 mJ/pulse, 150 mm focal length lens, and correlated with polar steady state and instantaneous pressure plots

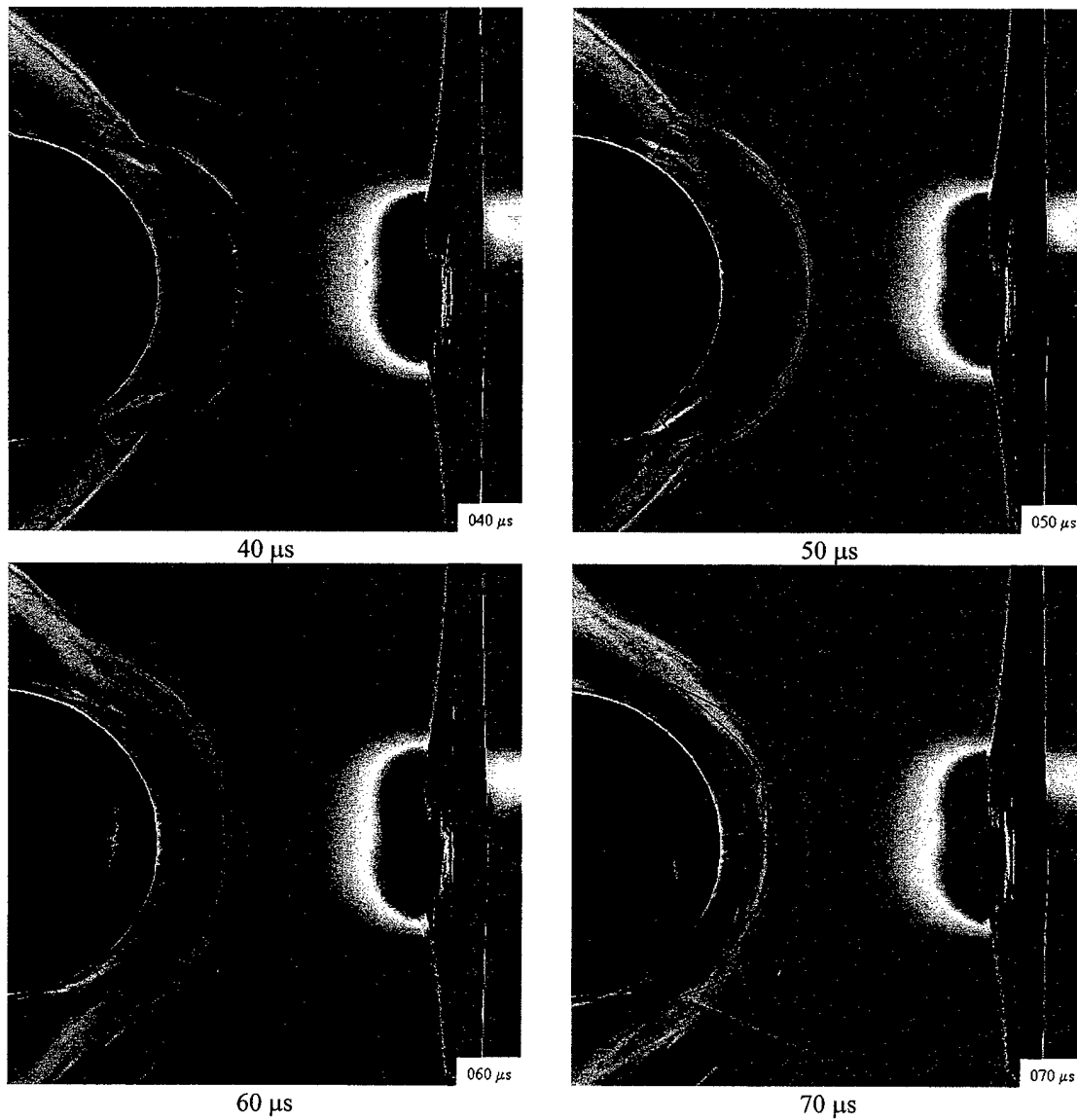


Figure 5.31 Phase averaged xenon Strobotac flash generated schlieren images of Mach 3.45 sphere with laser energy deposition 1.0 diameter upstream, 40, 50, 60, and 70 μ s after laser energy deposition, 258 mJ/pulse, 150 mm focal length lens, and correlated with polar steady state and instantaneous pressure plots

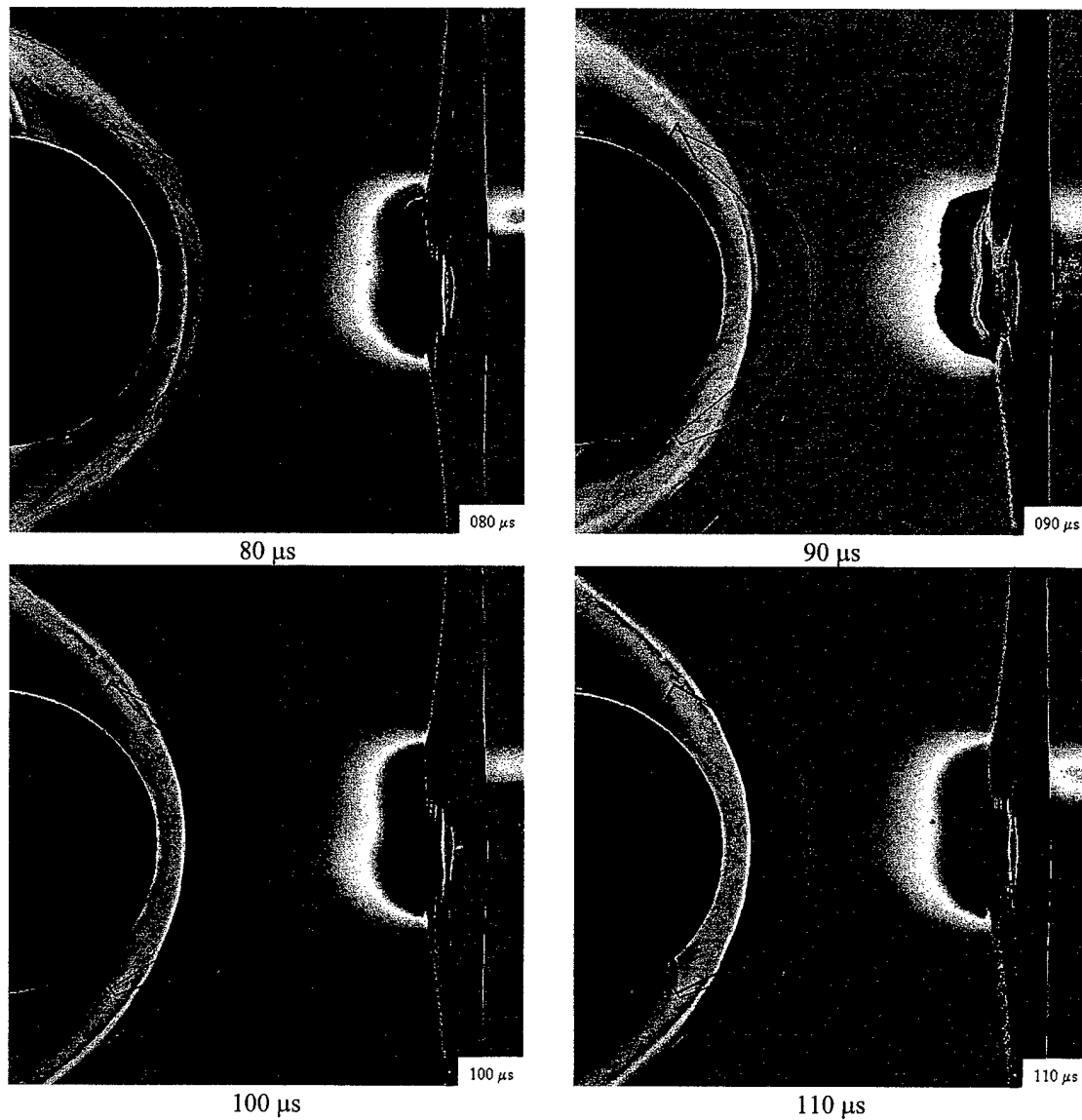


Figure 5.32 Phase averaged xenon Strobotac flash generated schlieren images of Mach 3.45 sphere with laser energy deposition 1.0 diameter upstream, 80, 90, 100, and 110 μs after laser energy deposition, 258 mJ/pulse, 150 mm focal length lens, and correlated with polar steady state and instantaneous pressure plots

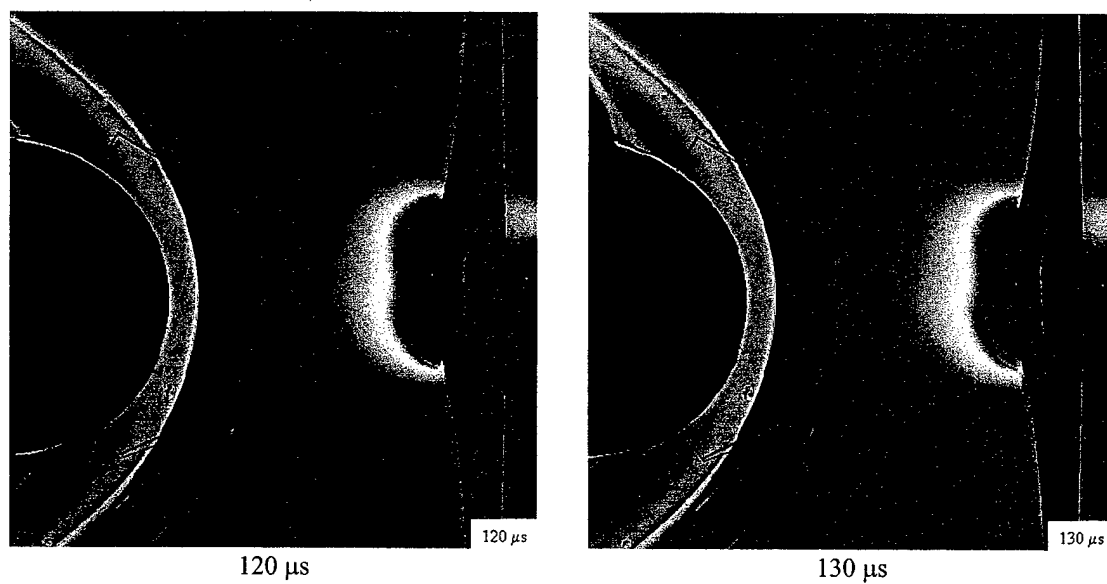


Figure 5.33 Phase averaged xenon Strobotac flash generated schlieren images of Mach 3.45 sphere with laser energy deposition 1.0 diameter upstream, 120, and 130 μ s after laser energy deposition, 258 mJ/pulse, 150 mm focal length lens, and correlated with polar steady state and instantaneous pressure plots

5.2.4 Surface Heat Transfer

The surface temperature of the hemisphere was measured from 0-45 degrees from the horizontal in the vertical symmetry plane for the sphere. Figure 5.34 shows the wall temperature of the sphere in the vertical symmetry plane as a function of time and gauge angle. Table 3.5 lists the measured angles for the eight gauges. Platinum thin film gauges were used to measure the temperature (see Section 3.6). The temperature plotted is given as the difference of the temperature and the ambient room temperature. From the temperature-time history, the heat transfer was calculated using Equation (3.19). The tunnel run times were targeted at 10 seconds based on the semi-infinite assumption for the determination of the heat flux (see Section 3.6.1 and 3.6.3.2). The temperature of the inside of the sphere was also recorded for each wind tunnel run to with an embedded thermocouple (see Figure 3.44) to assess the validity of the semi-infinite temperature requirement for the determination of the heat flux.

Table 5.2 Tunnel operating parameters for surface heat transfer measurement experiments

Mach number	3.45
Reynolds number based on sphere diameter, $Re_D = \frac{\rho V D}{\mu}$	1.905×10^6
Freestream viscosity, μ	$5.666 \times 10^{-6} \frac{\text{kg}}{\text{m s}}$
Stagnation pressure, p_0	$1.138 \times 10^6 \text{ Pa}$
Stagnation temperature, T_0	279 K
Stagnation density, ρ_0	$14.212 \frac{\text{kg}}{\text{m}^3}$
Freestream temperature, T	82.5 K
Freestream pressure, p	$1.602 \times 10^4 \text{ Pa}$
Freestream density, ρ	$0.676 \frac{\text{kg}}{\text{m}^3}$
Freestream velocity, V	628.1 m/s
Freestream speed of sound, a	182.1 m/s
Pitot pressure, p_{02}	$2.530 \times 10^5 \text{ Pa}$
Pitot density, ρ_{02}	$3.160 \frac{\text{kg}}{\text{m}^3}$

Figure 5.34 gives the measured sphere surface temperature as a function of gauge location and time. The temperature plotted is the difference between the wall temperature and the ambient room temperature,

denoted, $T - T_a$. Figure 5.35 shows the measured surface heat flux as a function of time and gauge location for the Mach 3.45 sphere. The heat flux has been non-dimensionalized with the absolute value of the van Driest stagnation point heat flux for a sphere (see Equation (3.23)). The data for the temperature in the case given in Figure 5.34 and Figure 5.35 is collected for a time resolution of 1 ms, or at a sampling frequency of 1 kHz. The cooling effect on the sphere during the wind tunnel run is observed in both the temperature and the heat flux plots. This cooling is associated with a drop in the stagnation temperature in the wind tunnel during its operation. This drop is, in turn, due to the expansion process of the air in the storage tanks (see discussion in Section 3.6.3.2). The measured heat flux (see Figure 3.41) agrees closely with van Driest (Equation (3.23)). Thus, the cooling is due to the temperature difference, $T_0 - T_w$. During the tunnel run, both T_0 and T_w drop. The van Driest stagnation point heat flux for a sphere can be rewritten as

$$q_0 = 0.763 \text{Pr}^{-0.6} \sqrt{\rho_{02} \mu_{02}} \sqrt{\frac{1}{R} \left(\frac{2(p_{02} - p_\infty)}{\rho_{02}} \right)^{\frac{1}{4}}} c_p (T_0 - T_w). \quad (5.8)$$

In this expression the only terms which vary during the tunnel run (after startup) are μ_{02} , T_0 , and T_w . The variation of μ_{02} during the tunnel run is small. Thus, the cooling to the sphere is due to the temperature difference $T_0 - T_w$ where $T_0 < T_w$.

The temperature and heat flux was also measured at a sampling frequency of 1 MHz. This high frequency data was limited to four channels for each test run of the wind tunnel. Therefore, for each test condition, two runs were made; the first for gauges 1-4, and the second for gauges 5-8. Twenty sets of data were collected at the 1 MHz frequency for each test condition. The temperature was reduced from the gauge voltage readout from the signal conditioner based on the calibration data given in Section 3.6.3.1. This temperature data was filtered with a digital filter. The digital filter was a low pass Hamming Window with a cutoff frequency of 80 kHz.

Figure 5.36 shows the heat flux calculated from Equation (3.19) for the eight gauge locations on the hemisphere with an energy deposition of 283 mJ/pulse and 1.0 diameter upstream of the sphere. The plotted contours are the heat flux non-dimensionalized with the van Driest stagnation heat flux. The absolute value of the stagnation point heat flux is used. By using the absolute value of the stagnation point heat flux, heating is positive, and cooling is negative. Figure 5.37 through Figure 5.44 gives the measured

surface temperature and the heat flux for each of the eight thin film gauges for the same test case. The temperature and the heat flux presented for each gauge is an average of 20 phase-locked data sets. The temperature in each case has an offset subtracted from it due to the stagnation temperature decrease during the operation of the wind tunnel (see Section 3.6.3.2). The scatter in the data is quantified by $\pm 1\sigma$ (where σ is the standard deviation) distributions shown by the error bars for different times on the temperature and the heat flux traces. As can be seen in the plots, the gauges are sensitive enough to pick up the heating due to the radiation and the blast wave from the spark source reflecting off of the surface of the sphere. These points are noted on the plots as R and B, respectively. The temperature increase due to the thermal spot reaching the sphere is only on the order of two degrees Kelvin. However, due to the small timescale, the heating flux rate to the sphere is large. This high heating rate is attributed to the derivative of the temperature with respect to time in Equation (3.17). After the blast wave reflection from the sphere, there is a cooling associated with the expansion wave hitting the sphere surface. This expansion fan is due to the lensing process of the bow shock and interface of the thermal spot interaction (see Section 5.2.3).

In Figure 5.36 the gauge locations are shown by the dashed lines, and Tecplot is used to interpolate the contour values between the gauges. For this test case the laser energy deposition was 1.0 diameter upstream and on centerline and consisted of a single laser pulse of 283 mJ/pulse at 10 Hz. Radiation heating from the laser spark can be seen by the ridge in the contour plot at time $t = 0$ across all of the gauges. Also, observed is the blast wave heating which can be seen by the ridge in the contour plot between 20 and 30 μ s. This blast wave heating can also be verified by the transmitted blast wave seen in the schlieren images corresponding to this case from 20 to 30 μ s in Figure 5.8. Also of interest is the lag in the blast wave heating detected by the gauges as the gauge angular position increases (note the curvature in the ridge as gauge angle increase in Figure 5.36). This lag in heating for the upper gauges is due to the fact that the blast wave hits the stagnation gauge first, and then successively the upper gauges.

After the blast wave heating effect, there is a cooling effect. This cooling effect is cooling effect due to the expansion fan hitting the surface of the sphere. This effect is clearly observed in the region of the contour plot following the blast wave ridge (see Figure 5.36 and Figure 5.37 - Figure 5.44).

Next, the heating due to the thermal spot impacting the sphere is detected from 50 to 100 μ s, and this heating also correlates with the schlieren images for 50 to 100 μ s for this test condition (see Figure 5.9 and

Figure 5.10). This surface heating from 50 to 100 μs also corresponds to the drop in measured pressure data observed in Figure 5.16, Figure 5.17, Figure 5.18 for the laser energy deposition 1.0 diameter upstream of the sphere. Moreover, a similar time lag in the heating is observed as the gauges increase in angle from 0 to 45 degrees from the horizontal. The lag is caused by the impact of the thermal spot hitting the stagnation gauge first, and then the latter gauges. Figure 5.36 shows the decrease in heating from 100 to 160 μs and this correlates with the schlieren images for the same time span (see Figure 5.11) as the thermal spot convects around the sphere and the sphere returns back to a steady state condition.

Figure 5.45 shows the heat flux for laser energy deposition upstream of the hemisphere model for a double laser energy deposition pulse separated by 5 μs and with both lasers phase locked and firing at 10 Hz. The plotted contours are the heat flux non-dimensionalized with the absolute value of the van Driest stagnation heat flux. The gauge locations are shown by the dashed lines, and Tecplot is used to interpolate the contour values between the gauges. The radiation heating at 0 μs and the blast wave heating can be seen from 20 to 30 μs . The thermal spot heat is observed from 50 to 100 μs . For the double pulse case when compared to the single pulse case does not have the severe increase in heating as seen in the thermal spot heating (see Figure 5.36). The heating is approximately 50% less than for the single pulse case. One possible explanation for this reduction in heat flux, might be a reduction in the spatial temperature gradient due to the double pulse. In other words, the double pulse would broaden the initial temperature distribution of the laser energy deposition since the first pulse would move downstream from the second pulse. This broadening of the temperature distribution, (see Equations (2.31) and (2.32)) would decrease the spatial temperature gradient. This decrease in temperature gradient would then lead to lower heat flux to the surface of the sphere as the thermal region convects about the sphere.

Figure 5.46 gives the heat flux for the hemisphere with single laser energy deposition at 0.6 diameters upstream and on centerline. Likewise, the plotted contours are the heat flux non-dimensionalized with the absolute value of the van Driest stagnation heat flux. The gauge locations are shown by the dashed lines, and Tecplot is used to interpolate the contour values between the gauges. The radiation heating is observed at 0 μs . However, the blast wave heating can be seen from 10 to 20 μs . This heating correlates the blast wave impact observed in the schlieren images for 10 to 20 μs of Figure 5.12. There is also a cooling effect due to the expansion fan hitting the surface of the sphere from the lensing process. The thermal spot

interaction occurs at 40 to 90 μs and is correlated with Figure 5.13 - Figure 5.14. The time lag of the heat transfer for the blast wave and the thermal spot interaction is also observed for the upper gauges. This lag for this test case is due to the stagnation point region interacting first with both the blast wave and thermal spot. Figure 5.47 - Figure 5.54 are the temperature and heat flux measurements for each of the individual eight gauges.

Figure 5.55 gives the heat flux for a double pulse laser energy deposition at 0.6 diameters upstream and on centerline. The radiation heating and the blast wave heating are observed and denoted on the plot for this double pulse test case. The heating due to the thermal spot is 40 to 50% less than the single laser pulse case. This lowering of the heat flux is similar to the effect seen for the double pulse 1.0 diameter upstream. The double pulse will lessen the spatial temperature gradient and, this broadening of the spatial temperature distribution, in turn, will lead to a lower heat flux to the surface of the sphere.

Figure 5.56 is the time integrated heat flux for each gauge for each of the four test cases described above. This figure gives the total energy flux to the gauge over the period of time of the interaction with the thermal spot generated by the laser perturbation. This integration puts the high heat fluxes observed for the interaction process into perspective. If the maximum energy flux from Figure 5.56, 0.02 mJ/mm^2 is then integrated across the face of the sphere, then the upper bound for the total energy fluxed through the sphere surface is 25 mJ. As an upper estimate, roughly only 9% of the energy from the laser energy deposition is transferred to the sphere. The rest of the energy from the laser deposition will still be contained in the flow, i.e. blast wave, turbulence, enthalpy, etc., and these forms of energy convect downstream in the flow.

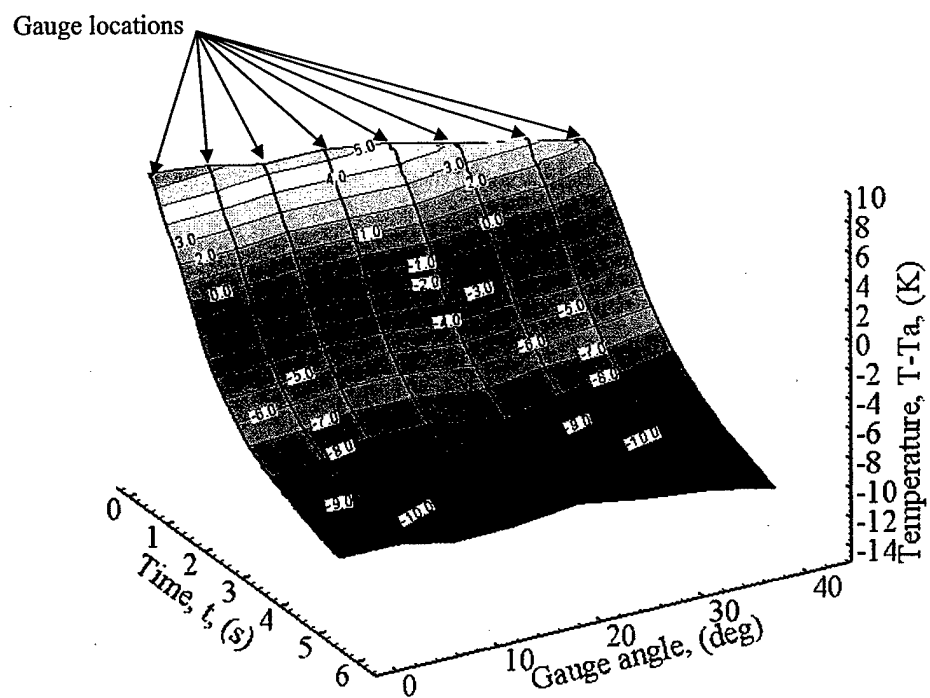


Figure 5.34 Wall temperature for the hemisphere without laser spark

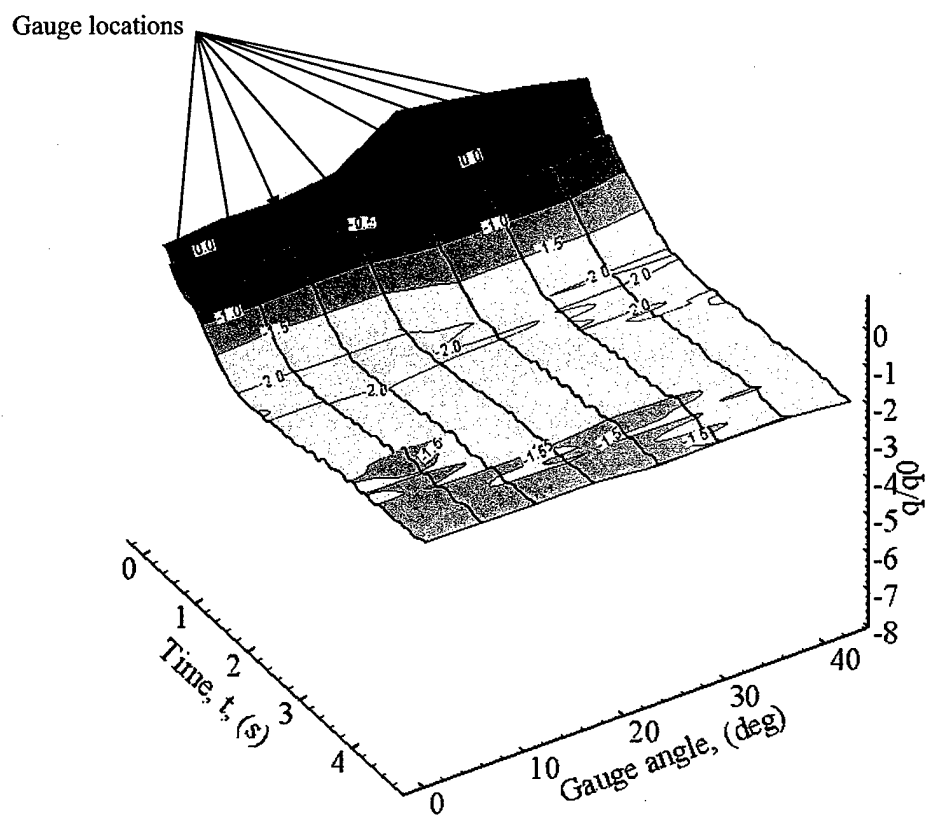


Figure 5.35 Wall heat flux without laser spark

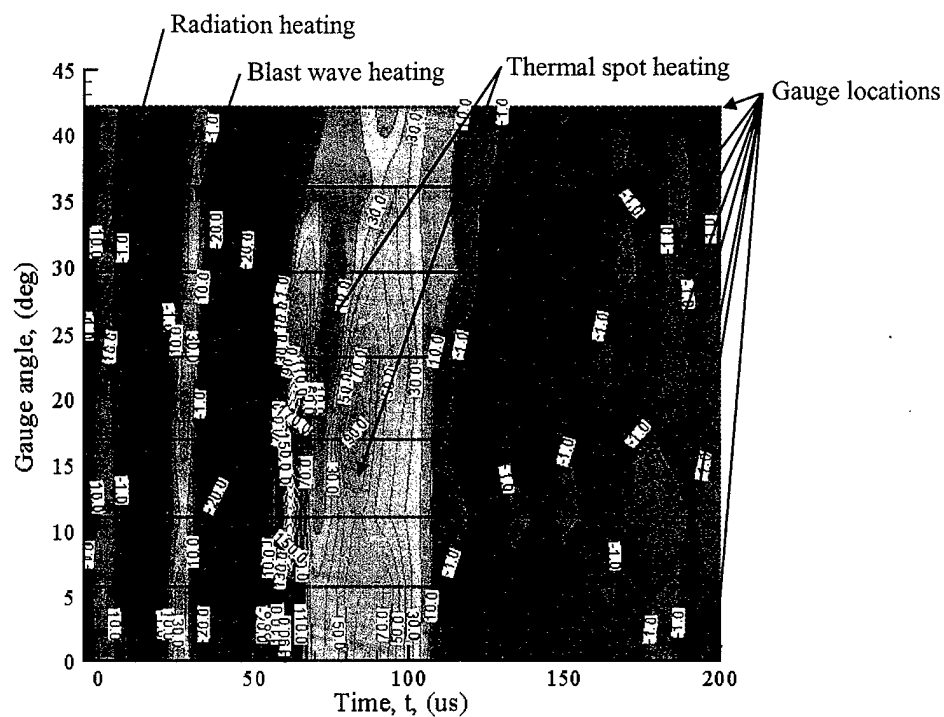


Figure 5.36 Measured wall heat flux on Mach 3.45 sphere and with laser energy deposition 1.0 diameter upstream and on the centerline axis, one laser pulse (10 Hz) at 283 mJ/pulse, 150 mm focal length lens

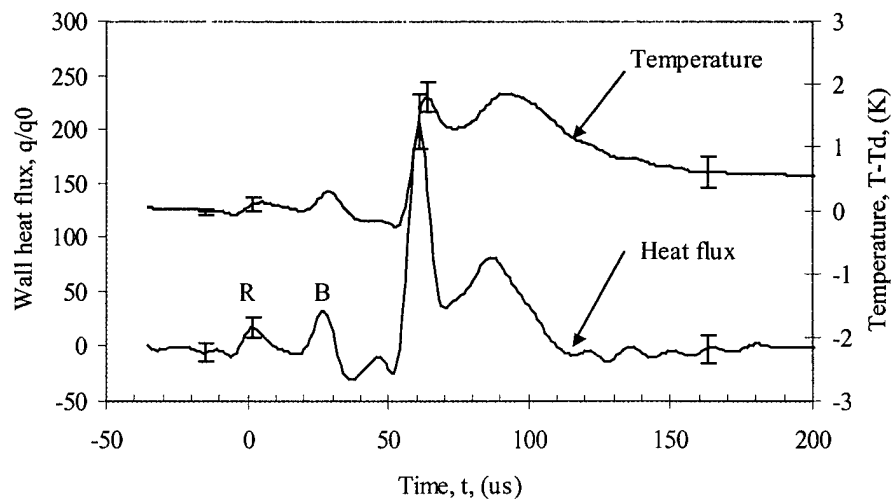


Figure 5.37 Measured wall heat flux and temperature for gauge 1 on Mach 3.45 sphere and with laser energy deposition 1.0 diameter upstream and on the centerline axis, one laser pulse (10 Hz) at 283 mJ/pulse, 150 mm focal length lens

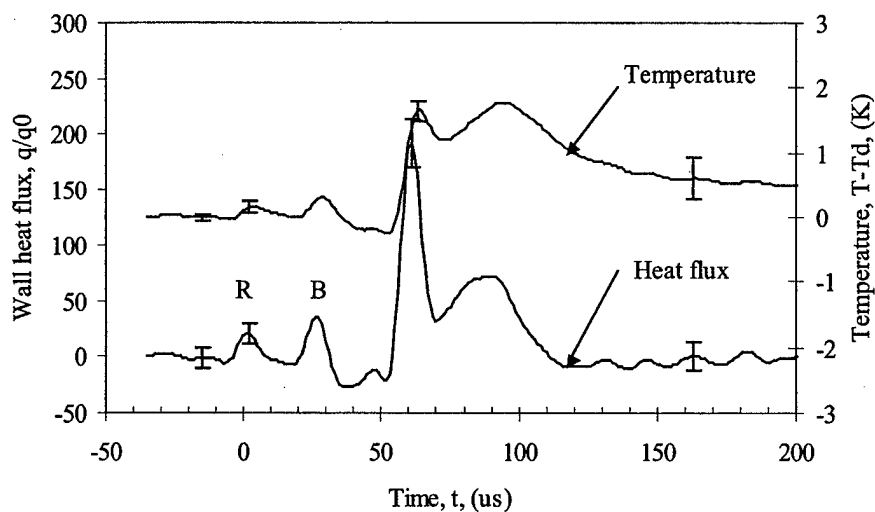


Figure 5.38 Measured wall heat flux and temperature for gauge 2 on Mach 3.45 sphere and with laser energy deposition 1.0 diameter upstream and on the centerline axis, one laser pulse (10 Hz) at 283 mJ/pulse, 150 mm focal length lens

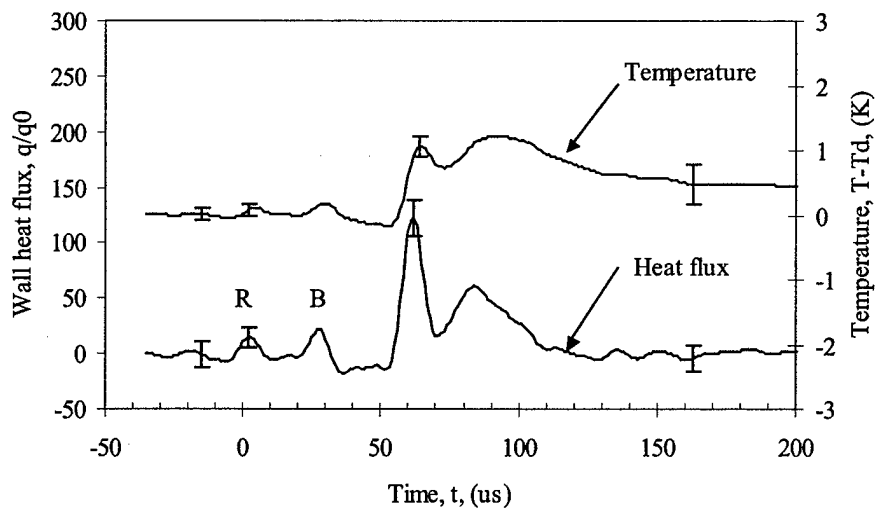


Figure 5.39 Measured wall heat flux and temperature for gauge 3 on Mach 3.45 sphere and with laser energy deposition 1.0 diameter upstream and on the centerline axis, one laser pulse (10 Hz) at 283 mJ/pulse, 150 mm focal length lens

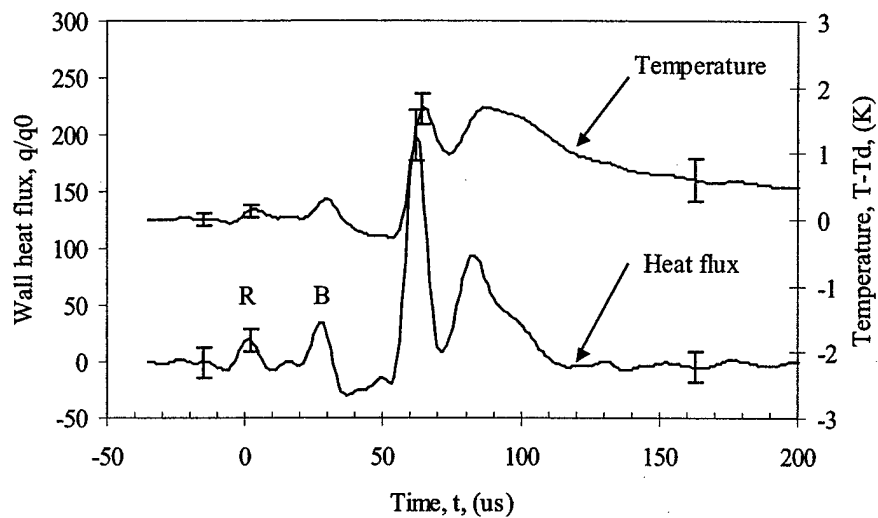


Figure 5.40 Measured wall heat flux and temperature for gauge 4 on Mach 3.45 sphere and with laser energy deposition 1.0 diameter upstream and on the centerline axis, one laser pulse (10 Hz) at 283 mJ/pulse, 150 mm focal length lens

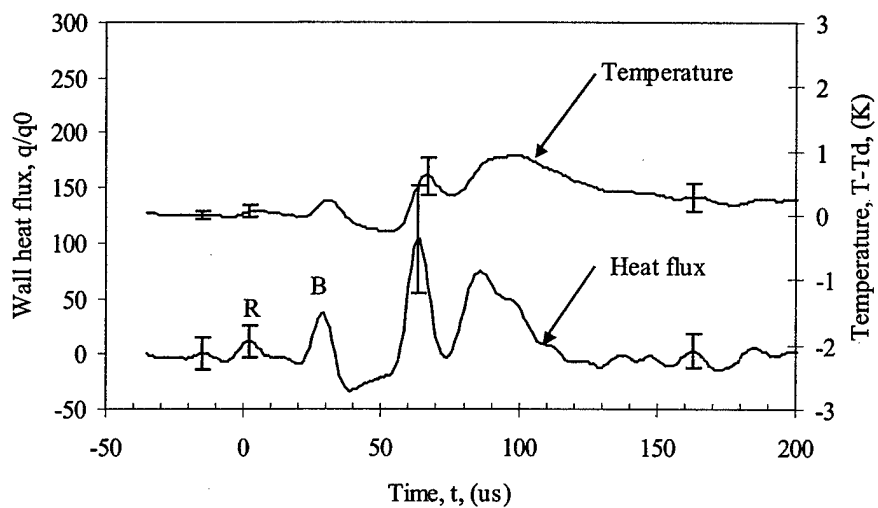


Figure 5.41 Measured wall heat flux and temperature for gauge 5 on Mach 3.45 sphere and with laser energy deposition 1.0 diameter upstream and on the centerline axis, one laser pulse (10 Hz) at 283 mJ/pulse, 150 mm focal length lens

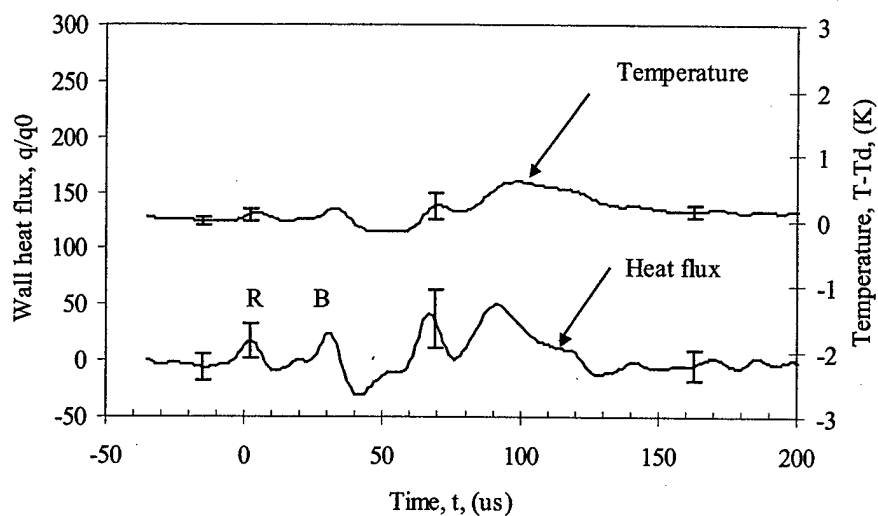


Figure 5.42 Measured wall heat flux and temperature for gauge 6 on Mach 3.45 sphere and with laser energy deposition 1.0 diameter upstream and on the centerline axis, one laser pulse (10 Hz) at 283 mJ/pulse, 150 mm focal length lens

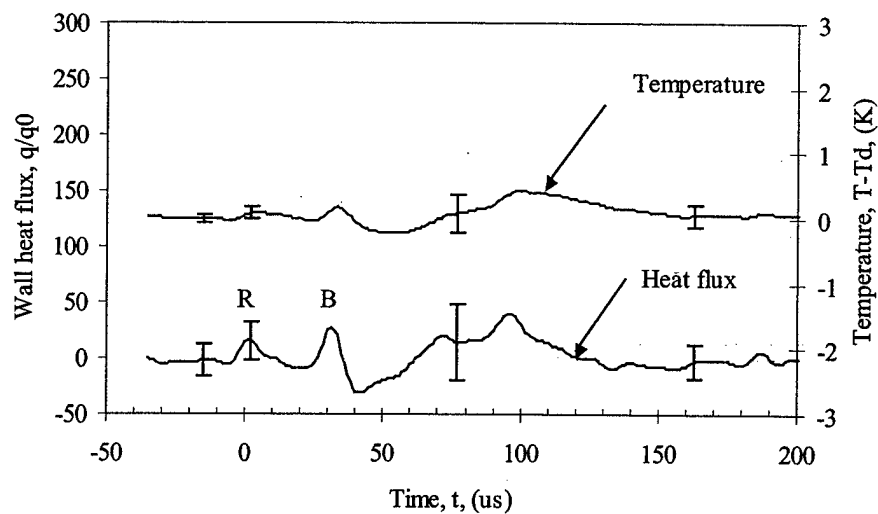


Figure 5.43 Measured wall heat flux and temperature for gauge 7 on Mach 3.45 sphere and with laser energy deposition 1.0 diameter upstream and on the centerline axis, one laser pulse (10 Hz) at 283 mJ/pulse, 150 mm focal length lens

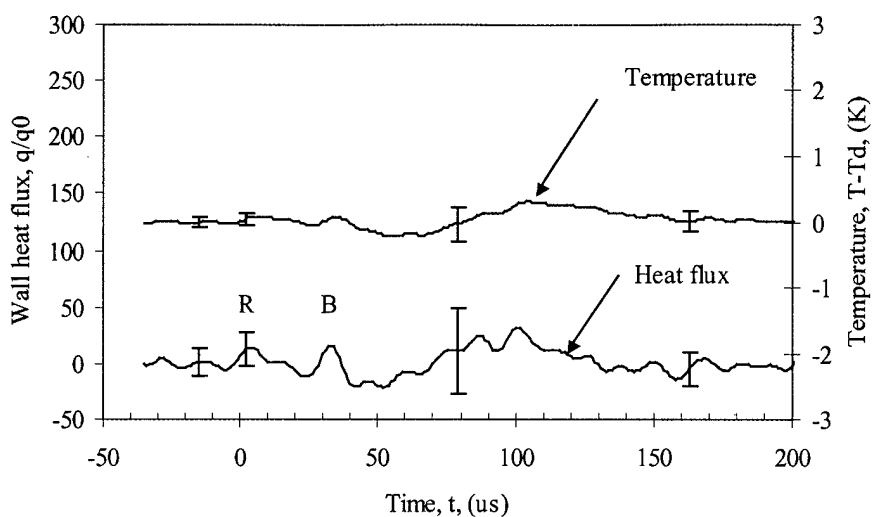


Figure 5.44 Measured wall heat flux and temperature for gauge 8 on Mach 3.45 sphere and with laser energy deposition 1.0 diameter upstream and on the centerline axis, one laser pulse (10 Hz) at 283 mJ/pulse, 150 mm focal length lens

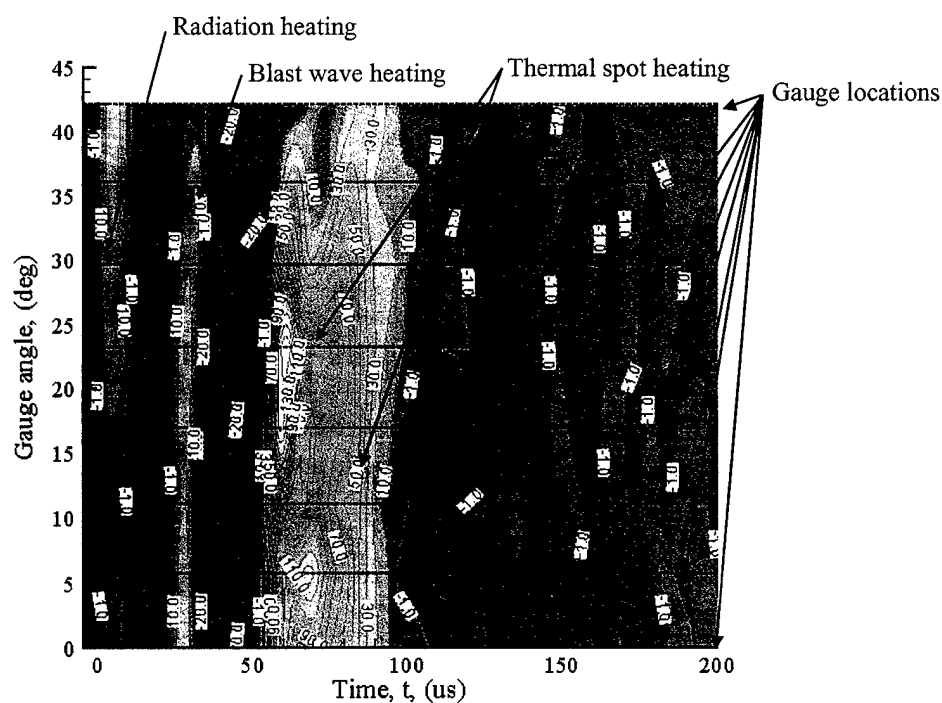


Figure 5.45 Measured wall heat flux on Mach 3.45 sphere and with laser energy deposition 1.0 diameter upstream and on the centerline axis, double laser pulse with 5 μ s separation (10 Hz) at 263 mJ/(double pulse), 150 mm focal length lens

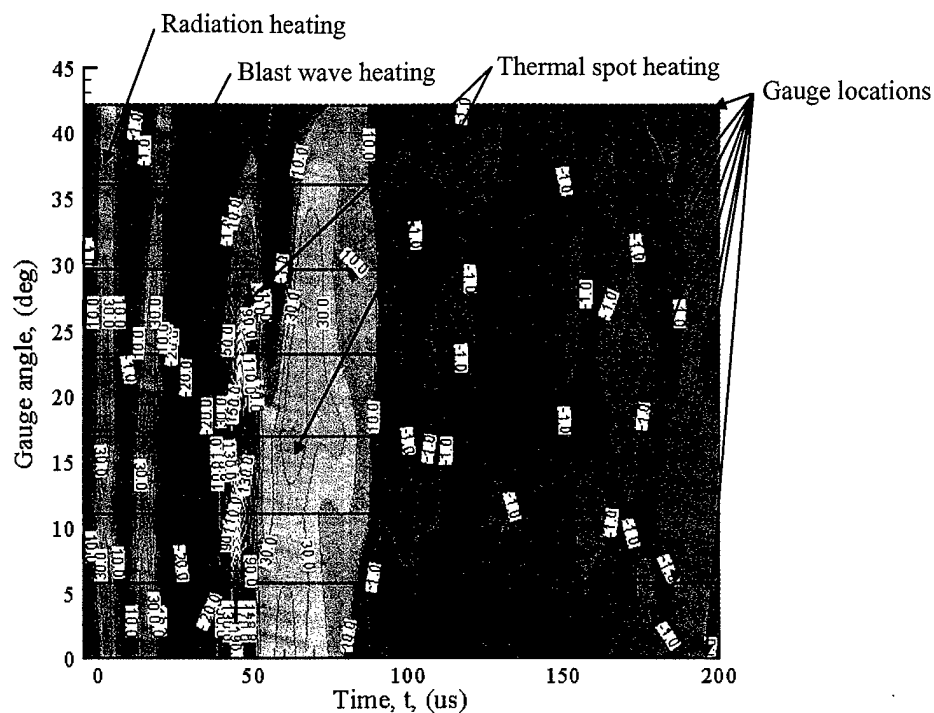


Figure 5.46 Measured wall heat flux on Mach 3.45 sphere and with laser energy deposition 0.6 diameters upstream and on the centerline axis, single laser pulse (10 Hz) at 283 mJ/pulse, 150 mm focal length lens

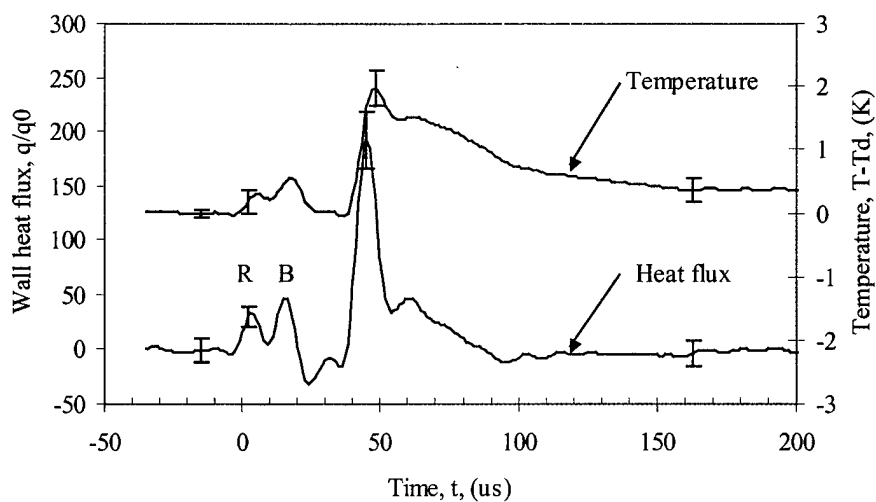


Figure 5.47 Measured wall heat flux and temperature for gauge 1 on Mach 3.45 sphere and with laser energy deposition 0.6 diameters upstream and on the centerline axis, one laser pulse (10 Hz) at 283 mJ/pulse, 150 mm focal length lens

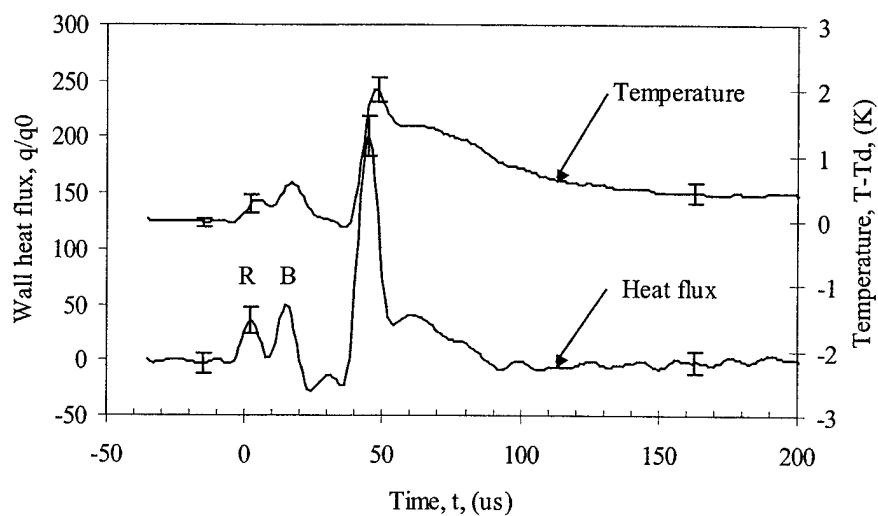


Figure 5.48 Measured wall heat flux and temperature for gauge 2 on Mach 3.45 sphere and with laser energy deposition 0.6 diameters upstream and on the centerline axis, one laser pulse (10 Hz) at 283 mJ/pulse, 150 mm focal length lens

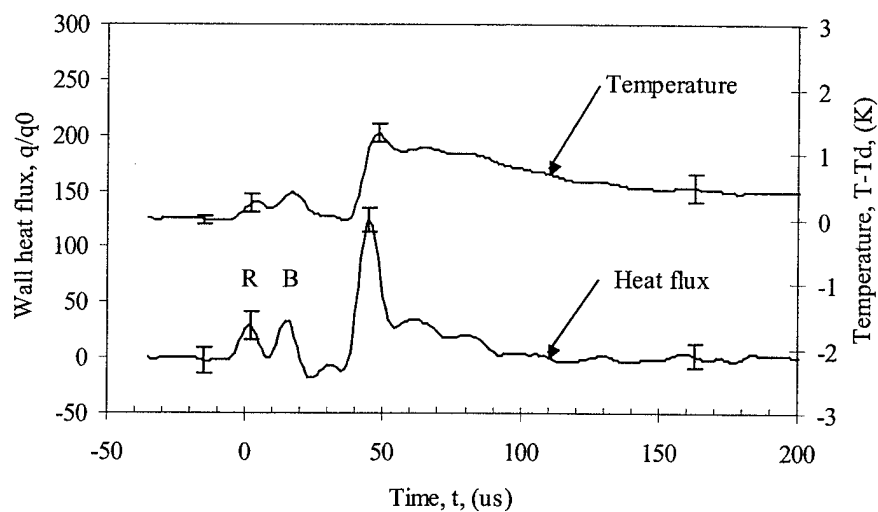


Figure 5.49 Measured wall heat flux and temperature for gauge 3 on Mach 3.45 sphere and with laser energy deposition 0.6 diameters upstream and on the centerline axis, one laser pulse (10 Hz) at 283 mJ/pulse, 150 mm focal length lens

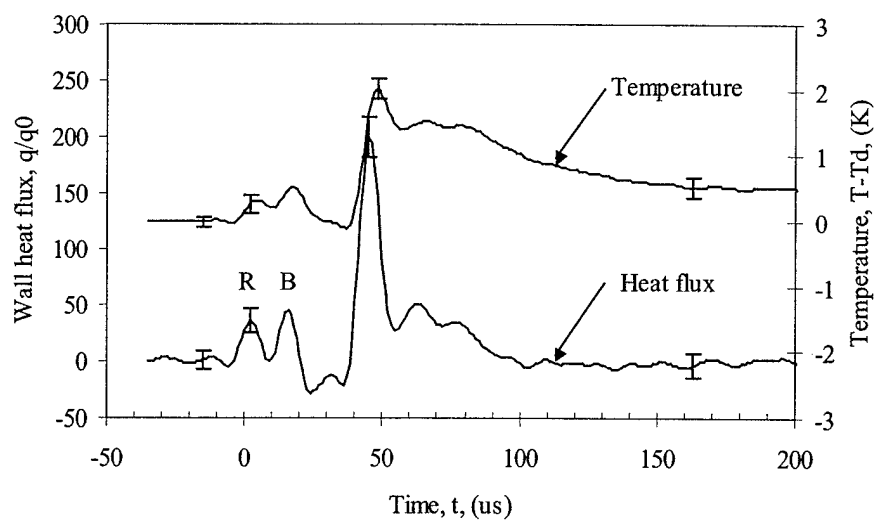


Figure 5.50 Measured wall heat flux and temperature for gauge 4 on Mach 3.45 sphere and with laser energy deposition 0.6 diameters upstream and on the centerline axis, one laser pulse (10 Hz) at 283 mJ/pulse, 150 mm focal length lens

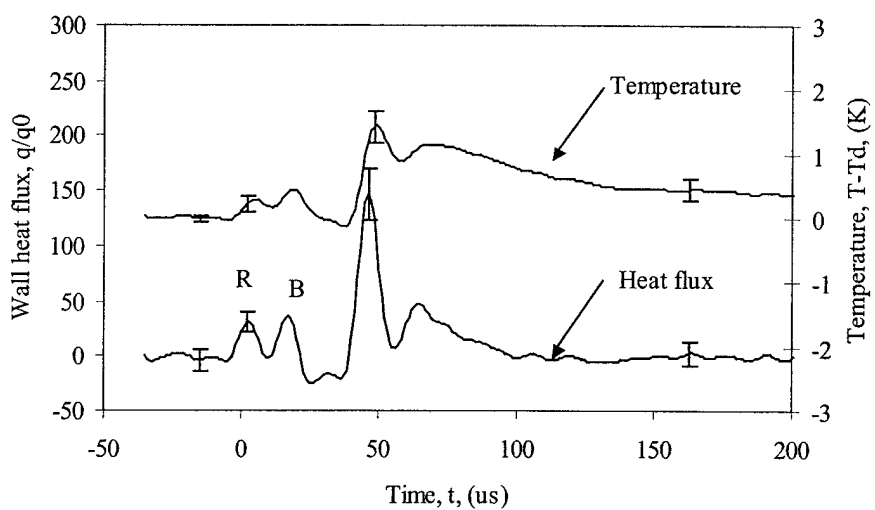


Figure 5.51 Measured wall heat flux and temperature for gauge 5 on Mach 3.45 sphere and with laser energy deposition 0.6 diameters upstream and on the centerline axis, one laser pulse (10 Hz) at 283 mJ/pulse, 150 mm focal length lens

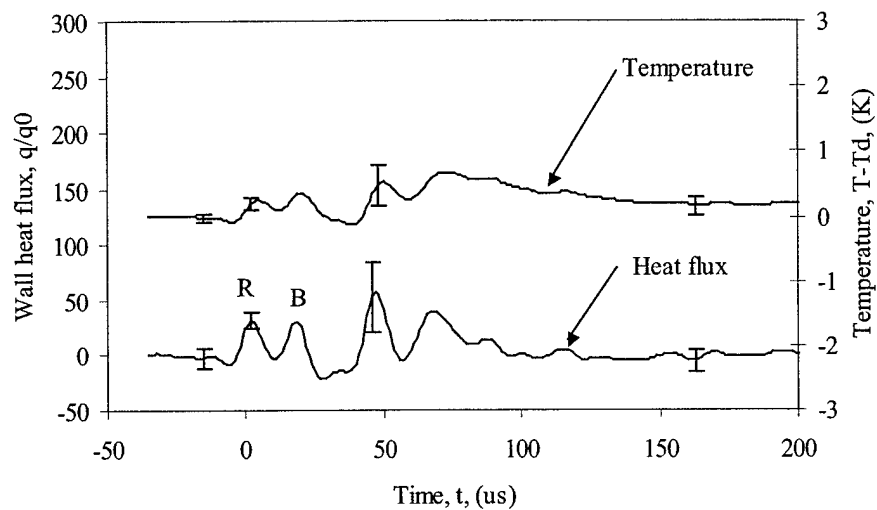


Figure 5.52 Measured wall heat flux and temperature for gauge 6 on Mach 3.45 sphere and with laser energy deposition 0.6 diameters upstream and on the centerline axis, one laser pulse (10 Hz) at 283 mJ/pulse, 150 mm focal length lens

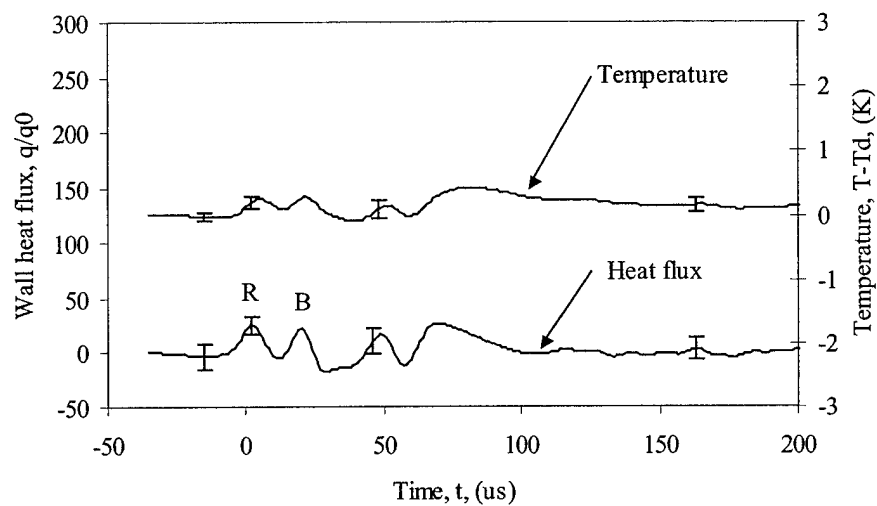


Figure 5.53 Measured wall heat flux and temperature for gauge 7 on Mach 3.45 sphere and with laser energy deposition 0.6 diameters upstream and on the centerline axis, one laser pulse (10 Hz) at 283 mJ/pulse, 150 mm focal length lens

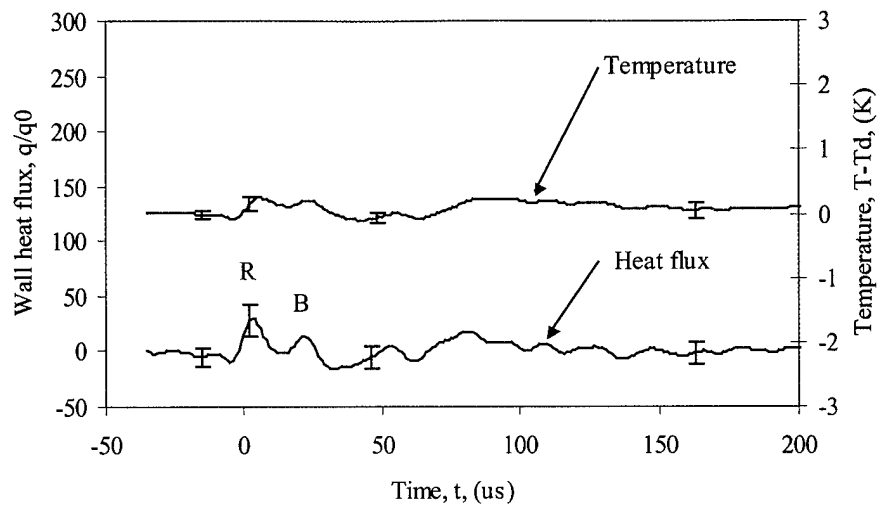


Figure 5.54 Measured wall heat flux and temperature for gauge 8 on Mach 3.45 sphere and with laser energy deposition 0.6 diameters upstream and on the centerline axis, one laser pulse (10 Hz) at 283 mJ/pulse, 150 mm focal length lens

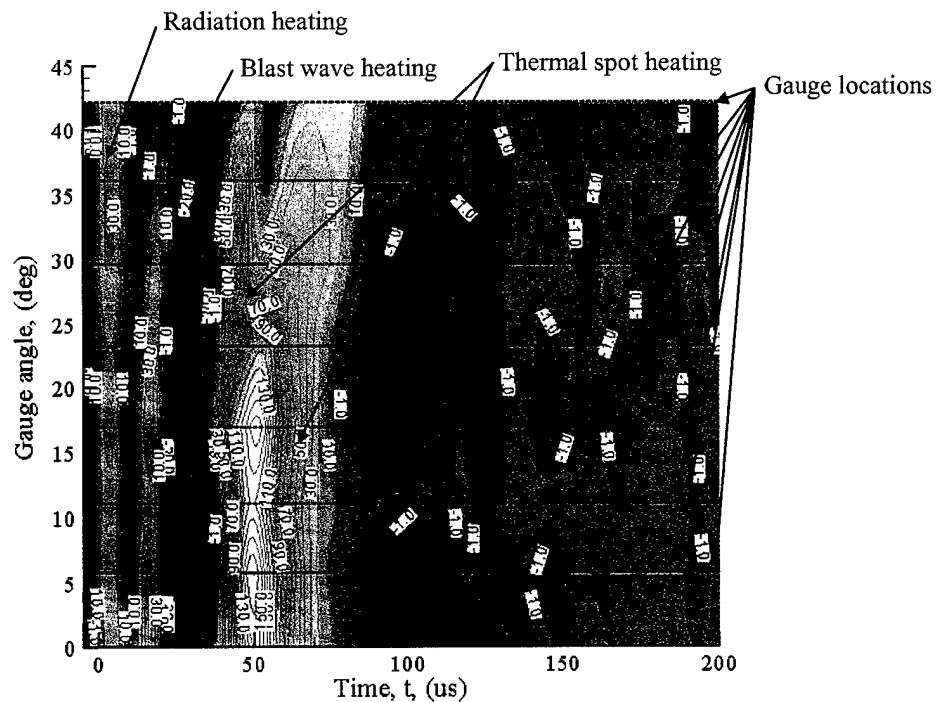


Figure 5.55 Measured wall heat flux on Mach 3.45 sphere and with laser energy deposition 0.6 diameters upstream and on the centerline axis, double laser pulse separated by 5 μ s (10 Hz) at 263 mJ/(double pulse), 150 mm focal length lens

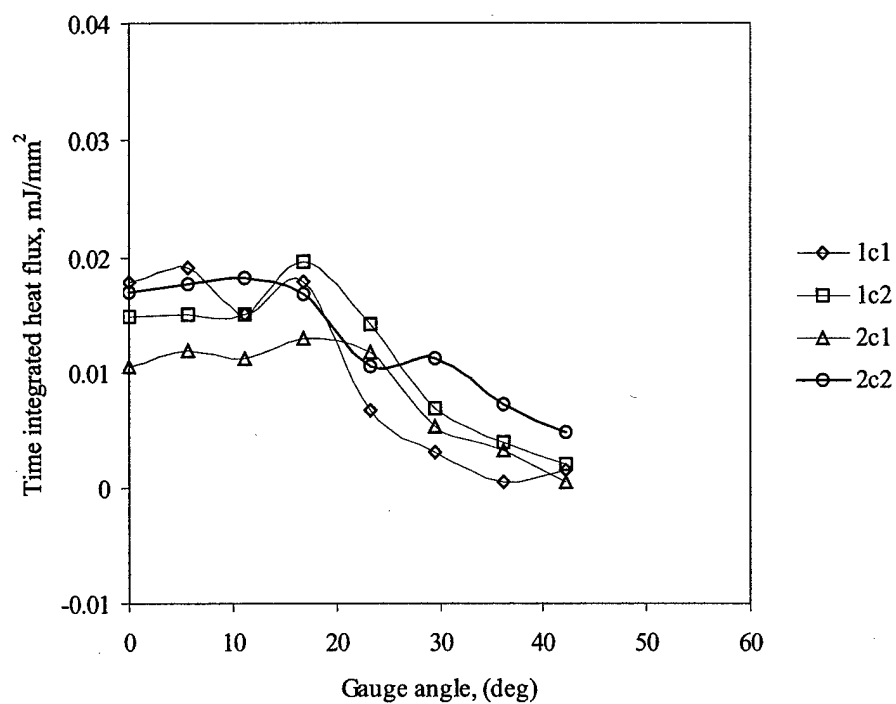


Figure 5.56 Time integrated heat flux for each of the gauges from small time scale data, 1c1 = single laser pulse 1.0 diameter upstream, 1c2 = single laser pulse 0.6 diameters upstream, 2c1 = double laser pulse 1.0 diameter upstream, and 2c2 = double laser pulse 0.6 diameters upstream

5.3 Sphere With Shock Impingement

The objective of the laser energy deposition tests upstream of the sphere with the shock impingement is to see if the severity of the aerothermal loads associated with the Edney Type IV shock/shock interaction can be reduced by perturbing the shock structure of the Edney Type IV interaction, e.g., by perturbing the embedded supersonic jet.

5.3.1 Steady State

Figure 5.57 shows the measured surface pressure for the Mach 3.45 sphere with the Edney Type IV shock impingement. The pressure has been non-dimensionalized with the freestream pitot pressure (see Equation (2.20)). The plot of the experimental data shows the characteristic rise in peak pressure due to the embedded supersonic jet of the Type IV interaction (see Section 2.4.1 and Figure 2.4). Also shown on the plot is the steady state pressure distribution for the sphere without the shock impingement (see Section 5.2.1). The increase in surface pressure attributable to the Edney Type IV shock impingement is readily seen in the comparison of the sphere alone distribution with the measured distribution for the shock impingement case. However, this measured peak pressure is most likely lower than the actual peak pressure due to the distribution of the pressure over the pressure gauge. Since the surface of the gauge cannot be made infinitesimally small, the pressure it senses will be an average of the pressure distributed over its surface. Therefore, any numerical simulations of this experimental arrangement should take into account the finite size of the pressure port diameter (see Section 3.5) and its averaging effect on the pressure sensed. D'Ambrosio [25] has demonstrated the necessity for accounting for this finite pressure sensor size when comparing experimental and numerical simulation data for the Edney Type IV interaction.

The two different data symbols in Figure 5.57 represent two data sets collected on two different days of wind tunnel testing. The steady state pressure data collected on the subsequent days of testing demonstrate the repeatability of the pressure measurements for these tests, similar to the repeatability of the sphere alone surface pressure tests described in Section 5.2.1.

Another factor can be attributed to the broadening of the pressure peak associated with the shock impingement. The compression ramp used to generate the impinging oblique shock was mounted to the

test section ceiling within the boundary layer. The shock generated with this ramp mounted in the boundary layer will fluctuate due to the unsteady effects associated with the turbulent boundary and ramp. [152] The fluctuations in the oblique shock will cause the shock interaction with the bow shock location to fluctuate. This, in turn, will cause the embedded supersonic jet of the Edney IV interaction to fluctuate.

Why does the surface pressure increase locally due to the Edney IV interaction? From the second law of Thermodynamics and with Equations (2.10), (2.11), (2.15), (2.16), and (2.19), the entropy change, $s_2 - s_1$, across a normal shock will be

$$s_2 - s_1 = -R \ln \left(\frac{p_{02}}{p_{01}} \right) = -R \ln \left[\left(\frac{\gamma + 1}{2\gamma M_1^2 - (\gamma - 1)} \right)^{\frac{\gamma}{\gamma-1}} \left(\frac{(\gamma + 1)M_1^2}{(\gamma - 1)M_1^2 + 2} \right)^{\frac{1}{\gamma-1}} \right] \quad (5.9)$$

where the subscripts 1 and 2 refer to the conditions upstream and downstream of the shock, respectively.

The drop in stagnation pressure across a normal shock at Mach 3.45 will then be $\frac{p_{02}}{p_{01}} = 0.22$. For

example, if the Mach 3.45 flow goes through an oblique shock with an angle of 30 degrees and then a normal shock corresponding to the conditions downstream of the oblique shock, the drop in stagnation pressure will be $\frac{p_{03}}{p_{01}} = 0.41$, where the subscript 3 refers to the conditions downstream of the

oblique/normal shock flow. Therefore, for this example, p_{03} will be 1.84 times greater than p_{02} . This argument can be carried further for more oblique shocks and a terminating normal shock. The drop in stagnation pressure will always be less for the compression through the series of oblique shocks and terminating normal shock when compared to the stagnation pressure drop across one normal shock. The entropy losses will be greater for the latter case and, therefore, will lead to a larger pressure drop according to Equation (5.9). For the Edney Type IV interaction, the flow through the supersonic embedded jet compresses through a series of oblique shocks and isentropic expansions (see Figure 2.4) and then through a terminal normal shock as it approaches the body surface. The stagnation pressure behind this supersonic embedded jet will be greater than the stagnation pressure behind the original bow shock. Thus, the Edney Type IV shock impingement leads to a peak pressure higher than the stagnation pressure on the body when the body is without the shock impingement.

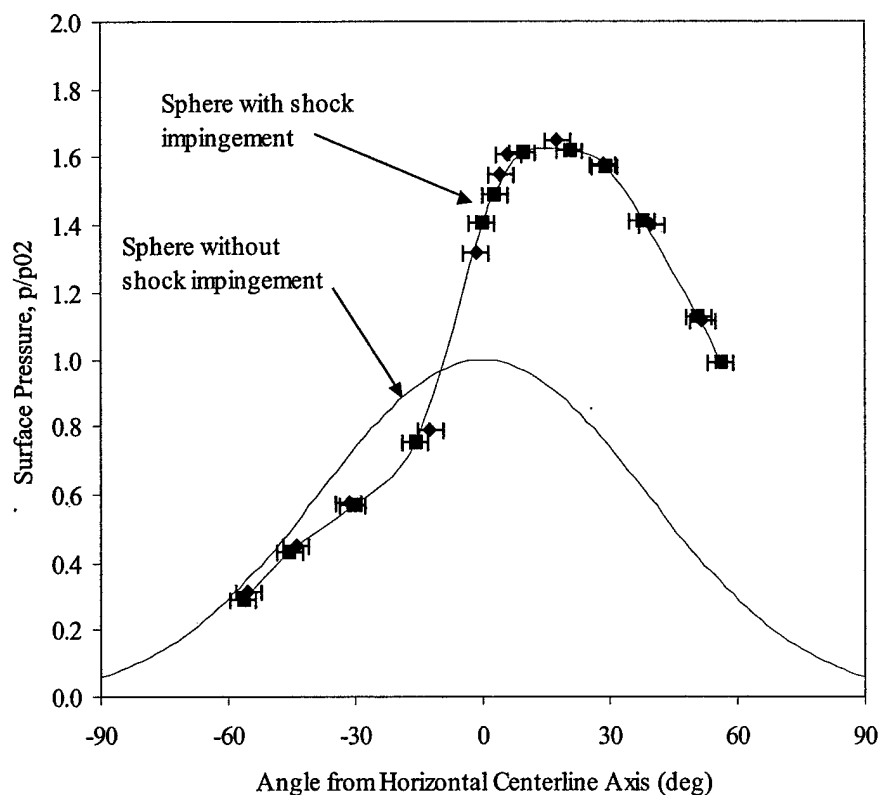


Figure 5.57 Measured surface pressure for Mach 3.45 sphere with Edney Type IV shock impingement

5.3.2 Flow Visualization

Various energy deposition locations were tested for the Mach 3.45 sphere with shock impingement (see Figure 5.2). In this section, time sequenced schlieren images are presented to qualitatively assess the effect of the laser energy perturbation on the sphere with an Edney Type IV shock/shock interaction. Quantitative surface pressure and heat transfer data are presented in the next section and correlated with the flow visualizations presented here.

The main flow features are diagrammed in Figure 5.58 for the laser energy deposition upstream of the Mach 3.45 sphere with the Edney Type IV interaction. All of the deposition locations were upstream of the bow shock and upstream of the oblique impinging shock. The laser deposition locations are noted in Figure 5.2, and the laser pulse width is 10 ns. The energy deposition is essentially instantaneous (see Figure 5.58 a)). As the thermal spot encounters the oblique shock, it will shear and cause the oblique shock

to distort three-dimensionally upstream (see Figure 5.58 b)). The shock perturbation will transmit to the Edney IV impingement location and perturb the shock structure locally at this point (see Figure 5.58 c)). This will cause a downward fluctuation in the embedded supersonic jet. As the thermal spot interacts with the oblique shock it will become elongated and stretched in the streamwise direction. It will also deflect downwards due to the downward velocity component behind the oblique shock. Next the thermal spot will interact with the shock structure creating a complex three-dimensional flow upstream of the sphere (see Figure 5.58 c)). The shocks on either side of the impinging shock will lens upstream due to the thermal interface and shock wave interaction. Obviously, the lensing will be different on the two sides of the oblique shock. The shock will move further upstream on the high side of the oblique shock. Complex shock interactions will form at the shock intersections (see Figure 5.58 d)). Finally, the spot will impact the sphere where some heat will be transferred to the sphere, convect around, and the shock will collapse back to the steady state Edney Type IV structure. In the locations tested, the spot was low enough that it interacted with the sphere. In other words, the spot was never located high enough where it would not impact the sphere and flow across the top. Attempts were made to locate the deposition location high enough so it would perturb the impinging shock but not impact the sphere. Burn damage was done to the test section windows and no attempt was made to continue these tests.

Figure 5.59 through Figure 5.63 are instantaneous schlieren images of the Mach 3.45 sphere with the Edney Type IV shock/shock interaction with laser energy deposition 1.0 diameter upstream and 0.45 diameters above the centerline. The images were taken with the laser/argon schlieren system described in Section 3.2.1. The time of each image is given below the image and represents the time of the image relative to the laser energy deposition at $t = 0$. As for the isolated sphere case presented in Section 5.2.2, the blast wave and thermal spot interaction can be seen in the images as the energy deposition interacts with the flow about the sphere.

There are two oblique shocks in the images. However, the upper one is due to a tunnel side wall effect with the compression ramp. This upper shock is not present in the center of the test section where the sphere model is located. Filtered Rayleigh scattering images (see Figure 5.64) were taken in the vertical center plane to verify that this upper shock was in fact a shock in the foreground and background and not a second impinging shock on the sphere. It also appears that the impinging oblique shock extends all the way

to the surface. This apparent shock extending to the surface is a three-dimensional effect of the schlieren, and it is the oblique shock in the background and foreground of the test section, and not a shock extending down to the surface of the model.

The supersonic embedded jet set up by the Edney Type IV shock/shock interaction (see Section 2.4.1) can clearly be seen in the image marked 0 μs in Figure 5.59. The light and dark regions within the supersonic jet can be seen in the schlieren image and correspond to the compression due to the transmitted and reflected oblique shocks and the expansion regions between the shear layers of the embedded jet. These compressions, expansions, and curvature of the embedded jet are typical of the Type IV interaction (see Figure 2.4). This supersonic embedded jet is what leads to the severe pressure and heat transfer loads to the body.

At 10 and 20 μs the blast wave can be seen propagating outward from the laser energy deposition location. However, in contrast to the laser energy deposition upstream of the sphere, the blast wave becomes distorted as it encounters the oblique shock wave created by the compression ramp mounted to the top of the test section. At 30 μs a distortion to the Edney Type IV shock structure begins. From 50 to 80 μs (see Figure 5.60 and Figure 5.61) the lensing of the bow shock occurs. However, in this case the lensing effect is distorted because of the difference in incident Mach numbers due to the impinging oblique shock. At 90 μs the shock structure begins to collapse back. A key observation is the apparent formation of a Type III interaction that can be seen at 120 and 130 μs (see Figure 5.62). The flow resumes steady state conditions by 160 μs and the reformation of the Type IV shock/shock structure.

Averaged schlieren images for this energy deposition location are presented in Section 5.3.3 with a correlation with the measured surface pressure.

Figure 5.65 through Figure 5.68 are instantaneous schlieren images for laser energy deposition upstream of the sphere with shock impingement now with the laser energy deposition located 0.6 diameters upstream and 0.2 diameters above the centerline. The images are a time sequence in 10 μs steps from 0 to 130 μs . For this closer energy deposition position, the sequence of interaction events occurs quicker as one would expect. The spacing between the blast wave effects and thermal spot interaction become less, and their attributable effects become less distinct.

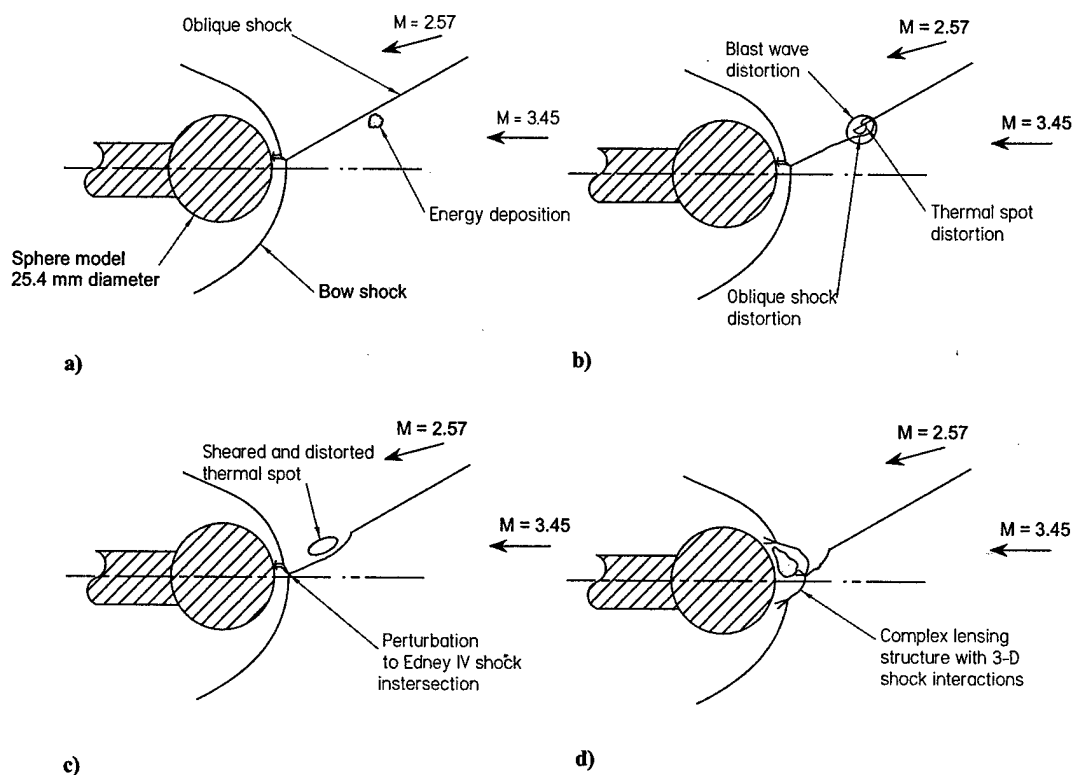


Figure 5.58 Flow features associated with laser energy deposition upstream of Mach 3.45 sphere with shock impingement, **a)** initial deposition, **b)** shearing of thermal spot, oblique shock distortion, and blast wave distortion, **c)** perturbation to Edney IV shock/shock interaction, and **d)** complex bow shock lensing, thermal spot interaction with sphere, and three-dimensional shock interactions

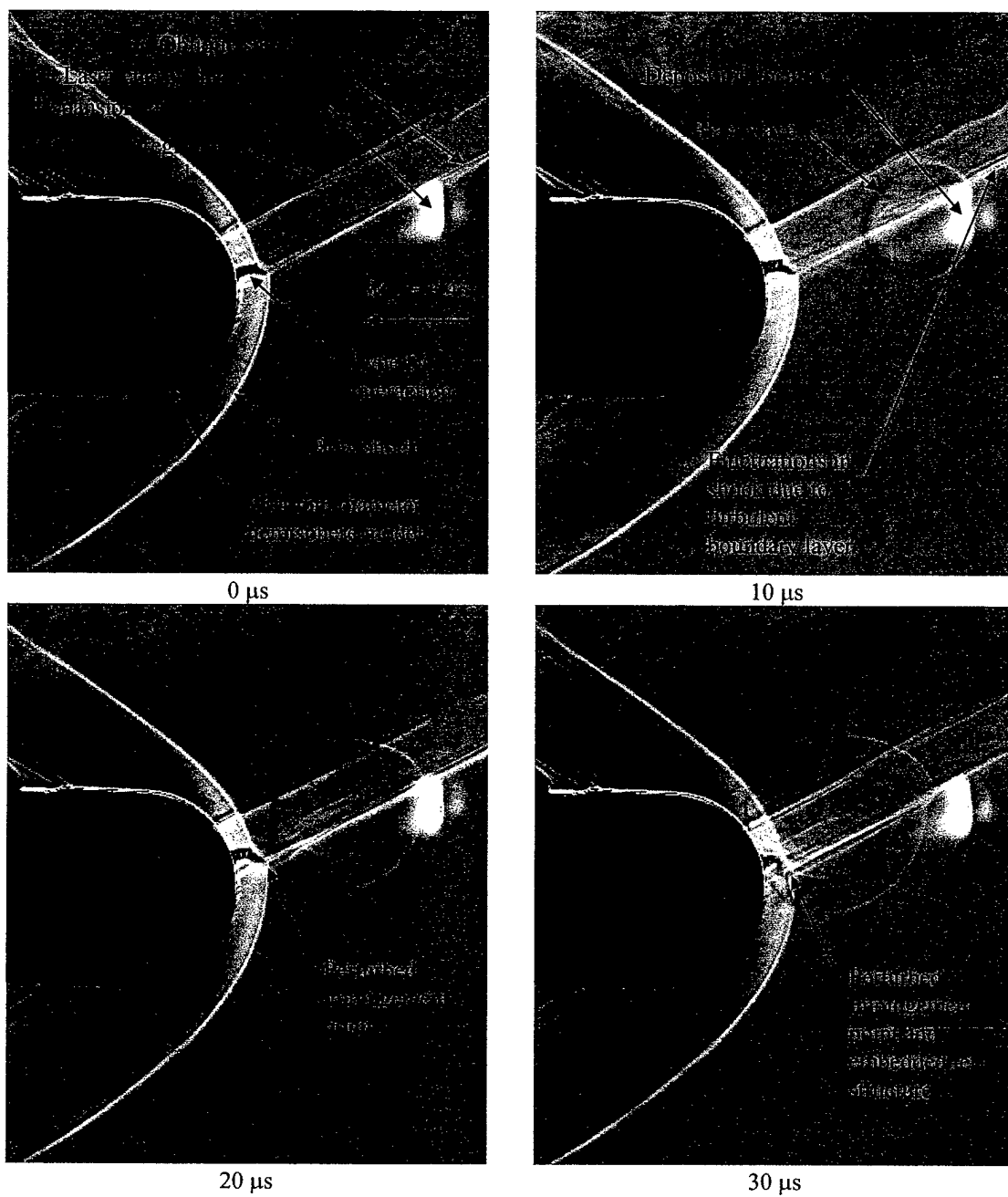


Figure 5.59 Instantaneous argon/laser generated schlieren images of Mach 3.45 sphere with Edney Type IV shock impingement and with laser energy deposition 1.0 diameter upstream and 0.45 diameters above the centerline axis, 0, 10, 20, and 30 μs after laser energy deposition, 283 mJ/pulse, 150 mm focal length lens

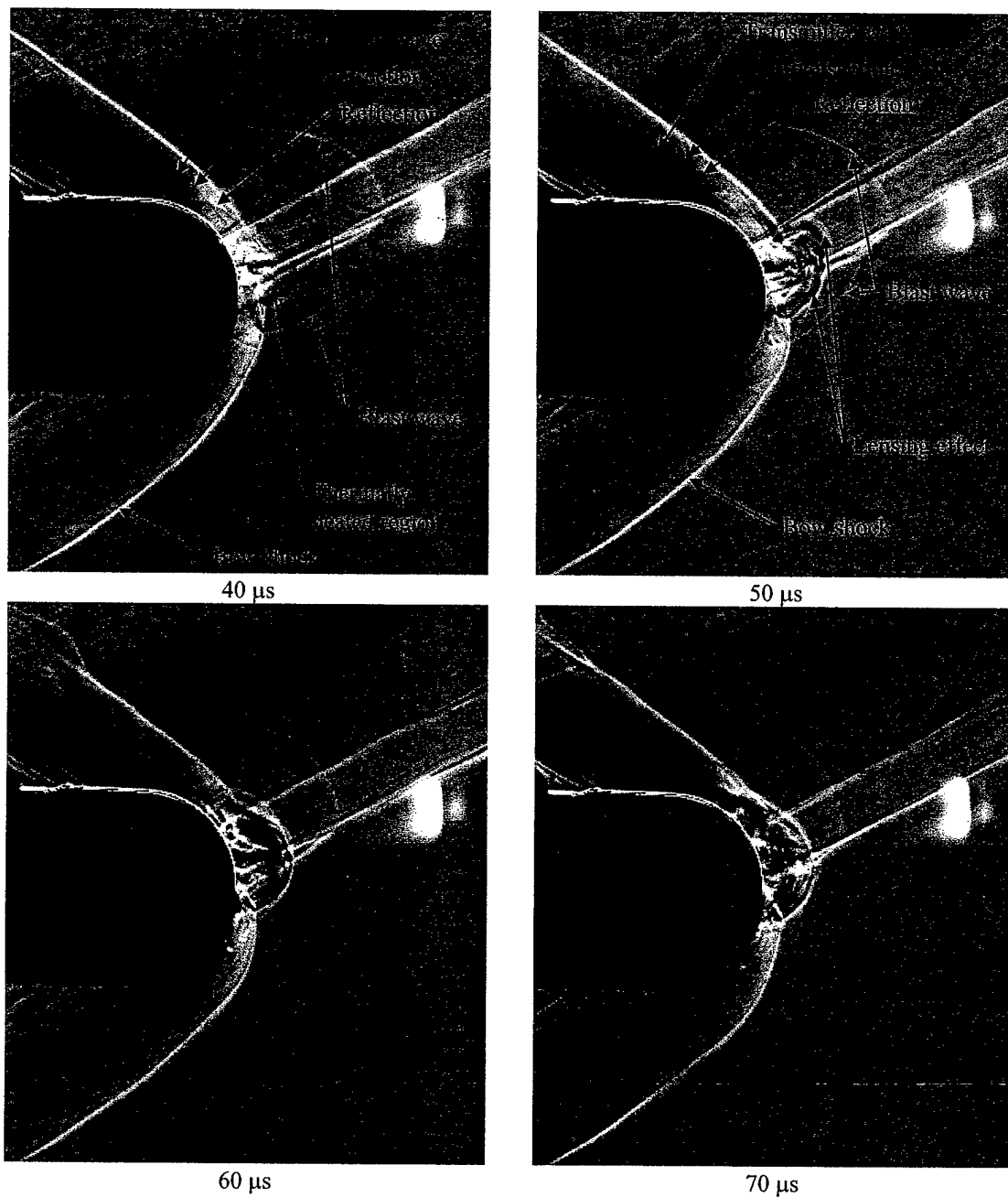


Figure 5.60 Instantaneous argon/laser generated schlieren images of Mach 3.45 sphere with Edney Type IV shock impingement and with laser energy deposition 1.0 diameter upstream and 0.45 diameters above the centerline axis, 40, 50, 60, and 70 μs after laser energy deposition, 283 mJ/pulse, 150 mm focal length lens

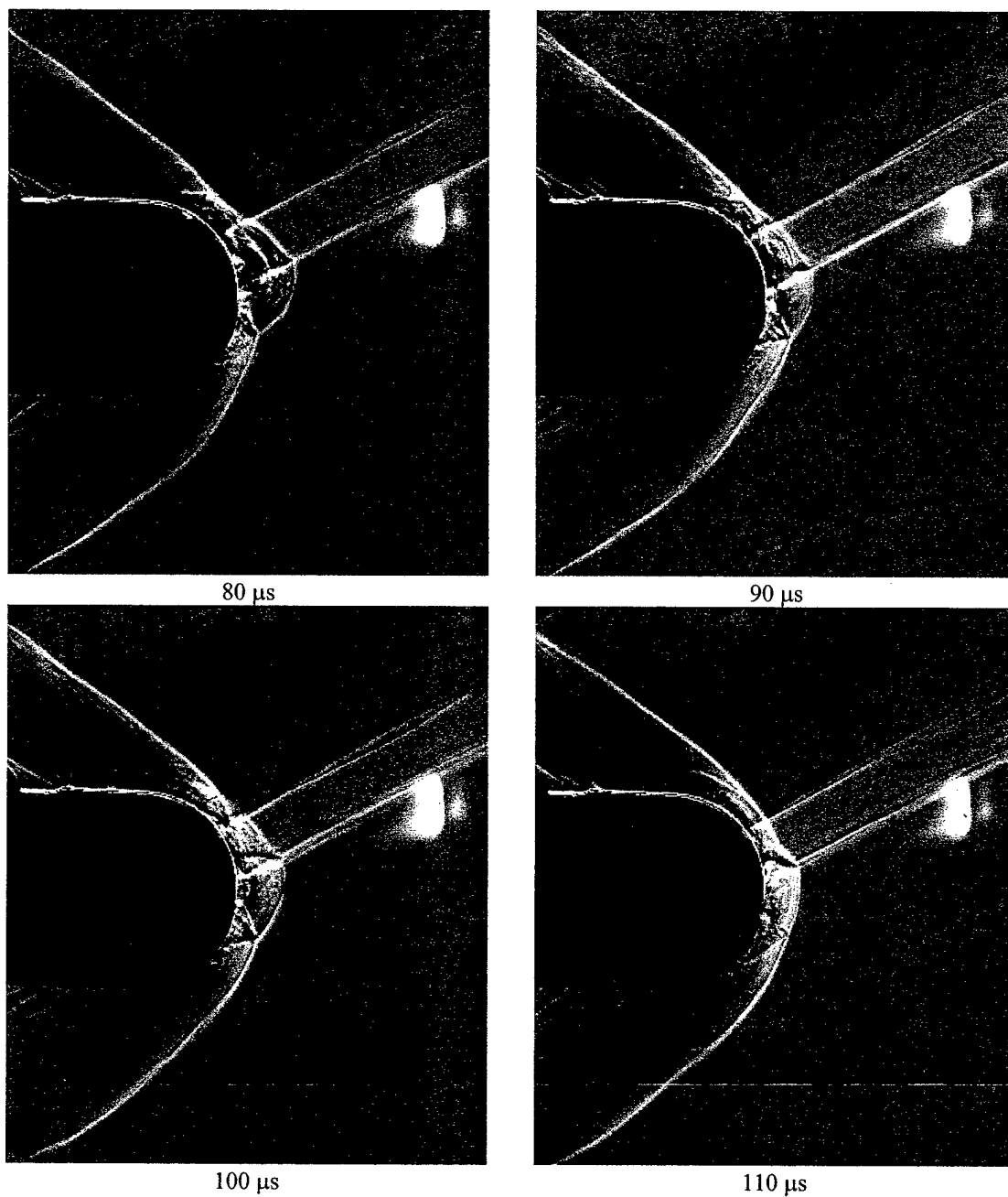


Figure 5.61 Instantaneous argon/laser generated schlieren images of Mach 3.45 sphere with Edney Type IV shock impingement and with laser energy deposition 1.0 diameter upstream and 0.45 diameters above the centerline axis, 80, 90, 100, and 110 μs after laser energy deposition, 283 mJ/pulse, 150 mm focal length lens

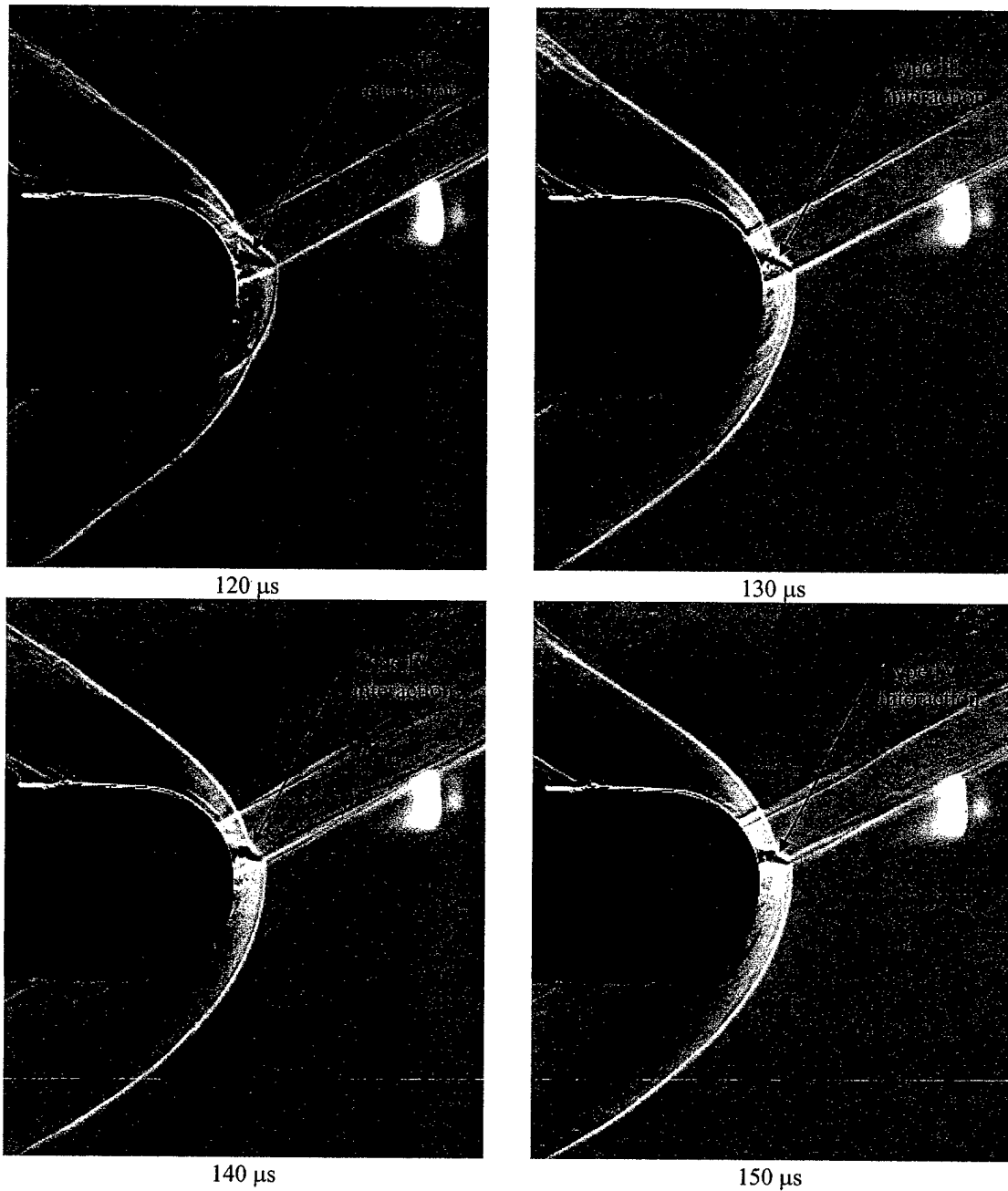


Figure 5.62 Instantaneous argon/laser generated schlieren images of Mach 3.45 sphere with Edney Type IV shock impingement and with laser energy deposition 1.0 diameter upstream and 0.45 diameters above the centerline axis, 120, 130, 140, and 150 μs after laser energy deposition, 283 mJ/pulse, 150 mm focal length lens

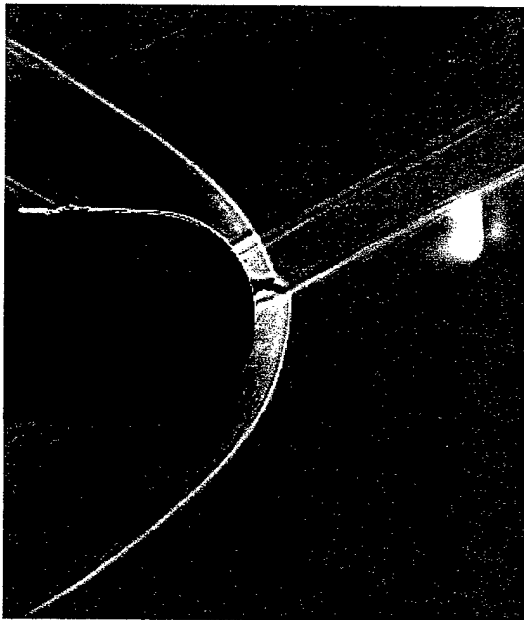
160 μ s

Figure 5.63 Instantaneous argon/laser generated schlieren images of Mach 3.45 sphere with Edney Type IV shock impingement and with laser energy deposition 1.0 diameter upstream and 0.45 diameters above the centerline axis, 160 μ s after laser energy deposition, 283 mJ/pulse, 150 mm focal length lens

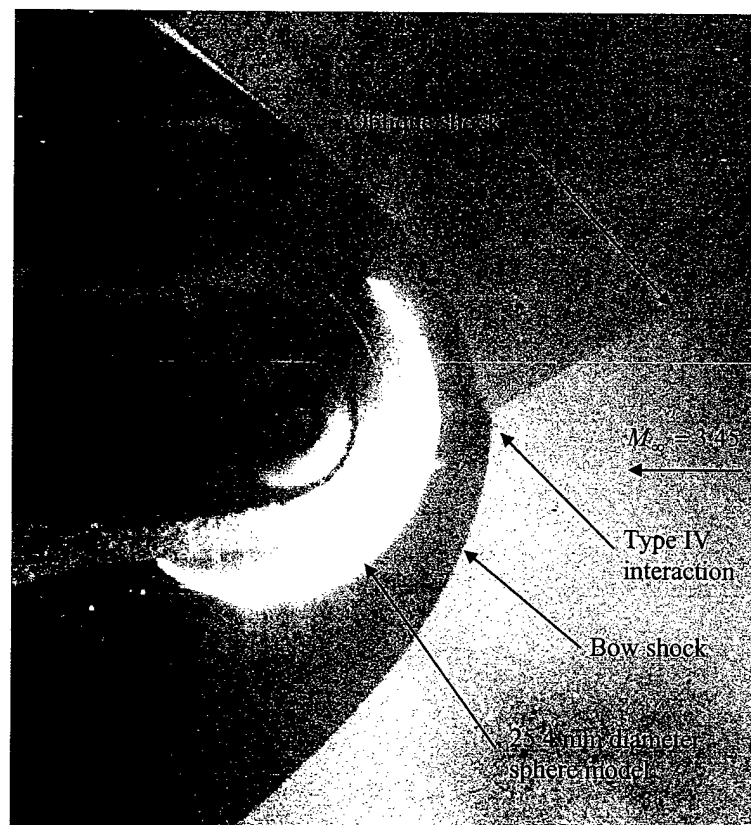


Figure 5.64 Filtered Rayleigh scattering image in vertical symmetry plane to verify one impinging shock

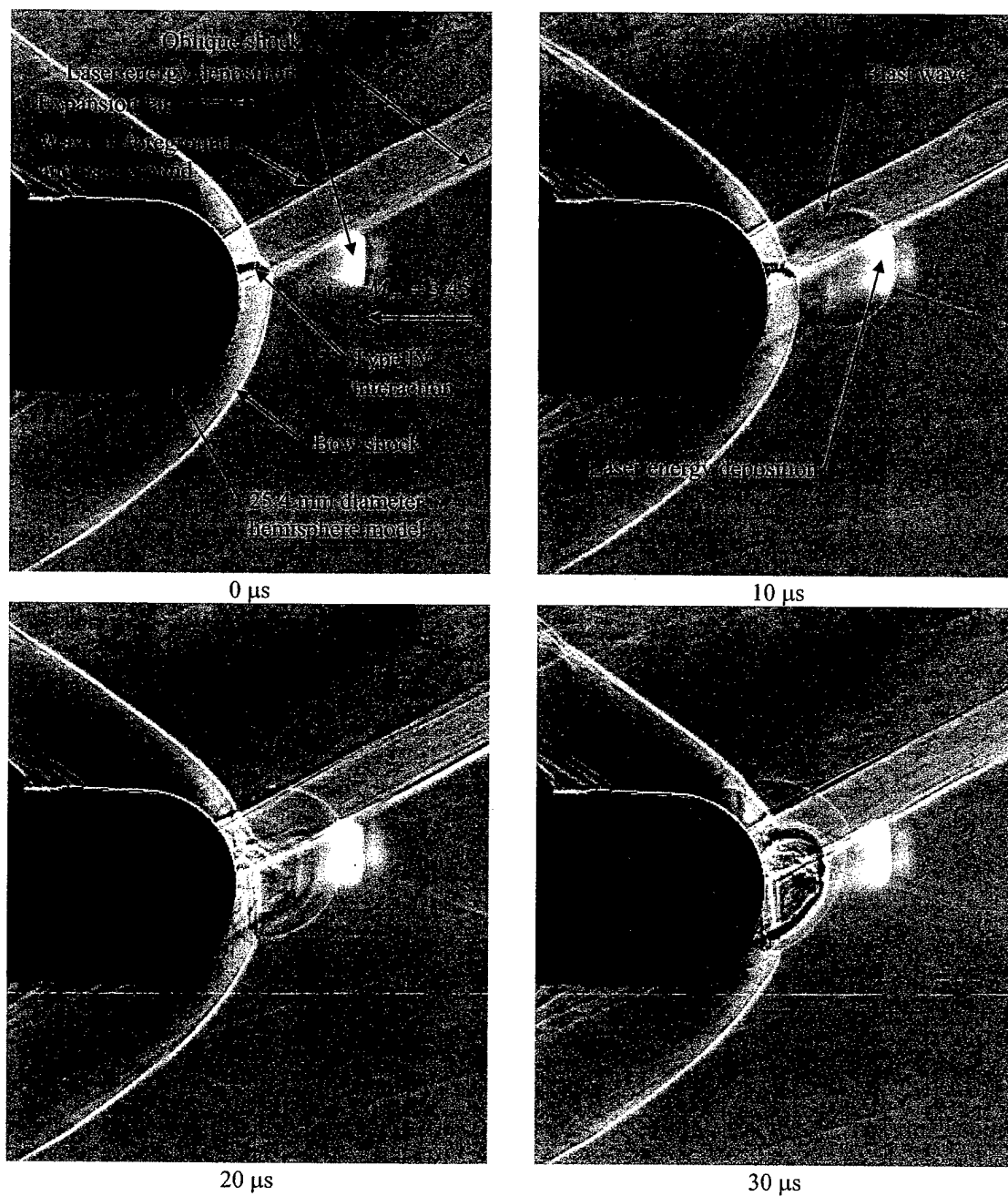


Figure 5.65 Instantaneous argon/laser generated schlieren images of Mach 3.45 sphere with Edney Type IV shock impingement and with laser energy deposition 0.6 diameter upstream and 0.2 diameters above the centerline axis, 0, 10, 20, and 30 μ s after laser energy deposition, 283 mJ/pulse, 150 mm focal length lens

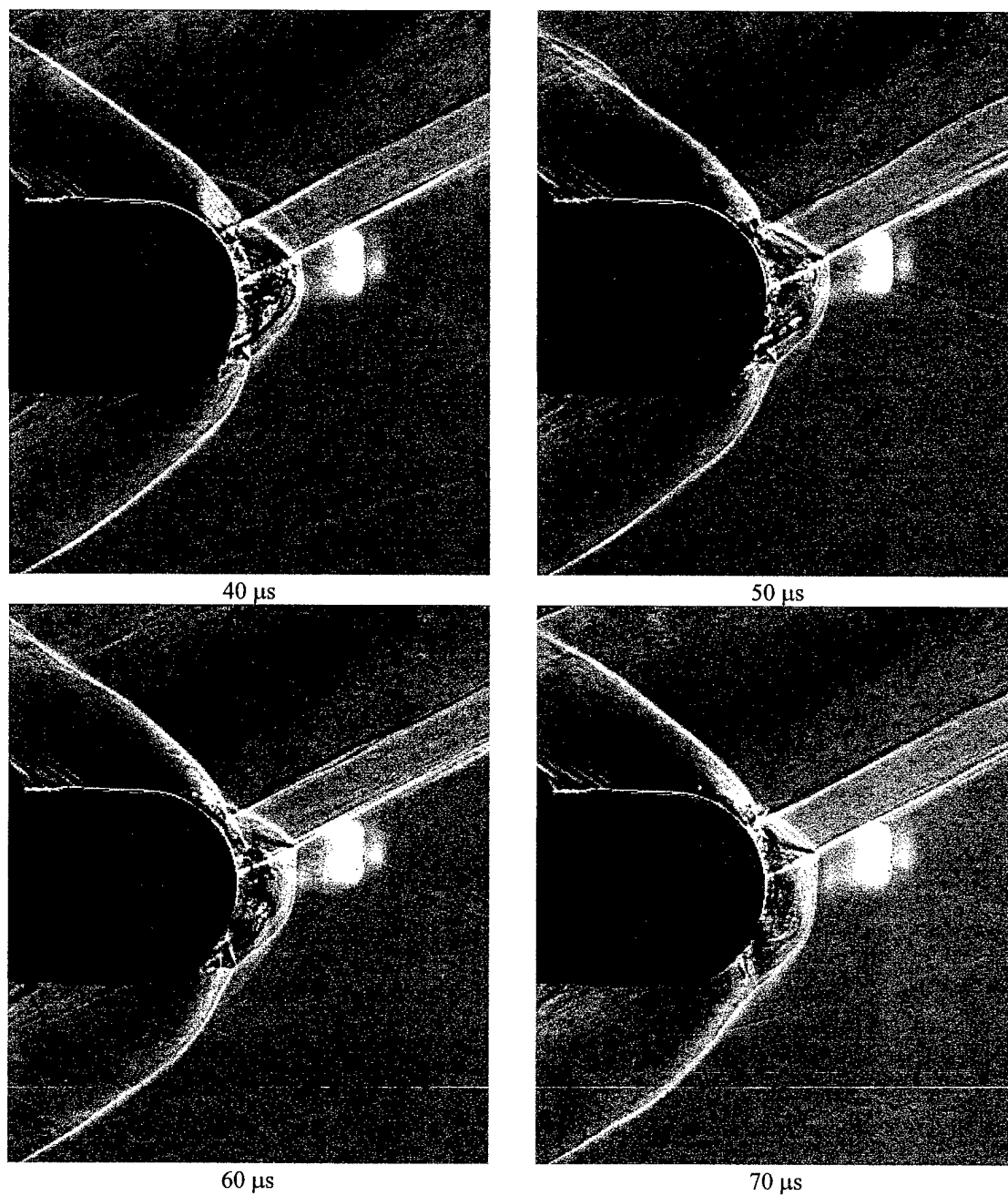


Figure 5.66 Instantaneous argon/laser generated schlieren images of Mach 3.45 sphere with Edney Type IV shock impingement and with laser energy deposition 0.6 diameter upstream and 0.2 diameters above the centerline axis, 40, 50, 60, and 70 μs after laser energy deposition, 283 mJ/pulse, 150 mm focal length lens

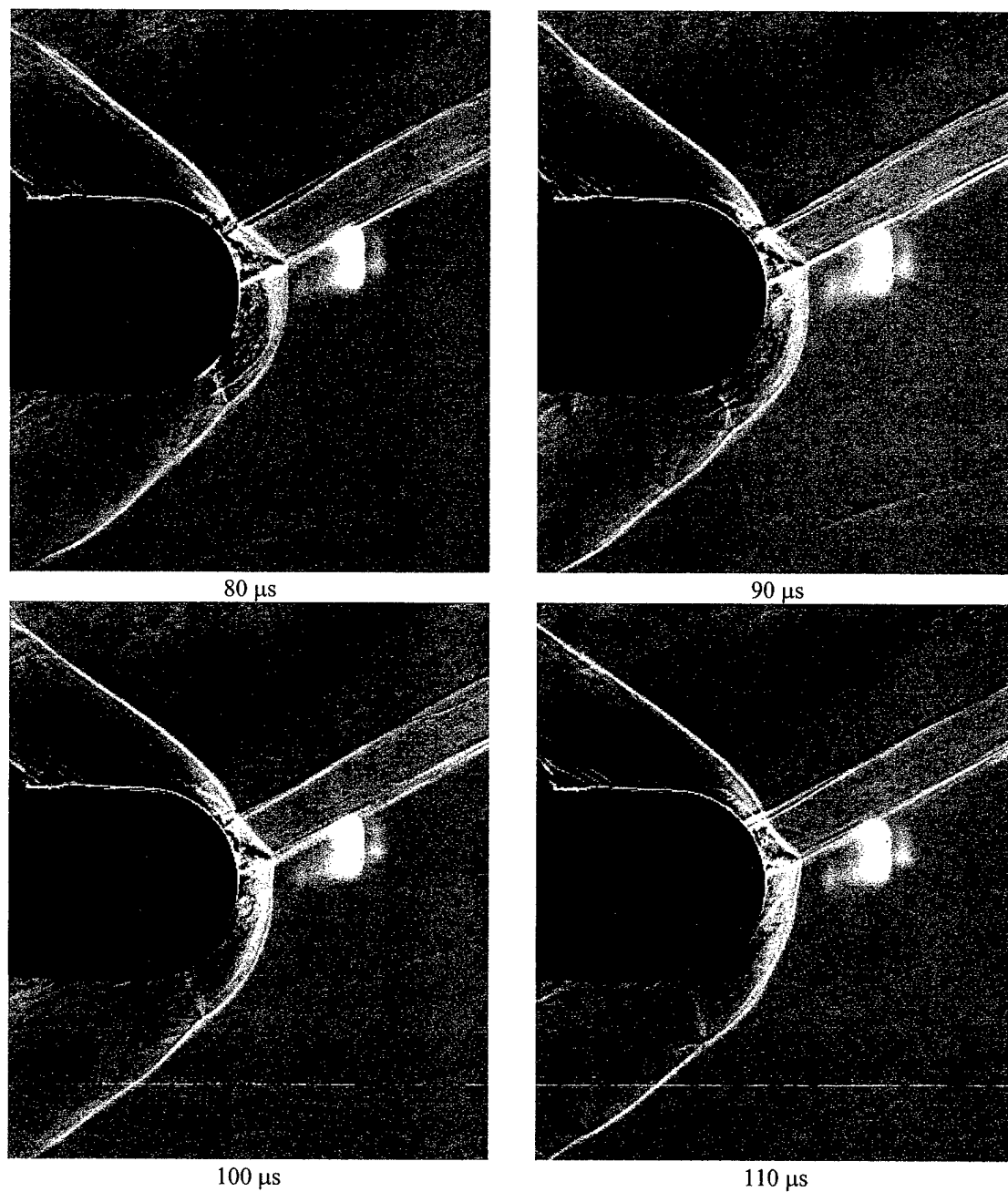


Figure 5.67 Instantaneous argon/laser generated schlieren images of Mach 3.45 sphere with Edney Type IV shock impingement and with laser energy deposition 0.6 diameter upstream and 0.2 diameters above the centerline axis, 80, 90, 100, and 110 μs after laser energy deposition, 283 mJ/pulse, 150 mm focal length lens

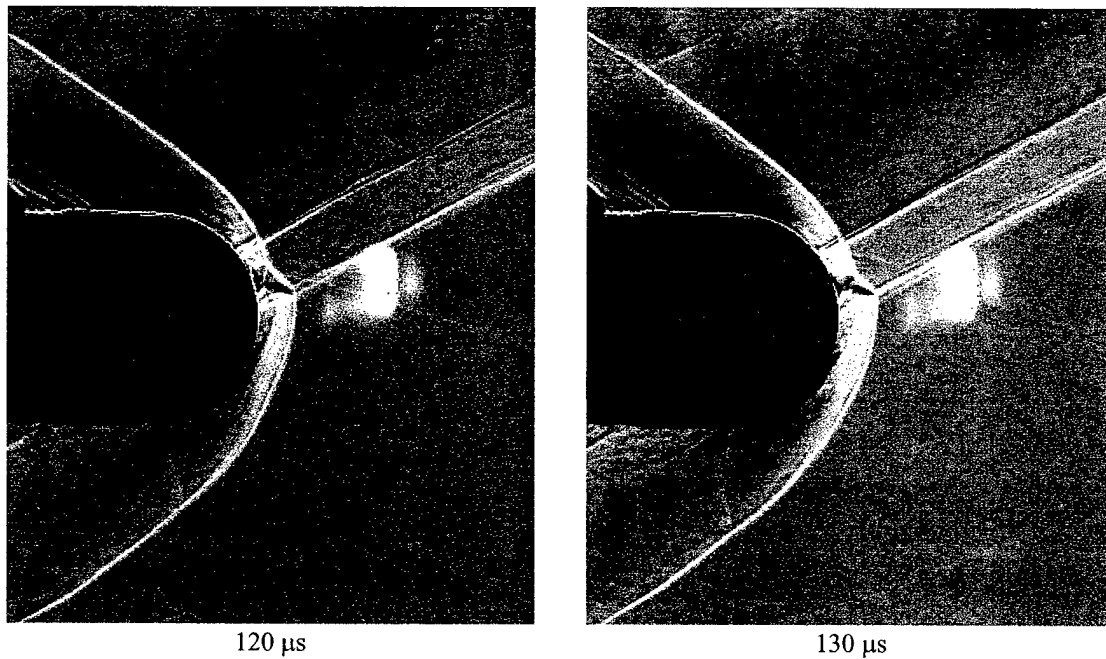


Figure 5.68 Instantaneous argon/laser generated schlieren images of Mach 3.45 sphere with Edney Type IV shock impingement and with laser energy deposition 0.6 diameter upstream and 0.2 diameters above the centerline axis, 120, and 130 μ s after laser energy deposition, 283 mJ/pulse, 150 mm focal length lens

5.3.3 Surface Pressure

A series of unsteady surface pressure measurements were done for laser energy deposition upstream of the sphere model with an Edney Type IV impinging shock. Table 5.3 lists the tunnel operating parameters for the surface pressure measurements. The pressure transducer, sphere model, and the wind tunnel are described in Chapter 3.

Table 5.3 Tunnel operating parameters for shock impingement surface pressure tests

Mach number	3.45
Reynolds number based on sphere diameter, $Re_D = \frac{\rho V D}{\mu}$	1.863×10^6
Freestream viscosity, μ	$5.753 \times 10^{-6} \frac{\text{kg}}{\text{m s}}$
Stagnation pressure, p_0	$1.138 \times 10^6 \text{ Pa}$
Stagnation temperature, T_0	283 K
Stagnation density, ρ_0	$14.012 \frac{\text{kg}}{\text{m}^3}$
Freestream temperature, T	83.7 K
Freestream pressure, p	$1.602 \times 10^4 \text{ Pa}$
Freestream density, ρ	$0.667 \frac{\text{kg}}{\text{m}^3}$
Freestream velocity, V	632.6 m/s
Freestream speed of sound, a	183.4 m/s
Pitot pressure, p_{02}	$2.530 \times 10^5 \text{ Pa}$
Pitot density, ρ_{02}	$3.12 \frac{\text{kg}}{\text{m}^3}$

Figure 5.69 and Figure 5.70 give the pressure port locations relative to the embedded jet impingement area for the surface pressure measurements with the two energy deposition locations.

Figure 5.71 and Figure 5.72 are plots of the surface pressure of the Mach 3.45 sphere with an Edney Type IV shock interaction and with laser energy deposition upstream of the sphere. The plots show the pressure as a function of time and pressure port location with the time $t = 0$ corresponding to the time of the laser deposition. Both plots show a decrease in pressure similar to the thermal spot interaction with the sphere without the shock impingement. The pressure has, likewise, been nondimensionalized with the freestream pitot pressure.

Figure 5.22 through Figure 5.33 show a correlation of the surface pressure for the same conditions as shown in Figure 5.71 and Figure 5.72 with ensemble averaged schlieren images. The schlieren system used for these images was the Strobotac system (see Section 3.2.1) with the schlieren flash phase locked with the laser energy deposition. All of the time sequenced schlieren images for the laser energy deposition upstream of the shock impingement structure show a perturbation to the embedded supersonic jet.

For the energy deposition location of 0.7 diameters upstream and 0.15 diameters above model centerline, there is an increase in the peak surface pressure 20 degrees above the centerline. This increase in the pressure at this location is due to a secondary shock interaction formed by the shock lensing process and subsequent embedded jet forming and impinging on the sphere surface. This shifts the impingement location of the oblique shock, and shifts the location of the embedded shock. Across the bottom portion of the sphere, the pressure decreases and then increases similar to the thermal interaction with the sphere alone.

For the second test case for the surface pressure measurements, the energy deposition location was at 0.7 diameters upstream and 0.28 diameters above the centerline. However, for this case there is no significant increase in the peak pressure. The surface pressure decreases across the face of the sphere, and the peak pressure is reduced by 30% due to the thermal interaction of the laser energy deposition with the shock structure upstream of the sphere.

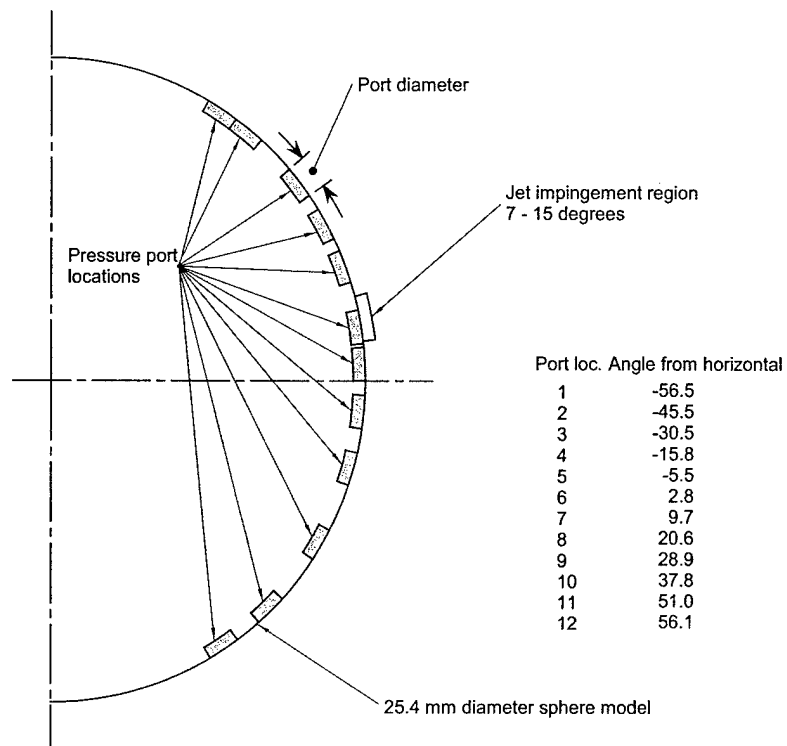


Figure 5.69 Pressure port locations with port diameter indicated and relative jet impingement region for surface pressure measurements for the energy deposition 0.7 diameters upstream and 0.15 diameters above model centerline

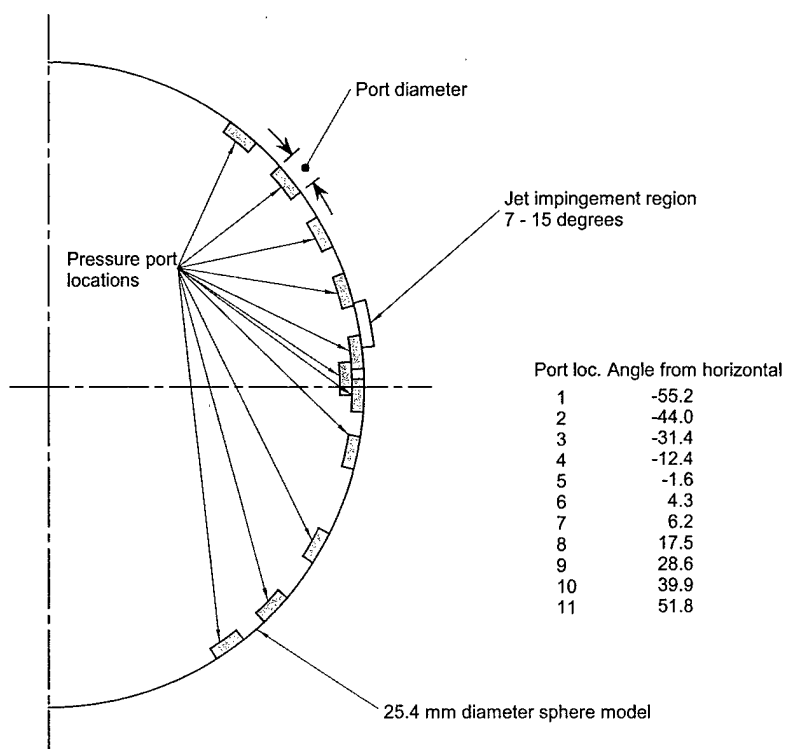


Figure 5.70 Pressure port locations with port diameter indicated and relative jet impingement region for surface pressure measurements for the energy deposition 0.7 diameters upstream and 0.28 diameters above model centerline

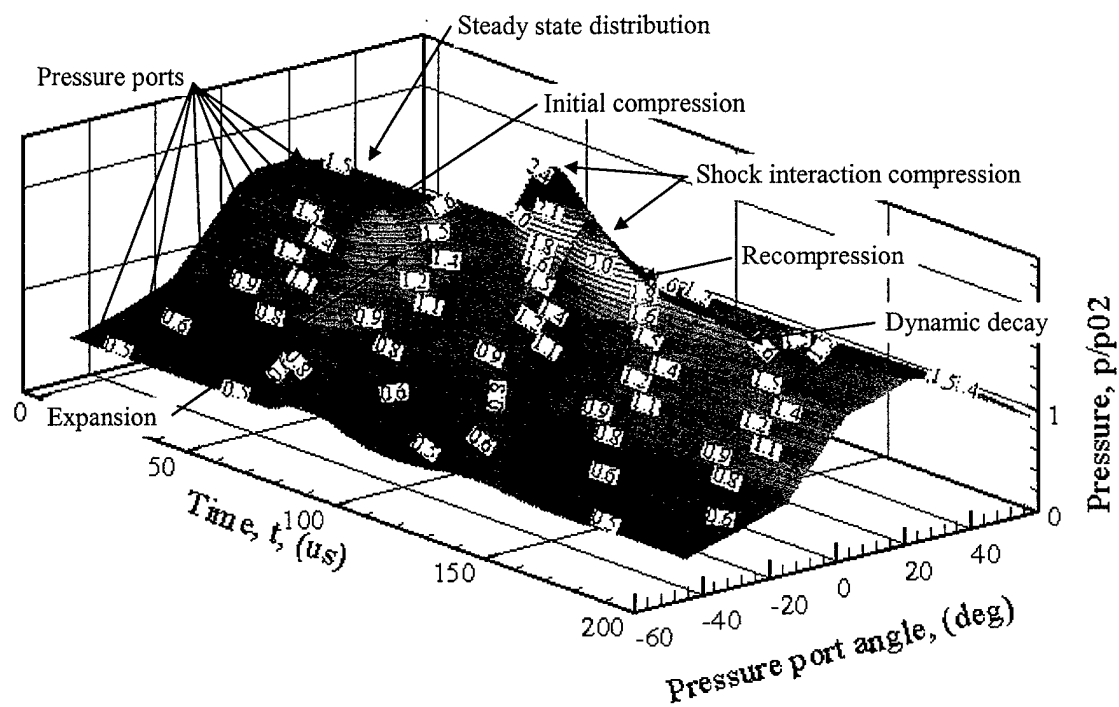


Figure 5.71 Surface pressure traces on the vertical symmetry plane around front of sphere in an Edney IV interaction with energy deposition 0.7 diameters upstream and 0.15 diameters above model centerline

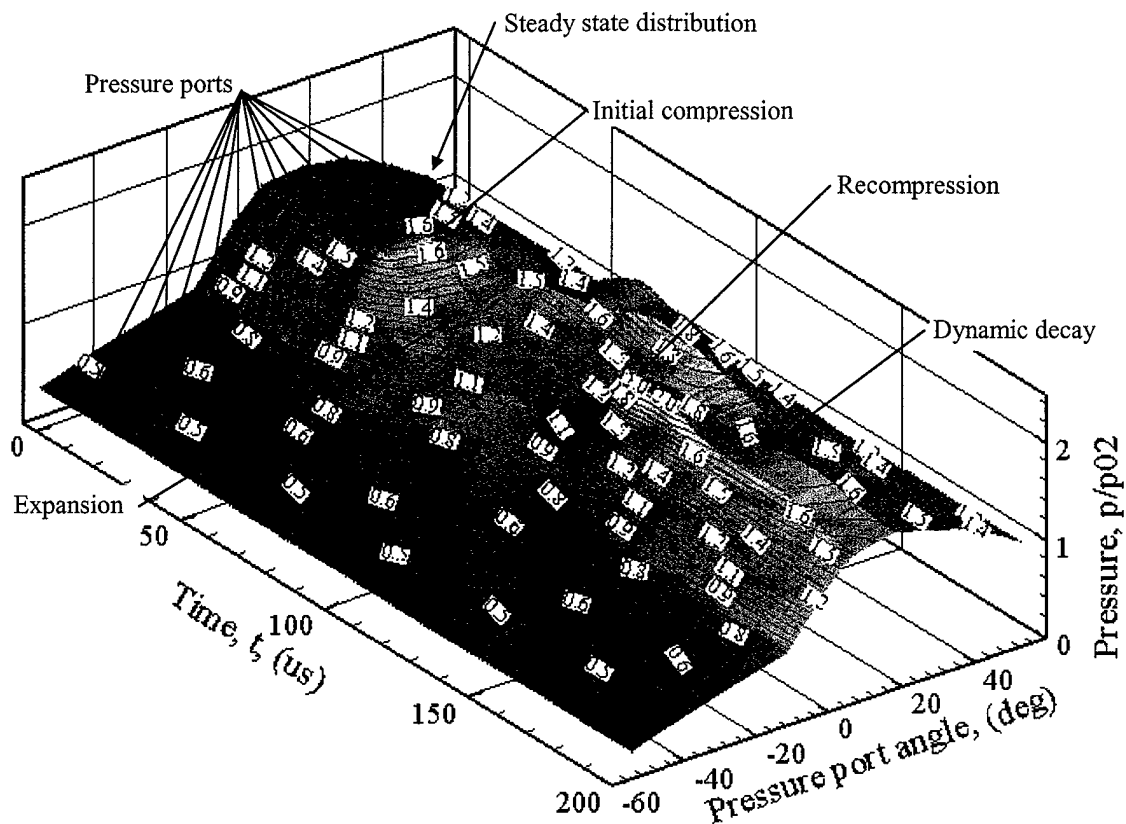


Figure 5.72 Surface pressure traces on the vertical symmetry plane around front of sphere in an Edney IV interaction with energy deposition 0.7 diameters upstream and 0.28 diameters above model centerline

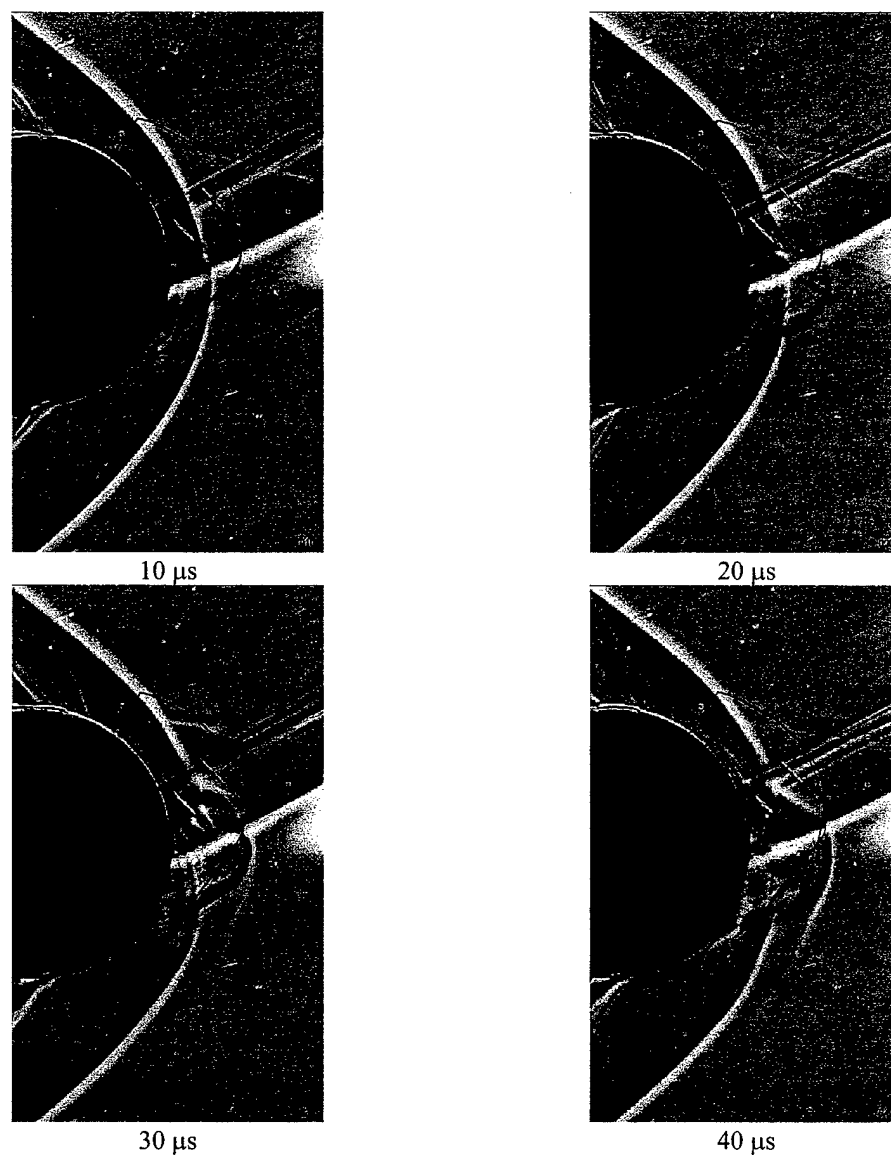


Figure 5.73 Phase averaged xenon Strobotac flash generated schlieren images of Mach 3.45 sphere with an Edney IV interaction with energy deposition 0.7 diameters upstream and 0.15 diameters above model centerline, 10, 20, 30, and 40 μs after laser energy deposition, 258 mJ/pulse, 150 mm focal length lens, and correlated with polar steady state and instantaneous pressure

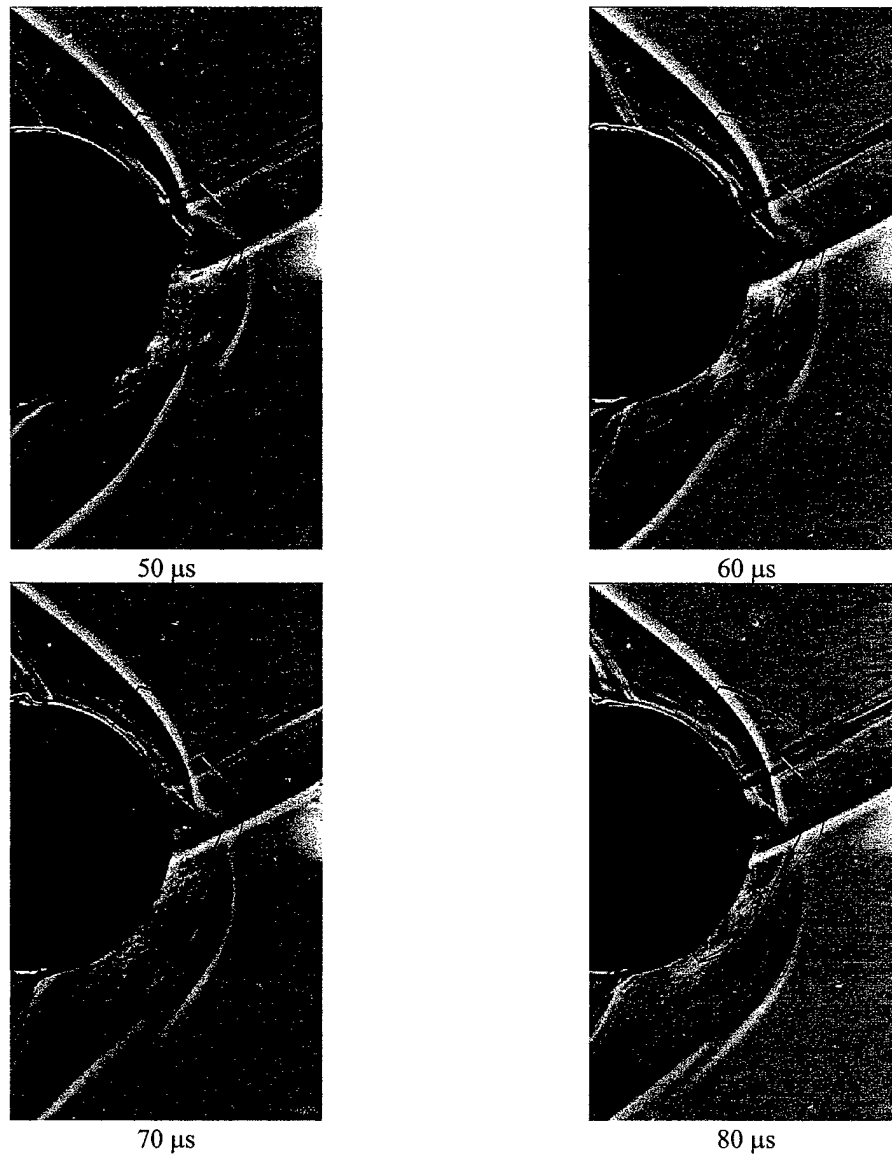


Figure 5.74 Phase averaged xenon Strobotac flash generated schlieren images of Mach 3.45 sphere with an Edney IV interaction with energy deposition 0.7 diameters upstream and 0.15 diameters above model centerline, 50, 60, 70, and 80 μ s after laser energy deposition, 258 mJ/pulse, 150 mm focal length lens, and correlated with polar steady state and instantaneous pressure

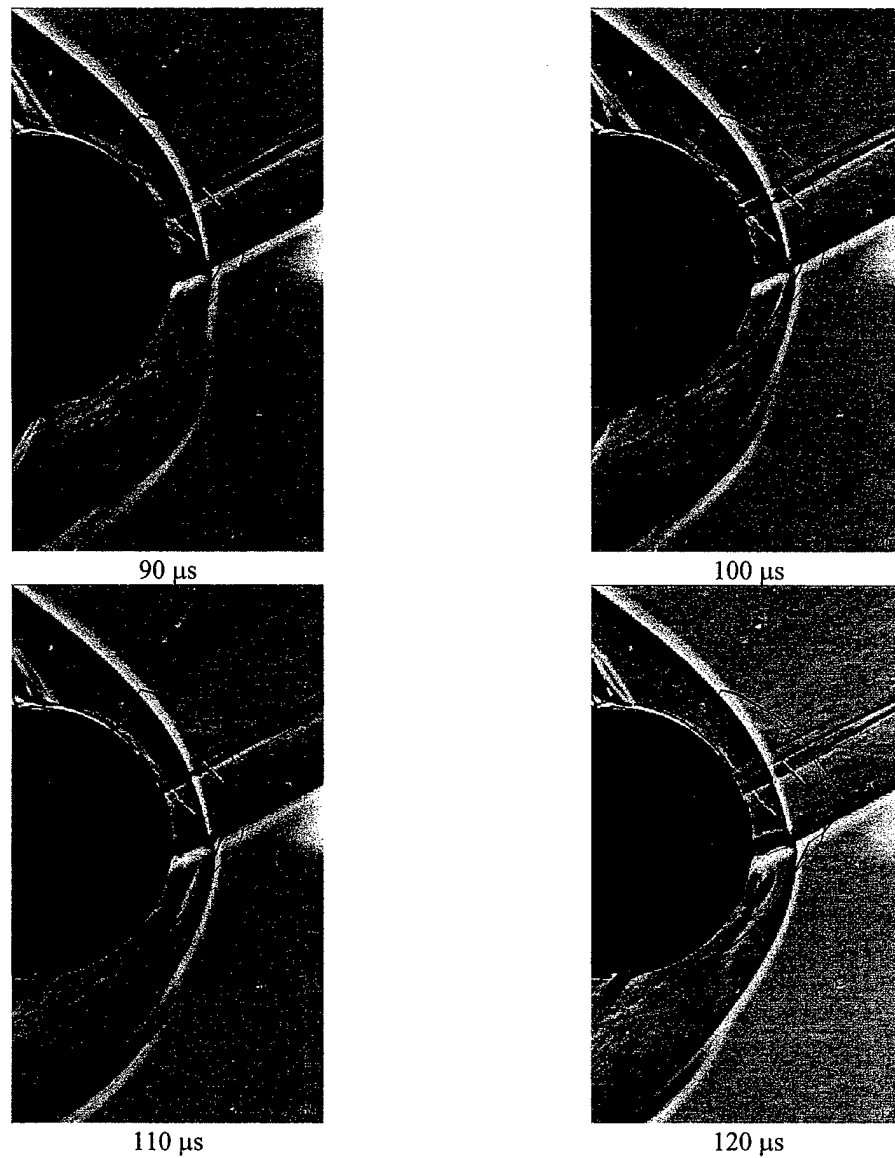


Figure 5.75 Phase averaged xenon Strobotac flash generated schlieren images of Mach 3.45 sphere with an Edney IV interaction with energy deposition 0.7 diameters upstream and 0.15 diameters above model centerline, 90, 100, 110, and 120 μ s after laser energy deposition, 258 mJ/pulse, 150 mm focal length lens, and correlated with polar steady state and instantaneous pressure

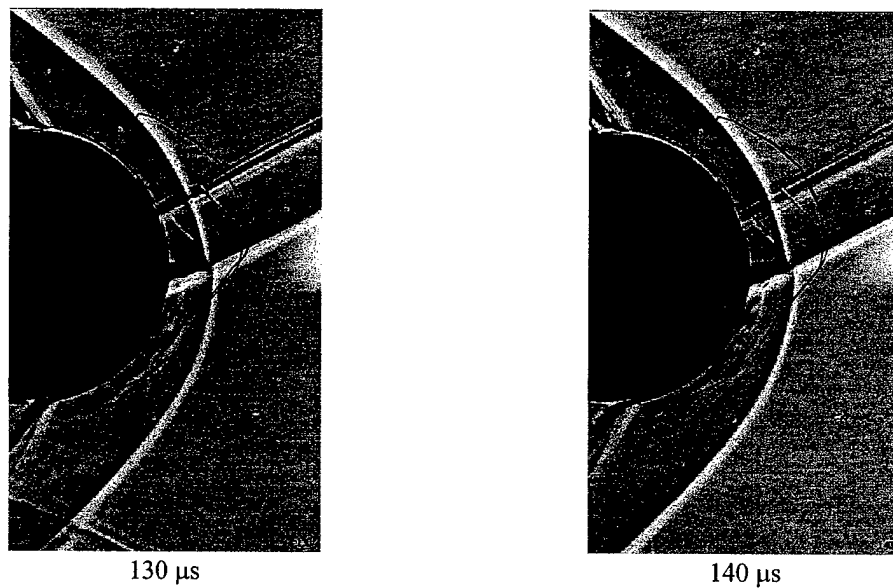


Figure 5.76 Phase averaged xenon Strobotac flash generated schlieren images of Mach 3.45 sphere with an Edney IV interaction with energy deposition 0.7 diameters upstream and 0.15 diameters above model centerline, 130, and 140 μ s after laser energy deposition, 258 mJ/pulse, 150 mm focal length lens, and correlated with polar steady state and instantaneous pressure

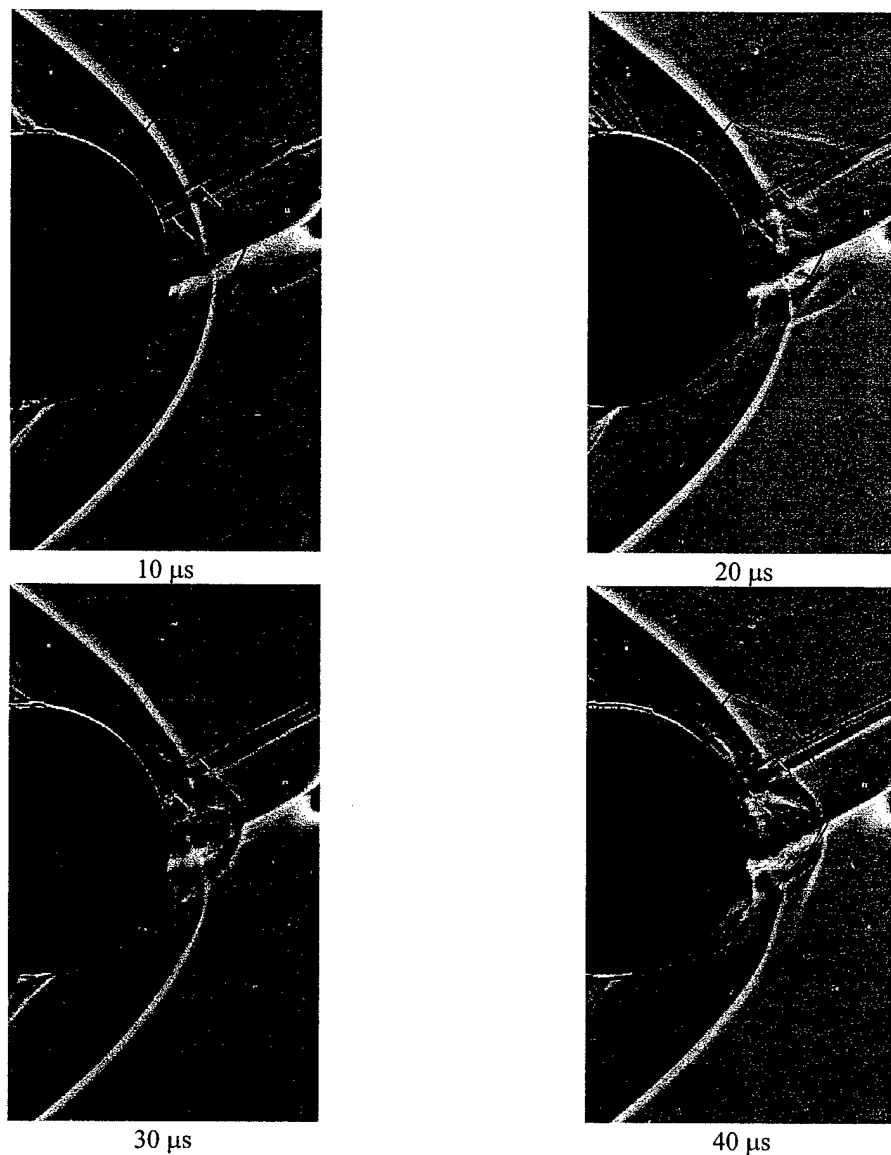


Figure 5.77 Phase averaged xenon Strobotac flash generated schlieren images of Mach 3.45 sphere with an Edney IV interaction with energy deposition 0.7 diameters upstream and 0.28 diameters above model centerline, 10, 20, 30, and 40 μs after laser energy deposition, 258 mJ/pulse, 150 mm focal length lens, and correlated with polar steady state and instantaneous pressure

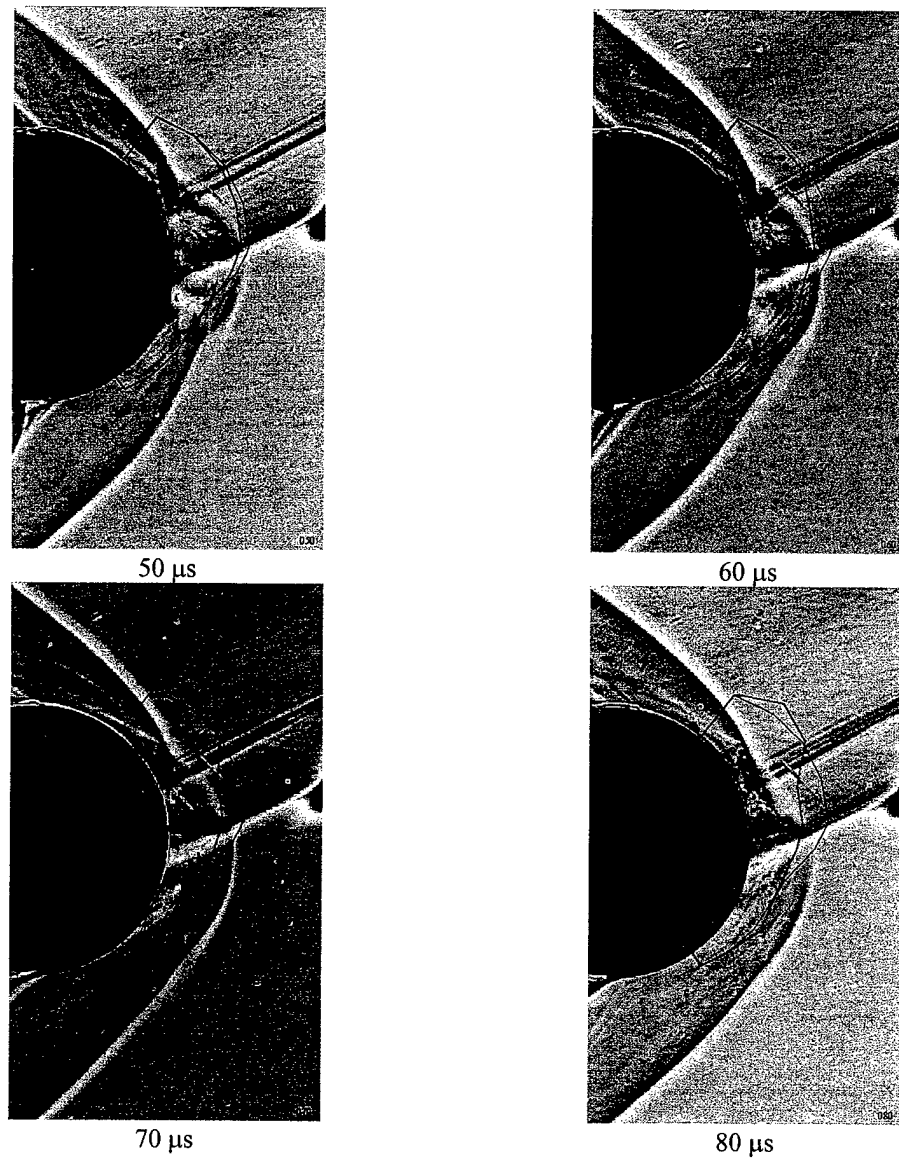


Figure 5.78 Phase averaged xenon Strobotac flash generated schlieren images of Mach 3.45 sphere with an Edney IV interaction with energy deposition 0.7 diameters upstream and 0.28 diameters above model centerline, 50, 60, 70, and 80 μs after laser energy deposition, 258 mJ/pulse, 150 mm focal length lens, and correlated with polar steady state and instantaneous pressure

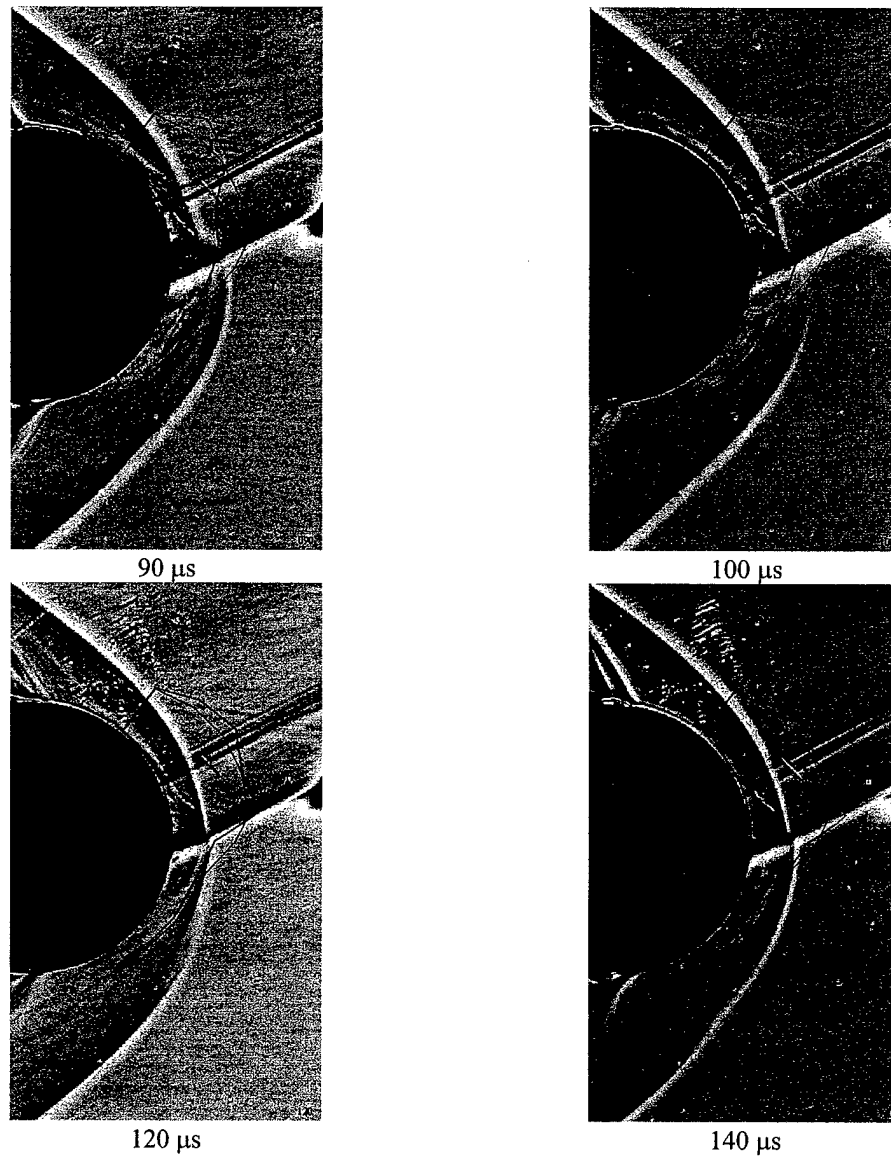


Figure 5.79 Phase averaged xenon Strobotac flash generated schlieren images of Mach 3.45 sphere with an Edney IV interaction with energy deposition 0.7 diameters upstream and 0.28 diameters above model centerline, 90, 100, 120, and 140 μ s after laser energy deposition, 258 mJ/pulse, 150 mm focal length lens, and correlated with polar steady state and instantaneous pressure

5.3.4 Surface Heat Transfer

The surface heat transfer and surface temperature was measured for the hemisphere model with an Edney Type IV shock/shock interaction. Table 5.4 lists the wind tunnel test section conditions for the shock impingement tests. The impinging oblique shock was generated by a 15 degree wedge mounted to the top of the test section (see Figure 3.15). This was the same wedge as used in the surface pressure measurements.

Table 5.4 Tunnel operating parameters for heat transfer measurements on sphere with shock impingement

Mach number	3.45
Reynolds number based on sphere diameter, $Re_D = \frac{\rho V D}{\mu}$	1.905×10^6
Freestream viscosity, μ	$5.666 \times 10^{-6} \frac{\text{kg}}{\text{m s}}$
Stagnation pressure, p_0	$1.138 \times 10^6 \text{ Pa}$
Stagnation temperature, T_0	279 K
Stagnation density, ρ_0	$14.212 \frac{\text{kg}}{\text{m}^3}$
Freestream temperature, T	82.5 K
Freestream pressure, p	$1.602 \times 10^4 \text{ Pa}$
Freestream density, ρ	$0.676 \frac{\text{kg}}{\text{m}^3}$
Freestream velocity, V	628.1 m/s
Freestream speed of sound, a	182.1 m/s
Pitot pressure, p_{02}	$2.530 \times 10^5 \text{ Pa}$
Pitot density, ρ_{02}	$3.160 \frac{\text{kg}}{\text{m}^3}$

Figure 5.80 gives the thin film platinum gauge locations and widths relative to the embedded jet impingement location for the temperature and heat transfer experiments on the Mach 3.45 sphere with shock impingement.

The temperature recorded for the eight gauge sphere model at a sampling rate of 1 kHz is plotted in Figure 5.81, and the wall heat flux is plotted in Figure 5.82 for the case of no laser energy deposition. The increase in heat transfer rate due to the shock impingement can readily be seen when these plots are compared to the sphere without shock impingement shown in Figure 5.34 and Figure 5.35. The

temperature and the heat flux for the stagnation point, gauge 1, are compared for the sphere with and without the Edney Type IV shock/shock interaction in Figure 5.83 and Figure 5.84. The effect of increased heat flux due to the shock impingement can clearly be seen in these plots. As for the sphere without the shock impingement, the sphere is cooling during the wind tunnel run. This cooling is due to the lower stagnation compared to the initial ambient temperature of the sphere surface. The stagnation temperature also drops during the operation of the wind tunnel (see discussion in Section 3.6.3.2) due to the expansion process in the air storage tanks.

The increase in heat flux associated with the Edney Type IV shock interaction can be attributed to the rise in stagnation pressure behind the embedded jet. Refer to the discussion given in Section 5.3.1 describing the increase in pressure associated with the shock/shock interaction. The van Driest equation for the stagnation point heat flux relates the heating to the stagnation pressure (see Equations (3.22), (3.23), and (3.24)). Since the stagnation pressure will increase behind the embedded jet, the heat flux will increase accordingly.

For the laser energy deposition upstream of the hemisphere with shock impingement, surface heat transfer data was collected for a sampling rate of 1 MHz. The same data reduction was applied to the data as for the laser energy deposition for the sphere without shock impingement (see Section 5.2.4).

Figure 5.85 gives the measured wall heat flux on Mach 3.45 sphere with Edney Type IV shock impingement and with laser energy deposition 1.0 diameter upstream and 0.45 diameters above the centerline axis for a single laser pulse at 283 mJ/pulse and a 150 mm focal length lens. Figure 5.86 - Figure 5.93 gives the measured temperature and heat flux for the each of the eight gauges. Error bars presented bound the measurement uncertainty for the data and represent the one standard deviation distribution in the data. These error bars are presented for various times. The laser was fired at a rate of 10 Hz. The gauge locations are shown by the dashed lines in Figure 5.85. Tecplot was used to interpolate the data between the gauges and generate the contour plots.

The radiation heating from the laser spark can be seen by the ridge in the contour plot at 0 μ s. The blast wave heating can be seen by the ridge denoted on the plot. Here the blast wave heating lags for the stagnation region gauges. The lag for this case is the reverse for the laser energy deposition upstream of the sphere discussed in Section 5.2.4. This reversal is due to the spot being located above centerline.

Therefore, the blast wave reaches the upper gauges first and then the lower stagnation gauges. The heating due to the blast wave can be correlated with the schlieren images for 20 to 30 μs in Figure 5.59. The heating of the sphere due to the thermal spot interaction occurs from 80 to 100 μs (see Figure 5.85). Here the heating is across the upper gauges, and this is due to the spot being located above the centerline, 0.45 diameters, for this case. The thermal spot interaction is also observed in the schlieren images for 80 to 100 μs in Figure 5.60 and Figure 5.61. The heating rate returns to a steady state by 160 μs .

After the blast wave heating effect from the laser spark and before the thermal spot reaches the sphere surface, there is a time span when the temperature drops and there is a cooling effect. This drop in temperature is associated with the expansion fan hitting the surface of the sphere from the lensing process described in Section 5.2.3.

Since the compression ramp to generate the oblique shock is in the boundary layer, the oblique shock will fluctuate. These fluctuations also cause a significant amount of the fluctuations in the amount of heating from the thermal spot. These fluctuations can be seen by the increase in the distribution about the mean in Figure 5.86 - Figure 5.93 for the thermal spot heating of the sphere model.

The thermal spot heating of the sphere with the shock impingement lags behind the thermal spot heating for the sphere alone for the energy deposition 1.0 diameter upstream. This 30 μs lag can be attributed to the spot being sheared and slowed down as it interacts with the oblique shock upstream of the model. This also causes the thermal spot to spread and elongate along the oblique shock during this shock interface interaction as it approaches the model.

Figure 5.94 plots the heat flux to the sphere for the Mach 3.45 sphere with Edney Type IV shock impingement and with laser energy deposition 1.0 diameter upstream and 0.45 diameters above the centerline axis for a double laser pulse separated by 5 μs , each laser phase locked at a firing rate of 10 Hz at 263 mJ/pulse and with a 150 mm focal length lens. No schlieren images are shown for the double pulse test case. Very little difference is observed between the double pulse and the single pulse cases.

Figure 5.95 gives the measured wall heat flux on Mach 3.45 sphere with Edney Type IV shock impingement and with laser energy deposition 0.6 diameters upstream and 0.2 diameters above the centerline axis for a single laser pulse, fired at 10 Hz at 283 mJ/pulse and with a 150 mm focal length lens. The radiation, blast wave, and thermal spot heating are denoted on the plot and can be correlated with the

schlieren images in Figure 5.65, - Figure 5.68. Figure 5.96 - Figure 5.103 present the measured temperature and the heat flux for gauges 1-8 for this test case.

Figure 5.104 shows the measured wall heat flux on Mach 3.45 sphere with Edney Type IV shock impingement and with laser energy deposition 0.6 diameters upstream and 0.2 diameters above the centerline axis for a double laser pulse separated by 5 μ s with the lasers phase locked and firing at 10 Hz at 263 mJ/pulse, and with a 150 mm focal length lens. The radiation, blast wave, and thermal spot heating are denoted on the plot. There were no schlieren images taken for this test case.

Figure 5.105 is the time integrated heat flux for each gauge for each of the four test cases described above. This figure gives the total energy flux to the gauge over the period of time of the interaction with the thermal spot generated by the laser perturbation. As for the sphere without the shock impingement, this integration puts the high heat fluxes observed for the interaction process into perspective. If the maximum energy flux from Figure 5.105, 0.03 mJ/mm² is then integrated across the face of the sphere, then the upper bound for the total energy fluxed through the sphere surface is 30 mJ. As an upper estimate, roughly only 11% of the energy from the laser energy deposition is transferred to the sphere. The rest of the energy from the laser deposition will still be contained in the flow, i.e. blast wave, turbulence, enthalpy, etc., and these forms of energy convect downstream in the flow.

In summary, the energy deposition tests upstream of the sphere with shock impingement are inconclusive on whether the heat flux can be beneficially modified. There are two reasons that hindered the heat transfer measurements. First, the ramp in the boundary causes the oblique shock to fluctuate, thereby, causing a fluctuation in the embedded jet. This jet will then sweep across the face of the sphere and average out the peak heating associated with the Type IV interaction. This will also cause fluctuations and an averaging in the measured temperature and consequently the heat transfer rate. Secondly, the heating associated with the thermal spot interaction is an order of magnitude greater than the heating measured for the shock impingement alone (compare the heating levels in Figure 5.82 and Figure 5.85 for instance). Therefore, it is impossible to distinguish the heating fluctuations caused by the oblique shock turbulent boundary layer interactions in addition to the fluctuations that might be present but masked by the high heating associated with the thermal spot interaction. However, the sensitivity of the gauges have been demonstrated by the detection of the spark radiation, blast wave heating, and the expansion cooling effect.

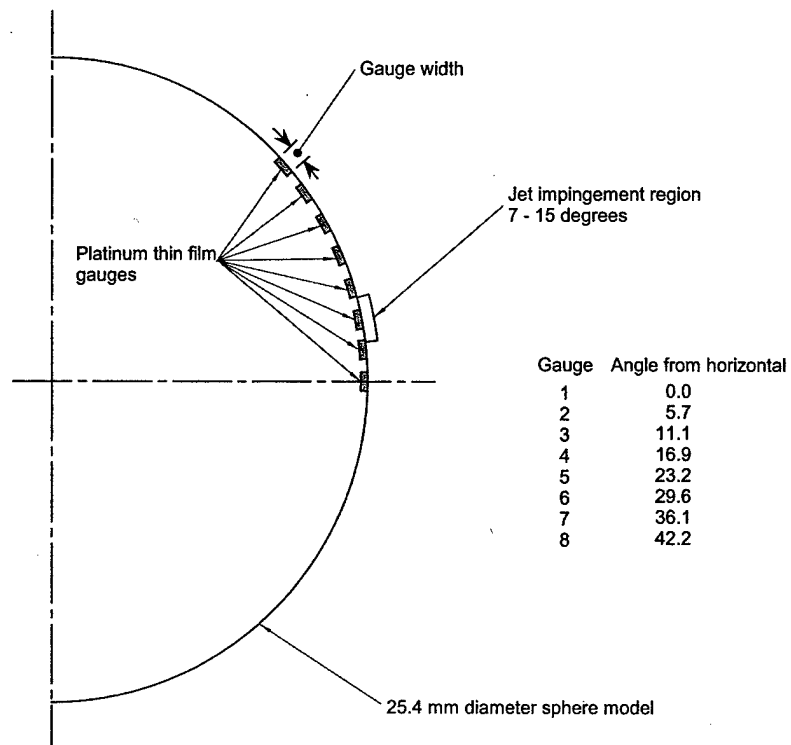


Figure 5.80 Thin film platinum gauge locations with gauge width indicated and relative jet impingement region for surface temperature and heat flux measurements

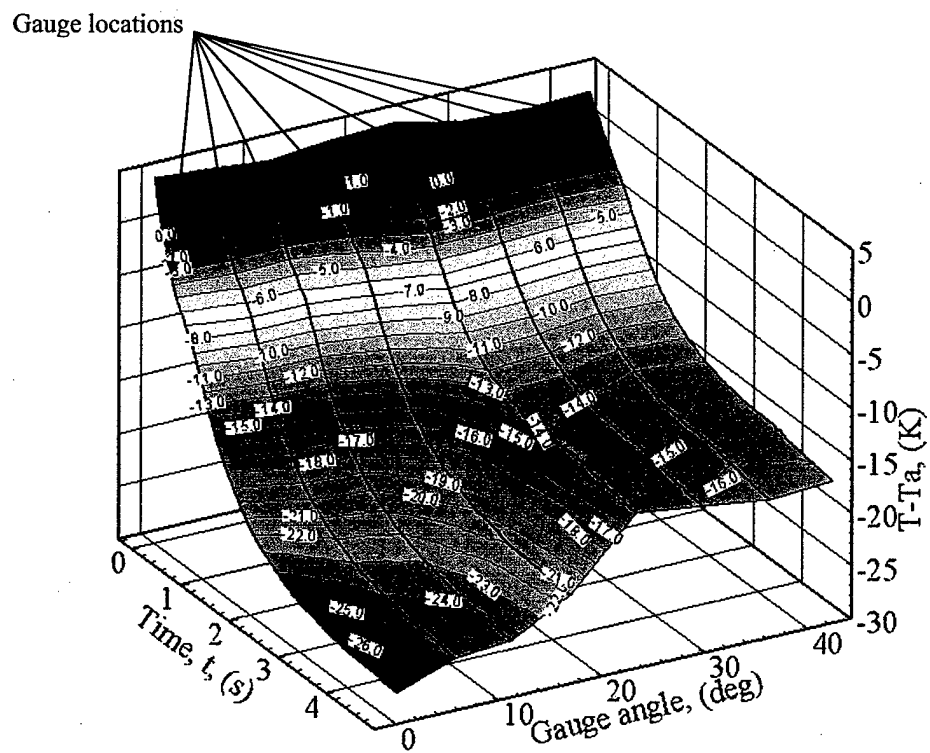


Figure 5.81 Hemisphere wall temperature with impinging shock and no laser spark

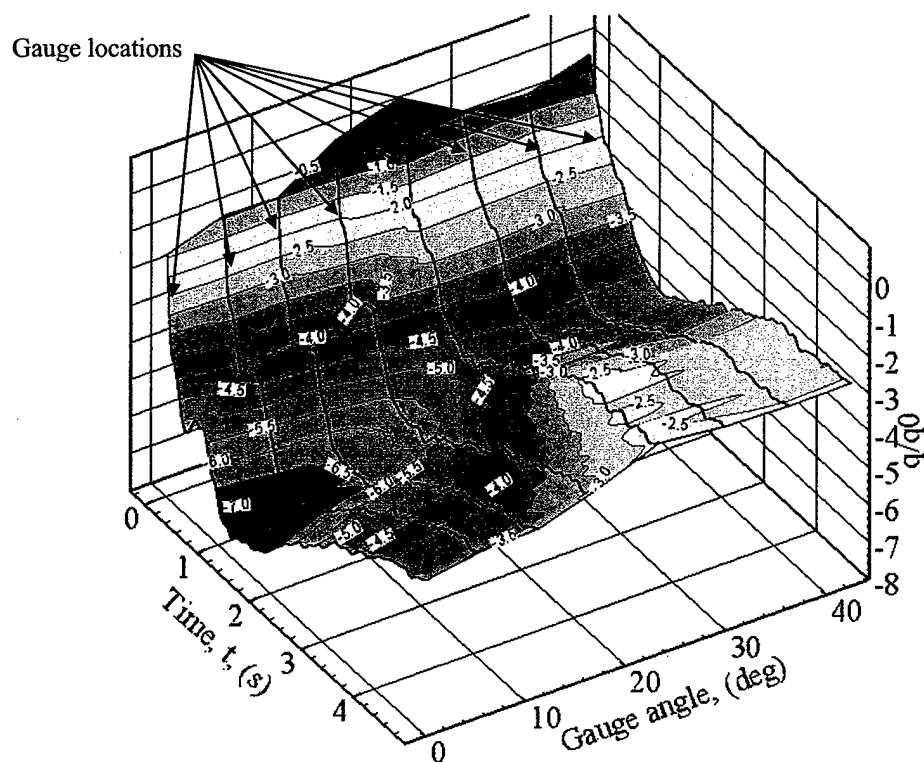


Figure 5.82 Wall heat flux, no laser spark

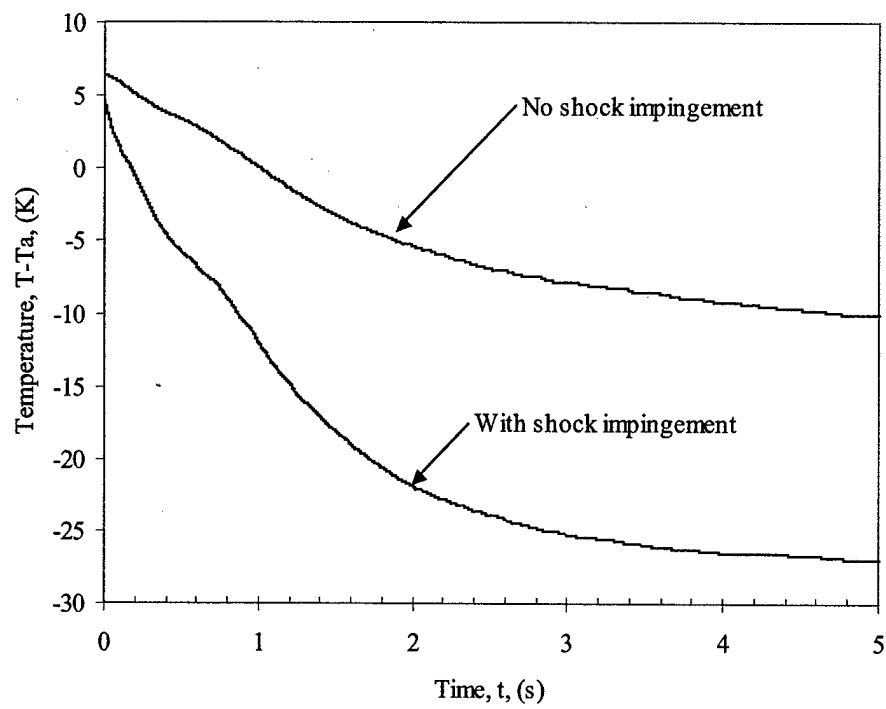


Figure 5.83 Comparison of stagnation point surface temperature for sphere with and without Edney Type IV shock/shock interaction

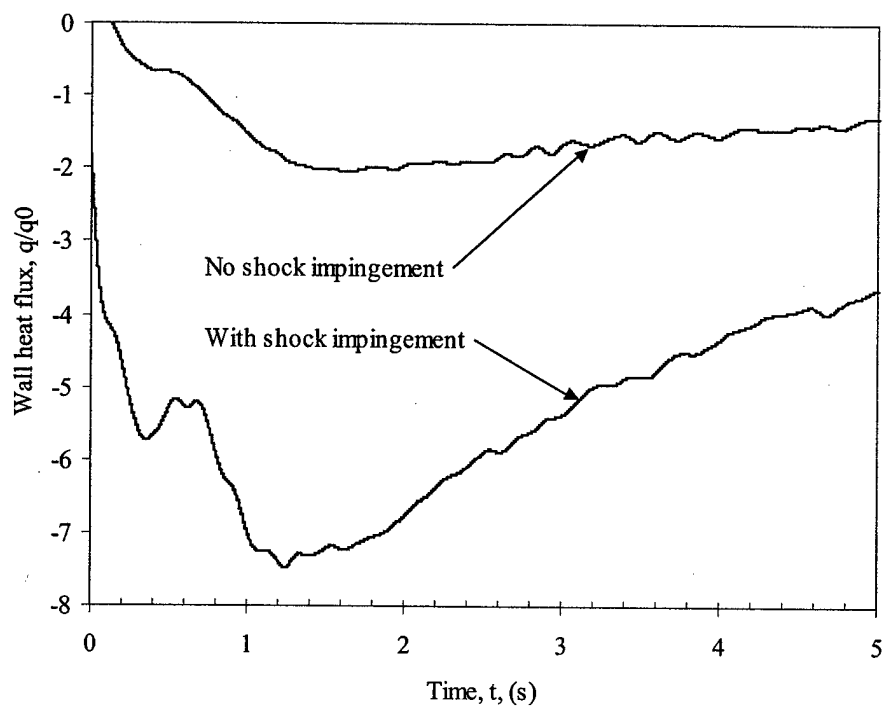


Figure 5.84 Comparison of stagnation point heat transfer for sphere with and without Edney Type IV shock/shock interaction

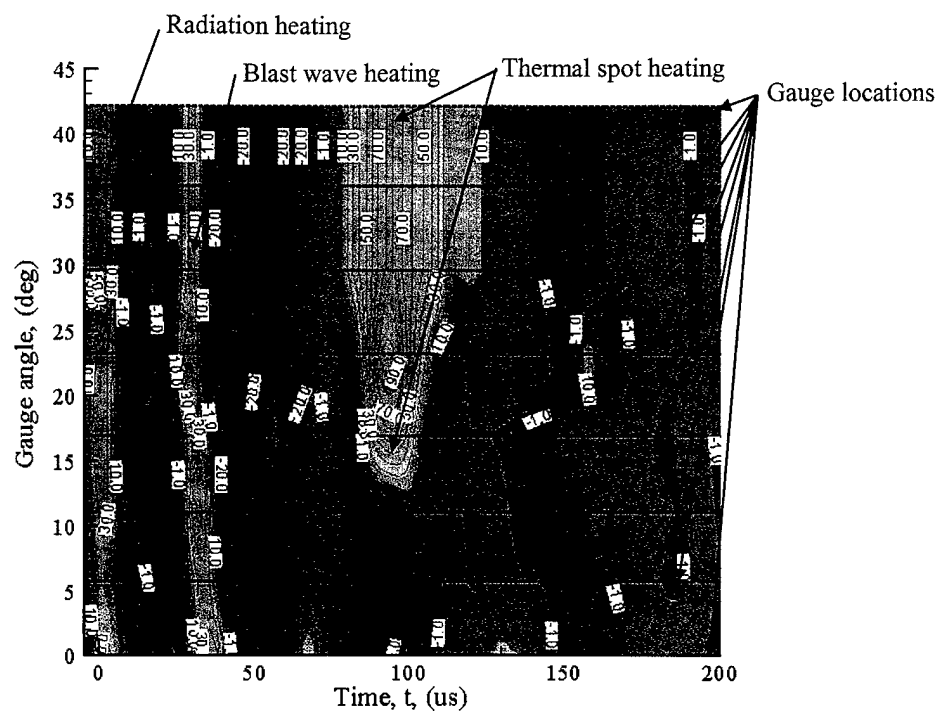


Figure 5.85 Measured wall heat flux on Mach 3.45 sphere with Edney Type IV shock impingement and with laser energy deposition 1.0 diameter upstream and 0.45 diameters above the centerline axis, one laser pulse (10 Hz) at 283 mJ/pulse, 150 mm focal length lens

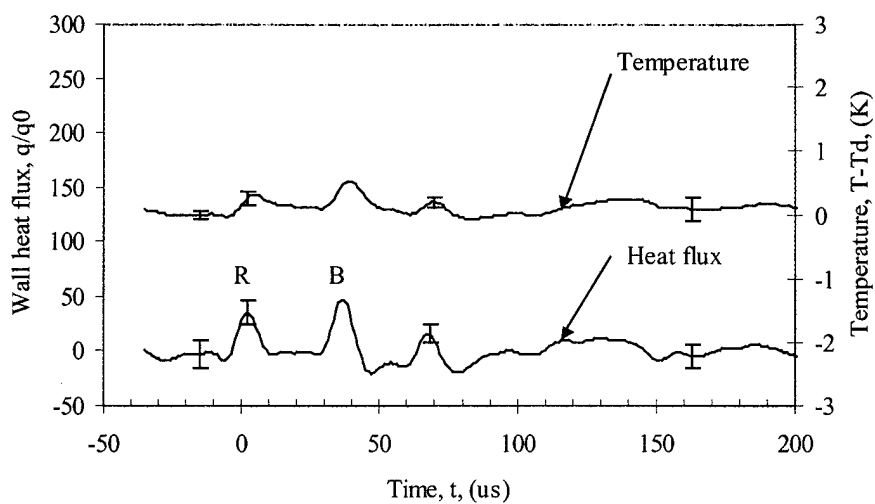


Figure 5.86 Measured wall heat flux and wall temperature for gauge 1 on Mach 3.45 sphere with Edney Type IV shock impingement and with laser energy deposition 1.0 diameter upstream and 0.45 diameters above the centerline axis, one laser pulse (10 Hz) at 283 mJ/pulse, 150 mm focal length lens

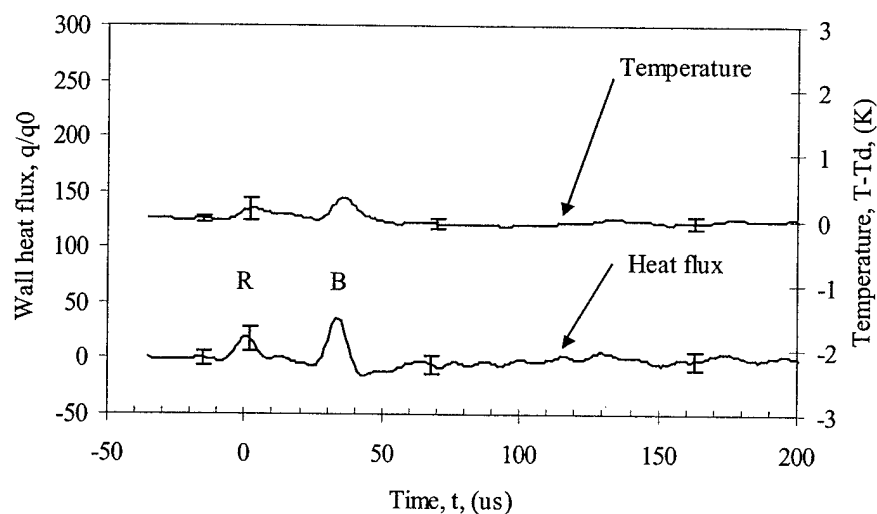


Figure 5.87 Measured wall heat flux and wall temperature for gauge 2 on Mach 3.45 sphere with Edney Type IV shock impingement and with laser energy deposition 1.0 diameter upstream and 0.45 diameters above the centerline axis, one laser pulse (10 Hz) at 283 mJ/pulse, 150 mm focal length lens

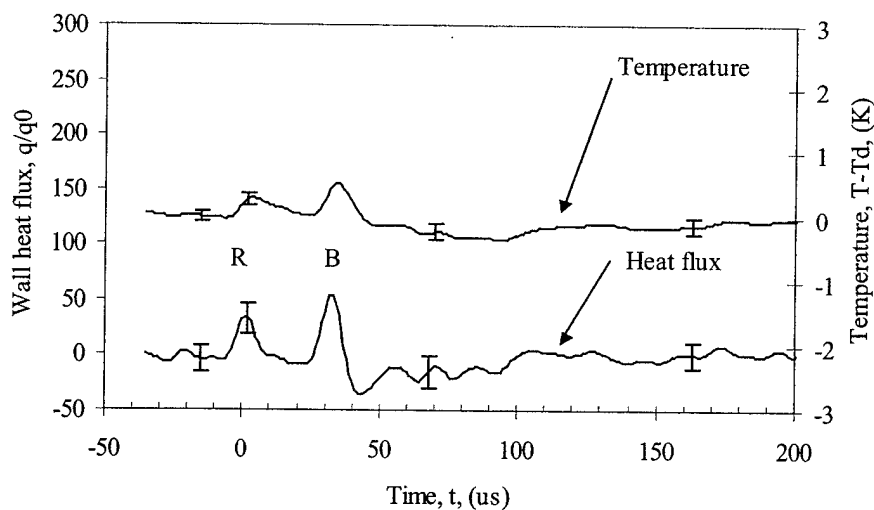


Figure 5.88 Measured wall heat flux and wall temperature for gauge 3 on Mach 3.45 sphere with Edney Type IV shock impingement and with laser energy deposition 1.0 diameter upstream and 0.45 diameters above the centerline axis, one laser pulse (10 Hz) at 283 mJ/pulse, 150 mm focal length lens

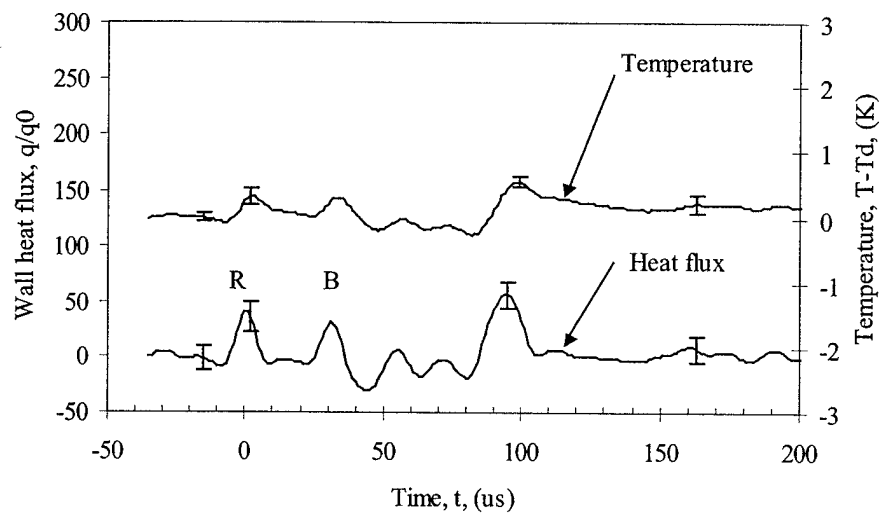


Figure 5.89 Measured wall heat flux and wall temperature for gauge 4 on Mach 3.45 sphere with Edney Type IV shock impingement and with laser energy deposition 1.0 diameter upstream and 0.45 diameters above the centerline axis, one laser pulse (10 Hz) at 283 mJ/pulse, 150 mm focal length lens

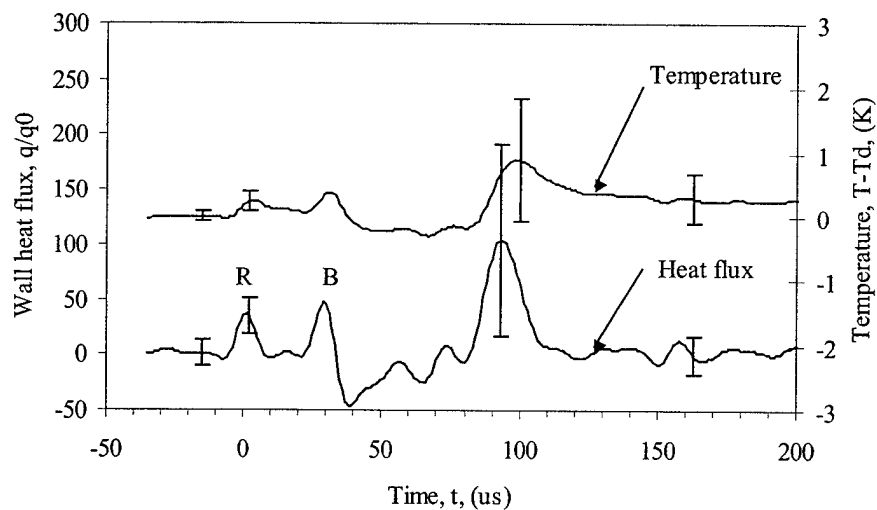


Figure 5.90 Measured wall heat flux and wall temperature for gauge 5 on Mach 3.45 sphere with Edney Type IV shock impingement and with laser energy deposition 1.0 diameter upstream and 0.45 diameters above the centerline axis, one laser pulse (10 Hz) at 283 mJ/pulse, 150 mm focal length lens

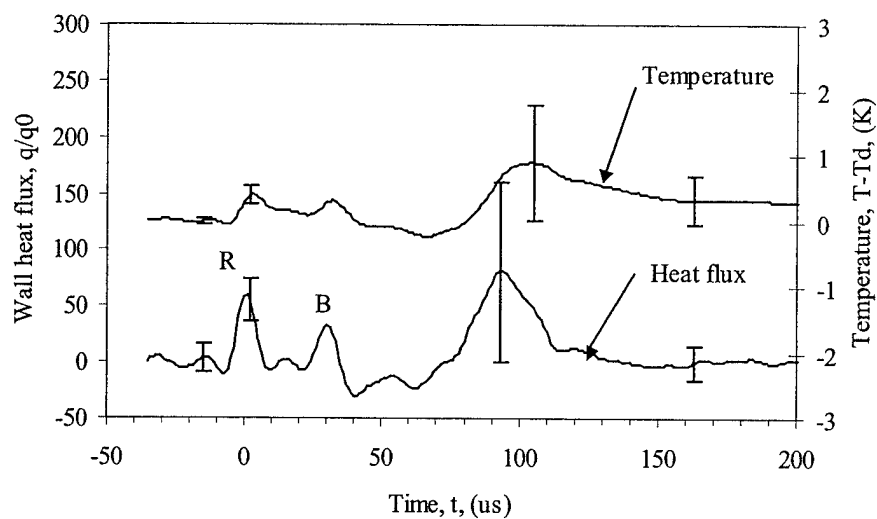


Figure 5.91 Measured wall heat flux and wall temperature for gauge 6 on Mach 3.45 sphere with Edney Type IV shock impingement and with laser energy deposition 1.0 diameter upstream and 0.45 diameters above the centerline axis, one laser pulse (10 Hz) at 283 mJ/pulse, 150 mm focal length lens

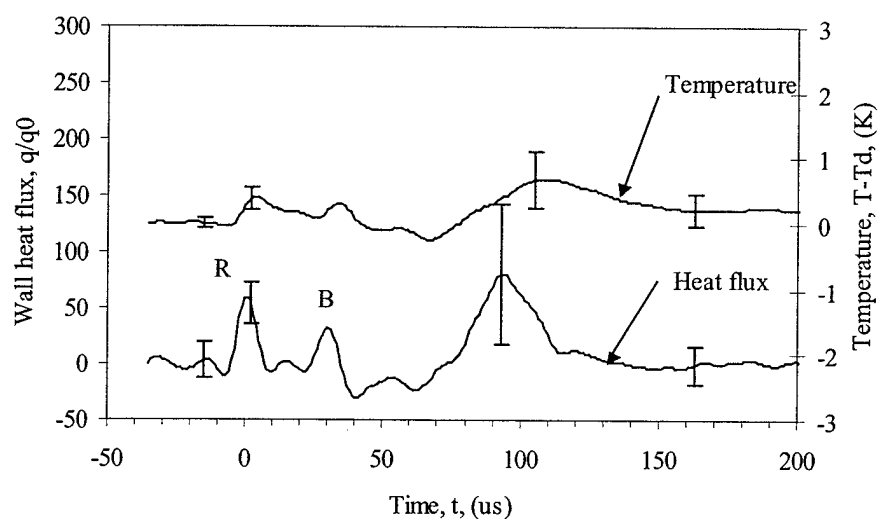


Figure 5.92 Measured wall heat flux and wall temperature for gauge 7 on Mach 3.45 sphere with Edney Type IV shock impingement and with laser energy deposition 1.0 diameter upstream and 0.45 diameters above the centerline axis, one laser pulse (10 Hz) at 283 mJ/pulse, 150 mm focal length lens

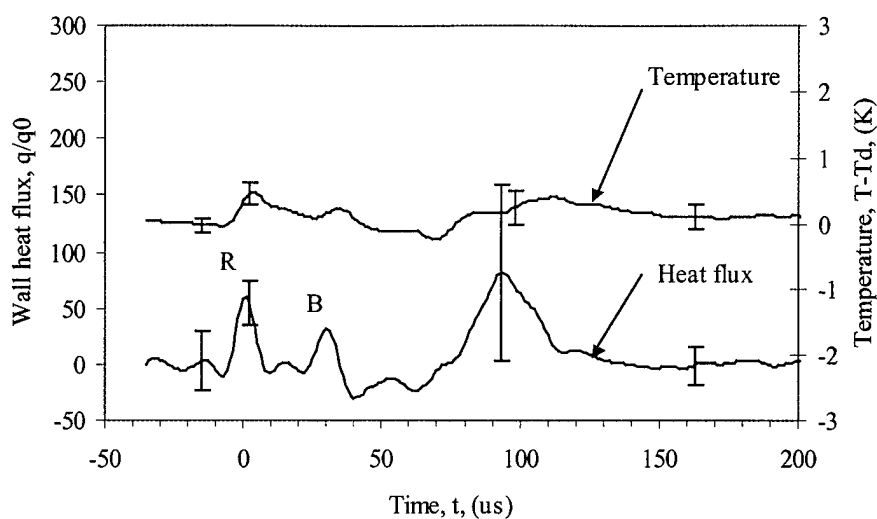


Figure 5.93 Measured wall heat flux and wall temperature for gauge 8 on Mach 3.45 sphere with Edney Type IV shock impingement and with laser energy deposition 1.0 diameter upstream and 0.45 diameters above the centerline axis, one laser pulse (10 Hz) at 283 mJ/pulse, 150 mm focal length lens

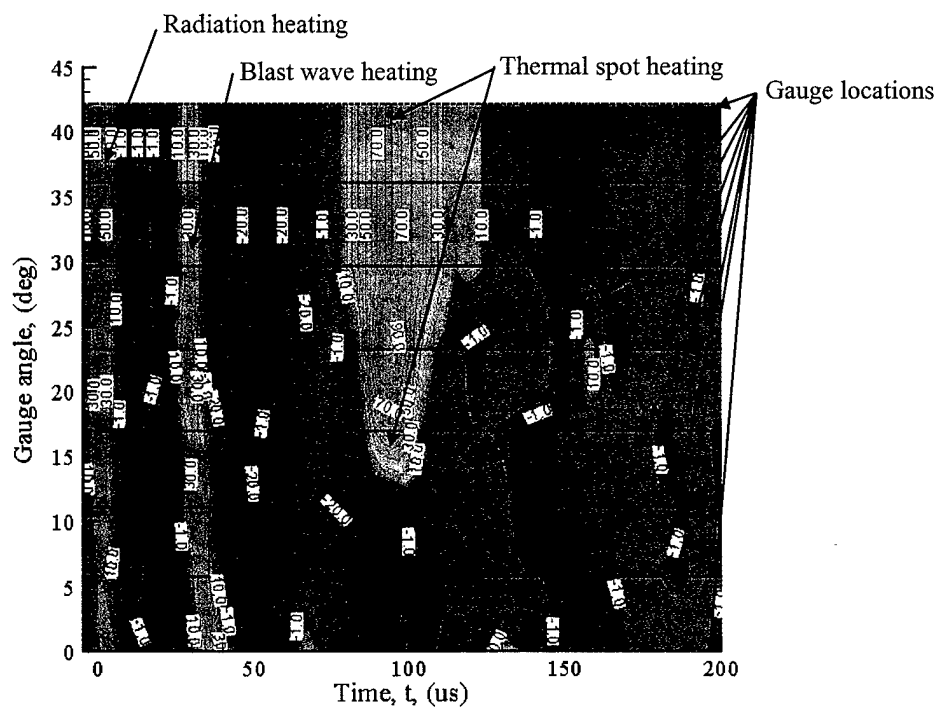


Figure 5.94 Measured wall heat flux on Mach 3.45 sphere with Edney Type IV shock impingement and with laser energy deposition 1.0 diameter upstream and 0.45 diameters above the centerline axis, double laser pulse separated by 5 μ s (10 Hz) at 263 mJ/pulse, 150 mm focal length lens

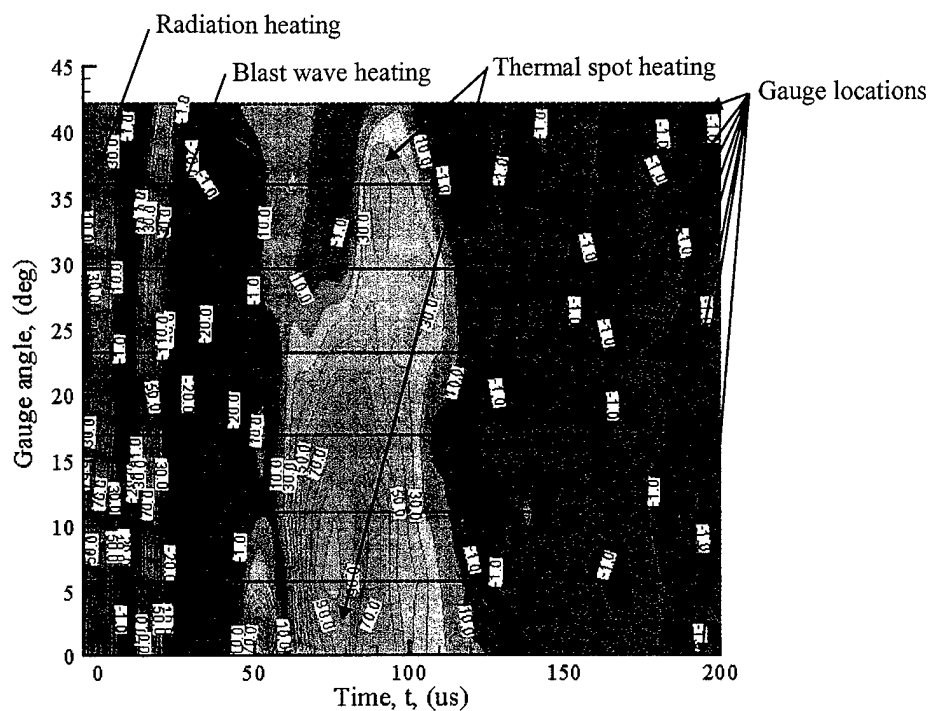


Figure 5.95 Measured wall heat flux on Mach 3.45 sphere with Edney Type IV shock impingement and with laser energy deposition 0.6 diameters upstream and 0.2 diameters above the centerline axis, one laser pulse (10 Hz) at 283 mJ/pulse, 150 mm focal length lens

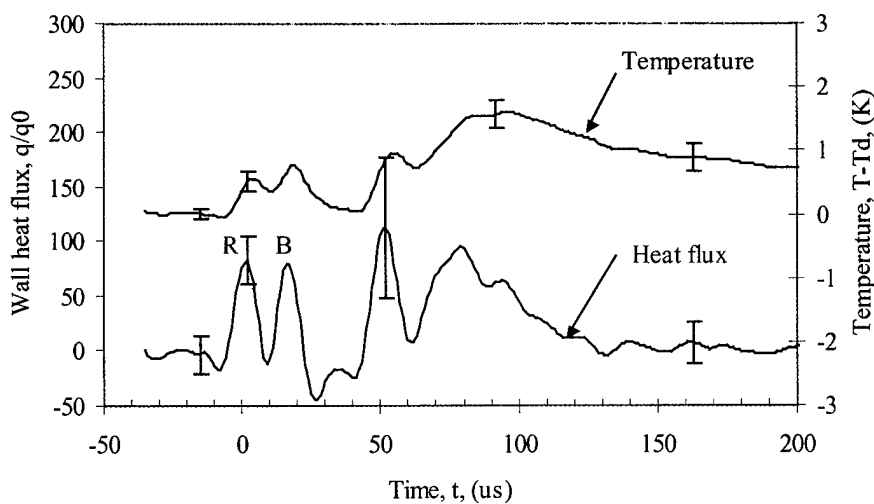


Figure 5.96 Measured wall heat flux and wall temperature for gauge 1 on Mach 3.45 sphere with Edney Type IV shock impingement and with laser energy deposition 0.6 diameters upstream and 0.2 diameters above the centerline axis, one laser pulse (10 Hz) at 283 mJ/pulse, 150 mm focal length lens

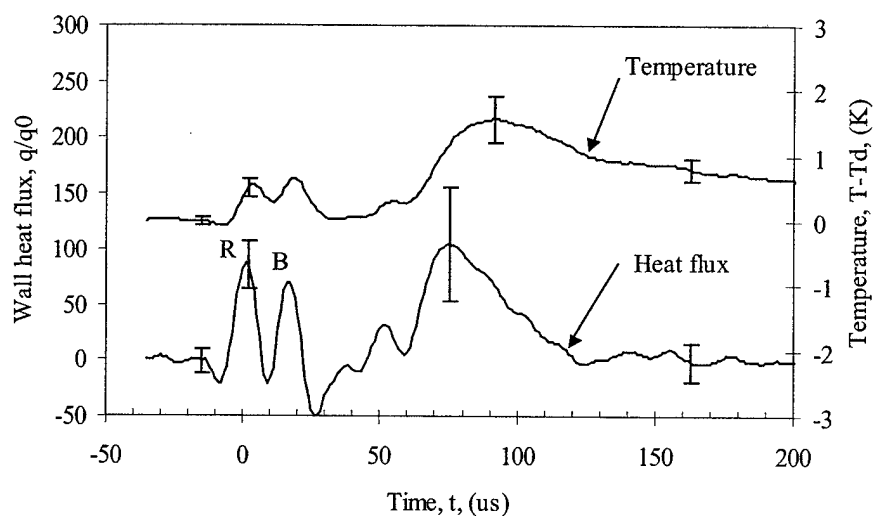


Figure 5.97 Measured wall heat flux and wall temperature for gauge 2 on Mach 3.45 sphere with Edney Type IV shock impingement and with laser energy deposition 0.6 diameters upstream and 0.2 diameters above the centerline axis, one laser pulse (10 Hz) at 283 mJ/pulse, 150 mm focal length lens

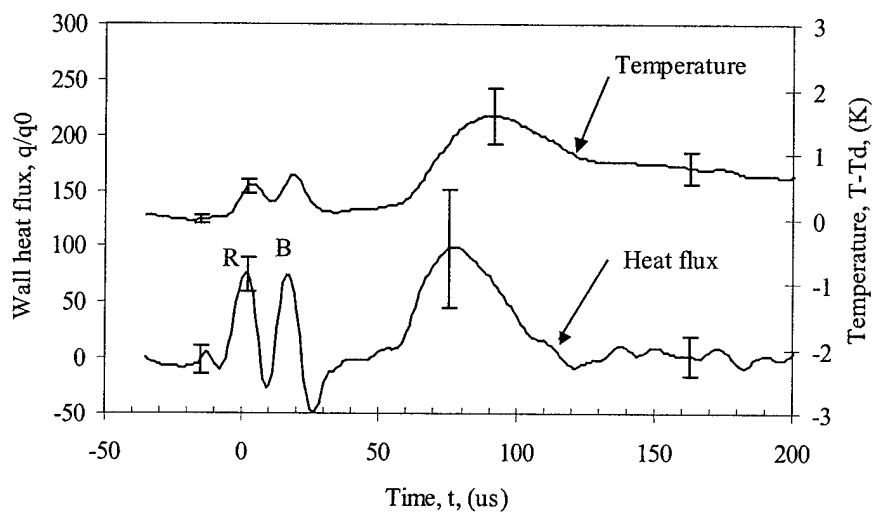


Figure 5.98 Measured wall heat flux and wall temperature for gauge 3 on Mach 3.45 sphere with Edney Type IV shock impingement and with laser energy deposition 0.6 diameters upstream and 0.2 diameters above the centerline axis, one laser pulse (10 Hz) at 283 mJ/pulse, 150 mm focal length lens

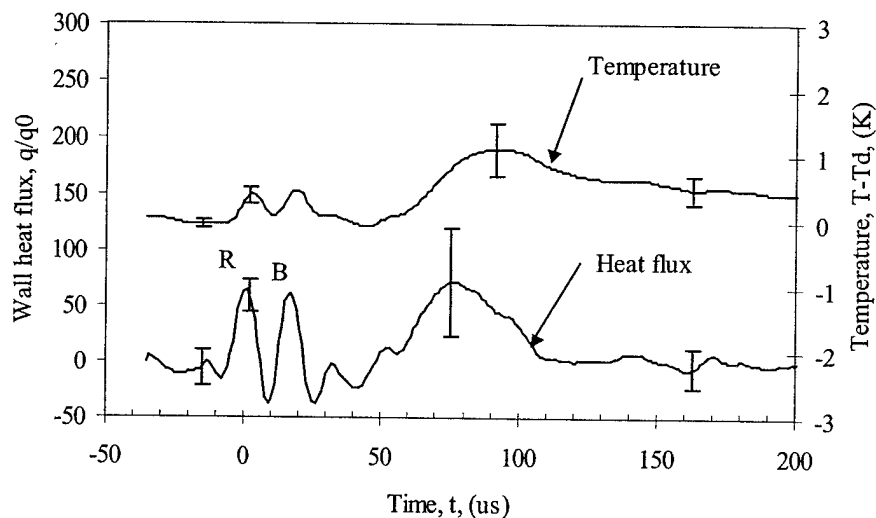


Figure 5.99 Measured wall heat flux and wall temperature for gauge 4 on Mach 3.45 sphere with Edney Type IV shock impingement and with laser energy deposition 0.6 diameters upstream and 0.2 diameters above the centerline axis, one laser pulse (10 Hz) at 283 mJ/pulse, 150 mm focal length lens

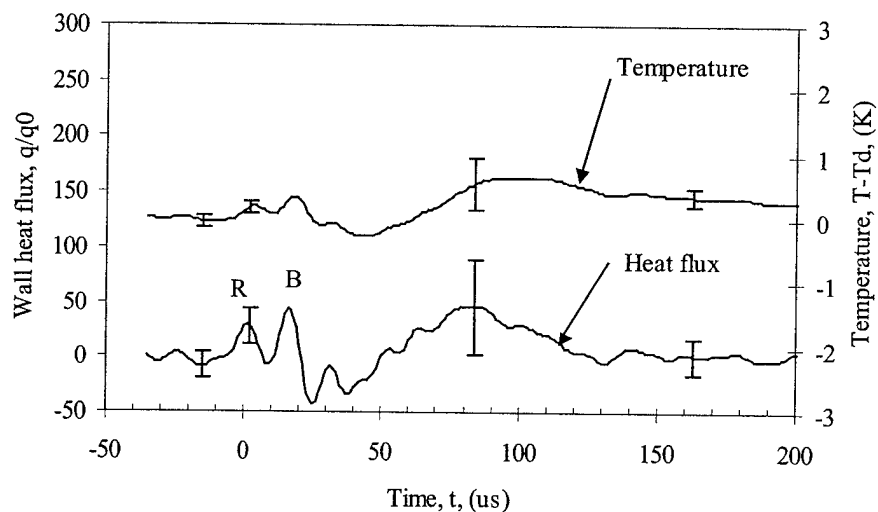


Figure 5.100 Measured wall heat flux and wall temperature for gauge 5 on Mach 3.45 sphere with Edney Type IV shock impingement and with laser energy deposition 0.6 diameters upstream and 0.2 diameters above the centerline axis, one laser pulse (10 Hz) at 283 mJ/pulse, 150 mm focal length lens

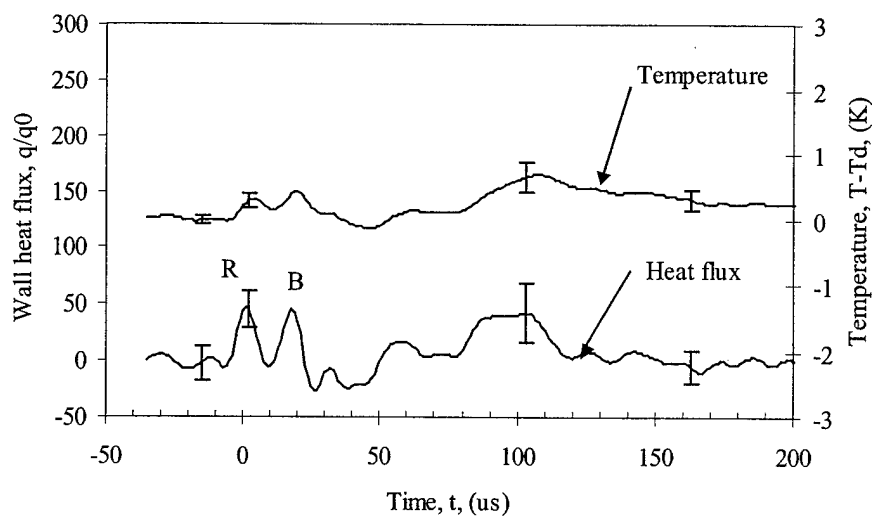


Figure 5.101 Measured wall heat flux and wall temperature for gauge 6 on Mach 3.45 sphere with Edney Type IV shock impingement and with laser energy deposition 0.6 diameters upstream and 0.2 diameters above the centerline axis, one laser pulse (10 Hz) at 283 mJ/pulse, 150 mm focal length lens

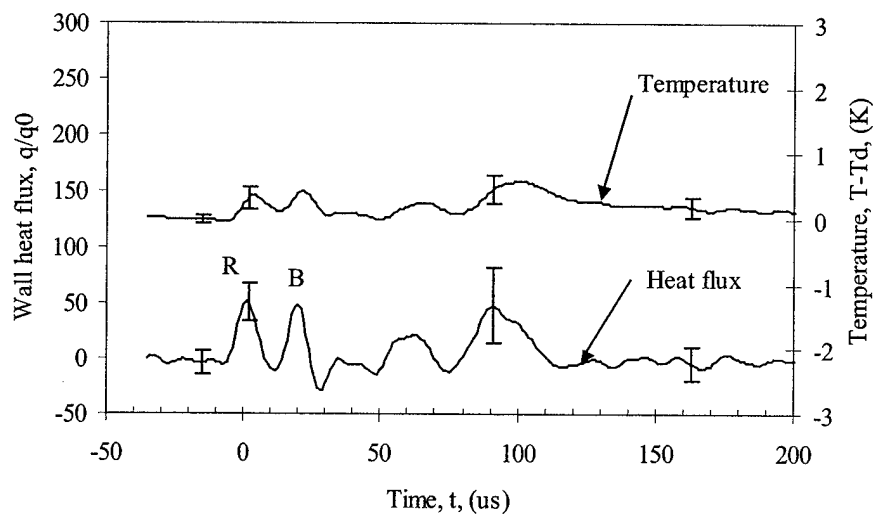


Figure 5.102 Measured wall heat flux and wall temperature for gauge 7 on Mach 3.45 sphere with Edney Type IV shock impingement and with laser energy deposition 0.6 diameters upstream and 0.2 diameters above the centerline axis, one laser pulse (10 Hz) at 283 mJ/pulse, 150 mm focal length lens

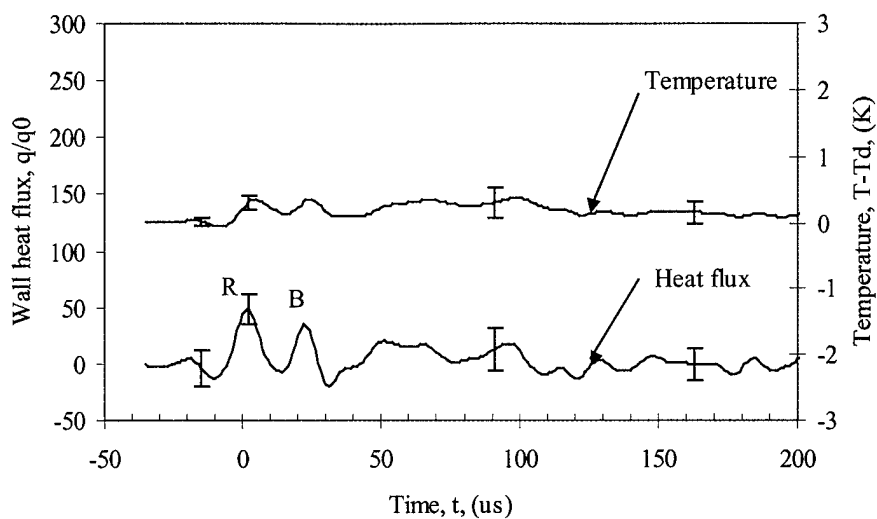


Figure 5.103 Measured wall heat flux and wall temperature for gauge 8 on Mach 3.45 sphere with Edney Type IV shock impingement and with laser energy deposition 0.6 diameters upstream and 0.2 diameters above the centerline axis, one laser pulse (10 Hz) at 283 mJ/pulse, 150 mm focal length lens

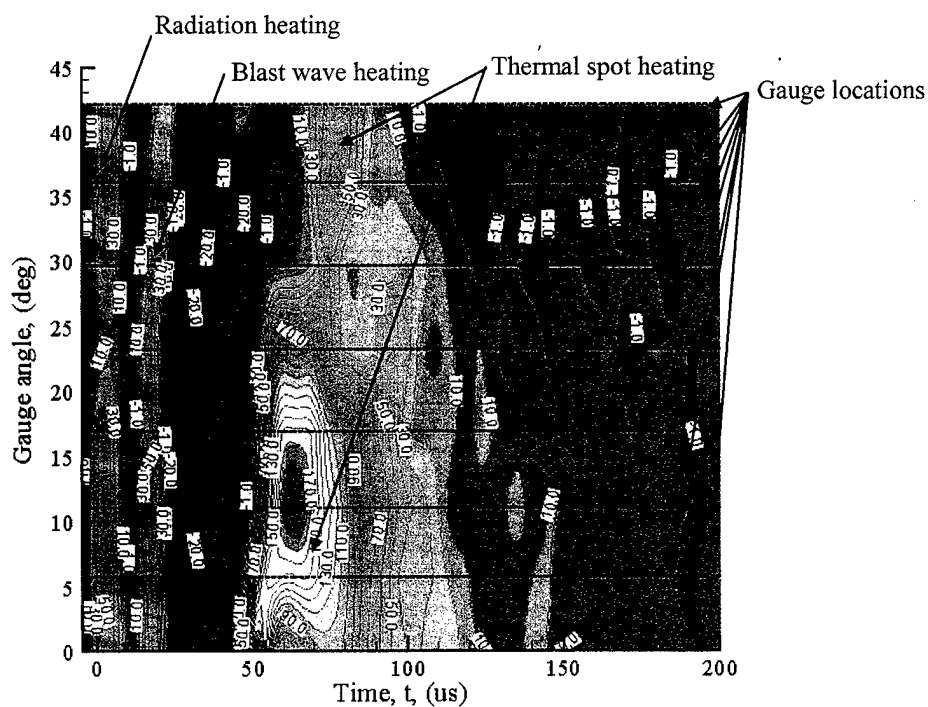


Figure 5.104 Measured wall heat flux on Mach 3.45 sphere with Edney Type IV shock impingement and with laser energy deposition 0.6 diameters upstream and 0.2 diameters above the centerline axis, double laser pulse separated by 5 μ s (10 Hz) at 263 mJ/pulse, 150 mm focal length lens

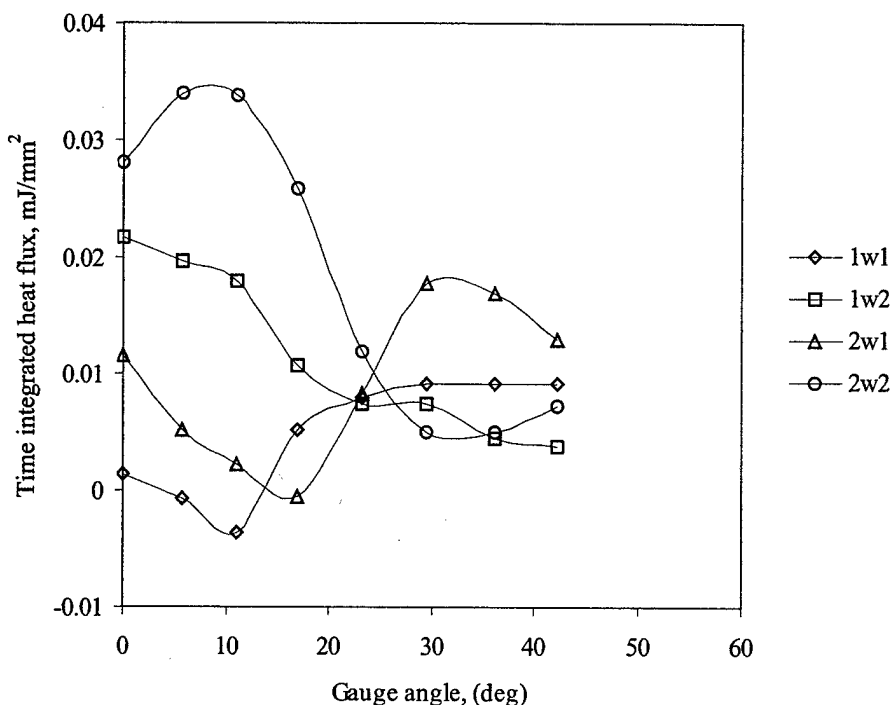


Figure 5.105 Time integrated heat flux for each of the gauges from small time scale data, 1w1 = single laser pulse 1.0 diameter upstream and 0.45 diameters above centerline, 1w2 = single laser pulse 0.6 diameters upstream and 0.2 diameters above centerline, 2w1 = double laser pulse 1.0 diameter upstream and 0.45 diameters above centerline, and 2w2 = double laser pulse 0.6 diameters upstream and 0.2 diameters above centerline

5.4 Summary

The goal was to effectively show that the severe aerothermal loads associated with the Edney Type IV shock impingement could be reduced by laser energy upstream of the shock/shock interaction region.

The pressure and heat transfer were measured for energy deposition upstream of the sphere without shock impingement as a baseline and for comparison to the shock impingement case. Schlieren images were taken for flow visualization of the interaction processes. The heat transfer data detects the radiation, blast wave heating, cooling of the expansion due to the thermal interface and bow shock interaction, and the thermal spot hitting the sphere surface. This blast wave heating was verified with the schlieren images. A reduction of 40% was measured in the stagnation pressure for the sphere without shock impingement.

The peak pressure associated with the Edney IV interaction was momentarily reduced by 30% by laser energy deposition upstream of the sphere with shock impingement. The heat transfer measurements were inconclusive in determining a reduction in heat transfer with laser energy deposition. Any reduction in heat transfer rate associated with the Type IV interaction could not be separated out from the heating associated with the thermal spot interaction with the sphere. However, as with the sphere without shock impingement the sensitivity of the gauges was demonstrated for tests conducted with laser energy deposition upstream of the sphere. Problems were also attributed to boundary layer shock interactions with the shock generator located within the test section boundary layer.

The schlieren images did show a significant effect on the shock structure for the energy deposition upstream of the Edney IV shock/shock interaction location. Locations for energy deposition that still perturb the shock structure but where the thermal spot does not impinge on the body might provide a means of mitigating the heat transfer associated with the shock impingement, and not cause excessive heating due to the spot. Additionally, rapid laser pulses of lower power might be effective in perturbing the Edney IV structure and minimizing the heat transfer of the thermal spot impingement.

Chapter 6

Crossing Shocks

6.1 Overview of Crossing Shock Tests

The objective of the crossing shock experiments was to see if the shock structure in the dual solution domain could be effectively transitioned through the used of laser energy deposition. The goal would be to reduce the total pressure losses associated with a normal shock by transitioning the Mach reflection to a regular reflection (see discussion in Section 2.4.2). Figure 6.1, Table 6.1, Figure 6.2, and Table 6.2 summarize the laser energy deposition locations for the test cases involving the crossing shocks. Qualitative flow assessments are made from time sequenced schlieren images obtained for these energy deposition locations in Section 6.2, and numerical simulation results are compared with one of the test cases in Section 6.3.

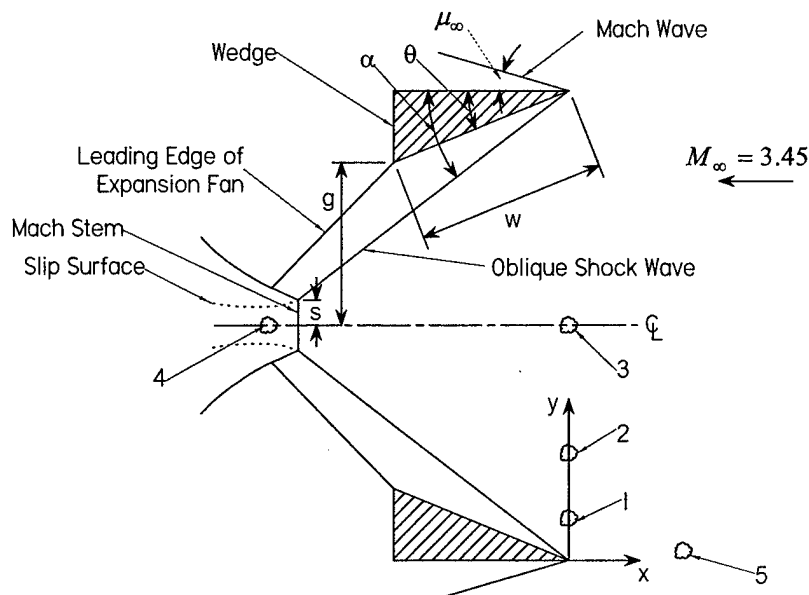
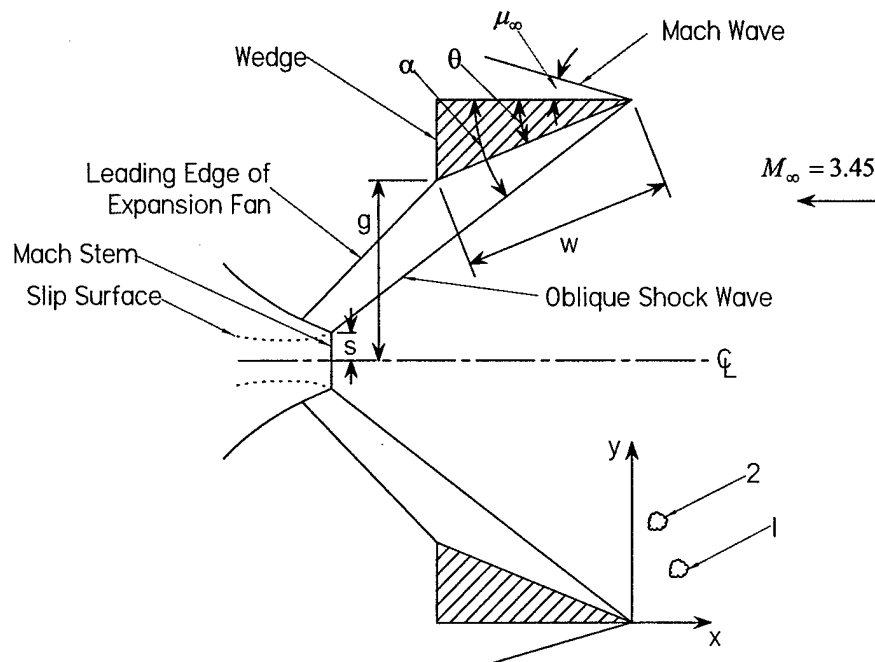


Figure 6.1 Energy deposition locations for wedges with span $b = 2.2w$ (image is drawn to scale)

Table 6.1 Laser deposition position and energy levels for wedges with span $b = 2.2w$

Position	Distance upstream from leading edge, x/w	Distance above leading edge, y/w	Energy (mJ/pulse)
1	-0.02	0.25	215
1	-0.02	0.25	105
2	-0.05	0.58	215
3	-0.02	0.95	215
4	-1.31	0.98	215
5	0.59	0.05	215

**Figure 6.2** Energy deposition locations for wedges with span $b = 4.0w$ (image is drawn to scale)**Table 6.2** Laser deposition position and energy levels for wedges with span $b = 4w$

Position	Distance upstream from leading edge, x/w	Distance above leading edge, y/w	Energy (mJ/pulse)
1	0.23	0.25	215
2	0.12	0.47	215

6.2 Flow Visualization

An experimental survey of energy deposition locations, energy levels, and wedge span widths was completed to assess the effects of laser energy deposition on the shock structures in the dual solution domain at Mach 3.45. Symmetric, 22 degree wedges, were tested in the wind tunnel with laser energy deposition. Two different span wedges, $2.2w$ and $4w$, were tested where w , the wedge length, was 25.4 mm (see Section 3.7 for details on the wedge models). Since the wedges had an angle of 22 degrees, the intersecting shock structure falls within the dual solution domain (see Section 2.4.2 and Figure 2.7). The $2.2w$ span wedges were tested with five different laser energy deposition locations, and schlieren flow visualization was used to determine the effect of the energy deposition on the shock structure. Dr. Hong Han numerically simulated the energy deposition for one of the locations and the experimental and computation results are compared in Section 6.3. The $4w$ span wedges were tested with two energy deposition locations. The two different span wedges were tested to determine three-dimensional spanwise effects on the flow structure.

Table 6.3 lists the tunnel operational parameters for the tests on the wedges, and Table 6.4 lists flow parameters for the wedges.

Figure 6.3 through Figure 6.6 give the time sequence of laser/argon schlieren images for laser energy deposition, at 215 mJ/pulse, and with deposition location aligned with leading edge of wedges and $0.25w$ above the leading edge (position 1). The wedge span is $b = 2.2w$, and the separation between the back of the wedges is $2g = 1.14w$. Due to the turbulence levels within the test section [136], the Mach stem solution occurs for this wind tunnel and wedge angle. The dependence of the Mach stem versus regular reflection solution on the turbulence levels has been demonstrated by Ivanov. [74] The blast wave from the laser energy deposition is clearly observed at 10 μ s. As time progresses the blast wave and thermal spot begin to interact with the oblique shock. By 40 μ s the blast wave interacts with the Mach stem at the oblique shock intersection point. Due to the lowering of the local Mach number around the thermal spot, the oblique shock generated by the bottom wedge moves upstream. Initial effects on the Mach stem can be seen from 40 to 50 μ s. By lowering the localized Mach number the effect is to pull the solution to the left in the dual solution domain (see Figure 2.7). The solution will then approach the lower boundary of the

dual solution domain. If the Mach number is decreased sufficiently, the regular reflection solution will occur. However, even if the boundary is not crossed, the Mach stem will still decrease. Both Ivanov [68] and Schmisser and Gaitonde [125] have demonstrated the decrease in Mach stem height as the lower boundary of the dual solution domain is approached by changing the wedge angle. Figure 6.22 gives the Mach stem height as the laser perturbation interacts with the shock structure for this test case. The Mach stem decreases to 30% of its original height. By 300 μ s the Mach stem has returned to its original height.

For the next test case, the energy was deposited at the same location, position 1 (see Figure 6.1), but at a lower amount of energy. The amount of energy was approximately half of the energy for the previous case. Figure 6.7 through Figure 6.9 give the time sequence of instantaneous schlieren images for laser energy deposition, at 105 mJ/pulse, with deposition location aligned with leading edge of wedges and 0.25 w above the leading edge. The wedge span is $b = 2.2w$, and the separation between the back of the wedges is $2g = 1.14w$. The same gross flow features are observed for this test case, however, the effect on the Mach stem is not as great as for the higher energy level discussed above. The Mach stem height is shown in Figure 6.22 as the shock structure interacts with the laser perturbation. The Mach stem is estimated to reduce to 40% of its original height.

Figure 6.10 through Figure 6.12 give the time sequence of instantaneous schlieren images for laser energy deposition, at 215 mJ/pulse with deposition location aligned with leading edge of wedges and 0.58 w above leading edge (position 2). The wedge span is $b = 2.2w$, and the separation between the back of the wedges is $2g = 1.14w$. In a like manner, the blast wave and the thermal spot interact with the wedge shock structure. However, there is less interaction of the thermal region with the wedge surface. The Mach stem heights for this test case are shown in Figure 6.22. The Mach stem is reduced to 25% of its original height.

Figure 6.13 through Figure 6.15 give the time sequence of instantaneous schlieren images for laser energy deposition, at 215 mJ/pulse with deposition location aligned with leading edge of wedges and on centerline (position 3). The wedge span is $b = 2.2w$, and the separation between the back of the wedges is $2g = 1.14w$. This test case increases the Mach stem by the lensing effect on the original Mach stem. The Mach stem is increased by 230% of its initial height and returns to the original height by 300 μ s. Additionally, a vortex pair formation is formed downstream of the Mach stem due to the interaction

process. This vortex pair formation is similar to the vortex formation when laser energy is deposited upstream of a Mach disk in an underexpanded jet. [2]

Figure 6.16 through Figure 6.19 give the time sequence of instantaneous schlieren images for laser energy deposition, at 215 mJ/pulse with deposition location behind Mach stem and on centerline (position 4). The wedge span is $b = 2.2w$, and the separation between the back of the wedges is $2g = 1.14w$. Figure 6.22 shows the Mach stem increase by 1.8 times its original height for this test case. There will be two effects in for these energy deposition position that will drive the Mach stem forward. First the blast wave from the spot will propagate upstream and interact with the Mach stem. Second, the pressure will increase in the subsonic region of the deposition region, and the temperature will increase. The local Mach number will decrease. All of these effects will increase the cause the Mach stem to move upstream.

Figure 6.20 through Figure 6.21 give the time sequence of instantaneous schlieren images for laser energy deposition, at 215 mJ/pulse with deposition location $0.59w$ upstream of leading edge and $0.05w$ above leading edge (position 5). The wedge span is $b = 2.2w$, and the separation between the back of the wedges is $2g = 1.14w$. Figure 6.22 shows the similar decrease in Mach stem height due to the energy deposition. The height for this test case decreases to 40% of the original height.

Figure 6.23 through Figure 6.26 give the time sequence of instantaneous schlieren images for laser energy deposition, at 215 mJ/pulse with deposition location $0.12w$ upstream of leading edge and $0.47w$ above leading edge (position 2 in Figure 6.2). The wedge span is $b = 4.0w$, and the separation between the back of the wedges is $2g = 1.19w$. No measurements were made for the Mach stem height. The energy deposition upstream of the larger span wedges contains the same type of evolving flow features as discussed above, i.e., the distortion of the oblique shock, perturbation of the intersection point, and decreasing/increasing Mach stem. However, qualitatively the effect on the Mach stem for the larger span wedges is not as great as for the smaller span wedges. The three-dimensional variation of the Mach stem will be different for the larger span wedges, and, therefore, the overall effect of the energy perturbation to the Mach stem will be less. In addition, by the nature of the schlieren, the images are integrated in the spanwise direction. This aspect could also mask some of the effect on shock structures for the energy deposition upstream of the larger span wedges.

Figure 6.27 gives the time sequence of instantaneous schlieren images for laser energy deposition, at 215 mJ/pulse with deposition location $0.23w$ upstream of leading edge and $0.25w$ above leading edge. The wedge span is $b = 4.0w$, and the separation between the back of the wedges is $2g = 1.19w$.

No measurements were made for the Mach stem height for the $b = 4w$ span wedges.

Table 6.3 Tunnel operational parameters for wedge tests

Mach number	3.45
Reynolds number based on wedge length, w , $Re_w = \frac{\rho V w}{\mu}$	1.863×10^6
Freestream viscosity, μ	$5.753 \times 10^{-6} \frac{\text{kg}}{\text{m s}}$
Stagnation pressure, p_0	$1.138 \times 10^6 \text{ Pa}$
Stagnation temperature, T_0	283 K
Stagnation density, ρ_0	$14.012 \frac{\text{kg}}{\text{m}^3}$
Freestream temperature, T	83.7 K
Freestream pressure, p	$1.602 \times 10^4 \text{ Pa}$
Freestream density, ρ	$0.667 \frac{\text{kg}}{\text{m}^3}$
Freestream velocity, V	632.6 m/s
Freestream speed of sound, a	183.4 m/s
Pitot pressure, p_{02}	$2.530 \times 10^5 \text{ Pa}$
Pitot density, ρ_{02}	$3.116 \frac{\text{kg}}{\text{m}^3}$

Table 6.4 Wedge flow parameters for Mach 3.45

Flow deflection angle, θ , (deg)	Shock angle, α , (deg)	L.E. exp. fan rel. to wedge, μ_z , (deg)
$\theta_{\text{vn}} = 20.48$	$\alpha_{\text{vn}} = 35.41$	26.51
$\theta_d = 23.68$	$\alpha_d = 39.28$	29.32
22	37.21	27.76

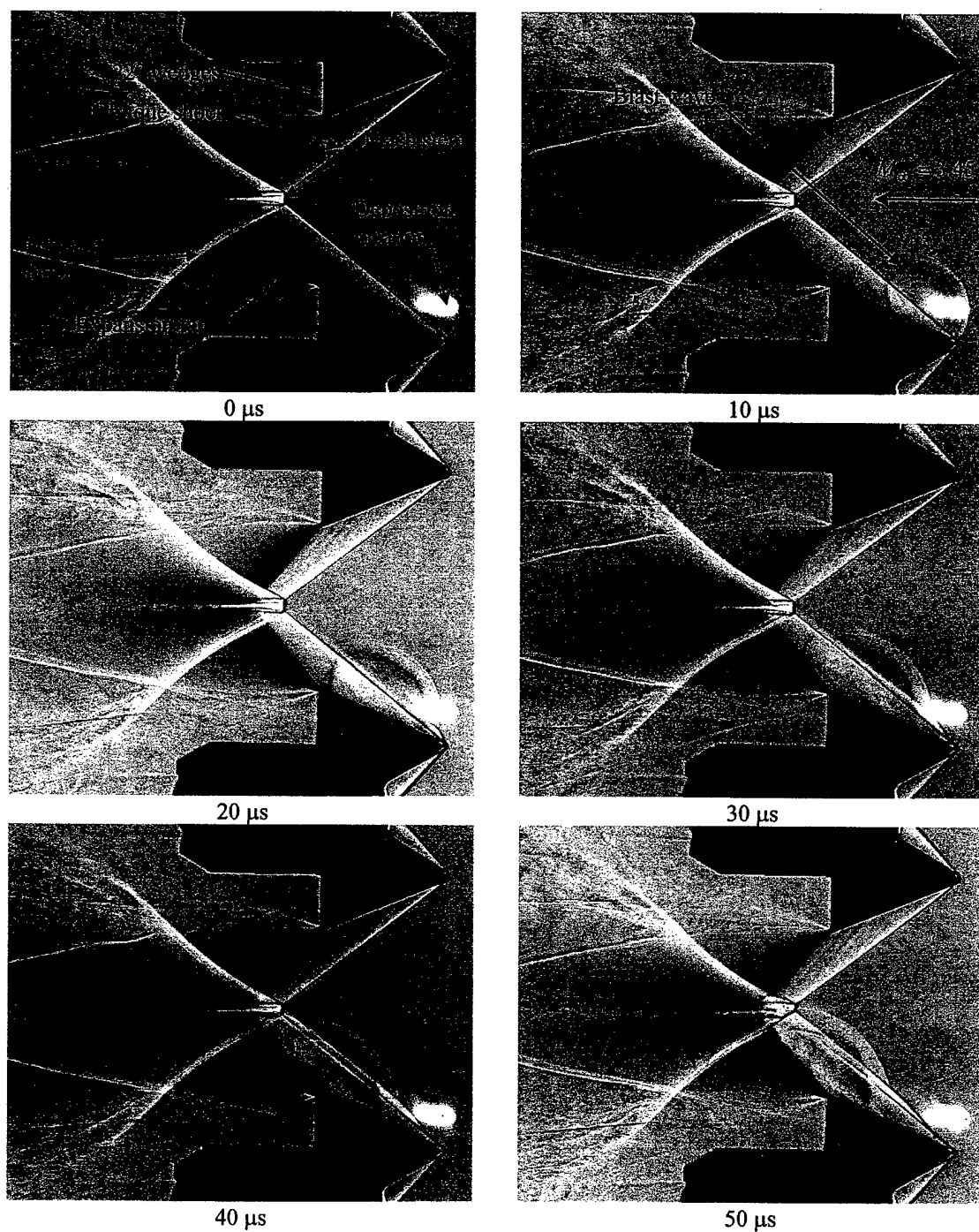


Figure 6.3 Instantaneous laser/argon schlieren time sequence of laser energy deposition at 215 mJ/pulse with deposition location $-0.02w$ from leading edge of wedges and $0.25w$ above leading edge for 0, 10, 20, 30, 40, and 50 μs delays, $2g = 1.14w$, and $b = 2.2w$

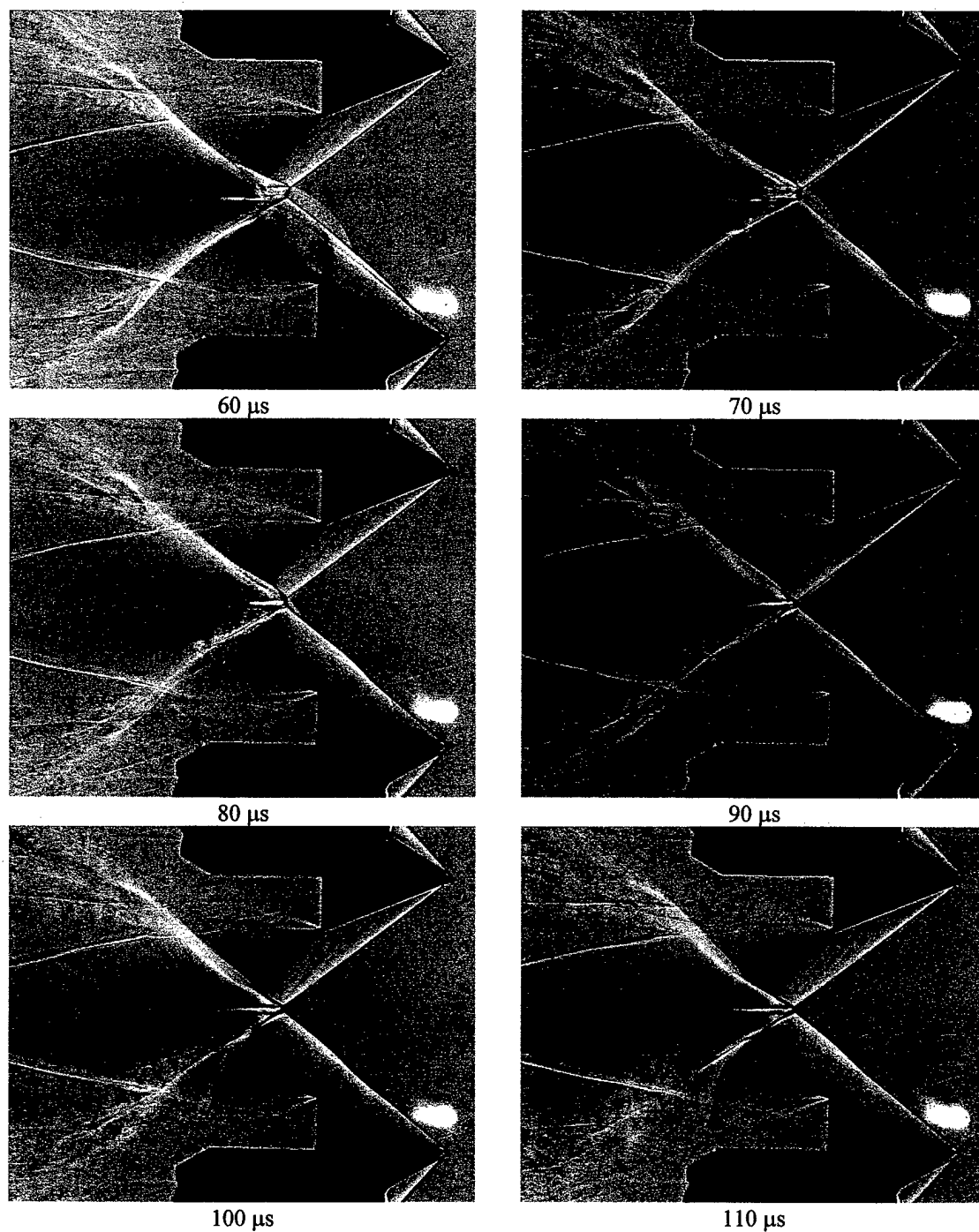


Figure 6.4 Instantaneous laser/argon schlieren time sequence of laser energy deposition at 215 mJ/pulse with deposition location $-0.02w$ from leading edge of wedges and $0.25w$ above leading edge for 60, 70, 80, 90, 100, and 110 μs delays, $2g = 1.14w$, and $b = 2.2w$

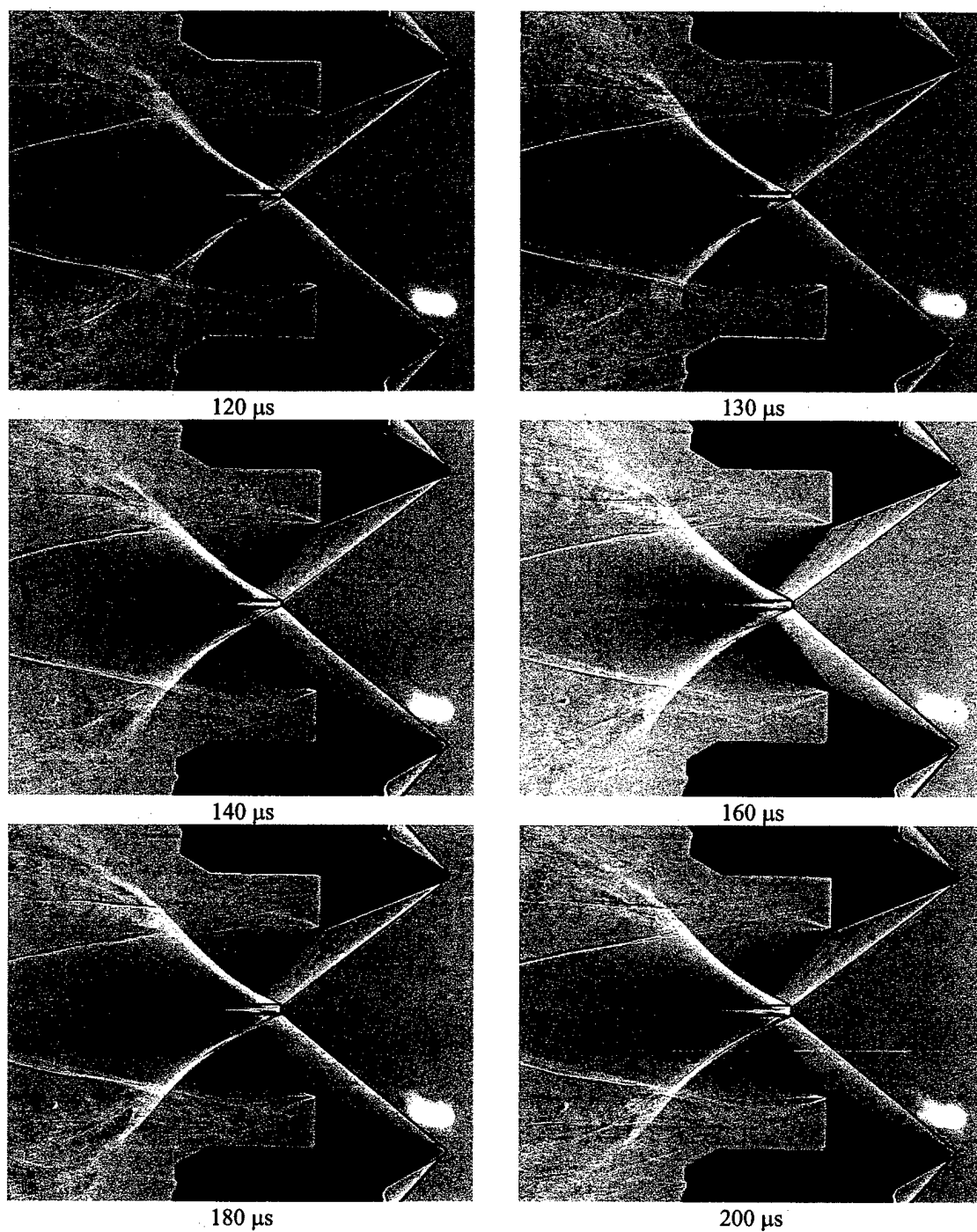


Figure 6.5 Instantaneous laser/argon schlieren time sequence of laser energy deposition at 215 mJ/pulse with deposition location $-0.02w$ from leading edge of wedges and $0.25w$ above leading edge for 120, 130, 140, 160, 180, and 200 μ s delays, $2g = 1.14w$, and $b = 2.2w$

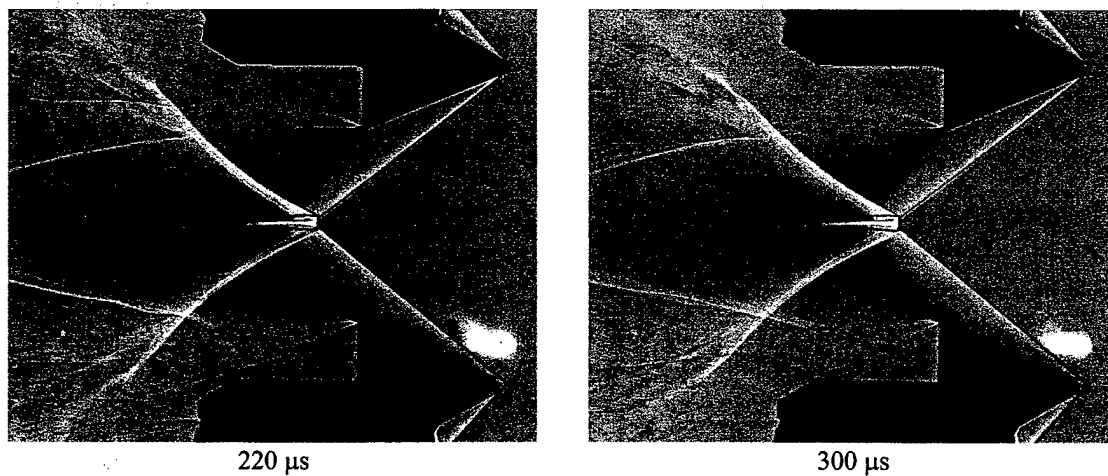


Figure 6.6 Instantaneous laser/argon schlieren time sequence of laser energy deposition at 215 mJ/pulse with deposition location $-0.02w$ from leading edge of wedges and $0.25w$ above leading edge for 220 and 300 μ s delays, $2g = 1.14w$, and $b = 2.2w$

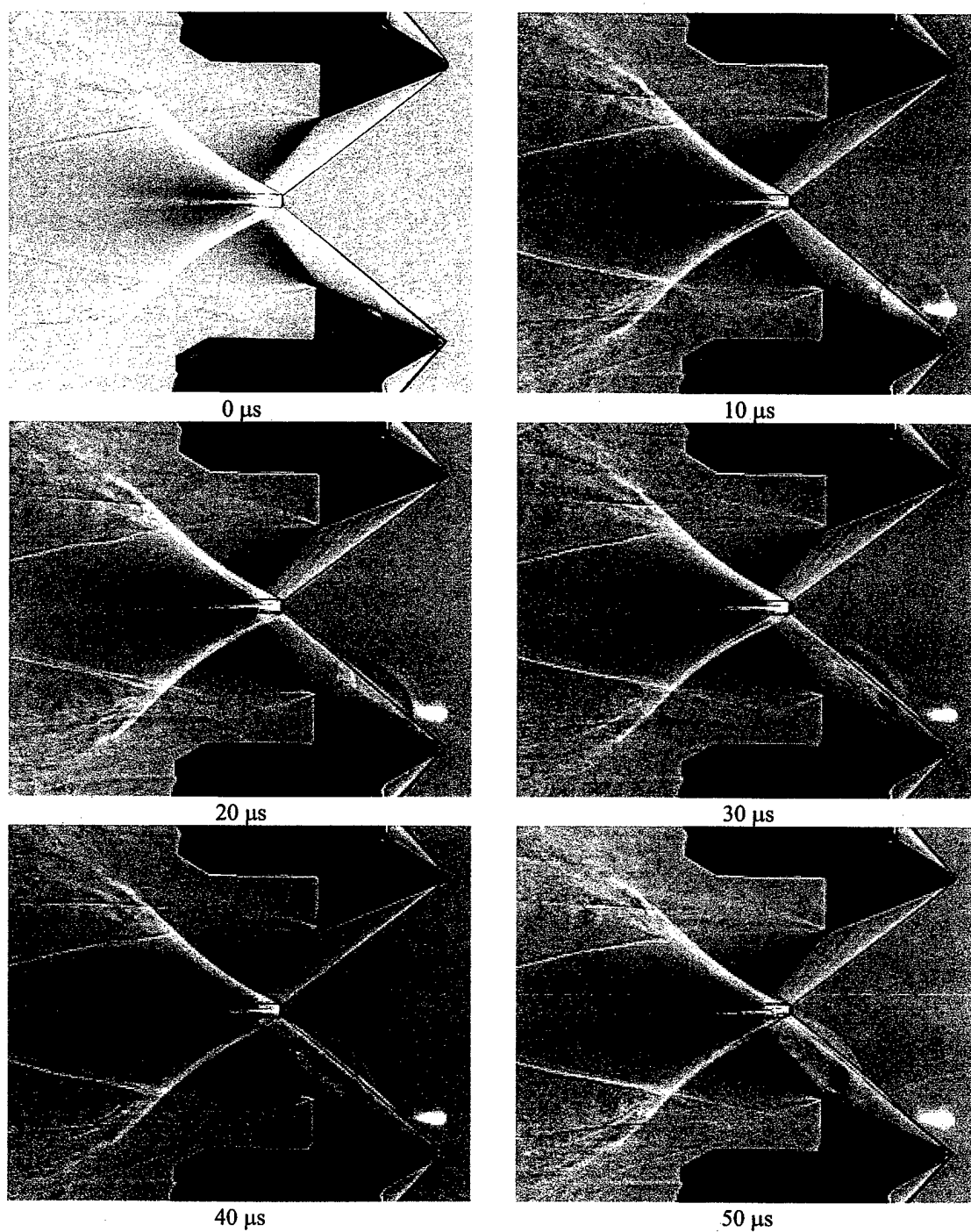


Figure 6.7 Instantaneous laser/argon schlieren time sequence of laser energy deposition at 105 mJ/pulse with deposition location $-0.02w$ from leading edge of wedges and $0.25w$ above leading edge for 0, 10, 20, 30, 40, and 50 μ s delays, $2g = 1.14w$, and $b = 2.2w$

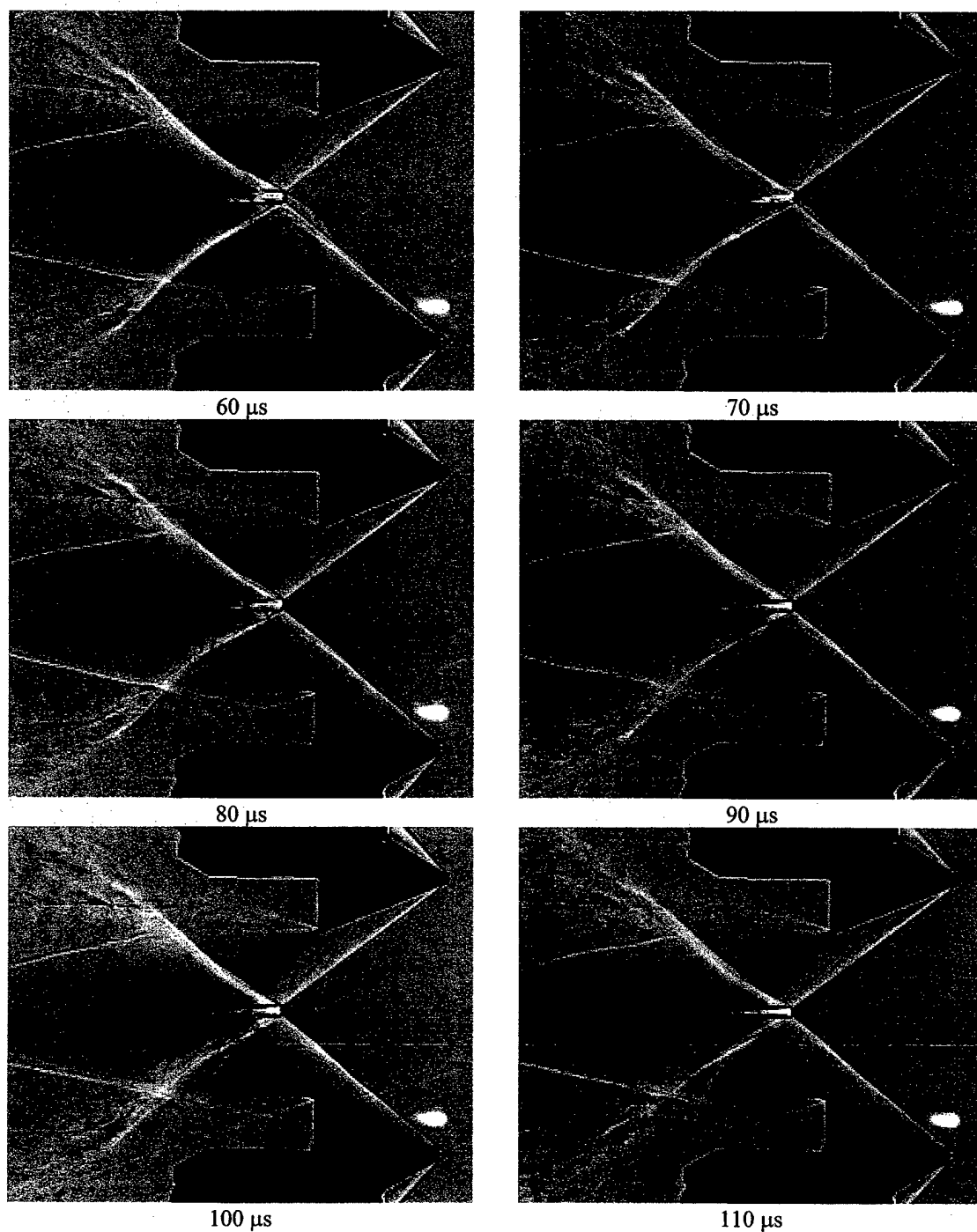


Figure 6.8 Instantaneous laser/argon schlieren time sequence of laser energy deposition at 105 mJ/pulse with deposition location $-0.02w$ from leading edge of wedges and $0.25w$ above leading edge for 60, 70, 80, 90, 100, and 110 μ s delays, $2g = 1.14w$, and $b = 2.2w$

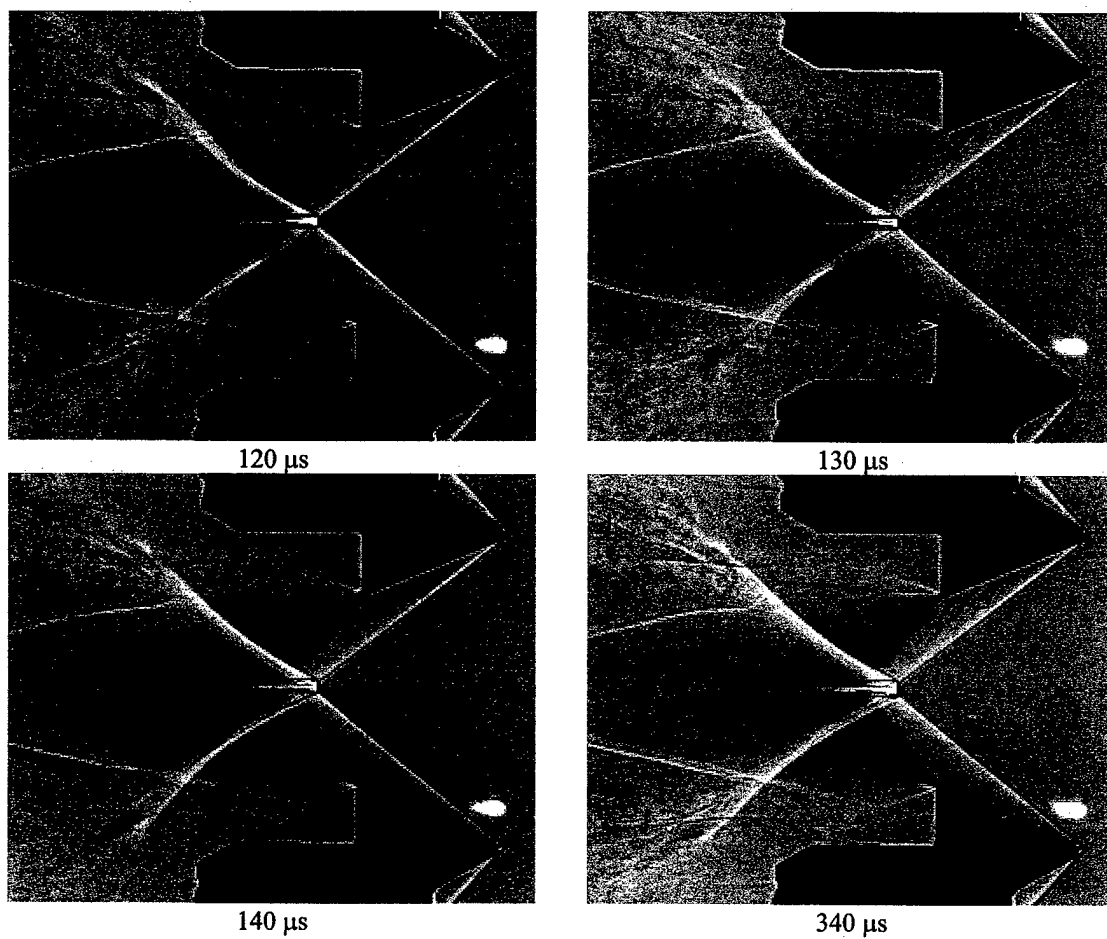


Figure 6.9 Instantaneous laser/argon schlieren time sequence of laser energy deposition at 105 mJ/pulse with deposition location $-0.02w$ from leading edge of wedges and $0.25w$ above leading edge for 120, 130, 140, and 340 μs delays, $2g = 1.14w$, and $b = 2.2w$

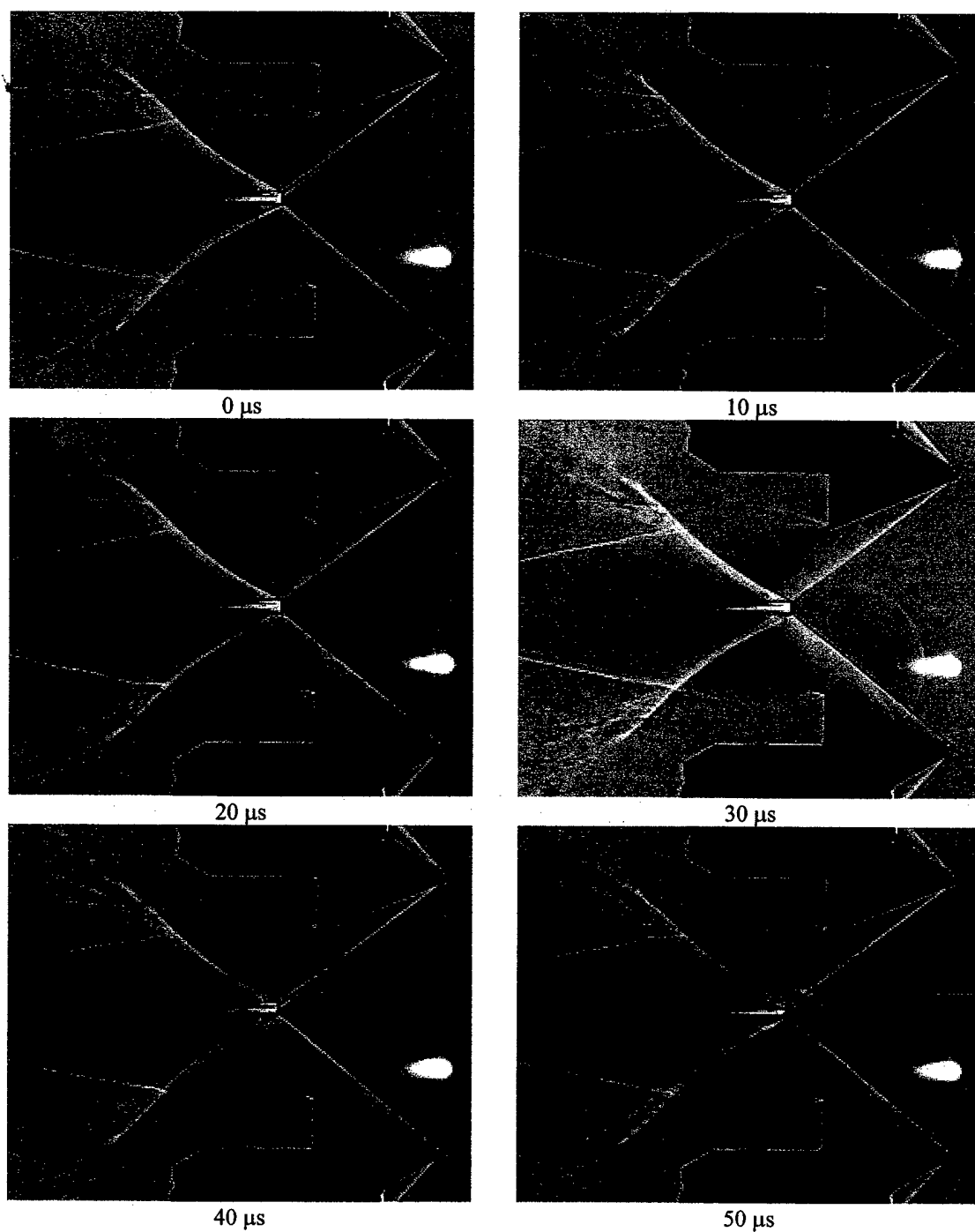


Figure 6.10 Instantaneous laser/argon schlieren time sequence of laser energy deposition at 215 mJ/pulse with deposition location $-0.05w$ from leading edge of wedges and $0.58w$ above leading edge for 0, 10, 20, 30, 40, and 50 μ s delays, $2g = 1.14w$, and $b = 2.2w$

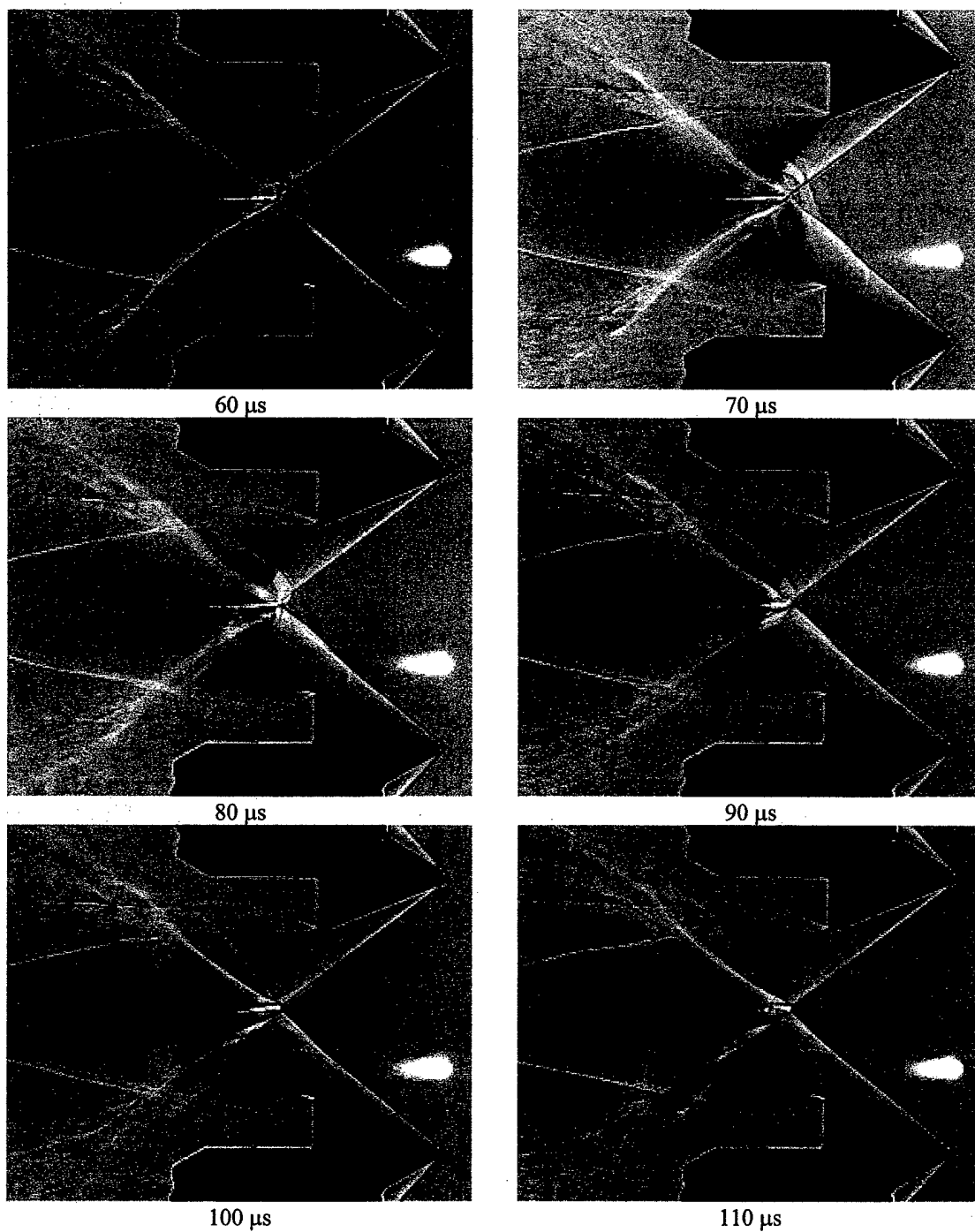


Figure 6.11 Instantaneous laser/argon schlieren time sequence of laser energy deposition at 215 mJ/pulse with deposition location $-0.05w$ from leading edge of wedges and $0.58w$ above leading edge for 60, 70, 80, 90, 100, and 110 μ s delays, $2g = 1.14w$, and $b = 2.2w$

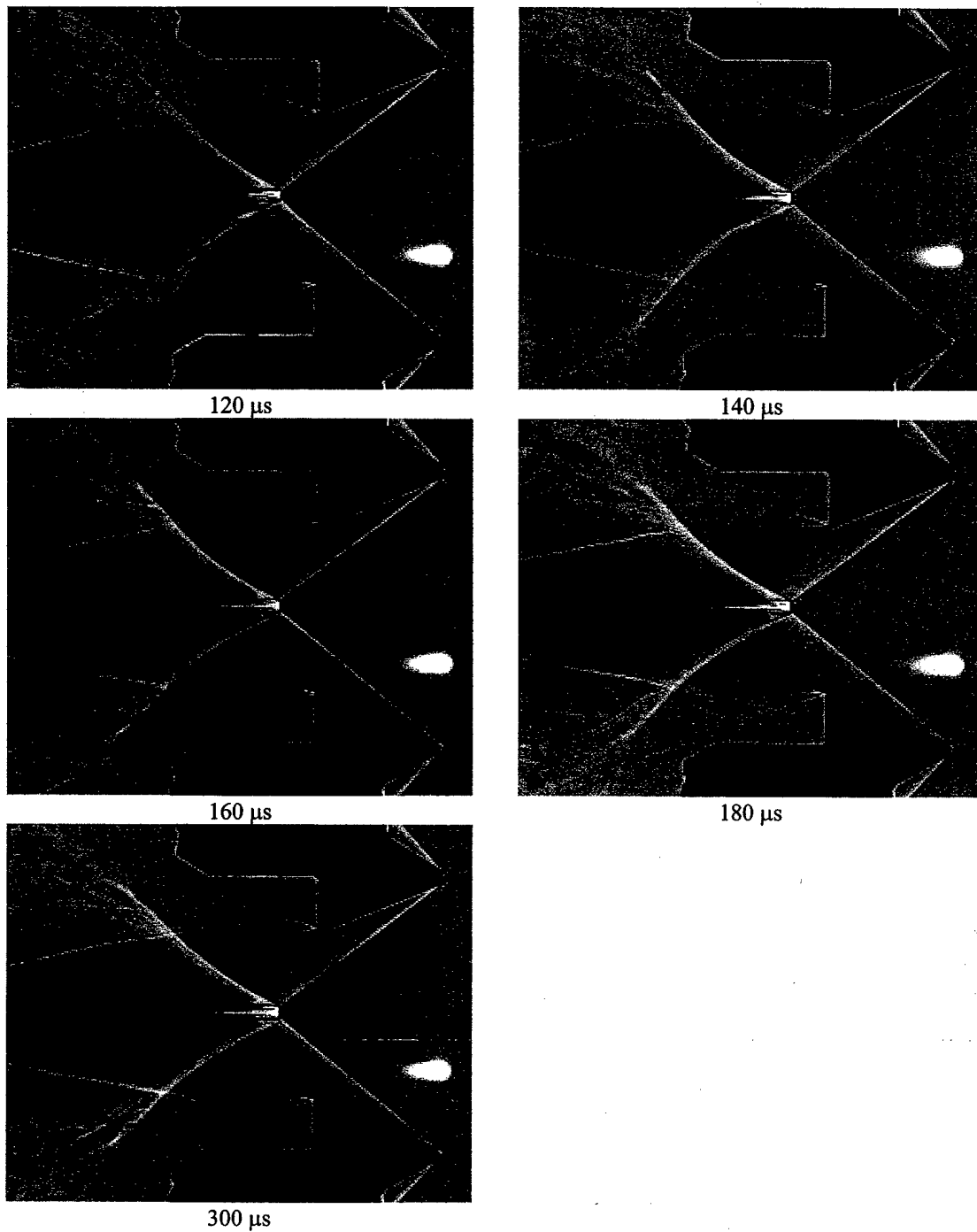


Figure 6.12 Instantaneous laser/argon schlieren time sequence of laser energy deposition at 215 mJ/pulse with deposition location $-0.05w$ from leading edge of wedges and $0.58w$ above leading edge for 120, 140, 160, 180, and 300, μs delays, $2g = 1.14w$, and $b = 2.2w$

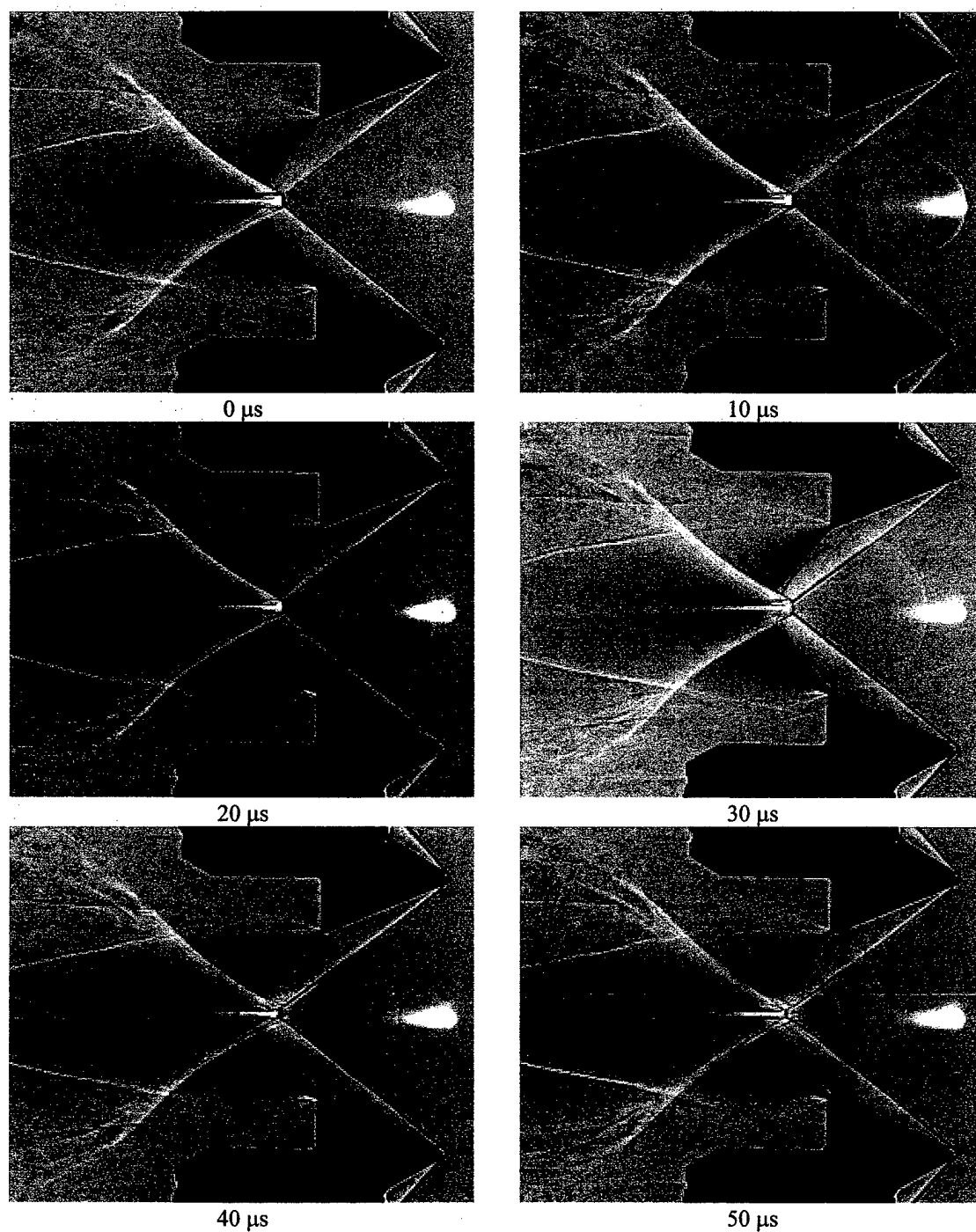


Figure 6.13 Instantaneous laser/argon schlieren time sequence of laser energy deposition at 215 mJ/pulse with deposition location $-0.02w$ from leading edge of wedges and $0.95w$ above leading edge for 0, 10, 20, 30, 40, and 50 μs delays, $2g = 1.14w$, and $b = 2.2w$

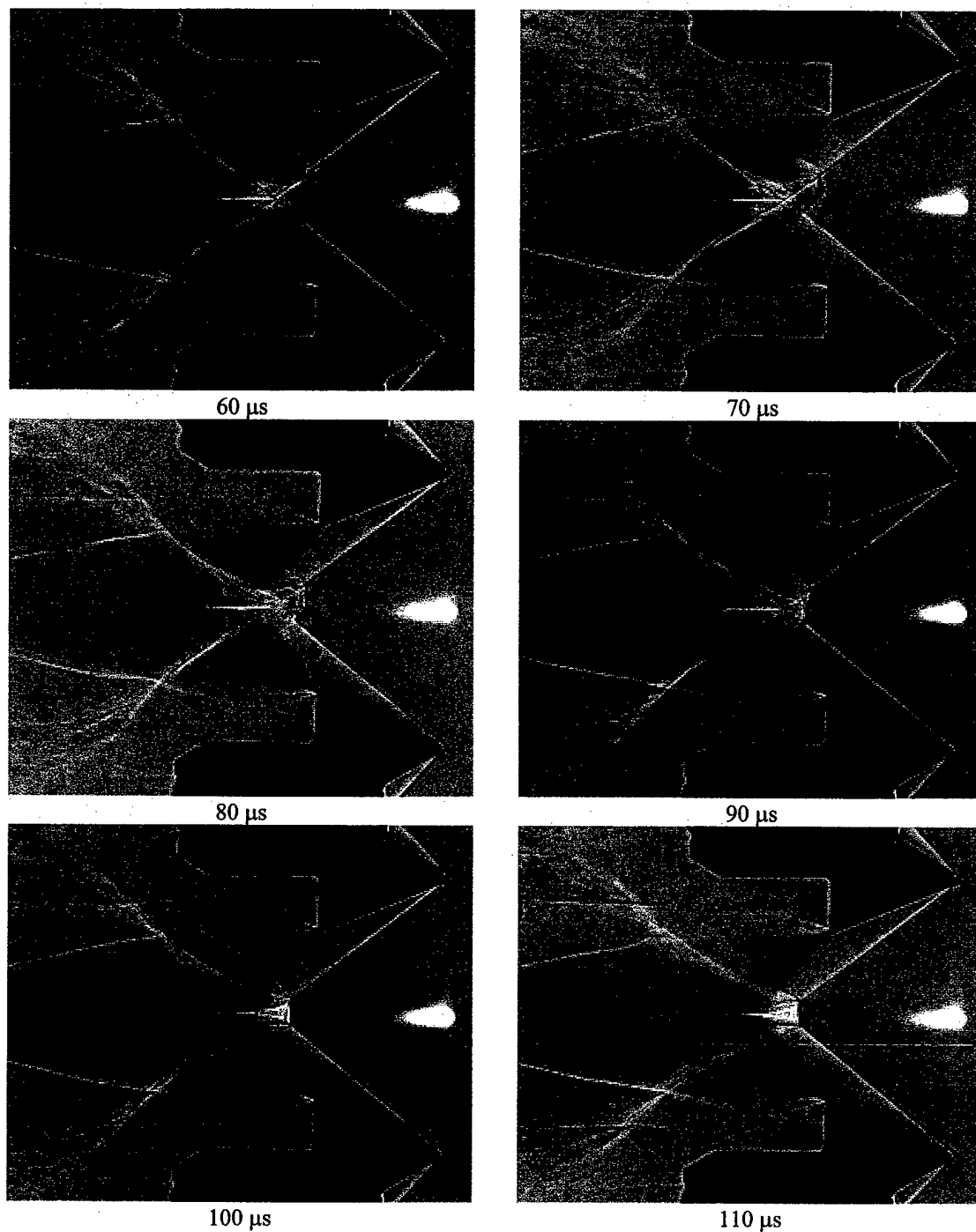


Figure 6.14 Instantaneous laser/argon schlieren time sequence of laser energy deposition at 215 mJ/pulse with deposition location $-0.02w$ from leading edge of wedges and $0.95w$ above leading edge for 60, 70, 80, 90, 100, and 110 μ s delays, $2g = 1.14w$, and $b = 2.2w$

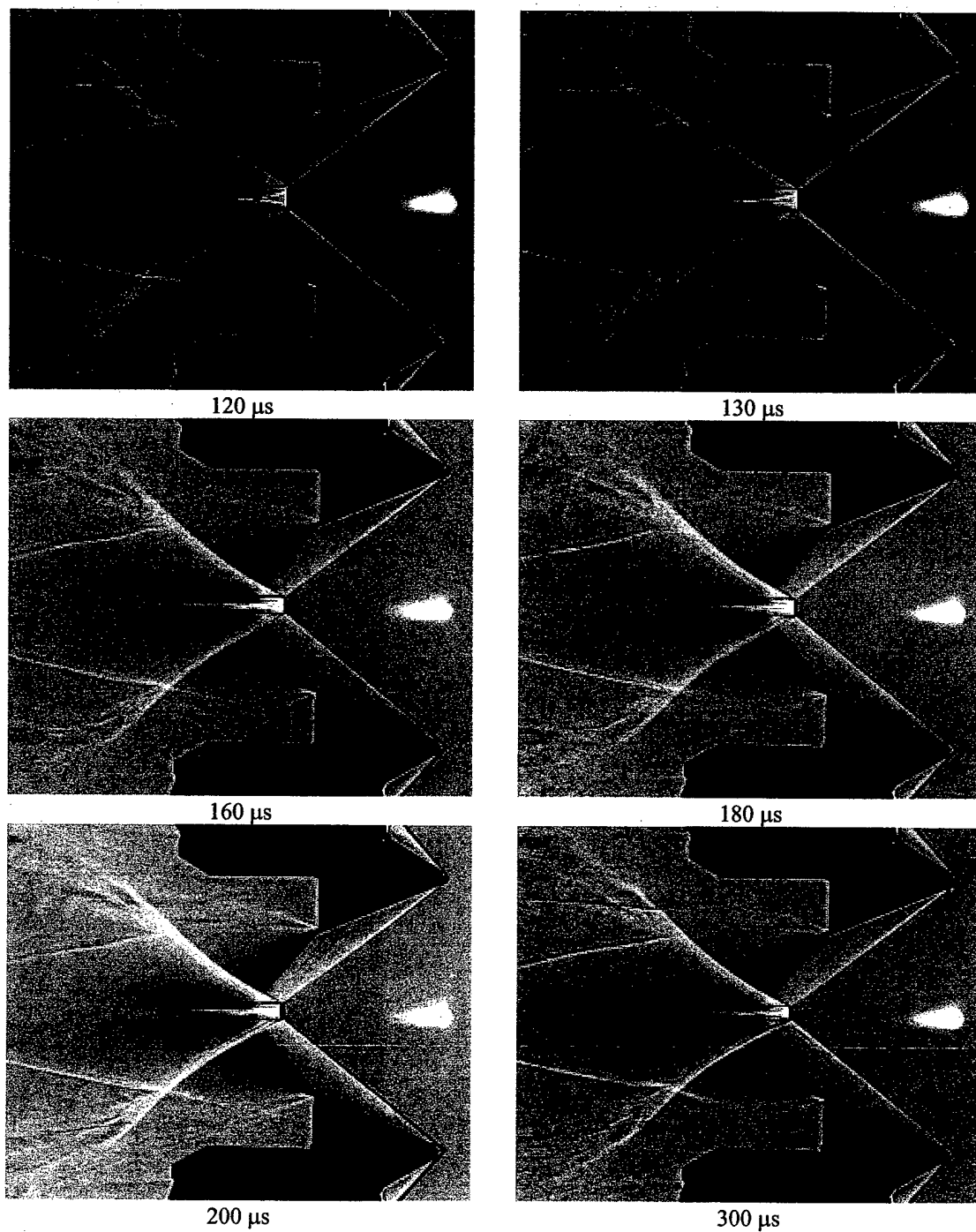


Figure 6.15 Instantaneous laser/argon schlieren time sequence of laser energy deposition at 215 mJ/pulse with deposition location $-0.02w$ from leading edge of wedges and $0.95w$ above leading edge for 120, 130, 160, 180, 200, and 300 μ s delays, $2g = 1.14w$, and $b = 2.2w$

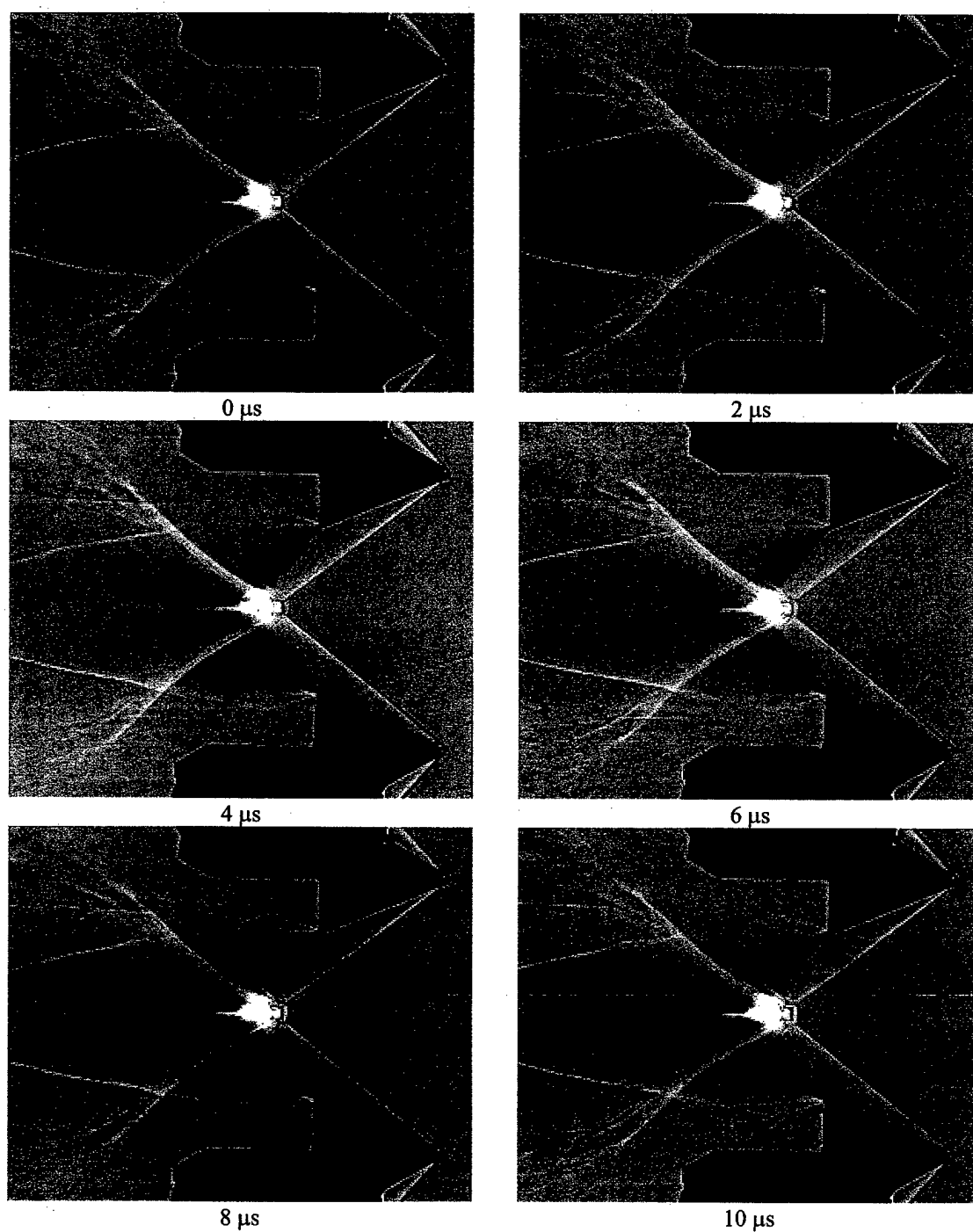


Figure 6.16 Instantaneous laser/argon schlieren time sequence of laser energy deposition at 215 mJ/pulse with deposition location $-1.31w$ from leading edge of wedges and $0.98w$ above leading edge for 0, 2, 4, 6, 8, and 10 μs delays, $2g = 1.14w$, and $b = 2.2w$

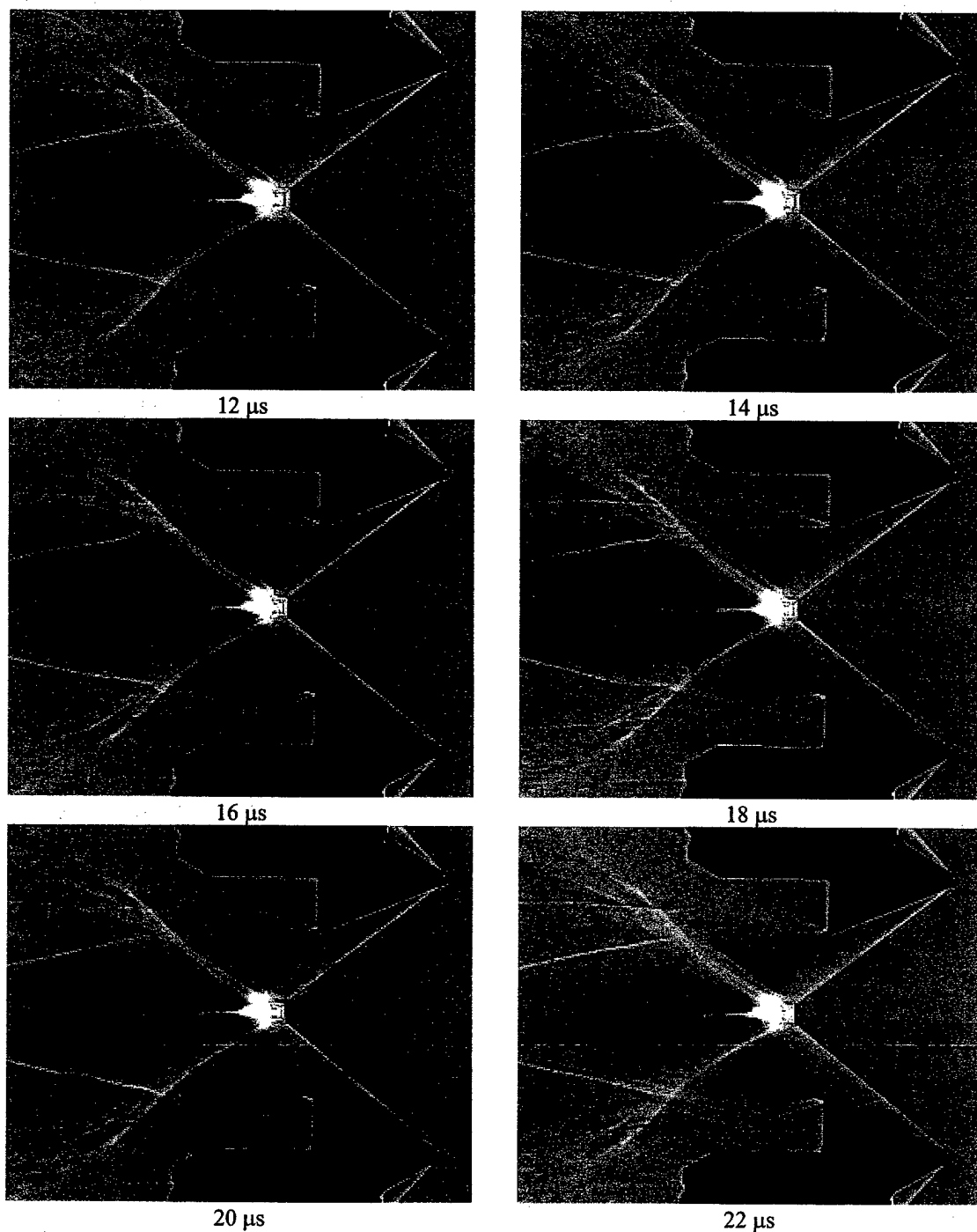


Figure 6.17 Instantaneous laser/argon schlieren time sequence of laser energy deposition at 215 mJ/pulse with deposition location $-1.31w$ from leading edge of wedges and $0.98w$ above leading edge for 12, 14, 16, 18, 20, and 22 μs delays, $2g = 1.14w$, and $b = 2.2w$

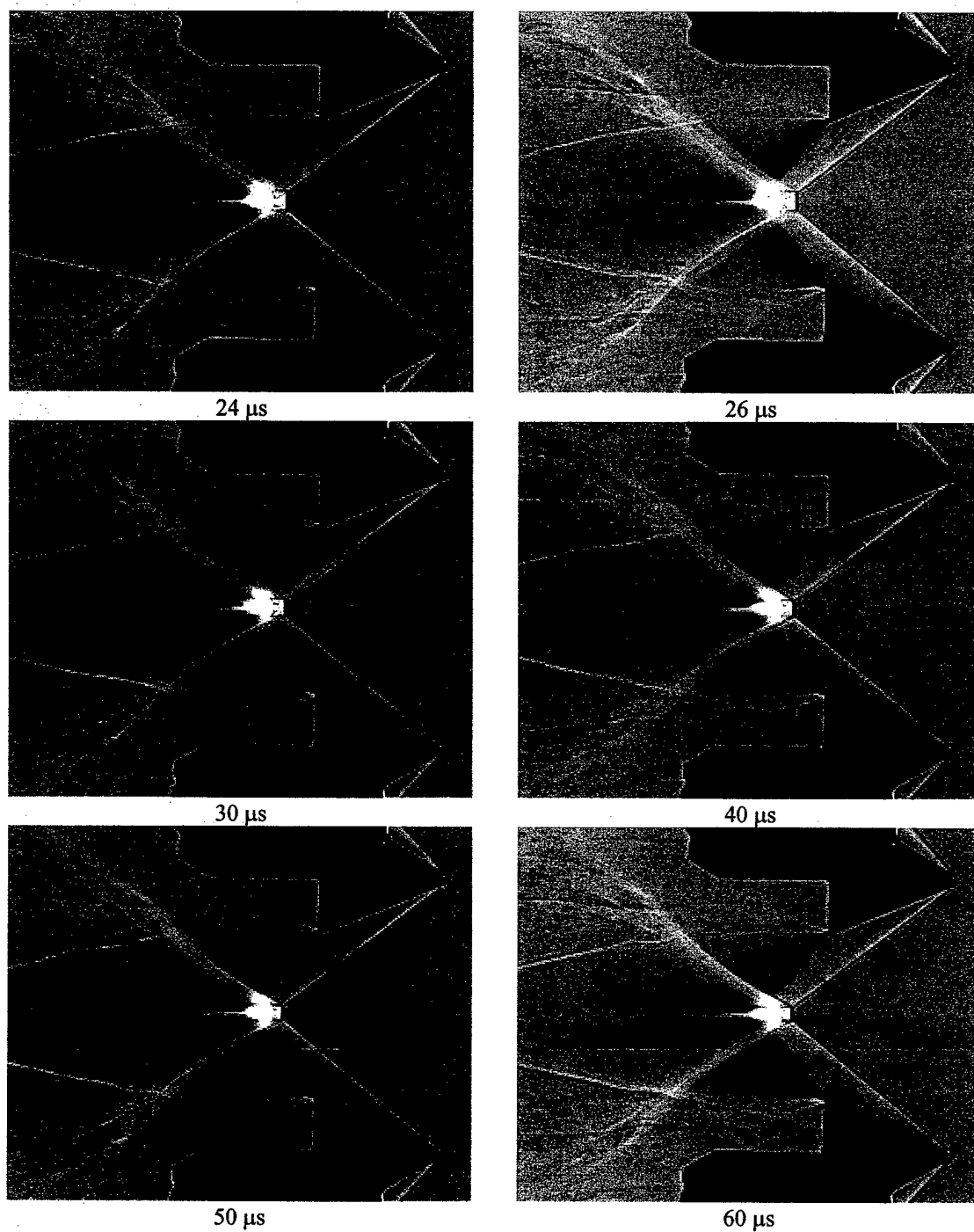
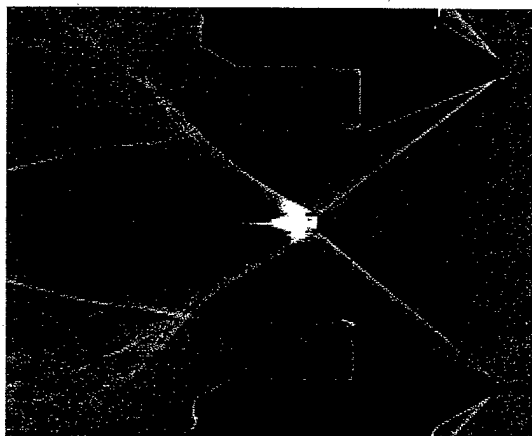


Figure 6.18 Instantaneous laser/argon schlieren time sequence of laser energy deposition at 215 mJ/pulse with deposition location $-1.31w$ from leading edge of wedges and $0.98w$ above leading edge for 24, 26, 30, 40, 50, and 60 μ s delays, $2g = 1.14w$, and $b = 2.2w$



70 μ s

Figure 6.19 Instantaneous laser/argon schlieren time sequence of laser energy deposition at 215 mJ/pulse with deposition location $-1.31w$ from leading edge of wedges and $0.98w$ above leading edge for 70 μ s delay, $2g = 1.14w$, and $b = 2.2w$

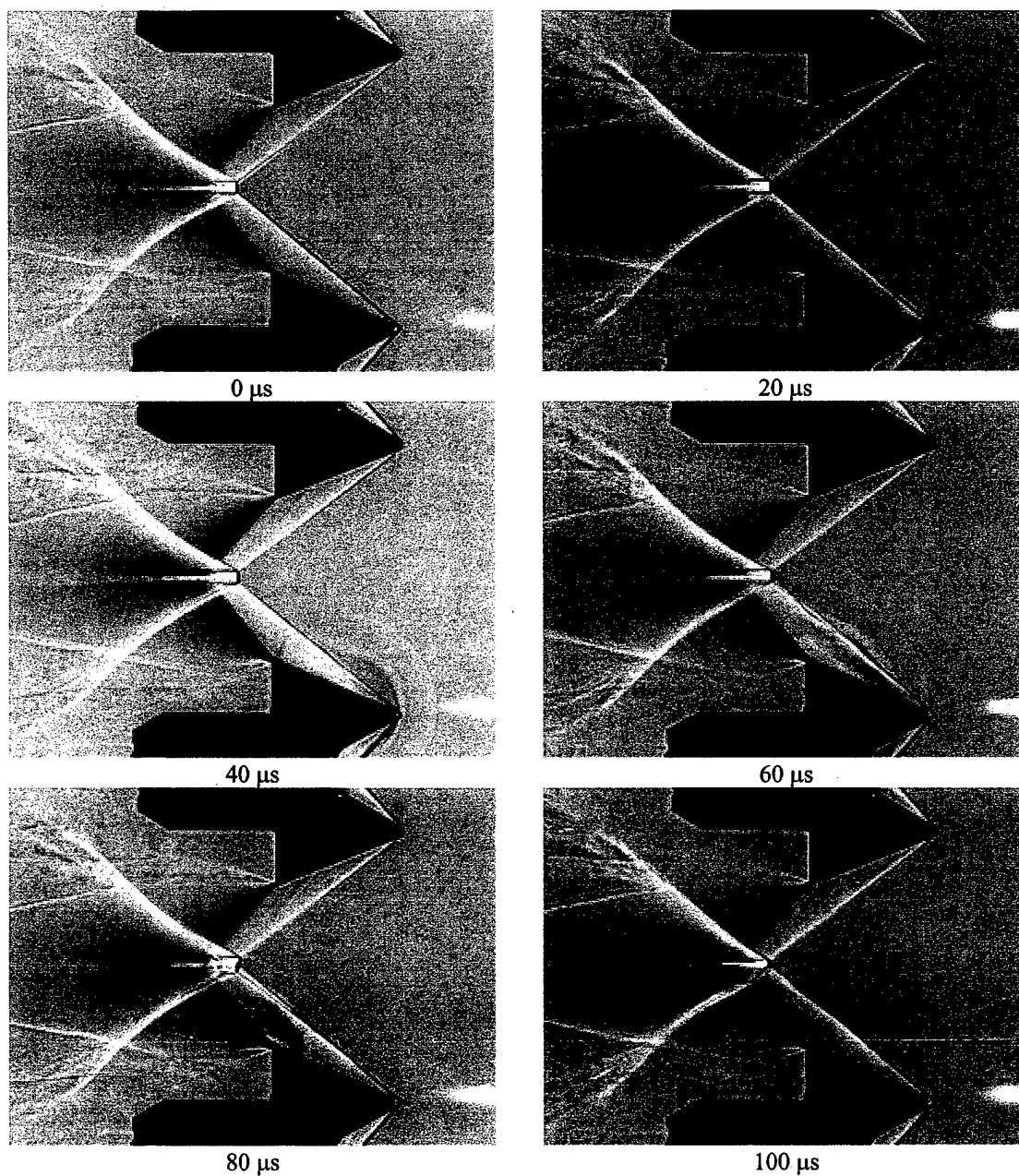


Figure 6.20 Instantaneous laser/argon schlieren time sequence of laser energy deposition at 215 mJ/pulse with deposition location $0.59w$ from leading edge of wedges and $0.05w$ above leading edge for 0, 20, 40, 60, 80, and 100 μ s delays, $2g = 1.14w$, and $b = 2.2w$

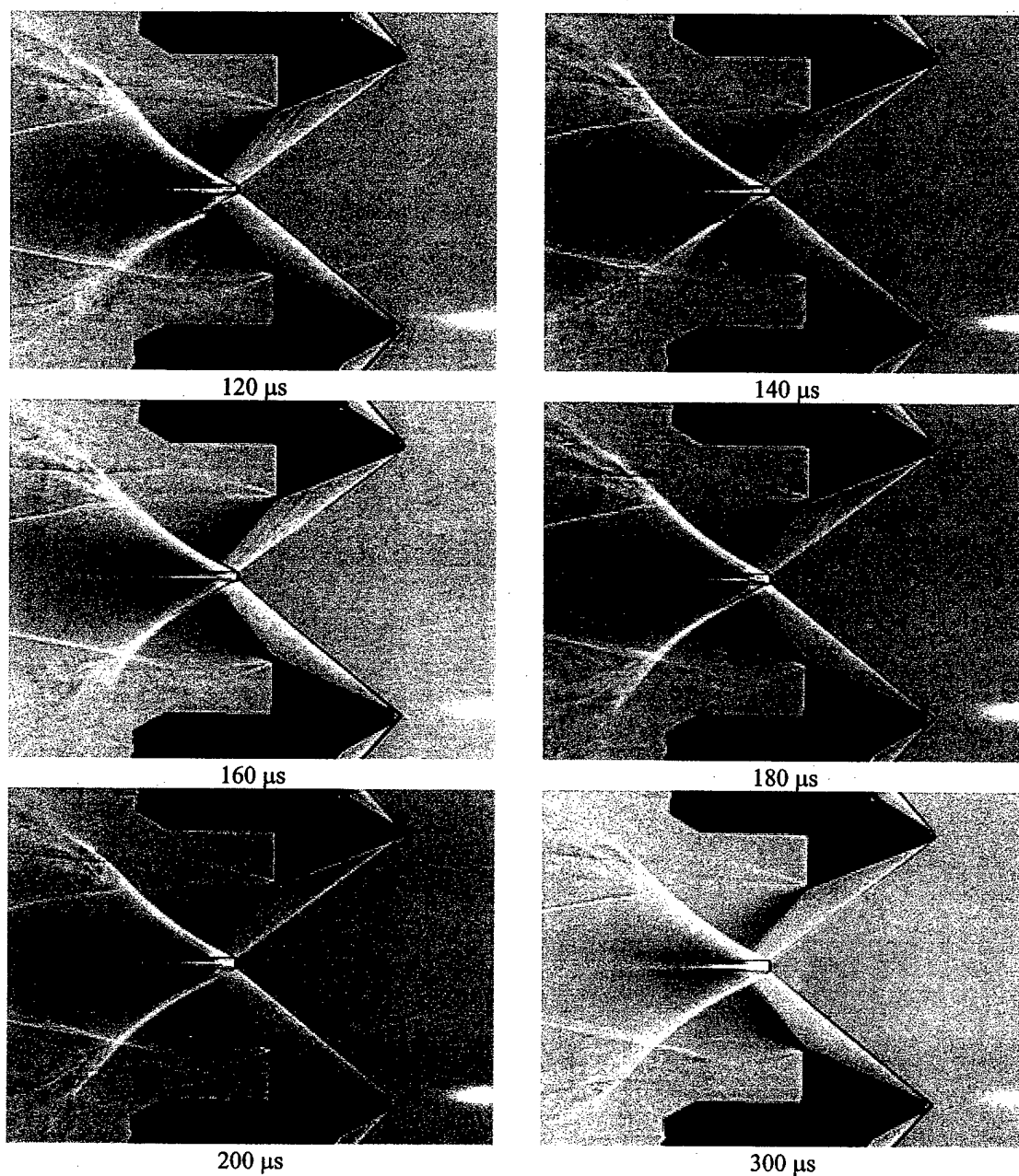


Figure 6.21 Instantaneous laser/argon schlieren time sequence of laser energy deposition at 215 mJ/pulse with deposition location $0.59w$ from leading edge of wedges and $0.05w$ above leading edge for 120, 140, 160, 180, 200, and 300 μ s delays, $2g = 1.14w$, and $b = 2.2w$

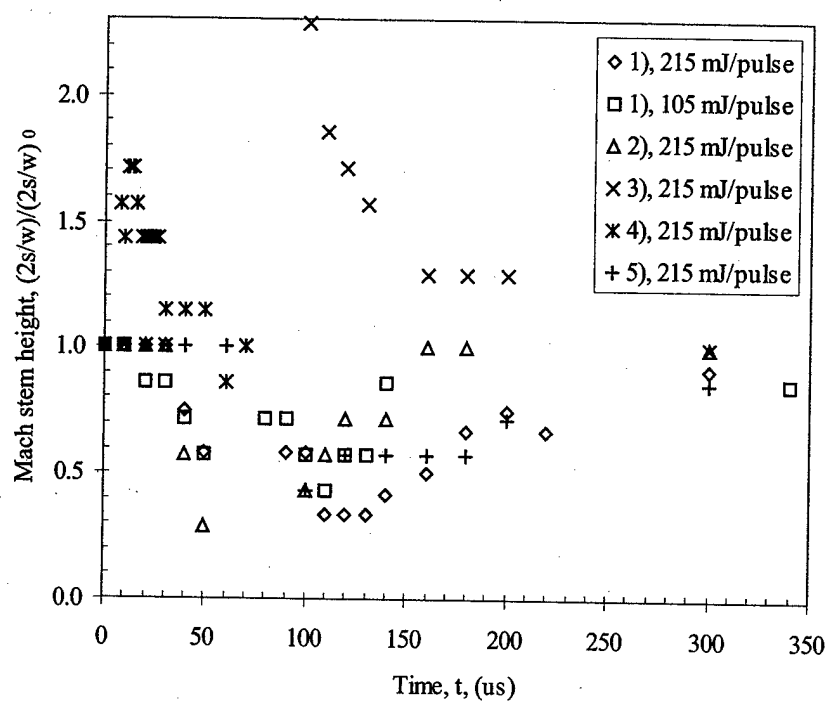


Figure 6.22 Mach stem heights after laser energy deposition at various locations for symmetric 22° wedges, $2g = 1.14w$ and $b = 2.2w$, the measurement uncertainty of the Mach stem height is $\pm 10\%$ (the position numbers and associated energy levels are noted in the legend and correspond to the numbers given in Figure 6.1)

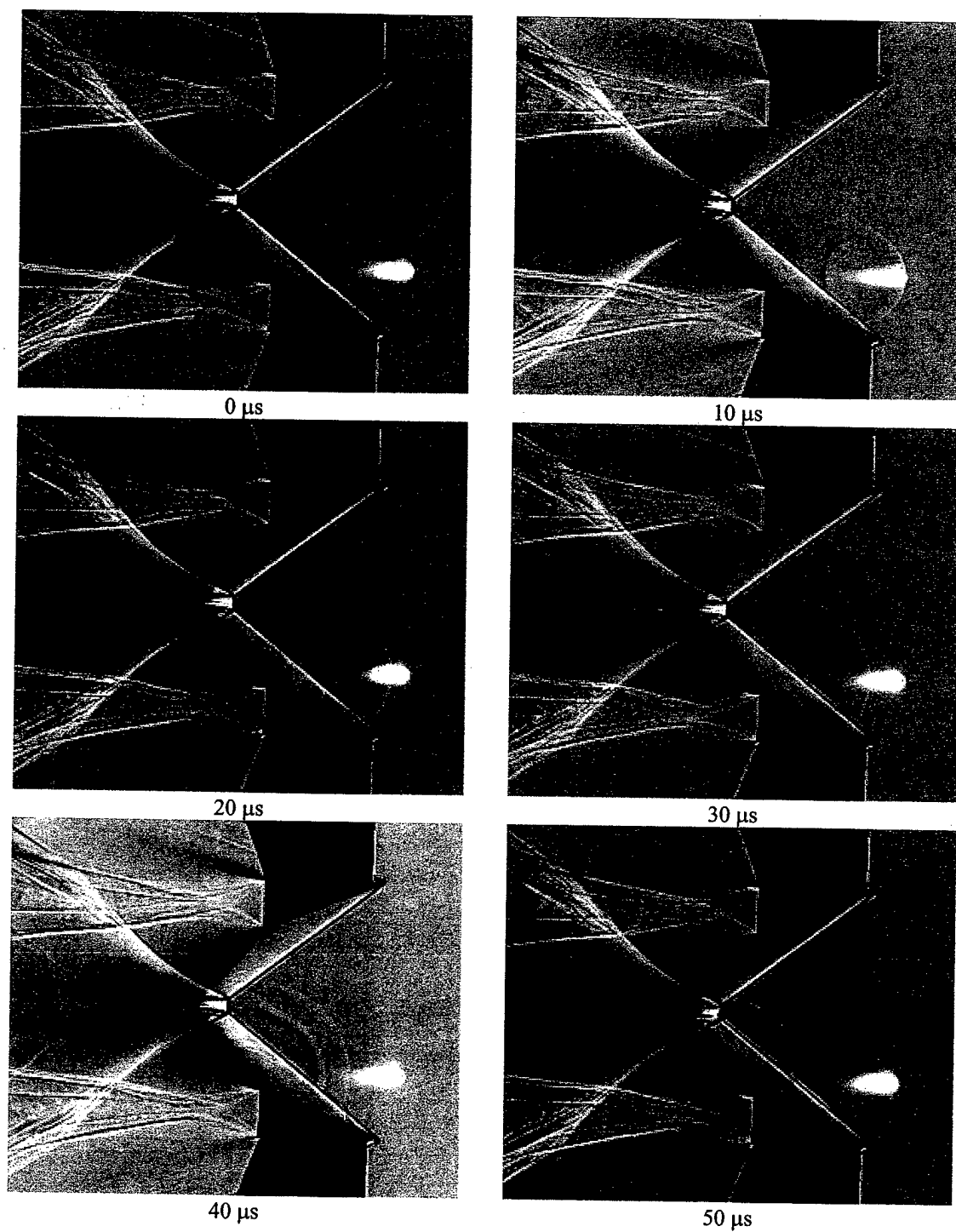


Figure 6.23 Instantaneous laser/argon schlieren time sequence of laser energy deposition at 215 mJ/pulse with deposition location $0.12w$ upstream of leading edge and $0.47w$ above leading edge for 0, 10, 20, 30, 40, and 50 μs delays, $2g = 1.19w$, and $b = 4w$

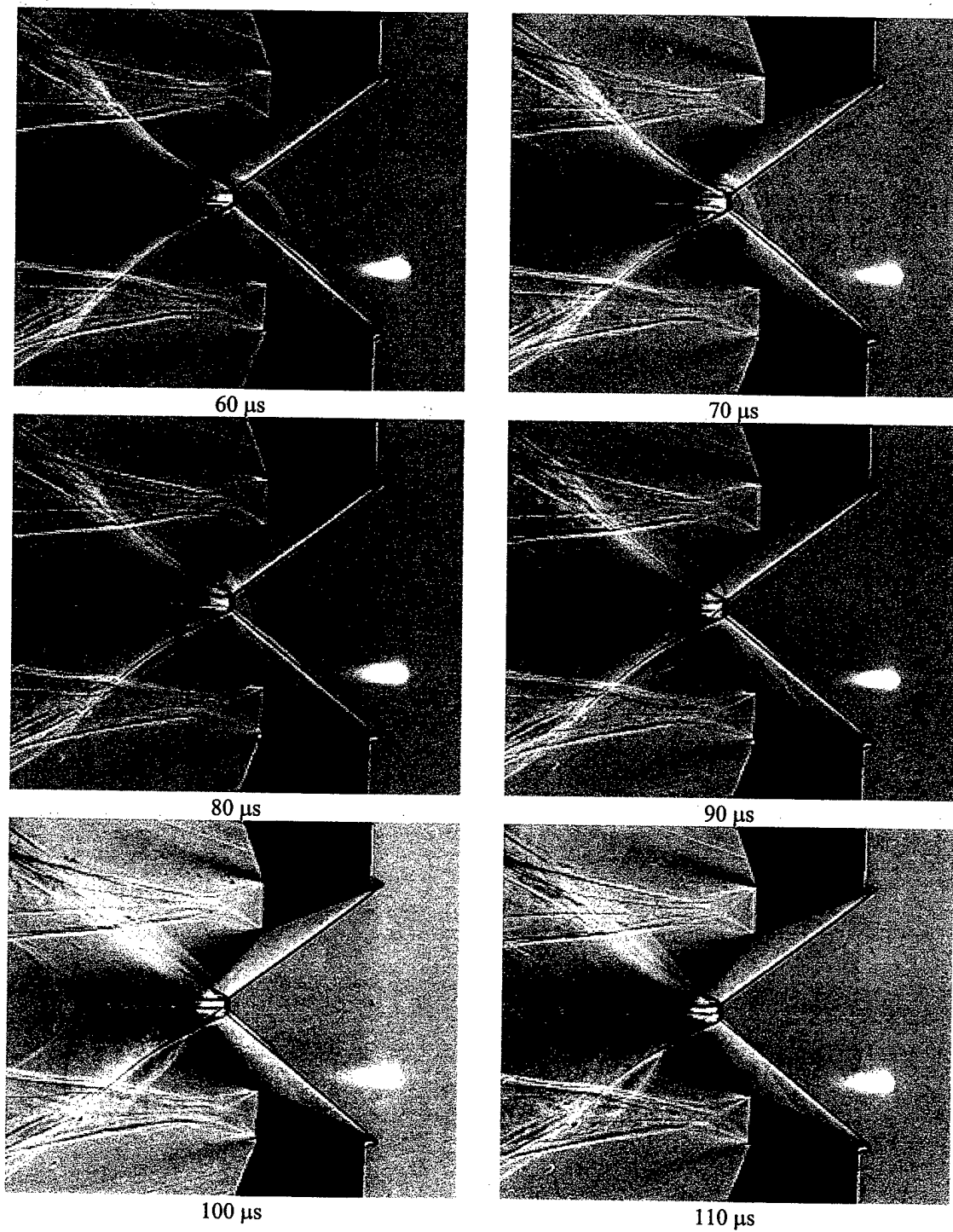


Figure 6.24 Instantaneous laser/argon schlieren time sequence of laser energy deposition at 215 mJ/pulse with deposition location $0.12w$ upstream of leading edge and $0.47w$ above leading edge for 60, 70, 80, 90, 100, and 110 μ s delays, $2g = 1.19w$, and $b = 4w$

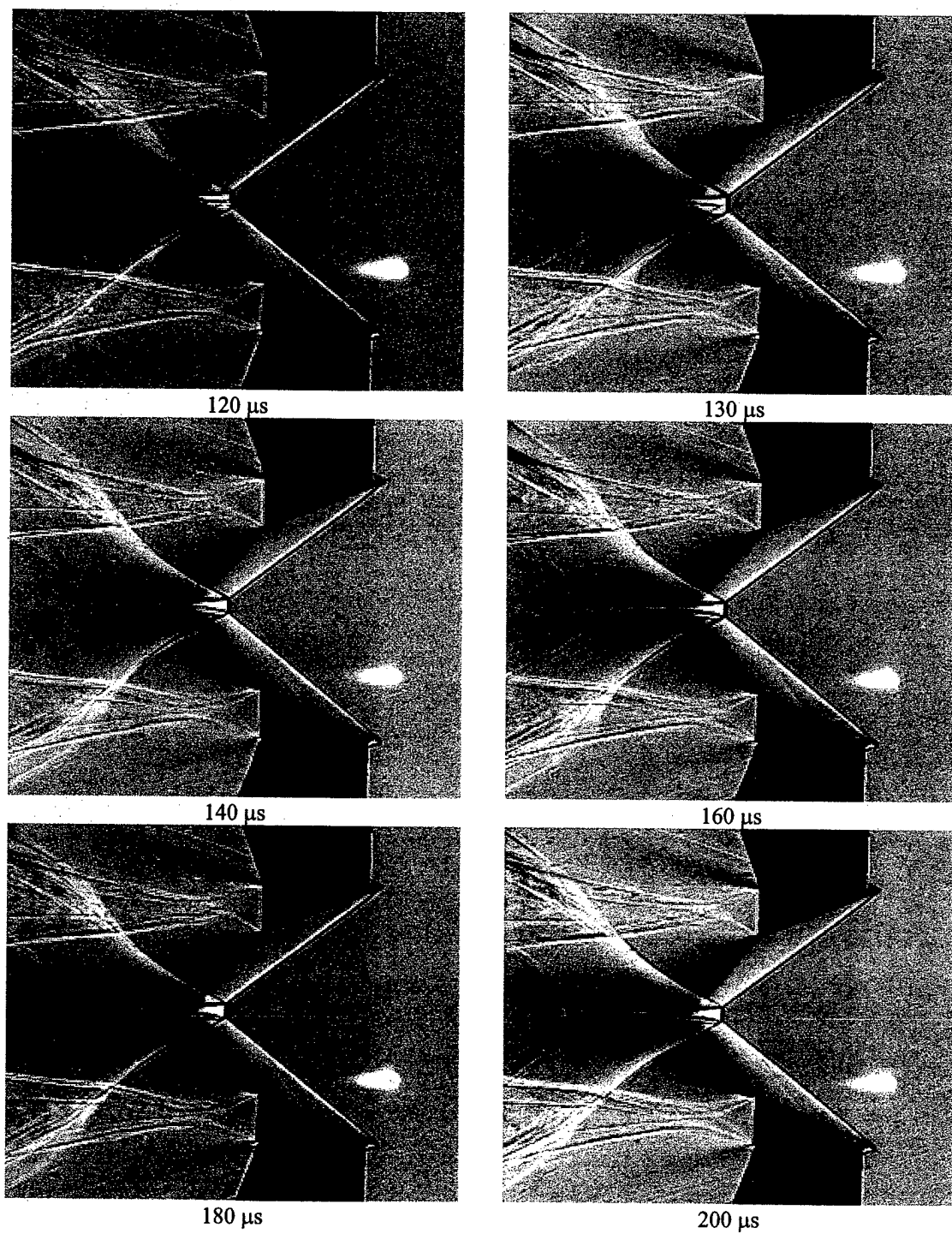
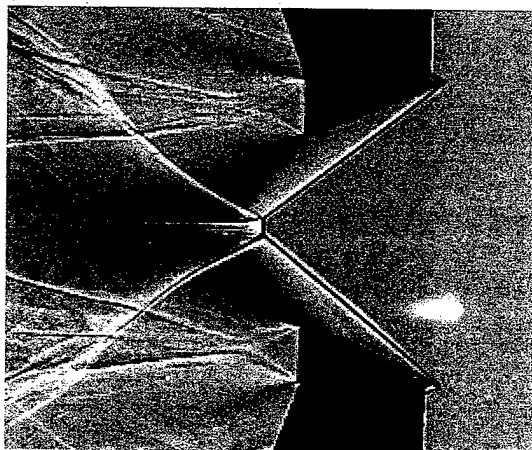


Figure 6.25 Instantaneous laser/argon schlieren time sequence of laser energy deposition at 215 mJ/pulse with deposition location $0.12w$ upstream of leading edge and $0.47w$ above leading edge for 120, 130, 140, 160, 180, and 200 μ s delays, $2g = 1.19w$, and $b = 4w$



220 μ s

Figure 6.26 Instantaneous laser/argon schlieren time sequence of laser energy deposition at 215 mJ/pulse with deposition location $0.12w$ upstream of leading edge and $0.47w$ above leading edge for 220 μ s delay, $2g = 1.19w$, and $b = 4w$

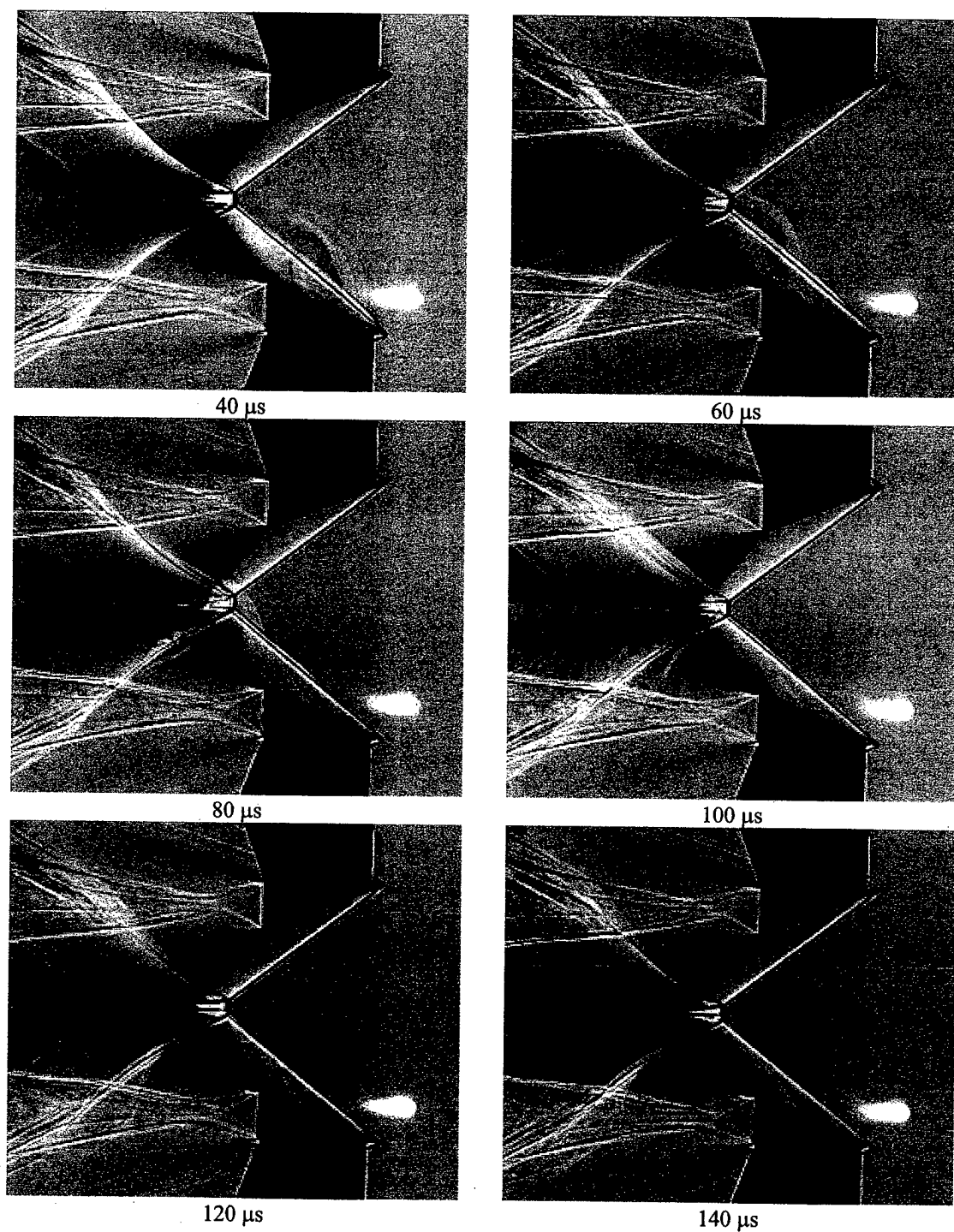


Figure 6.27 Instantaneous laser/argon schlieren time sequence of laser energy deposition at 215 mJ/pulse with deposition location $0.23w$ upstream of leading edge and $0.25w$ above leading edge for 120, 130, 140, 160, 180, and 200 μs delays, $2g = 1.19w$, and $b = 4w$

6.3 Comparison with Computational Model

In this Section the experimental schlieren images are compared to the computational schlieren images for one deposition location. The tunnel operational parameters for the experiment are listed in Table 6.5, and flow parameters for the wedges are listed in Table 6.4. Figure 6.28 through Figure 6.35 give the comparison for the experimental and numerical simulation for a sequence of images for the interaction of the laser energy deposition upstream of symmetric 22 degree wedges. The experimental schlieren images are an ensemble average of 5 to 10 images taken with the Strobotac schlieren system (see Section 3.2.1).

The computational domain is $3.5w \times 4w \times 2.2w$ where the dimensions are for the streamwise, vertical, and spanwise directions, respectively. The Euler simulation was performed with GASP. [3] Freestream boundary conditions were applied at the upstream boundary. Extrapolation conditions were applied at the outflow boundaries, and the inviscid slip condition applied at the boundaries of the wedges. The laser perturbation was modeled as a spherical temperature variation with a Gaussian distribution (see Section 2.3.2). The conditions for the simulation are second-order accuracy in space and second-order implicit relaxation algorithm in time. The grid resolution is such that there are 11 to 12 grid points along the Mach stem for the initial steady state condition for the Mach reflection in the shock intersection region.

The freestream density used in the simulation was 1.2 kg/m^3 compared to the freestream value of 0.66 kg/m^3 used in the simulation. This effectively reduces the energy level of the laser perturbation used in the simulation. Since the Euler equations are used and the laser spot is modeled as an initial temperature and pressure perturbation, then all the dimensionless dependent variables, e.g.,

$$\frac{u}{U_\infty}, \frac{v}{U_\infty}, \frac{w}{U_\infty}, \frac{p}{p_\infty}, \frac{\rho}{\rho_\infty}, \text{ and } \frac{T}{T_\infty}$$

are functions of the following dimensionless independent variables

$$\frac{x}{L}, \frac{y}{L}, \frac{z}{L}, \text{ and } \frac{tU_\infty}{L}$$

where L is a length scale, e.g., w , the wedge length shown in Figure 2.8, and the parameters

$$M_\infty, \frac{\Delta T_0}{T_\infty}, \frac{r_0}{L}, \text{ and } \gamma.$$

The temperature distribution is defined by (see Section 2.3.2)

$$\Delta T_0 = \frac{E}{\pi^{3/2} r_0^3 \rho_\infty c_v} \quad (6.1)$$

The temperature distribution used in the simulation is defined by

$$\left. \frac{\Delta T_0}{T_\infty} \right|_c = \frac{E_c}{\pi^{3/2} r_0^3 \rho_{\infty_c} c_{v_c}} \quad (6.2)$$

where the subscript c indicates the values used in the computation. The computational and the experimental densities are related by

$$\rho_{\infty_c} = \alpha \rho_{\infty_e} = 1.82 \rho_{\infty_e} \quad (6.3)$$

where the subscript e refers to the experimental condition. The computational temperature perturbation will then be given by

$$\left. \frac{\Delta T_0}{T_\infty} \right|_c = \frac{1}{\alpha} \left. \frac{E}{\pi^{3/2} r_0^3 \rho_{\infty_c} c_v} \right|_e \quad (6.4)$$

Therefore, the effective energy perturbation used in the numerical simulation was 155 mJ/pulse. Measurements made of the blast wave speed show the energy level to be approximately 130 mJ/pulse.

The computation was performed in two steps. First, the steady state solution for the symmetric wedges is converged with the simulation conditions corresponding to the tunnel test conditions. Next, the laser perturbation is applied as an instantaneous temperature distribution at the location corresponding to the experimental deposition location. The pressure distribution for this region is then determined from the ideal gas law whereby the density is assumed constant. The density in the perturbation region is assumed constant according to mass conservation. The mass cannot flux out of the region during the instantaneous laser perturbation. For the steady state condition, the measured Mach stem height from the numerical simulation is within 2% of the experimentally measured Mach stem height.

As seen in Figure 6.28, from 0-10 μ s the blast wave initially propagates outward from the laser energy deposition region and the spot begins to move downstream. Note: a piece of tape on the test section window is used to block the flash from the laser spark in the experimental images. This piece of tape is seen as the dark square in the experimental images. The flash from this laser spark saturates regions of interest in the Strobotac generated schlieren images.

From 20-30 μs , the blast wave interacts with the oblique shock, and by 30 μs the thermal spot begins to distort the bow shock forward. This perturbation propagates to the reflection region and begins to decrease the Mach reflection by 60 to 70 μs . As the thermal spot moves downstream the Mach stem continues to decrease due to the thermal interaction and the upstream blast wave interactions. Both the experimental and numerical results show the same trends of the Mach stem reduction. However, the flow perturbations are much larger in the numerical simulation. Part of this discrepancy can be attributed to the integral effect along the spanwise direction of the experimental schlieren. The numerical images shown, are center plane images and have not been integrated in the spanwise direction. This disparity can readily be seen in the images from 60 – 100 μs . There are other factors that might also contribute to this: 1) The numerical simulation is an Euler model and does not account for viscous effects. The experimental data definitely has viscous effects, i.e., boundary layer growth along the wedge surfaces, and shear layer growth downstream of the intersection region. 2) In the numerical simulation, the energy perturbation is a simplified gasdynamic model with spherical symmetry. It does not include any plasma effects, as well as, any geometrical asymmetries and initial vorticity. Future simulations with the models currently under development by Kandala and Candler [71] will determine the plasma and asymmetrical effects. 3) There is no turbulence modeled in the simulation. There is turbulence in the wind tunnel [136] and this leads to the back transition to the Mach reflection after the perturbation in the experimental data. 4) Lastly, the energy level used in the simulation could be overestimated. The measurements for the energy deposition levels give an upper bound (see Section 4.3). Blast wave measurements in quiescent air have accounted for some of the energy level discrepancy (see Section 4.4). Future spectrographic measurements are needed for more accurate temperature determination within the energy deposition region and for the calibration of the energy levels used in the models. Note that these spectrographic measurements will also aid in the verification of the plasmadynamic modeling of Kandala and Candler. [71]

The Mach stem height measurements from the experimental images and the numerical schlieren images are presented in Figure 6.36. In the experiment, the Mach stem is reduced to approximately 25% of its original height, and then resumes its initial height by 500 μs . In the numerical simulation, the Mach stem is transitioned to a regular reflection and remains stable for simulation times out to 230 μs . The simulation demonstrates the ability of the laser perturbation to effectively transition the solution of the Mach reflection

to the regular reflection within the dual solution domain. The experimental and the simulation results show a definite reduction in Mach stem height. Furthermore, the simulation effectively transitions the Mach stem to a stable regular reflection within the dual solution domain.

The author wishes to thank Dr. Hong Yan for her work in completing the numerical simulations.

Table 6.5 Tunnel operation parameters for the wedge tests

Mach number	3.45
Reynolds number based on wedge length, w , $Re_w = \frac{\rho V w}{\mu}$	1.750×10^6
Freestream viscosity, μ	$5.753 \times 10^{-6} \frac{\text{kg}}{\text{m s}}$
Stagnation pressure, p_0	$1.069 \times 10^6 \text{ Pa}$
Stagnation temperature, T_0	283 K
Stagnation density, ρ_0	$13.162 \frac{\text{kg}}{\text{m}^3}$
Freestream temperature, T	83.7 K
Freestream pressure, p	$1.505 \times 10^4 \text{ Pa}$
Freestream density, ρ	$0.626 \frac{\text{kg}}{\text{m}^3}$
Freestream velocity, V	632.6 m/s
Freestream speed of sound, a	183.4 m/s
Pitot pressure, p_{02}	$2.376 \times 10^5 \text{ Pa}$
Pitot density, ρ_{02}	$2.927 \frac{\text{kg}}{\text{m}^3}$

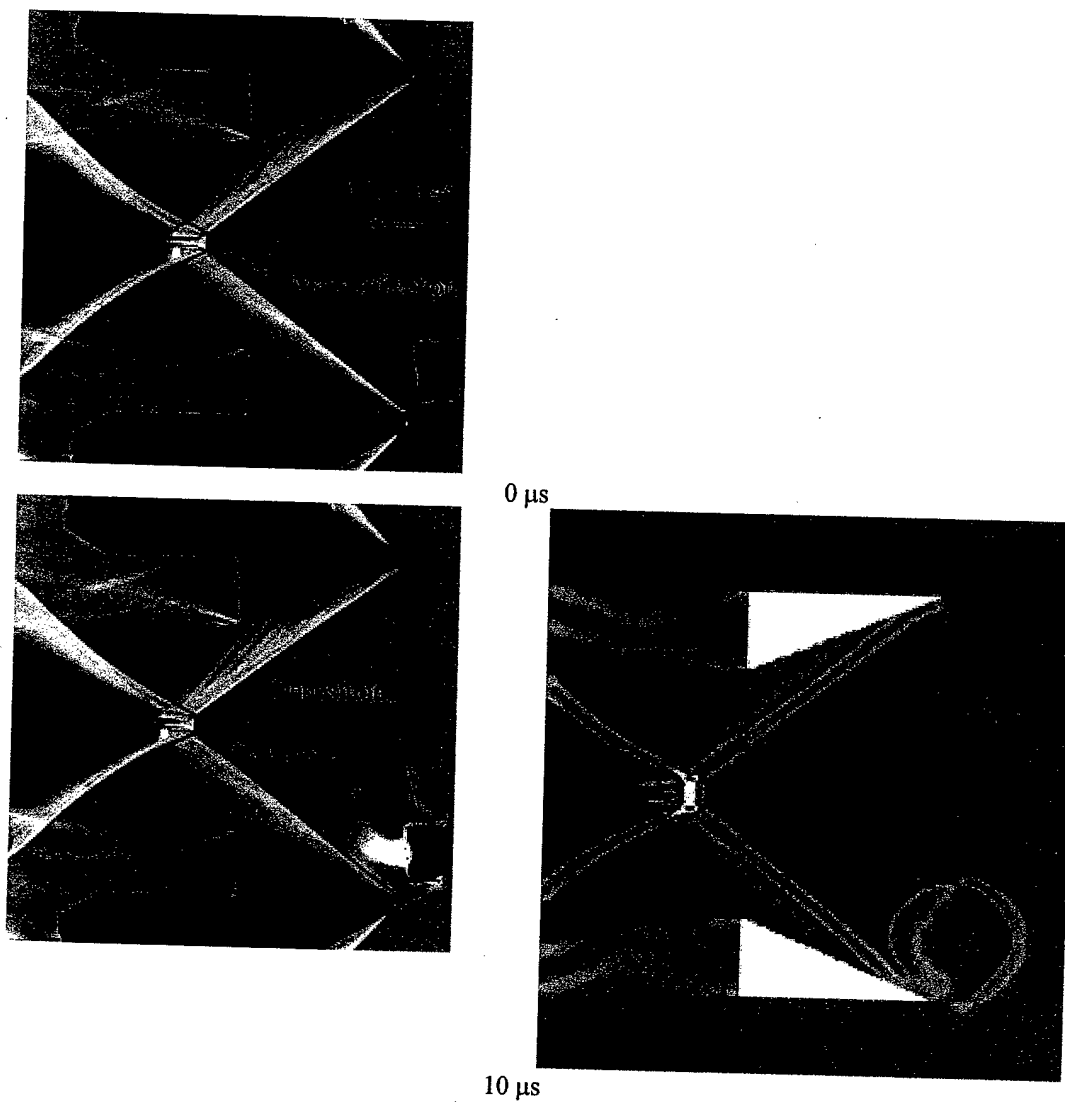


Figure 6.28 Experimental and numerical schlieren comparison for laser energy deposition upstream of 22 degree symmetric wedges at Mach 3.45 for time delays of 0 and 10 μ s

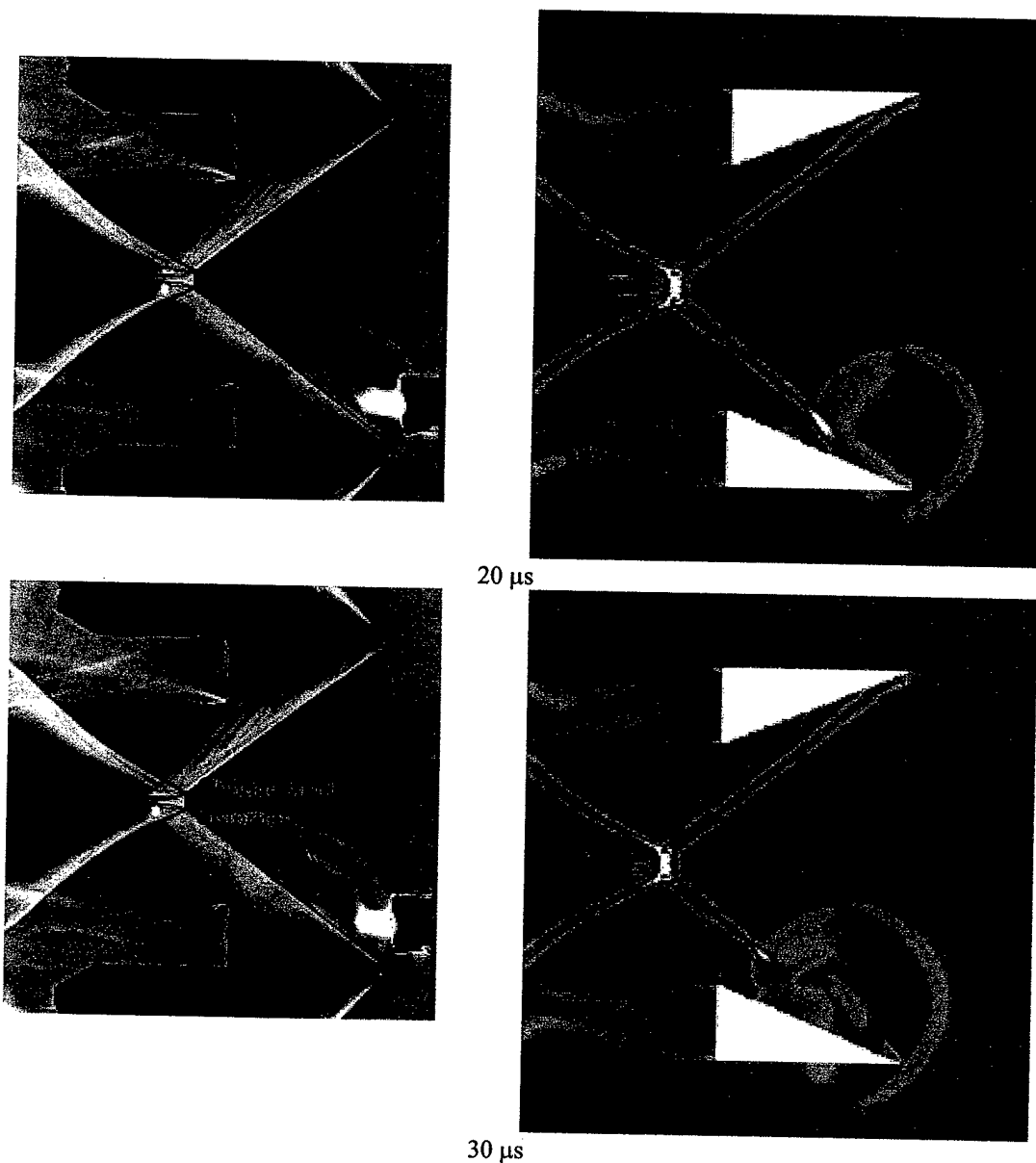


Figure 6.29 Experimental and numerical schlieren comparison for laser energy deposition upstream of 22 degree symmetric wedges at Mach 3.45 for time delays of 20 and 30 μs

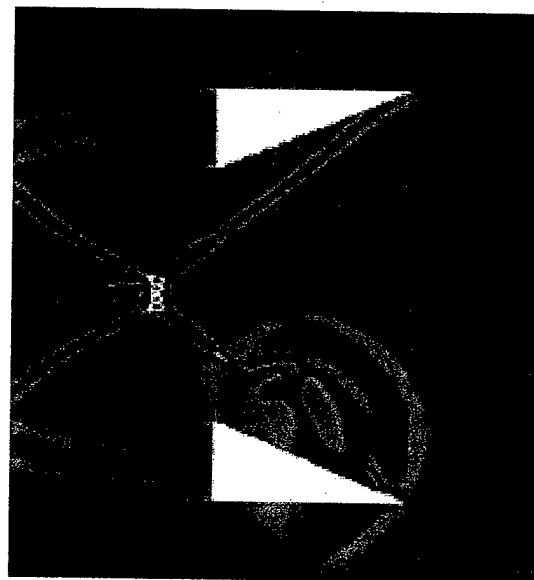
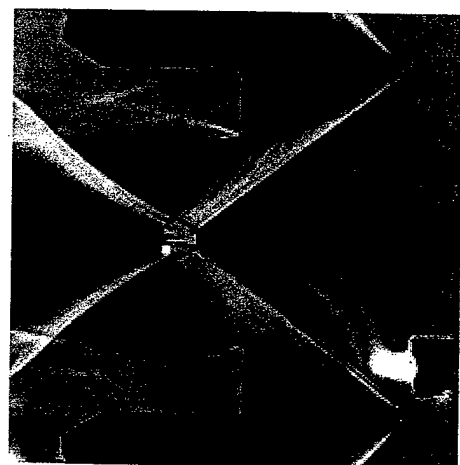
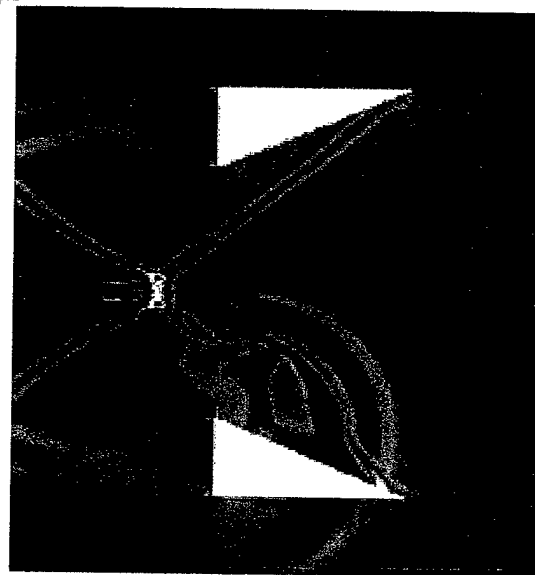
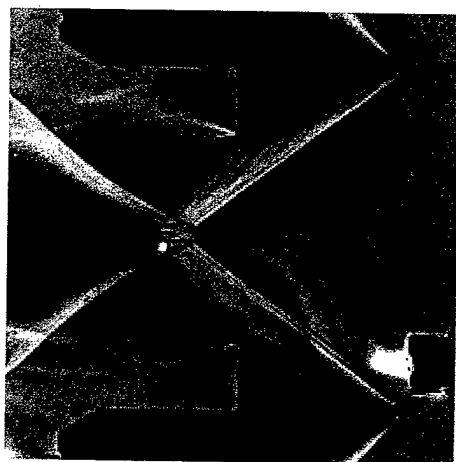
40 μ s50 μ s

Figure 6.30 Experimental and numerical schlieren comparison for laser energy deposition upstream of 22 degree symmetric wedges at Mach 3.45 for time delays of 40 and 50 μ s

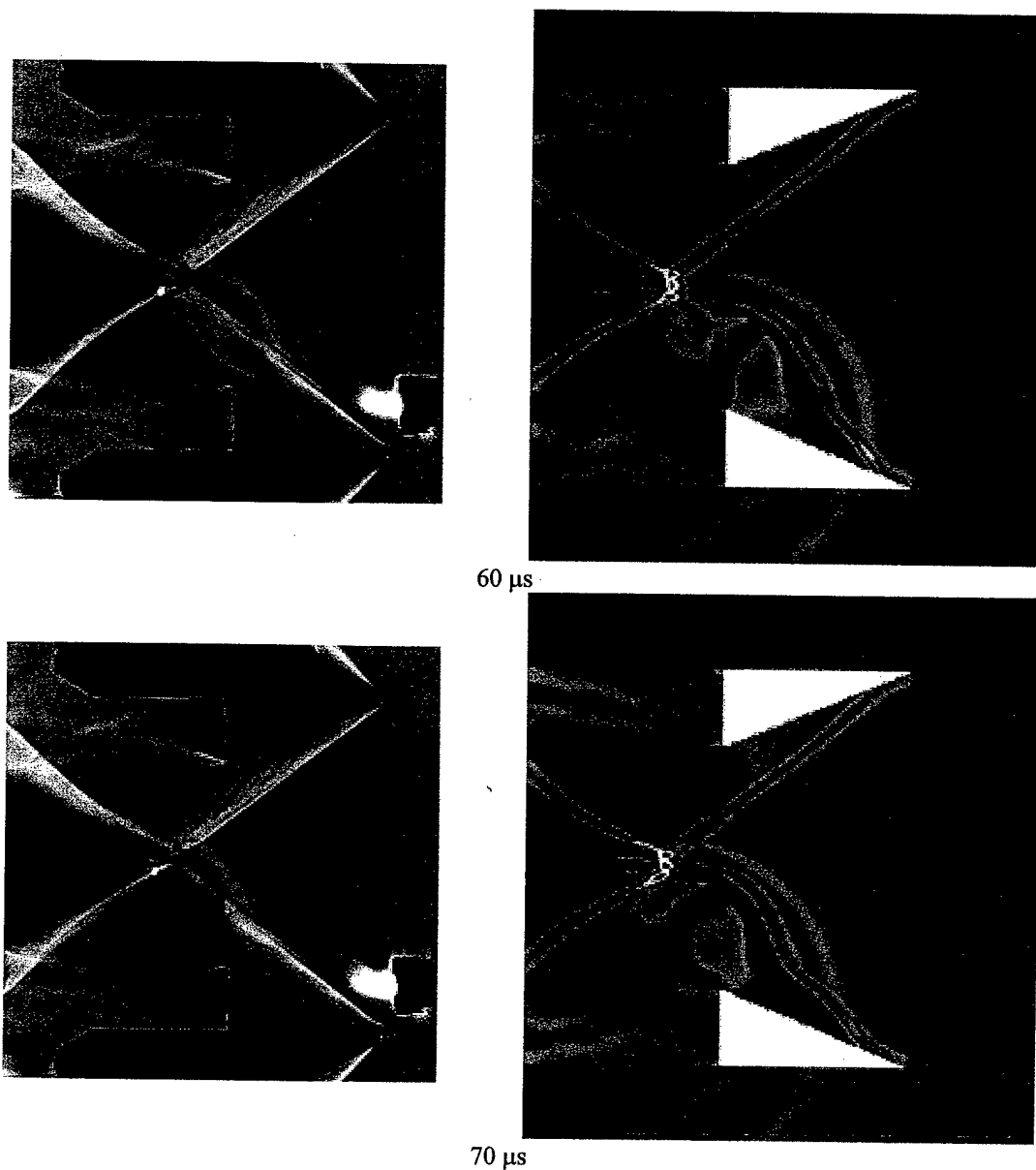


Figure 6.31 Experimental and numerical schlieren comparison for laser energy deposition upstream of 22 degree symmetric wedges at Mach 3.45 for time delays of 60 and 70 μs

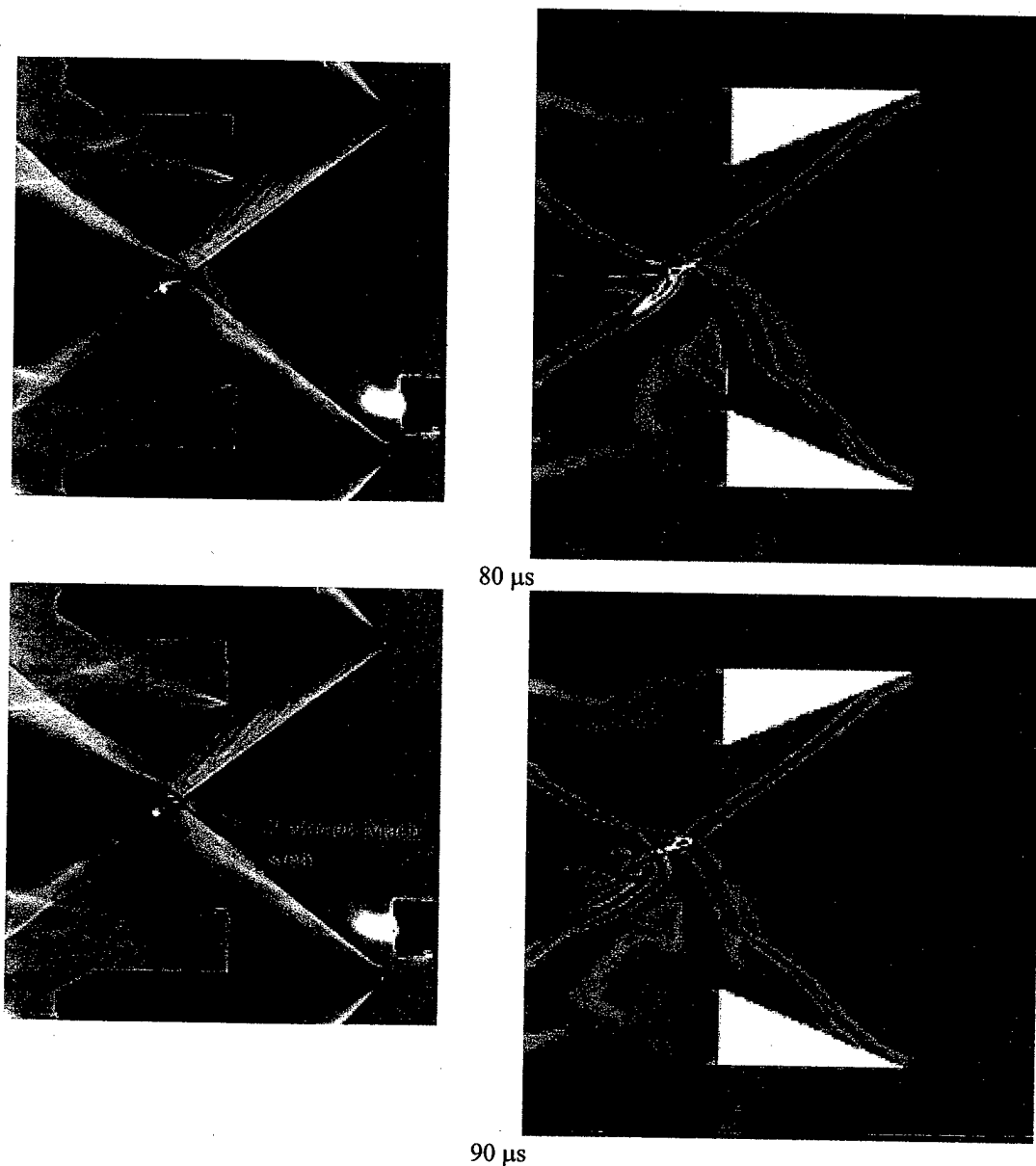


Figure 6.32 Experimental and numerical schlieren comparison for laser energy deposition upstream of 22 degree symmetric wedges at Mach 3.45 for time delays of 80 and 90 μ s

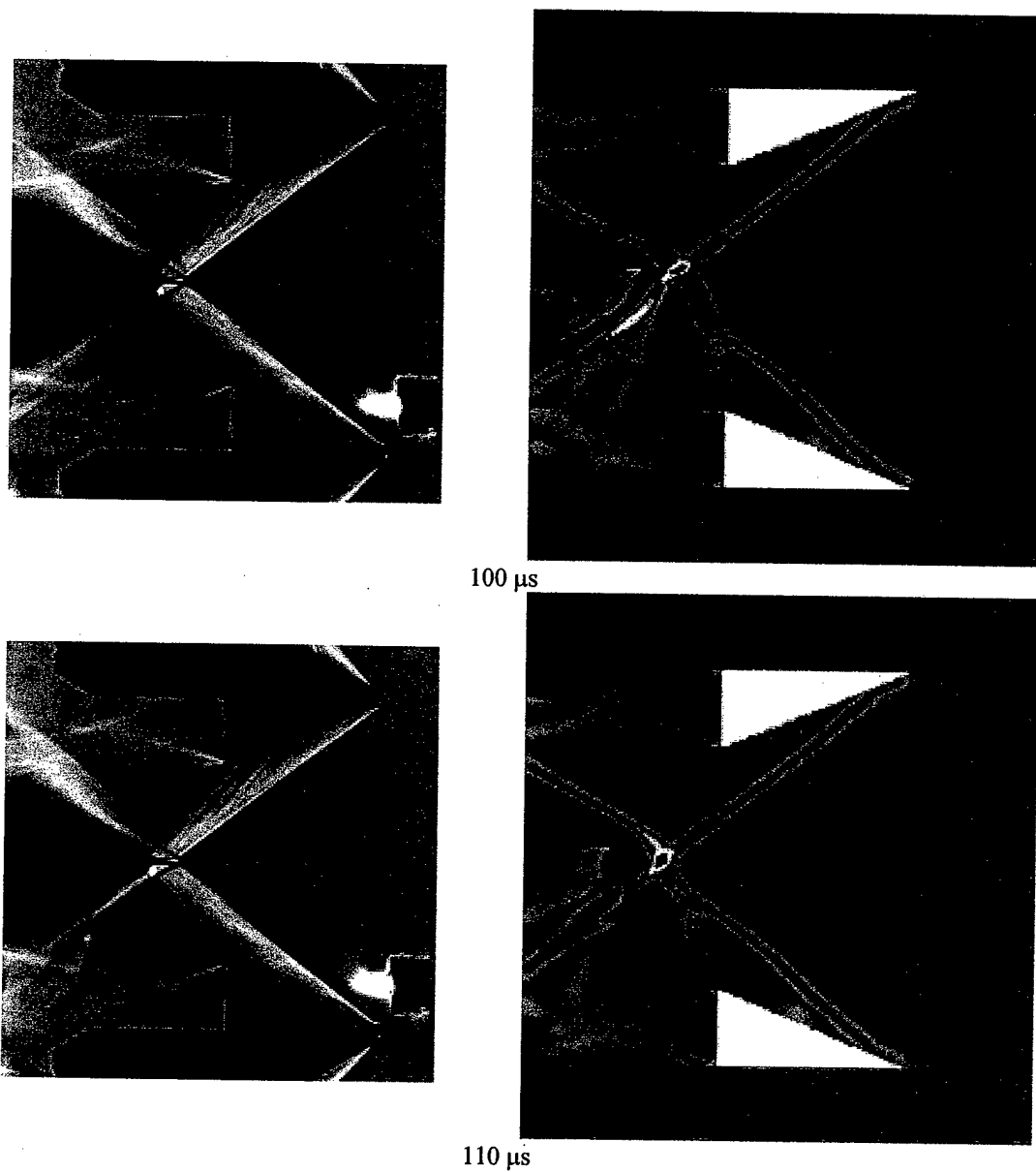


Figure 6.33 Experimental and numerical schlieren comparison for laser energy deposition upstream of 22 degree symmetric wedges at Mach 3.45 for time delays of 100 and 110 μ s

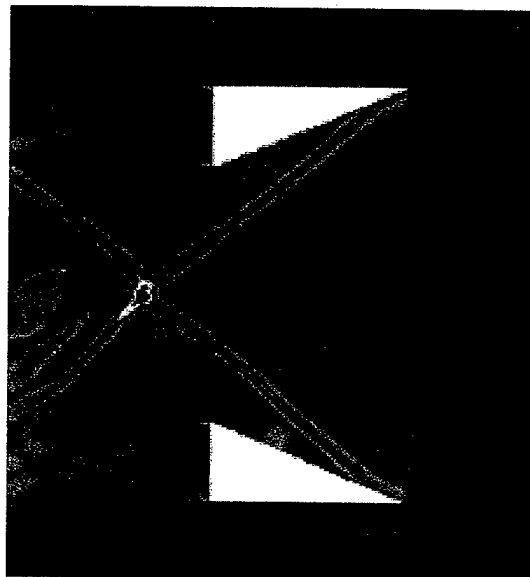
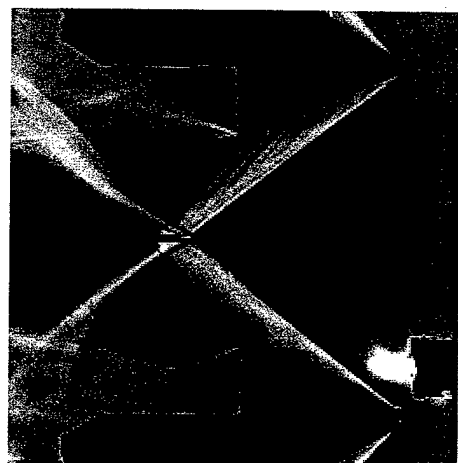
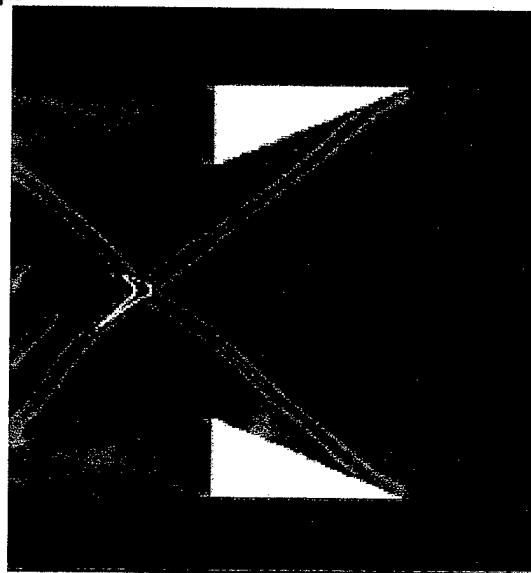
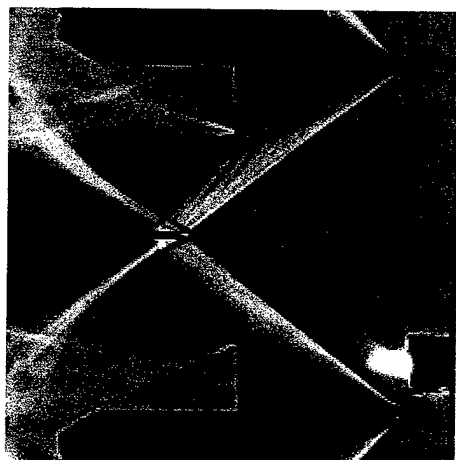
120 μ s130 μ s

Figure 6.34 Experimental and numerical schlieren comparison for laser energy deposition upstream of 22 degree symmetric wedges at Mach 3.45 for time delays of 120 and 130 μ s

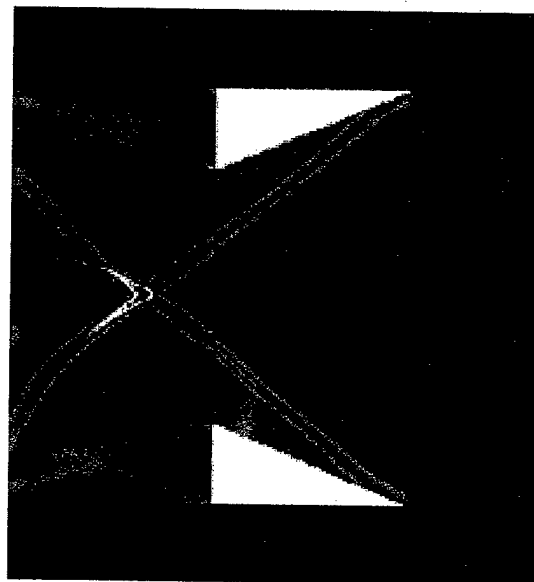
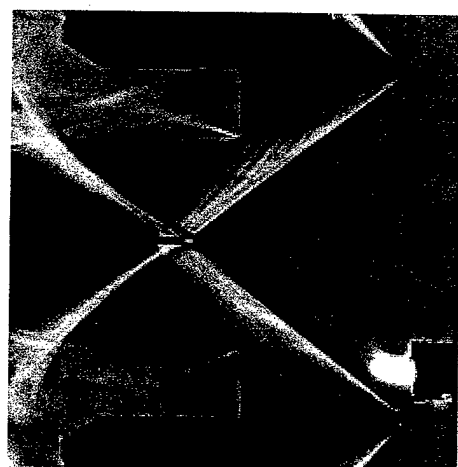
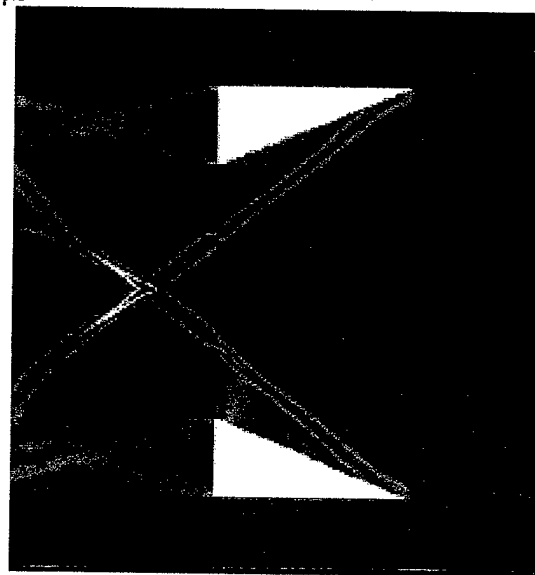
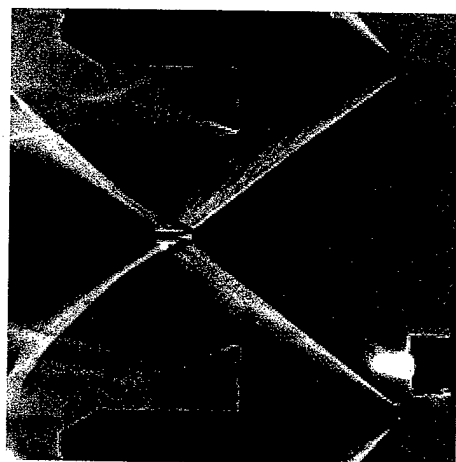
140 μ s150 μ s

Figure 6.35 Experimental and numerical schlieren comparison for laser energy deposition upstream of 22 degree symmetric wedges at Mach 3.45 for time delays of 140 and 150 μ s

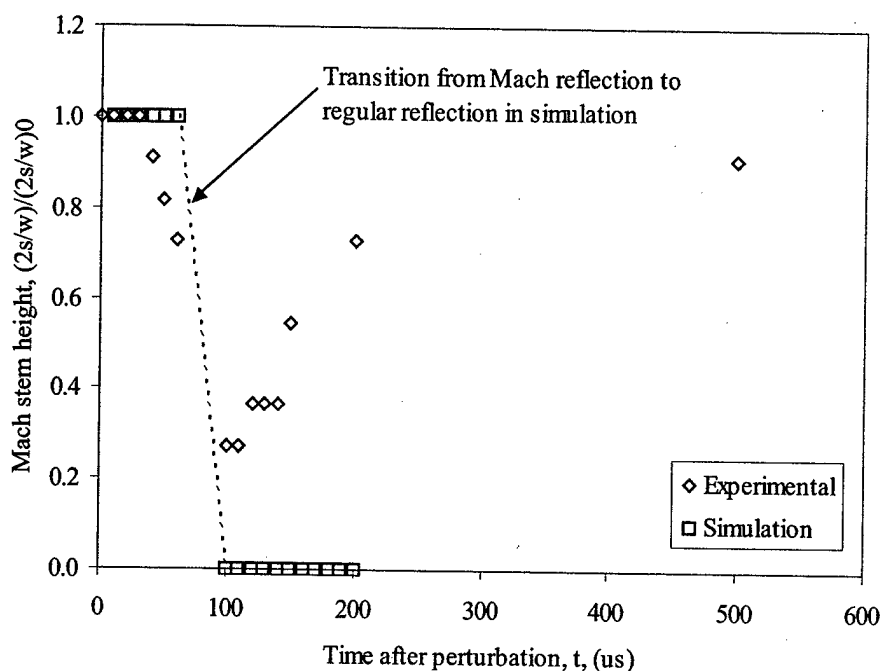


Figure 6.36 Mach stem height measurements from experimental and numerical simulation schlieren images as a function of time after the laser energy deposition (the uncertainty in the measurements is $\pm 10\%$)

6.4 Summary

An experimental survey of laser energy deposition applied to the symmetric shock structure in the dual solution domain was completed. Off centerline laser perturbations showed the ability to reduce the Mach stem height of the Mach reflection within the dual solution domain. The Mach stem height was reduced to 25% of its original height for this off-axis energy deposition. Applications of the laser perturbation on centerline increased the Mach stem height. Vortex generation downstream of the Mach stem was also observed and is comparable to the vortex generation created by laser energy deposition upstream of an axially symmetric Mach disk. Numerical simulations were compared to the experimental results and the same trends were observed. The numerical simulation showed the complete transition from the Mach reflection to the regular reflection. Furthermore, the transitioned regular reflection remained stable. Due to

turbulence levels within the wind tunnel, the experimentally reduced Mach stem did not remain stable and transitioned back to a larger, stable Mach stem height.

Three-dimensional effects were experimentally investigated with two different span wedges. The laser energy deposition had minimal effect on the Mach stem height for the $b = 4w$ span wedges. This reduced effect can be attributed to the three-dimensional Mach stem and to the integral effect of the schlieren images. In contrast, the laser energy deposition had a significant effect on the $b = 2.2w$ span wedges. The relation between the localized energy deposition to the wedge span should be investigated further to determine the three-dimensional effects.

Lastly, numerical simulations with better estimates of the energy deposition levels should be made and compared to the experimental data. Future spectrographic measurements will also provide data for energy deposition levels. Additionally, future simulations should include viscous effects, turbulence modeling, and asymmetries in the deposition region.

Chapter 7

Electric Arc and Laser Energy Excitation of Compressible

Axisymmetric Jet Shear Layer

7.1 Overview of Shear Layer Tests

Efficient combustion of fuel and oxidizer in high speed flows requires a threshold of mixing between fuel and oxidizer streams. Shear layer perturbation by energy deposition provides a means of inducing large scale structures in the shear layer. These large scale structures, in turn, would promote mixing of the fluids on either side of the shear layer. This enhanced mixing would lead to more efficient combustion.

Two energy deposition methods (electric arcing and laser induced optical breakdown) were used to force and control compressible mixing layers of axisymmetric jets. The energy deposition forcing methods have been experimentally investigated with the schlieren technique, particle image velocimetry, Mie scattering, and static pressure probe diagnostic techniques. Two jets perfectly expanded with nozzle exit Mach numbers of 0.85 and 1.38 were tested and examined with schlieren imaging for electric arc frequencies ranging from 1-18 kHz. Similar structures were observed for comparable Strouhal numbers between the subsonic and supersonic jets. The Mach 1.38 jet shear layer was forced with a single pulse laser energy deposition. The large-scale structure forced with the laser perturbation was characterized with schlieren imaging, measurements of the velocity and vorticity fields, and the pressure history. The core and braid regions were identified and correlated with the pressure data. The single pulse laser perturbation was demonstrated as an effective way to induce large-scale structures in a compressible shear layer. It was demonstrated that the laser spark (capable of 40 mJ/pulse) was more effective at inducing a large-scale structure than the electric arc (capable of 1 mJ/pulse) in the compressible shear layer. In terms of the frequency of pulses, the laser was capable of pulsing at 10 Hz, and the electric arc was capable of pulsing from 1-18 kHz.

Table 7.1 summarizes the tests completed in this study. Most of the emphasis was placed on the Mach 1.38 jet since the enhancement of mixing in the supersonic case was the primary objective of this experiment.

Table 7.1 Summary of axisymmetric jet shear layer perturbation experiments

Axisymmetric Nozzle Mach Number	Diagnostic technique	Perturbation Method	Energy Level (mJ)	Pulse Frequency	Experimental Objective
0.85	schlieren	Electric arc	1	0 – 15 kHz	Energy level and pulse frequency effect on forcing of shear layer
1.38	3 Comp. PIV			0 – 18 kHz	
				10 kHz	
		5	10 Hz		
		10			
	20				
	40	Temporal evolution of forced structure			
				2 Comp. PIV	
			schlieren		
Mie					
Pressure probe					

7.2 Electric Arc Forcing

The first task in investigating the arc excitation was to investigate which arc pulse frequencies amplified the growth of the mixing layer. The growth of the mixing layer was qualitatively assessed based on the schlieren images taken for varying arc pulse frequencies. These results could then be compared to those in forced subsonic jets. To accomplish this analysis, schlieren images were taken for a range of arc excitation frequencies for each nozzle. Schlieren images with the electric arc perturbation are given in Figure 7.1 and Figure 7.2 for the Mach 0.85 and 1.38 nozzles, respectively. Each image is an average of 50 frames synchronized to the excitation pulse. The excitation arc pulse is located in the left shear layer just above the nozzle surface. Each schlieren image is oriented with the test nozzle at the bottom of the image and the jet flow direction going from bottom-to-top. The knife edge for the schlieren system is vertical so the intensity gradient is observed across the shear layer of the jet. The images show the uniformity of the flow and no strong shocks are observed for the supersonic Mach 1.38 case. The tungsten rod (electrode), described in the Test Apparatus Section above, can be seen at the lower left of each image. In each figure, the undisturbed jet is shown at the

left. Images are shown with increasing arc pulse frequency from left to right. The spacing in the perturbation to the shear layer decreases as the arc frequency increases, as the figures clearly show.

The non-dimensional quantity characterizing the forcing frequency to the shear layer is given by the Strouhal number and is expressed by

$$St_D = \frac{f D}{U} \quad (7.1)$$

where f is the frequency of the disturbance, D is the characteristic length (the diameter of the nozzle in this case), and U is a characteristic speed of the fluid (here it is the magnitude of the exit velocity of the jet).

For shear layers of subsonic jets a Strouhal number between 0.25 and 0.5 has been reported as the most amplified forcing frequency. [316] For the Mach 0.85 jet, all frequencies (see Figure 7.1) showed some perturbation to the shear layer. The most effective frequency for amplifying the perturbation to the shear layer and creating the largest structures occurs over a range of 4 to 11 kHz corresponding to Strouhal numbers of 0.22 to 0.49. As the frequency increases, the number of modes increases, but it appears that the structure size decreases. At the lower frequencies a disturbance on the opposing side is also observed. This gives the jet core an overall periodic wave structure.

The effect of the forcing is reduced for the Mach 1.38 jet, as would be expected (see Figure 7.2). The compressibility effects reduce the size of the structures. The same periodic wavy jet structure is observed as seen in the subsonic jet, however the supersonic case is less pronounced. Between pulses the flow travels further for the supersonic shear layer giving a larger separation between the structures when compared to the subsonic jet forced at the same frequency. The first structure can be seen in each of the schlieren images for the differing frequencies. For the lower frequencies the induced structures in the shear layer are isolated until they grow and begin to interact downstream. For the Mach 1.38 jet the most effective, long lasting, and uniform perturbation seems to occur between 10 to 18 kHz, corresponding to Strouhal numbers of 0.32 to 0.56. The large-scale structures in the Mach 1.38 jet shear layer do not grow as rapidly as the structures in the Mach 0.85 jet, as indicated by the longer streamwise extent of the jet core for the Mach-1.38 jet. The periodic wavy nature of the jet (as seen at Mach 0.85) is also apparent in the Mach 1.38 jet at the higher forcing frequencies, though the magnitude is much less. The arc-pulse generator was limited to 20 kHz and 1 mJ of energy per pulse. To induce large-scale structures on the same

scale as those forced in the subsonic case, a larger energy pulse may be needed. Martins *et al* [87] have used a glow discharge to force the shear layer but a lower Reynolds number. This is the first time an arc discharge has been used at a high Reynolds number and high Mach number.

Figure 7.3 gives the three Cartesian contour plots of the components of velocity with the u - v vector field overlay (where the convective rate has been subtracted from the v component in the vector plots) and the z -component of vorticity for the unperturbed Mach-1.38 jet. The jet is perfectly expanded and is free of any shocks (see the schlieren image for the unperturbed jet in Figure 7.2). The coordinate system for the PIV data is oriented such that the xy -plane slices through the core of the jet with y pointing in the streamwise direction. The jet flow shown in the PIV plots is oriented from bottom-to-top and the positive z -axis points out of the page (see also Figure 3.50). The PIV data ranges from 3.5 to 8 diameters downstream of the nozzle of the jet. The z -component of vorticity is computed from the averaged velocity fields and is given by

$$\Omega_z = \frac{\partial \langle v \rangle}{\partial x} - \frac{\partial \langle u \rangle}{\partial y} \quad (7.2)$$

where $\langle \cdot \rangle$ indicates the averaged velocity components. The averages are computed from an ensemble of 500 instantaneous PIV data sets. The core velocity ranges from 400 m/s at the bottom to 370 m/s at the top. The isentropic velocity at the exit of the jet is 408 m/s. The x and z -components of velocity are less than three percent of the core. These components could be due to a slight tilt in the PIV sheet, not a large enough sample for the averages, and PIV inaccuracies. The vorticity peaks in the shear layer and decreases in the streamwise direction. The decrease in the vorticity is directly related to the decrease in the velocity gradients in the streamwise direction, as seen in the u and v components. Furthermore, the linearity of the contours in the y direction of the z -component of the vorticity, Ω_z , show a linear growth of the mixing layer in the streamwise direction. In a similar manner, Smits and Dussauge [320] describe a linear growth rate for the structures, whereby the growth of the structures would control the growth of the mixing layer, within a compressible shear layer in the streamwise direction.

Figure 7.4 gives the contour plots of the x , y , and z -components of velocity with u - v vector field overlays and the z -component of vorticity for the case where the shear layer of the Mach 1.38 jet is excited with the electric arc at 10 kHz. The v component in the vector fields, as in Figure 7.3, has the convective

rate subtracted. The same axis system as described above applies, and the same region of the jet is interrogated with the PIV system. An ensemble of 500 phase-locked PIV fields were used to calculate the averages as above. The y -component shows only a slight perturbation at $y/D = 5.5$; the core velocity in this region decreases by 5 percent. The impact of the arc forcing is more visible on the x -component of velocity. The opposing directions of u on either side of the structure indicate a roller structure in the region of $y/D = 5.5 - 7$. Little, or no effect, is seen in the z -component of velocity, w . The confinement of the vorticity component, Ω_z , appears to have spread, and its magnitude within the shear layer decreased slightly. Thus, one might say "a larger hammer" is needed to force the shear layer.

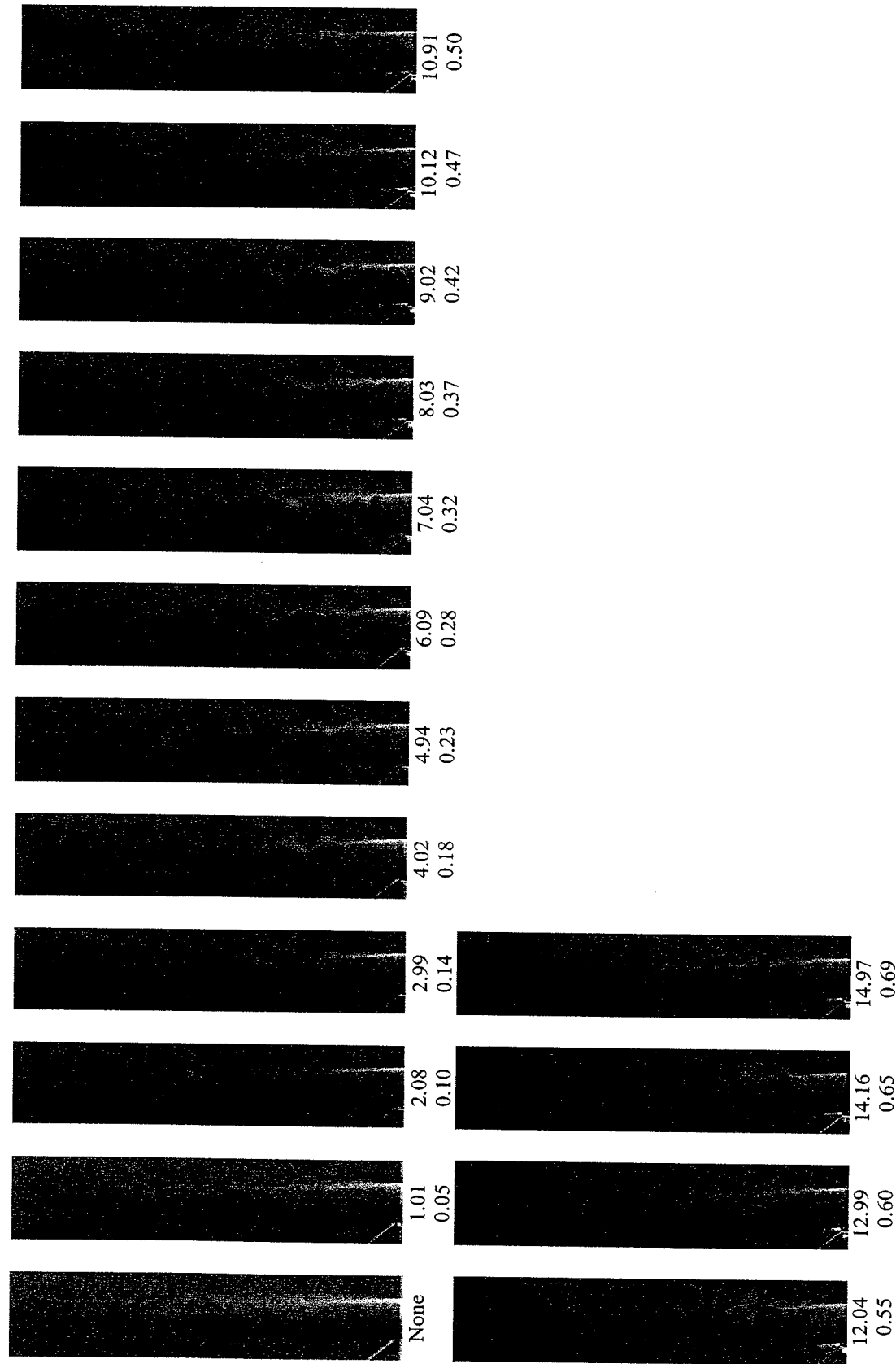


Figure 7.1 Schlieren images of electric arc shear layer perturbation in Mach 0.85 jet (top numbers are pulse frequency in kHz and bottom are Strouhal numbers)

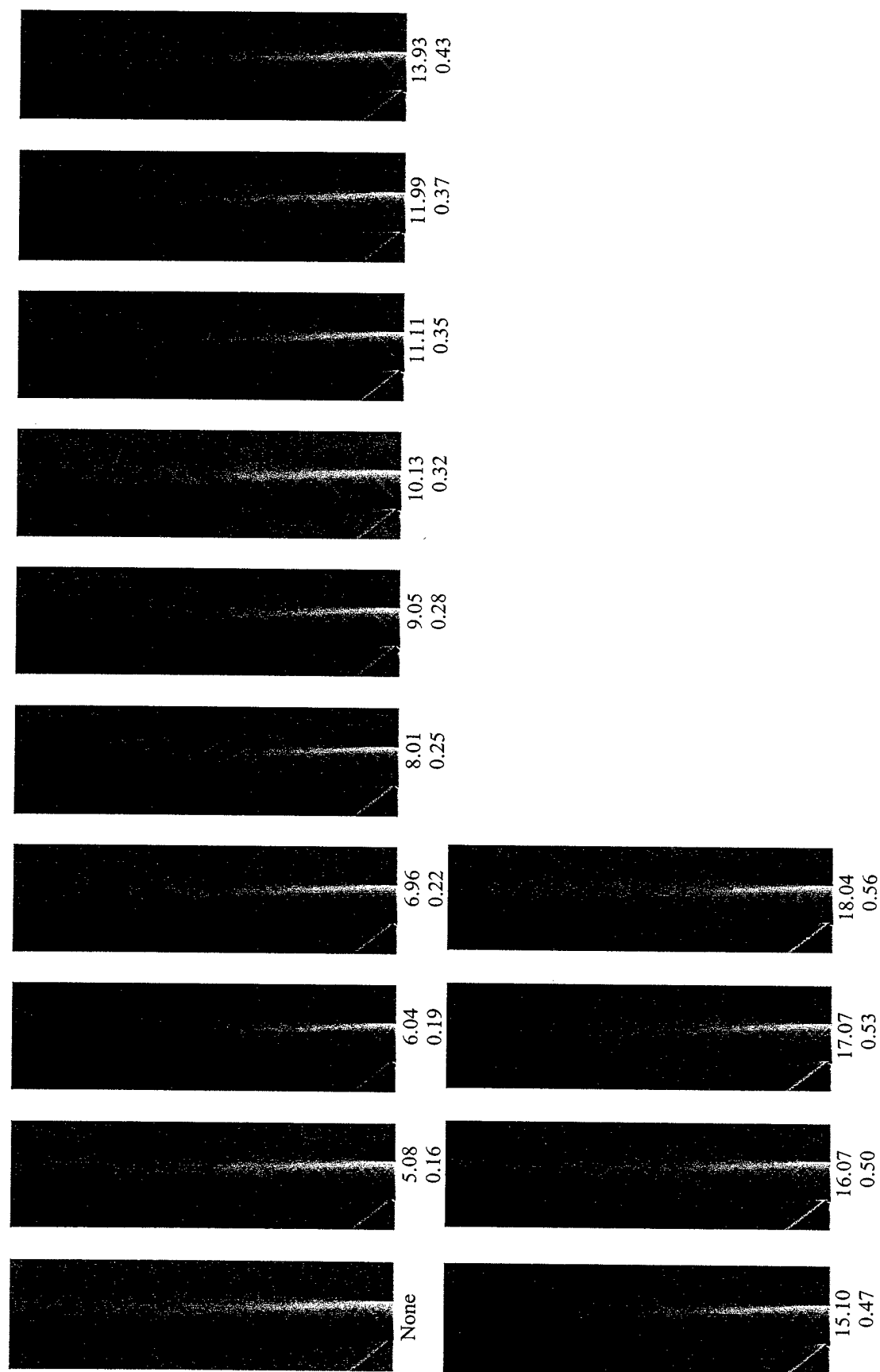


Figure 7.2 Schlieren images of electric arc shear layer perturbation in Mach 1.38 jet (top numbers are pulse frequency in kHz and bottom are Strouhal numbers)

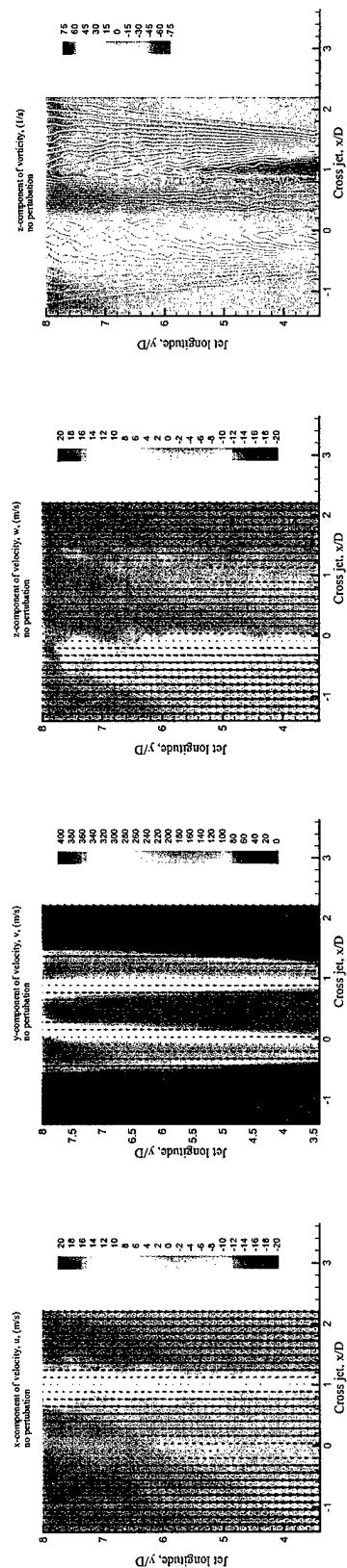


Figure 7.3 Contour plots of three Cartesian velocity components with u - v vector field overlays (the vector fields are plotted with the convective velocity subtracted from the v component) and z -component of vorticity for the Mach 1.38 jet with no perturbation

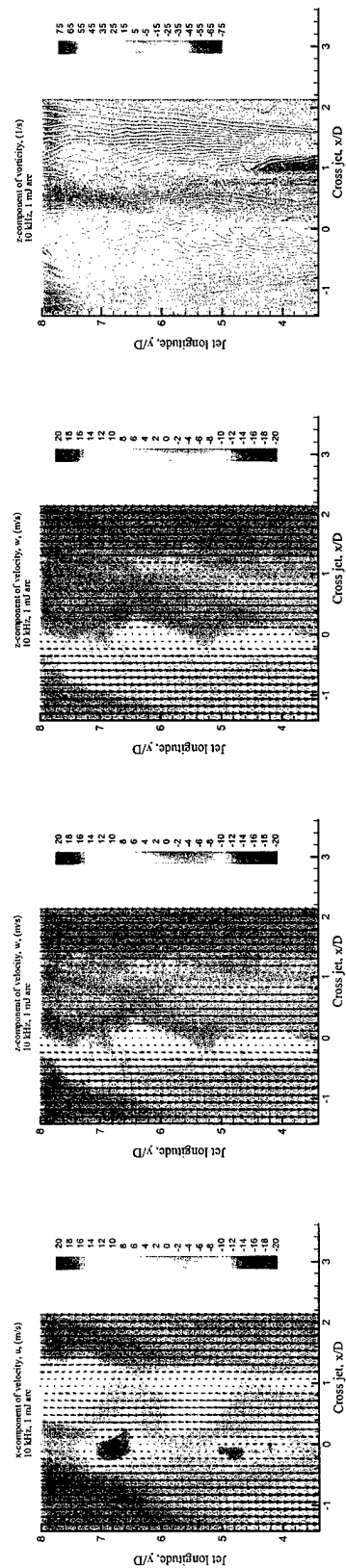


Figure 7.4 Contour plots of three Cartesian velocity components with u - v vector field overlays (the vector fields are plotted with the convective velocity subtracted from the v component) and z -component of vorticity for the Mach 1.38 jet with 10kHz 1mJ electric arc perturbation

7.3 Laser Discharge Forcing

Figure 7.5 gives a time series of schlieren images (same vertical knife edge orientation as used for the arc forced jets) for the Mach 1.38 jet perturbed with a 40 mJ laser pulse. Of course, we are restricted to a single energy deposition pulse perturbation to the shear layer in terms of the time and length scales of the flow. This is in contrast to the arc perturbation, whereby the interaction of several pulses could be observed due to the higher pulse frequency (see Figure 7.2). The images in Figure 7.5 show the same type structure as seen in Figure 7.1 and Figure 7.2 except here there is only a single pulse. Note that the block on the bottom left of each image protects the camera from the laser discharge flash. The blast wave and a reflected wave from the laser spark can be seen in the images at 50 and 100 μsec of delay. As the large-scale structure travels downstream, a secondary structure is observed to develop within the opposing shear layer. A tertiary structure also forms below the primary structure on the forced side. These secondary and tertiary structures associated with the single pulse are also observed in the PIV data discussed below.

Figure 7.6 gives the u , v , and w velocity components and the Ω_z vorticity component for the Mach 1.38 jet perturbed with a single laser pulse of 40 mJ. Similarly, the vector field, u - v , has been plotted on top of the contour plots where the convective rate has been subtracted from the v component in the vector field plots. The velocity components again are an ensemble average of 500 phase-locked instantaneous velocity fields at 220 μsec after the laser perturbation. The vorticity was determined from the averaged velocity components with Equation (7.2). The same probe region is used both with and without perturbation (and for both arcing and laser sparking, i.e. $y/D = 3.5 - 8$). The y -component of velocity, v , shows the large-scale structure extending into the jet core. The velocity in the core decreases by 10 percent. The secondary structure on the opposing shear layer can be seen below and to the right of the larger primary structure. A large effect of the laser perturbation can be seen in the x -component of velocity. The opposing directions of the velocity component, u , indicate a roller-type structure at approximately $y/D = 5.5$ and the turning of the jet core around the structure. The z -component shows a tilted structure with opposite sign in front of and behind the vortex core. However, the feature is fairly weak when compared to the magnitude of the x -component of velocity. There appears to be a three-dimensional swirl where the flow is coming out of the plane behind the structure and into the plane in front of the structure. This three-dimensional effect

develops from the initial perturbation and evolves as the core velocity flows around it. The vorticity component, Ω_z , shows the field to be thicker in the region of the large-scale structure and with a lower magnitude due to the fact that the shear layer has large velocity change over a smaller region compared to the smaller roller type structure. The vorticity plot also shows the secondary structure on the opposing shear layer lagging behind the primary structure at $y/D = 4.8$. The magnitude of the vorticity component decreases by 40 percent from the isolated vorticity in the shear layer. A third structure is also located at $y/D = 4$. This primary, secondary, and tertiary structure formation is also evident in the schlieren images (see Figure 7.5).

Figure 7.7 compares the y -component of velocity and the z -component of vorticity for increasing laser energy deposition pulses ranging from 5 to 40 mJ/pulse. Again, the contour plots of the y -component of velocity are shown with the u - v vector field where the convective rate has been subtracted from the v component. The size of the large-scale structure increases as the energy deposition level increases; the size of the structure increases by 40 percent when the energy is increased from 5 to 40 mJ/pulse. Moreover, the size of the structure can also be deduced from the y -component of velocity plots as indicated by the indentation to the jet core. The secondary structure is not as evident at the lower energy levels on the opposing shear layer. The tertiary structure lagging behind the primary structure is invariant with energy level (at $y/D = 4$ for this interrogation time). For the energy-level tests the plots are an average of 50 images, and the vorticity component was determined with Equation (7.2).

Three component PIV data was obtained for the 40 mJ/pulse laser excitation across the full volume of the Mach 1.38 jet 220 μ sec after the excitation pulse. The volume of velocity data was created by 21 planar fields of PIV data taken across the jet in 1-mm increments. The planar fields were phase averaged (50 for each plane location) and then assembled to produce the volume of average velocity data in the z direction. Figure 7.8 shows the deformation to the jet core due to the laser excitation pulse where the 320 m/s isosurface is plotted. The large-scale structure is located at $y/D = 5$. The same axis system is used as for the aforementioned cases. The core does slightly pinch off at the top of the forced structure. The structure extends into the jet core, and the flow in the core moves around the large-scale structure as shown by the isosurface. Figure 7.9 shows the magnitude of vorticity (based on the full three-dimensional velocity field)

in three orthogonal planes across the jet in the vicinity of the forced large-scale structure. The magnitude of the vorticity is given by

$$\Omega = \sqrt{\Omega_x^2 + \Omega_y^2 + \Omega_z^2} \quad (7.3)$$

where the z-component of vorticity is given by Equation (7.2), and the x and y components are, likewise,

$$\Omega_x = \frac{\partial \langle w \rangle}{\partial y} - \frac{\partial \langle v \rangle}{\partial z}, \quad (7.4)$$

and

$$\Omega_y = \frac{\partial \langle u \rangle}{\partial z} - \frac{\partial \langle w \rangle}{\partial x}. \quad (7.5)$$

Note that the vorticity components are computed from the averaged velocity fields. Again, it is observed that the vorticity has increased outside the region of the unperturbed shear layer. This extension and amplification of the vorticity in the jet region is a direct indication of the size and location of the large-scale structure. The increased vorticity in this region would also indicate increased circulation and, thus, increased mixing.

Figure 7.10 shows the x-component of vorticity across three orthogonal planes in the jet at 220 μ s after the laser deposition. This component shows a migration out of its normal plane due to the formation of the large scale structure. For an unperturbed jet, this component would normally be confined to the top and bottom of the jet in this figure.

Figure 7.11 shows the y-component of vorticity across three orthogonal planes in the jet at 220 μ s after the laser deposition. Here it is observed that the large scale structure induces streamwise vorticity in the jet.

Figure 7.12 shows the z-component of vorticity across three orthogonal planes in the jet at 220 μ s after the laser deposition. Like the x-component, the z-component of vorticity is developed in the jet due to the large scale structure. For an unperturbed jet, this component of vorticity would be confined to left and right sides, respectively in this orientation of the figure.

Figure 7.13 through Figure 7.17, and Figure 7.18 show the time evolution of the jet with the 40 mJ/pulse perturbation. The large structure induced by the laser energy deposition can clearly be seen moving downstream. In each figure the column corresponds to an instant in time. In each column the first

two graphs shown are the u and v velocity component contour plot, where the u - v vector field plots (where the convective rate has been subtracted from the v component) are overlaid. The third graph is the z -component of vorticity computed from the velocity data with Equation (7.2). In this case, the velocity data is an average of 50 PIV phase-locked images at each time step. The field of view covers $y/D = 1.4 - 6.8$. The last image shown at the bottom of each column of figures is a corresponding Mie scattering image. The Mie scattered images are an average of 100 images. Overlaid with the Mie scattering images are pressure probe locations where pressure measurements were recorded. The sliding bar charts at the right of the Mie scattering images give the averaged result of 500 recorded pressure traces where the pressure is normalized with the ambient pressure. Each pressure bar chart is aligned horizontally with the corresponding probe in the figures. The whiskers on the bar chart indicate the \pm one standard deviation, σ , of the measured pressure fluctuations. The structure is also observed to grow as it travels down the shear layer. Moreover, the density gradients given by the schlieren images correspond to the PIV data and the Mie scattering images obtained for the 40 mJ perturbation (see Figure 7.5). For each diagnostic the large-scale structure created by the laser energy deposition can clearly be observed as it moves within the mixing layer. The graphs of the vorticity show that this large structure has diffused some of the localized vorticity contained in the shear layer into the jet core. The movement of this vorticity into the jet core can be seen with greater detail in Figure 7.9 where the full vorticity magnitude is shown.

Three-dimensional effects are also observed in the time series PIV data. As noted previously, a structure can be seen to form on the opposing side of the shear layer, and another structure is also observed lagging the initial large-scale forced structure on the same side where perturbation occurred. These additional structures are also shown in the schlieren and Mie scattering images. The convective speed of the structure was measured as 250 m/s based on the Mie scattering averaged images and 260 m/s measured from the PIV images. These observed convective rates are much closer to the theoretical (220 m/s) than the empirically determined (342 m/s) values (see Table 3.9). The empirically determined value does not match well for this large forced structure. Furthermore, this convection velocity is constant over the observed times.

In addition, the large-scale structure grows approximately twice in size based on the vorticity plots from 100 to 260 μ sec. Likewise, the Mie scattering images show growth in the large-scale structure as more

moist ambient air is entrained in the structure due to its increase in size. The velocity plots and Mie scattering images also show the formation of secondary and tertiary structures in the opposing shear layer and forced side shear layer - both lagging behind the primary structure.

The pressure plots from the three static pressure probes show a minimum when the cores of the primary and tertiary structures pass the probe (see also Figure 7.18). A peak pressure is observed when the braid region between the two structures passes. Considering the model of the large-scale structure as presented by Papamoschou and Roshko, [318] a peak in pressure in the braid region corresponds to the stagnation point created as the two streams across the shear layer meet in a frame of reference translating with the structure. The minimums in the pressure traces correspond to the core regions of the large-scale structures. Figure 7.18 gives the averaged pressure data traces for the three vertical pressure probe locations. The top plot in Figure 7.18 is the trace for the upstream probe; the middle is the middle probe, and the bottom plot is the downstream probe. The probes were positioned vertically above the laser perturbation location. The traces giving the $\pm\sigma$ for the pressure data are also shown on the plots. For reference, the times of 100, 220, and 260 μsec are highlighted on the plots and correspond to the time interval for the sequence of PIV data and Mie images, the delay time of the volumetric data, and laser energy-level data discussed above. Time at zero corresponds to the perturbation initiation. The average convective velocity of the stagnation point (based on the peak-to-peak pressure data) is 257 m/s - in close agreement with the other measurements from the Mie scattering images and the PIV data. Table 7.2 summarizes the various convective velocities based on the theory, and the measurements made in this series of experiments. The data for the convective speed from these experiments does not correlate with the empirically derived formulation of Murakami and Papamoschou [98] given by Equation (2.42). Their empirical formulation was based on data obtained with a coaxial jet apparatus. In addition, for increasing convective Mach number, the data used for the empirical fit showed considerable spread and poor correlation with the fit. In the data presented here, the convective rates show better agreement with the theory of Papamoschou [104] given by Equation (2.41).

Table 7.2 Comparison of convective velocity for forced large-scale structure

Theory (m/s)		Measurement (m/s)		
Eq. (2.41)	Eq. (2.42)	PIV	Mie	Pres.
220	342	260	250	257

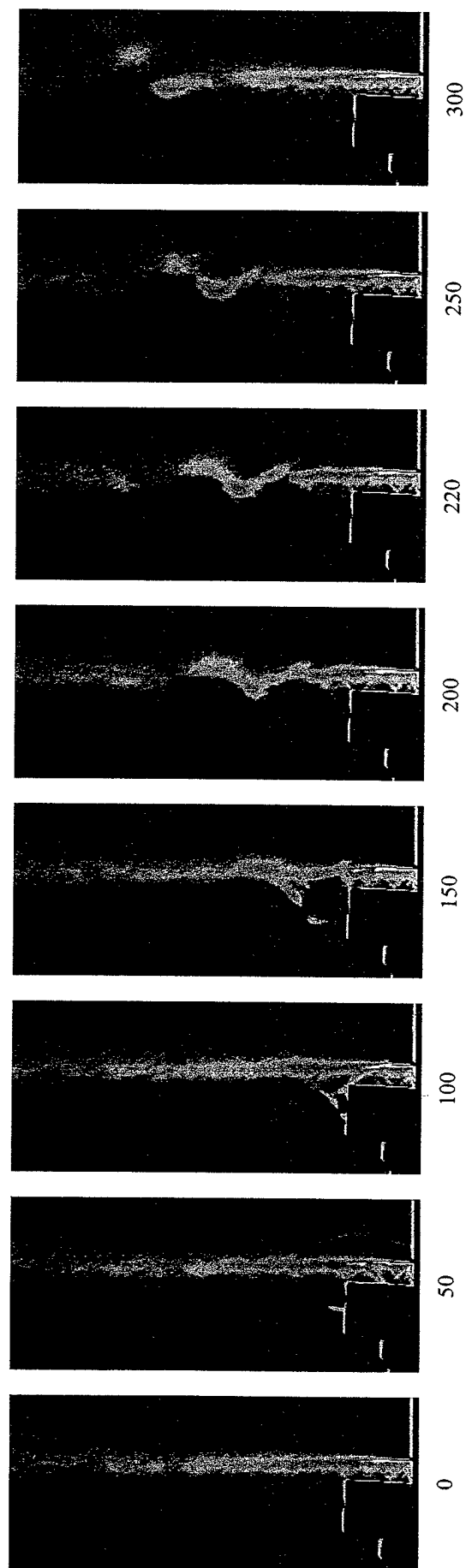


Figure 7.5 Schlieren images for increasing time delays (given in μs below each image) after 40 mJ laser excitation pulse in shear layer of Mach 1.38 jet

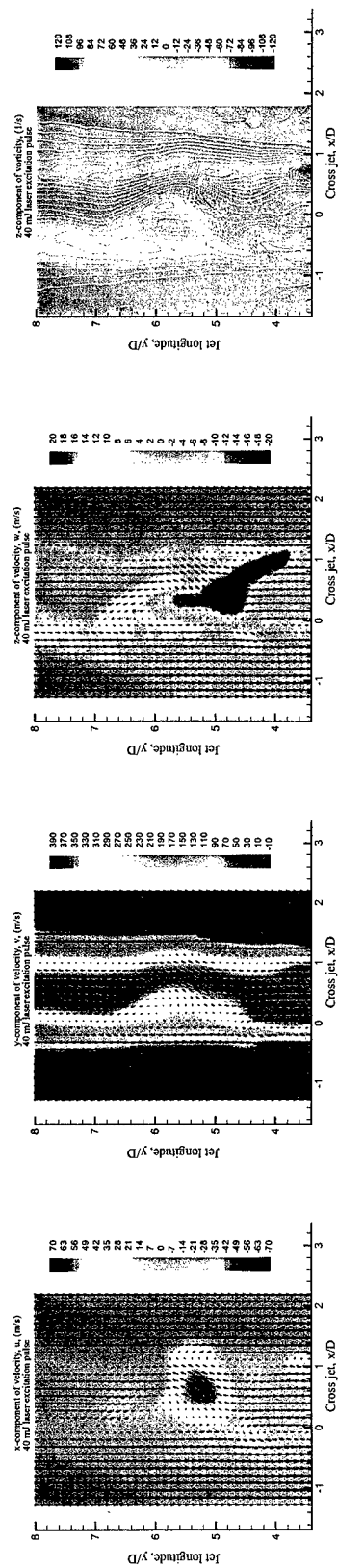


Figure 7.6 Contour plots of three Cartesian velocity components with u - v vector field overlays (the vector fields are plotted with the convective velocity subtracted from the v component) and z -component of vorticity for Mach 1.38 jet $220 \mu\text{s}$ after a 40 ml laser spark perturbation

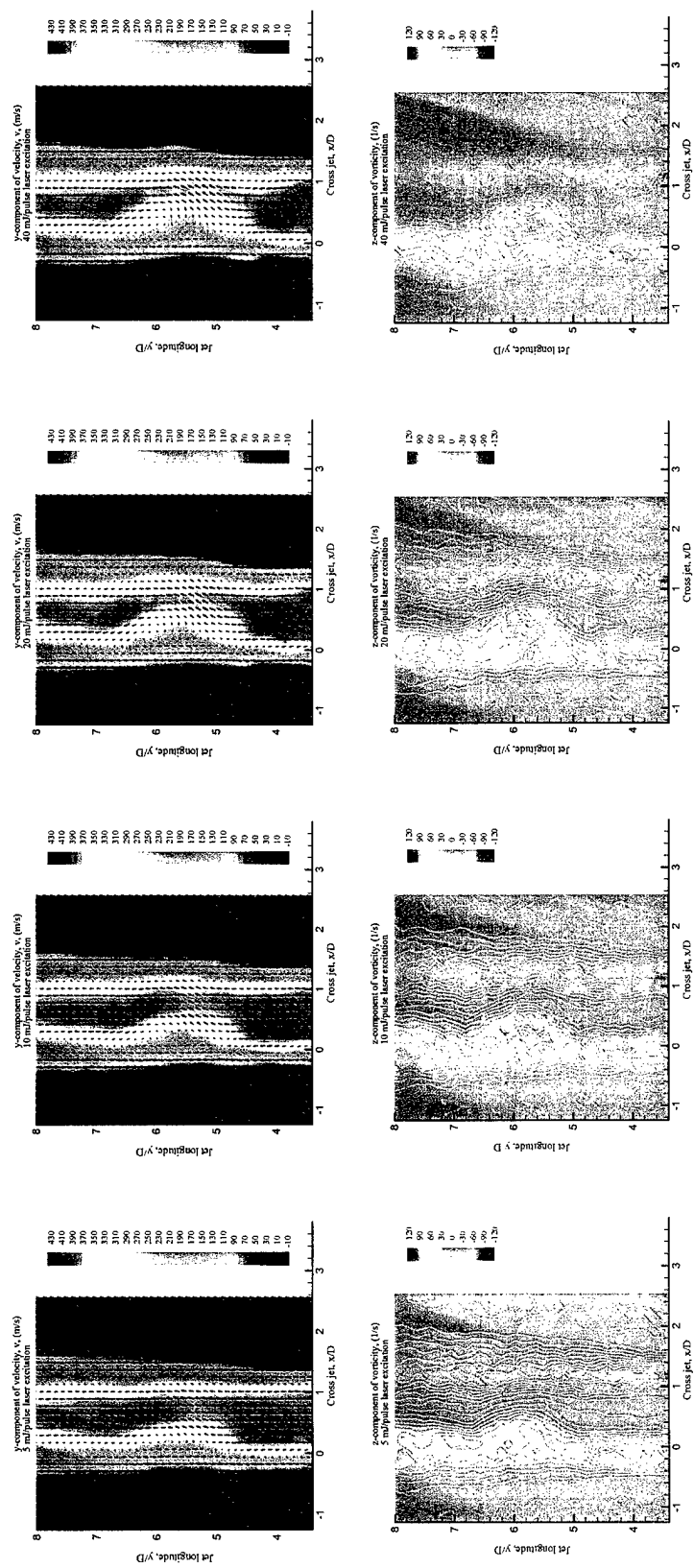


Figure 7.7 Comparison of the velocity and z-component of vorticity for laser perturbations of 5, 10, 20, and 40 mJ/pulse at 220 μ s (note the convective rate has been subtracted from the v component in the vector field plots)

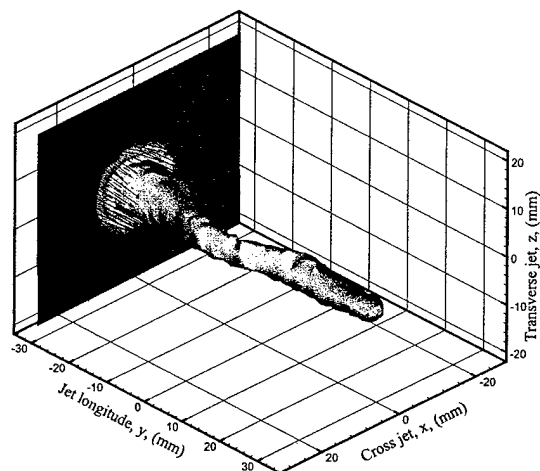


Figure 7.8 Deformation of jet core due to 40 mJ laser excitation pulse (320 m/s velocity magnitude isosurface)

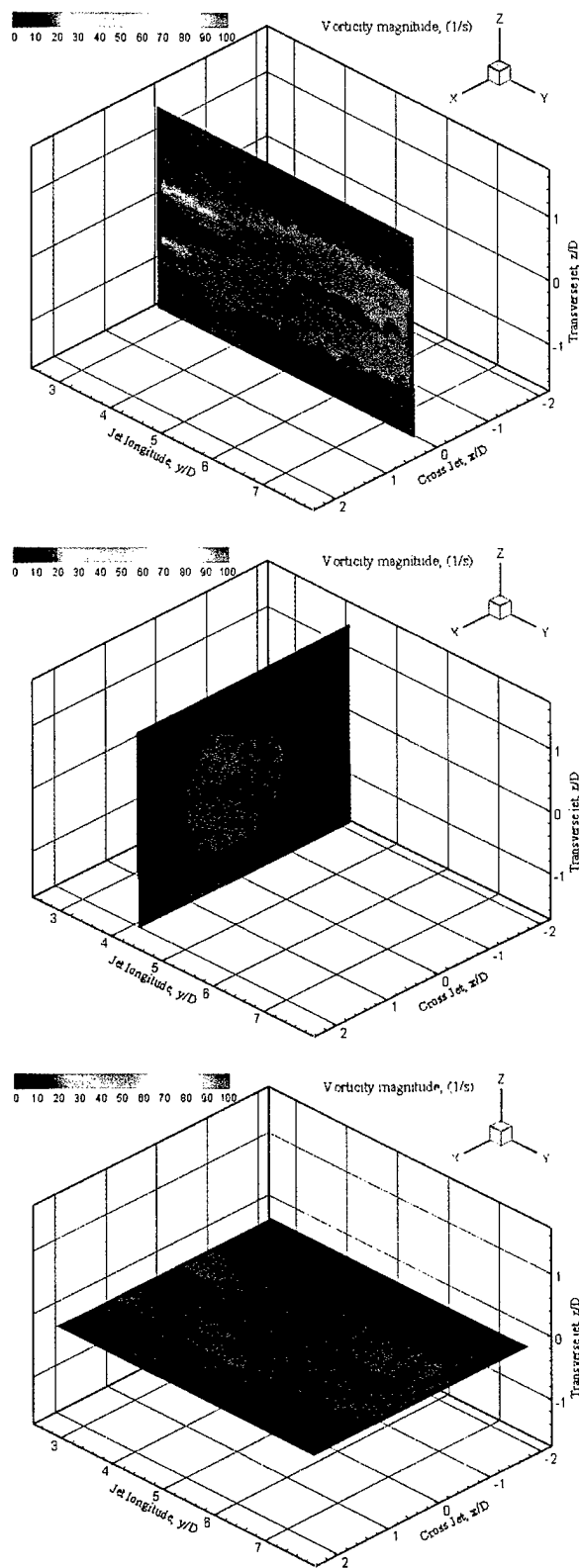


Figure 7.9 Vorticity magnitude in jet 220 μ s after 40 mJ laser excitation pulse

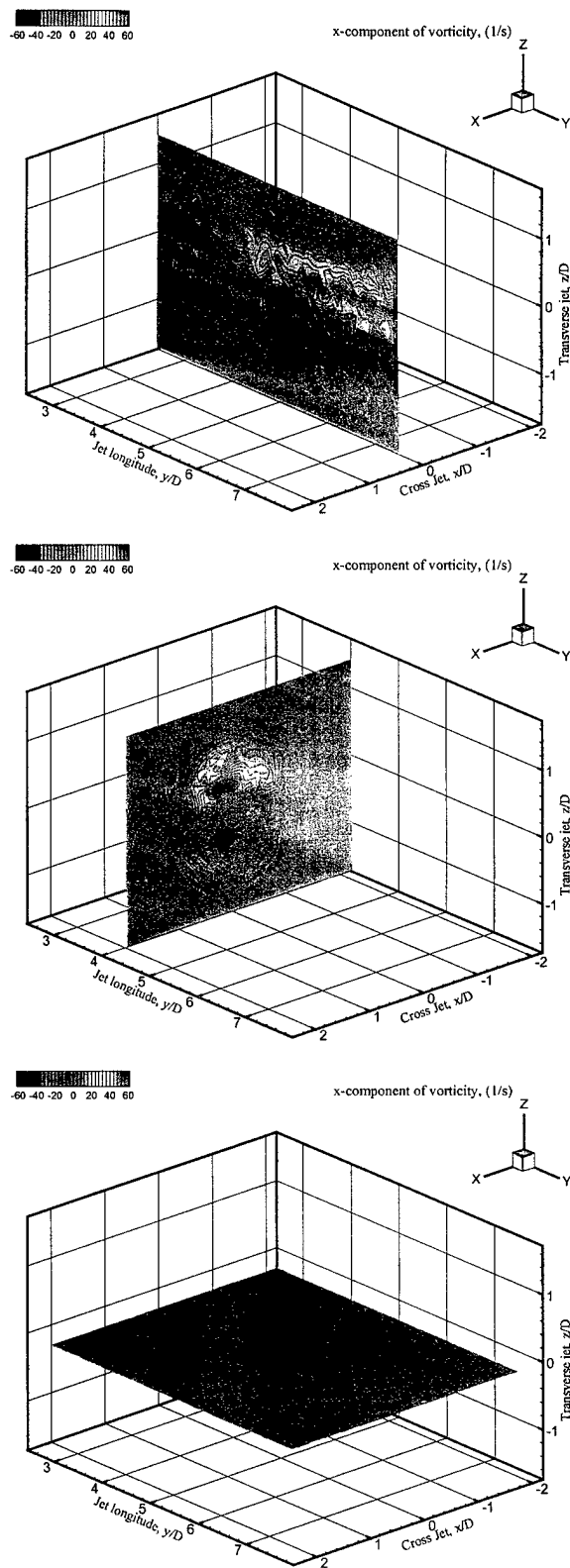


Figure 7.10 The x-component of vorticity at $220 \mu s$ after 40 mJ laser excitation pulse

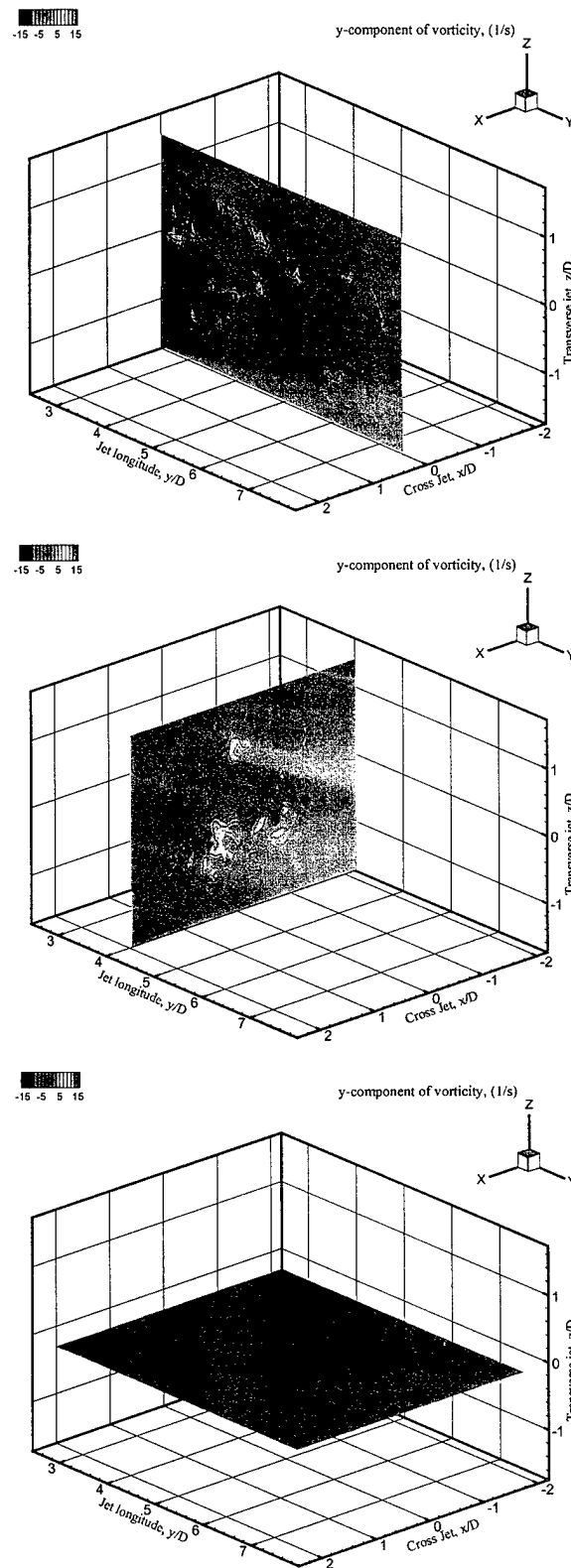


Figure 7.11 The y-component of vorticity at 220 μs after 40 mJ laser excitation pulse

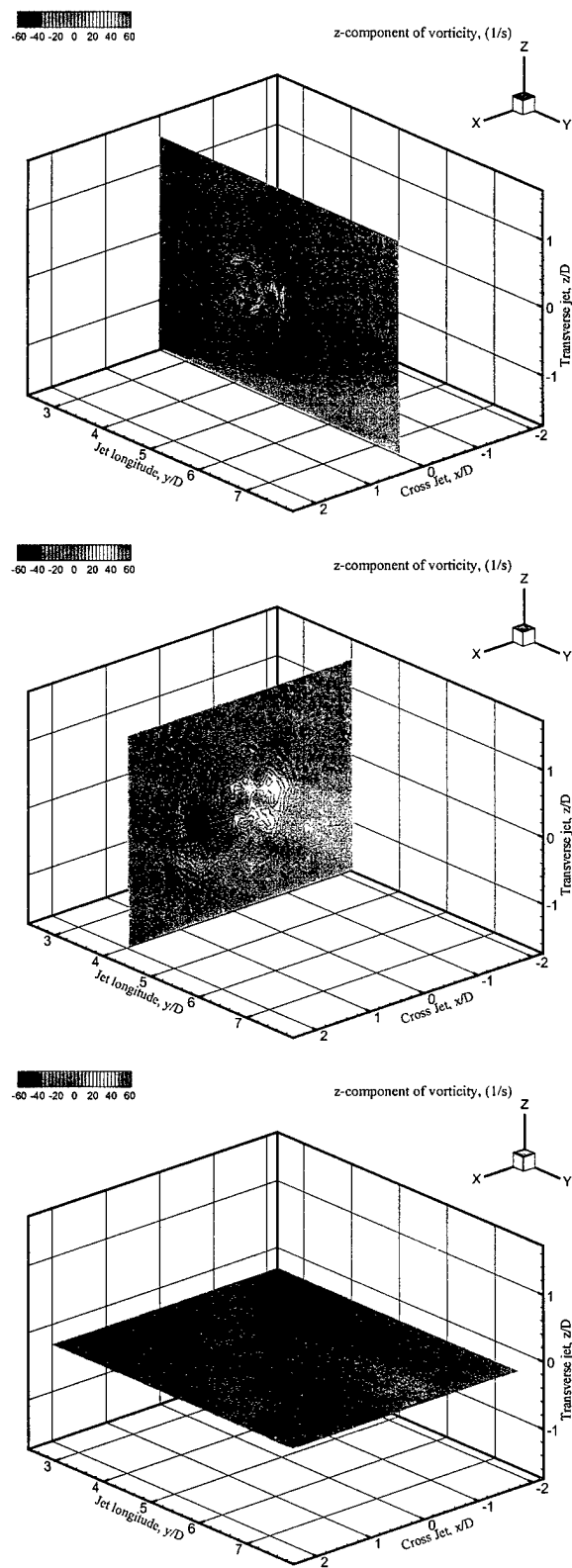


Figure 7.12 The z-component of vorticity at $220 \mu s$ after 40 mJ laser excitation pulse

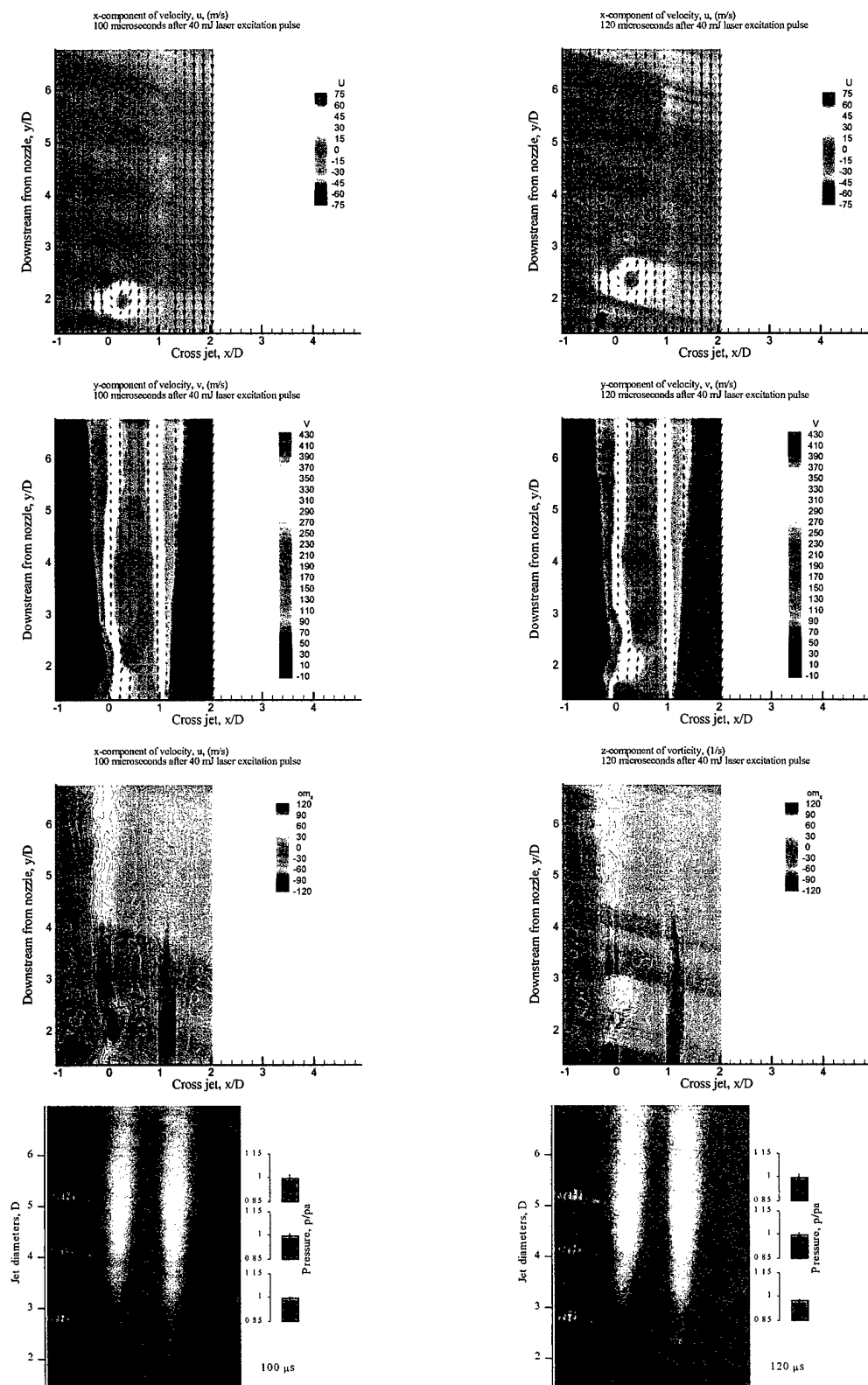


Figure 7.13 Temporal evolution of the x-component of velocity, u , y-component of velocity, v , and z-component of vorticity, Ω_z , correlated with Mie scattering images and pressure probe data at 100 - 120 μs

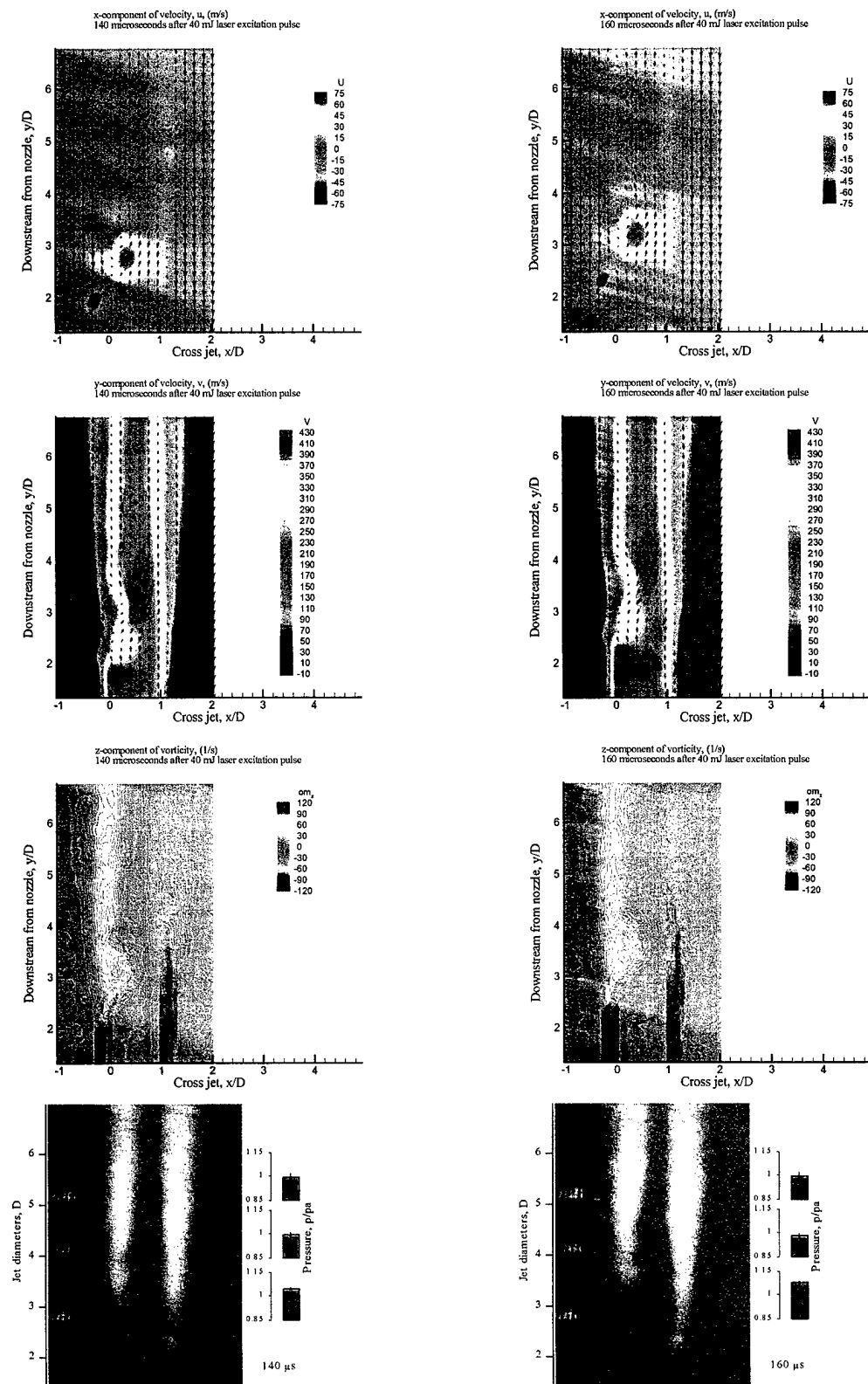


Figure 7.14 Temporal evolution of the x -component of velocity, u , y -component of velocity, v , and z -component of vorticity, Ω_z , correlated with Mie scattering images and pressure probe data at 140 - 160 μs

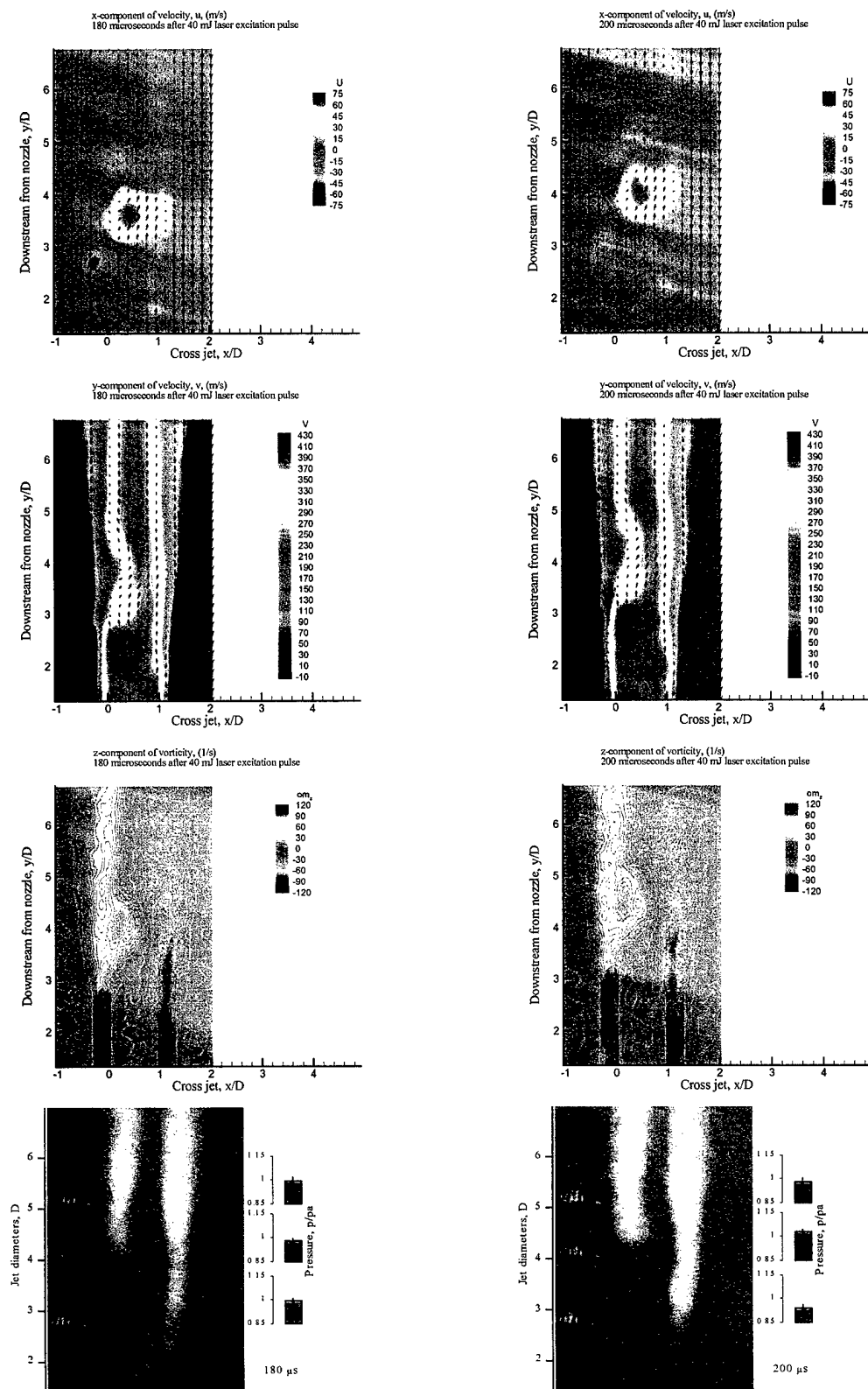


Figure 7.15 Temporal evolution of the x-component of velocity, u , y-component of velocity, v , and z-component of vorticity, Ω_z , correlated with Mie scattering images and pressure probe data at 180 - 200 μs

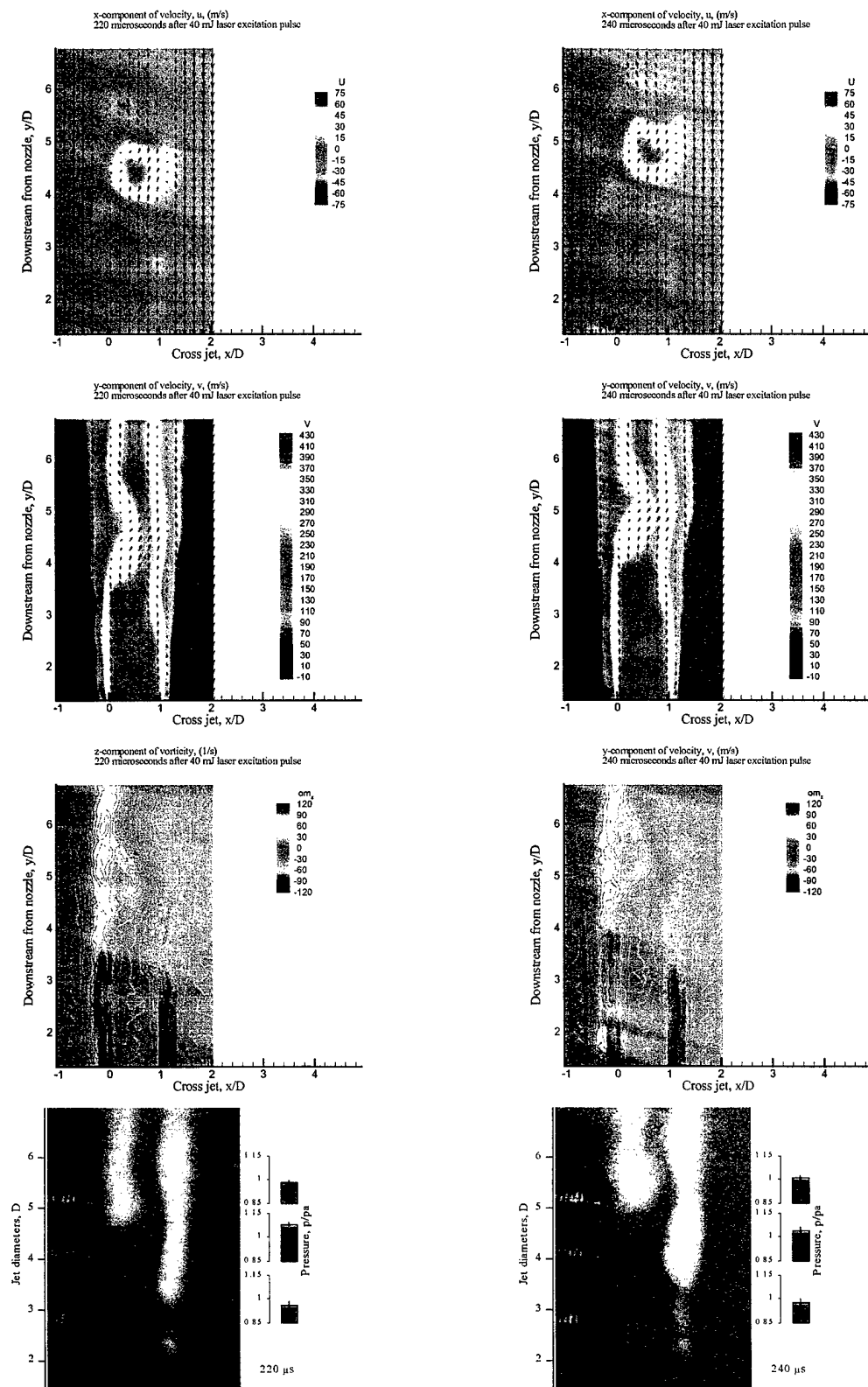


Figure 7.16 Temporal evolution of the x-component of velocity, u , y-component of velocity, v , and z-component of vorticity, Ω_z , correlated with Mie scattering images and pressure probe data at 220 - 240 μ s

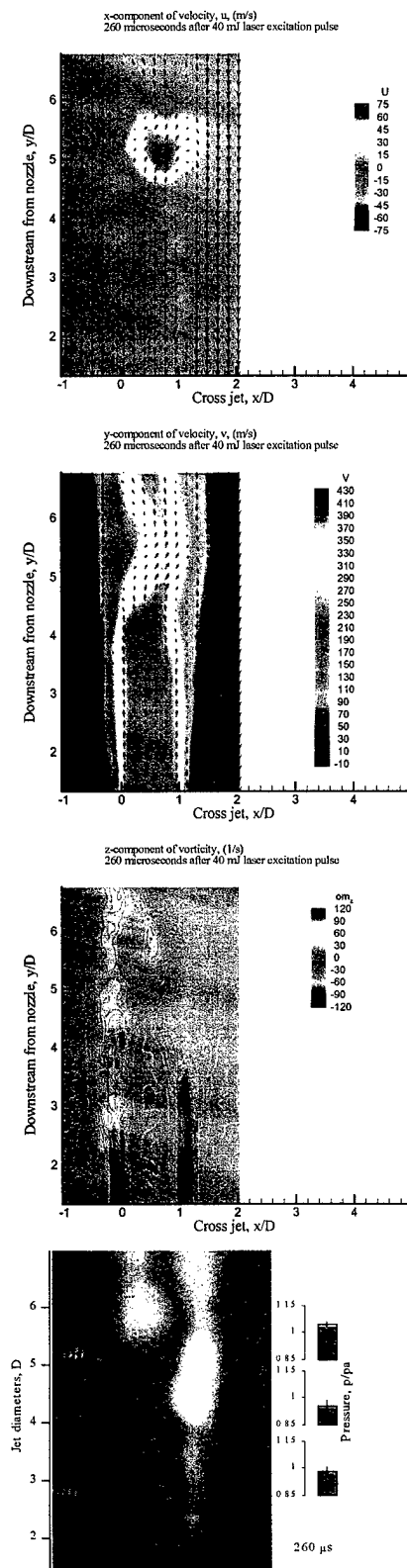


Figure 7.17 Temporal evolution of the x -component of velocity, u , y -component of velocity, v , and z -component of vorticity, Ω_z , correlated with Mie scattering images and pressure probe data at 260 μ s

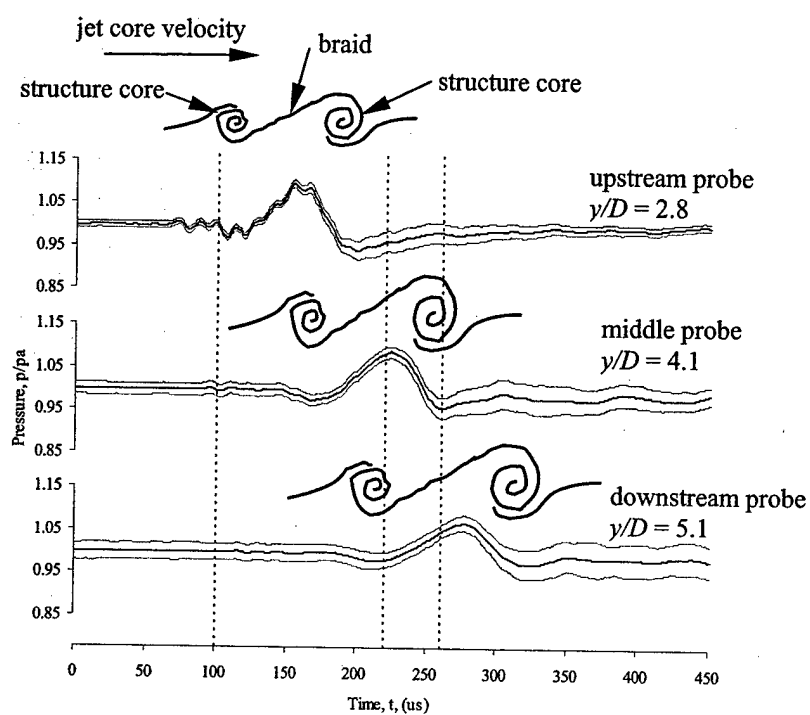


Figure 7.18 Vertical pressure probe (upstream, middle, and downstream) traces and correlation with large-scale structures

7.4 Summary

A method of forcing and controlling supersonic mixing layers has been demonstrated in Mach 0.85 and 1.38 axisymmetric jets. Two types of excitation were investigated: a multi-pulse electric arc and a focused laser beam. The most amplified frequency for the electric arc forcing was found to be in the same range as for subsonic jets. Although the arc provided some perturbation to the flow, the energy was found to be too low, especially for the Mach 1.38 jet, to have a dramatic impact on the flow structure. Single laser pulse excitation was effective creating a large-scale structure containing well-defined core and braid regions, as shown with the velocity and static pressure measurements. This structure contained a primary vortex with an elongated secondary structure separated by a stagnation point in a frame of reference moving at the convective velocity. Particle image velocimetry data was obtained for the flow field and used to describe the structure of the perturbed shear layer. This information was collaborated with quantitative pressure data and with qualitative schlieren images. The laser perturbation is an effective means of inducing a large-scale structure in a compressible shear layer.

*Now I lay me down to sleep
I pray the Lord my soul to keep
May angels watch me through the night
and wake me with the morning light.*

Unknown

Chapter 8

Conclusion

8.1 Key Discoveries

The objectives of this research effort were to explore the realm of using energy deposition to control various compressible flow phenomena in a localized manner. Specifically, energy deposition was applied to the mitigation of the adverse Edney Type IV shock/shock interaction upstream of a blunt body, modification of the shock structure within the intersecting shock dual solution domain, and the forcing of large scale structures in a compressible axisymmetric shear layer.

Initial qualitative and quantitative data was collected for the laser energy deposition into quiescent air. Precision measurements were made of the blast wave speed as a function of various energy levels. Currently, this database is being used to calibrate the numerical models of Yan *et al* [151] and Kandala and Candler. [71] The measurements for the blast wave and energy levels show good agreement with the spherical model of Yan *et al* [151]. The pressure probe measurements did not compare well with the simulations and differed by 40%. The non-intrusive laser deposition measurements by Boguszko *et al* [14] are well justified and will provide additional model calibration data. These numerical models will provide the initial conditions for the more complex modeling involved with laser energy deposition upstream of the blunt body and for the intersecting shocks.

One objective of this research effort was to demonstrate the feasibility of reducing the peak pressure (and, ultimately, peak heat transfer) associated with the Edney IV shock impingement condition through the use of laser energy deposition. The steady state surface pressure measurements had excellent correlation with steady state Euler simulation results. For the unsteady flow associated with the laser perturbation, surface pressure measurements show a 40% decrease in surface pressure during the 50

microsecond thermal spot interaction time as observed for the case of a sphere in Mach 3.45 flow with varying levels of energy deposition upstream of the bow shock. The laser excitation pulse width is 10 nanoseconds versus the 50 microsecond transient effect on the flow. Surface heat transfer measurements were made for the Mach 3.45 sphere as well. Excellent time response and sensitivity were demonstrated with the thin film gauges. The gauges were able to measure the heat transfer associated with the radiation, blast wave, and thermal interaction associated with the laser energy deposition.

The peak surface pressure associated with the Edney IV interaction was reduced by 30% momentarily by the flow perturbation created by the upstream laser discharge. However, the experiments did not show the desired effect of reducing the heat transfer by perturbing the flow with energy deposition.

In terms of the crossing shock investigation, experiments show a reduction of the Mach stem by 80% for asymmetric laser energy deposition upstream of the shock structures generated by $22^\circ \times 22^\circ$ wedges at Mach 3.45. Qualitative comparisons were made between numerical and experimental schlieren images and general agreement between the two.

A method of forcing and controlling supersonic mixing layers has been demonstrated in Mach 0.85 and 1.38 axisymmetric jets. Two types of excitation were investigated: a multi-pulse arc and a focused laser beam. The most amplified frequency for the electric arc forcing was found to be in the same range as for subsonic jets. Although the arc provided some perturbation to the flow, the energy was found to be too low, especially for the Mach 1.38 jet, to have a dramatic impact on the flow structure. Single laser pulse excitation was effective creating a large-scale structure containing well-defined core and braid regions, as shown with the velocity and static pressure measurements. This structure contained a primary vortex with an elongated secondary structure separated by a stagnation point in a frame of reference moving at the convective velocity. The Mie scattering images, PIV data, and pressure data was correlated. The laser was effective at creating a large scale structure in the axisymmetric shear layer.

8.2 Areas for Further Research

The following discussion suggests areas recommended for future research in the areas of laser energy deposition into quiescent air, upstream of a blunt body, upstream of the crossing shocks, and into compressible shear layers.

Asymmetric deposition volumes need to be investigated to study the effects of the asymmetric plasma formation process. The vortex ring formation due to the asymmetric formation process needs to be quantified and numerically modeled. The vorticity could then be developed as an initial condition in simpler model and included in the initial conditions for the future modeling of energy deposition into complex, high speed flows. The effect of the vorticity on the flow structures in the high speed flows could then be characterized. The non-intrusive measurements of the flow properties are well justified and will provide for further verification and validation of the model development effort. Both models and experiments for multi-pulse depositions should be made. Initial investigative results were obtained for double pulse depositions in the heat transfer experiments. In addition, density effects on the deposition process should be characterized by study the deposition in lower density gases. This could be accomplished by conducting blast wave experiments in the supersonic facility. Here the laser absorption process could be characterized for the deposition into the lower density air within the test section.

Follow-on experiments are needed for the shock impingement test cases with the shock generator outside of the test section boundary layer. This presents a major challenge because of the operational starting limitations of the wind tunnel. However, by removing the oblique shock generation from the boundary layer, a more stable shock impingement location can be obtained. Fluctuations to the shock from the boundary layer can be separated from induced controlled perturbations. The deposition location upstream of the sphere with the shock impingement should be moved higher so that the thermal spot does not impact the sphere. These tests would indicate if the spot can effectively perturb the embedded jet due to the Type IV interaction enough to reduce the peak heat transfer loads. Different Mach number and higher stagnation temperature flows should be tested with the laser energy deposition to determine Mach number effects and the effectiveness of reducing heat transfer at higher surface heat flux conditions.

The laser energy deposition tests need to be conducted in a quiet facility to determine the ability of transitioning to a reduced Mach stem, and then assessing the stability of this Mach stem, or regular reflection. Further experiments (such as laser sheet lighting) and simulations done to further characterize the three-dimensional effects of the laser energy deposition on the shock structures.

In the area of the jet shear layer perturbations, proper orthogonal decomposition [61, 11, 130, 51, 20, 31] should be considered to analyze the induced large-scale structure from the PIV data fields. [108, 45]

This list could go on indefinitely as there seems to be a multitude of high speed flow phenomena where energy deposition might be applied. The research summarized in this dissertation should provide some of the necessary approaches and techniques as the research continues in this exciting field of high speed flow control.

References

- ¹ Adelgren, R., Elliott, G., Crawford, J., Carter, C., Grosjean, D., and Donbar, J., "Axisymmetric Jet Shear Layer Excitation Induced by Electric Arc Discharge and Focused Laser Energy Deposition," AIAA Paper No. 2002-0729, 2002.
- ² Adelgren, R., Elliott, G., Knight, D., Zheltovodov, A., Beutner T.J., "Energy Deposition in Supersonic Flows," AIAA Paper No. 2001-0885, Jan. 2001.
- ³ Aerosoft, Inc., *GASP Version 3, The General Aerodynamic Simulation Program, Computational Flow Analysis Software for the Scientist and Engineer, User's Manual*, Aerosoft, Inc., 1996.
- ⁴ Alexandrov, A., Vidyakin, N., Lakutin, V., et al, "On a Possible Mechanism of Interaction of a Shock Wave with the Decaying Plasma of a Laser Spark in Air", *Zhurnal Technicheskaya Fizika*, 1986, Vol. 56, p. 771.
- ⁵ Anderson, E.E., *Introduction to Modern Physics*, Saunders College Publishing, 1982, pp. 81-84.
- ⁶ Anderson, J.D., *Hypersonic and High Temperature Gas Dynamics*, AIAA, 2000, pp. 213-259.
- ⁷ Baker, W.E., *Explosions in Air*, University of Texas Press, 1973.
- ⁸ Baravian, G., Godart, J., and Sultan, G., "Multiphoton Ionization of Molecular Nitrogen by a Neodymium-glass Laser," *Physical Review A*, Vol. 25, No. 3, 1982.
- ⁹ Ben-Dor, G., Elperin, T., and Golshtein, E., "Monte Carlo Analysis of the Hysteresis Phenomenon in Steady Shock Wave Reflections," *AIAA Journal*, Vol. 35, No. 11, 1997, pp. 1777-1779.
- ¹⁰ Ben-Dor, G., Elperin, T., Li, H., and Vasiliev, E., Chpoun, A., and Zeitoun, D., "Dependence of Steady Mach Reflections on the Reflecting-wedge Trailing-Edge Angle," *AIAA Journal*, Vol. 35, No. 11, 1997, pp. 1780-1782.
- ¹¹ Berkooz, G., Holmes, P., Lumley, J.L., "The Proper Orthogonal Decomposition in the Analysis of Turbulent Flows," *Annual Review of Fluid Mechanics*, Vol. 25, 1993, pp. 539 - 575.
- ¹² Berry, Scott A., and Nowak, Robert J., "Fin Leading-Edge Sweep Effect on Shock-Shock Interaction at Mach 6," *Journal of Spacecraft and Rockets*, Vol. 34, No. 4, July-August 1997.
- ¹³ Bogdanoff, D.W., "Compressibility Effects in Turbulent Shear Layers," *AIAA Journal*, Vol. 21, pp. 926-927.
- ¹⁴ Boguszko, M., Elliott, G., and Carter, C., "Filtered Rayleigh Scattering for Fluid/Thermal Systems," AIAA Paper No. 2002-3233, 2002.
- ¹⁵ Buck, G.A., Li, Y., "Numerical and Experimental Studies of Spark-Induced Impulsive Acoustic Disturbances in Compressible Flow," AIAA Paper No. 2001-0890, 2001.
- ¹⁶ Burcham, F. W. Jr., Nugent, J., "Local Flow Field around a Pylon-mounted Dummy Ramjet Engine on the X-15-2 Airplane for Mach Numbers 2.0 to 6.7," NASA TN D-5638.
- ¹⁷ Carl, M., Hannemann V., Eitelberg G., "Shock/Shock Interaction Experiments in the High Enthalpy Shock Tunnel Gottingen," 36th AIAA Aerospace Sciences Meeting and Exhibit, Reno, NV, January 11-15, 1998.
- ¹⁸ Cherniy, G. G., "Some Recent Results in Aerodynamic Applications of Flows with Localized Energy Addition", AIAA Paper No. 99-4819, 1999.

- ¹⁹ Chpoun, A., Passerel, D., Li, H., and Ben-Dor, "Reconsideration of Oblique Shock Wave Reflections in Steady Flows. Part 1. Experimental Investigation," *Journal of Fluid Mechanics*, Vol. 301, 1995, pp. 19-35.
- ²⁰ Citriniti, J.H., George, W.K., "Reconstruction of the Global Velocity Field in the Axisymmetric Mixing Layer Utilizing the Proper Orthogonal Decomposition," *Journal of Fluid Mechanics*, Vol. 418, 2000, pp. 137 - 166.
- ²¹ Clemens, N.T., and Mungal, M.G., "Two- and Three-Dimensional Effects in the Supersonic Mixing Layer," *AIAA Journal*, Vol. 30, No. 4, 1992, pp.973-981.
- ²² Cook, W.J., and Felderman, E.J., "Reduction of Data from Thin-Film Heat Transfer Gages: A Concise Numerical Technique," *AIAA Journal*, Vol. 4, No. 3, 1966, pp. 561-562.
- ²³ Corke, T., Jumper, E., Post, M., Orlov, D., McLaughlin, T., "Application of Weakly-Ionized Plasmas as Wing Flow-control Devices," AIAA Paper No. 2002-0350, 2002.
- ²⁴ Crawford, J.B., and Elliott, G.S., "Multiple Laser Excitation for Enhancement of Large Scale Structures," AIAA Paper 99-0998, 1999.
- ²⁵ D'Ambrosio, D., "Numerical Prediction of Laminar Shock/Shock Interactions in Hypersonic Flow," AIAA Paper No. 2002-0582, 2002.
- ²⁶ Damon, E.K., and Tomlinson, R.G., "Observation of Ionization of Gases by a Ruby Laser," *Applied Optics*, Vol. 2, No. 5, 1963.
- ²⁷ Dally, J.W., Riley, W.F., and McConnell, K.G., *Instrumentation for Engineering Measurements*, John Wiley & Sons, Inc., 1984.
- ²⁸ Dana, W.H., "The X-15 Airplane - Lessons Learned," AIAA Paper No. 1993-0309, 1993.
- ²⁹ Day, M.J., Mansour, N.N., and Reynolds, W.C., "Nonlinear Stability and Structure of Compressible Reacting Mixing Layers," *Journal of Fluid Mechanics*, Vol. 446, 2001, pp. 375 - 408.
- ³⁰ Debiasi, M. and Papamoschou, D., "Noise from Imperfectly Expanded Supersonic Coaxial Jets," *AIAA Journal*, Vol. 39, No. 3, 2001, pp. 388 - 395.
- ³¹ Delville, J., "Characterization of the Organization in Shear Layers via the Proper Orthogonal Decomposition," *Applied Scientific Research*, Vol. 53, 1994, pp. 263 - 281.
- ³² Dors, I., Parigger, C., and Lewis, J., "Fluid Dynamics Effects Following Laser-induced Optical Breakdown," AIAA Paper No. 2000-0717, 2000.
- ³³ Edney, B., "Anomalous Heat Transfer and Pressure Distributions on Blunt Bodies at Hypersonic Speeds in the Presence of an Impinging Shock," The Aeronautical Research Institute of Sweden, FAA Report 115, 1968.
- ³⁴ Elliott, G.S., Beutner, T.J., "Molecular filter based planar Doppler velocimetry," *Progress in Aerospace Sciences*, Pergamon, Vol. 35, 1999, pp. 799-845.
- ³⁵ Elliott, G.S., Crawford, J., and Mosedale, A., "Forcing of Compressible Mixing Layers Using Laser Excitation," *AIAA Journal*, Vol. 36, No. 9, pp.1730 - 1732.
- ³⁶ Elliott, G.S., Crawford, J.B., and Mosedale, A., "Enhancement of Large Scale Structures in Supersonic Axisymmetric Jets Using Laser Excitation," AIAA Paper No. 98-0331, 1998.
- ³⁷ Elliott, G.S., Samimy, M., and Arnette, S.A., "The Evolution of Large Scale Structure in Compressible Mixing Layers," 9th Symposium on Turbulent Shear Flows, Kyoto, Japan, 1993.

- ³⁸ Elliott, G.S., and Samimy, M., "Compressibility Effects in Free Shear Layers," *Physics of Fluids A*, Vol. 2, No.7, pp. 1231 – 1240, 1990.
- ³⁹ Fay, J.A., and Riddell, F.R., "Theory of Stagnation Point Heat Transfer in Dissociated Air," *Journal of the Aeronautical Sciences*, Vol. 25, No. 2, February, 1958, pp. 73-86.
- ⁴⁰ Frame, Michael J., and Lewis, Mark J., "Analytical Solution of the Type IV Shock Interaction," *Journal of Propulsion and Power*, Vol. 13, No. 5, 1997.
- ⁴¹ Georgievski, P., and Levin, V., "Unsteady Interaction of a Sphere with Atmospheric Temperature Inhomogeneity at Supersonic Speed", *Mekhanika Zhidkosti i Gaza*, No. 4, June 1993, pp. 174-183.
- ⁴² Goebel, S.G., and Dutton, J.C., "Experimental Study of Compressible Turbulent Mixing Layers," *AIAA Journal*, Vol. 29, No. 4, 1991, pp. 538 – 545.
- ⁴³ Goldstein, R.J., "Optical Systems for Flow Measurement: Shadowgraph, Schlieren, and Interferometric Techniques," *Fluid Mechanic Measurements*, ed. by Goldstein, R.J., Hemisphere Publishing Corporation, 1983, pp. 377-397.
- ⁴⁴ Goldston, R.J., and Rutherford, P.H., *Introduction to Plasma Physics*, Institute of Physics Publishing, 1995, pp. 180-184.
- ⁴⁵ Graftieaux, L., Michard, M., and Grosjean, N., "Combining PIV, POD, and Vortex Identification Algorithms for the Study of Unsteady Turbulent Swirling Flows," *Measurement Science and Technology*, Vol. 12, 2001, pp. 1422 – 1429.
- ⁴⁶ Gutmark, E.J., Schadow, K.C., and Yu, K.H., "Mixing Enhancement in Supersonic Free Shear Flows," *Annual Review of Fluid Mechanics*, Vol. 27, 1995, pp. 375-417.
- ⁴⁷ Hall, J.L., Dimotakis, P.E., and Rosemann, H., "Experiments in Nonreacting Compressible Shear Layers," *AIAA Journal*, Vol., 31, No. 12, 1993, pp. 2247 – 2254.
- ⁴⁸ Hannemann, V., and Schnieder, M., "Shock-Shock Interaction in High Enthalpy Flow," John Wiley & Sons, ECCOMAS 98.
- ⁴⁹ Harvey, J.K., Holden, M.S., and Wadhams, T.P., "Code Validation Study of Laminar Shock/Boundary Layer and Shock/Shock Interactions in Hypersonic Flow, Part B: Comparison with Navier-Stokes and DSMC Solutions," AIAA Paper No. 2001-1031, 2001.
- ⁵⁰ Henderson, L.F., "The Reflection of a Shock Wave at a Rigid Wall in the Presence of a Boundary Layer," *Journal of Fluid Mechanics*, Vol. 30, pp. 699-722, 1967.
- ⁵¹ Hilberg, D. Lazik, W., Fielder, H.E., "The Application of Classical POD and Snapshot POD in a Turbulent Shear Layer with Periodic Structures," *Applied Scientific Research*, Vol. 53, 1994, pp. 283 - 290.
- ⁵² Hileman, J., Samimy, M., "Turbulent Structures and the Acoustic Far Field of a Mach 1.3 Jet," *AIAA Journal*, Vol. 39, No. 9, pp. 1716 – 1727.
- ⁵³ Holden, M.S., *Atmospheric Interceptor Technology CD, Version 4.0*, U.S. Army SMDC, Sterling Research Corporation, 2001.
- ⁵⁴ Holden, M.S., and Kolly, J., "Measurements of Heating in Regions of Shock/Shock Interaction in Hypersonic Flow," AIAA Paper No. 95-0640, 1995.
- ⁵⁵ Holden, M., Kolly, J., and Martin, S., "Shock/shock Interaction Heating in Laminar and Low-Density Hypersonic Flows," AIAA Paper No. 96-1866, 1996.

- ⁵⁶ Holden, M.S. and Rodriguez, K.M., "Studies of Shock/Shock Interaction on Smooth and Transpiration-Cooled Hemispherical Nosetips in Hypersonic Flow," NASA Contractor Report 189585, April 1994.
- ⁵⁷ Holden, M.S., Rodriguez, K.M., and Nowak, R.J., "Studies of Shock/Shock Interaction on Smooth and Transpiration - Cooled Hemispherical Nosetips in Hypersonic Flow," AIAA Paper No. 91-1765, 1991.
- ⁵⁸ Holden, M.S., and Wadhams, T.P., "Code Validation Study of Laminar Shock/Boundary Layer and Shock/Shock Interactions in Hypersonic Flow, Part A: Experimental Measurements," AIAA Paper No. 2001-1031, 2001.
- ⁵⁹ Holden, M.S., Wieting, A.R., Moselle, J.R., and Glass, C., "Studies of Aerothermal Loads Generated in Regions of Shock/Shock Interaction in Hypersonic Flow," AIAA Paper No. 88-0477, 1988.
- ⁶⁰ Ho, C.M., and Huerre, P., "Perturbed Free Shear Layers," *Annual Review of Fluid Mechanics*, Vol. 16, 1984, pp. 365 - 424.
- ⁶¹ Holmes, P., Lumley, J.L., and Berkooz, G., *Turbulence, Coherent Structures, Dynamical Systems and Symmetry*, Cambridge University Press, 1996.
- ⁶² Hornung, H., Oertel, H., and Sandeman, R., "Transition to Mach Reflection of Shock Waves in Steady and Pseudosteady Flow With and Without Relaxation," *Journal of Fluid Mechanics*, Vol. 90, pp. 541-560.
- ⁶³ Hornung, H., Robinson, M., "Transition from Regular to Mach Reflection of Shock Waves Part 2," *Journal of Fluid Mechanics*, Vol. 123, 1982, pp. 155-164.
- ⁶⁴ Howatson, A.M., *An Introduction to Gas Discharges*, 2nd ed., Pergamon Press, Elmsford, NY, 1976.
- ⁶⁵ Hoyaax, M.F., *Arc Physics*, Springer-Verlag, New York, NY, 1968.
- ⁶⁶ Hsu, K. and Parpia, I.H., "Simulation of Multiple Shock-Shock Interference Patterns on a Cylindrical Leading Edge," *AIAA Journal*, Vol. 34, No. 4, 1996.
- ⁶⁷ Ivanov, M.S., Kharitonov, A.M., and Khotyanovsky, D.V., "Numerical and Experimental Study of 3D Steady Shock Wave Interactions," AIAA Paper No. 2001-0740, 2001.
- ⁶⁸ Ivanov, M., Markelov, G., Kudryavtsev, A., and Gimelshein, S., "Numerical Analysis of Shock Wave Reflection Transition in Steady Flows," *AIAA Journal*, Vol. 36, No. 11, 1998, pp. 2079-2086.
- ⁶⁹ Jenkins, D.R., *Hypersonics Before the Shuttle, a Concise History of the X-15 Research Airplane*, Monographs in Aerospace History, No. 18, NASA Publication SP-2000-4518, June 2000.
- ⁷⁰ Jiang, Z., Takayama, K., Moosad, K.P.B., Onoreda, O., Sun, M., "Numerical and Experimental Study of a Micro-Blast Wave Generated by Pulsed-laser Beam Focusing," *Shock Waves*, Springer-Verlag, 1998, pp. 337-349.
- ⁷¹ Kandala, R., Candler, G.V., "Computational Modeling of Localized Laser Energy Deposition in Quiescent Air," AIAA Paper No. 2002-2160, 2002.
- ⁷² Keenan, J.H., Chao, J., and Kaye, J., *Gas Tables: Thermodynamic Properties of Air, Products of Combustion and Component Gases, Compressible Flow Functions*, 2nd ed., John Wiley and Sons, 1980, p.29.
- ⁷³ Keldysh, L.V., "Ionization in the Field of a Strong Electromagnetic Wave," *Soviet Physics JETP*, Vol. 20, No. 5, 1965.

- ⁷⁴ Khotyanovsky, D.V., Kudryavtsev, A.N., and Ivanov, M.S., "Numerical Study of Transition between Steady Regular and Mach Reflection Caused by Free-stream Perturbations," 22nd International Symposium on Shock Waves, Paper No. 3700, 1999.
- ⁷⁵ Kinnear, K.M., and Lu, F.K., "Design, Calibration, and Testing of Transient Thin Film Heat Transfer Gauges," AIAA Paper No. 98-2504, 1998.
- ⁷⁶ Knight, D., "RTO WG 10: Test Cases for CFD Validation of Hypersonic Flight," AIAA Paper No. 2002-0433, 2002.
- ⁷⁷ Knight, D., Kuchinskiy, V., Kuranov, A., and Sheikin, E., "Aerodynamic Flow Control at High Speed Using Energy Deposition," 4th Workshop on MagnetoPlasma Aerodynamics for Aerospace Applications, Institute for High Temperatures, Russian Academy of Sciences, Moscow, Russia, April 9-11, 2002.
- ⁷⁸ Levin, V. and Terent'eva, L., "Supersonic Flow Over a Cone with Heat Release in the Neighborhood of the Apex," *Mekhanika Zhidkosti i Gaza*, No. 2, 1993, pp. 110-114.
- ⁷⁹ Li, H., Ben-Dor, G., "A Parametric Study of Mach Reflection in Steady Flows," *Journal of Fluid Mechanics*, Vol. 341, 1997, pp. 101-125.
- ⁸⁰ Liepmann, H.W., and Roshko, A., *Elements of Gasdynamics*, John Wiley and Sons, 1957.
- ⁸¹ Ligrani, P.M., Camci, C., and Grady, M.S., "Thin Film Heat Transfer Gage Construction and Measurement Details," von Karman Institute for Fluid Dynamics, Technical Memorandum 33, November 1982.
- ⁸² Lind, C.A., "Effect of Geometry on the Unsteady Type-IV Shock Interaction," *Journal of Aircraft*, Vol. 34, No. 1, 1997.
- ⁸³ Lind, C.A., Lewis, M.J., "Computational Analysis of the Unsteady Type IV Shock Interaction of Blunt Body Flows," *Journal of Propulsion and Power*, Vol. 12, No. 1, 1996.
- ⁸⁴ Lind, C.A., Lewis, M.J., "Unsteady Characteristics of a Hypersonic Type IV Shock Interaction," *Journal of Aircraft*, Vol. 32, No. 6, 1995.
- ⁸⁵ Lobb, R.K., "Experimental Measurement of Shock Detachment Distance on Spheres Fired in Air at Hypervelocities," *The High Temperature Aspects of Hypersonic Flow*, Pergamon, 1964, pp. 519-527.
- ⁸⁶ Maker, P.D., Terhune, R.W., Savage C.M., "Optical Third Harmonic Generation," *Quantum Electronics, Proceedings of the 3rd International Congress*, Paris, 1963, ed. Grivet P., Bloembergen, N., Vol. 2, Columbia University Press, New York, 1964, pp. 1559-1572.
- ⁸⁷ Martins, S., Kinzie, K.W., and McLaughlin, D.K., "Wave Structure of Coherent Instabilities in a Planar Shear Layer," AIAA Paper No. 94-0822, 1994.
- ⁸⁸ Markelov, G.N., Pivkin, I.V., and Ivanov, M.S., "Impulsive Wedge Rotation Effects on the Transition from Regular to Mach Reflection," 22nd International Symposium on Shock Waves, Paper No. 2851, 1999.
- ⁸⁹ McGuire, J.B., "Fluid Dynamic Perturbations Using Laser Induced Breakdown," Masters Thesis, Purdue University, 1994.
- ⁹⁰ Meyerand, R.G., and Haught, A.F., "Gas Breakdown at Optical Frequencies," *Physical Review Letters*, Vol. 11, No. 9, 1963.
- ⁹¹ Meyerand, R.G., and Haught, A.F., "Optical-Energy Absorption and High-Density Plasma Production," *Physical Review Letters*, Vol. 13, No. 1, 1964.

- ⁹² Miles, R.B., Lempert, W.R., "Flow Diagnostics in Unseeded Air," AIAA Paper No. 90-0624, 1990.
- ⁹³ Miles, R., Martinelli, S., Macheret, S., Shneider, M., Girgis, I., Zaidi, S., Mansfield, D., Siclari, M., Smereczniak, P., Kashuba, R., and Vogel, P., "Suppression of Sonic Boom by Dynamic Off-body Energy Addition and Shape Optimization," AIAA Paper No. 2002-0150, 2002.
- ⁹⁴ Mink, R.W., "Optical Frequency Electrical Discharges in Gases," *Journal of Applied Physics*, Vol. 35, 1964.
- ⁹⁵ Modlin, J.M., and Colwell, G.T., "Surface Cooling of Scramjet Engine Inlets Using Heat Pipe, Transpiration, and Film Cooling," *Journal of Thermophysics and Heat Transfer*, Vol. 6, No. 3, July-Sept. 92.
- ⁹⁶ Molder, S., Timofeev, E.V., Dunham, C.G., McKinley, S., Voinovich, P.A., "On Stability of Strong and Weak Reflected Shocks," *Shock Waves*, Vol. 10, 2000, pp. 389-393.
- ⁹⁷ Morgan, G. C., "Laser-induced breakdown of gases," *Rep. Prog. Phys.*, 38, 1975, pp. 621-665.
- ⁹⁸ Murakami, E., and Papamoschou, D., "Eddy Convection in Coaxial Supersonic Jets," *AIAA Journal*, Vol. 38, No. 4, 2000, pp. 628 - 635.
- ⁹⁹ Myrabo, L. N., Raizer, Y. P., "Laser-induced Air Spike for Advanced Transatmospheric Vehicles," 25th AIAA Plasmadynamics and Lasers Conference, June 20-23, 1994, Colorado Springs, CO.
- ¹⁰⁰ Niemz, M.H., "Threshold Dependence of Laser-Induced Optical Breakdown on Pulse duration," *Applied Physics Letters*, Vol. 66, No. 10, 1995.
- ¹⁰¹ Nowak, R.J., Holden, M.S., and Wieting, A.R., "Shock/Shock Interference on a Transpiration Cooled Hemispherical Model," AIAA Paper No. 90-1643, 1990.
- ¹⁰² Panda, J. and Seasholtz, R.G., "Experimental Investigation of Density Fluctuations in High-speed Jets and Correlation with Generated Noise," *Journal of Fluid Mechanics*, Vol. 450, 2002, pp. 97-130.
- ¹⁰³ Pandey, A.K., "Thermoviscoplastic Response of Engine-Cowl Leading Edge Subjected to an Oscillating Shock-Shock Interaction," *Journal of Spacecraft*, Vol. 30, No. 6.
- ¹⁰⁴ Papamoschou, D., "Experimental Investigation of Heterogeneous Compressible Shear Layers," Ph.D. Thesis, California Institute of Technology, 1986.
- ¹⁰⁵ Papamoschou, D., "Structure of the Compressible Turbulent Shear Layer," *AIAA Journal*, Vol. 29, No. 5, pp. 680 - 681, 1991.
- ¹⁰⁶ Papamoschou, D. and Debiase, M., "Directional Suppression of Noise from a High-Speed Jet," *AIAA Journal*, Vol. 39, No. 3, 2001, pp. 380 - 387.
- ¹⁰⁷ Papamoschou, D., and Roshko, A., "The Compressible Turbulent Shear Layer," *Journal of Fluid Mechanics*, Vol. 197, 1988, pp. 453 - 477.
- ¹⁰⁸ Patte-Rouland, B., Lalizel, G., and Rouland, E., "Flow Analysis of an Annular Jet by Particle Image Velocimetry and Proper Orthogonal Decomposition," *Measurement Science and Technology*, Vol. 12, 2001, pp. 1401 - 1412.
- ¹⁰⁹ Pilyugin, N., Talipov, R., Khlebnikov, V., "Supersonic Flow over the Bodies by the Flow with Physical-Chemical Heterogeneity," *Thermophysics of High Temperatures*, 1997, Vol. 35, No. 2, pp. 322-336 (in Russian).
- ¹¹⁰ Pope, A., and Goin, K.L., *High Speed Wind Tunnel Testing*, Robert E. Krieger Publishing Company, Malabar, Florida, Reprint Edition, 1978, (Original Edition, 1965).

- ¹¹¹ Pot, T., Chanetz, B., Lefebvre, M., Bouchardy, P., "Fundamental Study of Shock/Shock Interference in Low Density Flow: Flowfield Measurements by DLCARS," 21st International Symposium on Rarefied Gas Dynamics, Marseille, France, July 26-31, 1998.
- ¹¹² Purpura C., Chanetz, J., Delery, J., Grasso, F., "Type III and Type IV Shock/Shock Interferences: Theoretical and Experimental Aspects," 21st International Symposium on Rarefied Gas Dynamics, Marseille, France, July 26-31, 1998.
- ¹¹³ Raffel, M., Willert, C., and Kompenhans, J., *Particle Image Velocimetry, a Practical Guide*, Springer-Verlag, Berlin, Germany, 1998.
- ¹¹⁴ Raizer, Y. P., "Breakdown and Heating of Gases Under the Influence of a Laser Beam," *Soviet Physics USPEKHI*, Volume 8, Number 5, 1966, pp. 650-673.
- ¹¹⁵ Raizer, Y. P., *Gas Discharge Physics*, 2nd ed., Springer-Verlag, New York, NY, 1997.
- ¹¹⁶ Raizer, Y. P., *Laser-Induced Discharge Phenomena*, Consultants Bureau, New York, NY, 1977.
- ¹¹⁷ Riddle, J.P., Furukawa, G.T., and Plumb, H.H., "Platinum Resistance Thermometry," *Measurements in Heat Transfer, Second Edition*, Edited by Eckert, E.R.G., and Goldstein, R.J., McGraw-Hill, 1976, pp. 25-102.
- ¹¹⁸ Riggins, D., Nelson, H.F., Johnson, E., "Blunt-Body Wave Drag Reduction Using Focused Energy Deposition," *AIAA Journal*, Vol. 37, No. 4, April 1999.
- ¹¹⁹ Root, R.G. "Modeling of Post-Breakdown Phenomena," *Laser-induced Plasmas and Applications*, ed. by Radziemski, L.J., Cremers, D.A., Marcel Dekker, Inc., New York, NY, 1989, pp. 69-101.
- ¹²⁰ Roth, J.R., Sherman, D.M., and Wilkinson, S.P., "Boundary Layer Flow Control with a One Atmosphere Uniform Glow Discharge Surface Plasma," AIAA Paper 98-0328, 36th ASM Meeting, Reno, NV, 1998.
- ¹²¹ Roth, J.R., Sherman, D.M., Wilkinson, S.P., "Electrohydrodynamic Flow Control with a Glow-Discharge Surface Plasma," *AIAA Journal*, Vol. 38, No. 7, July 2000, pp. 1166 - 1172.
- ¹²² Samtaney, R., "Vorticity in Shock-Accelerated Density-Stratified Interfaces: An analytical and Computational Study," PhD Thesis, Rutgers University, 1993.
- ¹²³ Schlichting, H., and Gersten, K., *Boundary Layer Theory*, 8th ed., Springer, 2000, pp. 241-265.
- ¹²⁴ Schmisser, J.D., "Receptivity of the Boundary Layer on a Mach-4 Elliptic Cone to Laser-Generated Localized Freestream Perturbations," Ph.D. Thesis, Purdue University, 1997.
- ¹²⁵ Schmisser, J.D., Gaitonde, D.V., "Numerical Simulation of Mach Reflection in Steady Flows," AIAA Paper No. 2001-0741, 2001.
- ¹²⁶ Schultz, D.L., and Jones, T.V., "Heat-transfer Measurements in Short-duration Hypersonic Facilities," AGARDograph No. 165, North Atlantic Treaty Organization Advisory Group for Aerospace Research and Development, 1973.
- ¹²⁷ Scott, C.J., "Transient Experimental Techniques for Surface Heat Flux Rates," *Measurements in Heat Transfer, Second Edition*, Edited by Eckert, E.R.G., and Goldstein, R.J., McGraw-Hill, 1976, pp. 383-392.
- ¹²⁸ Seebeck, T.J., "Magnetische Polarisation der Metalle und Erze durch Temperature-Differenz," *Abh. Konigl. Akad. Wiss. Berlin*, 1822-1833, p. 265.

- ¹²⁹ Simeonides, G., "The VKI Hypersonic Wind Tunnels and Associated Measurement Techniques," Technical Memorandum 46, von Karman Institute, 1990.
- ¹³⁰ Sirovich, L., "Turbulence and the Dynamics of Coherent Structures, Parts I, II, and III," Quarterly Journal of Applied Mathematics, Brown University, 1987.
- ¹³¹ Slessor, M.D., Bond, C.L., and Dimotakis, P.E., "Turbulent Shear-Layer Mixing at High Reynolds Numbers: Effects of Inflow Conditions," *Journal of Fluid Mechanics*, Vol. 376, 1998, pp. 115 – 138.
- ¹³² Smith, David C., "Laser Induced Gas Breakdown and Plasma Interaction," 38th Aerospace Sciences Meeting and Exhibit, January 10-13, 2000, Reno, NV.
- ¹³³ Smith, R.J., *Electronics: Circuits and Devices, Third Edition*, John Wiley & Sons, 1987, pp. 118-124.
- ¹³⁴ Smits, A.J., and Dussauge, J., *Turbulent Shear Layers in Supersonic Flow*, American Institute of Physics, 1996.
- ¹³⁵ Stiener, H., Gretler, W., Hirschler T., "Numerical Solution for Spherical Laser-driven Shock Waves," *Shock Waves*, Springer-Verlag, 1998, pp. 139-147.
- ¹³⁶ Stroehle, Eric J., "The Design and Construction of a Wind Tunnel for Education and Research," Masters Thesis, Rutgers University, New Jersey, Oct 1999.
- ¹³⁷ Svetsov, V., Popova, M., Rybakov, V., Artemiev, V., Medveduk, S., "Jet and Vortex Flow Induced by Anisotropic Blast Wave: Experimental and Computational Study," *Shock Waves*, Springer-Verlag, 7, 1997, pp. 325-334.
- ¹³⁸ Tam, C.K.W., and Zaman, K.B.M.Q., "Subsonic Jet Noise from Nonaxisymmetric and Tabbed Nozzles," *AIAA Journal*, Vol. 38, No. 4, 2000, pp. 592 – 599.
- ¹³⁹ Taylor, G.I., "The Formation of a Blast Wave by a Very Intense Explosion: I Theoretical Discussion," *Proc. Roy. Soc.*, Vol. 201, 1950, pp. 159-174.
- ¹⁴⁰ Tretyakov, P.K., Fomin, V.M., Yakovlev, V.I., "New Principles of Control of Aerophysical Processes. Research Development", Proc.: International Conference on the Methods of Aerophysical Research, September 2-6, Novosibirsk, Russia, 1996, Part 2, pp. 210-220.
- ¹⁴¹ Urban, W.D., Watanabe, S., and Mungal, M.G., "Velocity Field of the Planar Shear Layer: Compressibility Effects," AIAA paper No. 98-0697, 1998.
- ¹⁴² van Driest, E.R., "The Problem of Aerodynamic Heating," *Aeronautical Engineering Review*, October 1956, pp. 26-40.
- ¹⁴³ van Wie, D.M., White, M.E., and Corpening, G.P., "NASP Inlet Design and Testing Issues," *Johns Hopkins APL Technical Digest*, Vol. 11, Nos. 3 and 4, 1990.
- ¹⁴⁴ von Neumann, J., *Collected Works*, Vol. 6, 1963, pp. 239-299, Pergamon Press (article originally published in 1943).
- ¹⁴⁵ Vuillon, J., Zeitoun, D., Ben-Dor, G., "Reconsideration of Oblique Shock Wave Reflections in Steady Flows. Part 2. Numerical Investigation," *Journal of Fluid Mechanics*, Vol. 301, 1995, pp. 37-50.
- ¹⁴⁶ Watts, J.D., "Flight Experience with Shock Impingement and Interference Heating on the X-15-2 Research Airplane," NASA TM X-1669, October 1968.
- ¹⁴⁷ Watts, J.D., Olinger, F. V., "Heat-transfer Effects of Surface Protuberances on the X-15 Airplane," NASA TM-1566, May 1968.

- ¹⁴⁸ Wieting, A.R., and Holden, M.S., "Experimental Study of Shock Wave Interference Heating on a Cylindrical Leading Edge at Mach 6 and 8," AIAA Paper No. 87-1511, 1987.
- ¹⁴⁹ Yamamoto, Y., Nagai, S., Koyama, S., Hirabayashi, N., and Hozumi, K., "CFD Analysis and Wind Tunnel Experiments of Hypersonic Shock-Shock Interaction Heating for Two Hemi Sphere Cylinder Problem," AIAA Paper No. 2002-0217, 2002.
- ¹⁵⁰ Yan, H., Adelgren, R., Elliott, G., Knight, D., Buetner, T., Ivanov, M., Kudryavtsev, A., and Khotyanovsky, D., "Laser Energy Deposition in Intersecting Shocks," AIAA Paper No. ,2002.
- ¹⁵¹ Yan, H., Adelgren, R., Elliott, G., Knight, D., Boguszko, M., Ivanov, M., Kudryavtsev, A., and Khotyanovsky, D., "Laser Energy Deposition in Quiescent Air Part II," AIAA Paper for ASM 2003.
- ¹⁵² Yan, H., Knight, D., and Zheltovodov, A., "Large Eddy Simulation of Supersonic Compression Corner Using ENO Scheme," *DNS/LES Progress and Challenges*, edited by Liu, C., Leonidas, S., and Beutner, T., Third AFOSR International Conference, 2001.
- ¹⁵³ Zel'dovich, Y.B., and Raizer, Y.P., *Physics of Shock Waves and High-Temperature Hydrodynamic Phenomena*, edited by Hayes, W., and Probstein, F., Dover Publications, Inc., 2002 (Original English 2 Volume set published in 1966).
- ¹⁵⁴ Zhong, X., "Application of Essentially Nonoscillatory Schemes to Unsteady Hypersonic Shock-Shock Interference Heating Problems," *AIAA Journal*, Vol. 32, No. 8, August 1994.

Vita

Russell G. Adelgren

Education

Bachelor of Science, Aeronautical Engineering, Embry-Riddle Aeronautical University, 1989

Master of Engineering, Engineering Mechanics, University of Florida, 1994

United States Air Force Squadron Officer School, 1996

Experience

Active duty officer, United States Air Force, July 1989 - present

Project officer for office automation, Air Force Armament Laboratory, Eglin Air Force Base, Florida, July 1989 - November 1990

Aeroballistic research engineer, Wright Laboratory, Eglin Air Force Base, Florida, December 1990 - May 1994

Test manager for space and missile systems, Headquarters Air Force Operational Test and Evaluation Center, Kirtland Air Force Base, New Mexico

Course director and instructor of mathematical sciences, United States Air Force Academy, Colorado Springs, Colorado

Graduate student of mechanical and aerospace engineering, Department of Mechanical and Aerospace Engineering, Rutgers - The State University of New Jersey

Publications

Hathaway, Adelgren, and Brown, "Expert Systems and Ballistic Range Data Analysis," AIAA 17th Aerospace Ground Testing Conference, Nashville, Tennessee, July 1992

Adelgren and Hathaway, "Aeroballistic Range Data Analysis Using an Expert System," Test Technology Symposium VI, Johns Hopkins University, March 1993.

Winchenbach, Adelgren, and McClenahan, "Launching a Surf Zone Mine Countermeasure Explosive Array from a Double Barreled Single Stage Compressed Gas Gun," 44th Meeting of the Aeroballistic Range Association, Munich, Germany, September 1993

Hathaway and Adelgren, "HAVE DASH Free-Flight Range Test Results," Wright Lab Technical Report 94-7083, 1994

Ranum, Sutton, and Adelgren, "PGU-31/B 40-millimeter Cartridge Phase II Testing," Air Force Development Test Center Technical Report 94-03, 1994

Adelgren, Lashinski, and Ray, "Operational Considerations for Reusable Launch Vehicles," Space Technology and Applications International Forum, 2nd Conference on Next Generation Launch Systems, Albuquerque, New Mexico, January 1997

Adelgren, "Multivariable Calculus Pollinated with Basic Mechanical Physics," Mathematical Association of America Mathfest 98, Contributed papers on Mathematics Across the Disciplines, Toronto, Canada, July 1998

- Adelgren, Elliott, Knight, Zheltovodov, and Buetner, "Laser Energy Deposition Upstream of a One Inch Diameter Sphere with an Edney Type IV Shock Structure in the 6 Inch by Inch Mach 3.45 Facility," Report RU-TR-MAE-211, Department of Mechanical and Aerospace Engineering, Rutgers University, September 2000
- Adelgren, Elliott, Knight, Zheltovodov, and Buetner, "Energy Deposition in Supersonic Flows," AIAA Paper 2001-0885, 39th AIAA Aerospace Sciences Meeting and Exhibit, 8-11 January 2001
- Adelgren, Elliott, Knight, and Zheltovodov, "Localized Pulsed Laser Energy Deposition in the Vicinity of an Underexpanded Transverse Wall Jet in Mach 3.45 Flow," Report RU-TR-MAE-212, Department of Mechanical and Aerospace Engineering, Rutgers University, 4 July 2001
- Adelgren, Elliott, Knight, and Ivanov, "Preliminary Study of Localized Pulsed Laser Energy Deposition Effects on Shock Structures and Mach/Regular Reflection Dual Solution Domain at Mach 3.45," Report RU-TR-MAE-213, Department of Mechanical and Aerospace Engineering, Rutgers University, 21 July 2001
- Adelgren, Elliott, Knight, Buetner, Ivanov, and Zheltovodov, "Laser Energy Deposition in Transverse Wall Jets and Intersecting Shocks," Workshop on Thermochemical Processes in Plasma Aerodynamics, Hypersonic System Research Institute, St. Petersburg, Russia, September 2001
- Adelgren, Boguszko, Elliott, and Knight, "Shock Propagation Measurements for Nd:YAG Laser Induced Breakdown in Quiescent Air," Report RU-TR-MAE-214, Department of Mechanical and Aerospace Engineering, Rutgers University, October 2001
- Adelgren, Elliott, Knight, Zheltovodov, and Buetner, "Localized Flow Control in Supersonic Flows by Pulsed Laser Energy Deposition," Third Workshop on Magneto and Plasma Aerodynamics for Aerospace Applications, IVTAN, Moscow, Russia, April 2001
- Adelgren, Elliott, Crawford, Carter, Grosjean, and Donbar, "Axisymmetric Jet Shear Layer Excitation Induced by Electric Arc Discharge and Focused Laser Energy Deposition," AIAA Paper 2002-0729, 40th AIAA Aerospace Sciences Meeting and Exhibit, 14-17 January 2002
- Yan, Adelgren, Elliott, Knight, Buetner, Ivanov, Kudryavtsev, and Khotyanovsky, "Laser Energy Deposition in Quiescent Air and Intersecting Shocks," Fourth Workshop on Magneto and Plasma Aerodynamics for Aerospace Applications, Institute of High Temperatures, Russian Academy of Sciences, Moscow, Russia, 8-10 April 2002
- Yan, Adelgren, Elliott, Knight, Buetner, and Ivanov, "Laser Energy Deposition in Intersecting Shocks," First AIAA Flow Control Conference, St. Louis, MO, 2002.
- Adelgren, Yan, Elliott, Knight, Zheltovodov, and Ivanov "Localized Flow Control by Laser Energy Deposition Applied to Edney IV Shock Impingement and Intersecting Shocks," Accepted for AIAA ASM, 2003.
- Yan, Adelgren, Elliott, Knight, Boguszko, Ivanov, Kudryavtsev, and Khotyanovsky, "Laser Energy Deposition in Quiescent Air Part II," Accepted for AIAA ASM, 2003.

Awards and Decorations

- United States Air Force Academy, Math Department Company Grade Officer of the Quarter, 1998
- Air-to-Surface Weapons Systems Program Office, External Support Individual of the Quarter, 1992
- Air Force Armament Lab Company Grade Officer of the Quarter, 1990
- Three Air Force Commendation Medals

Expert Marksmanship Award for the M-9 Pistol

Magna Cum Laude graduation honors, Embry-Riddle Aeronautical University, 1989

Dean's List, 9 semesters, Embry-Riddle Aeronautical University, 1984-1989

Air Force Reserve Officer Training Corps Scholarship

Embry-Riddle Aeronautical University Academic Scholarship

Sigma Gamma Tau Engineering Honor Society

Pi Mu Epsilon National Honorary Mathematics Society